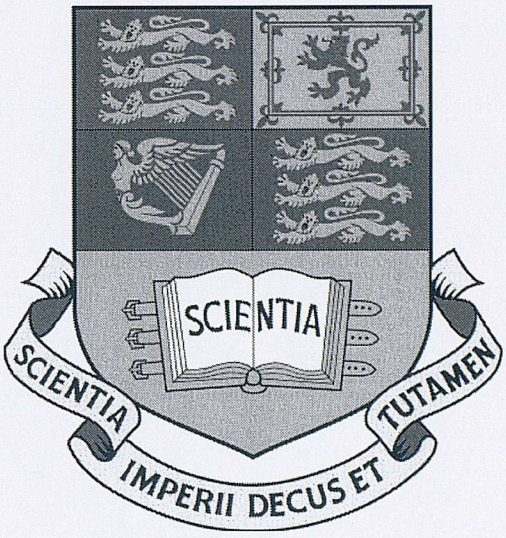
PHASE CHANGE OF SINGLE COMPONENT FLUIDS AND MIXTURES IN ANNULAR FLOW



Jader Riso Barbosa, Jr., M.Sc., B.Sc.

A thesis submitted in partial fulfilment of the requirements for the degree of Doctor of Philosophy of the University of London and for the Diploma of Imperial College of Science, Technology and Medicine

Department of Chemical Engineering and Chemical Technology, Imperial College of Science, Technology and Medicine, London, SW7 2BY

April 2001

"We had suffered, starved and triumphed,
grovelled down yet grasped at glory, grown bigger
in the bigness of the whole. We had seen God
in His splendours, heard the text that Nature renders.
We had reached the naked soul of man."

E. Shackleton

Abstract

This thesis is dedicated to the study of flow boiling of single component fluids and multicomponent mixtures in vertical pipes at high qualities. Both theoretical and experimental investigations were carried out with the objective of improving fundamental knowledge of hydrodynamics and phase change heat transfer in annular flow.

The diabatic experiments had the objective of studying the nature of nucleate boiling in upward steam-water annular flow. A specially constructed, electrically heated, annulus visualisation test section ($d_{eq} = 12.9$ mm) was used to observe directly the interaction between disturbance waves and bubble nucleation through the analysis of high-speed video recordings. It was found that disturbance waves seem to locally trigger off the activity of nucleation sites as they travel along the channel. Local measurements of the heater wall temperature, and hence of heat transfer coefficient, were carried out using a radiation equilibrium thermocouple which could be traversed along the heated section. An analysis of the Onset of Nucleate Boiling (ONB) in climbing films was also implemented.

Adiabatic experiments were carried out to investigate the behaviour of the fraction of the liquid entrained as droplets in the region of transition between the churn and annular flow regimes. An isokinetic probe was used, which enabled the simultaneous measurement of the gas and entrained liquid mass fluxes. The campaign was performed in a 10.8 m long, 31.8 mm internal diameter test section (LOTUS facility) over a wide range of flow conditions. The profiles of local droplet concentration characterise churn flow as a region in which the radial gradients of concentration tend to disappear with increasing gas flowrate. As annular flow takes place, the local concentration is virtually constant with respect to radial position and gas flowrate. As far as the determination of the fraction of liquid entrained as droplets at the onset of annular flow is concerned, the experimental results are of particular interest to annular flow computer simulation codes as it provides a basis for calculating the initial condition for the mass conservation equations. With that objective in mind, an empirical correlation was developed to predict the fraction of liquid entrained as droplets at the onset of annular flow.

The modelling work on heat transfer deals with phase change of multicomponent mixtures at high qualities. A differential phenomenological model of the annular flow regime is proposed so as to describe the deterioration of the heat transfer coefficient observed by Kandlbinder (1997) for boiling of binary and ternary hydrocarbon mixtures in a 25.4 mm internal diameter, vertical pipe. The set of correlations for droplet entrainment and deposition by Govan (1990) was extended to cope with the so-called mixture effects. Use was also made of a Colburn-Drew type formulation for calculation of interfacial parameters (mass fluxes, compositions and temperature). The formulation gives a very good prediction of bulk and wall temperatures and of heat transfer coefficients determined experimentally.

A simple mathematical model to describe the formation of waves characteristic of the churn flow regime is also proposed. Previous work (Govan, 1990), in which high-speed video recordings were carried out, used a test section with a specially constructed transparent liquid inlet and showed clearly the process of wave formation. The model, which is based on integral mass and momentum conservation principles, predicts the wave velocity and distance travelled by the waves. It also provides estimates of wave parameters, such as critical amplitude, length and flow rates that are consistent with the experimental observations.

Acknowledgements

To Professor G.F. Hewitt FRS FREng, whose enthusiasm, devotion and achievement in multiphase flow science are, above all, an example of life. It is impossible to convey in few words all my gratitude and admiration for this extraordinary man.

To Professor S.M. Richardson FREng for a most valuable co-supervision in the last year of this project.

To Dr. C.J. Lawrence, Dr. M.A. Mendes-Tatsis (Imperial College) and Dr. V.V. Wadekar (HTFS, Harwell) for their friendship and support through the various stages of my PhD studies.

To the technical staff of the Department of Chemical Engineering and Chemical Technology, Bob King, Bob Brace, Sam Jones, Richard Wallington (Machine Workshop), Malcolm Dix and Peter Arnold (Electronics Division) for making ideas work.

To all my Multiphase Flow friends for their camaraderie and support.

To Gregor König, for his assistance in operating the LOTUS Facility during his attachment from the University of Karlsruhe as a Diploma student.

To Dr. Thomas Kandlbinder for providing me with the multicomponent boiling database.

To my mother, for her unconditional love.

To the Brazilian National Research Council (CNPq) and to the Overseas Research Scholarship (ORS) Scheme for their financial support.

Contents

1 Introduction **45**

1.1 Multiphase Flow 45

1.2 Objectives 46

1.3 Overview 48

2 Literature Review and Background **51**

2.1 Introduction and Organisation 51

2.2 Adiabatic vertical two-phase flow 52

2.2.1 Flow patterns 52

2.2.2 Flow pattern transitions 56

2.2.3 Annular flow 66

2.2.4 Churn flow 85

2.3 Flow boiling of single component fluids 104

2.3.1 The classical interpretation 106

2.3.2 Onset and suppression of nucleation in forced convective boiling . . 110

2.3.3 Other interpretations and secondary nucleation 119

2.3.4 Heat transfer in upwards annular flow 121

2.3.5 Correlations 122

2.3.6 Critical Heat Flux (CHF) 130

2.4 Flow boiling of multicomponent mixtures 134
2.4.1 Phase equilibrium in multicomponent systems 135
2.4.2 A summary of experimental investigations 137
2.4.3 Modelling and prediction of phase change in multicomponent systems 140
2.4.4 Review of Prediction Methods for Convective Boiling of Mixtures . 143
2.4.5 Forced convective boiling of ternary and multicomponent mixtures . 154
2.5 Summary 155

3 An Experimental Investigation of Nucleate Boiling in Annular Flow 157
3.1 Introduction 157
3.2 Experiments 159
3.2.1 Experimental apparatus 159
3.2.2 Heat transfer coefficient estimation 166
3.2.3 Visualisation equipment 168
3.2.4 Experimental Procedure 168
3.3 Experimental Results 170
3.3.1 Visualisation at a fixed position 170
3.3.2 Wave axial development 184
3.3.3 Heat transfer measurements 197
3.3.4 Error analysis 207
3.4 Prediction of ONB in climbing films 208
3.4.1 Onset and suppression of nucleation in forced convection 208
3.4.2 Interpretation of the present data set 211
3.4.3 Results 214
3.5 Summary 214

4 A Model for Flow Boiling of Multicomponent Mixtures 217

4.1 Introduction 218

4.1.1 Motivation 218

4.1.2 Hydrodynamic equilibrium considerations 219

4.1.3 The influence of droplet interchange 224

4.1.4 Mass transfer considerations 226

4.1.5 Nucleate boiling considerations 228

4.2 Hydrodynamics 229

4.2.1 Droplet interchange 229

4.2.2 Mass and momentum conservation 234

4.2.3 Additional closure relationships for hydrodynamics 237

4.3 Heat and mass transfer 239

4.3.1 Binary systems 239

4.3.2 Multicomponent systems 244

4.3.3 Calculation of the wall temperature 247

4.4 Solution of the governing equations 249

4.4.1 Numerical schemes and algorithm 249

4.5 Droplet interchange and condensation 251

4.6 Results 254

4.6.1 Convective boiling of hydrocarbon mixtures 254

4.6.2 Dryout Prediction of Single Components and Mixtures 283

4.6.3 Predictions of condensation data 298

4.7 Summary 300

5 Droplet Entrainment at the Onset of Annular Flow 303

5.1 Introduction 304

5.2 Background 308
5.3 Experimental apparatus 312
5.3.1 The LOTUS Facility 312
5.3.2 Pressure gradient measurement 314
5.3.3 The Isokinetic Probe Technique 316
5.3.4 Entrained fraction measurement 322
5.3.5 Experimental procedure 325
5.4 Results 325
5.4.1 Local mass fluxes, velocities and droplet concentration 325
5.4.2 Liquid entrainment in the churn-annular region 330
5.4.3 Entrained fraction and pressure gradient 339
5.4.4 A correlation for liquid entrained fraction at the onset of annular flow 341
5.4.5 Measurement uncertainty 342
5.4.6 Annular flow modelling and the onset of entrainment 346
5.5 Summary 348

6 A Theoretical Analysis of Interfacial Waves in Churn-Annular Flow 351

6.1 Conservation principles 351
6.2 Wave shape and volumetric relationships 353
6.3 Force balance over the coherent wave 358
6.4 Solution of conservation equations 363
6.5 Analytical results 365
6.6 Summary 368

7 Conclusions and Future Work 369

7.1 Visualisation of nucleate boiling in annular flow 369
7.1.1 Conclusions 369

7.1.2 Future Work 371
7.2 Modelling of forced convective multicomponent boiling 372
7.2.1 Conclusions 372
7.2.2 Future Work 375
7.3 Entrainment at the onset of annular flow 375
7.3.1 Conclusions 375
7.3.2 Future Work 377
7.4 Modelling of churn flow waves 377
7.4.1 Conclusions 377
7.4.2 Future Work 378

A Visualisation Data of Nucleate Boiling in Annular Flow **379**

B Heat and mass transfer in the liquid film (Shock, 1976) **391**

C Operating Instructions for the LOTUS Facility **395**

D Data for the Entrained Fraction near the Onset of Annular Flow **401**

E Papers covering the work described in this thesis **409**

List of Figures

2.1 The flow regimes in vertical gas-liquid flow (Collier and Thome, 1994). . . 54

2.2 The flow pattern map by Hewitt and Roberts (1969). 55

2.3 Correlation for inception of entrainment (Azzopardi, 1997). 71

2.4 Data for film flow rate obtained by Gill and co-workers for different liquid injection devices. Conversion factors: 1 in = 25.4 mm, 1 lb h^{-1} = 1.26 × 10^{-4} kg s^{-1}. 72

2.5 The correlation for droplet entrainment rate by Govan (1990). 76

2.6 The correlation for droplet deposition rate by Govan (1990). 77

2.7 The incremental length of vertical pipe in annular flow. 79

2.8 Pressure gradient in vertical two-phase flow (Owen, 1986). 88

2.9 Postulated mechanism of churn flow (Hewitt *et al.*, 1985). 89

2.10 Experimental arrangements with a porous wall outlet used by Govan *et al.* (1991). 90

2.11 Experimental results for flooding, deflooding and and downflow with a porous wall inlet (Govan *et al.*, 1991). 91

2.12 Comparison of pressure gradient and hold-up with and without a falling film below the injector (Govan *et al.*, 1991). 92

2.13 Variation of entrained fraction with gas velocity (Wallis, 1962). 93

2.14 Experimental arrangement used in the visualisation study of Govan (1990). 95

2.15 Wave position versus time (Govan, 1990). 96

2.16 Film flow and entrained droplet flow in an annulus (Hewitt and Hall-Taylor, 1970). 101

2.17 Entrained fraction and pressure gradient in the churn-annular region (Fore and Dukler, 1995). 103

2.18 Flow patterns in a vertical evaporator tube (Collier and Thome, 1994). . . 105

2.19 Data on convective boiling (Dengler and Addoms, 1956). 107

2.20 The model for bubble growth and illustration of waiting period and temperature profiles (Hsu, 1962). 112

2.21 Variation of film flow with length for uniformly heated tubes with unheated zones (Bennett *et al.*, 1967b). 133

2.22 Variation of the flow rate of entrained droplets with local quality (Bennett *et al.*, 1967b). 134

2.23 Phase diagram for an non-azeotropic binary mixture. 136

2.24 Phase diagram for an non-azeotropic ternary mixture. 137

2.25 Example of deterioration of the heat transfer coefficient at high qualities for boiling of mixtures. Experimental conditions: Mixture 0.7/0.3 n-pentane/iso-octane (mass fraction), $p = 2.2$ bara, $\dot{m}_T = 500$ kg m^{-2} s^{-1} (nominal), $\dot{q}_w = 40$ kW m^{-2} (Kandlbinder, 1997). 139

2.26 Temperature profiles and boiling regimes for convective evaporation (Thome and Shock, 1984). 141

2.27 Illustration of liquid phase temperature profiles; (a) wall temperature controlled case, (b) heat flux controlled case (Wadekar, 1990). 142

2.28 Axial variation of interface concentration for annular flow heat transfer to ethanol-water mixtures. Legend: 1 - no mass transfer resistance in both phases, 2 - no mass transfer resistance in liquid, 3 - no mass transfer resistance in vapour, 4 - no mass transfer resistance in either phase, dotted line represents a calculation based on an equilibrium flash (Shock, 1976). . 152

2.29 Axial variation of interface temperature for annular flow heat transfer to ethanol-water mixtures. Legend: 1 - no mass transfer resistance in both phases, 2 - no mass transfer resistance in liquid, 3 - no mass transfer resistance in vapour, 4 - no mass transfer resistance in either phase, dotted line represents a calculation based on an equilibrium flash (Shock, 1976). 153

3.1 The experimental apparatus. Key to components: 1.Pressure reducing valve; 2.Steam drier/superheater; 3.Orifice plate; 4.Water preheater; 5.Mono pump; 6.Water flowmeter; 7.Test section; 8.Heater terminals; 9.Reflux condenser; 10.Vacuum pump. 160

3.2 A schematic of the steam drier/superheater. 161

3.3 A schematic of the connections between a flow measuring element (orifice plate or venturi) and a manometer (Bean, 1971). 162

3.4 The test section for the nucleate boiling visualisation experiments. 164

3.5 Illustration of the heat conduction problem in the heated section. 167

3.6 (a) Region of smooth film between disturbance waves, (b) a disturbance wave. Experimental conditions: $p_{in} = 1.9$ bar, $\dot{m}_T = 30.2$ kg m^{-2} s^{-1}, $X = 0.63$, $\dot{q}_w = 0$ W m^{-2}. 171

3.7 Illustration of nucleation in a smooth film between waves. Experimental conditions: $p_{in} = 1.9$ bar, $\dot{m}_T = 30.2$ kg m^{-2} s^{-1}, $X_{in} = 0.63$, $\dot{q}_w = 158.7$ kW m^{-2}, $\Delta T_{in} \approx 30$ K. 172

3.8 Droplet entrainment from the crest of a disturbance wave. Experimental conditions: $p_{in} = 2.0$ bar, $\dot{m}_T = 27.3$ kg m^{-2} s^{-1}, $X_{in} = 0.77$, $\dot{q}_w = 146.2$ kW m^{-2}, $\Delta T_{in} \approx 30$ K. 174

3.9 Nucleation and droplet entrainment at a low film flow rate. Experimental conditions: $p_{in} = 1.9$ bar, $\dot{m}_T = 24.0$ kg m^{-2} s^{-1}, $X_{in} = 0.87$, $\dot{q}_w = 195.8$ kW m^{-2}, $\Delta T_{in} \approx 30$ K. 175

3.10 Fully developed nucleate boiling in the liquid film. Experimental conditions: $p_{in} = 2.0$ bar, $\dot{m}_T = 30.2$ kg m^{-2} s^{-1}, $X_{in} = 0.63$, $\dot{q}_w = 485.6$ kW m^{-2}, $\Delta T_{in} \approx 30$ K. 177

3.11 Identification of active nucleation sites in the wave region. Experimental conditions: $p_{in} = 1.9$ bar, $\dot{m}_T = 30.2$ kg m^{-2} s^{-1}, $X_{in} = 0.63$, $\dot{q}_w = 158.7$ kW m^{-2}, $\Delta T_{in} \approx 30$ K. 178

3.12 Identification of active nucleation sites in the wave region. Experimental conditions: $p_{in} = 1.9$ bar, $\dot{m}_T = 24.0$ kg m^{-2} s^{-1}, $X_{in} = 0.87$, $\dot{q}_w = 195.8$ kW m^{-2}, $\Delta T_{in} \approx 30$ K. 179

3.13 Identification of active nucleation sites in the wave region. Experimental conditions: $p_{in} = 2.0$ bar, $\dot{m}_T = 27.3$ kg m^{-2} s^{-1}, $X_{in} = 0.77$, $\dot{q}_w = 146.2$ kW m^{-2}, $\Delta T_{in} \approx 30$ K. 180

3.14 Turbulent viscosity distribution in the disturbance wave calculated using a low Reynolds number $\kappa - \varepsilon$ model (Jayanti and Hewitt, 1997). 181

3.15 Temperature contours in the disturbance wave calculated using a low Reynolds number $\kappa - \varepsilon$ model. Interface at saturation (Jayanti and Hewitt, 1997). . 182

3.16 Variation of disturbance waves frequency with wall heat flux. Experimental conditions (Mass fluxes are initial values): Run 0824-1, p_{in} = 1.6 bar, $\dot{m}_G$ = 14.2 kg m^{-2} s^{-1}, $\dot{m}_L$ = 8.0 kg m^{-2} s^{-1}, $\Delta T_{in} \approx$ 10 K, Run 0824-2, p_{in} = 2.1 bar, $\dot{m}_G$ = 22.0 kg m^{-2} s^{-1}, $\dot{m}_L$ = 8.0 kg m^{-2} s^{-1}, $\Delta T_{in} \approx$ 10 K, Run 0830, p_{in} = 2.0 bar, $\dot{m}_G$ = 19.0 kg m^{-2} s^{-1}, $\dot{m}_L$ = 11.2 kg m^{-2} s^{-1}, $\Delta T_{in} \approx$ 10 K. 183

3.17 Illustration of axial development of the flow. Experimental conditions: p_{in} = 1.9 bar, $\dot{m}_T$ = 33 kg m^{-2} s^{-1} (nominal), X_{in} = 0.65, $\dot{q}_w$ = 460 kW m^{-2} (nominal: at frames indicating the presence of a heat flux. Others: $\dot{q}_w$ = 0), $\Delta T_{in} \approx$ 30 K (in *top of heater* frames. Approximately 10 K in others). 185

3.18 The injection of liquid through the porous sintered section. Experimental conditions: p_{in} = 1.9 bar, $\dot{m}_T$ = 32.1 kg m^{-2} s^{-1}, X = 0.66, $\dot{q}_w$ = 0 kW m^{-2}. 186

3.19 Illustration of the flow at the junction between the sinter and the calming section. Experimental conditions: p_{in} = 1.9 bar, $\dot{m}_T$ = 32.1 kg m^{-2} s^{-1}, X = 0.66, $\dot{q}_w$ = 0 kW m^{-2}. 188

3.20 Illustration of the flow at the junction between the calming section and the heater. Experimental conditions: p_{in} = 1.9 bar, $\dot{m}_T$ = 32.1 kg m^{-2} s^{-1}, X = 0.66, $\dot{q}_w$ = 0 kW m^{-2}. 189

3.21 Illustration of the flow at the junction between the calming section and the heater. Experimental conditions: p_{in} = 1.9 bar, $\dot{m}_T$ = 32.1 kg m^{-2} s^{-1}, X_{in} = 0.66, $\dot{q}_w$ = 309.6 kW m^{-2}, $\Delta T_{in} \approx$ 10 K. 190

3.22 Illustration of the flow at the junction between the calming section and the heater. Experimental conditions: p_{in} = 1.9 bar, $\dot{m}_T$ = 32.1 kg m^{-2} s^{-1}, X_{in} = 0.66, $\dot{q}_w$ = 437.2 kW m^{-2}, $\Delta T_{in} \approx$ 10 K. 191

3.23 Variation of disturbance waves frequency with distance along the heater. Experimental conditions: $p_{in} = 1.9$ bar, $\dot{m}_T = 32.1$ kg m^{-2} s^{-1}, $X = 0.66$, $\dot{q}_w = 0$ kW m^{-2}. 192

3.24 Wave frequency as a function of dimensionless distance (Hall-Taylor and Nedderman, 1968). 193

3.25 Wave velocity correlation (Hall-Taylor and Nedderman, 1968). 194

3.26 Comparison of the present data with the wave velocity correlation (Hall-Taylor and Nedderman, 1968). 195

3.27 Comparison of wave frequency data with data of Shearer (1964) and Hall-Taylor and Nedderman (1968). 196

3.28 Profiles of measured wall temperature along the heated section. Experimental conditions: $\overline{p} = 1.6$ bar (nominal), $\dot{m}_{G,in} = 23$ kg m^{-2} s^{-1} (nominal), $\dot{q}_w = 326.9$ kW m^{-2}, $\Delta T_{in} \approx 10$ K, Run 0523b: $\dot{m}_{L,in} = 12.8$ kg m^{-2} s^{-1}, Run 0523f: $\dot{m}_{L,in} = 19.2$ kg m^{-2} s^{-1}, Run 0523g: $\dot{m}_{L,in} = 22.4$ kg m^{-2} s^{-1}. 198

3.29 Variation of the experimental (average) heat transfer coefficient with wall heat flux. 199

3.30 Predictions of the heat transfer coefficient by the various correlations. Experimental conditions: $\overline{p} = 1.42$ bar, $\dot{m}_T = 38.1$ kg m^{-2} s^{-1}, $\dot{q}_w = 33.4$ kW m^{-2}, $\overline{\Delta T}_w = 5.0$ K, $\Delta T_{in} \approx 10$ K. 200

3.31 Predictions of the heat transfer coefficient by the various correlations. Experimental conditions: $\overline{p} = 1.52$ bar, $\dot{m}_T = 32.6$ kg m^{-2} s^{-1}, $\dot{q}_w = 202.3$ kW m^{-2}, $\overline{\Delta T}_w = 21.5$ K, $\Delta T_{in} \approx 10$ K. 201

3.32 Predictions of the heat transfer coefficient by the various correlations. Experimental conditions: $\overline{p} = 1.55$ bar, $\dot{m}_T = 38.9$ kg m^{-2} s^{-1}, $\dot{q}_w = 326.9$ kW m^{-2}, $\overline{\Delta T}_w = 28.34$ K, $\Delta T_{in} \approx 30$ K. 202

3.33 Predictions of the heat transfer coefficient using the Bennett *et al.* (1961) correlation. 203

3.34 Predictions of the heat transfer coefficient using the Chen (1966) correlation. 203

3.35 Predictions of the heat transfer coefficient using the Shah (1982) correlation. 204

3.36 Predictions of the heat transfer coefficient using the Kandlikar (1990) correlation. 204

3.37 Predictions of the heat transfer coefficient using the Liu and Winterton (1991) correlation. 205

3.38 Predictions of the heat transfer coefficient using the Steiner and Taborek (1992) correlation. 206

3.39 Typical boiling curves indicating the appearance of active nucleation sites. Experimental conditions: Run 0515. $\overline{p} = 1.5$ bar, $\dot{m}_T = 36.0$ kg m^{-2} s^{-1}, $\Delta T_{in} \approx 30$ K; Run 0524. $\overline{p} = 1.3$ bar, $\dot{m}_T = 38.1$ kg m^{-2} s^{-1}, $\Delta T_{in} \approx 10$ K; Run 0619. $\overline{p} = 1.5$ bar, $\dot{m}_T = 25$ kg m^{-2} s^{-1}, $\Delta T_{in} \approx 10$ K. 209

3.40 Geometry of the annular channel. 212

3.41 Predictions of the onset of nucleate boiling. 215

4.1 Evaporation of mixtures in annular flow. (a) Real situation, (b) Implicitly assumed in design (no droplets). 220

4.2 Phase diagram for a binary non-azeotropic mixture. 221

4.3 Saturation temperature against enthalpy for binary mixtures. 222

4.4 Calculations of (a) wall temperature and (b) heat transfer coefficient using the simplified droplet interchange formulation (Kandlbinder *et al.*, 1998). Conditions of calculations: mixture n-pentane/iso-octane (0.7/0.3 mole fraction), $p = 3.2$ bar, $\dot{q}_w = 49.3$ kW m^{-2}, $\dot{m}_T = 305.0$ kg m^{-2} s^{-1}. 225

4.5 An illustration of the model. 230

4.6 Mass conservation over an incremental pipe length. 234

4.7 Schematic of the model for interphase transfer. 240

4.8 Droplet interchange and condensation of mixtures in annular flow. 252

4.9 Comparison of predicted and experimental dimensionless heat transfer coefficients (Nusselt number) for condensation of refrigerants with the correlation of Tang (1997). Data of Cavallini *et al.* (2000). 253

4.10 Schematic diagram of the High Pressure Boiling Facility. 255

4.11 $e^{0,m}$ for different initial entrained fractions; mixture 1, $p = 2.3$ bar, $\dot{q}_w = 57.7$ kW m^{-2}, $\dot{m}_T = 286.6$ kg m^{-2} s^{-1}. 258

4.12 $e^{0,m}$ for different initial entrained fractions; mixture 1, $p = 6.0$ bar, $\dot{q}_w = 60.2$ kW m^{-2}, $\dot{m}_T = 295.0$ kg m^{-2} s^{-1}. 258

4.13 Mean concentration of n-pentane in the liquid film and in the droplets; mixture 1, $p = 6.1$ bar, $\dot{q}_w = 68.4$ kW m^{-2}, $\dot{m}_T = 503.8$ kg m^{-2} s^{-1}. 260

4.14 Mean concentration of n-pentane in the liquid film and in the droplets; mixture 2, $p = 2.2$ bar, $\dot{q}_w = 49.3$ kW m^{-2}, $\dot{m}_T = 297.1$ kg m^{-2} s^{-1}. 260

4.15 Mean concentration of n-pentane in the liquid film and in the droplets; mixture 1, $p = 6.0$ bar, $\dot{q}_w = 60.2$ kW m^{-2}, $\dot{m}_T = 295.0$ kg m^{-2} s^{-1}. 261

4.16 Profiles of absolute pressure; mixture 1, $p = 3.2$ bar, $\dot{q}_w = 49.3$ kW m^{-2}, $\dot{m}_T = 305.0$ kg m^{-2} s^{-1}. 263

4.17 Profiles of absolute pressure; mixture 2, $p = 2.2$ bar, $\dot{q}_w = 40.7$ kW m^{-2}, $\dot{m}_T = 195.8$ kg m^{-2} s^{-1}. 263

4.18 Predictions of wall, interface and core temperature; mixture 1, $p = 2.3$ bar, $\dot{q}_w = 49.8$ kW m^{-2}, $\dot{m}_T = 292.8$ kg m^{-2} s^{-1}. 265

4.19 Predictions of wall, interface and core temperature; mixture 1, $p = 3.2$ bar, $\dot{q}_w = 49.3$ kW m^{-2}, $\dot{m}_T = 305.0$ kg m^{-2} s^{-1}. 265

4.20 Predictions of wall, interface and core temperature; mixture 1, $p = 6.0$ bar, $\dot{q}_w = 60.2$ kW m^{-2}, $\dot{m}_T = 295.0$ kg m^{-2} s^{-1}. 266

4.21 Predictions of wall, interface and core temperature; mixture 1, $p = 10.0$ bar, $\dot{q}_w = 49.8$ kW m^{-2}, $\dot{m}_T = 299.2$ kg m^{-2} s^{-1}. 266

4.22 Predictions of heat transfer coefficient; mixture 1, $p = 2.3$ bar, $\dot{q}_w = 49.8$ kW m^{-2}, $\dot{m}_T = 292.8$ kg m^{-2} s^{-1}. 267

4.23 Predictions of heat transfer coefficient; mixture 1, $p = 3.2$ bar, $\dot{q}_w = 49.3$ kW m^{-2}, $\dot{m}_T = 305.0$ kg m^{-2} s^{-1}. 267

4.24 Predictions of heat transfer coefficient; mixture 1, $p = 6.0$ bar, $\dot{q}_w = 60.2$ kW m^{-2}, $\dot{m}_T = 295.0$ kg m^{-2} s^{-1}. 268

4.25 Predictions of heat transfer coefficient; mixture 1, $p = 10.0$ bar, $\dot{q}_w = 49.8$ kW m^{-2}, $\dot{m}_T = 299.2$ kg m^{-2} s^{-1}. 268

4.26 Profiles of bulk and interfacial concentration of n-pentane in the vapour core; mixture 1, $p = 6.1$ bar, $\dot{q}_w = 68.4$ kW m^{-2}, $\dot{m}_T = 503.8$ kg m^{-2} s^{-1}. . 270

4.27 Profiles of bulk and interfacial concentration of n-pentane in the vapour core; mixture 1, $p = 3.2$ bar, $\dot{q}_w = 49.3$ kW m^{-2}, $\dot{m}_T = 305.0$ kg m^{-2} s^{-1}. . 270

4.28 Profiles of enthalpy released or absorbed by the droplets normalised by the wall heat flux; mixture 1, $p = 6.0$ bar, $\dot{q}_w = 60.2$ kW m^{-2}, $\dot{m}_T = 295.0$ kg m^{-2} s^{-1}. 271

4.29 Profiles of enthalpy released or absorbed by the droplets normalised by the wall heat flux; mixture 1, $p = 3.2$ bar, $\dot{q}_w = 49.3$ kW m^{-2}, $\dot{m}_T = 305.0$ kg m^{-2} s^{-1}. 271

4.30 Predictions of local wall temperature by various methods; mixture 1, $p = 2.3$ bar, $\dot{q}_w = 49.8$ kW m^{-2}, $\dot{m}_T = 292.8$ kg m^{-2} s^{-1}. 272

4.31 Predictions of local wall temperature by various methods; mixture 1, $p = 3.2$ bar, $\dot{q}_w = 49.3$ kW m^{-2}, $\dot{m}_T = 305.0$ kg m^{-2} s^{-1}. 273

4.32 Predictions of local wall temperature by various methods; mixture 1, p = 6.1 bar, $\dot{q}_w = 60.2$ kW m^{-2}, $\dot{m}_T = 295.0$ kg m^{-2} s^{-1}. 273

4.33 Predictions of local heat transfer coefficients by various methods; mixture 1, $p = 2.3$ bar, $\dot{q}_w = 49.8$ kW m^{-2}, $\dot{m}_T = 292.8$ kg m^{-2} s^{-1}. 274

4.34 Predictions of local heat transfer coefficients by various methods; mixture 1, $p = 3.2$ bar, $\dot{q}_w = 49.3$ kW m^{-2}, $\dot{m}_T = 305.0$ kg m^{-2} s^{-1}. 274

4.35 Predictions of local heat transfer coefficients by various methods; mixture 1, $p = 6.1$ bar, $\dot{q}_w = 60.2$ kW m^{-2}, $\dot{m}_T = 295.0$ kg m^{-2} s^{-1}. 275

4.36 Predictions of average heat transfer coefficient. 276

4.37 Behaviour of average heat transfer coefficient predictions with pressure. . . 276

4.38 Behaviour of average heat transfer coefficient predictions with total mass flux. 277

4.39 Behaviour of average heat transfer coefficient predictions with wall heat flux.277

4.40 Profiles of liquid phase concentration; mixture 3, $p = 2.3$ bar, $\dot{q}_w$ = 40.5 kW m^{-2}, $\dot{m}_T = 297.5$ kg m^{-2} s^{-1}. 279

4.41 Profiles of vapour phase concentration; mixture 3, $p = 2.3$ bar, $\dot{q}_w$ = 40.5 kW m^{-2}, $\dot{m}_T = 297.5$ kg m^{-2} s^{-1}. 279

4.42 Distributions of Diffusion Interaction Parameters; mixture 3, $p = 3.1$ bar, $\dot{q}_w = 49.5$ kW m^{-2}, $\dot{m}_T = 296.0$ kg m^{-2} s^{-1}. 280

4.43 Distributions of Diffusion Interaction Parameters; mixture 3, $p = 6.0$ bar, $\dot{q}_w = 48.9$ kW m^{-2}, $\dot{m}_T = 300.5$ kg m^{-2} s^{-1}. 280

4.44 Distributions of wall, interface and core temperatures; mixture 3, $p = 6.0$ bar, $\dot{q}_w = 48.9$ kW m^{-2}, $\dot{m}_T = 300.5$ kg m^{-2} s^{-1}. 281

4.45 Distributions of wall, interface and core temperatures; mixture 3, $p = 3.1$ bar, $\dot{q}_w = 49.5$ kW m^{-2}, $\dot{m}_T = 296.0$ kg m^{-2} s^{-1}. 281

4.46 Heat transfer coefficient predictions; mixture 3, $p = 2.3$ bar, $\dot{q}_w = 40.5$ kW m^{-2}, $\dot{m}_T = 297.5$ kg m^{-2} s^{-1}. 282

4.47 Heat transfer coefficient predictions; mixture 3, $p = 3.1$ bar, $\dot{q}_w = 49.5$ kW m^{-2}, $\dot{m}_T = 296.0$ kg m^{-2} s^{-1}. 282

4.48 Predictions of average heat transfer coefficient in annular flow. 284

4.49 Behaviour of predicted average heat transfer coefficient with pressure. . . . 284

4.50 Behaviour of predicted average heat transfer coefficient with total mass flux. 285

4.51 Behaviour of predicted average heat transfer coefficient with wall heat flux. 285

4.52 Temperature profiles in a run in which dryout occurred; mixture 1, $p = 6.1$ bar, $\dot{q}_w = 30.5$ kW m^{-2}, $\dot{m}_T = 92.3$ kg m^{-2} s^{-1}. 286

4.53 Predictions of critical quality for single components. 288

4.54 Predictions of critical quality for mixtures. 288

4.55 Predictions of dryout for single components using the modified entrainment and deposition correlations. 291

4.56 Predictions of dryout for mixtures using the modified entrainment and deposition correlations. 291

4.57 CHF versus pressure for single components. 293

4.58 CHF versus inlet subcooling for single components. 293

4.59 CHF versus total mass flux for single components. 294

4.60 CHF versus pressure for mixtures. 294

4.61 CHF versus inlet subcooling for mixtures. 295

4.62 CHF versus total mass flux for mixtures. 295

4.63 Variation of the surface tension of pentane/iso-octane mixture with axial distance and concentration; mixture 2, $p = 2.2$ bar, $\dot{q}_w = 49.3$ kW m^{-2}, $\dot{m}_T = 297.1$ kg m^{-2} s^{-1}. 296

4.64 Illustration of the effects of the modification in the interchange correlations on the wall temperature and heat transfer coefficient predictions; mixture 1, $p = 3.2$ bar, $\dot{q}_w = 49.3$ kW m^{-2}, $\dot{m}_T = 305.0$ kg m^{-2} s^{-1}. 297

4.65 Comparison of calculated CHF using the present formulation and the correlation by Katto and Ohno (1984); SC, single component; M, mixture. . . 298

4.66 Liquid film concentration in condensation. R-407C, $p = 17$ bar, $\dot{q}_w = -33.7$ kW m^{-2}, $\dot{m}_L = 402$ kg m^{-2} s^{-1}. 301

4.67 Liquid film and droplet concentration in condensation (hypothetical case); mixture 1, $p = 2.3$ bar, $\dot{q}_w = -49.8$ kW m^{-2}, $\dot{m}_L = 292.8$ kg m^{-2} s^{-1}. . . 301

4.68 Liquid film and droplet concentration in evaporation (initial entrained fraction assumed equal to 10%); mixture 1, $p = 2.3$ bar, $\dot{q}_w = -49.8$ kW m^{-2}, $\dot{m}_L = 292.8$ kg m^{-2} s^{-1}. 302

4.69 Prediction of condensation heat transfer coefficients for R-407C. 302

5.1 Results of take off through a porous wall section (air-water annular flow). $d_T = 0.032$ mm, $p = 1.5$ bara, $U_{LS} = 0.08$ m s^{-1}, $U_{GS} = 17.4$ m s^{-1} (Azzopardi and Zaidi, 2000). 306

5.2 Results of take off through a porous wall section (air-water churn flow). $d_T = 0.032$ mm, $p = 1.5$ bara, $U_{LS} = 0.08$ m s^{-1}, $U_{GS} = 4.4$ m s^{-1} (Azzopardi and Zaidi, 2000). 307

5.3 Local liquid mass flux profiles (Gill *et al.*, 1964). 309

5.4 Local liquid mass flux profiles (Gill *et al.*, 1964). 310

5.5 Local droplet concentration profiles (Gill *et al.*, 1964). 311

5.6 Local droplet concentration profiles (Gill *et al.*, 1964). 312

5.7 A diagram of the LOTUS air-water facility. 313

5.8 Operating range of the LOTUS Facility (Watson, 1999). 315

5.9 Schematic diagram of the liquid purge system. 316

5.10 Isokinetic probe sampling principle. 317

5.11 The isokinetic probe used in the present study and the mounting section. Not to scale (Khor, 1998). 319

5.12 A detailed view of the tip of the isokinetic probe (Khor, 1998). 320

5.13 Experimental setup for gas and liquid collection using the isokinetic sampling probe. 321

5.14 Traversing positions attained by the isokinetic probe and averaging dimensions. 323

5.15 Liquid collection using the isokinetic probe. Experimental conditions: $p =$ 3 bara, $\dot{m}_L = 45$ kg m^{-2} s^{-1}, $U^*_{GS} = 1.3$. 324

5.16 Local liquid mass flux profiles. $p = 2.1$ bara, $\dot{m}_L = 126.3$ kg m^{-2} s^{-1}. . . . 326

5.17 Local liquid mass flux profiles. $p = 3.7$ bara, $\dot{m}_L = 216.0$ kg m^{-2} s^{-1}. . . . 327

5.18 Local gas velocity profiles. $p = 2.1$ bara, $\dot{m}_L = 126.3$ kg m^{-2} s^{-1}. 327

5.19 Local gas velocity profiles. $p = 3.7$ bara, $\dot{m}_L = 216.0$ kg m^{-2} s^{-1}. 328

5.20 Profiles of local droplet concentration. $p = 2.1$ bara, $\dot{m}_L = 126.3$ kg m^{-2} s^{-1}.329

5.21 Profiles of local droplet concentration. $p = 3.7$ bara, $\dot{m}_L = 216.0$ kg m^{-2} s^{-1}.329

5.22 Volumetric flow ratio. $p = 2.0$ bara (nominal). 330

5.23 Volumetric flow ratio. $p = 3.6$ bara (nominal). 331

5.24 Volumetric flow ratio. $p = 5.2$ bara (nominal). 331

5.25 Liquid entrained fraction as a function of the total liquid mass flux. $p = 2.0$ bara (nominal). 332

5.26 Liquid entrained fraction as a function of the total liquid mass flux. $p = 3.6$ bara (nominal). 332

5.27 Liquid entrained fraction as a function of the total liquid mass flux. $p = 5.0$ bara (nominal). 333

5.28 Mechanisms of entrainment and drop break-up (Azzopardi, 1983). 335

5.29 Map for droplet break-up mechanism (Azzopardi,1983). 336

5.30 Liquid entrained fraction as a function of the absolute pressure. (a) $\dot{m}_L =$ 13 kg m^{-2} s^{-1} (nominal), (b) $\dot{m}_L = 23$ kg m^{-2} s^{-1} (nominal), (c) $\dot{m}_L = 48$ kg m^{-2} s^{-1} (nominal). 337

5.31 Liquid entrained fraction as a function of the absolute pressure. (a) $\dot{m}_L =$ 130 kg m^{-2} s^{-1} (nominal), (b) $\dot{m}_L = 218$ kg m^{-2} s^{-1} (nominal), (c) $\dot{m}_L =$ 300 kg m^{-2} s^{-1} (nominal). 338

5.32 Entrainment and experimental pressure gradient in the churn-annular region. $p = 2.0$ bara, $\dot{m}_L = 47.0$ kg m^{-2} s^{-1} (nominal). 339

5.33 Entrainment and experimental pressure gradient in the churn-annular region. $p = 2.0$ bara, $\dot{m}_L = 138.0$ kg m^{-2} s^{-1} (nominal). 340

5.34 Prediction of entrained fraction using the proposed correlation. 341

5.35 A comparison between experimental and predicted equilibrium entrained fraction according to various methods. 348

5.36 Effect of system pressure on the prediction of the equilibrium entrained fraction according to various methods. 349

5.37 Effect of liquid mass flux on the prediction of the equilibrium entrained fraction according to various methods. 350

6.1 An illustration of the problem geometry. 352

6.2 Measured churn flow wave shapes based on the visualisation experiments of Hewitt *et al.* (1985). 355

6.3 The assumed geometry of the wave. 355

6.4 Illustration and model of flowrates in and out of the wave. 357

6.5 Force balance over a coherent wave. 358

6.6 The boundary layer hypothesis for wall shear stress. 362

6.7 Wave position versus time. Symbols refer to Sequences in Govan (1990) experiments. 367

6.8 Calculated wave velocity distributions. 368

List of Tables

2.1 Response of disturbance waves to variations in system parameters. 68

2.2 Wave frequencies and velocities from visualisation experiments (Govan, 1990). 97

2.3 X and K values for Katto and Ohno (1984) correlation. 132

3.1 Dimensions of the test section for the boiling visualisation experiments. . . 165

3.2 Experimental conditions for the heat transfer tests. 197

3.3 Errors of various correlations in predicting the heat transfer coefficient. . . 206

3.4 Estimated uncertainty of measured parameters used in the determination of the experimental heat transfer coefficient. 207

4.1 Estimated uncertainty of measured values used in the determination of the experimental heat transfer coefficient. 256

4.2 Test matrix for two-phase experiments (Kandlbinder, 1997). 257

4.3 Values of $e^{0,m}$, at $z_A = 1m$, for different values of initial entrained fraction. 259

4.4 Summary of conditions in calculations of $e^{0,m}$. 261

5.1 Dimensions of the isokinetic sampling probe. 318

5.2 A comparison of entrained fraction obtained using a porous sinter and the isokinetic probe. 343

5.3 Uncertainties of measured parameters. 344

6.1 Results obtained using the mathematical model. 366

A.1 Wave velocity and frequency data. Experimental conditions: Run 0824a, $p_{in} = 1.6$ bar, $\dot{m}_T = 24.9$ kg m^{-2} s^{-1}, $X_{in} = 0.68$, $\dot{q}_w = 0$ kW m^{-2}, $\Delta T_{in} \approx$ 30 K. 379

A.2 Wave velocity and frequency data. Experimental conditions: Run 0824c, $p_{in} = 1.6$ bar, $\dot{m}_T = 24.9$ kg m^{-2} s^{-1}, $X_{in} = 0.68$, $\dot{q}_w = 0$ kW m^{-2}, $\Delta T_{in} \approx$ 30 K. 380

A.3 Wave velocity and frequency data. Experimental conditions: Run 0824e, $p_{in} = 1.6$ bar, $\dot{m}_T = 22.2$ kg m^{-2} s^{-1}, $X_{in} = 0.64$, $\dot{q}_w = 73.1$ kW m^{-2}, $\Delta T_{in} \approx 30$ K. 380

A.4 Wave velocity and frequency data. Experimental conditions: Run 0824f, $p_{in} = 1.6$ bar, $\dot{m}_T = 22.2$ kg m^{-2} s^{-1}, $X_{in} = 0.64$, $\dot{q}_w = 125.3$ kW m^{-2}, $\Delta T_{in} \approx 30$ K. 380

A.5 Wave velocity and frequency data. Experimental conditions: Run 0824h, $p_{in} = 2.1$ bar, $\dot{m}_T = 30.1$ kg m^{-2} s^{-1}, $X_{in} = 0.73$, $\dot{q}_w = 0$ kW m^{-2}, $\Delta T_{in} \approx$ 30 K. 381

A.6 Wave velocity and frequency data. Experimental conditions: Run 0824k, $p_{in} = 2.1$ bar, $\dot{m}_T = 30.1$ kg m^{-2} s^{-1}, $X_{in} = 0.73$, $\dot{q}_w = 189.5$ kW m^{-2}, $\Delta T_{in} \approx 30$ K. 381

A.7 Wave velocity and frequency data. Experimental conditions: Run 0829b, $p_{in} = 2.0$ bar, $\dot{m}_T = 33.7$ kg m^{-2} s^{-1}, $X_{in} = 0.62$, $\dot{q}_w = 96.6$ kW m^{-2}, $\Delta T_{in} \approx 30$ K. 381

A.8 Wave velocity and frequency data. Experimental conditions: Run 0830a, $p_{in} = 2.0$ bar, $\dot{m}_T = 30.2$ kg m^{-2} s^{-1}, $X_{in} = 0.63$, $\dot{q}_w = 0$ kW m^{-2}, $\Delta T_{in} \approx$ 30 K. 382

A.9 Wave velocity and frequency data. Experimental conditions: Run 0830b, p_{in} = 2.0 bar, $\dot{m}_T$ = 30.2 kg m^{-2} s^{-1}, X_{in} = 0.63, $\dot{q}_w$ = 96.1 kW m^{-2}, $\Delta T_{in} \approx$ 30 K. 382

A.10 Wave velocity and frequency data. Experimental conditions: Run 0830c, p_{in} = 2.0 bar, $\dot{m}_T$ = 30.2 kg m^{-2} s^{-1}, X_{in} = 0.63, $\dot{q}_w$ = 158.7 kW m^{-2}, $\Delta T_{in} \approx$ 30 K. 383

A.11 Wave velocity and frequency data. Experimental conditions: Run 0830d, p_{in} = 2.0 bar, $\dot{m}_T$ = 30.2 kg m^{-2} s^{-1}, X_{in} = 0.63, $\dot{q}_w$ = 276.7 kW m^{-2}, $\Delta T_{in} \approx$ 30 K. 383

A.12 Wave velocity and frequency data. Experimental conditions: Run 0830e, p_{in} = 2.0 bar, $\dot{m}_T$ = 30.2 kg m^{-2} s^{-1}, X_{in} = 0.63, $\dot{q}_w$ = 485.6 kW m^{-2}, $\Delta T_{in} \approx$ 30 K. 384

A.13 Wave velocity and frequency data. Experimental conditions: Run 1027a, Position from the bottom of heater = 0 m, p_{in} = 1.9 bar, $\dot{m}_T$ = 32.1 kg m^{-2} s^{-1}, X_{in} = 0.60, $\dot{q}_w$ = 0 kW m^{-2}, $\Delta T_{in} \approx$ 10 K. 384

A.14 Wave velocity and frequency data. Experimental conditions: Run 1027b, Position from the bottom of heater = 0 m, p_{in} = 1.9 bar, $\dot{m}_T$ = 32.1 kg m^{-2} s^{-1}, X_{in} = 0.60, $\dot{q}_w$ = 0 kW m^{-2}, $\Delta T_{in} \approx$ 10 K. 385

A.15 Wave velocity and frequency data. Experimental conditions: Run 1027c, Position from the bottom of heater = 0.065 m, p_{in} = 1.9 bar, $\dot{m}_T$ = 32.1 kg m^{-2} s^{-1}, X_{in} = 0.60, $\dot{q}_w$ = 0 kW m^{-2}, $\Delta T_{in} \approx$ 10 K. 385

A.16 Wave velocity and frequency data. Experimental conditions: Run 1027d, Position from the bottom of heater = 0.065 m, p_{in} = 1.9 bar, $\dot{m}_T$ = 32.1 kg m^{-2} s^{-1}, X_{in} = 0.60, $\dot{q}_w$ = 0 kW m^{-2}, $\Delta T_{in} \approx$ 10 K. 386

A.17 Wave velocity and frequency data. Experimental conditions: Run 1027e, Position from the bottom of heater = 0.105 m, p_{in} = 1.9 bar, $\dot{m}_T$ = 32.1 kg m^{-2} s^{-1}, $X_{in} = 0.60$, $\dot{q}_w = 0$ kW m^{-2}, $\Delta T_{in} \approx 10$ K. 387

A.18 Wave velocity and frequency data. Experimental conditions: Run 1027f, Position from the bottom of heater = 0.105 m, p_{in} = 1.9 bar, $\dot{m}_T$ = 32.1 kg m^{-2} s^{-1}, $X_{in} = 0.60$, $\dot{q}_w = 0$ kW m^{-2}, $\Delta T_{in} \approx 10$ K. 387

A.19 Wave velocity and frequency data. Experimental conditions: Run 1027g, Position from the bottom of heater = 0.135 m, p_{in} = 1.9 bar, $\dot{m}_T$ = 32.1 kg m^{-2} s^{-1}, $X_{in} = 0.60$, $\dot{q}_w = 0$ kW m^{-2}, $\Delta T_{in} \approx 10$ K. 388

A.20 Wave velocity and frequency data. Experimental conditions: Run 1027h, Position from the bottom of heater = 0.135 m, p_{in} = 1.9 bar, $\dot{m}_T$ = 32.1 kg m^{-2} s^{-1}, $X_{in} = 0.60$, $\dot{q}_w = 0$ kW m^{-2}, $\Delta T_{in} \approx 10$ K. 388

A.21 Wave velocity and frequency data. Experimental conditions: Run 1027i, Position from the bottom of heater = 0.205 m, p_{in} = 1.9 bar, $\dot{m}_T$ = 32.1 kg m^{-2} s^{-1}, $X_{in} = 0.60$, $\dot{q}_w = 0$ kW m^{-2}, $\Delta T_{in} \approx 10$ K. 389

A.22 Wave velocity and frequency data. Experimental conditions: Run 1027j, Position from the bottom of heater = 0.205 m, p_{in} = 1.9 bar, $\dot{m}_T$ = 32.1 kg m^{-2} s^{-1}, $X_{in} = 0.60$, $\dot{q}_w = 0$ kW m^{-2}, $\Delta T_{in} \approx 10$ K. 389

C.1 List of valves in the LOTUS rig. 400

D.1 Entrained fraction data. Experimental conditions: $p = 2.1$ bara (nominal), $\dot{m}_L = 15$ kg m^{-2} s^{-1} (nominal). 401

D.2 Entrained fraction data. Experimental conditions: $p = 3.6$ bara (nominal), $\dot{m}_L = 12$ kg m^{-2} s^{-1} (nominal). 402

D.3 Entrained fraction data. Experimental conditions: $p = 5.0$ bara (nominal), $\dot{m}_L = 12$ kg m^{-2} s^{-1} (nominal). 402

D.4 Entrained fraction data. Experimental conditions: $p = 1.9$ bara (nominal), $\dot{m}_L = 22$ kg m^{-2} s^{-1} (nominal). 402

D.5 Entrained fraction data. Experimental conditions: $p = 3.5$ bara (nominal), $\dot{m}_L = 23$ kg m^{-2} s^{-1} (nominal). 403

D.6 Entrained fraction data. Experimental conditions: $p = 5.0$ bara (nominal), $\dot{m}_L = 23$ kg m^{-2} s^{-1} (nominal). 403

D.7 Entrained fraction data. Experimental conditions: $p = 1.8$ bara (nominal), $\dot{m}_L = 48$ kg m^{-2} s^{-1} (nominal). 403

D.8 Entrained fraction data. Experimental conditions: $p = 3.6$ bara (nominal), $\dot{m}_L = 48$ kg m^{-2} s^{-1} (nominal). 404

D.9 Entrained fraction data. Experimental conditions: $p = 5.0$ bara (nominal), $\dot{m}_L = 48$ kg m^{-2} s^{-1} (nominal). 404

D.10 Entrained fraction data. Experimental conditions: $p = 2.1$ bara (nominal), $\dot{m}_L = 126$ kg m^{-2} s^{-1} (nominal). 404

D.11 Entrained fraction data. Experimental conditions: $p = 3.8$ bara (nominal), $\dot{m}_L = 128$ kg m^{-2} s^{-1} (nominal). 405

D.12 Entrained fraction data. Experimental conditions: $p = 5.2$ bara (nominal), $\dot{m}_L = 105$ kg m^{-2} s^{-1} (nominal). 405

D.13 Entrained fraction data. Experimental conditions: $p = 2.0$ bara (nominal), $\dot{m}_L = 218$ kg m^{-2} s^{-1} (nominal). 405

D.14 Entrained fraction data. Experimental conditions: $p = 3.7$ bara (nominal), $\dot{m}_L = 215$ kg m^{-2} s^{-1} (nominal). 406

D.15 Entrained fraction data. Experimental conditions: $p = 5.1$ bara (nominal), $\dot{m}_L = 214$ kg m^{-2} s^{-1} (nominal). 406

D.16 Entrained fraction data. Experimental conditions: $p = 2.0$ bara (nominal), $\dot{m}_L = 331$ kg m^{-2} s^{-1} (nominal). 407

D.17 Entrained fraction data. Experimental conditions: $p = 3.2$ bara (nominal), $\dot{m}_L = 330$ kg m^{-2} s^{-1} (nominal). 407

D.18 Entrained fraction data. Experimental conditions: $p = 5.0$ bara (nominal), $\dot{m}_L = 302$ kg m^{-2} s^{-1} (nominal). 408

Nomenclature

Roman

Symbol	*Quantity*	*SI unit*
A	Area	m^2
A	Amplitude	m
$[B_G]$	Matrix of mass transfer coefficients	m s^{-1}
Bo	Boiling number	-
c	Tracer concentration	-
C	Droplet deposition concentration	kg m^{-3}
C	Concentration of droplets in the core	-
CHF	Critical heat flux	W m^{-2}
c_p	Specific heat capacity at constant pressure	J kg^{-1} K^{-1}
C_{mix}	Mixture correction factor	-
Co	Convective number	-
d_a	Outer diameter of annulus	m
d_c	Characteristic diameter	m
d_o	Inner diameter of annulus	m
d_p	Droplet diameter	m

Symbol	*Quantity*	*SI unit*
d_T	Tube diameter	m
D	Deposition rate	kg m^{-2} s^{-1}
e	Fraction of liquid entrained as droplets	-
e_∞	Equilibrium entrained fraction	-
$e^{j,m}$	Parameter defined in Eq. 4.38	-
E	Entrainment rate	kg m^{-2} s^{-1}
f	Friction factor	-
f	Frequency	Hz
F	Enhancement/correction factor in heat transfer correlation	-
F	Function in Eqs. 4.23	m s^{-2}
F	Force	N
Fr	Froude number	-
g	Acceleration due to gravity	m s^{-2}
h	Specific enthalpy	J kg^{-1}
h	Humidity	-
I	Electrical current	A
$[I]$	Unit Matrix	-
I_p	Diffusion interaction coefficient	-
K	Kutateladze number	-
k_D	Deposition rate coefficient	m s^{-1}
L	Length	m
Le	Lewis number	-

Symbol	*Quantity*	*SI unit*
$\dot{m}$	Mass flux	kg m^{-2} s^{-1}
M	Mass	kg
M_w	Molecular weight	kg $kmol^{-1}$
$\dot{M}$	Mass flow rate	kg m^{-2}
n	Flux of droplets per unit area of tube wall	m^{-2} s^{-1}
N_p	Number of data points	-
NEQ	Number of equations	-
NOC	Number of components	-
NOD	Flux of droplets per unit tube cross-sectional area	m^{-2} s^{-1}
On	Ohnhezoge number	-
p	Pressure	Pa
P	Perimeter	m
Pr	Prandtl number	-
$\dot{q}$	Heat flux	W m^{-2}
$\dot{Q}$	Internal heat generation rate	W m^{-3}
$\dot{\mathbf{Q}}$	Heat rate	W
r	Radial co-ordinate	m
r_i	Inner radius of heated section	m
r_o	Outer radius of heated section	m
r_T	Tube radius	m
R	Electrical resistance	m
R	Universal gas constant (=8.315)	J mol^{-1} K^{-1}
Re	Reynolds number	-

Symbol	*Quantity*	*SI unit*
s	Thickness of layer (film method)	m
S	Suppression factor in heat transfer correlation	-
Sc	Schmidt number	-
$[Sc]$	Schmidt number matrix	-
Sr	Strouhal number	-
t	Time	s
t	Pipe wall thickness	m
T	Temperature	K
U	Velocity	m s^{-1}
U_M	Mixture velocity	m s^{-1}
V	Voltage	V
V	Volume	m^3
$\dot{V}$	Volumetric flow rate	m^3 s^{-1}
We	Weber number	-
x	Concentration of liquid (mass fraction)	-
X	Quality	-
X_{tt}	Martinelli parameter	-
y	Concentration of vapour (mass fraction)	-
y	Auxiliary radial co-ordinate	m
z	Axial co-ordinate	m

Greek

Symbol	*Quantity*	*SI unit*
α	Heat transfer coefficient	W m^{-2} K^{-1}
β	Volumetric flow ratio	-
β_{12}	Mass transfer coefficient	m s^{-1}
δ	Thickness of film or layer	m
δ_{ij}	Maxwell-Stefan diffusion coefficients	m^2 s^{-1}
δ_{ts}	Thickness of thermal laminar sub-layer	m
Δ_{12}	Mass diffusivity	m^2 s^{-1}
$[\Delta]$	Matrix of mass diffusivity coefficients	m^2 s^{-1}
Δh_v	Latent heat of vaporisation	J kg^{-1}
ΔT_{bp}	Boiling range	K
ε	Void fraction	-
η	Viscosity	N s m^{-2}
θ	Temperature difference	K
κ	Thermal diffusivity	m^2 s^{-1}
λ	Thermal conductivity	W m^{-1} K^{-1}
ν	Kinematic viscosity	m s^{-2}
ϕ	Finite flux correction factor for mass transfer	-
ϕ_T	Finite flux correction factor for heat transfer	-
$[\Phi]$	Finite flux correction matrix for mass transfer	-
φ	Angle	rad
ρ	Density	kg m^{-3}
ϱ	Electrical resistivity	Ω m

Symbol	*Quantity*	*SI unit*
σ	Surface tension	N m^{-1}
τ	Shear stress	N m^{-2}
Ψ	Parameter defined in Eq. 4.25	m^3
Ψ_m	Marsh and Mudawar (1989) parameter	-
Ω	Parameter defined in Eq. 4.24	m s^{-1}

Subscripts

Symbol	*Meaning*
∞	Location away from interface or wall
a	Accelerational
b	Bulk
bub	Bubble point temperature
$buoy$	Buoyancy
c	Creation
C	Homogeneous core
$crit$	Critical
D	Deposition
dew	Dew point temperature
$disp$	Dispersion
E	Equilibrium
eq	Equivalent
exp	Experimental
f	Frictional
FC	Forced convection
g	Gravitational
G	Gas (vapour)
GC	Gas (vapour) in the core
GO	All flux as gas (vapour)
HS	Heated section

Symbol	*Meaning*
i	Component identifier
I	Interface
L	Liquid phase
LE	Entrained liquid
LF	Liquid film
LFC	Critical liquid film
LO	All fiux as liquid
OA	Onset of annular flow
mac	Macro-convective
mic	Micro-convective
mix	Mixture
NB	Nucleate boiling
ONB	Onset of nucleate boiling
ov	Overall
p	Droplet
r	Reduced property
s	Substrate
S	Superficial
sat	Saturation
sl	Slug
T	Total
TB	Taylor bubble

Subscripts

Symbol	*Meaning*
tp	Two-phase
w	Wall
W	Wave

Superscripts

Symbol	*Meaning*
$\bar{}$	Average value
$\tilde{}$	Molar quantity
$\bullet$	Finite flux
j, k, m	Axial co-ordinate (section) counters

Chapter 1

Introduction

1.1 Multiphase Flow

Multiphase flow is everywhere. From environmental phenomena to chemical processes and power generation, it is difficult to find a relevant problem which does not involve two or more phases.

However young the science of Multiphase Flow may appear to be, the practical application of some of its basic principles had certainly been around earlier than the Industrial Revolution, when the first phase change equipment were designed and operated. Since then, engineers have been improving human existence on earth and even making life possible outside it through the application of the knowledge of fluid mechanics and heat transfer in multiphase systems.

The affirmation of Multiphase Flow as a field of science in its own right came in the mid-20th century, basically as a requirement for the development of the nuclear industry. The high safety standards set by the latter could only be met if accurate prediction methods and design methodologies were employed. This prompted efforts from engineers all over the globe to improve the basic phenomenological understanding and to devise reliable

prediction methods for multiphase systems.

Nowadays, economic and environmental aspects dictate the future needs of the research in Multiphase Flow. However, from offshore oil and gas recovery and transport to the cooling of electronic equipment, the challenge of improving our fundamental knowledge and building better models and prediction methods remains the same.

1.2 Objectives

This thesis is concerned with the most important flow regime in the most important geometry, namely annular flow of gas and liquid in a vertical tube. In such flows, part of the liquid flows as a liquid film on the channel wall whereas the remainder flows as droplets entrained in the gas core. The importance of annular flow stems from the large occurrence of annular flow in the power and process industries. As a consequence, annular flow is also the most studied of all flow regimes.

Although numerous experimental and theoretical investigations have been conducted in annular flow over the past five decades or so, some fundamental aspects of this flow regime are not yet fully understood.

For instance, in multicomponent systems, experiments carried out at Harwell and at Imperial College have shown that the heat transfer coefficient often decreases with increasing vapour fraction (quality) (Kandlbinder, 1997). This fact seems to contradict what one would expect for single component systems, i.e., an increase in the heat transfer coefficient with increasing quality.

Momentum, energy and mass transfer processes take place in a very complex manner in annular flow of multicomponent mixtures. In addition to the so-called mixture effects, which give rise to gradients of concentration in the radial and axial directions, other phenomena may contribute to the observed decrease in heat transfer. As will be shown

in this thesis, non-equilibrium effects associated with the formation of droplets in annular flow play a vital role in explaining the heat transfer coefficient deterioration. A new model describing such non-equilibrium effects will be presented.

In this new model for evaporating multicomponent annular flow, the fraction of the liquid phase entrained as droplets and the concentration of the components in the liquid film and in the droplets were calculated as a function of the distance along the channel. The heat transfer coefficient was then calculated for the predicted liquid phase and component distribution. Two important questions arising in the analysis were as follows,

1. What is the fraction of the liquid phase which is entrained as droplets at the point along the channel where annular flow is initiated?

2. What is the role of nucleate boiling in heat transfer in annular flow?

These two questions were the focus of the experimental studies which formed part of the work.

As the flow proceeds along the channel and the vapour content of the flow rises, the *flow regime* changes successively from bubbly flow, to slug flow, to churn-annular flow and finally to annular flow. Recognising the importance of the boundary conditions (and particularly the entrained fraction) for annular flow at the transition from churn-annular flow, attention has been focused on the churn-annular regime itself. This has involved the measurement of entrained fraction in both churn-annular and annular flow in the boundary region and the development of an analytical description of the waves from which the entrained droplets derive in churn-annular flow.

A clear view of the phenomenon of phase change in annular flow requires the identification of the heat transfer processes occurring in the liquid film. There has been a serious debate in the literature concerning the nature of the nucleate boiling heat transfer mechanism at high vapour fraction flows. A more traditional school of thought suggests that nucleate

boiling is gradually suppressed (and forced convection becomes more significant) as the quality increases (Collier and Thome, 1994). A challenging interpretation (Mesler, 1977) suggests that the thinning of the liquid film may actually promote nucleation and that the droplet interchange mechanism may provide conditions under which nucleation is maintained even at wall superheats lower that those required to sustain nucleation.

Visualisation experiments coupled with measurements of the wall temperature of the heater provide qualitative and quantitative information on the phase change heat transfer in annular flow. In addition, by using a specially constructed annulus test section, a direct observation of the interaction of disturbance waves and the activity of nucleation sites can be made. As will be seen, under the conditions investigated, the disturbance waves seem to locally *trigger off* the activity of the nucleation sites.

The objective of this thesis is to address the issues described above and to contribute to their clarification at a fundamental level.

1.3 Overview

This thesis is organised as follows. Chapter 2 presents a review of the literature for diabatic and adiabatic gas-liquid systems. In Chapter 3, experiments aimed at elucidating the nature of nucleate boiling in steam-water annular flow are described. In Chapter 4, a model for phase change of multicomponent mixtures in annular flow is presented. The results are compared with those obtained by Kandlbinder (1997) for hydrocarbon mixtures undergoing phase change in a vertical pipe. Chapter 5 describes a series of adiabatic air-water tests aimed at determining the fraction of the total liquid flow entrained as droplets at the churn-annular transition. Chapter 6 puts forward a simple mathematical model to describe the formation of waves in churn-annular flow. The model is calibrated and compared with high-speed visualisation data by Govan (1990). Finally, conclusions and

recommendations for future work are presented in Chapter 7.

Chapter 2

Literature Review and Background

2.1 Introduction and Organisation

This review is mainly concerned with two-phase gas-liquid flow of single component fluids and multicomponent mixtures of miscible fluids in vertical round tubes. Both adiabatic and diabatic cases are considered. Also, more attention is paid to high vapour mass fraction flows as the understanding of some of their features is the principal objective of this study.

This chapter is organised as follows. Section 2.2 introduces the subject of two-phase flow in vertical tubes by describing the existing flow regimes and the mechanisms of transition between them. This is carried out within the context of adiabatic systems. Section 2.3 deals with phase change heat transfer to single component fluids. A physical description of the boiling process as well as a review of prediction methods are presented. Multicomponent systems undergoing phase change are dealt with in Section 2.4.

2.2 Adiabatic vertical two-phase flow

2.2.1 Flow patterns

Multiphase flow problems in engineering embrace two complex phenomena, the turbulence in each of the phases and the dynamics of the two-phase interface(s). In order to gain understanding of the physics and to provide reliable and inexpensive solutions to the problems, several methods of flow classification based on both experimental and theoretical studies were developed over the past decades.

A natural way to tackle two-phase flow problems is to relate them in some way to a single phase flow counterpart. For instance, the *homogeneous model* treats the two-phase mixture as a single phase fluid with average physical properties. Other examples are the pioneering works of Martinelli and collaborators (Martinelli and Nelson, 1948; Lockhart and Martinelli, 1949), who dealt with the prediction of pressure drop by introducing a two-phase multiplier to the pressure drop of an equivalent single phase flow (same total or phasic flow rate).

In some cases, the level of accuracy desired to the solution requires the knowledge of the configuration of the interface(s) for a given set of flow parameters. Designating a *flow pattern* is a way of classifying, based on subjective and objective criteria, the various configurations attained by the phase interface(s) in internal flows of multiphase mixtures. A presentation of the experimental techniques developed and used to characterise flow patterns in multiphase flow was given by Hewitt (1978).

The acknowledged flow patterns in vertical flow are shown in Fig. 2.1. These are as follows (in order of increasing quality), bubbly flow, plug (or slug) flow, churn flow, annular flow and wispy-annular flow [1]. A qualitative description of the flow patterns is given by Collier

[1] Other flow patterns may also be identified, for example mist flow, where the liquid is solely dispersed as droplets in a continuous gas core (usually associated with post-dryout flows).

and Thome (1994),

a. Bubbly flow. The gas or vapour phase is dispersed as discrete bubbles of approximately the same size in a continuous liquid phase;

b. Plug flow. The gas flows as large bullet-shape (Taylor) bubbles. The gas in the bubble is separated from the pipe wall by a descending film of liquid. The liquid flow is contained in liquid slugs which separate successive gas bubbles. These slugs may or may not contain smaller entrained gas bubbles;

c. Churn flow. The gas or vapour flows in a chaotic manner through the liquid which is mainly displaced to the channel wall. The liquid flow has an oscillatory or time varying character. The net transport of liquid is upwards and carried out by large waves travelling over a film substrate. Section 2.2.4 presents a review of works carried out in churn flow;

d. Annular flow. The annular pattern is undoubtedly the dominant configuration, prevailing from qualities of to a few percent up to values close to unity. The liquid phase flows as an annular film coating the wall of the tube, whereas the gas phase flows in the core. The film interface is covered by ripple (small wavelength, small amplitude) waves and by disturbance (longer wavelength, larger amplitude) waves. Disturbance waves travel at velocities greater than that of the liquid film and have a height many times greater than the average thickness of the film. They are also the main source of droplet entrainment, a process by which small liquid drops are formed from the tips of the disturbance waves and are drawn into the gas flow. After travelling for a while in the gas core, the droplets eventually re-deposit back on to the film at a distance downstream. The mass exchange process between the continuous and dispersed liquid streams is commonly referred to as the entrainment

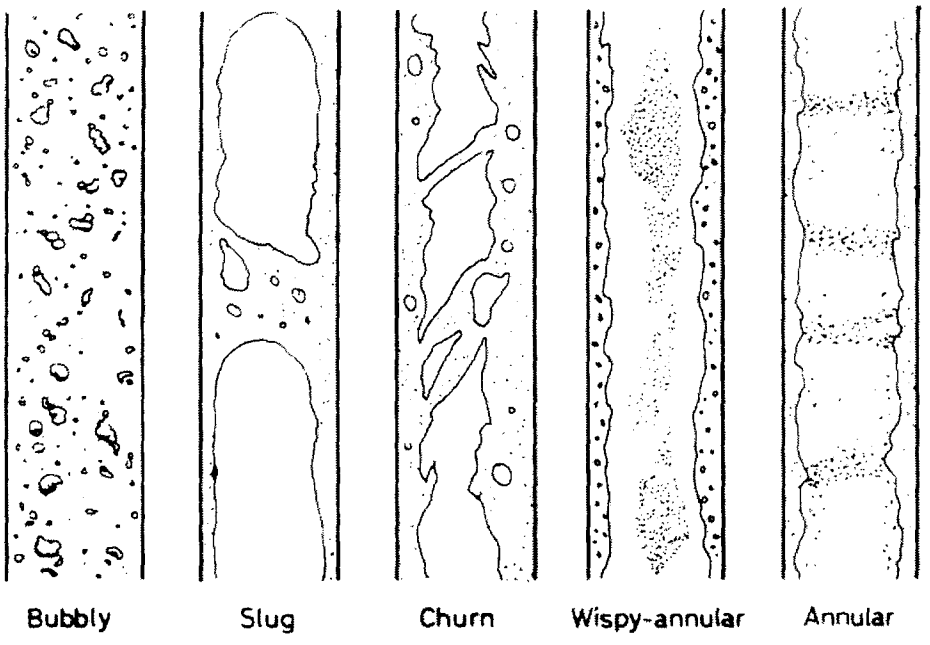


Figure 2.1: The flow regimes in vertical gas-liquid flow (Collier and Thome, 1994).

and deposition mechanism. A more detailed description of the annular flow regime is given in Section 2.2.3;

e. Wispy-annular flow. The flow in this region takes the form of a relatively thick liquid film on the walls of the pipe together with a considerable amount of liquid entrained in a central gas or vapour core. The liquid in the film is aerated by small gas bubbles and the entrained liquid phase appears as large droplets which have agglomerated into long irregular filaments or wisps. This region occurs at high mass velocities.

The different flow patterns can be allocated in a chart called a *flow pattern map*. The flow patterns are represented as areas on the plot, whose coordinates are the actual superficial velocities (mean velocity of each phase if flowing alone in the pipe) or generalised parameters containing these velocities. An example of a flow pattern map for vertical

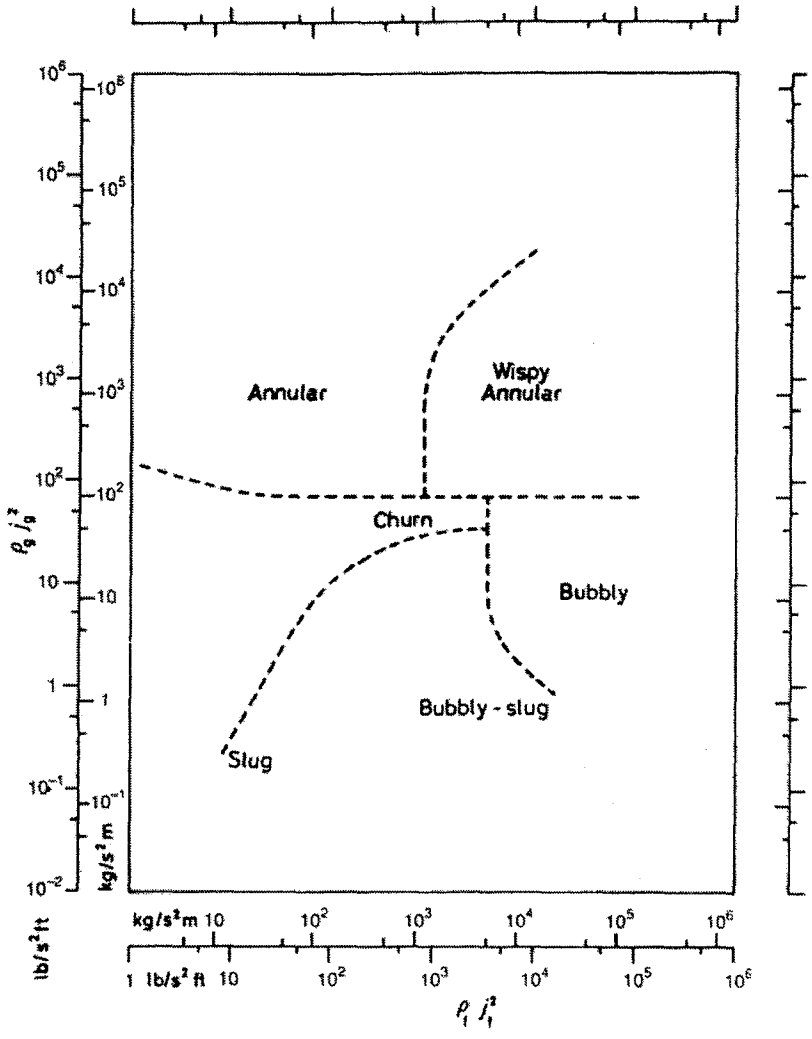


Figure 2.2: The flow pattern map by Hewitt and Roberts (1969).

flow is that proposed by Hewitt and Roberts (1969) (see Fig. 2.2) from observations of low-pressure air-water and high-pressure steam-water flows in vertical round tubes with internal diameters ranging from 10 to 30 mm.

It must be clear that flow pattern maps simply delineate approximate boundaries. Momentum fluxes alone (or a more generalised parameter) may be adequate to represent one particular transition, but it is very unlikely that this same parameter will also be suitable for a different transition governed by a different balance of forces. A more refined

approach is to treat each transition individually and to provide separate criteria based on phenomenological aspects of that transition.

A description of the most widely used transition criteria between the various flow regimes of vertical two-phase gas-liquid flow is carried out in the next section.

2.2.2 Flow pattern transitions

As seen before, flow pattern classification involves subjective criteria (like visual observation) which are sometimes prone to be questionable. A more scientific way of establishing boundaries between flow patterns involves measurement of flow properties such as local void fraction and phase velocities and also an indication of how these relate to a change of flow regime.

Flow pattern transition is an active area of research. Over the years, numerous studies and models have been developed so as to accurately describe and predict pattern transitions and associated phenomena. A summary of the cases of interest to this study is presented below,

a. Bubbly flow to slug flow transition. Possibly, the best criterion to corroborate the transition from bubbly flow to slug flow is that based on a critical gas volume fraction, $\bar{\varepsilon}_{crit}$. This idea was pursued by Taitel *et al.* (1980) and by Mishima and Ishii (1984) who suggested that $\bar{\varepsilon}_{crit} = 0.25$ and $\bar{\varepsilon}_{crit} = 0.30$, respectively. More sophisticated approaches were taken by Pauchon and Banerjee (1986) and by Lu and Zhang (1994). Pauchon and Banerjee postulated that the transition is related to the formation of 'void waves' (i.e., regions of high gas concentration in which coalescence is enhanced). They used an inviscid two-fluid formulation to determine the gaseous void propagation velocity and solved the governing equations using the method of characteristics and predicted that the transition from bubbly to slug flow

takes place when $\bar{\varepsilon}_{crit} = 0.26$. Other work on void waves includes that of Biesheuvel and Gorissen (1990) and Bouré (1997). Lu and Zhang (1994) postulated that the transition takes place when the interfacial area density (or interfacial surface area per unit volume), $\frac{P_I}{A}$, reaches a maximum (P_I is the interfacial perimeter). Their analysis was based on a combination of one-dimensional, steady-state, frictionless, fully developed momentum conservation equations for the gas and liquid phases, using interfacial closure relationships (e.g.,bubble drag coefficient, bubble diameter). Lu and Zhang's results gave a transition value of $\bar{\varepsilon}_{crit} = 0.30$ using refrigerant R-12 under adiabatic conditions. Good agreement between experiments and a modified theory incorporating heat addition effects was obtained for diabatic flows of refrigerant R-12.

b. Slug flow to churn flow transition. In the last twenty years or so, many studies were carried out, and on this particular transition. Basically, there are four main theories that provide explanations for the slug to churn transition in vertical pipes. Dukler and Taitel (1986), treat churn flow as an entrance phenomenon. They see churn flow as a case of unstable slug flow (with short liquid slugs and Taylor bubbles) which will evolve into a stable slug flow pattern further downstream through coalescence of the Taylor bubbles. Dukler and Taitel developed a relationship for the length of the entrance region, L_e, required to form stable slugs,

$$L_e = 42.6 d_T \left[\frac{U_M}{(g d_T)^{0.5}} + 0.29 \right], \tag{2.1}$$

where U_M is the mixture velocity, i.e., the sum of the superficial velocities of the two phases and d_T is the internal diameter of the tube.

This transition criterion appears to be heavily based on visual observations of the flow pattern. Moreover, an assessment of the validity of such a model is difficult

due to a disagreement concerning the definition of churn flow. As will be seen in Section 2.2.4, the type of flow that Dukler and collaborators refer to as churn flow may not be the same pattern recognised as churn flow by Hewitt and co-workers. This semantic problem will be clarified later.

The second school of thought (Brauner and Barnea, 1986) attributes the collapse of the liquid slug to excessive aeration of a slug unit. In other words, as the superficial gas velocity increases, the mean void fraction in the liquid slug reaches a critical value and this leads to the collapse of the liquid slugs due to bubble coalescence. This critical void fraction is assumed to be the same as that at the transition between slug and bubbly flow for the same mixture velocity, U_M. Therefore, the transition to churn flow will take place when the void fraction in the liquid slug, ε_{sl}, is greater than the bubble maximum volumetric package, taken as $\varepsilon_{max} = 0.52$. Brauner and Barnea give the following expression for the void fraction in the liquid slug,

$$\varepsilon_{sl} = 0.058 \left[d_c \left(\frac{2 f_m U_M^3}{d_T} \right)^{0.4} \left(\frac{\rho_L}{\sigma} \right)^{0.6} - 0.725 \right]^2 , \tag{2.2}$$

where,

$$d_c = \min \left[d_{c,disp}, d_{c,buoy} \right] , \tag{2.3}$$

$$d_{c,disp} = 2 \left(\frac{0.4\sigma}{g \Delta\rho} \right)^{0.5} , \tag{2.4}$$

$$d_{c,buoy} = \frac{3 \rho_L f_m U_M^2}{8 g \Delta\rho \cos\varphi} , \tag{2.5}$$

and φ is the inclination from the horizontal. The friction factor, f_m is given by,

$$f_m = 0.046 \left(\frac{\nu_L}{U_M d_T} \right)^{0.2}. \tag{2.6}$$

The third approach (Mishima and Ishii, 1984; Chen and Brill, 1997) attributes the transition to churn flow to the collapse of relatively short, highly aerated liquid slugs. This is caused by instabilities in the wake of Taylor bubbles. According to Mishima and Ishii (1984), the transition from slug to churn flow takes place when,

$$\varepsilon > \bar{\varepsilon}_{TB}, \tag{2.7}$$

where ε is the mean void fraction and $\bar{\varepsilon}_{TB}$ is the mean void fraction over the Taylor bubble. $\bar{\varepsilon}_{TB}$ is given by,

$$\bar{\varepsilon}_{TB} = 1 - 0.813 \left[\frac{(C_0 - 1) U_M + 0.35 \left(\frac{\Delta \rho g d_T}{\rho_L} \right)^{0.5}}{U_M + 0.75 \left(\frac{\Delta \rho g d_T}{\rho_L} \right)^{0.5} \left(\frac{\Delta \rho g d_T^3 \rho_L}{\eta_L^2} \right)^{\frac{1}{18}}} \right]^{0.75}. \tag{2.8}$$

The mean void fraction, ε is evaluated using a drift flux model,

$$\varepsilon = \frac{U_{GS}}{\left[C_0 U_M + 0.35 \left(\frac{g d_T \Delta \rho}{\rho_L} \right)^{0.5} \right]}, \tag{2.9}$$

with, $C_0 = 1.2 - 0.2 \left(\frac{\rho_G}{\rho_L} \right)^{0.5}$ for round tubes.

Chen and Brill (1997) postulate that the transition to churn flow takes place when,

$$\frac{L_{sl}}{L_u} < 0.15, \tag{2.10}$$

$$\varepsilon_{sl} > 0.52, \tag{2.11}$$

where L_{sl} is the length of the slug and L_u is the length of the slug unit (liquid slug plus Taylor bubble). ε_{sl} is the gas void fraction in the liquid slug.

For known physical properties, geometry and a given liquid flow rate, the superficial gas velocity at which the transition takes place is calculated by substituting the criteria in a set of conservation and closure equations.

The fourth theory (Nicklin and Davidson, 1962; McQuillan and Whalley, 1985; Jayanti and Hewitt, 1992) attributes the slug-to-churn transition to flooding of the liquid film surrounding the Taylor bubble. The links between flooding and churn flow are presented later in 2.2.4. For the moment, it suffices to say that the physical foundation of the criterion lies on the similarity of pressure drop and holdup characteristics between the phenomena of churn flow following flooding and "ordinary" churn flow (Govan *et al.*, 1991) and also on the fact that the gas velocity required to initiate flooding in a falling film of very small flow rate is approximately the same as that at the slug-to-churn transition (Wallis, 1961).

The model by Jayanti and Hewitt (1992) is presented below. It is an improvement of the methodology put forward by McQuillan and Whalley (1985) in that it accounts for the effect of the length of the Taylor bubble and to allow for turbulence in the falling film surrounding the Taylor bubble. According to Jayanti and Hewitt (1992), the transition takes place when,

$$\sqrt{U_{bS}^*} + m\sqrt{U_{fS}^*} > 1, \tag{2.12}$$

where U_{bS}^* and U_{fS}^* are dimensionless characteristic superficial velocities modified to represent the gas and liquid flow rates in the Taylor bubble region and m is the Taylor bubble length effect factor. These are given by,

$$U_{bS}^{*} = U_{bS}\left[\frac{\rho_G}{g d_T \Delta\rho}\right]^{0.5}, \tag{2.13}$$

$$U_{fS}^{*} = U_{fS}\left[\frac{\rho_L}{g d_T \Delta\rho}\right]^{0.5}, \tag{2.14}$$

$$U_{bS} = \left[1 - \frac{4\delta}{d_T}\right]\left[1.2U_M + 0.35\left(\frac{g d_T \Delta\rho}{\rho_L}\right)^{0.5}\right], \tag{2.15}$$

$$U_{fS} = U_{bS} - U_M, \tag{2.16}$$

$$m = \begin{cases} 1 & ; \text{ if } \frac{L_{TB}}{d_T} > 120 \\ 0.1928 + 0.01089\frac{L_{TB}}{d_T} - 3.754 \times 10^{-5}\left(\frac{L_{TB}}{d_T}\right)^2 & ; \text{ if } \frac{L_{TB}}{d_T} \leq 120. \end{cases} \tag{2.17}$$

L_{TB} is the length of the Taylor bubble calculated through a liquid phase mass balance,

$$U_{LS} = U_{sl}\left(1 - \varepsilon_{sl}\right)\frac{L_{sl}}{L_{sl} + L_{TB}} - U_{fS}\frac{L_{sl}}{L_{sl} + L_{TB}}, \tag{2.18}$$

where U_{sl} is the slug velocity, L_{sl} is the length of the slug, ε_{sl} is the void fraction in the liquid slug. Jayanti and Hewitt (1992) suggest that close to the transition $U_{sl} = U_M$, $L_{sl} = 12 d_T$ and $\varepsilon_{sl} = 0.5$.

An additional equation relating the falling film thickness, δ, and velocity, U_{fS}, is needed. This is given by the correlation by Brotz (1954),

$$U_{fS} = 39.66\frac{\delta}{d_T}\left\{g d_T \frac{\Delta\rho}{\rho_L}\left[1 - \left(1 - \frac{4\delta}{d_T}\right)^{0.5}\right]\right\}^{0.5}. \tag{2.19}$$

Jayanti and Brauner (1994) evaluated the performance of the above methods using the experimental data by Owen (1986) for vertical, air-water, adiabatic two-phase flows in a 20 m long, 31.8 mm internal diameter pipe (LOTUS facility). They found that the model by Taitel and Dukler (1986) implied that 'churn' flow would disappear after lengths between 200 and 360 tube diameters. Owen, however, observed churn flow at a distance of 625 diameters downstream to the point of water injection. Thus, at least for that case, this theory is not valid. The predictions of the Brauner and Barnea (1986) model were in line with Owen's experimental data at high liquid flow rates, but not at low flow rates. Jayanti and Brauner (1994) attributed this fact to the limitation of the Brauner and Barnea's model in predicting gas holdup in short liquid slugs and does not rule out the idea of excessive slug aeration as a mechanism for slug-to-churn transition. The model by Jayanti and Hewitt (1992), presented a much better prediction than that of McQuillan and Whalley (1985) for the whole range of liquid flow rates. This may be attributed to the inclusion of the column length effect parameter defined by Eq. 2.17.

Watson and Hewitt (1999) investigated experimentally the effect of pressure on the transition from slug to churn flow. They concluded that the gas superficial velocity required to trigger the transition decreases with increasing system pressure. Watson and Hewitt also compared the experimental data with the transition models presented above and the best performance was that of the model by Jayanti and Hewitt (1992).

Results from recent experiments on gas-liquid flow in vertical annuli (Das *et al.*, 1999a) strengthened the evidence that flooding in the Taylor bubble is the main mechanism behind the slug-to-churn transition. In annuli, the transition is marked by the collapse of asymmetric slug flow (the Taylor bubbles form open annular

rings) and by the restoration of symmetry in phase distribution. Das *et al.* pointed out that this fact indicates that the slug-to-churn transition initiates in the Taylor bubble region and that phenomena taking place in the liquid slug region, namely bubble coalescence (Barnea and Brauner, 1986) and Taylor bubble wake effects (Mishima and Ishii, 1984; Chen and Brill, 1997) cannot be used to explain the transition mechanism. Direct observation of the evolution of the flow field along the test section also ruled out the entry length effect (Taitel *et al.*, 1980) as a mechanism of transition. On the other hand, visual observations of elongation and collapse of Taylor bubbles with increasing gas flow rate favoured the flooding approach.

For the slug-to-churn transition, Das *et al.* (1999b) obtained a good prediction using the Jayanti and Hewitt (1992) model adapted for the annular geometry. The modifications to the Jayanti and Hewitt model are as follows,

1. the characteristic diameter in the dimensionless superficial velocities in an annulus is $(d_o + d_a)$, where d_o and d_a are the inner and outer annulus diameters;
2. the velocity of the rising Taylor bubble is given by,

$$U_{bS} = 1.2U_M + 0.323\sqrt{g\,(d_o + d_a)}; \tag{2.20}$$

3. the flooding constant (Eq. 2.12) is taken as 0.85.

c. Churn flow to annular flow transition. As the superficial gas velocity increases, the interfacial shear stress becomes significant and flow reversals characteristic of churn flow cease to exist. The liquid film gets thinner, the flow becomes unidirectional and the annular flow regime is established. Ripples and disturbance waves start to appear, and the pressure gradient eventually begins to increase with increasing gas superficial velocity. A number of definitions for the transition to annular flow

may arise from these processes. These are as follows, (i) at the flow reversal point, i.e., the point where the gas flow rate is sufficient to carry all the liquid upwards; (ii) at the pressure drop minimum (see Fig. 2.8), that occurs due to the decreasing trends of pressure gradient with increasing gas flow rate observed in fully developed churn flow; (iii) at the condition of zero mean wall shear, which is negative in churn flow and positive in annular flow; and (iv) at the point of continuously positive local wall shear stress, which must take place when the liquid film flow is entirely unidirectional.

Of all the above criteria, the flow reversal condition is the mostly used due to its easy experimental observation and because there are simple relationships to determine it. The wall shear stress conditions are difficult to evaluate as they require detailed measurements close to the wall. The minimum pressure gradient criterion is somewhat dubious. As will be seen in Section 2.2.4, for some conditions, the pressure drop minimum occurs in fully developed annular flow. The visual observations of the flow regime transitions by Owen (1986) support this argument. Also, the pressure gradient also includes the gravitational component, and thus does not wholly reflect the frictional or interfacial behaviour.

Taitel *et al.* (1980) suggested that the transition to annular flow is governed by the behaviour of the entrained droplets. The limiting gas velocity, i.e., the gas velocity at which the entrained droplets become suspended, is given by,

$$U_{GS} = 3.2 \left[\frac{g\sigma \left(\rho_L - \rho_G\right)}{\rho_G^2} \right]^{1/4}. \tag{2.21}$$

A more used criterion is that proposed by Hewitt and Wallis (1963) (also Wallis, 1969), which uses the flooding correlation,

$$\sqrt{U^*_{GS}} + \sqrt{U^*_{LS}} \approx 1, \tag{2.22}$$

with zero liquid downflow, U^*_{LS} equal to zero. The dimensionless superficial velocities in Eq. 2.22 are given by,

$$U^*_{GS,LS} = U_{GS,LS}\sqrt{\frac{\rho_{G,L}}{gd_T\left(\rho_L - \rho_G\right)}}. \tag{2.23}$$

Alternative dimensionless velocities can be defined in terms of the surface tension, σ (Kutateladze numbers). A correlation based on these is as follows (Pushkina and Sorokin, 1969),

$$K_G = 3.2, \tag{2.24}$$

$$K_G = U_{GS}\frac{\sqrt{\rho_G}}{\left[g\sigma\left(\rho_L - \rho_G\right)\right]^{1/4}}. \tag{2.25}$$

Whalley (1996) presents a simplified but very illustrative analysis of correlations for the transition to fully cocurrent annular flow.

d. Annular flow to wispy-annular flow transition. Wallis (1969) suggests, based on electrical probe measurements of liquid 'wisps' in the gas core, that a criterion for this transition is,

$$U_{GS} = \left(7 + 0.06\frac{\rho_L}{\rho_G}\right)U_{LS}, \tag{2.26}$$

for the case where $U^*_{LS} > 1.5$. According to Collier and Thome (1994), the wispy-annular region corresponds to the region where U^*_{GS} is greater than unity and U^*_{LS} is greater than 2.5 to 3.

2.2.3 Annular flow

Annular flow is the most important flow regime because of its extensive practical application. In the majority of cases of interest, the flow is turbulent in both phases and there is a substantial amount of liquid entrained as droplets in the vapour core. Understanding the droplet generation process and the behaviour of droplets whilst travelling in the core are key parameters to the development of hydrodynamic and heat transfer models for annular flow.

'Ideal annular flow', i.e., that in which the gas and liquid phases are totally separated (no entrainment) and the interface is *smooth*, rarely occurs in practice. This is because the gas flow rates are high enough to trigger the appearance of interfacial waves and of droplets entrained in the gas core. The pioneering works of Levy (1952), Calvert and Williams (1955), Anderson and Mantzouranis (1960) and Hewitt (1961) (an extension of the Dukler (1960) analysis of falling films for upwards co-current flow) provided analytical solutions for this ideal case. In spite of their limited range of applicability, these studies were valuable as they introduced basic concepts, such as the triangular relationship (Hewitt, 1961), which are used in modelling codes up to this date.

The liquid film in annular flow

In annular flow, the liquid film is not of a simple nature. Rather, it is covered by waves of diverse lengths and amplitudes. The small-wavelength waves (ripples) are present throughout the range of gas and liquid flow rates. However, above a critical liquid film Reynolds number, large wavelength, high amplitude waves start to form. These are called disturbance waves. Several of their unique characteristics have been listed by Levy (1999). These are as follows,

1. the ratio of the wave amplitude to the mean film thickness is of the order of 5;

2. the velocity of the disturbance waves is, as a rule of thumb, ten per cent of the superficial gas velocity;

3. the wave surface is not smooth, and within the waves there are many sub-peaks and troughs;

4. the wave is rather long by comparison to its amplitude;

5. the wave spacing is not uniform and can have a multipeak distribution function. The wave spacing decreases as the liquid flow is increased and the gas flow rate is increased;

6. the wave frequency is initially high (near the liquid injector) and drops as the waves coalesce. The wave frequency increases with liquid flow rate;

7. waves never break up or pass through each other. Sometimes, they merge to form one high-velocity wave which slows down thereafter.

It is believed that disturbance waves are created through the same mechanism ~~by which~~ turbulent bursts in single phase flow boundary layers. Martin and Azzopardi (1985) compared the the initial frequencies of these waves in vertical annular flow with those of turbulent bursts in single phase water flow. Table 2.1 summarises the response of disturbance waves to changes in various system parameters (Wolf, 1995).

A detailed study of the structure of liquid films in vertical annular flows was carried out by Wolf (1995). He made use of experimental and analytical tools to gather both instantaneous, local and average information about the behaviour of the liquid film in annular flow. Amongst many findings which confirmed and quantified some of the main characteristics of disturbance waves described above, those which involved the analysis of wall shear stress and film thickness time traces are the most interesting. Cross correlation

Table 2.1: Response of disturbance waves to variations in system parameters.

Increasing	Wave velocity	Wave frequency	Coherence
Gas mass flux	↗	↗	↗
Liquid mass flux	—	↗ (slightly)	—
pipe diameter	—	↘	↘
Gas density	↘	↗	not investigated
axial distance	—	↘	not investigated

of these signals indicated an apparent lag between the peak in shear stress and a peak in film thickness. This also allowed an estimate of the flow rates in the substrate film and in the disturbance waves, respectively.

More recently, a very detailed study on the turbulent structure of the liquid film in annular flow was carried out by Vassallo (1999). Vassallo carried out measurements using hot-film anemometry and concluded that, at conditions far from the flow reversal boundary ($U^*_{GS} \approx 2.4$), the velocity distribution in the liquid film approaches the single phase universal velocity (log-law) profile. At low superficial gas velocities, where the film is thicker, he suggested that a modified log-law should be used with a smaller value of the intercept constant. This is an indication that the wall shear is affected by the film structure. In fact, the structure of the film increases the wall shear stress for a given velocity profile in the film.

Droplets in annular flow

Droplets are generated by the shear action of the gas phase flowing over the liquid film. This fact can be verified through an experiment in which the measurement of the liquid film flow rate of an adiabatic annular flow is carried out at points downstream of the

liquid inlet (the liquid film is carefully introduced, e.g., using a porous wall section). It can be observed that the liquid film flow rate decreases monotonically with distance.

An experimental investigation of the process of droplet creation (Azzopardi and Whalley, 1980) showed that this phenomenon is strongly correlated to the inception of disturbance waves in the liquid film. In an experiment in which annular flow was artificially created by introducing the liquid film via a porous sinter, they noticed that, if the film flow rate was set at a value just below that required for disturbance wave creation and a small volume of liquid was suddenly injected into the film, a small number of waves were created. The flow at the top of the pipe was observed by means of a high-speed ciné camera used in conjunction with a special axial viewing device. Before the waves were created no drops were present. Subsequent to injection, drops were seen; the number of drops increased as the waves approached the end of the pipe. Once the waves had passed out of the pipe, no droplets were seen.

It has been suggested (Cousins *et al.*, 1965) that film flow rate below which no entrainment takes place should be defined by a critical film Reynolds number, $Re_{LFC} = \dot{m}_{LF} d_T \eta_L^{-1}$. Four criteria for disturbance wave inception and entrainment are summarised below.

1. The criterion of Ishii and Grolmes (1975). In this criterion, the authors suggested that the mechanism behind the start of entrainment is the penetration of the boundary layer of the gas. They proposed a critical Reynolds number,

$$Re_{LFC} = \left[\frac{y^+}{0.347} \left(\frac{\rho_L}{\rho_G} \right)^{1/2} \frac{\eta_G}{\eta_L} \right]^{3/2}, \tag{2.27}$$

   where y^+ is the dimensionless distance from the wall (assumed to be equal to 10).

2. The criterion of Asali *et al.* (1984). Asali *et al.* used a disturbance wave stability analysis to determine Re_{LFC}. They found that the critical Reynolds number was a

weak function of the group $\frac{\eta_L}{\eta_G}\sqrt{\frac{\rho_G}{\rho_L}}$ and put forward a graphical correlation. This was then fitted by Owen (1986),

$$Re_{LFC} = \exp\left[5.305 + 0.657\left(\frac{\eta_G}{\eta_L}\right)\left(\frac{\rho_L}{\rho_G}\right)^{0.5}\right]. \tag{2.28}$$

3. The criterion of Owen (1986). Owen modified the correlation of Asali *et al.* (1984) to account for evaporation of the liquid film and obtained,

$$Re_{LFC} = \exp\left[5.8405 + 0.4249\left(\frac{\eta_G}{\eta_L}\right)\left(\frac{\rho_L}{\rho_G}\right)^{0.5}\right]. \tag{2.29}$$

4. The criterion of Azzopardi (1997). Azzopardi revisited an existing criterion (Azzopardi *et al.*, 1983), which, by dimensional analysis, suggested that the appropriate dimensionless groups to correlate the liquid Reynolds number at the inception of entrainment were the Ohnhezoge number, $On = \frac{\eta_L}{\sqrt{\sigma\rho_L d_T}}$ and the ratio of the Weber number and the gas Reynolds number, $\frac{We}{Re_G} = \frac{\eta_G U_{GS}}{\sigma}$. Figure 2.3 illustrates the graphical correlation suggested by Azzopardi (1997).

Most of the data used in the above correlations to develop the mentioned criteria were obtained under adiabatic conditions. However, use was made of various fluid combinations to investigate the effect of surface tension and liquid viscosity.

A description of the mechanisms of atomisation by which droplets are created will be dealt with in Chapter 5. Here, it is sufficient to say that there are two main mechanisms of droplet formation, bag break-up and ligament break-up (Azzopardi, 1983). The former is characteristic of lower gas and liquid flow rates and the latter is observed at higher flow rates. Perhaps a more important fact to notice at this point is that the amount of liquid flowing as entrained droplets is extremely sensitive to the method of liquid injection. This behaviour is illustrated in Fig. 2.4 where data obtained at Harwell (Gill *et al.*,

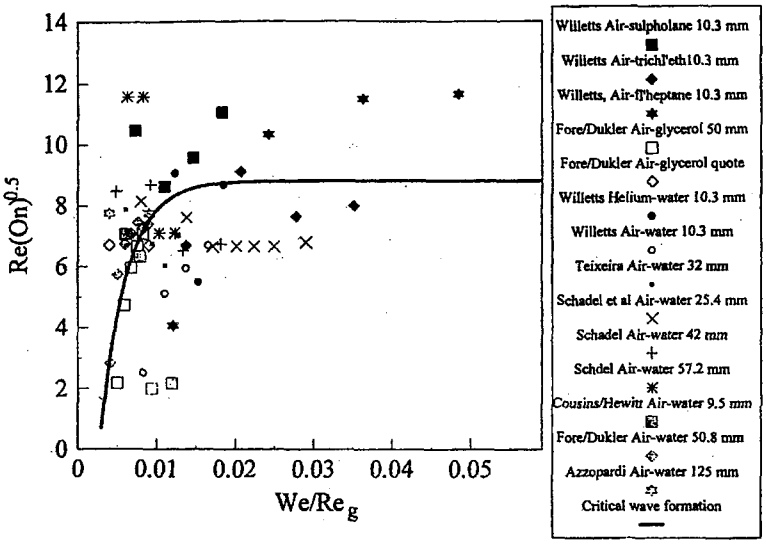


Figure 2.3: Correlation for inception of entrainment (Azzopardi, 1997).

1963, 1964; Gill and Hewitt, 1966) are shown for the extreme cases of porous sinter and central jet injectors respectively. Comparisons of calculated values with these data are also presented. The measured liquid film flow rate for both centre jet and porous wall injectors is plotted as a function of distance from the injection point for the same inlet flow rates and pressure. The marked differences, even after 200 inches (approximately 5 m), between the two injectors will be noted. However, related variations occur in liquid film thickness and pressure gradient and, when the results for film flow rate are compared with those predicted by the relationships for turbulent film flow (Hewitt, 1961), the predicted values are close to the measured ones.

The results in Fig. 2.4 lead to the conclusion that the annular flow problem has more than one possible solution and, in an experiment in which the annular flow pattern is created artificially, the method of injection of the liquid phase is extremely important in determining dependent flow parameters.

It has been shown (Hewitt and Hall-Taylor, 1970) that, at very large distances (several hundred diameters), adiabatic annular flows tend to *hydrodynamic equilibrium*, i.e., a

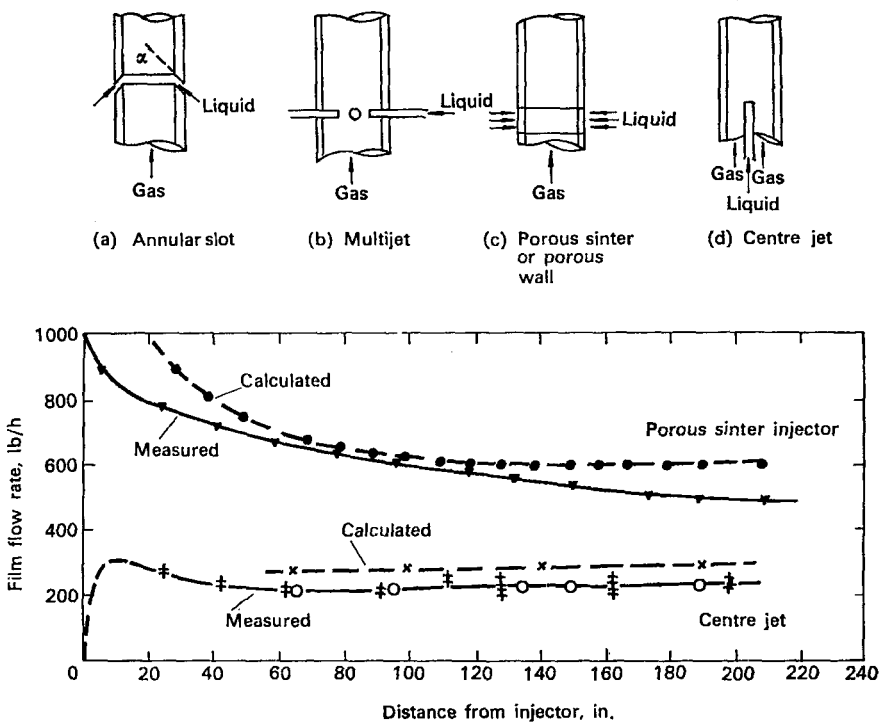


Figure 2.4: Data for film flow rate obtained by Gill and co-workers for different liquid injection devices. Conversion factors: 1 in = 25.4 mm, 1 lb h^{-1} = 1.26 × 10^{-4} kg s^{-1}.

state in which the rate of droplet deposition is approximately equal to that of droplet entrainment and the entrained fraction (mass flow rate of entrained liquid divided by the total liquid flow rate) remains approximately constant. The rates cannot become exactly equal, and true equilibrium cannot be obtained, because the decrease in gas density as the gas passes down the tube alters the position of equilibrium. Nevertheless, such large *equilibrium* distances are not realistic of industrial equipment which undoubtedly operate in the *entry region.*

The challenge of measuring separately rates of entrainment and deposition remained through the 1970's and part of the 1980's. One of the earliest correlations for droplet entrainment and deposition was proposed by Hutchinson and Whalley (1973). The correlation used the concept of hydrodynamic equilibrium between entrainment and deposition and assumed a similarity between the equation for the two processes. The entrainment correlation is based on an equilibrium concentration, C_E, which is sought to be proportional to the following dimensionless group,

$$C_E \propto \left(\frac{\tau_I \delta}{\sigma}\right), \tag{2.30}$$

Hutchinson and Whalley claimed that the dimensionless parameter in the equation above would be suitable for representing the entrainment phenomenon as it is the ratio between disruptive (interfacial shear) and containment (surface tension) forces acting on the liquid film. The entrainment rate, E, is measured in units of mass of fluid leaving unit area of tube wall per unit time.

The rate of droplet deposition, D, can be described by the following equation (Cousins and Hewitt, 1968),

$$D = k_D C_E, \tag{2.31}$$

where D is the droplet deposition rate (mass per unit area of tube wall per unit time) and k_D is a droplet mass transport or deposition coefficient. If approximate equilibrium has been reached the deposition and entrainment rates are almost equal, and so E can be calculated from the equation above.

Later work dealt with entrainment and deposition rates in a different way. Ueda (1979) measured the axial film flow rate gradient at different distances and used information about the rate of deposition to derive the entrainment rate. Ueda presented the following relationship in dimensional form (SI units),

$$E = 3.54 \times 10^{-3} \left[\frac{\tau_I}{\sigma} \left(\frac{U_{LS}}{\sigma} \right)^{0.60} \right]^{0.57}, \tag{2.32}$$

valid for $\frac{\tau_I}{\sigma} \left(\frac{U_{LS}}{\sigma} \right)^{0.60} > 120$. As pointed out by Azzopardi (1997), the main disadvantage of using such an approach is that it involves two unknowns, viz., the rates of droplet entrainment and deposition, and only one equation.

By injecting a tracer into the film at a known concentration, it is possible to assess the rates of droplet entrainment and deposition independently by measuring the profile of concentration in the film along the pipe. A combination of the mass balance equations for the liquid film and for the concentration of the tracer in the liquid film gives (Azzopardi, 1997),

$$\frac{d}{dz} \ln \left(\frac{c_{LF}}{c_E} - 1 \right) = \frac{4D}{\dot{m}_L d_T} \left[e \left(1 - e \right) \right]^{-1}, \tag{2.33}$$

where c_{LF} is the local concentration of tracer in the liquid film and c_E is the mixing-cup concentration of tracer defined as, at the film inlet, $c_E = c_{LF,0} \left(1 - e_0 \right)$.

Equation 2.33 can be combined with the mass balance on an element of liquid film,

$$\frac{d}{dz} \dot{m}_{LF} = \frac{4}{d_T} \left(D - E \right), \tag{2.34}$$

to give D and E. This technique was firstly proposed by Quandt (1965) and used by many investigators ever since.

One of the most comprehensive set of correlations for entrainment and deposition of droplets in annular flow is that proposed by Govan (1990). He correlated 2354 data points (1366 for entrainment and 988 for deposition) from 22 sources, encompassing 9 different gas-liquid combinations. The equations by Govan are as follows,

$$E = \begin{cases} 0 & \text{if } \dot{m}_{LF} \leq \dot{m}_{LFC} \\ 5.75 \times 10^{-5} \dot{m}_{GC} \left[\frac{\rho_L d_T}{\sigma \rho_G^2} (\dot{m}_{LF} - \dot{m}_{LFC})^2 \right]^{0.316} & \text{if } \dot{m}_{LF} > \dot{m}_{LFC}, \end{cases} \tag{2.35}$$

where $\dot{m}_{LFC}$ is a critical liquid film mass flux below which no entrainment takes place. It is given by (Owen, 1986),

$$\dot{m}_{LFC} = \frac{\eta_L}{d_T} \exp \left[5.8504 + 0.4249 \left(\frac{\eta_G}{\eta_L} \right) \left(\frac{\rho_L}{\rho_G} \right)^{0.5} \right]. \tag{2.36}$$

The droplet deposition rate is expressed as,

$$D = k_D C, \tag{2.37}$$

where C is the concentration of droplets in the core,

$$C = \frac{\dot{m}_{LE}}{\frac{\dot{m}_{GC}}{\rho_G} + \frac{\dot{m}_{LE}}{\rho_{LE}}}, \tag{2.38}$$

and the deposition transfer coefficient, k_D, is calculated as follows,

$$k_D = \begin{cases} 0.18 \left(\frac{\sigma}{\rho_G d_T} \right)^{0.5} & \text{if } \frac{C}{\rho_G} \leq 0.3 \\ 0.083 \left(\frac{\rho_G}{C} \right)^{0.65} \left(\frac{\sigma}{\rho_G d_T} \right)^{0.5} & \text{if } \frac{C}{\rho_G} > 0.3. \end{cases} \tag{2.39}$$

Plots of the entrainment and deposition correlations are shown in Figs. 2.5 and 2.6. Considerable scatter is present in both distributions.

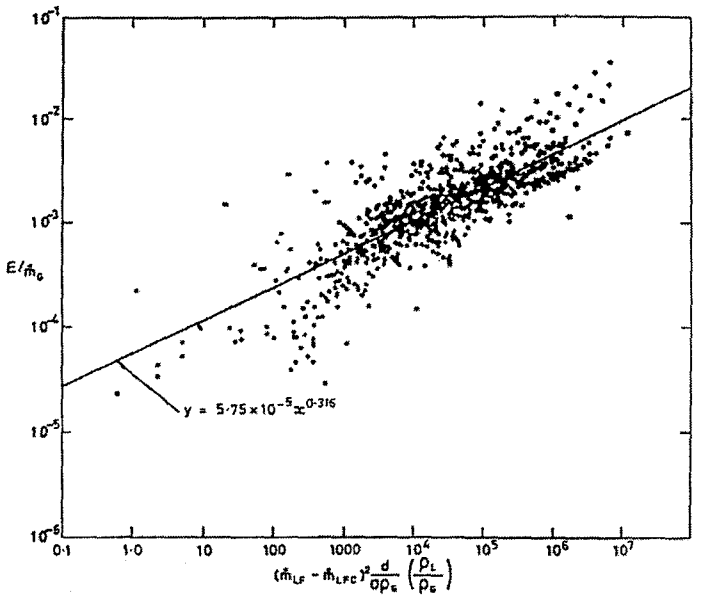


Figure 2.5: The correlation for droplet entrainment rate by Govan (1990).

The set of correlations for entrainment and deposition rates by Schadel *et al.* (1990) is another example of a droplet interchange model. This is summarised below.

$$\frac{E}{U_{GS}\sqrt{\rho_L \rho_G}} = \frac{k_a}{\pi d_T}\left(\dot{M}_{LF} - \dot{M}_{LFC}\right), \tag{2.40}$$

where $k_a = 4.97$, 4.36 and 4.33×10^{-4} m s kg^{-1} for $d_T = 25.4$, 42.0 and 57.2 mm, respectively.

$$D = \begin{cases} \frac{0.034}{d_T^{0.6}} \frac{\dot{M}_{LE}}{\dot{V}_G} & \text{if } \frac{\dot{M}_{LE}}{\dot{V}_G} \leq \frac{0.078}{d_T^{0.6}} \\ \frac{0.021}{d_T^{0.6}} & \text{if } \frac{\dot{M}_{LE}}{\dot{V}_G} > \frac{0.078}{d_T^{0.6}}, \end{cases} \tag{2.41}$$

where $\dot{V}_G$ is the volumetric flow of gas in m^3 s^{-1}.

Recent droplet interchange studies were presented by Azzopardi and Zaidi (2000) and Kataoka *et al.* (2000). Azzopardi and Zaidi (2000) applied the light scattering (Malvern) technique to obtain further entrainment data in a 38 mm internal diameter pipe. Kataoka

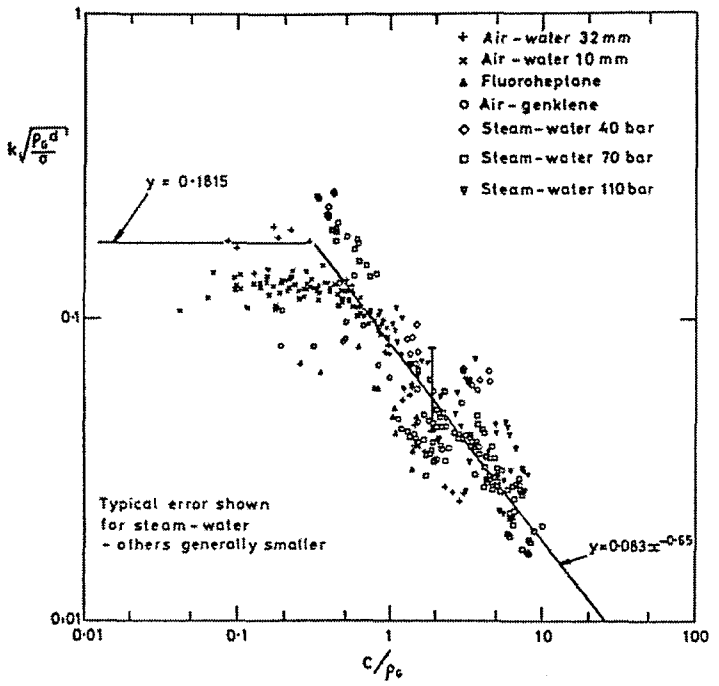


Figure 2.6: The correlation for droplet deposition rate by Govan (1990).

et al. proposed new correlations for entrainment and deposition rates. From the point of view of improvement of current annular flow predictions, it is unlikely that these would offer any benefit since they are based on a database already used in previous studies (Govan *et al.*, 1988; Govan, 1990).

Although remarkable progress has been made towards a better understanding and prediction of droplet entrainment and deposition in annular flow, there is still a number of phenomena yet to be explored in this fascinating field. As will be seen in this thesis, the effect of physical properties (mainly of non-aqueous systems), the droplet flow behaviour in the proximity to the churn flow boundary and the effect of the presence of an imposing heat flux are some of the challenges faced by those who attempt to improve the models for such flows.

Annular flow modelling

A mass and momentum balance over the incremental length of pipe in which the flow is in the annular regime provides the following conservation equations (see Fig. 2.7.a),

mass flow rate of the liquid film,

$$\frac{d}{dz}\dot{m}_{LF} = \frac{P_I}{A}(D - E), \tag{2.42}$$

mass flow rate of entrained droplets,

$$\frac{d}{dz}\dot{m}_{LE} = \frac{P_I}{A}(E - D), \tag{2.43}$$

momentum of liquid film,

$$-(1-\varepsilon_C)\frac{dp}{dz} - (1-\varepsilon_C)\rho_L g + \frac{P_I \tau_I}{A} - \frac{P_{wL}\tau_{wL}}{A} + \frac{P_I}{A}(DU_{pd} - EU_{pc}) = 0, \tag{2.44}$$

momentum of gas core,

$$-\varepsilon_C \frac{dp}{dz} - \varepsilon_C \rho_G g - \frac{P_I \tau_I}{A} - F_d \varepsilon_C = 0, \tag{2.45}$$

momentum of entrained droplets,

$$-\varepsilon_C \varepsilon_d (\rho_L - \rho_G) + F_d \varepsilon_C - \frac{P_I}{A}(DU_{pd} - EU_{pc}) = 0. \tag{2.46}$$

In the above equations, ε_C is the fraction of the cross-sectional area of the pipe, A, occupied by the core (liquid plus entrained droplets). The entrained droplets occupy a fraction ε_d of the core or a fraction $\varepsilon_C \varepsilon_d$ of the pipe cross section. The liquid film occupies a fraction $(1 - \varepsilon_C)$. P_{wL} is the portion of the pipe perimeter in contact with the liquid phase. P_I is the interfacial perimeter. F_d is the resultant drag force per unit volume on the droplets. E and D are the rates of droplet entrainment and deposition per unit

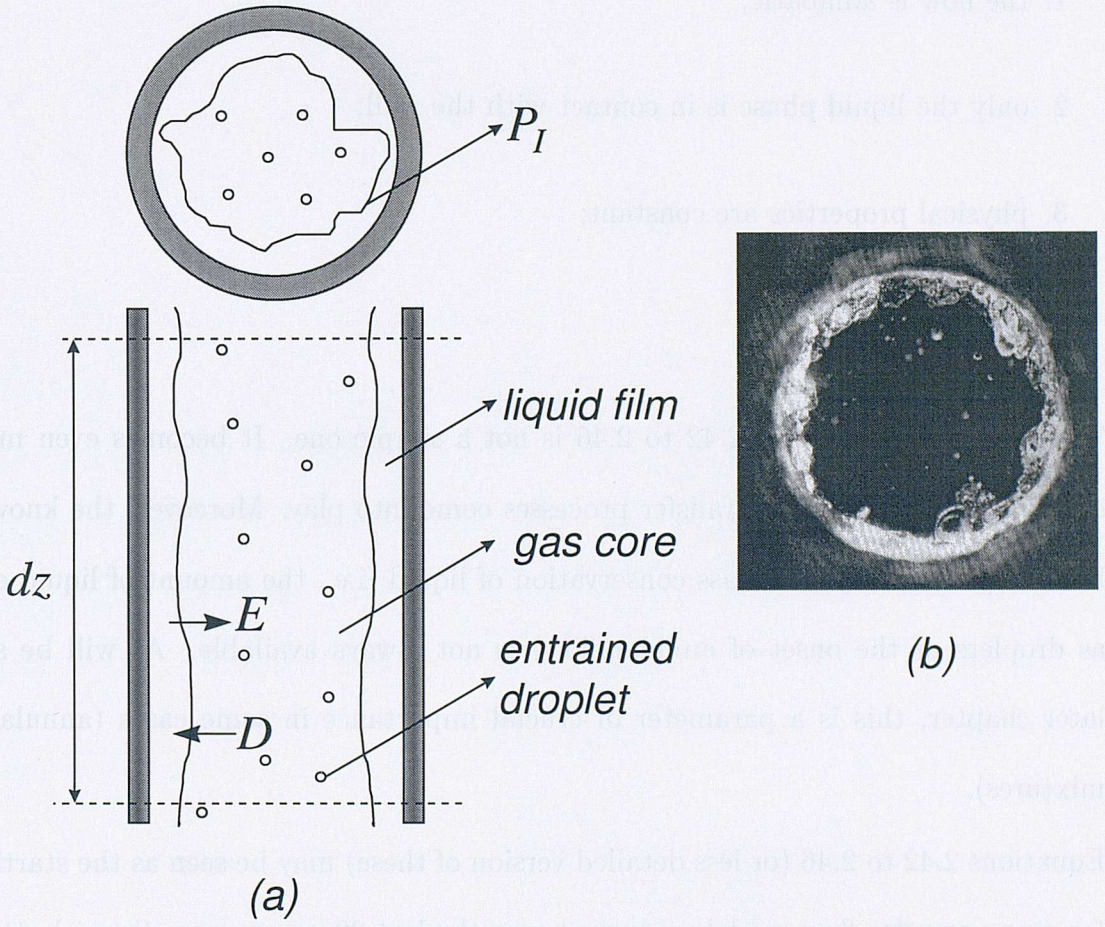


Figure 2.7: The incremental length of vertical pipe in annular flow.

interfacial area. U_{pc} and U_{pd} are the velocities of droplets at the moment of entrainment and of deposition, respectively. Figure 2.7.b, an axial-view photograph from Hewitt and Hall-Taylor (1970), serves to illustrate the liquid and gas fields and the interface structure. In order to derive the above set of equations, the following assumptions were made,

1. the flow is adiabatic;

2. only the liquid phase is in contact with the wall;

3. physical properties are constant;

4. $\frac{\partial}{\partial t} = 0$.

The task of solving Eqs. 2.42 to 2.46 is not a simple one. It becomes even more difficult when heat and mass transfer processes come into play. Moreover, the knowledge of boundary conditions for mass conservation of liquid (i.e., the amount of liquid entrained as droplets at the onset of annular flow) is not always available. As will be seen in a later chapter, this is a parameter of crucial importance in some cases (annular flow of mixtures).

Equations 2.42 to 2.46 (or less detailed version of these) may be seen as the starting point for many annular flow models proposed over the last 30 years or so. Several attempts to simplify these equations by introducing assumptions and new closure relationships were carried out by many investigators. Amongst many of such models, one may cite those of Moeck and Stachiewicz (1972), Whalley *et al.* (1974), Dobran (1983), Schadel *et al.* (1990), Govan (1990), Nigmatulin *et al.* (1996), and Fu and Klausner (1997).

The objective of this section is not to review the development of each model, but rather to concentrate on the issues regarding the development of the model that is employed in the present study.

A recourse which simplifies considerably the momentum equations presented above is to treat the droplet core as a homogeneous mixture. By doing so, it is hypothesised that the flow in the droplet core is that of a fluid with physical properties averaged over the proportion of each phase in the homogeneous mixture. Moreover, closure relationships for, say, the interfacial shear stress can be devised and correlated based on such a hypothesis. Usually, the influence of the liquid film on the gas core flow is expressed through the interfacial friction faction, f_I. From a single phase flow analogy,

$$f_I = \frac{2\tau_I}{\rho_C U_C^2} = f\left(Re_G, \epsilon\right), \tag{2.47}$$

where ϵ is the equivalent sand roughness of the film in m.

In pursuance of an expression for f_I which would give reliable predictions for annular two-phase flow, many authors proposed empirical correlations between ϵ and the thickness of the liquid film, δ (Gill *et al.*, 1963). These would serve to provide the link between the film thickness and interfacial shear stress and, eventually, pressure drop. Examples of such correlations are those by Wallis (1969),

$$f_I = f_G\left(1 + 360\frac{\delta}{d_T}\right), \tag{2.48}$$

where,

$$f_G = 0.079 Re_G^{-0.25}, \tag{2.49}$$

and by Hewitt and Whalley (1978),

$$f_I = f_{SC}\left[1 + 24\left(\frac{\rho_{LF}}{\rho_G}\right)^{1/3}\frac{\delta}{d_T}\right], \tag{2.50}$$

where f_{SC} is the friction factor for a single phase flow in a tube with the same diameter, homogeneous core density ρ_C, homogeneous core velocity U_C and viscosity equal to that

of the gas phase, calculated using the Blasius friction factor relationship (Eq. 2.49).

A more refined relationship for f_I was later put forward by Owen (1986), who showed that the turbulent mixing length in the gas core is reduced in the presence of droplets. The relationship for f_I was adapted from the classical Nikuradse equation and is as follows,

$$\sqrt{\frac{2}{f_I}} = A_r + \frac{1}{K_{tp}}\left[\ln\left(\frac{r_I}{\epsilon_e}\right) - 1.5 + \frac{2\delta}{r_T}\ln\left(\frac{r_T}{\delta}\right)\frac{\delta}{r_T}\right], \tag{2.51}$$

where r_I and r_T are the interface and tube radius, respectively. A_r is the Nikuradse sand roughness parameter determined experimentally. ϵ_e is the effective interfacial roughness height, which only affects the flow in the gas core if ϵ exceeds the laminar layer in the gas core as follows,

$$\epsilon_e = \epsilon - \frac{5d_T}{Re_G}\sqrt{\frac{2}{f_G}}. \tag{2.52}$$

The von Kármán constant, K_{tp}, was correlated by,

$$K_{tp} = \exp\left(-1.9786 + 0.9381\frac{\rho_G U_{GS}^2}{\rho_C U_C^2}\right). \tag{2.53}$$

Another simplifying assumption is the one regarding the velocity distribution in the liquid film. In many applications, the liquid film Reynolds number is such that, by analogy with single phase flow, some turbulence would be occurring. Hewitt and Hall-Taylor (1970) showed that single phase flow theories give satisfactory predictions of parameters such as film flow rate and thickness. The film flow rate in dimensionless form is given by,

$$\dot{M}_{LF}^{+} = \frac{\dot{M}_{LF}}{\pi d_T \eta_L}\int_0^{\delta^+} u_{LF}^{+} d\mathrm{y}^{+}, \tag{2.54}$$

where y^{+} and δ^{+} are the co-ordinate $\mathrm{y} = r_T - r$ and the film thickness in dimensionless form. These are given by,

$$\mathrm{y}^+ = \frac{\rho_L u^* \mathrm{y}}{\eta_L}, \tag{2.55}$$

and,

$$\delta^+ = \frac{\rho_L u^* \delta}{\eta_L}. \tag{2.56}$$

u^+_{LF} is the dimensionless liquid film velocity given by,

$$u^+_{LF} = \frac{u_{LF}}{u^*}, \tag{2.57}$$

where u^* is the friction velocity,

$$u^* = \sqrt{\frac{\tau_w}{\rho_L}}. \tag{2.58}$$

Typically, the von Kármán or Universal velocity profile is used. This is given by,

$$u^+_{LF} = \begin{cases} \mathrm{y}^+ & \text{for } \mathrm{y}^+ \leq 5 \\ -3.05 + 5\ln(\mathrm{y}^+) & \text{for } 5 < \mathrm{y}^+ \leq 30 \\ 5.46 + 2.5\ln(\mathrm{y}^+) & \text{for } \mathrm{y}^+ > 30. \end{cases} \tag{2.59}$$

Integration of the equations above gives the following relationships for the dimensionless liquid film flow rate,

$$\dot{M}^+_{LF} = \begin{cases} \frac{1}{2}\delta^{+2} & \text{for } 0 < \delta^+ \leq 5 \\ 12.45 - 8.05\delta^+ + 5\delta^+\ln(\delta^+) & \text{for } 5 < \delta^+ \leq 30 \\ -214 + 8\delta^+ 2.5\delta^+\ln(\delta^+) & \text{for } \delta^+ > 30. \end{cases} \tag{2.60}$$

The liquid film in annular flow is usually very thin and the effect of curvature can be, most of the times, neglected. In this case, a force balance on the liquid film gives (Hewitt and Hall-Taylor, 1970),

$$\tau\,(y) \approx \tau_I \approx \text{constant}, \tag{2.61}$$

and Eq. 2.58 can be approximated by,

$$u^* = \sqrt{\frac{\tau_I}{\rho_L}}. \tag{2.62}$$

Equations 2.60 to 2.62 provide a unique triangular relationship (Hewitt, 1961) between the liquid film flow rate, the liquid film thickness and the interfacial shear stress. This means that at any point within the channel, if two of the parameters are known, the third one can be calculated through Eqs. 2.60 to 2.62. In such an analysis, the shear stress is often superseded by the pressure gradient, calculated through the force balance,

$$\frac{dp}{dz} = \frac{4}{d_T - 2\delta}\tau_I. \tag{2.63}$$

Experimental validation of the triangular relationship has been carried out using the extensive database of Gill *et al.* (1963, 1964) and Gill and Hewitt (1966) (see Hewitt and Hall-Taylor, 1970).

In Chapter 4, an annular flow model which deals with phase change of multicomponent mixtures is derived. The modelling issues discussed above will be briefly reviewed and some new features will be introduced.

Recent developments

Some of the recent developments in annular flow modelling employed Computational Fluid Dynamics (CFD) tools in order to gain further understanding about the behaviour of disturbance waves and the liquid film. The studies by Wolf (1995) and Jayanti and Hewitt (1997) confirmed that the disturbance waves are zones of turbulent recirculation travelling over a laminar substrate. They were also able to quantify the roles of interfacial

shear and resolved normal (body) forces in the interaction between the gas and liquid phases. They found that the latter contributes for only about 10% of the inter-phasis force.

As far as heat transfer is concerned, Jayanti and Hewitt (1997) showed that, by considering the heat transfer in the wave and substrate regions separately, better agreement between predicted and experimental heat transfer coefficients for evaporation can be found. One-dimensional analyses which use the logarithmic profile approach coupled with the Reynolds analogy between momentum and heat transfer often overestimate the heat transfer by as much as 50% (Hewitt and Hall-Taylor, 1970). This matter is explored further in Section 2.3.4

A word of caution about CFD predictions must be said in the sense that, although they help elucidating the prevailing mechanisms in wavy interfaces, they are far from generating definitive answers. A number of hypotheses is generally made, which may compromise the local physics of the phenomena is some cases.

2.2.4 Churn flow

Characteristics of the flow regime

Churn flow is probably the most complex, least understood regime in gas-liquid flow in vertical pipes. As seen in the literature, disagreement between authors concerns not only to issues regarding the physics of the flow or the mechanisms of transition to the churn flow regime (Nicklin and Davidson, 1962; Mishima and Ishii, 1984; Dukler and Taitel, 1986) but also questions about the existence of churn flow as a separate regime (Mao and Dukler, 1993; Hewitt and Jayanti, 1993; Jayanti *et al.*, 1993).

Here, churn flow is defined as a regime which occurs after the breakdown of slug flow as velocity and/or quality increase. As seen before, in churn flow, the large Taylor bubbles

characteristic of slug flow have disappeared but, when churn flow is viewed from the outside through a transparent tube, characteristic reversals in flow velocity are observed. This regime has been given the name churn flow for many decades (see Hewitt and Hall-Taylor, 1970) but its detailed characteristics have not been widely investigated, despite the fact that the regime occurs over a relatively large range of flow conditions. Some confusion has been caused in the literature by the term 'churn' being used in at least two other contexts,

1. The 'churn turbulent' bubbly flow regime as defined, for instance, by Zuber and Findlay (1965). Essentially, this regime is delineated to allow specific forms of the drift-flux model to be used over certain ranges of gas and liquid velocity;

2. The 'churn flow' regime defined by Taitel *et al.* (1980). This was seen as a form of developing slug flow; the longer the pipe, the more likely the flow was to correspond to classical slug (or plug) flow rather than to a flow with apparently churning motion which was defined, in this case, as the churn flow regime.

The present author believes it appropriate to retain the older designation of churn flow as an important regime occurring between slug flow and annular flow.

Visualisation studies by Hewitt *et al.* (1985) reveal the nature of the churn flow regime. Essentially, it has similarities to annular flow in that there is a continuous gas core in the centre of the channel and a liquid layer near the channel wall. Nicklin and Davidson (1962) used the alternative name 'semi-annular' flow which also recognised the often annular nature of the churn flow regime. However, it is important to make a distinction between annular flow and churn flow since its characteristics are so very different. The characteristics which distinguish it from annular flow are as follows,

1. The breakdown of slug flow is accompanied by a very rapid increase in pressure gradient due to intensified wave activity and friction. This is well illustrated by the

pressure gradient data obtained by Owen (1986), an example which is shown in Fig. 2.8. In this figure, the dimensionless gas velocity, U^*_{GS}, is given by,

$$U^*_{GS} = U_{GS}\left[\frac{\rho_G}{gd_T\left(\rho_L - \rho_G\right)}\right]^{1/2}, \tag{2.64}$$

For $U^*_{GS} \geq 0.4$, as the gas flow rate increases, the pressure gradient *decreases* with increasing gas flow rate (the liquid flow rate being constant) due to the decreasing intensity of the gas-liquid interaction. Eventually, the pressure gradient begins to increase again as annular flow is entered. This behaviour is characteristic of churn flow and it is very different from that observed in annular flow;

2. The flow mechanism in churn flow was established in the visualisation tests of Hewitt *et al.* (1985). In those experiments, photochromic dye tracing was used and, by matching the refractive index of the tube wall and the liquid phase, it was possible to get simultaneous visualisation of the interface and of the instantaneous velocity profile. The liquid is transported upwards in large waves which pick up liquid from a falling film ahead of them and shed liquid which forms a falling film behind them. The flow mechanism suggested by Hewitt *et al.* (1985) is illustrated in Fig. 2.9.

   The origin of the large waves is similar to those which cause the 'flooding' phenomenon in countercurrent gas-liquid flow. It is perhaps helpful here to review measurements which were made by Govan *et al.* (1991), whose test section is illustrated in Fig. 2.10. A vertical 31.8 mm internal diameter tube was used in these experiments, with the liquid being injected through an inlet sinter (section of porous wall tubing) and then removed through an outlet sinter as shown in Fig. 2.10. Gas entered at the bottom of the test section and passed up the tube, the gas flow being fully developed before it met the liquid (this is an important point; quite different results are obtained if the gas flow is not developed).

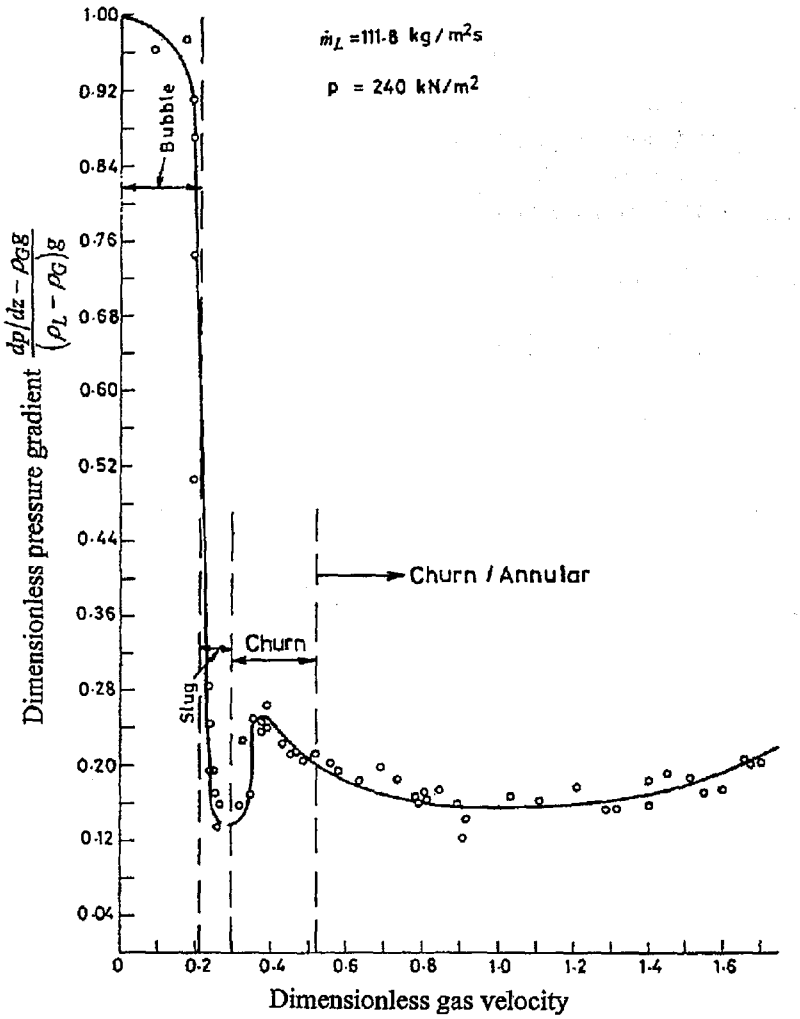


Figure 2.8: Pressure gradient in vertical two-phase flow (Owen, 1986).

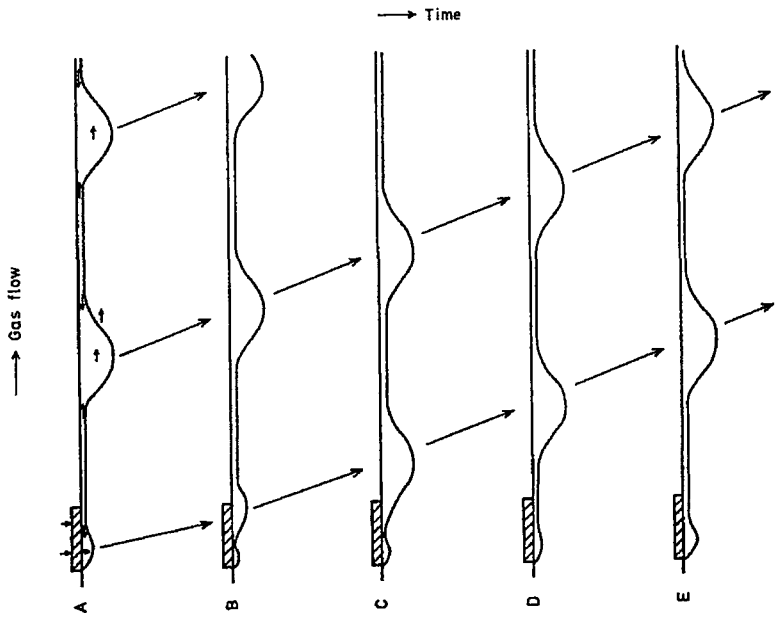


Figure 2.9: Postulated mechanism of churn flow (Hewitt *et al.*, 1985).

Flooding occurs in this situation by the formation of a single wave near the outlet sinter which is then transported upwards by the gas phase and passes beyond the inlet sinter and into the upper part of the channel. After this point, part of the liquid flows upwards from the injection point and part of it flows downwards (see the line marked 'downflow' on Fig. 2.11). The results shown in Fig. 2.11 are for falling film lengths (i.e., distance between inlet and outlet porous wall sections) $L = 0.3$ and $L = 1.0$ m, respectively.

The region above the injector is, in fact flowing in churn flow and the same results would have been obtained for this region in the absence of the downflow portion. This was proved by Govan *et al.* (1991) by comparing pressure gradient and hold-up in the region above the liquid injector both with and without the falling liquid film below the injector. These results are shown in Fig. 2.12. In this figure, ϵ_L is the liquid hold-up and $-\frac{dp}{dz}$ is the pressure gradient. The liquid flow rate is that of the

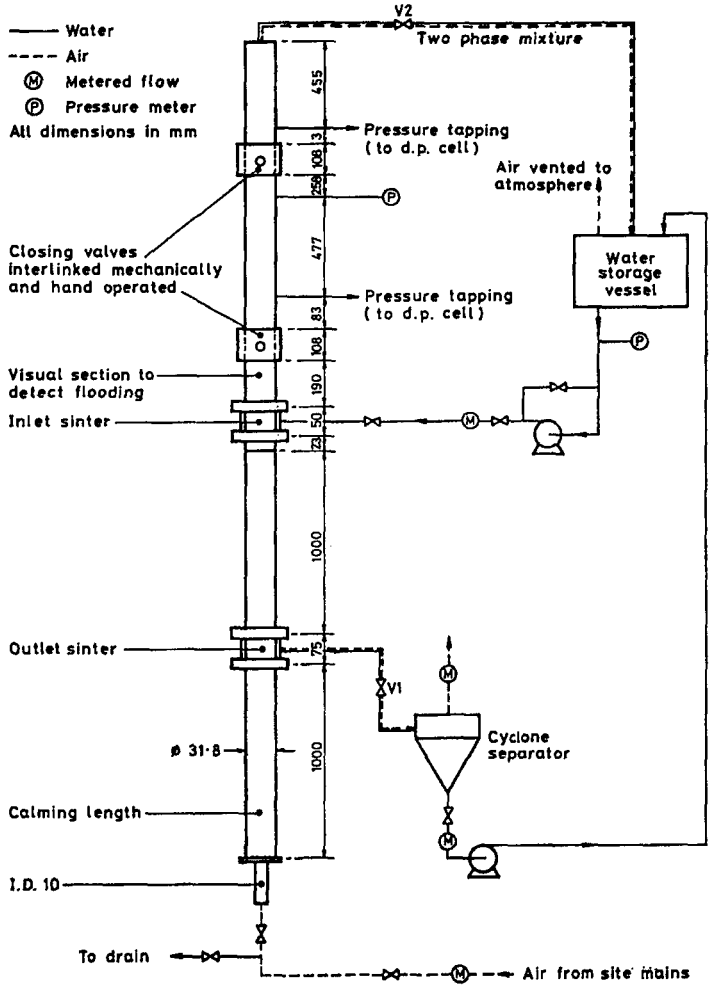


Figure 2.10: Experimental arrangements with a porous wall outlet used by Govan *et al.* (1991).

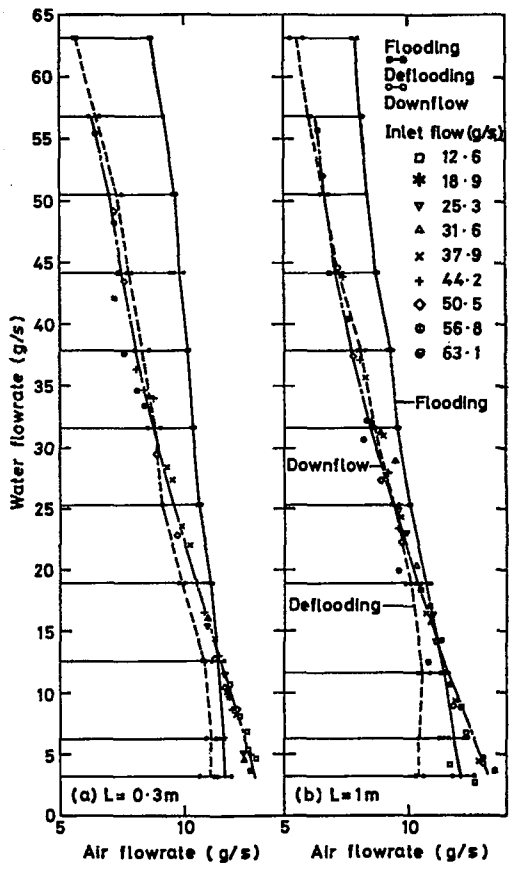


Figure 2.11: Experimental results for flooding, deflooding and and downflow with a porous wall inlet (Govan *et al.*, 1991).

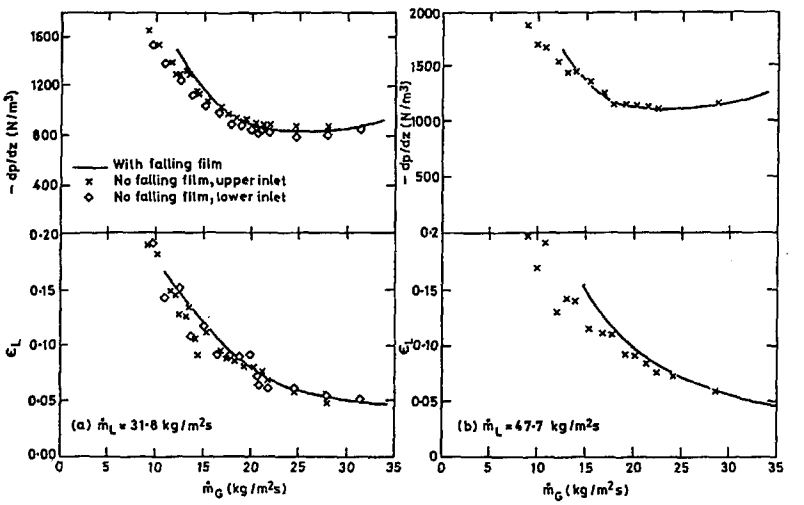


Figure 2.12: Comparison of pressure gradient and hold-up with and without a falling film below the injector (Govan *et al.*, 1991).

liquid *flowing upwards* in the case where there was a falling liquid film downwards below the liquid injector or the *total liquid flow* in the absence of the down flowing film. Thus, the transition to churn flow is characterised by the capability of forming flooding-type waves and there is an intimate connection between the flooding phenomenon and the existence of churn flow. In fact, flooding within the Taylor bubble in slug flow is, as seen previously, the most likely explanation of the slug-churn transition (Jayanti and Hewitt, 1992, Jayanti *et al.*, 1993);

3. The large flooding waves are broken up to form droplets as they pass along the channel and a reasonably large fraction of the liquid can be entrained as droplets. Figure 2.13 shows results obtained by Wallis (1962) who showed that the entrained fraction *decreases* with increasing gas velocity in what is clearly churn flow to a minimum value before *increasing* again in annular flow. In downwards co-current flow, the flooding type waves are not formed and the entrained fraction goes smoothly to zero as gas flow rate is decreased.

The above features of churn flow are ones which make the regime very distinct from

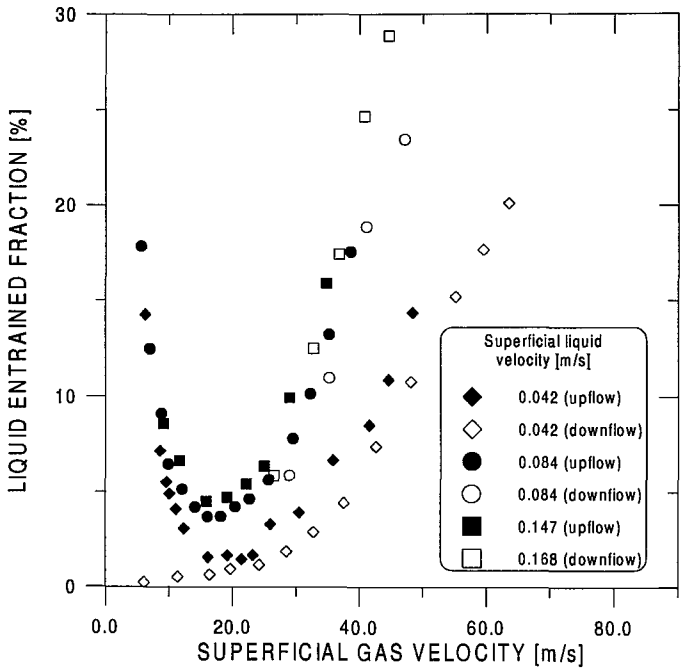


Figure 2.13: Variation of entrained fraction with gas velocity (Wallis, 1962).

annular flow, hence the need for a separate designation.

Although a large amount of work has been done in detailed characterisation of annular flow, there has been relatively little on churn flow. In addition to the visualisation work by Hewitt *et al.* (1985), Govan (1990) used special visualisation methods (namely a transparent liquid injector) to observe the formation of the waves in churn flow and their translation along the channel after formation.

Churn flow visualisation experiments (Govan, 1990)

Since some of its experimental results are of interest to the modelling work presented in Chapter 6, a detailed description of the visualisation studies by Govan (1990) is given in the present section.

Govan (1990) devised an experimental apparatus for investigation of churn flow in which

visualisation of events near the liquid entry point were made possible due to the use of a transparent liquid injector. This consisted of a length of plastic tubing through which a large number of holes were drilled, giving a smooth liquid entry analogous to that produced by a porous wall.

The experimental arrangement used in Govan's study is shown in Fig. 2.14. Air was fed to the bottom of the test section and water pumped into a transparent parallel-sided casing surrounding the inlet section. Liquid entering this inlet section left the system by either of two routes, (i) *upwards* through the rig separator, or (ii) *downwards*, being removed by an outlet sintered section.

The air removal from the outlet sinter (removing the down-falling liquid) was minimized using valve V1, and the test section pressure was maintained at 1.33 bar using valve V2. The experimental procedure was as follows: the air flow was started at the desired value and then liquid passed into the transparent injection device at a low flow rate. Under these circumstances the liquid passed downwards as a falling film (countercurrent to the gas flow rate) and passed out of the system through the outlet sinter. The gas flow rate was then increased until flooding occurred. A large wave was formed near the outlet sinter, was transported upwards by the gas and initiated churn flow in the upper part of the section. Waves were then repeatedly formed in the region of the liquid inlet and could be observed clearly. Liquid continued to flow downwards (corresponding to the 'downflow' curve on Fig. 2.11) but this liquid was now in a sub-flooded state (see Fig. 2.11). Thus, there are essentially two regions, one above the injector which is in churn flow and one below the injector which is of falling film flow with a countercurrent gas flow. The downward flow rate was estimated from the downwards flow curve shown in Fig. 2.11, allowing the upward flow rate to be estimated.

Govan captured the flow behaviour at the water inlet using a high-speed video camera. He measured the wave frequencies, velocities and the position of a chosen wave along the

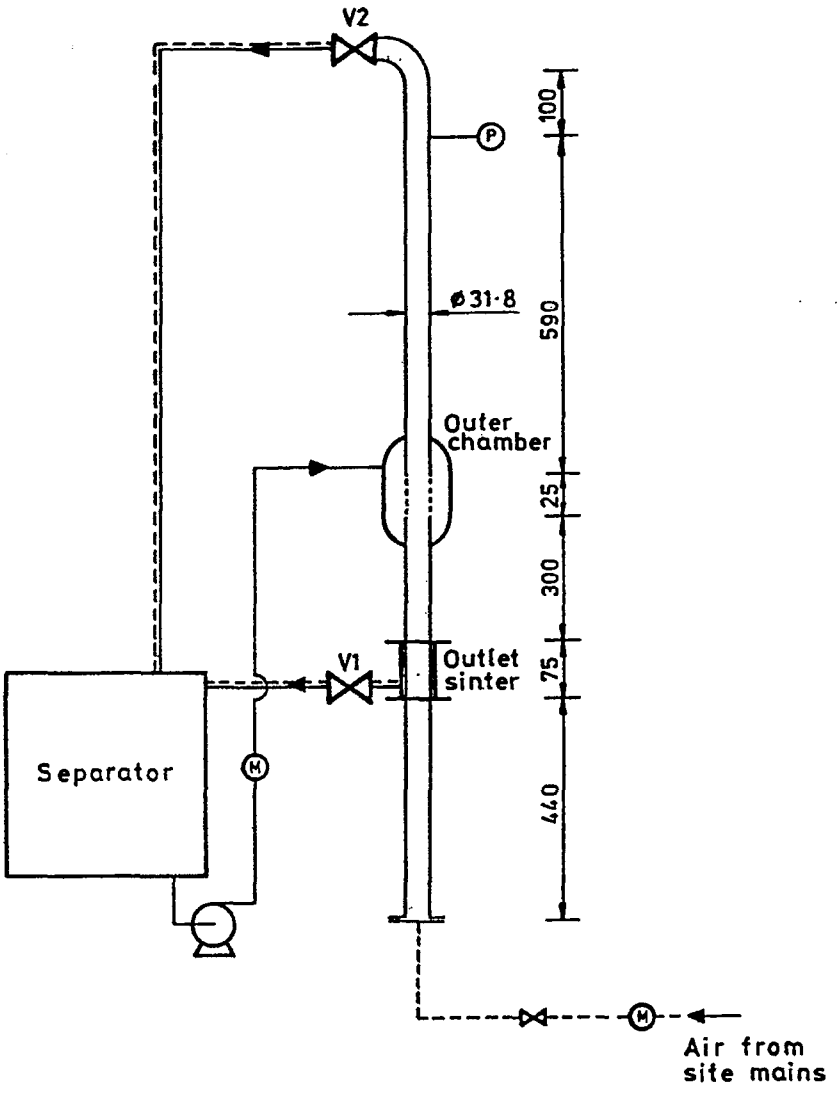


Figure 2.14: Experimental arrangement used in the visualisation study of Govan (1990).

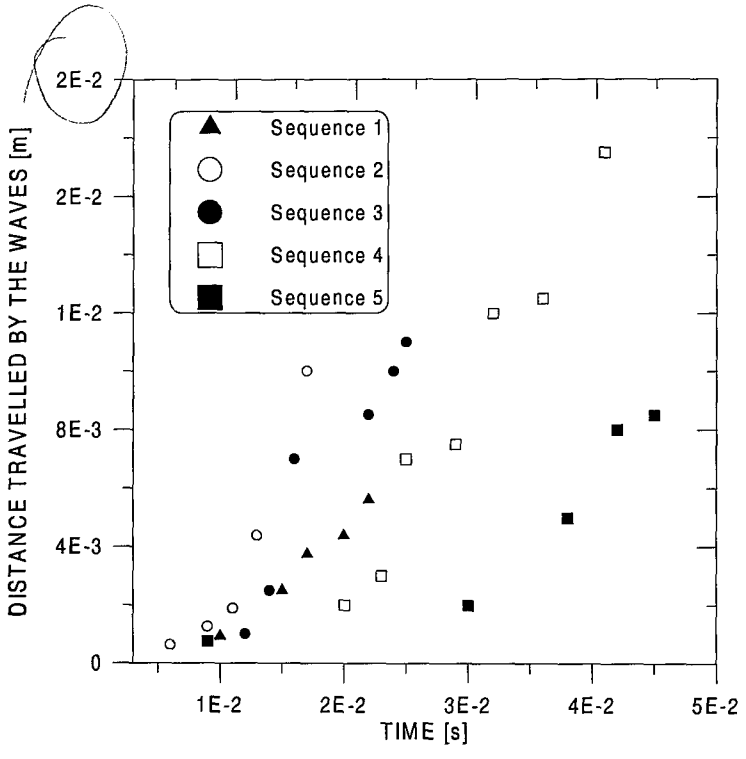


Figure 2.15: Wave position versus time (Govan, 1990).

section as a function of time. From an observation of the video footage produced, several characteristics of the waves could be analysed (such as flow reversals, liquid entrainment, etc.) and, in general, these were in agreement with the mechanisms postulated by Hewitt *et al.* (1985) and illustrated in Fig. 2.9.

Table 2.2 shows the flow rates used in Govan's visualisation experiments, together with the mean wave frequencies calculated from his video recordings. Govan reported that individual waves show considerable variations about the mean, especially at high liquid/low gas flows. As expected, the wave frequency increases with increasing liquid flow (because the waves grow more quickly) and with increasing gas flow (because the critical amplitude is less and thus achieved more quickly). However, the effect is rather small in both cases. Figure 2.15 shows typical measurements of wave position (relative to the bottom of the porous section where the waves generally form) versus time from the start of the growth of the wave.

Table 2.2: Wave frequencies and velocities from visualisation experiments (Govan, 1990).

No of video Sequence	$\dot{M}_G$ $\times 10^{-3}$ [kg/s]		U_G [m/s]	$\dot{M}_L$ $\times 10^{-3}$ [kg/s]	$\dot{M}_{LU}$ $\times 10^{-3}$ [kg/s]
1	8.3		6.5	27	-
2	8.3		6.5	42	7
3	6.8		5.3	103	51
4	4.5		3.5	105	32
5	3.6		2.8	108	27
No of video Sequence	Total time [ms]	No of waves	Frequency [Hz]	Net upflow per wave $\times 10^{-3}$ [kg]	Wave velocity [m/s]
1	3305	41	12.4	-	0.46
2	4895	65	13.3	0.5	1.34
3	4904	78	15.9	3.2	0.75
4	5008	52	10.4	3.1	0.70
5	5498	54	9.8	2.8	0.52

With exception of the wave measured in Sequence 1, whose behaviour is rather anomalous, the measurements are very consistent, showing that as the gas velocity is decreased the growth/acceleration period is longer and the mean velocity is lower, as would be expected. Values of the mean velocity are given in Table 2.2 and compared with the gas superficial velocity. With the exception of Sequence 1, the wave velocity is around 20% of the superficial gas velocity.

Churn flow models

Jayanti and Brauner (1994) put forward a model particularly devoted to the prediction of churn flow parameters, namely pressure gradient and void fraction. They applied force balances on the gas core and on the tube as follows,

$$-\frac{dp}{dz} = \frac{4}{d_T}\frac{\tau_I}{\sqrt{\varepsilon}} + \rho_G g, \tag{2.65}$$

$$-\frac{dp}{dz} = \frac{4}{d_T}\tau_{wL} + \left[\rho_L\left(1-\varepsilon\right) + \rho_G\varepsilon\right] g. \tag{2.66}$$

In Eq. 2.66, τ_{wL} is the average wall shear stress (accounting for the fact that only the liquid is in contact with the wall). Jayanti and Brauner (1994) suggested that τ_{wL} may be calculated based on the net liquid flow rate alone and that its time-varying nature can be neglected. Thus,

$$\tau_{wL} = \frac{1}{2}\rho_L f_L \left(\frac{U_{LS}}{1-\varepsilon}\right)^2. \tag{2.67}$$

f_L is estimated using single phase flow relationships. Therefore, for $Re_L < 2100$,

$$f_L = \frac{16}{Re_L}, \tag{2.68}$$

and for $Re_L > 2100$,

$$f_L = 0.079 Re_L^{-0.25}. \tag{2.69}$$

In a similar manner, the average interfacial shear stress can be written as,

$$\tau_I = \frac{1}{2}\rho_G f_I \left(\frac{U_{GS}}{\varepsilon}\right)^2, \tag{2.70}$$

where f_I is the interfacial friction factor. Jayanti and Brauner suggested, based on comparisons with the experimental results by Govan *et al.* (1991), that f_I would be best estimated by an average of the correlations by Bharathan (see Bharathan and Wallis, 1983) (for the post-flooding regime in countercurrent flow) and by Wallis (1969) (for annular flow),

$$f_I = \frac{1}{2}\left(f_{I_{Bharathan}} + f_{I_{Wallis}}\right), \tag{2.71}$$

where,

$$f_{I_{Bharathan}} = 0.005 + 14.4\,(1-\varepsilon)^{2.04}, \tag{2.72}$$

$$f_{I_{Wallis}} = 0.005 + 0.375\,(1-\varepsilon). \tag{2.73}$$

Jayanti and Brauner (1994) compared the pressure gradient predictions using the above model with the experimental results by Owen (1986). They claimed that almost all data points (covering a liquid mass flux range of 5 to 400 kg m^{-2} s^{-1}) are predicted well and lie within $\pm 20\%$ of the measured pressure gradient.

Interfacial friction factors for churn-annular flow

Several attempts were made in order to develop separate correlations for the interfacial friction factor in churn flow. In a more complete report of Bharathan's work (Bharathan

and Wallis, 1983), the post-flooding regime friction factor was correlated by the following expression (including the diameter of the pipe as a parameter),

$$f_I = 0.005 + 10^{\left(-0.56+\frac{9.07}{d_T^*}\right)} \left[\frac{d_T^*\,(1-\varepsilon)}{4}\right]^{\left(1.63+\frac{4.74}{d_T^*}\right)}, \tag{2.74}$$

where,

$$d_T^* = d_T \sqrt{\frac{(\rho_L - \rho_G)\, g}{\sigma}}. \tag{2.75}$$

For $d_T = 0.0318$ m, Eq. 2.74 reduces to Eq. 2.72.

Alternative relationships for f_I have been proposed by Abe *et al.* (1991) and Kelly and Freitas (1993).

Entrainment in the churn-annular region

The earlier work by Wallis (1962) was the first to provide some information on the behaviour of the entrained fraction in the churn flow region. Wallis carried out experiments in a 12.7 mm internal diameter vertical pipe. The results by Wallis are shown in Fig. 2.13 for both cocurrent upflow and downflow conditions. The difference in entrained fraction behaviour between these two cases suggests that there is some entrainment activity associated with the sub-annular region ($U_{GS}^* < 1$) in upflow. At what seems to be the region of minimum pressure gradient, i.e., the region of transition between churn flow and annular flow ($0.9 < U_{GS}^* < 1.2$), the entrained fraction goes through a minimum before starting to increase again. Hewitt and Hall-Taylor (1970) reported a similar behaviour for flow in annuli. In this study, film removal devices were employed at both inner (porous sinter method) and outer (slit device) surfaces. The shape of the entrained fraction curve is very similar to that of Wallis (see Fig. 2.16).

Gill *et al.* (1964) also observed an increase in the entrained fraction in the churn flow

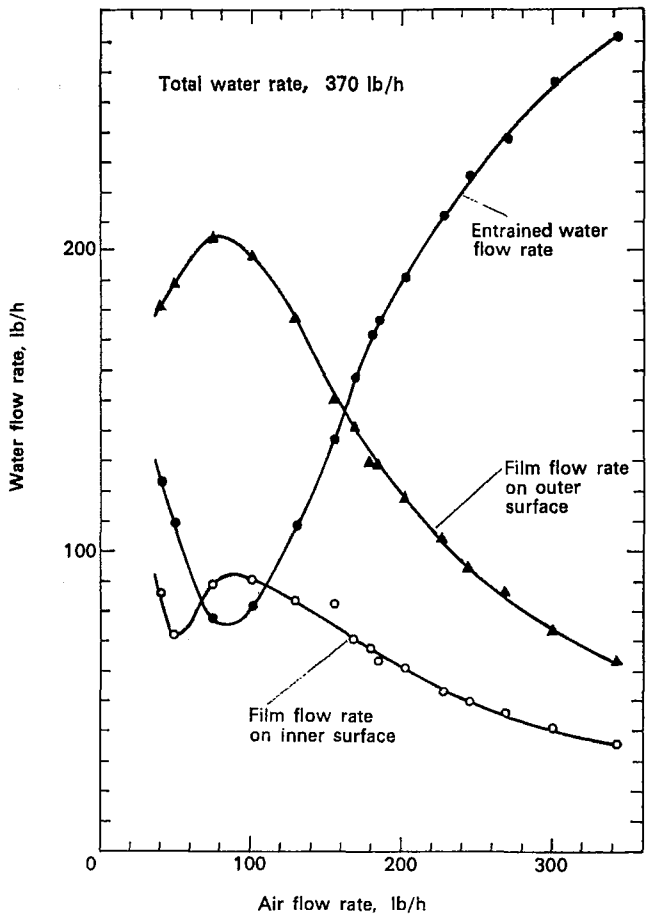


Figure 2.16: Film flow and entrained droplet flow in an annulus (Hewitt and Hall-Taylor, 1970).

region, but did not systematically investigate this phenomenon. However, their conclusions on the distinct behaviour of droplet concentration in this region have led to further exploration of these phenomena by the present author (see Chapter 5). Basically, they observed that the local droplet concentration in the gas core is approximately constant for fully cocurrent annular flow, but not for churn flow (where it is generally higher).

Verbeek *et al.* (1993) investigated the effect of pipe diameter and of physical properties on the entrainment curve. They observed that the minimum in the entrainment curve is shifted to higher gas velocities for large tube diameter (50.8 and 101.6 mm), low surface tension and high liquid viscosity systems.

Entrained fraction data in annular flow at low gas flow rates were also generated by Fore and Dukler (1995). They also measured film thickness, droplet velocity, droplet diameter, deposition rate, wall shear stress and pressure gradient. It is interesting to notice that the similarity in the *loci* of minimum of the pressure gradient and entrained fraction distributions was only partially supported by their work. Fore and Dukler carried out experiments in a 50.8 mm internal diameter vertical pipe at pressures close to atmospheric using air-water ($\eta_L = 1$ cp) and air-50% glycerin/water ($\eta_L = 6$ cp) systems. For the lower viscosity system, the minima of the pressure gradient and entrained fraction profiles took place at $U^*_{GS} \approx 1$. However, the data trend for the more viscous mixture is, as shown in Fig. 2.17, very different. In this case, the entrained fraction does not exhibit a minimum at the flow reversal point but, as reported by Verbeek *et al.* (1993), at a higher gas velocity. Unfortunately, for the reported air-50% glycerin/water data of Fore and Dukler, gas velocities were not high enough in order to characterise the entrainment curve minima. Based on the information above, it can be postulated that only the entrainment of droplets from the waves is inhibited by an increase in η_L. The process of formation and, of course, the existence of these waves is not affected since the pressure gradient trends remain unchanged (see Fig. 2.17). Experimental investigations in line with those by Hewitt *et*

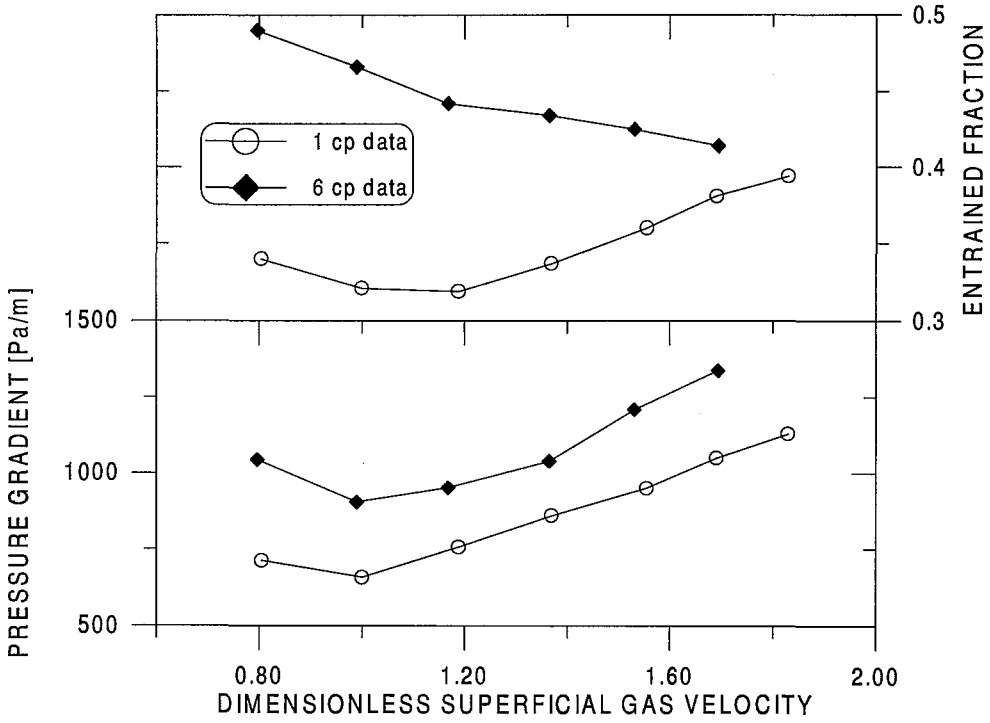


Figure 2.17: Entrained fraction and pressure gradient in the churn-annular region (Fore and Dukler, 1995).

al. (1985) should validate such a hypothesis.

Recent studies by Azzopardi (Azzopardi, 2000; Azzopardi and Zaidi, 2000) also provided some insight into the problem of droplet entrainment at low gas flow rates. Azzopardi and Zaidi (2000) carried out experiments using a light scattering technique in a 38.0 mm internal diameter vertical test section and determined the liquid entrained fraction for $U^*_{GS} \geq 1$ over a wide range of conditions. Although they did not venture into the low gas velocity region, the studies of Azzopardi and Zaidi (2000) strengthen the concept of the trend of higher entrainment at lower gas velocities.

2.3 Flow boiling of single component fluids

In this part of the literature survey, the subject of phase change heat transfer is brought to attention. More specifically, this section deals with the mechanisms by which, as a result of an energy transfer to the system, liquid is transformed into vapour. These mechanisms are known as *boiling* and *evaporation.*

Dhir (1998) defines boiling (or more rigorously nucleate boiling) as a phase change process in which vapour bubbles are formed either on a heated surface or in a superheated liquid layer adjacent to a heated surface. It differs from evaporation at pre-existing vapour-liquid interfaces because it also involves creation of such interfaces at discrete sites on the heated surface.

Figure 2.18 from Collier and Thome (1994) illustrates the situation of upwards flow of an initially single phase liquid in a vertical round tube subjected to an uniform wall heat flux. After a region of single phase heat transfer, nucleate boiling starts at the wall. Initially, the bubbles collapse as they detach from the wall and reach the core of the stream, which is still subcooled. Later, at what is defined as the point of Net Vapour Generation (NVG), there is a permanent presence of vapour bubbles in the core. As the quality increases,

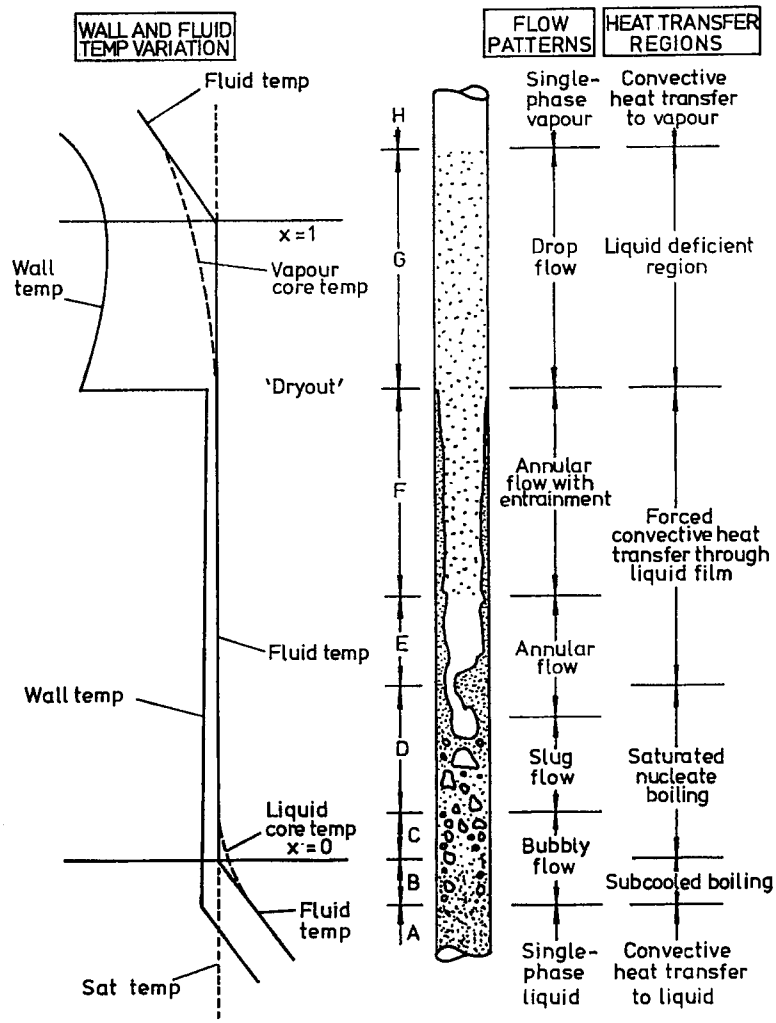


Figure 2.18: Flow patterns in a vertical evaporator tube (Collier and Thome, 1994).

the flow configuration evolves as portrayed in Fig. 2.1. When the annular regime is entered, droplet entrainment and deposition come into play. With further increase of vapour fraction, the liquid film thins and eventually dries out leading a sharp increase in the wall temperature and consequently a deterioration of the heat transfer coefficient as shown in Fig. 2.18. This point is referred to as the dryout point. The entrained droplets may persist over several tube diameters before evaporating completely in the superheated vapour.

It should be emphasized that this review is devoted to saturated boiling. Therefore, the subject of subcooled boiling will not be dealt with. The reader is referred to Butterworth and Shock (1982) and Collier and Thome (1994) for information on this matter.

2.3.1 The classical interpretation

Dengler and Addoms (1956) were possibly the first to report that at least two different heat transfer mechanisms were responsible for phase change from liquid to vapour in a tube. As pointed out by Bennett *et al.* (1980), Dengler and Addoms found that much of their forced convective boiling data, if normalised by the heat transfer coefficient for the two-phase mixture flowing with liquid phase properties, could be uniquely correlated by the Martinelli parameter, X_{tt}, given by,

$$X_{tt} = \left(\frac{1-X}{X}\right)^{0.9} \left(\frac{\rho_G}{\rho_L}\right)^{0.5} \left(\frac{\eta_L}{\eta_G}\right)^{0.1}. \tag{2.76}$$

However, as it can be observed in Fig. 2.19, there were a number of sets of data which gave heat transfer coefficients higher than the "purely" convective data. They attributed this difference to nucleate boiling. They also observed that when nucleation apparently existed, the deviation of the observed heat transfer coefficient from their calculated "purely" convective coefficient was greatest at low values of $\frac{1}{X_{tt}}$. At larger values of $\frac{1}{X_{tt}}$, the experimental coefficient converged with the calculated coefficient from their "purely" convective correlation.

The measured heat transfer coefficient trends observed by Dengler and Addoms suggest that the heat transfer coefficient is a combination of two mechanisms, nucleate boiling and forced convection. At low qualities (generally lower than a few per cent), there is a dominance of nucleate boiling. At high qualities (generally those characteristic of the annular flow regime), nucleate boiling is suppressed and forced convection is the dominant

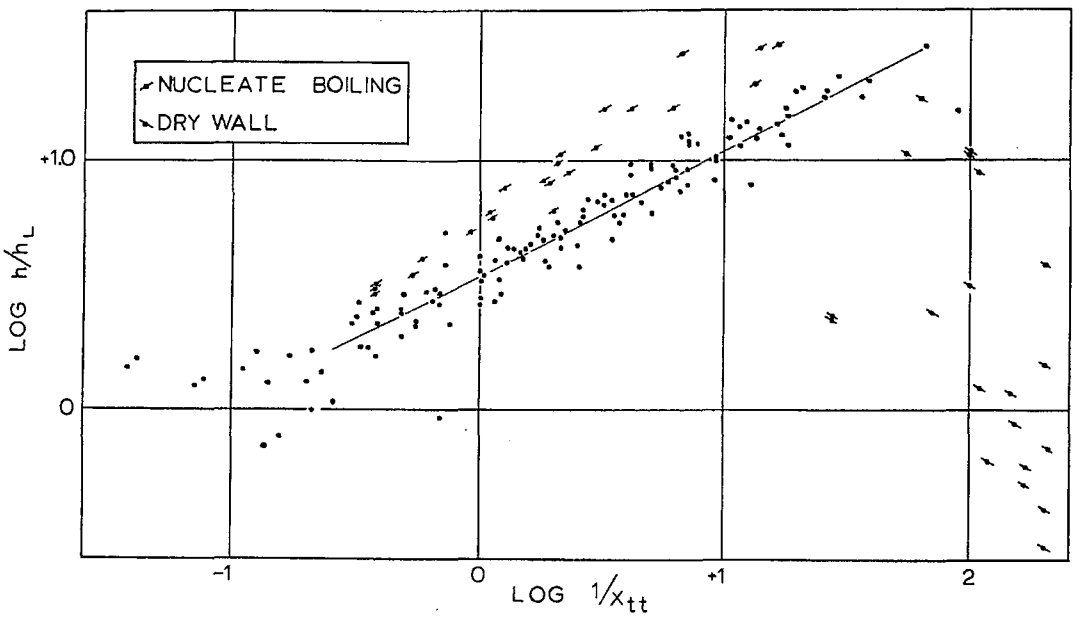


Figure 2.19: Data on convective boiling (Dengler and Addoms, 1956).

mechanism. This interpretation of the experimental results in forced convective boiling will be termed here, mainly due to historical reasons, as the *classical interpretation.*

Other early works that provided experimental evidence which gave support to the classical interpretation of flow boiling heat transfer are those by Bennett *et al.* (1961), Guerrieri and Talty (1956) and Bergles and Rohsenow (1964).

In pursuance of an accurate representation of the mechanisms, various authors have proposed a number of physical models which can be used to describe the phenomenon of forced convective boiling. However, an agreement on how the quantitative combination between the nucleate boiling and convective portions takes place has not yet been achieved. Moreover, amongst the various correlations and methods proposed for the prediction of flow boiling, the form (and even the existence) of enhancement and suppression contributions to the nucleate boiling and convective portions is a rather disputable point in the literature. Some of the challenging views that oppose to the classical interpretation are

discussed in a later section.

Modelling of phase change in forced convective systems relies on observing the way in which the various system parameters — like heat flux, system pressure, heated surface finishing, mass flux, quality etc.— affect both modes of heat transfer. Some of the qualitative features arising from such observations are as follows,

1. purely convective evaporation is not (or very little) affected by the heat flux to the surface. On the other hand, this exerts a strong influence on nucleate boiling, as the number density of sites that become active increases with increasing surface heat flux;

2. in the nucleate boiling dominant region, an increase in pressure increases the nucleate boiling heat transfer coefficient. This is because the superheat required to generate the same over-pressure in the bubble to sustain its growth is reduced (reduction in the slope of the saturation pressure curve). For the forced convective region, an increase in pressure reduces the ratio between the liquid and vapour densities. Therefore, when a given mass of liquid evaporates, a larger volume of vapour is generated at lower pressures. This means that the vapour velocity decreases with increasing pressure for a given quality and mass flux. Such an effect leads to a decrease in the interfacial shear stress, an increase in the film thickness and a decrease in the heat transfer coefficient with increasing pressure. Thus, there is a great propensity towards nucleate boiling dominance at high pressures;

3. surface finish is a key parameter to nucleate boiling, since imperfections (cavities and scratches) entrap vapour or gases and act as bubble nuclei. The more imperfect the surface, the higher the nucleation activity, leading to a more efficient nucleation process. In principle, forced convection is not so affected by the surface finishing condition of the heater (though there may be an effect if the surface is very rough);

4. in the forced convective region, an increase in mass flux or in quality (i.e., an increase in effective velocity) enhances the heat transfer coefficient. On the other hand, nucleate boiling is suppressed as the decreasing wall superheat is unable to sustain wall nucleation.

Most of the remarks above concerning nucleate boiling are based on observations of pool boiling, i.e., nucleate boiling under natural convection conditions. Due to the system's relative simplicity (specially in performing experiments), the literature devoted to pool boiling is much greater than that to flow boiling. Many correlations were proposed for various heater geometries (Forster and Zuber, 1955; Stephan and Abdelsalam, 1980; Cooper, 1984). A deep phenomenological insight is given in the recent review by Dhir (1998).

Based on these introductory paragraphs, it can be concluded that modelling the nucleate boiling contribution in convective systems is a major challenge in boiling research. Section 2.3.2 presents a review of previous work on the subject of suppression of nucleate boiling in convective systems. In Section 2.3.3, an alternative view of the classical interpretation of the roles of the nucleation and convective contributions is addressed. Section 2.3.4 sheds some light on heat transfer issues specifically concerned with the annular flow regime. Finally, the main correlations for predicting the heat transfer coefficient in convective boiling are presented in Section 2.3.5.

Another very important problem in this field concerns the prediction of Critical Heat Flux (CHF). In annular flow, this corresponds to the point at which the liquid film disappears and the pipe wall comes into direct contact with the vapour stream. The normal way of dealing with CHF is to use empirical correlations to predict its onset. However, an accurate and reliable prediction of the *dryout* point must involve phenomenological modelling of the flow. This is dealt with in Section 2.3.6.

2.3.2 Onset and suppression of nucleation in forced convective boiling

As far as the transfer of heat from the surface to the superheated liquid is concerned, the suppression of nucleate boiling and the initiation of nucleate boiling are the same problem, the only difference being the direction from which . the critical temperature difference (superheat) required to sustain nucleation and bubble growth is approached.

This temperature difference may be found by considering initially the equation defining the mechanical equilibrium of a spherical vapour nucleus of radius r^* in a liquid at constant temperature and pressure. The pressure difference between the pressure above the planar surface (interface), p_∞, and that corresponding to saturation, p_{sat} can be approximated by (Collier and Thome, 1994),

$$p_\infty - p_{sat} = \frac{2\sigma}{r^*}\left(1 + \frac{\rho_G}{\rho_L}\right). \tag{2.77}$$

The superheat corresponding to the pressure difference above can be calculated using the Clausius-Clapeyron equation and the ideal gas law,

$$\frac{dp}{dT} = \frac{\Delta h_v}{T}\left(\frac{1}{\rho_G} - \frac{1}{\rho_L}\right). \tag{2.78}$$

If the specific volume of the liquid is small ($\frac{1}{\rho_G} \gg \frac{1}{\rho_L}$) and,

$$M_w \frac{p}{\rho_G} = \mathrm{R}T, \tag{2.79}$$

then,

$$\frac{1}{p}dp = \frac{\Delta h_v M_w}{\mathrm{R}T^2}dT. \tag{2.80}$$

Integrating Eq. 2.80 and simplifying for $\left(\frac{2\sigma}{p_{sat}r^*}\right) \ll 1$ gives (see Collier and Thome, 1994),

$$\Delta T_{sat} = \frac{RT_{sat}^2}{\Delta h_v M_w} \frac{2\sigma}{p_{sat} r^*} = \frac{2\sigma T_{sat}}{\rho_G \Delta h_v r^*}. \tag{2.81}$$

The theoretical work by Hsu (1962) shed some light on the mechanisms which lead to the incipience of boiling on a heated surface. It was the first successful attempt to correlate the size of cavities present on the surface (and the range over which these are active) and the temperature of the surface.

In this section, the model by Hsu (1962) is described in detail for the case of a constant wall heat flux. The bubble growth model is schematically presented in Fig. 2.20. The bubble nucleus has originated from residual vapour from the preceding bubble, which was left in the cavity. The bubble will grow inside a transient thermal layer of thickness δ_{ts}, whose cyclic growth re-starts each time a bubble departs and relatively cool bulk liquid replaces the void left by the detached bubble.

The transient conduction model for the superheated layer is given by,

$$\frac{\partial \theta}{\partial t} = \kappa_L \frac{\partial^2 \theta}{\partial y^2}, \tag{2.82}$$

with boundary conditions,

$$\theta = 0 \quad \text{at} \quad t = 0, \tag{2.83}$$

$$\theta = 0 \quad \text{at} \quad y = \delta_{ts} \quad \text{for all } t, \tag{2.84}$$

and at $t > 0$,

$$\frac{\partial \theta}{\partial y} = -\frac{\dot{q}_w}{\lambda_L} \quad \text{at} \quad y = 0, \tag{2.85}$$

where $\theta = T - T_\infty$.

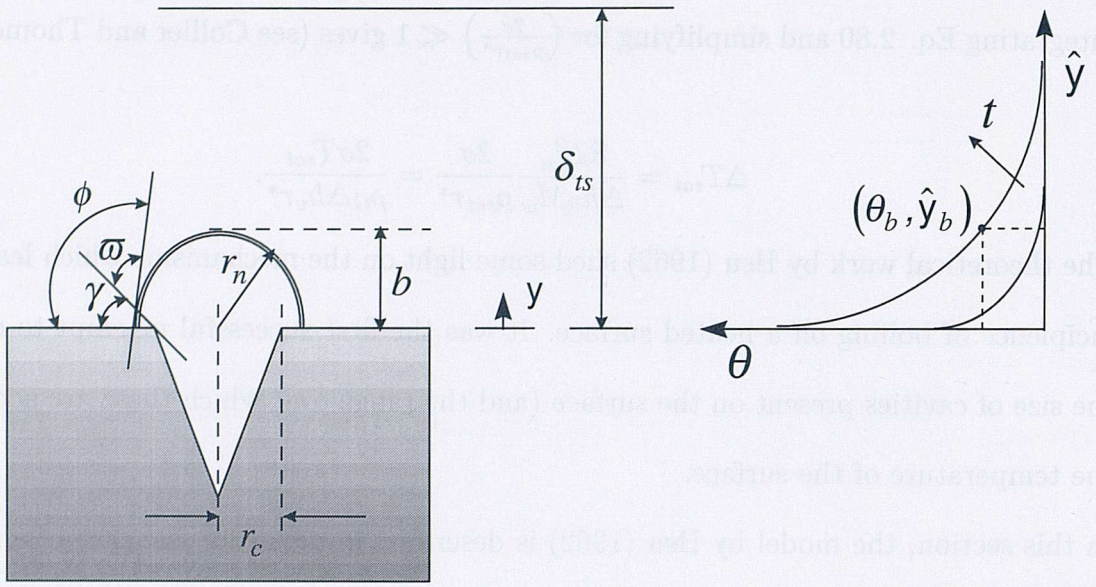


Figure 2.20: The model for bubble growth and illustration of waiting period and temperature profiles (Hsu, 1962).

The solution of the temperature profile is,

$$\frac{\theta}{\frac{\dot{q}_w \delta_{ts}}{\lambda_L}} = 2\sqrt{\hat{t}} \sum_{n=0}^{\infty} (-1)^n \left[\mathbf{i}\,\mathrm{erfc}\ \frac{(2n+1) - \hat{y}}{2\sqrt{\hat{t}}} - \mathbf{i}\,\mathrm{erfc}\ \frac{(2n+1) + \hat{y}}{2\sqrt{\hat{t}}} \right], \tag{2.86}$$

where $\hat{t} = \frac{\kappa_L t}{\delta_{ts}^2}$ and $\hat{y} = \frac{\delta_{ts} - y}{\delta_{ts}}$.

One of the main contributions of the theory by Hsu (Hsu, 1962) is the introduction of the concept of the waiting period. The hypothesis behind this concept is that the bubble nucleus will not grow unless the surrounding liquid is warmer than the bubble temperature so that there is a net heat flux to the bubble to provide the heat of vaporisation. When the bubble starts to grow, the waiting period ends. The end of the waiting period is reached when $\theta(y, t) = \theta_b$ at $y = b$, where b is the bubble nucleus height and θ_b is the temperature required for bubble growth.

Hsu (1962) found θ_b by applying the Clausius-Clapeyron equation (Eq. 2.81),

$$\theta_b = \theta_{sat} + \frac{2\sigma T_{sat}}{\Delta h_v \rho_G r_n}, \tag{2.87}$$

where r_n is the bubble nucleus radius. Hsu found a relationship between b, r_n and the cavity radius, r_c, by assuming that the bubble nucleus has the shape of a truncated sphere (see Fig. 2.20). Under these assumptions, the following relationships can be derived,

$$b = \left(\frac{1+\cos\phi}{\sin\phi}\right) r_c = C_1 r_c, \tag{2.88}$$

$$r_n = \left(\frac{1}{\sin\phi}\right) r_c = C_2 r_c, \tag{2.89}$$

$$b = (1+\cos\phi)\, r_n = C_3 r_n,\ C_3 = \frac{C_1}{C_2}. \tag{2.90}$$

Hsu assumes that $C_1 = 2$, $C_2 = 1.25$, $C_3 = 1.6$.

After some algebraic manipulation, Hsu arrived at (in dimensionless parameters),

$$\frac{\theta_b}{\frac{\dot{q}_w \delta_{ts}}{\lambda_L}} = \frac{\theta_{sat}}{\frac{\dot{q}_w \delta_{ts}}{\lambda_L}} + \left(\frac{2\sigma T_{sat} C_3}{\Delta h_v \rho_G \delta_{ts} \frac{\dot{q}_w \delta_{ts}}{\lambda_L}}\right) \frac{1}{1-\hat{y}_b}, \tag{2.91}$$

where $\hat{y}_b = \frac{\delta_{ts}-b}{\delta_{ts}}$. Whenever Eq. 2.91 is satisfied, this marks the end of the waiting period. In other words, the waiting period corresponds to the $\hat{t}$ at which the temperature profile (Eq. 2.86) intersects the particular co-ordinate $(\frac{\theta_b}{\frac{\dot{q}_w \delta_{ts}}{\lambda_L}}, \hat{y}_b)$. At $\hat{t} \to \infty$, the temperature profile reduces to the linear form,

$$\frac{\theta}{\frac{\dot{q}_w \delta_{ts}}{\lambda_L}} = \hat{y}, \tag{2.92}$$

and the intersection points between Eqs. 2.91 and 2.92 represent the upper and lower limits for $\hat{y}_b$. Thus, the cavities with $\hat{y}_b$ falling in between the limiting points ($\hat{y} = \hat{y}_b^*$) and finite waiting times are the *effective* ones. Those outside this range are the *ineffective* ones.

The value of $\hat{y}_b^*$ for the limiting points can be determined by substituting,

$$\frac{\theta_b}{\frac{\dot{q}_w \delta_{ts}}{\lambda_L}} = \hat{y}_b, \tag{2.93}$$

in Eq. 2.87. This gives,

$$\hat{y}_b^{*^2} - \left(1 + \frac{\theta_{sat}}{\frac{\dot{q}_w \delta_{ts}}{\lambda_L}}\right) \hat{y}_b^* + \frac{2\sigma T_{sat} C_3}{\Delta h_v \rho_G \delta_{ts} \frac{\dot{q}_w \delta_{ts}}{\lambda_L}} + \frac{\theta_{sat}}{\frac{\dot{q}_w \delta_{ts}}{\lambda_L}} = 0. \tag{2.94}$$

Using (from Fig. 2.20),

$$r_c = \frac{b}{C_1} = \frac{\delta_{ts}\,(1 - \hat{y}_b)}{C_1}, \tag{2.95}$$

Hsu (1962) solved 2.94 to obtain the minimum and maximum radius of active cavities. These are given by,

$$r_{c,max} = \frac{\delta_{ts}}{2C_1}\left[1 - \frac{\theta_{sat}}{\frac{\dot{q}_w \delta_{ts}}{\lambda_L}} + \sqrt{\left(1 - \frac{\theta_{sat}}{\frac{\dot{q}_w \delta_{ts}}{\lambda_L}}\right)^2 - \frac{8\sigma T_{sat} C_3 \lambda_L}{\dot{q}_w \delta_{ts}^2 \rho_G \Delta h_v}}\right], \tag{2.96}$$

$$r_{c,min} = \frac{\delta_{ts}}{2C_1}\left[1 - \frac{\theta_{sat}}{\frac{\dot{q}_w \delta_{ts}}{\lambda_L}} - \sqrt{\left(1 - \frac{\theta_{sat}}{\frac{\dot{q}_w \delta_{ts}}{\lambda_L}}\right)^2 - \frac{8\sigma T_{sat} C_3 \lambda_L}{\dot{q}_w \delta_{ts}^2 \rho_G \Delta h_v}}\right]. \tag{2.97}$$

From Eqs. 2.96 and 2.97, it is clear that no cavity will be effective unless the discriminant is positive. Therefore,

$$\frac{\lambda_L}{\dot{q}_w}\left(\frac{\dot{q}_w \delta_{ts}}{\lambda_L} - \theta_{sat}\right)^2 \leq \frac{8\sigma T_{sat} C_3}{\rho_G \Delta h_v}. \tag{2.98}$$

Finally, the criterion for the onset of nucleation is given by,

$$\dot{q}_w = \frac{\lambda_L}{\delta_{ts}}\left[\theta_{sat} + \frac{4\sigma C_3 T_{sat}}{\delta_{ts} \Delta h_v \rho_G} + \sqrt{\left(2\theta_{sat} + \frac{4\sigma C_3 T_{sat}}{\delta_{ts} \Delta h_v \rho_G}\right)\left(\frac{4\sigma C_3 T_{sat}}{\delta_{ts} \Delta h_v \rho_G}\right)}\right]. \tag{2.99}$$

Hsu (1962) applied the same analytical treatment to the case of constant surface temperature. He arrived at the following expression for the wall superheat required for the onset of nucleation,

$$\frac{\delta_{ts}\left(\theta_w - \theta_{sat}\right)^2}{\theta_w} \leq \frac{8\sigma T_{sat} C_3}{\rho_G \Delta h_v}. \tag{2.100}$$

Equations 2.98 and 2.100 are interchangeable if the following transformation is used,

$$\frac{\delta_{ts}}{\theta_w} = \frac{\lambda_L}{\dot{q}_w}. \tag{2.101}$$

Davis and Anderson (1966) applied a theory analogous to that of Hsu (1962) to calculate the onset of nucleate boiling in forced convection. Basically, they equated the slopes of the temperature profile and of the Clausius-Clapeyron equation to find the critical bubble radius for the onset of nucleation. One of the differences between the Hsu (1962) and Davis and Anderson (1966) theories is concerned with the definition of the temperature profile close to the wall. Both theories consider a linear dependence with distance, but the reference parameters are different. In dimensional form, the Hsu temperature profile (Eq. 2.92) is given by,

$$T = T_\infty + \frac{\dot{q}_w}{\lambda_L}\left(\delta_{ts} - \mathrm{y}\right), \tag{2.102}$$

and the Davis and Anderson profile is given by,

$$T = T_w - \frac{\dot{q}_w}{\lambda_L}\mathrm{y}. \tag{2.103}$$

It is interesting to note that the addition of Eqs. 2.102 and 2.103 results in Eq. 2.101. The criterion of Davis and Anderson (1966) is given by,

$$\left(T_w - T_{sat}\right)^2 = \frac{8 C_1 \sigma T_{sat} \dot{q}_w}{\lambda_L \Delta h_v}\left(\frac{1}{\rho_G} - \frac{1}{\rho_L}\right), \tag{2.104}$$

where C_1 is assumed equal to 1 (hemispherical bubble nucleus).

The graphical correlation of Bergles and Rohsenow (1964) often gives results very similar to those given by Eq. 2.104. Bergles and Rohsenow correlated their incipience data for water using the following relationship,

$$(T_w - T_{sat}) = 0.556 \left(\frac{\dot{q}_w}{1082 p^{1.156}} \right)^{0.463 p^{0.0234}}, \tag{2.105}$$

in SI units (p in bar).

In a very interesting paper, Kenning and Cooper (1965) investigated the flow field around an artificial bubble nucleus (air-water system). They then used this information, i.e., the velocity profile, to obtain the temperature distribution, which enabled them to propose a criterion for the incipience of nucleation. This is given by,

$$(T_w - T_{sat}) = 1.33 \frac{\dot{q}_w \eta_L}{\lambda_L \sqrt{\tau_w \rho_L}} \left[\frac{2\sigma \rho_L T_{sat} \lambda_L \tau_w}{\dot{q}_w \eta_L^2 \Delta h_v} \left(\frac{1}{\rho_G} - \frac{1}{\rho_L} \right) \right]^{0.6}. \tag{2.106}$$

Kenning and Cooper's (1965) correlation is valid over the range,

$$0.6 < \left[\frac{2\sigma \rho_L T_{sat} \lambda_L \tau_w}{\dot{q}_w \eta_L^2 \Delta h_v} \left(\frac{1}{\rho_G} - \frac{1}{\rho_L} \right) \right] < 20, \tag{2.107}$$

for water with an accuracy of $\pm 50\%$.

Marsh and Mudawar (1989) carried out detailed experiments on nucleate boiling in turbulent falling films (using water and FC-72) and also developed a theoretical model for predicting the onset of nucleate boiling for turbulent falling films. Their approach adapted earlier boiling incipience models (Bergles and Rohsenow, 1964; Davis and Anderson, 1966) so as to cope with the presence of waves and with the turbulence in the falling film. In stead of assuming a linear liquid temperature profile in the laminar sublayer (Davis and Anderson, 1966), they employed a turbulent film temperature profile. For the constant wall heat flux case, the temperature gradient is given by,

$$\frac{dT_L}{dy} = -\frac{\dot{q}_w}{\lambda_L}\left[1 + \frac{Pr_L}{Pr^*}\frac{\nu^*}{\nu_L}\right]^{-1}, \tag{2.108}$$

where Pr^* and ν^* are the turbulent Prandtl number and turbulent kinematic viscosity (Kays and Crawford, 1993).

The superheated vapour temperature profile obtained from the Clausius-Clapeyron equation was used (with the assumption of a constant value of $T\left(\frac{1}{\rho_G} - \frac{1}{\rho_L}\right)\Delta h_v^{-1}$),

$$T_E = T_{sat} + \frac{T_{sat}\left(\frac{1}{\rho_G} - \frac{1}{\rho_L}\right)}{\Delta h_v}\frac{2\sigma}{r}, \tag{2.109}$$

where r is the bubble radius.

As seen before, the tangency radius (the radius of the first cavity at which boiling occurs) is found by equating the slopes of T_L and T_E. In addition to their slopes being equal, T_E and T_I must also be equal at the point of tangency. After applying the appropriate substitutions, Marsh and Mudawar (1989) arrived at,

$$T_{wi} - T_{sat} = \left[\frac{8\sigma T_{sat}\left(\frac{1}{\rho_G} - \frac{1}{\rho_L}\right)\dot{q}_w}{\Delta h_v \lambda_L}\right]^{1/2} \Psi_t^{1/2}, \tag{2.110}$$

where Ψ_t is the turbulent boundary layer profile multiplier defined as,

$$\Psi_t = \frac{\left[\frac{1}{2} + \frac{1}{2}\int_0^1 \frac{\left[1+\frac{Pr_L}{Pr^*}\frac{\nu^*}{\nu_L}\right]}{\left[1+\frac{Pr_L}{Pr^*}\frac{\nu^*}{\nu_L}\right]} d\left(\frac{y}{r_{tan}}\right)\right]^2}{\left[1 + \frac{Pr_L}{Pr^*}\frac{\nu^*}{\nu_L}\right]}. \tag{2.111}$$

In addition to the boundary layer multiplier, Marsh and Mudawar introduced Ψ_w, the multiplier accounting for the effects of waves, turbulent eddies and for the curvature of the isotherms around the growing bubbles. As far as the effect of the waves is concerned, Marsh and Mudawar claim that a very complex flow pattern is characterised by the existence of turbulent bursts at the wall that are continuously interrupted by the passage of the waves. Rearranging and rewriting Eq. 2.110 gives,

$$\dot{q}_w = \frac{\Delta h_v \lambda_L}{8\sigma T_{sat}\left(\frac{1}{\rho_G} - \frac{1}{\rho_L}\right)} \left(T_{wi} - T_{sat}\right)^2 \frac{1}{\Psi_m}, \tag{2.112}$$

where,

$$\Psi_m = \Psi_t \Psi_w. \tag{2.113}$$

A least squares approximation to the water incipience data by Marsh and Mudawar gave an empirical value of $\Psi_m = 3.5$ with a mean error of 5.2%. They attribute this large value of Ψ_m to the pronounced waviness of the film flow. If the evaporative heat transfer coefficient is known, Marsh and Mudawar propose an alternative method of determining Ψ_m. By combining Eq. 2.112 and,

$$\dot{q}_w = \alpha_E \left(T_{wi} - T_{sat}\right), \tag{2.114}$$

the incipient wall superheat becomes,

$$\left(T_{wi} - T_{sat}\right) = \frac{1}{\Gamma}\Psi_m, \tag{2.115}$$

where,

$$\frac{\Delta h_v \lambda_L}{8\sigma T_{sat}\left(\frac{1}{\rho_G} - \frac{1}{\rho_L}\right)\alpha_E}. \tag{2.116}$$

Based on visual observation of the flow, Marsh and Mudawar postulated a heat transfer mechanism by which the waves in the film actually trigger off bubble nucleation. In their words, ' ...during nucleate boiling, a larger wall superheat is created upon the passage of large waves, providing more favourable conditions for nucleation compared to the thin film between the large waves. At the point of incipience, wall regions which are instantaneously favourable for bubble growth due to the passage of large waves are quickly covered with

thin film flow, which, together with the turbulent eddies, tend to deprive wall cavities of the superheat required for nucleation... '.

The interaction between the activity of bubble nucleation sites and disturbance waves in annular flow has been observed by Hewitt and collaborators at Harwell in the 1960's (Hewitt *et al.*, 1965). Their high-speed cinematography sequences showed that as the thickness of the liquid film varied with the presence of the disturbance waves, so did the intensity of the nucleation of the sites. In their experiments, the waves also seemed to *trigger off* rather than *suppress* nucleation activity. The amount of experimental evidence (number of ciné sequences) from this experiments is very small and, at the time, the authors did not attempt to provide an explanation for the observed phenomenon. Therefore, one of the objectives of the present study is to revive these experiments by carrying out extensive high-speed recording of such flows.

2.3.3 Other interpretations and secondary nucleation

Mesler (1977) contested the view that forced convection is the dominant heat transfer mechanism at high qualities by re-examining the data of Dengler and Addoms (1956). Mesler claimed that the positive slope of the data trend in Fig. 2.19 is not due to the enhancement of forced convection but to the inclusion of the same variable in the quantities being plotted against each other. He also showed that a model postulating nucleate boiling as the dominant mechanism could correlate Dengler and Addoms data as well as purely nucleate boiling data.

The question about the existence and importance of nucleate boiling at high qualities is fundamental and has generated a serious debate in the literature (Standiford, 1978; Beattie and Lawther, 1979; Beattie and Green, 1984).

The theory of Mesler is supported by experimental evidence (Williams and Mesler, 1967),

which indicated bubble growth within the microlayer underneath preceding bubbles. Simultaneously, local heat transfer fluxes up to ten times the average were detected. Reports that the heat transfer coefficient at high qualities and high mass fluxes can be predicted using a nucleate boiling correlation are available (Beattie and Green, 1984).

Experimental evidence is also widely obtainable to support the suppression of nucleation at high quality flows. Amongst many examples, one may cite those in which the measured heat flux (Hewitt *et al.*, 1965) or wall superheat (Kandlikar *et al.*, 1995) required to sustain nucleation increased with increasing quality and/or mass flux.

The essential evidence of the dominant heat transfer mechanism in annular flow is the examination of the $\dot{q}_w$ versus $(T_w - T_{sat})$ relationship. Aounallah *et al.* (1982) carried out tests to resolve the problem by taking highly accurate measurements of $(T_w - T_{sat})$ in a system in which quality and film thickness are decoupled from the heat flux. This is achieved by having an adiabatic equilibrium [1] section between the bottom heater (steam generation) and the top heater (test section). They found, for water at $p = 1$ bar, X up to 0.42, $(T_w - T_{sat})$ up to 10 K and $\dot{q}_w$ up to 175 kW m^{-2}, that $\dot{q}_w$ was directly proportional to $(T_w - T_{sat})$; an indication that no nucleate boiling occurred.

Butterworth and Shock (1982) suggested that an interesting test in an experimental arrangement similar to that of Aounallah *et al.* (1982) would be to set up a nucleate boiling situation with subcooled bulk flow in the upper heater and then to increase the heat load in the lower heater to see whether the linear relationship between $\dot{q}_w$ and $(T_w - T_{sat})$ still prevails.

The hydrodynamic features of annular flow may provide conditions under which nucleation can take place even if bubble generation is suppressed at the heated wall. Mesler and Mailen (1977) observed that in a thin falling film, the deposition of droplets which were

[1] A discussion of equilibrium annular flow and the effect of phase change on the entrainment is curve is presented in Section 2.3.6

ejected from the surface of the film due to bubble burst, caused entrainment of gas bubbles into the liquid film (in a way analogous to a water jet impinging on a free surface). If the liquid film is sufficiently thin, the gas (in the form of tiny bubbles) may be able to reach the supersaturated liquid region close to the surface of the heater. There, the small bubbles may act as sites (even at lower wall superheats), continuously maintaining the nucleation process. In fact, Mesler and Mailen (1977) observed that new bubbles do grow from the disturbances in the film where bubble rupture has occurred.

Attempts to elucidate the role of this *secondary nucleation* in equilibrium upward annular flows were made by Chan (1990) and by Sun (1996). The aim of their experimental works was to obtain values for the heat transfer coefficient, under identical hydrodynamic equilibrium conditions, for evaporating and condensing flows. They claimed that, if secondary nucleation was an important mechanism, then heat transfer coefficients for evaporation would be higher than those for condensation. The data obtained by Chan indicated that secondary nucleation effects were relevant as evaporation heat transfer coefficients were considerably higher. However, the accuracy of Chan's experiments was somewhat low. A need for accuracy improvements led to the investigations by Sun, who modified the test section previously used by Chan and carried out a new series of evaporation/condensation experiments. The new results showed virtually no difference between heat transfer coefficients in evaporation and condensation.

2.3.4 Heat transfer in upwards annular flow

In Section 2.2.3, it was mentioned that one-dimensional analyses which use the logarithmic profile approach coupled with the Reynolds analogy between momentum and heat transfer largely overpredict the heat transfer coefficient (at least for evaporation of water).

In this case the convective heat transfer coefficient is given by,

$$\alpha = \frac{\rho_L c_{pL} u^*}{T_I^+}, \tag{2.117}$$

where T_I^+ is the dimensionless interface temperature calculated through an integration of the thermal eddy diffusivity profile (Hewitt and Hall-Taylor, 1970). This is given by,

$$T_I^+ = \begin{cases} \delta^+ Pr_L & \text{for } 0 < \delta^+ \leq 5 \\ 5Pr_L + 5\ln\left[1 + Pr_L\left(\frac{\delta^+}{5} - 1\right)\right] & \text{for } 5 < \delta^+ \leq 30 \\ 5Pr_L + 5\ln\left(1 + 5Pr_L\right) + 2.5\ln\left(\frac{\delta^+}{30}\right) & \text{for } \delta^+ > 30. \end{cases} \tag{2.118}$$

Several attempts to correct the heat transfer coefficient overprediction were made over the years. The most common is the suggestion of a damping factor to account for turbulent reduction near the interface (Mudawwar and El-Masri, 1986).

A more sophisticated approach was put forward by Dobran (1983), who developed an expression for the momentum diffusivity of a wavy layer (he suggested that the liquid film is divided into a continuous layer and a disturbed wavy layer). He found good agreement with experimental data by adjusting to 0.5 the value of an effective Prandtl number defined as the ratio of the wavy layer momentum to the corresponding thermal diffusivity.

Clearly, as suggested by the CFD predictions of Jayanti and Hewitt (1997), the way forward seems to be a more phenomenological description of the flow in the film, i.e., with a distinction between the substrate and wave regions. Although such an approach may be still not practical, evidence of its feasibility has been demonstrated more than 20 years ago (Brumfield and Theofanous, 1976).

2.3.5 Correlations

As suggested by Collier and Thome (1994), boiling models can be classified by how the nucleate boiling and convective boiling coefficients are combined to obtain the total heat

transfer coefficient. The general power law type of model is of the form,

$$\alpha = [\alpha_{NB}^n + \alpha_{FC}^n]^{1/n} . \tag{2.119}$$

A simple addition (with $n = 1$) of the nucleate boiling and forced convective coefficients, which can be weighted or not by enhancement or suppression factors (Chen, 1966), is referred to as an *additive* model. The use of $1 < n < \infty$ leads to an *asymptotic* model, as the value of α tends to the higher of the two contributions. Finally, $n = \infty$ is the case of choosing the larger of the two coefficients.

The Chen correlation

The Chen (1966) correlation is of the additive type. The nucleate boiling contribution is calculated by the correlation by Forster and Zuber (1955) multiplied by a suppression factor S to account for the reduction of effective superheat caused by the coexistence of the forced convective mechanism. For the enhancement of the convective heat transfer coefficient, a parameter F is introduced which was shown by Chen through a Reynolds analogy to be represented as a function of the Martinelli parameter.

The heat transfer coefficient is given by,

$$\alpha = \alpha_{FC} F + \alpha_{NB} S, \tag{2.120}$$

where,

$$\alpha_{FC} = 0.023 \frac{\lambda_L}{d_T} Re_L^{0.8} Pr_L^{0.4}, \tag{2.121}$$

$$Re_L = \frac{\dot{m}_L d_T}{\eta_L}, \tag{2.122}$$

$$Pr_L = \frac{\eta_L c_{pL}}{\lambda_L}, \tag{2.123}$$

$$F = \begin{cases} 1 & \text{if } \frac{1}{X_{tt}} > 0.1 \\ 2.35\left[\frac{1}{X_{tt}} + 0.213\right]^{0.736} & \text{if } \frac{1}{X_{tt}} \leq 0.1, \end{cases} \tag{2.124}$$

$$\frac{1}{X_{tt}} = \left(\frac{\rho_L}{\rho_G}\right)^{0.5} \left(\frac{\eta_G}{\eta_L}\right)^{0.1} \left(\frac{X}{1-X}\right)^{0.9}, \tag{2.125}$$

$$\alpha_{NB} = 0.00122 \frac{\lambda_L^{0.79} c_{pL}^{0.45} \rho_L^{0.49} \Delta T_{sat}^{0.24} \Delta p_{sat}^{0.75}}{\sigma^{0.5} \eta_L^{0.29} \rho_G^{0.24} \Delta h_V}, \tag{2.126}$$

$$S = \frac{1}{1 + 2.53 \times 10^{-6} Re_{tp}^{1.17}}, \tag{2.127}$$

$$\Delta T_{sat} = T_w - T_{sat}, \tag{2.128}$$

$$\Delta p_{sat} = p_{sat}(T_w) - p_{sat}(T_{sat}), \tag{2.129}$$

and,

$$Re_{tp} = Re_L F^{1.25}. \tag{2.130}$$

The Shah correlation

The correlation by Shah (1982) is an upgrade of an earlier correlation by the same author. It is an example of a correlation of the third kind, i.e., one in which the greater of the nucleate boiling and convective components is used. It is also a classical example of correlations that are based on the boiling and convective numbers, Bo and Co. The correlation is as follows,

$$\frac{\alpha}{\alpha_L} = \max\left(F_{FC}, F_{NB}\right), \tag{2.131}$$

where E_{FC} and E_{NB} are the convective and boiling enhancement factors. These are given by,

$$F_{FC} = 1.8Co^{-0.8}, \tag{2.132}$$

and,

If $Co > 1.0$,

$$F_{NB} = \begin{cases} 230Bo^{0.5} & ; \text{if } Bo \geq 3 \times 10^{-4} \\ 1 + 46Bo^{0.5} & ; \text{if } Bo < 3 \times 10^{-4}. \end{cases} \tag{2.133}$$

If $0.1 < Co \leq 1.0$,

$$F_{NB} = GBo^{0.5} \exp\left(2.47Co^{-0.1}\right). \tag{2.134}$$

If $Co \leq 0.1$,

$$F_{NB} = GBo^{0.5} \exp\left(2.47Co^{-0.15}\right), \tag{2.135}$$

where G is equal to 14.7 if $Bo \geq 11 \times 10^{-4}$, or 15.3 if $Bo < 11 \times 10^{-4}$.

The Bjorge et al. correlation

Bjorge *et al.* (1982) proposed a correlation which is, for the high quality region ($X > 0.05$), of the additive type and, for the low quality region, of the asymptotic type (with $n = 2$). In terms of the total heat flux (for the high quality region),

$$\dot{q} = \dot{q}_{FC} + \dot{q}_{NB}\left[1 - \left(\frac{\Delta T_{ONB}}{\Delta T_{sat}}\right)^3\right], \tag{2.136}$$

where,

$$\Delta T_{ONB} = \frac{8\sigma T_{sat}\alpha_{FC}}{\lambda_L \Delta h_v}\left(\frac{1}{\rho_G} - \frac{1}{\rho_L}\right). \tag{2.137}$$

The forced convective contribution is correlated by,

$$\dot{q}_{FC} = \frac{Re_L^{0.9} Pr_L F(X_{tt})\lambda_L}{F_2 d_T}\Delta T_{sat}, \tag{2.138}$$

where,

$$F(X_{tt}) = 0.15\left[\frac{1}{X_{tt}} + 2.0\left(\frac{1}{X_{tt}}\right)^{0.32}\right], \tag{2.139}$$

and,

$$F_2 = \begin{cases} 5Pr_L + 5\ln\left(1 + 5Pr_L\right) + 2.5\ln\left(0.0031 Re_L^{0.812}\right) & ; \text{if } Re_L > 1125 \\ 5Pr_L + 5\ln\left[1 + Pr_L\left(0.0964 Re_L^{0.585} - 1\right)\right] & ; \text{if } 50 < Re_L < 1125 \\ 0.0707 Pr_L Re_L^{0.5} & ; \text{if } Re_L < 50. \end{cases} \tag{2.140}$$

The nucleate boiling contribution is calculated from,

$$\frac{\dot{q}_{NB}}{\eta_L \Delta h_v}\sqrt{\frac{\sigma}{g\left(\rho_L - \rho_g\right)}} = B_M \frac{\lambda_L^{0.5}\rho_L^{17/8} c_{pL}^{19/8}\rho_G^{1/8}}{\eta_L \Delta h_v^{7/8}\left(\rho_L - \rho_G\right)^{9/8}\sigma^{5/8} T_{sat}^{1/8}}\Delta T_{sat}^3, \tag{2.141}$$

where $B_M = 1.89 \times 10^{-14}$ in SI units. Bjorge *et al.* recommend this correlation for boiling of water in tubes. The heat transfer coefficient is given by $\frac{\dot{q}}{(T_w - T_{sat})}$.

The Kandlikar correlation

Kandlikar (1990) correlated over 5000 data points for various fluids. He proposed the following correlation,

$$\frac{\alpha}{\alpha_L} = C_1 Co^{C_2}\left(25 Fr_{LO}\right)^{C5} + C_3 Bo^{C_4} F_{fl}, \tag{2.142}$$

where α_L is calculated using the Dittus-Boelter correlation (see Eq. 2.121). Co is the convective number, Bo is the boiling number, Fr_{LO} is the liquid Froude number calculated using the total mass flux and F_{fl} is a fluid dependent parameter (for water, $F_{fl} \approx 1$). The constants C_1 to C_5 assume different values depending on the flow orientation and dominant heat transfer mechanism. In the convective boiling dominant region ($Co < 0.65$), $C_1 = 1.136$, $C_2 = -0.9$ and $C_3 = 667.2$. In the nucleate boiling dominant region ($Co > 0.65$), $C_1 = 0.6683$, $C_2 = -0.2$ and $C_3 = 1058.0$. $C_4 = 0.7$ (always). $C_5 = 0.3$, unless for vertical tubes and horizontal tubes with $Fr_{lo} > 0.04$, when it is equal to 0.

The Liu and Winterton correlation

Liu and Winterton (1991) proposed a correlation of the asymptotic type. The heat transfer coefficient is given by,

$$\alpha^2 = (F\alpha_{LO})^2 + (S\alpha_{NB})^2, \tag{2.143}$$

where α_{LO} is calculated from the Dittus-Boelter equation with the entire mass flow rate flowing as liquid, and α_{NB} is calculated using the Cooper (1984) correlation,

$$\alpha_{NB} = 55 p_r^{0.55} q_w^{2/3} \left(-\log_{10} p_r\right)^{-0.55} M_w^{-0.5}. \tag{2.144}$$

The enhancement and suppression factors are given by,

$$F = \left[1 + XPr_L \left(\frac{\rho_L}{\rho_G} - 1\right)\right]^{0.35}, \tag{2.145}$$

and,

$$S = \left(1 + 0.055 F^{0.1} Re_{LO}^{0.16}\right)^{-1}. \tag{2.146}$$

For flow in annuli, Liu and Winterton suggest the use of an equivalent diameter given by,

$$d_H = \frac{4 \times \text{ flow area}}{\text{heated perimeter}} = \frac{d_a^2 - d_o^2}{d_o^2}, \tag{2.147}$$

where d_a and d_o are the outer and inner diameters of the annular channel.

Liu and Winterton claim that Eq. 2.143 predicts saturated flow boiling data with ±20.5% deviation. Others correlations perform closely, except for the Chen (1966) correlation. This may be due to the inclusion of horizontal flow data.

The Steiner and Taborek correlation

The correlation by Steiner and Taborek (1992) was developed from a large data bank of more than 13000 data points. It is the method recommended by Collier and Thome (1994). The asymptotic expression is given by,

$$\alpha = \left[(F\alpha_{LO})^3 + (F_{NB}\alpha_{NB,O})^3\right]^{1/3}, \tag{2.148}$$

where F is the two-phase multiplier (Eq. 2.149). α_{LO} is calculated from the Gnielinski (1976) correlation based on the total flow as liquid.

$$F = \left[(1-X)^{1.5} + 1.9X^{0.6}\left(\frac{\rho_L}{\rho_G}\right)^{0.35}\right]^{1.1}. \tag{2.149}$$

F_{NB} is the nucleate boiling correction factor expressed as,

$$F_{NB} = F_{PF}\left(\frac{\dot{q}}{\dot{q}_0}\right)^{nf}\left(\frac{d_T}{d_{T0}}\right)^{-0.4}\left(\frac{R_p}{R_{p0}}\right)^{0.133} F_M, \tag{2.150}$$

where F_M is a molecular weight correction (0.72 for water). R_{p0}, d_{T0} and $\dot{q}_0$ are standard reference values (equal to 1 μm, 0.01 m and 150 kW m^{-2} respectively). F_{PF} and nf are the pressure correction factor and the heat flux correction exponent. These are given by,

$$F_{PF} = 2.816p_r^{0.45} + \left(3.4 + \frac{1.7}{1-p_r^7}\right)p_r^{3.7}, \tag{2.151}$$

and,

$$nf = 0.8 - 0.1 \exp\left(1.75 p_r\right). \tag{2.152}$$

The authors present the values of α_{NB} in tabular form.

The Bennett et al. correlation

The Bennett *et al.* (1961) correlation is one that does not follow the general form given by Eq. 2.119. The correlation was devised based on a database obtained for boiling in annuli and has a general form similar to those of Guerrieri and Talty (1956) and Dengler and Addoms (1956). However, in contrast with these works, Bennett *et al.* (1961) found a slight but systematic effect of the heat flux in the convective region. For constant quality and flow rate, the dependence can be expressed as,

$$\alpha \propto \dot{q}_w^{0.11}. \tag{2.153}$$

In its final form, the correlation for the *convection* dominated data is given by,

$$\frac{\alpha}{\alpha_L} = 0.64 \dot{q}_w^{0.11} \left(\frac{1}{X_{tt}}\right)^{0.74}, \tag{2.154}$$

where $\dot{q}_w$ is expressed in Btu h^{-1} ft^{-2}. α_L is calculated using the Dittus-Boelter relationship as follows,

$$\alpha_L = 0.023 \frac{\lambda_L}{d_e} \left[\frac{d_e \dot{m} (1 - X)}{\eta_L}\right]^{0.8} \left[\frac{c_{pL} \eta_L}{\lambda_L}\right]^{0.4}, \tag{2.155}$$

where d_e is the equivalent diameter for an annulus.

Later, Collier *et al.* (1964) recommended that better results with the Bennett *et al.* (1961) correlation were obtained if physical properties were evaluated at the film temperature, T_f, given by,

$$T_f = T_{sat} + 0.33\Delta T_{sat}, \tag{2.156}$$

with T in ^oF.

2.3.6 Critical Heat Flux (CHF)

The two main methods of correlating CHF data are,

1. in terms of the heat flux as a function of quality,
2. in terms of the quality at dryout as a function of the length between the onset of bulk boiling and the dryout point.

As pointed out by Hewitt (1996), neither approach to correlation has any fundamental justification; each representation may be more advantageous in some instances than the other. The two correlating parameters are related as follows,

$$CHF = \frac{\dot{m}_T d_T \Delta h_v}{4z}\left[X_{cr} + \frac{cp_L\left(\Delta T_{sub}\right)_{inlet}}{\Delta h_v}\right]. \tag{2.157}$$

The most widely used correlation for CHF is that of Katto and Ohno (1984). Other correlations, as well as standard CHF data tables can be found in text books (Collier and Thome, 1994). The Katto and Ohno (1984) correlation is given by,

$$CHF = \mathsf{X}\dot{m}_T\left[\Delta h_v + \mathsf{K}\Delta h_{sub}\right]. \tag{2.158}$$

The terms X and K are functions of three groups, $Z' = \frac{z}{d_T}$, $R' = \frac{\rho_G}{\rho_L}$ and $W' = \left[\frac{\sigma\rho_L}{\dot{m}_T^2 z}\right]$. The variables X_1 to X_5 are given by,

$$\mathsf{X}_1 = \frac{CW'^{0.043}}{Z'}, \tag{2.159}$$

$$\mathsf{X}_2 = \frac{0.1R'^{0.133}W'^{0.333}}{1+0.0031Z'}, \tag{2.160}$$

$$\mathsf{X}_3 = \frac{0.098R'^{0.133}W'^{0.433}Z'^{0.27}}{1+0.0031Z'}, \tag{2.161}$$

$$\mathsf{X}_4 = \frac{0.0384R'^{0.6}W'^{0.173}}{1+0.28W'^{0.233}Z'}, \tag{2.162}$$

$$\mathsf{X}_5 = \frac{0.234R'^{0.513}W'^{0.433}Z'^{0.27}}{1+0.0031Z'}. \tag{2.163}$$

The variables K_1 to K_3 are given by,

$$\mathsf{K}_1 = \frac{0.261}{CW'^{0.043}}, \tag{2.164}$$

$$\mathsf{K}_2 = \frac{0.833\left[0.0124+(1/Z')\right]}{R'^{0.133}W'^{0.333}}, \tag{2.165}$$

$$\mathsf{K}_3 = \frac{1.12\left[1.52W'^{0.233}+(1/Z')\right]}{R'^{0.6}W'^{0.173}}. \tag{2.166}$$

The value of C is given by,

$$C = \begin{cases} 0.25 & ;\text{ if } Z' < 50 \\ 0.25 + 9\times10^{-4}\left(Z'-50\right) & ;\text{ if } 50 < Z' < 150 \\ 0.34 & ;\text{ if } Z' > 150. \end{cases} \tag{2.167}$$

The appropriate values of X and K are chosen according to Table 2.3.

The Katto and Ohno (1984) correlation is valid over the following ranges of data, $0.01 < z < 8.8$ m, $0.001 < d_T < 0.038$ m, $0.0003 < R' < 0.41$, $3\times10^{-9} < W' < 2\times10^{-2}$.

The inadequacy of the correlation approach was demonstrated in the experiments of Bennett *et al.* (1967b) , who determined the dryout heat flux for a 4.26 m long, 12.6 mm

Table 2.3: X and K values for Katto and Ohno (1984) correlation.

For	$R' < 0.15$	$R' > 0.15$
If	$X_1 < X_2$, $X = X_1$	$X_1 < X_5$, $X = X_1$
	$X_1 > X_2$ and $X_2 < X_3$ } $X = X_2$	$X_1 > X_5$ and $X_5 > X_4$ } $X = X_5$
	$X_1 > X_2$ and $X_2 > X_3$ } $X = X_3$	$X_1 > X_5$ and $X_5 < X_4$ } $X = X_4$
	$K_1 > K_2$, $K = K_1$	$K_1 > K_2$, $K = K_1$
	$K_1 < K_2$, $K = K_2$	$K_1 < K_2$ and $K_2 < K_3$ } $K = K_2$
		$K_1 < K_2$ and $K_2 > K_3$ } $K = K_3$

internal diameter tube in which a 0.61 m long unheated section (a "cold patch") could be located at different distances along the pipe. They observed a systematic change in the critical heat flux depending on the location of the cold patch. This fact is better illustrated in Figs. 2.21 and 2.22. In Fig. 2.21, film flow rate measurements for uniformly heated tubes with cold patches near the inlet and near the outlet are reported. Figure 2.22 shows the same results in terms of the entrained liquid flow rate as a function of local quality. The effect of the cold patch is due to a relaxation of the system towards hydrodynamic equilibrium (when the rates of entrainment and deposition are equal). Dryout occurs

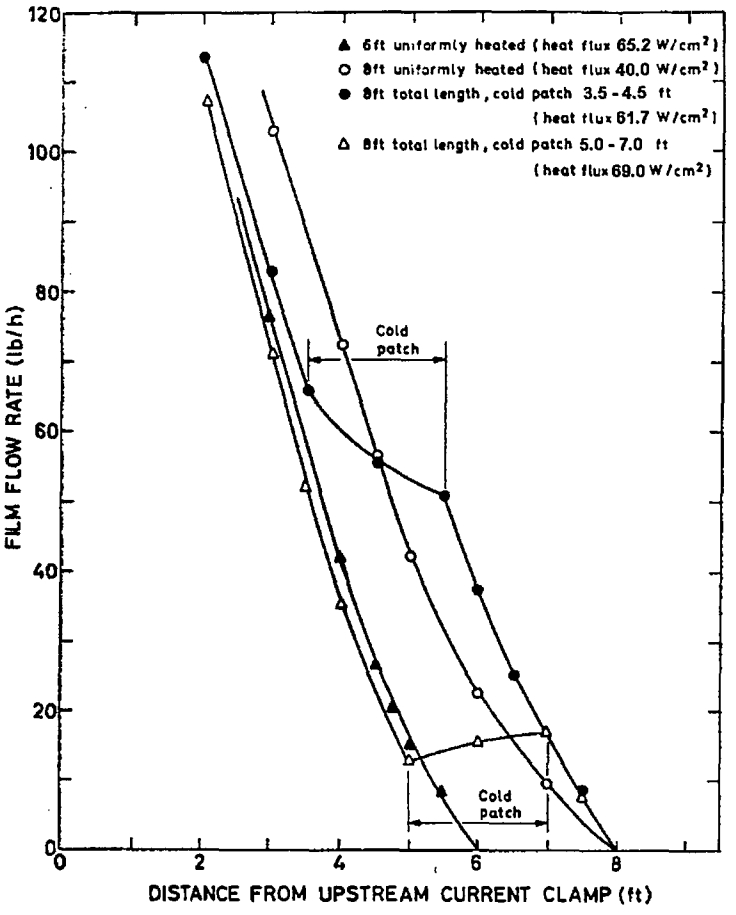


Figure 2.21: Variation of film flow with length for uniformly heated tubes with unheated zones (Bennett *et al.*, 1967b).

when the entrained flow equals the total liquid flow.

It is clear from the information above that only a phenomenological approach would provide reliable predictions of the dryout problem. Such an approach is undertaken by means of annular flow modelling as presented in Section 2.2.3. Naturally, such a task would involve the knowledge of the rates of droplet entrainment and deposition and the dryout position is given by the distance at which $\dot{m}_{LF} = 0$.

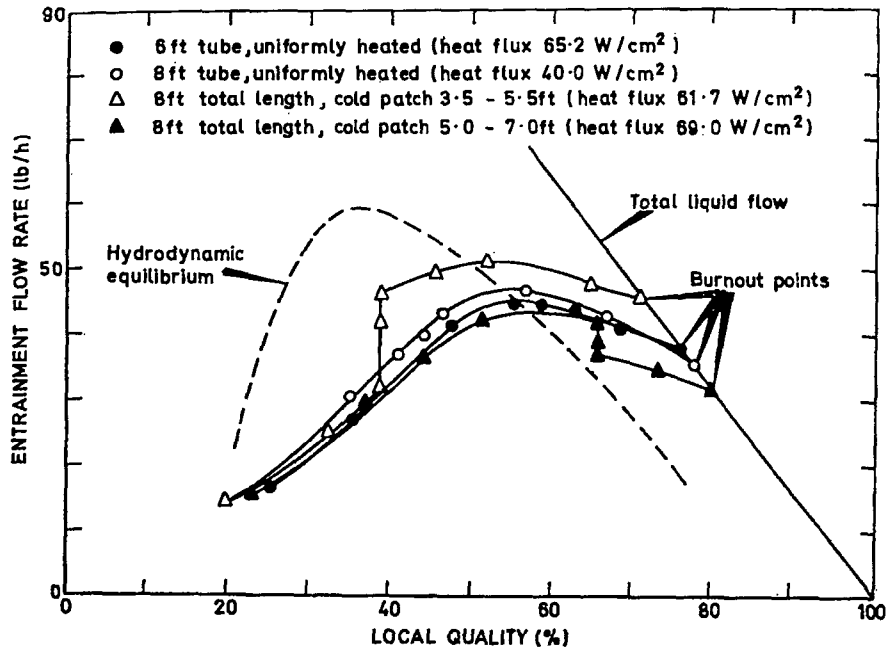


Figure 2.22: Variation of the flow rate of entrained droplets with local quality (Bennett *et al.*, 1967b).

2.4 Flow boiling of multicomponent mixtures

A detailed knowledge of the phenomena involved in boiling of mixtures is of great importance in the chemical, process and refrigeration industries. In the past three decades or so, efforts have been made towards gaining a better understanding of local mechanisms such as bubble formation and growth and multicomponent diffusion. However, despite the evident advances, there is a dearth of adequately predictive and design methods for forced convective boiling of mixtures. The majority of methods has very little physical basis and most of heat transfer calculations rely on empirical corrections to coefficients calculated for pure substances.

In this section, the available calculation methodologies for forced convective boiling of mixtures are reviewed. These are presented in order of increasing complexity, the complexity depending on the detail with which mass transfer calculations are executed.

Before discussing these calculation methodologies, however, a brief review of phase equilibrium in multicomponent systems is presented, followed by a review of some of the experimental work undertaken in the field of multicomponent phase change.

2.4.1 Phase equilibrium in multicomponent systems

Phase equilibrium thermodynamics describes the relationships between the physical parameters of a given system (e.g., pressure, temperature, volume and composition) existing between two or more phases in direct contact when those are in a state of equilibrium. Bett *et al.* (1975) define the equilibrium state as one which (i) does not change over the time scale of interest, and (ii) a small change made to it can be reversed to its initial state.

The usefulness of phase equilibrium calculations is that it allows the prediction of various properties in each phase knowing only a limited number of physical properties of the system (for instance, saturation pressure and composition of the liquid phase).

Phase equilibrium diagrams, such as the one depicted in Fig. 2.23 for a binary mixture at a constant pressure, serve to visualise the relationships between pressure, temperature and composition in the phases. The more volatile, or lighter, component is that with the lower saturation temperature at the pressure of interest.

The dew point and the bubble point lines are shown in Fig. 2.23. The dew point line denotes the variation in *equilibrium* vapour mole (or mass) fraction with saturation temperature. The bubble point line depicts the functional dependency of the *equilibrium* liquid mole (or mass) fraction on the saturation temperature.

For *non-azeotropic* (or *zeotropic*) mixtures, the following relationships always hold,

$$\begin{aligned} \tilde{y}_i &\geq \tilde{x}_i \quad \text{for the lighter component} \\ \tilde{y}_i &\leq \tilde{x}_i \quad \text{for the heavier component.} \end{aligned} \tag{2.168}$$

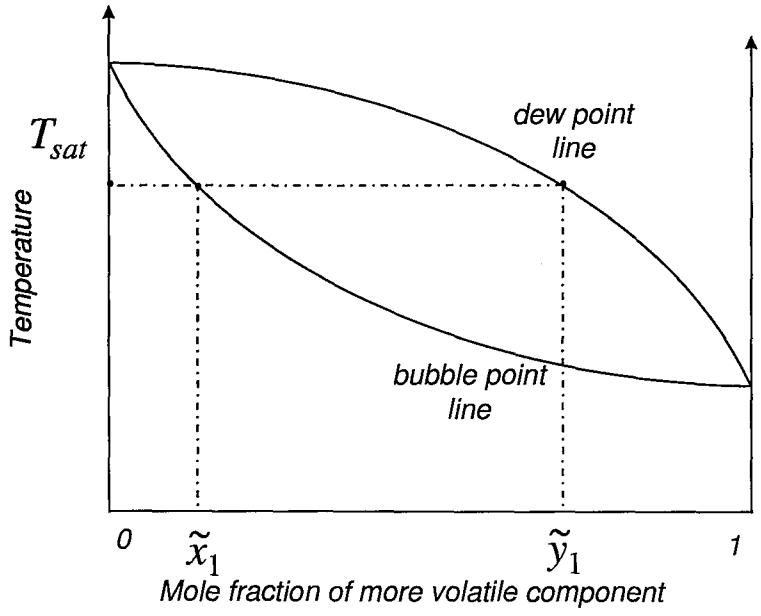


Figure 2.23: Phase diagram for an non-azeotropic binary mixture.

In some mixtures, significant differences in intermolecular forces lead to the formation of an azeotrope. This happens when, at one (or more) particular composition the dew point and bubble point temperatures are equal and the mixture behaves as a single component fluid.

Figure 2.24 shows a phase diagram for a non-azeotropic ternary mixture. In this figure, component 1 represents the most volatile component and component 3 the least volatile. *Ideal* systems are those that follow Raoult's law. This law states that the vapour mole fraction of component i is directly proportional to the liquid mole fraction via the ratio of its saturation vapour pressure at the same temperature to the total system pressure,

$$\tilde{y}_i = \tilde{x}_i \frac{p_i}{p}. \tag{2.169}$$

Equation 2.169 is of practical use for predicting equilibrium in mixtures such as those in Fig. 2.23, but is of limited general use because of the assumptions from which it is

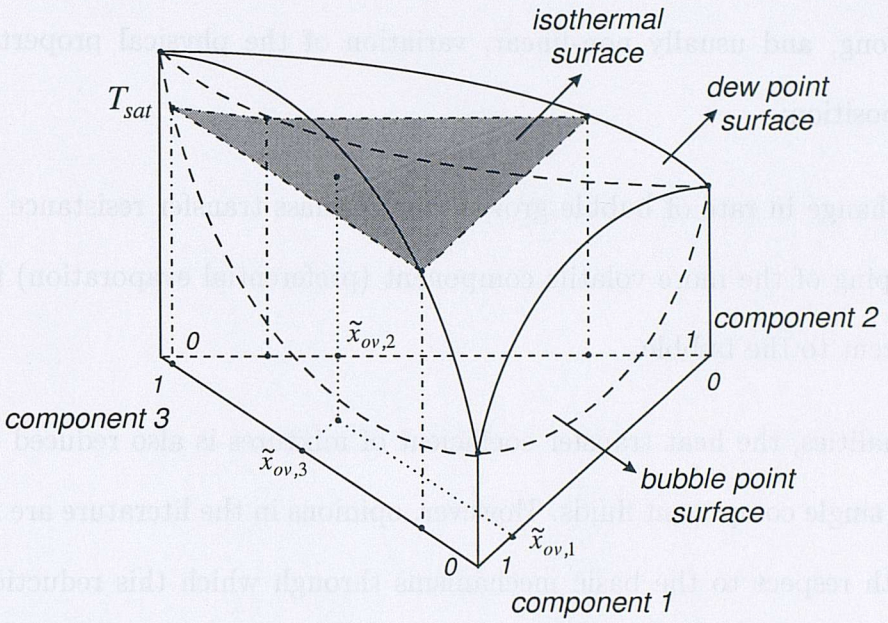


Figure 2.24: Phase diagram for an non-azeotropic ternary mixture.

derived. Effects due to a departure from the ideal behaviour are better accounted for using more sophisticated methods, such as Equations of State (Peng and Robinson, 1976) and the Principle of Corresponding States.

2.4.2 A summary of experimental investigations

Kandlbinder (1997) carried out an excellent review of the experimental work on forced convective boiling of multicomponent mixtures and a similar discussion will not be pursued here. Rather, the aim of the present section is to make use of the review by Kandlbinder in a more qualitative appraisal of the problem.

At the present time, there is a consensus that, in the nucleate boiling dominant region, the heat transfer coefficient for a mixture is reduced when compared with that of the single components under similar conditions. This observation is endorsed by vast experimental evidence (Shock, 1982; Thome and Shock, 1984). In essence, the decrease in the boiling

heat transfer coefficient is a combination of mainly two effects,

1. a strong, and usually non-linear, variation of the physical properties with local composition;

2. the change in rate of bubble growth due to mass transfer resistance caused by the stripping of the more volatile component (preferential evaporation) from the layer adjacent to the bubble.

At high qualities, the heat transfer coefficient of mixtures is also reduced in comparison to those of single component fluids. However, opinions in the literature are not yet clearly formed with respect to the basic mechanisms through which this reduction takes place (Shibata *et al.*, 1994; Fujita and Tsutsui, 1998).

Results presented in this thesis indicate that an additional mechanism characteristic of the annular regime, namely, the effect of the axial gradient of liquid concentration on droplet interchange between the liquid film and the gas core may also be responsible, together with mass transfer resistance, for the deterioration of the heat transfer coefficient at high qualities. These issues are explored in detail in Chapter 4.

Figure 2.25, from Kandlbinder (1997) illustrates the heat transfer coefficient deterioration at high qualities. Similar behaviour was observed by many investigators for both vertical (Celata *et al.*, 1993) and horizontal tube orientations (Wettermann and Steiner, 2000).

A recent experimental study of flow boiling of water-methanol mixtures in vertical pipes was carried out by Shatto (1998). He performed tests for various concentrations and two pipe diameters (15.9 and 19.1 mm internal diameter). The total mass fluxes ranged from 30 to 220 kg m^{-2} s^{-1} and the heat fluxes from 10 to 110 kW m^{-2}. A wide range of qualities was investigated. Shatto found that in the nucleate boiling dominant region, the mixtures showed a very strong degradation in heat transfer compared to the pure components. He proposed a correlation of the additive type in which the forced convective component also

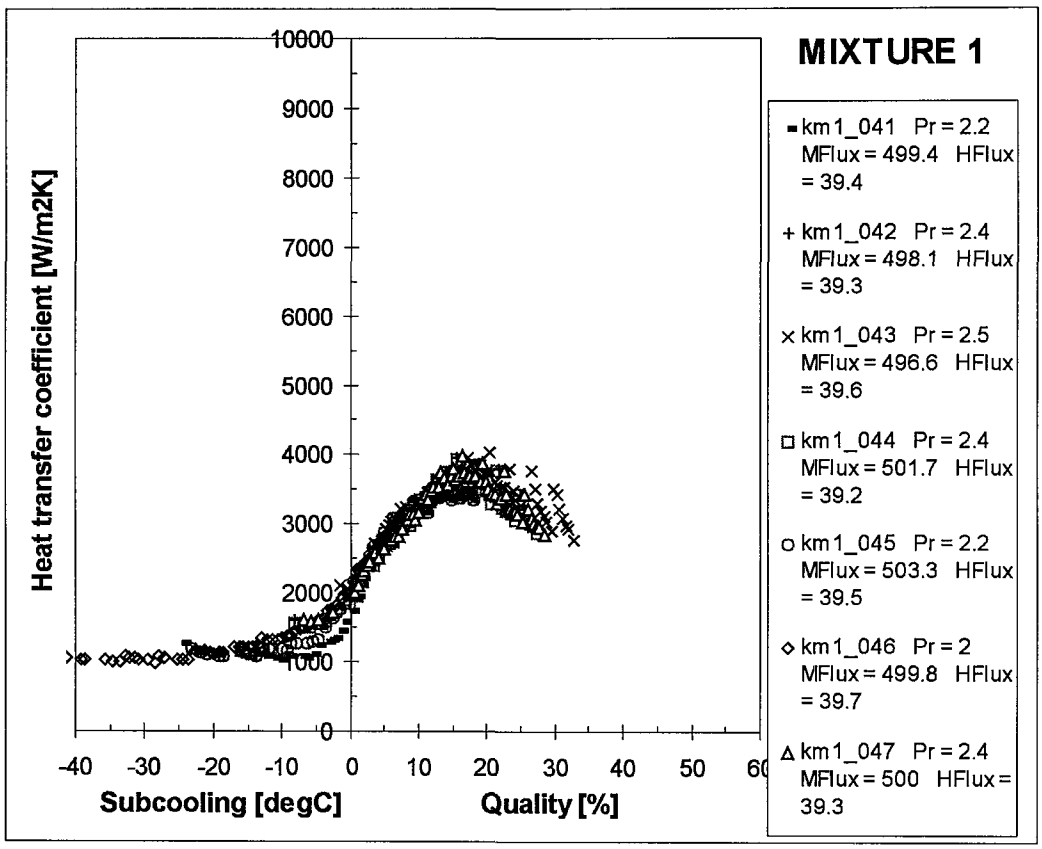


Figure 2.25: Example of deterioration of the heat transfer coefficient at high qualities for boiling of mixtures. Experimental conditions: Mixture 0.7/0.3 n-pentane/iso-octane (mass fraction), $p = 2.2$ bara, $\dot{m}_T = 500$ kg m^{-2} s^{-1} (nominal), $\dot{q}_w = 40$ kW m^{-2} (Kandlbinder, 1997).

had a correction factor for the effect of mass transfer resistance in the vapour core and non-equilibrium due to slip between the phases.

Shatto (1998) also compared the database with the correlations of Bennett and Chen (1980) and Kandlikar (1998). The Bennett and Chen (1980) correlation overpredicted the data for pure methanol and also predicted strong mass transfer resistance effects in situations where it appeared to be negligible. The Kandlikar (1998) correlation underpredicted most of his data. He attributed this to the fact that nucleation might be present in most of his data.

2.4.3 Modelling and prediction of phase change in multicomponent systems

In multicomponent evaporating systems, the difference in volatility between the components gives rise to axial gradients of concentration (and hence of saturation temperature) in both liquid and vapour streams due to the preferential evaporation of the more volatile component(s) even when local component equilibrium occurs. Fig. 2.26, reproduced from Thome and Shock (1984), illustrates the axial distributions of saturation and wall temperature for a mixture and for a single component undergoing phase change in a tube. As the quality increases, the liquid phase becomes richer in the less volatile component and the fluid saturation temperature increases (in many cases, overcoming the decrease associated with the negative axial pressure gradient).

The heat transfer coefficient in mixture systems is normally defined by the following equation,

$$\alpha = \frac{\dot{q}_w}{(T_w - T_E)}, \tag{2.170}$$

where $\dot{q}_w$ is the heat flux imposed to the walls of the tube, T_w is the temperature of

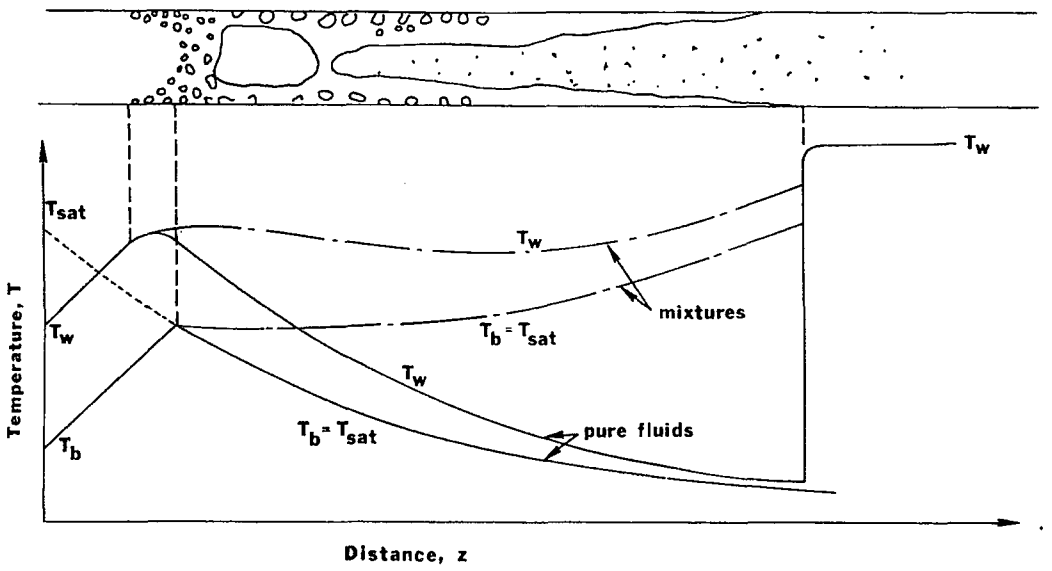


Figure 2.26: Temperature profiles and boiling regimes for convective evaporation (Thome and Shock, 1984).

the inner wall of the tube and T_E is the flow equilibrium bulk temperature calculated from the local mean enthalpy and pressure. For the cases of boiling and evaporation, $T_E = T_{bub}$. As seen before, it is a commonly acknowledged experimental fact that heat transfer coefficients for mixtures are lower than those for pure fluids with identical physical properties.

In annular flow, in the absence of nucleation, the decrease associated with mixture effects takes place in different ways depending on the form of heating imposed to the surface (Wadekar, 1990). For simplicity, a case in which droplet interchange is assumed not to exist is depicted (see Fig. 2.27).

In the wall temperature controlled case, the decrease in α is due to the reduction in the temperature driving force is from $T_w - T_{bub}(\tilde{x}_b)$ to $T_w - T_{bub}(\tilde{x}_I)$. In the heat flux controlled case, the rise in the interface temperature does not change the temperature driving force. Rather, it must remain unchanged so that the product of the local (film)

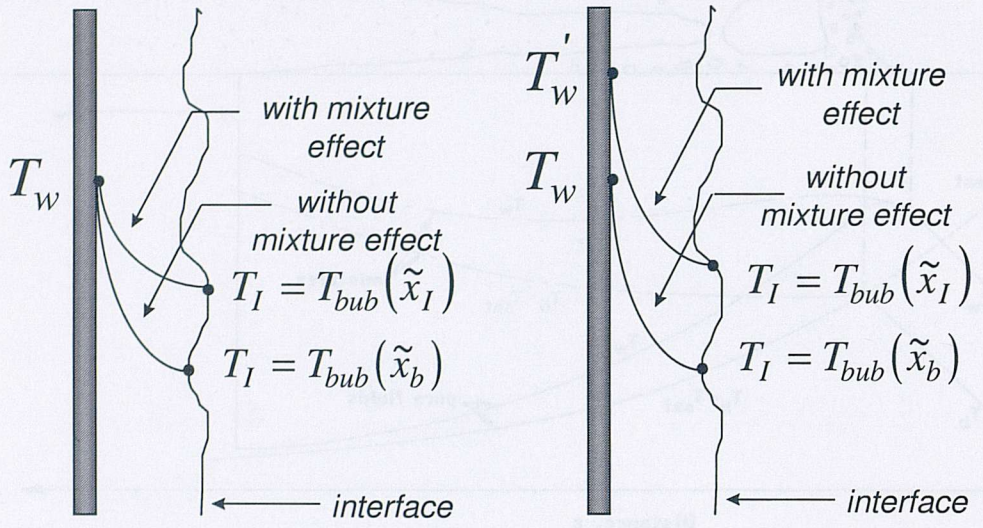


Figure 2.27: Illustration of liquid phase temperature profiles; (a) wall temperature controlled case, (b) heat flux controlled case (Wadekar, 1990).

heat transfer coefficient and the driving force is equal to the applied heat flux [2]. The increase in wall temperature from T_w to T_w' is illustrated in Fig. 2.27.b.

So what causes the decrease in α observed so systematically in the literature for the constant heat flux case? The answer is practicality. For engineering design calculations, it is more convenient to define α in terms of $T_w' - T_{bub}(\tilde{x}_b)$ than $T_w' - T_{bub}(\tilde{x}_I)$, where T_w' is generally determined experimentally. Because $T_{bub}(\tilde{x}_b)$ is lower than $T_{bub}(\tilde{x}_I)$, the ratio of the wall heat flux to the design based wall superheat is also lower. It is therefore expected that conventional prediction methods that do not take these effects into account will overestimate the experimental heat transfer coefficient.

[2] It is implicitly assumed that the liquid film heat transfer coefficient is independent of mixture effects. The validity of such a hypothesis will be discussed in Chapter 4 and in Appendix B

2.4.4 Review of Prediction Methods for Convective Boiling of Mixtures

As mentioned before, several methods are available in the literature to calculate forced convective boiling heat transfer to mixtures. The degree of complexity of such methodologies lies basically on the way mass transfer effects within the phases are assessed. Here, the methods are gathered in three main groups, (i) correlations, (ii) equilibrium methods and (iii) film (or Colburn) methods. These are extensively discussed below.

Correlations

Predictive methods for boiling of pure fluids form the basis for development of methods for mixtures. Of all correlations for pure fluids, the most widely used is the one proposed by Chen (1966) (see Section 2.3.5). An adaptation of the Chen correlation for mixtures was proposed by Bennett and Chen (1980), based on data obtained with an ethylene glycol-water mixture. Modified enhancement and suppression factors, F_{mix} and S_{mix}, were proposed so as to cope with mixture effects in both nucleate boiling and convective portions. These are as follows,

$$F_{mix} = F\left(\frac{Pr_L + 1}{2}\right)^{0.444}\left[1 - \frac{(1-y)\,\dot{q}_w}{\rho_L \Delta h_V \beta_{12_L} \Delta T}\frac{\partial T_{sat}}{\partial x}\right], \tag{2.171}$$

$$S_{mix} = S\left[1 - \frac{c_{pL}\,(y-x)}{\Delta h_V}\frac{\partial T_{sat}}{\partial x} Le_L^{1/2}\right]^{-1}. \tag{2.172}$$

The Lewis number, Le, is defined as the ratio between the thermal and mass diffusivities. x and y are the concentrations of the more volatile component in the liquid and in the vapour, respectively. The mass transfer coefficient for the liquid, β_{12_L}, is calculated via a Dittus-Boelter relationship using a modified two-phase Reynolds number in the form,

$$Re_{tp} = Re_L \left[F \left(\frac{Pr_L + 1}{2} \right)^{0.444} \right]^{1.25}. \tag{2.173}$$

It may be worth mentioning that Wadekar (1994) pointed out and rectified a conceptual error in the derivation of the local mixture effects modelling equations by Bennett and Chen (1980). According to Wadekar, the term corresponding to the bulk motion, $d\dot{m}_{ev}x_b$, where $d\dot{m}_{ev}$ is the rate of liquid vaporisation and x_b is the liquid bulk composition, was omitted by Bennett and Chen (1980).

Celata *et al.* (1993) compared both Chen (1966) and Bennett and Chen (1980) correlations for boiling of refrigerant mixtures. They found that the performance of the correlation for pure fluids is very similar to that for mixtures. The Chen (1966) correlation showed only a slightly larger scatter in the data for an error band greater than $\pm 20\%$. The correlation by Mishra *et al.* (1981) was also implemented, but it showed lower accuracy.

Palen (1992) also suggested the use of a modified form of the correlation by Chen (1966) for boiling of mixtures. In this case, no correction was proposed for the forced convective contribution. The heat transfer coefficient is given by,

$$\alpha = \alpha_{FC}F + \alpha_{NB}k_{mix}S, \tag{2.174}$$

where k_{mix} is a mixture correction factor defined by Palen and Small (1964) as,

$$k_{mix} = \exp(-0.027\Delta T_{bp}), \tag{2.175}$$

and ΔT_{bp} is the boiling range (difference between the dew point and bubble point temperatures).

Kandlbinder (1997), after comparing the performance of several correlations for boiling of mixtures, concluded that, though none of the existing correlations performed well, the correlation by Chen (1966) with correction suggested by Palen (1992) gave the best

results. Thus, the Chen/Palen formulation was chosen to be one of the methods for calculating wall temperatures compared in the present thesis. More recently, Kandlikar (1998) proposed an upgraded correlation for binary systems based on a correlation for pure fluids (Kandlikar, 1990). This incorporates the volatility parameter,V_1 , to account for severe suppressions observed for mixtures with larger volatility differences. V_1 is given by,

$$V_1 = \frac{c_{pL}}{\Delta h_v}\left(\frac{\kappa}{\Delta_{12}}\right)^{0.5}\frac{dT_{bub}}{dx_1}(y_1 - x_1). \tag{2.176}$$

This volatility parameter was originally proposed by Scriven (1959) and is usually termed as the Scriven number, Sn.

The correlation by Kandlikar (1998) is divided into three regions as follows,

Region 1: Near-azeotropic region; $V_1 \leq 0.03$

In this region, the correlation for pure fluids (Kandlikar, 1990) with mixture properties is applicable. This is given by the larger of α_{NBD} and α_{CBD}, namely the nucleate boiling and forced convective boiling dominant regions. These are given by,

$$\alpha_{NBD} = 0.6683Co^{-0.2}(1-x)^{0.8}\alpha_{LO} + 1058.0Bo^{0.7}(1-x)^{0.8}F_{Fl}\alpha_{LO}, \tag{2.177}$$

and

$$\alpha_{CBD} = 1.136Co^{-0.9}(1-x)^{0.8}\alpha_{LO} + 667.2Bo^{0.7}(1-x)^{0.8}F_{Fl}\alpha_{LO}, \tag{2.178}$$

where F_{Fl} is tabled by Kandlikar (1998) for various substances and α_{LO} is given by the correlations of Pethukov and Popov (1963) or Gnielinski (1976).

Region 2: Moderate diffusion-induced suppression region; $0.03 < V_1 < 0.2$ **and** $Bo > 1 \times 10^{-4}$

In this region, convective boiling dominates as nucleation is suppressed due to mass diffusion resistance. The heat transfer coefficient is given by,

$$\alpha_{CBD} = 1.136Co^{-0.9}(1-x)^{0.8}\alpha_{LO} + 667.2Bo^{0.7}(1-x)^{0.8}F_{Fl}\alpha_{LO}. \tag{2.179}$$

Region 3: Severe diffusion-induced suppression region; (a) $0.03 < V_1 < 0.2$ **and** $Bo \leq 1 \times 10^{-4}$ **and (b)** $V_1 \geq 0.2$

$$\alpha_{CBD} = 1.136Co^{-0.9}(1-x)^{0.8}\alpha_{LO} + 667.2Bo^{0.7}(1-x)^{0.8}F_{Fl}\alpha_{LO}F_D, \tag{2.180}$$

where the diffusion-induced suppression factor, F_D, is given by,

$$F_D = \frac{0.678}{1+V_1}. \tag{2.181}$$

According to Kandlikar (1998), the severe diffusion-induced suppression region is dominated by the convective terms. The nucleate boiling contribution in this region is further reduced due to the large difference in composition between the two phases.

Equilibrium or Silver, Bell and Ghaly (SBG) methods

Equilibrium methods for condensation were firstly devised by Silver (1947) and later, independently, by Bell and Ghaly (1973). Palen *et al.* (1980) were the first to use the methodology to evaporation of a pure component (water) in the presence of an inert gas (air). Later, Sardesai *et al.* (1982) proposed an extension to problems in which nucleate boiling also occurs. Here, the set of equations derived by Bell and Ghaly (1973) will be presented and then followed by the corrections of Sardesai *et al.* (1982). Subsequently, the main assumptions adopted in the derivation will be discussed.

The idea behind the equilibrium approach is quite simple, no direct computation of resistances to mass transfer are made and it is then postulated that these are accounted for in the calculation of the heat transfer resistances. It is worthwhile mentioning at this stage that, as the theory was devised for filmwise condensation, the geometry of the problem is that of a liquid film coating the inner wall of a circular tube.

The total heat flux $\dot{q}$ in the transfer of an amount of heat $d\dot{\mathbf{Q}}$ through an increment of area dA, is defined as,

$$\dot{q} = \frac{d\dot{\mathbf{Q}}}{dA}, \tag{2.182}$$

and the sensible heat flux to the vapour (gas) core is,

$$\dot{q}_{GC} = \frac{d\dot{\mathbf{Q}}_{GC}}{dA}. \tag{2.183}$$

A combination of Eqs. 2.182 and 2.183 yields,

$$\frac{\dot{q}_{GC}}{\dot{q}} = \frac{d\dot{\mathbf{Q}}_{GC}}{d\dot{\mathbf{Q}}}. \tag{2.184}$$

If one makes the (minor) assumption that all the heat absorbed in heating the liquid film crosses the whole thickness of the film, it is possible to write,

$$\dot{q} = \alpha_{LF}(T_w - T_I), \tag{2.185}$$

where α_{LF} is the heat transfer coefficient to the liquid film. Also writing a similar expression for the sensible heating of the vapour,

$$\dot{q}_{GC} = \alpha_{GC}(T_I - T_{GC}). \tag{2.186}$$

Eliminating T_I from Eqs. 2.185 and 2.186 one gets,

$$\dot{q} = \frac{1}{\frac{1}{\alpha_{LF}} + \frac{Z}{\alpha_{GC}}}(T_{GC} - T_w). \tag{2.187}$$

Thus,

$$\alpha = \frac{1}{\frac{1}{\alpha_{LF}} + \frac{Z}{\alpha_{GC}}}, \tag{2.188}$$

where,

$$Z = \frac{\dot{q}_{GC}}{\dot{q}} = \frac{d\dot{\mathbf{Q}}_{GC}}{d\dot{\mathbf{Q}}}. \tag{2.189}$$

In order to simplify the analysis of Eq. 2.189, two further assumptions are made. These are as follows,

1. The parameter Z is evaluated on the basis of an equilibrium phase change curve, i.e., the vapour phase condition can be evaluated based on equilibrium conditions at a given pressure. Z is thus given by,

$$Z = X c_{pGC} \frac{dT_{sat}}{dh}, \tag{2.190}$$

where $\frac{dT_{sat}}{dh}$ is the slope of the temperature-enthalpy curve for the mixture and X is the quality (fraction of the total mass flow which is vapour);

2. α_{GC} is calculated for the gas phase flowing alone in the system. No corrections are made for two-phase flow effects (waves on the interface, entrainment etc.). However, a correction for mass transfer effects was proposed by McNaught (1979) based on film theories.

An attempt to incorporate nucleate boiling to the methodology described above was made by Sardesai *et al.* (1982). They postulate that the total heat flux is made up of a sum of forced convective and nucleate boiling portions,

$$\dot{q} = \alpha_{FC}(T_w - T_I) + \alpha_{NB}(T_w - T_{GC}), \tag{2.191}$$

where α_{NB} must be corrected for mixture effects. If the main assumptions of the SBG methodology (equilibrium and saturated vapour phase) still hold, then T_{GC} is equivalent to the bubble point temperature at the system pressure and concentration x_b. Combining Eqs. 2.184, 2.187 and 2.191 gives,

$$\alpha = \frac{1 + \frac{\alpha_{NB}}{\alpha_{FC}}}{\frac{1}{\alpha_{FC}} + \frac{Z}{\alpha_{GC}}}. \tag{2.192}$$

More recently, Murata and Hashizume (1993) developed a more elaborated equilibrium model based on that of Sardesai *et al.* (1982). The heat transfer coefficient in smooth tubes is given by,

$$\alpha = \frac{F\alpha_L + S\alpha_{NB}}{1 + Xc_{pG}\frac{\partial T_{sat}}{\partial h}|_p \left(\frac{F\alpha_L}{\alpha_G}\right)}. \tag{2.193}$$

The liquid phase heat transfer coefficient is given by,

$$\alpha_L = 0.023\frac{\lambda_L}{d_T} Re_L^{0.8} Pr_L^{0.4}, \tag{2.194}$$

where,

$$F = 2.44\left(\frac{1}{X_{tt}}\right)^{0.863}. \tag{2.195}$$

The vapour phase heat transfer coefficient is given by,

$$\alpha_G = \alpha_G^* \sqrt{\varepsilon_G}, \tag{2.196}$$

where the void fraction is given by,

$$\varepsilon_G = \left[1 + \frac{(1-X)}{X}\sqrt{\frac{\rho_G}{\rho_L}}\right]^{-1}, \tag{2.197}$$

and,

$$\alpha_G^* = \rho_G c_{pG} U_G \frac{f_G}{2}\left[1 + 12.7\sqrt{f_G}2\left(Pr_G^{2/3} - 1\right)\right], \tag{2.198}$$

where $U_G = \frac{U_{GS}}{\varepsilon_G}$ and $f_G = \frac{\sqrt{\varepsilon_G} d_T}{2\rho_G U_G^2}\frac{dp}{dz}_f$. The frictional pressure gradient is given by,

$$\frac{dp}{dz}_f = \Phi_L^2 \frac{dp}{dz}_L, \tag{2.199}$$

where,

$$\Phi_L = 1 + 2.1\left(\frac{1}{X_{tt}}\right)^{0.9}, \tag{2.200}$$

and,

$$\frac{dp}{dz}_L = \left(\frac{0.184}{Re_L^{0.2}}\right)\frac{\dot{m}_L^2}{2 d_T \rho_L}. \tag{2.201}$$

The nucleate boiling heat transfer coefficient is given by,

$$\alpha_{NB} = \frac{\alpha_{NB_1}\tilde{x}_1 + \alpha_{NB_2}(1 - \tilde{x}_1)}{1 + F_{NB}(\tilde{y}_1 - \tilde{x}_1)}, \tag{2.202}$$

where the reduction in the nucleate boiling heat transfer is accounted for in a form of the Stephan and Körner (1969) mixture correction factor ($F_{NB} = 15$).

α_{NB_1} and α_{NB_2} are the pure component nucleate pool boiling heat transfer coefficients calculated from the Nishikawa *et al.* (1982) correlation.

$$\alpha_{NB_{1,2}} = 31.4\frac{p_{crit_{1,2}}^{0.2} F_p}{M_{w_{1,2}}^{0.1} T_{crit_{1,2}}^{0.9}}\dot{q}_w^{0.8} \tag{2.203}$$

where,

$$F_p = \left(\frac{p}{p_{crit_{1,2}}}\right)^{0.23} \left[1 - 0.99\left(\frac{p}{p_{crit_{1,2}}}\right)\right]^{-0.9}. \tag{2.204}$$

The suppression factor, S, by Bennett *et al.* (1980) was used,

$$S = \left[1 - \exp\left(-\frac{F\alpha_L\delta}{\lambda_L}\right)\right]\left(\frac{F\alpha_L\delta}{\lambda_L}\right)^{-1}, \tag{2.205}$$

where δ is a characteristic length given by,

$$\delta = C_d\left[\frac{\sigma}{g\left(\rho_L - \rho_G\right)}\right]^{1/2}. \tag{2.206}$$

and C_d is an empirical constant with a value of 0.08.

Finally, Murata and Hashizume (1993) suggested that $\frac{\partial T_{sat}}{\partial h}|_p$ should be calculated from the Peng and Robinson (1976) equation. They proposed an iterative solution for the set of equations presented above and suggested that properties of the equivalent pure fluid should be used in the calculations. Good results were obtained using this methodology for boiling of refrigerants (R123/R134a) in smooth and grooved tubes.

Film Methods

A more refined class of models are those in which the mass transfer effects are treated separately and locally. This is carried out using Fick's Law in one or in both phases.

As far as evaporation problems are concerned, Shock (1976) investigated theoretically the purely convective region by writing mass balances for the components over an element of fluid as the sum of diffusive and net flow portions (normal to the liquid-vapour interface),

$$-d\left(\dot{M}_L x_b\right) = 2\pi r_I \dot{m}_{I_L} dz - \frac{d\dot{M}_L}{dz} x_I dz, \tag{2.207}$$

$$d\left(\dot{M}_G y_b\right) = 2\pi r_I \dot{m}_{I_G} dz - \frac{d\dot{M}_G}{dz} y_I dz, \tag{2.208}$$

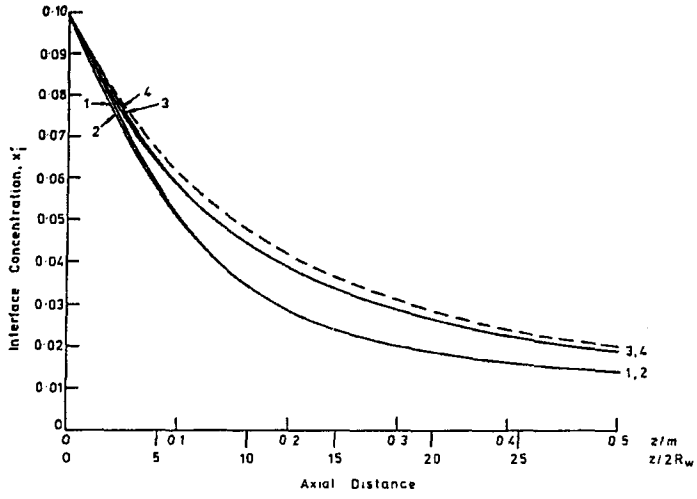


Figure 2.28: Axial variation of interface concentration for annular flow heat transfer to ethanol-water mixtures. Legend: 1 - no mass transfer resistance in both phases, 2 - no mass transfer resistance in liquid, 3 - no mass transfer resistance in vapour, 4 - no mass transfer resistance in either phase, dotted line represents a calculation based on an equilibrium flash (Shock, 1976).

where $\dot{m}_{I_{L,G}}$ are the interfacial fluxes of liquid and vapour.

Closure relationships for heat and mass transfer on the vapour side were given by the Chilton-Colburn analogy. In the liquid film, mass transfer was calculated via an extension of the method of Hewitt (1961) for heat transfer in single component flows. The model was applied to water-ethanol mixtures and, as the main conclusion, it can be said that the role of mass transfer resistance within the phases was found to be not very important in the cases studied. Mass transfer resistance in the liquid film was small compared to that of the vapour core, but even the latter had only a small significance in calculating the interfacial temperature. This fact is more clearly illustrated in Figs. 2.28 and 2.29, where the evolution of interfacial concentration and temperature are presented for cases in which mass transfer resistances were considered or not in both cases.

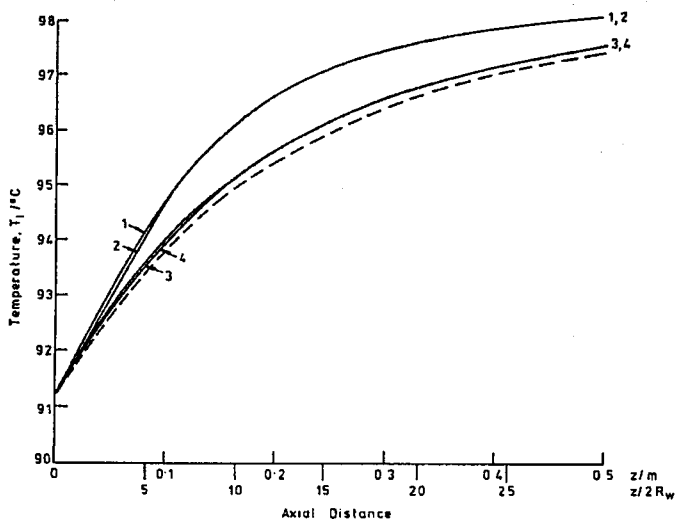


Figure 2.29: Axial variation of interface temperature for annular flow heat transfer to ethanol-water mixtures. Legend: 1 - no mass transfer resistance in both phases, 2 - no mass transfer resistance in liquid, 3 - no mass transfer resistance in vapour, 4 - no mass transfer resistance in either phase, dotted line represents a calculation based on an equilibrium flash (Shock, 1976).

Thome and Shock (1984) pointed out the conclusions arising from the work of Shock (1976) may not be valid for systems with wider boiling ranges (as the hydrocarbon mixtures studied in the present thesis). In addition, the effects due to droplet interchange and to interfacial roughness were not assessed by Shock's formulation.

2.4.5 Forced convective boiling of ternary and multicomponent mixtures

Processes involving boiling of mixtures of two or more substances are widely encountered in industry. However, despite the technological relevance, there is a dearth of adequately predictive and design methods for forced convective boiling of multicomponent mixtures. The majority of methods available in the literature for phase change of mixtures deal with the binary case. Moreover, of the number of studies devoted to the multicomponent case, most are related to condensation. A fairly refined methodology, and yet applicable to condenser design, is that based on film (or Colburn) methods. Taylor and Krishna (1993) gave a comprehensive review of the generalisations of Fick's Law for multicomponent systems and their application to a Colburn method calculation framework. Basically, two approaches are used, (i) the effective diffusivity method, where each constituent is assumed to transfer at a rate equal to that at which it would transfer if it alone were present in an arbitrarily chosen reference species at the same concentration, and (ii) the so-called interactive method, a more refined theory put forward by Toor (1964) and Stewart and Prober (1964), that assumes a linear dependence of the diffusive fluxes on *all* concentration driving forces. A description of calculation procedures for condenser design using both approaches is also presented by Webb (1995).

A model for boiling of ternary refrigerant mixtures in horizontal pipes was proposed by Zhang *et al.* (1997). In the forced convective dominant region, use was made of a film

methodology in which an effective diffusivity approach was employed to calculate the interfacial mass fluxes. Similarly to the work of Shock (1976), Zhang *et al.* (1997) found that, for R32/R125/R134A (23/25/52% mass fraction) and R32/R134A (30/70% mass fraction), the mass transfer resistance in the liquid phase was negligible. They also found no essential difference between the mechanisms of boiling heat transfer in binary and ternary systems.

To the present author's knowledge, no interactive model was ever tested for multicomponent boiling.

2.5 Summary

This chapter presented a critical appraisal of experimental and analytical work on two-phase flow and heat transfer at high qualities in vertical pipes. Both single component and mixture cases were addressed.

The main purpose of this review was to introduce the background information on the subject so that the material presented in the following chapters can be evaluated with respect to its contribution to the field.

Chapter 3

An Experimental Investigation of Nucleate Boiling in Annular Flow

This chapter is concerned with experimental investigations of heat transfer in annular two-phase flow. The experiments aimed at elucidating the nature of nucleate boiling in annular flow by observing the interaction between disturbance waves and the activity of nucleation sites. In Section 3.2, the experimental facility for the visualisation experiments is described. Section 3.3 presents the results from the visualisation campaign as well as temperature and heat transfer coefficient measurements for a range of conditions. Section 3.4 advances a modelling framework devoted to the prediction of the Onset of Nucleate Boiling (ONB) in climbing films characteristic of annular flow in annuli. A brief summary of the work undertaken is presented in Section 3.5.

3.1 Introduction

Little is known about the role of nucleate boiling in high quality phase change systems. As seen in Chapter 2, many authors support the idea that a suppression of this phenomenon

exists at high qualities. Others claim that this may be the dominant mechanism of heat transfer in such situations.

A fact beyond doubt is that the hydrodynamics of the annular regime gives rise to complex interactions between waves, droplets and bubbles. Amongst these, one may cite phenomena such as bubble sliding and bursting, liquid entrainment, nucleation suppression and enhancement etc.

Early visualisation experiments carried out at the UK Atomic Energy Research Establishment, Harwell (Hewitt *et al.*, 1965) showed that disturbance waves in the liquid film can *locally* trigger off the nucleation site activity. As will be seen later, in the light of current understanding of bubble nucleation in convective systems, this observation is somewhat contradictory.

The amount of experimental evidence (number of ciné sequences) from the Harwell experiments is very small and, at the time, the authors did not attempt to provide an explanation for the observed phenomenon. Therefore, one of the goals of the present study is to revive these experiments by carrying out high-speed recording of such flows.

The work described in this chapter deals with the visualisation of nucleate boiling in steam-water annular two-phase flows. A high-speed video recording system is used to observe more closely the interaction between disturbance waves and bubble nucleation. A specially constructed annular test section enables a direct observation of the flow field.

A quantitative evaluation of the heat transfer in such a system was also made possible through the use of a sliding equilibrium thermocouple (Bennett *et al.*, 1961) to measure the temperature along the heated wall. This allowed the determination of the local heat transfer coefficient in such flows.

3.2 Experiments

3.2.1 Experimental apparatus

Figure 3.1 illustrates the boiling visualisation apparatus. Steam from the site mains is reduced in pressure to about 2 bara and passed through a steam drier (and superheater). The steam drier was designed so as to keep the inlet steam free of liquid droplets. It was constructed from a 1.1 m section of 76.2 mm (3") internal diameter stainless steel pipe, in which two 3 kW electrically heated Incoloy 800 rod elements were inserted. These were bent and placed as shown in Fig. 3.2. Wet (or saturated) steam from the site mains enters at the bottom of the drier. A temperature control system was constructed and a temperature sensor placed in its core. The power to the heating elements was delivered so as to keep a constant temperature (normally 393 to 403 K) in the drier. The superheated steam leaves the drier through a 90^o bend located at the centre line of the drier and connected to the steam outlet via a standard fitting. It is believed that, by introducing this outlet design, droplets that might still exist in the exit stream would impinge on the highly superheated walls of the 90^o section and evaporate instantaneously. A relief valve (4.27 bar) was also installed downstream of the steam drier.

After receiving the required degrees of superheat, the dry steam flow rate is measured using a standard orifice plate (designed according to BS 1042) coupled to an inverted air-water U-tube manometer. The connections between the orifice plate and the U-tube manometer were made according to the recommendations of the ASME for horizontal steam pipelines (Bean, 1971). A schematic of the connections is shown in Fig. 3.3 from Bean (1971). Although some of the components in the figure are not to scale with those in the Imperial College facility, the figure serves to illustrate the experimental arrangement. The purpose of this arrangement is to reduce to a minimum the effects of condensation at the interface between the primary fluid (superheated steam) and the manometric fluid (water). At the

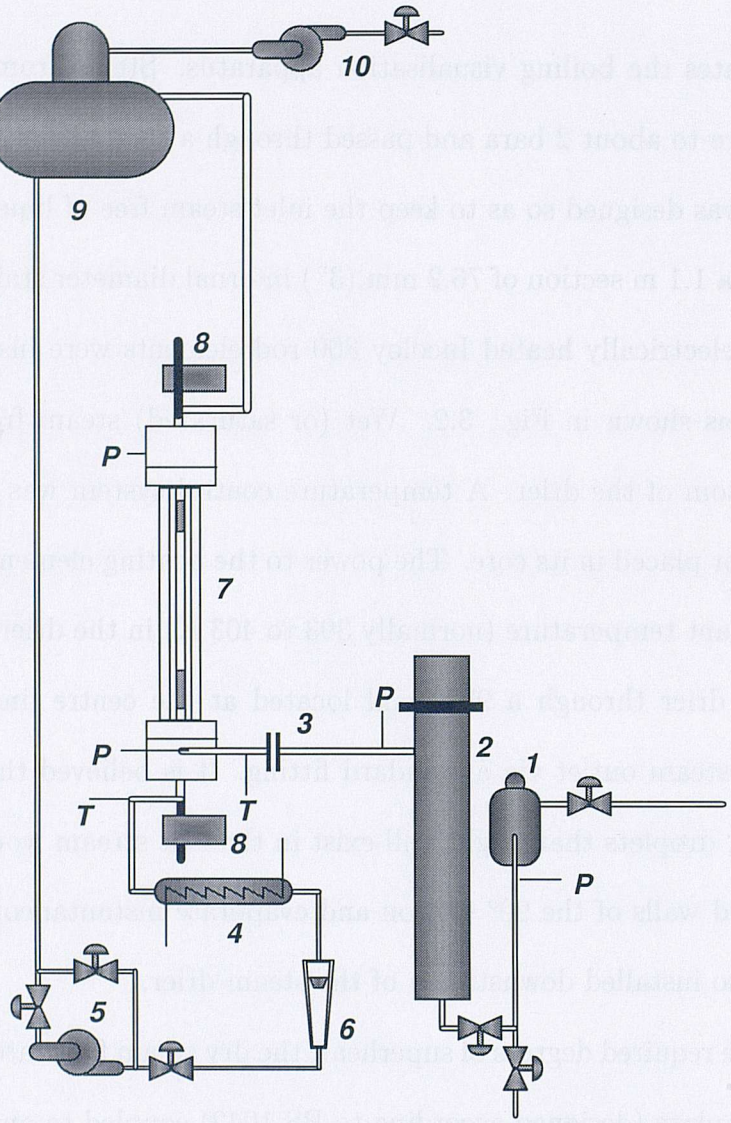


Figure 3.1: The experimental apparatus. Key to components: 1.Pressure reducing valve; 2.Steam drier/superheater; 3.Orifice plate; 4.Water preheater; 5.Mono pump; 6.Water flowmeter; 7.Test section; 8.Heater terminals; 9.Reflux condenser; 10.Vacuum pump.

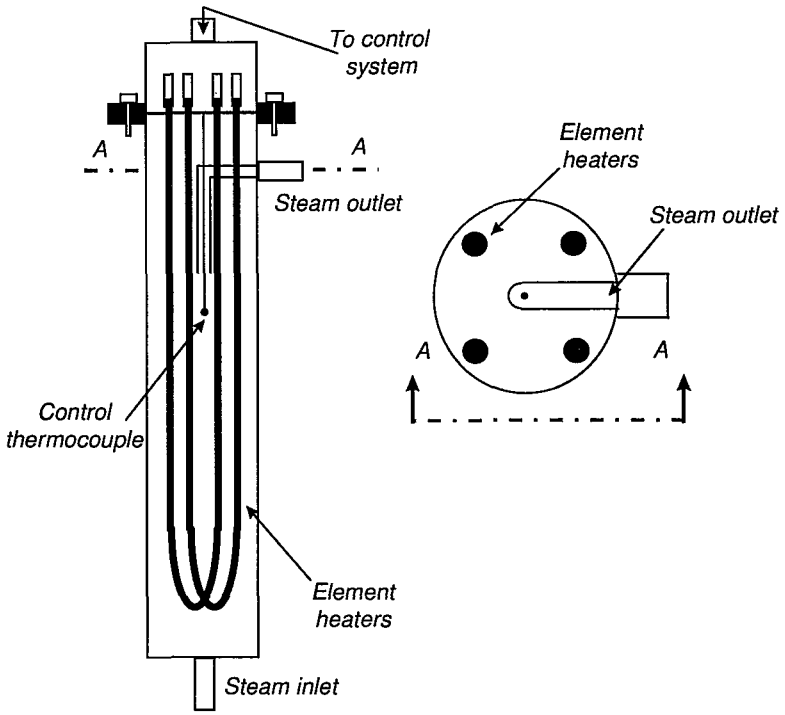


Figure 3.2: A schematic of the steam drier/superheater.

beginning of an experimental session, the reservoirs (A and B) are filled with water up to levels which are equalised by having the air vents open for a few moments. This procedure also equalises the air-water interfaces in the inverted U-tube manometer. To avoid the spillage of manometric water into the superheated steam line during the experiments, it was ensured that the volume of each reservoir was greater than the volume of the maximum height difference in the U-tube manometer.

Distilled water is fed to the test section by a Mono pump through an electrically heated (2 kW) pipe preheater and a calibrated rotameter (Platon OMN 1037).

The test section is schematically described in Figure 3.4. The top and bottom headers are made of brass and mounted on an aluminium support in such a way that they can be traversed independently along the support. This allows the distance between the headers to be easily (and accurately) set to accommodate the glass tubes. The aluminium support

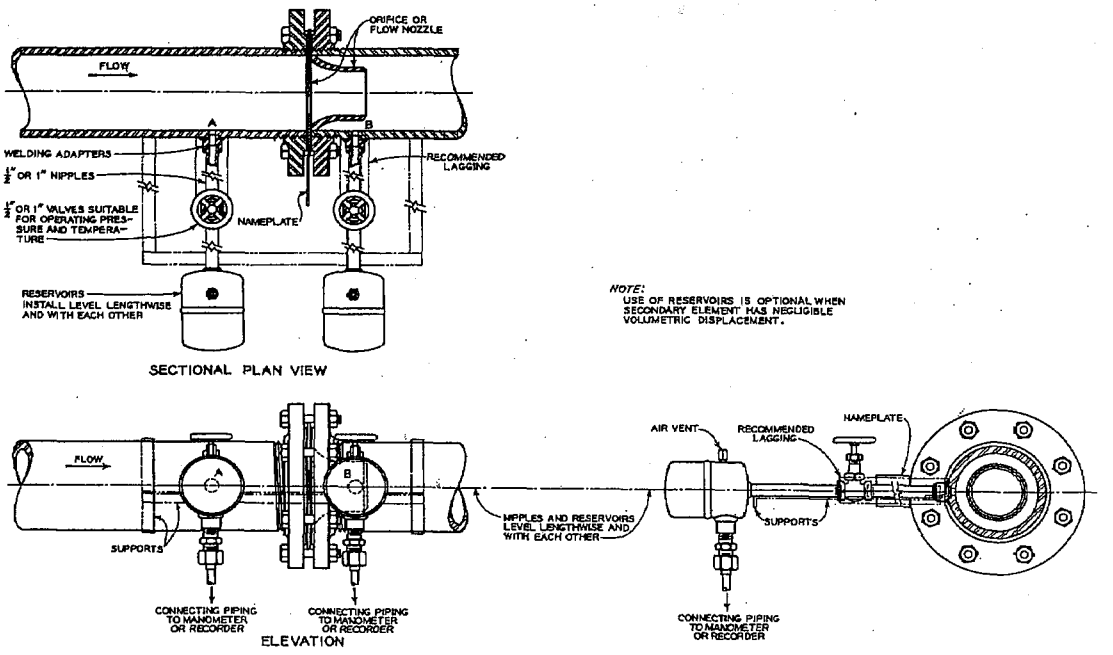


Figure 3.3: A schematic of the connections between a flow measuring element (orifice plate or venturi) and a manometer (Bean, 1971).

is mounted on two brackets which were fixed on the wall and accurately aligned vertically. The water is injected at the bottom end of the test section and passed through a sintered tube section of the same diameter as the inner surface of the annulus. It is then forced to flow as a film coating the inner surface of the heated inner tube. The film is dragged upwards by the steam entering at the bottom header in the annular gap between the heater and a glass tube which allows a direct observation of the flow. Condensation at the inner wall of the glass tube is prevented by passing hot air through an external gap. Compressed air from the site mains is heated up to around 373 K using two 750 W electrical air process heaters (manufactured by Hotwatt) arranged in series. The air is evenly distributed around the external gap inlet located at the bottom header.

The heated section of the inner rod is made of 321 stainless steel. The remainder of the heated inner rod is made from a thick wall copper tube and extends through glands in the headers to enable electrical connections to be made. The basic dimensions of the test section are summarised in Table 3.1.

The outer diameter of the sinters and of the thick wall copper tubes is identical to that of the heater, i.e., 19.05 mm.

Power is delivered to the heater via passing a low voltage, high amperage electrical current through the inner rod. Electrical connection between the transformer and each one of the copper clamps is made via eight 70 mm^2 welding cables. The 50 Hz AC current is set by means of a Variac-controlled transformer. The maximum current is of the order of 1000 A giving a voltage drop of approximately 20 V and a maximum power of the order of 20 kW.

The current is measured using a Crompton induction meter (ratio 2500/5). The output current (between 0 and 2 A) from the induction meter is sent to a multimeter. The voltage across the two copper clamps is measured using a standard panel voltmeter ($\pm$ 0.5 V). The power is calculated from the product of the measured voltage and current through

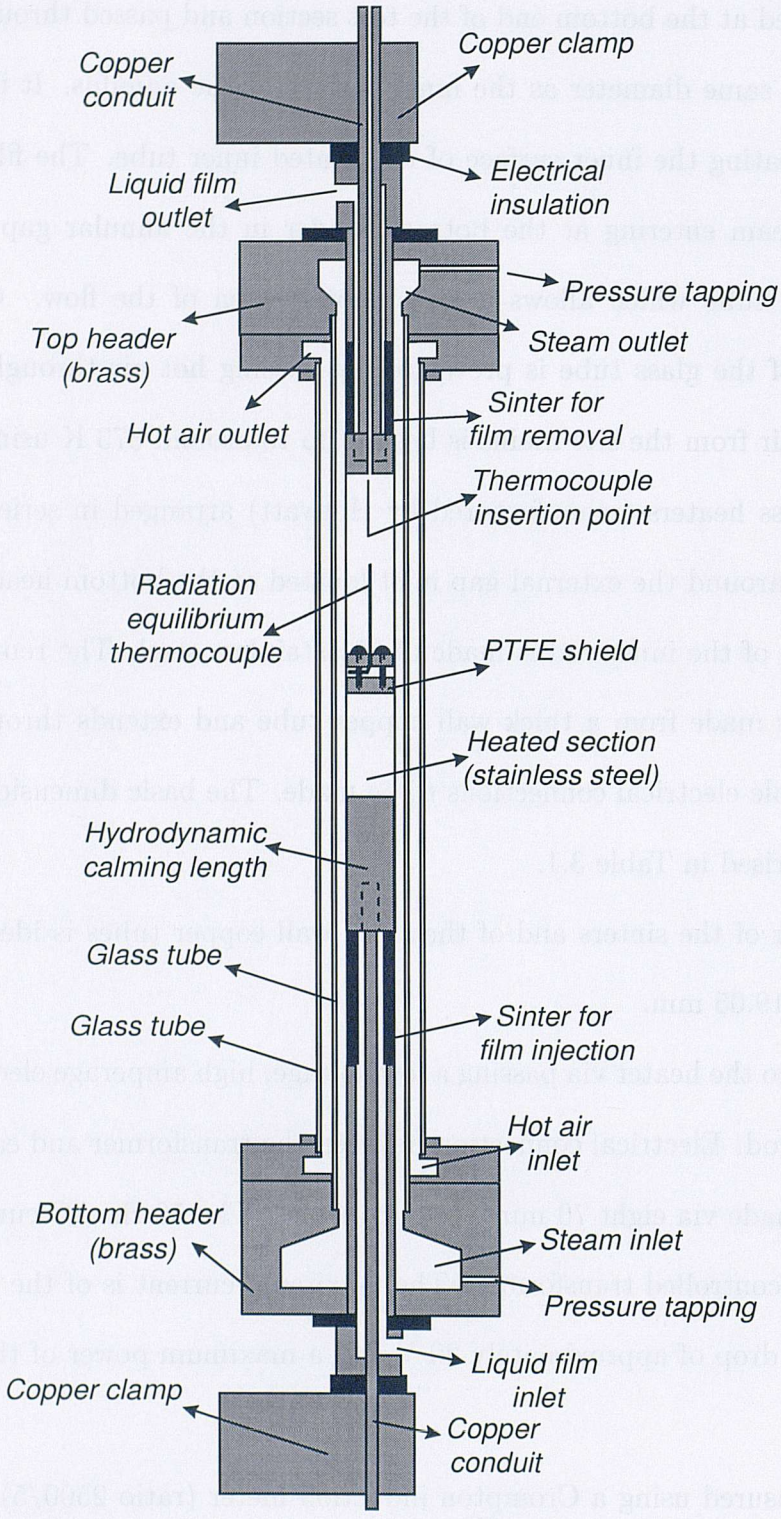


Figure 3.4: The test section for the nucleate boiling visualisation experiments.

Table 3.1: Dimensions of the test section for the boiling visualisation experiments.

Parameter	Dimension
Outer diameter of the inner rod	19.05 mm (3/4")
Inner diameter of the inner glass tube	32 mm
Inner diameter of the outer glass tube	48 mm
Wall thickness of glass tubes	2 mm
Length of calming section	90 mm
Length of inlet sinter	77 mm
Length of heater (stainless steel)	320 mm
Thickness of heater wall	0.56 mm
Total length of test section (between outer edges of headers)	790 mm
Length of visualisation section (between inner edges of headers)	565 mm

the heater.

Owing to the design of the bottom header and the hollow tube, conditions may be set in which the steam loses almost all of its superheat to the surroundings and to the water; this means that, under those conditions, at the point where the water leaves the sinter, both it and the steam can be very close to the saturation temperature. However, as will be discussed in Section 3.2.4, the elimination of remaining liquid subcooling is dealt with in a more direct way.

Absolute pressures at the top and bottom ends of the test section are measured using absolute pressure transducers (Druck 130W, 0 to 2 bara) and the saturation temperature

at a given point in the test section is calculated through a linear interpolation between the saturation temperature values corresponding to the pressure readings.

The transducers are of the strain gauge type and the output signal is linear. They were calibrated by the manufacturer ($\pm$ 0.1 % of absolute pressure).

Temperatures at various locations were measured using minerally insulated chromel-alumel Type K thermocouples calibrated up to 423 K. The uncertainty in the thermocouple readings was $\pm$ 0.5 K (except for the radiation equilibrium thermocouple — see Section 3.2.2, whose uncertainty was of the order of $\pm$ 0.1 K).

Thermal insulation of the pipe work is carried out using 20 to 25 mm thick foiled phenolic foam pipe sections or 20 mm elastomeric (armaflex) pipe sections.

3.2.2 Heat transfer coefficient estimation

The heat transfer coefficient is calculated by estimating the temperature of the outer surface of the heated section. This is done by measuring the temperature of the inner surface of the thin-wall heater using a sliding thermocouple which can be traversed vertically inside the hollow inner rod (Bennett *et al.*, 1961). The couple does not touch the tube but relies on radiation equilibrium with the inner surface at any cross-section of the core. Such an arrangement requires insulation from radiation other than that emanating from a small heated length immediately adjacent to the couple. This is achieved by bending the tip of the couple towards the pipe wall and encapsulating it in a PTFE shield. The sliding thermocouple arrangement is also shown in Figure 3.4. The thermocouple is a 1 m long, 1.5 mm outside diameter, Inconel sheathed minerally insulated chromel-alumel Type K thermocouple. The thermocouple is connected to a Fluke 51 thermometer display.

Having measured the temperature of the inner surface of the thin-wall heater, T_{w_i}, the temperature of the outer wall, T_{w_o}, is estimated by solving a steady-state heat conduction

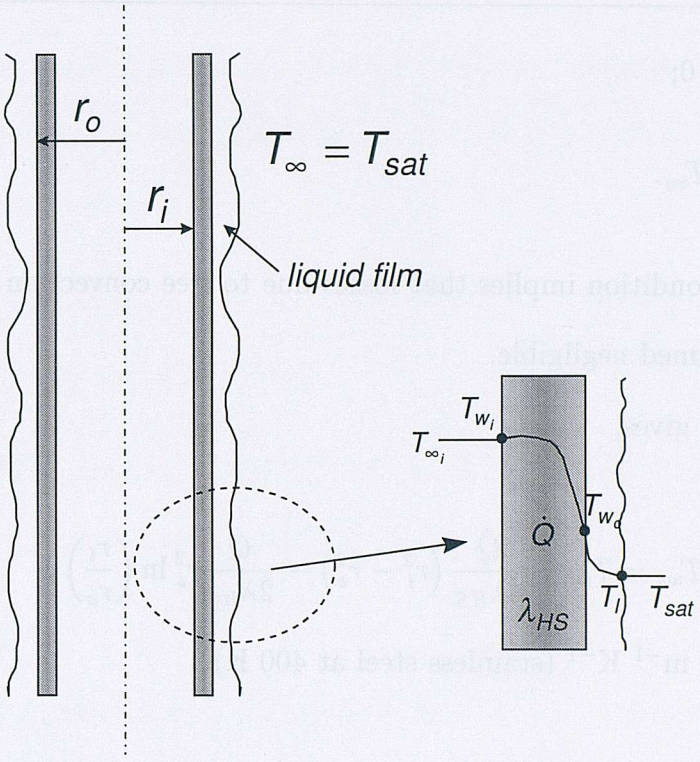


Figure 3.5: Illustration of the heat conduction problem in the heated section.

equation for the heater geometry (see Fig. 3.5).

In cylindrical coordinates, the differential equation for one dimensional heat conduction is given by,

$$\frac{1}{r}\frac{d}{dr}\left(r\frac{dT}{dr}\right) + \frac{\dot{Q}}{\lambda_{HS}} = 0. \tag{3.1}$$

$\dot{Q}$ is the internal heat generation rate defined as (in W m^{-3}),

$$\dot{Q} = \frac{I^2 R_{HS}}{V_{HS}} = \frac{I^2 \varrho_{HS}}{4\pi^2 r_o^2 \mathrm{t}}, \tag{3.2}$$

where t is the thickness of the heated section wall, r_o^2 is the outer radius of the heated section, I is the current and ϱ_{HS} is the resistivity of the heated section material. For 321 stainless steel, $\varrho = 0.78\Omega$ mm^2 m^{-1}.

The boundary conditions for Eq. 3.1 are as follows,

1. at $r = r_i$, $\frac{dT}{dr} \approx 0$;

2. at $r = r_i$, $T = T_{w_i}$.

The first boundary condition implies that losses due to free convection within the cylindrical cavity are assumed negligible.

An integration of 3.1 gives,

$$T_{w_o} = T_{w_i} + \frac{\dot{Q}}{4\lambda_{HS}}\left(r_i^2 - r_o^2\right) - \frac{\dot{Q}}{2\lambda_{HS}} r_i^2 \ln\left(\frac{r_i}{r_o}\right), \tag{3.3}$$

where $\lambda_{HS} = 16.6$ W m^{-1} K^{-1} (stainless steel at 400 K).

3.2.3 Visualisation equipment

A direct observation of the flow is carried out using a high-speed video recording system. The Kodak Ektapro 2000 camera is equipped with a Canon Macro 50 mm lens and capable of producing video footage at up to 2000 frames per second. The system is linked to a computer for data acquisition.

Illumination was carried out using two 500 W halogen lamps.

3.2.4 Experimental Procedure

In the temperature measurement sessions, the liquid film and steam flow rates and inlet temperatures are firstly adjusted. The electrical power to the heater is then gradually increased. For each value of heat flux, when steady-state is attained, the wall temperature is measured at various distances (typically 10) along the heater. It is assumed that steady-state is reached when the thermocouple reading at the initial traversing position is constant (This generally takes place 5 to 10 minutes after the wall heat flux is set). The wall temperature measurements were performed over a length of approximately 0.21

m from the top of the heated section. For the conditions investigated in the experiments, any residual subcooling in the liquid film is therefore eliminated in the first 0.11 m from the bottom of the heated length.

Before each run the heating power was raised substantially to promote vigorous nucleation in order to minimize hysteresis effects.

The heater surface characteristics were not analysed nor was the surface mechanically treated prior to the experiments. However, the heater was kept clean during the experimental campaign.

The procedure for investigating the onset of nucleation is identical to that suggested by Hewitt *et al.* (1965). The heated section was closely observed for the first appearance of an active nucleation site, its location and power being noted.

In the flow visualisation sessions, the interaction between disturbance waves and bubble nucleation was investigated using the high-speed video system. The camera was mounted on a tripod and aimed at the heated portion of the test section. The field of view was of the order of 30 mm by 50 mm. Due to operational difficulties, the visualisation and temperature measurement sessions could not be performed simultaneously. Nevertheless, one value of the wall temperature (generally at the top end of the heater) was recorded for each visualisation run. This was basically to monitor the heater temperature for a (unwanted) sudden rise associated with burnout.

After several attempts, it was found that the best illumination arrangement was achieved by having one of two light sources located below or above the aiming line of the camera, with the source arranged in a way such that the light rays are nearly parallel to the heater. This promoted the reflection of light on the rougher and thicker portions of the film, and thus increased the contrast between the wavy and smooth regions.

3.3 Experimental Results

The present section describes both qualitative and quantitative results obtained in this study. Results of boiling visualisation at a fixed position along the heater are shown in Section 3.3.1. Section 3.3.2 presents the visualisation results obtained from runs in which the camera was placed at several positions along the test section. Wave frequencies and velocities obtained from the high-speed video footage are also presented in Sections 3.3.1 and 3.3.2. All the features described in these sections were observed from a careful analysis of the video recordings. Because it is easier to identify such features in the moving video sequences, the printed stills are accompanied by labels and drawings. Finally, quantitative heat transfer measurements are presented in Section 3.3.3.

3.3.1 Visualisation at a fixed position

In this section, still frames extracted from the video footage at a fixed position (approximately 0.25 m from the bottom end of the stainless steel heater, a position at which liquid film subcooling effects no longer exist) are presented. In all pictures, the section of the inner rod under investigation appears as a dark horizontal cylinder in the middle of the frames. The dark line at the very bottom of the pictures is the wall of the inner glass tube. The direction of flow is from right to left.

Figures 3.6.a and 3.6.b show respectively the region of smooth film between consecutive disturbance waves and a disturbance wave on the liquid film in an experimental run in which $\dot{q}_w = 0$. The rough nature of the wave region can be distinguished due to the reflection of light at the film interface.

In Fig. 3.7, a sequence in which bubble nucleation takes place in the smooth film region is illustrated. A full nucleation cycle of a single bubble can be observed (indicated by a white arrow). The bubble grows in frames 3.7.a to 3.7.d and bursts in 3.7.e. This is

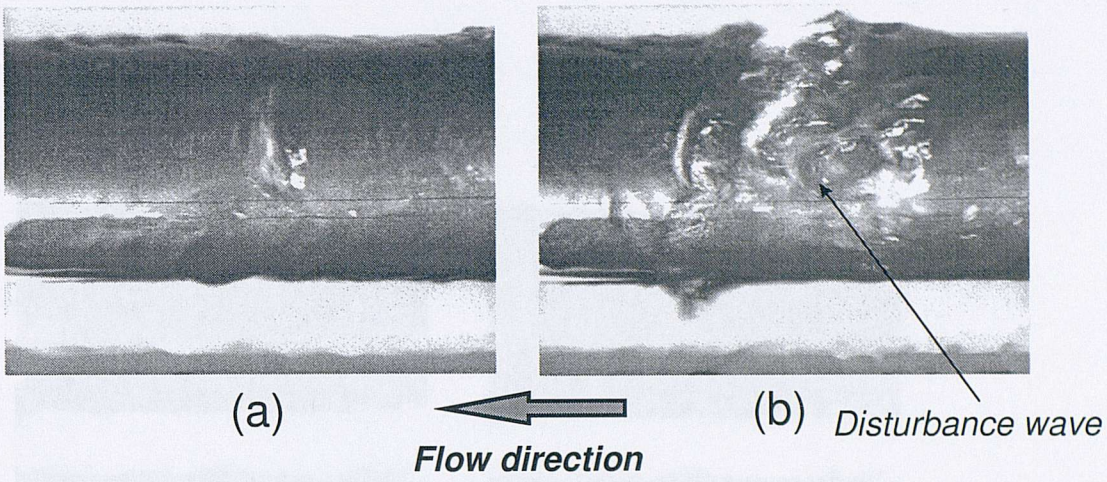


Figure 3.6: (a) Region of smooth film between disturbance waves, (b) a disturbance wave. Experimental conditions: $p_{in} = 1.9$ bar, $\dot{m}_T = 30.2$ kg m^{-2} s^{-1}, $X = 0.63$, $\dot{q}_w = 0$ W m^{-2}.

not the only visible nucleation site. Other sites are identifiable (black arrows), though their cycles were not in the same period of the referred site. The time interval between consecutive frames is 1 ms.

It should be stressed that it is extremely difficult to observe nucleation and droplet entrainment phenomena in the still photographs. Nucleation sites are clearly observed in the videos as bubbles are produced and depart from them. Thus, a nucleation site is seen as a fixed position at which a 'flickering' activity characteristic of bubble formation and departure is observed. The location of nucleation sites which are active before the wave passes over them are seen to be preserved as the waves passes by. More nucleation sites are activated in the tail region of the disturbance wave and these additional sites are *deactivated* before the next wave arrives. However, sites in the same position are *reactivated* in the tail region of the next disturbance wave.

Entrained droplets are seen clearly in the videos as moving 'streaks' travelling much faster than the waves. Again, this behaviour is very difficult to capture in still photographs; the human eye is a very powerful processor of dynamic visual evidence!

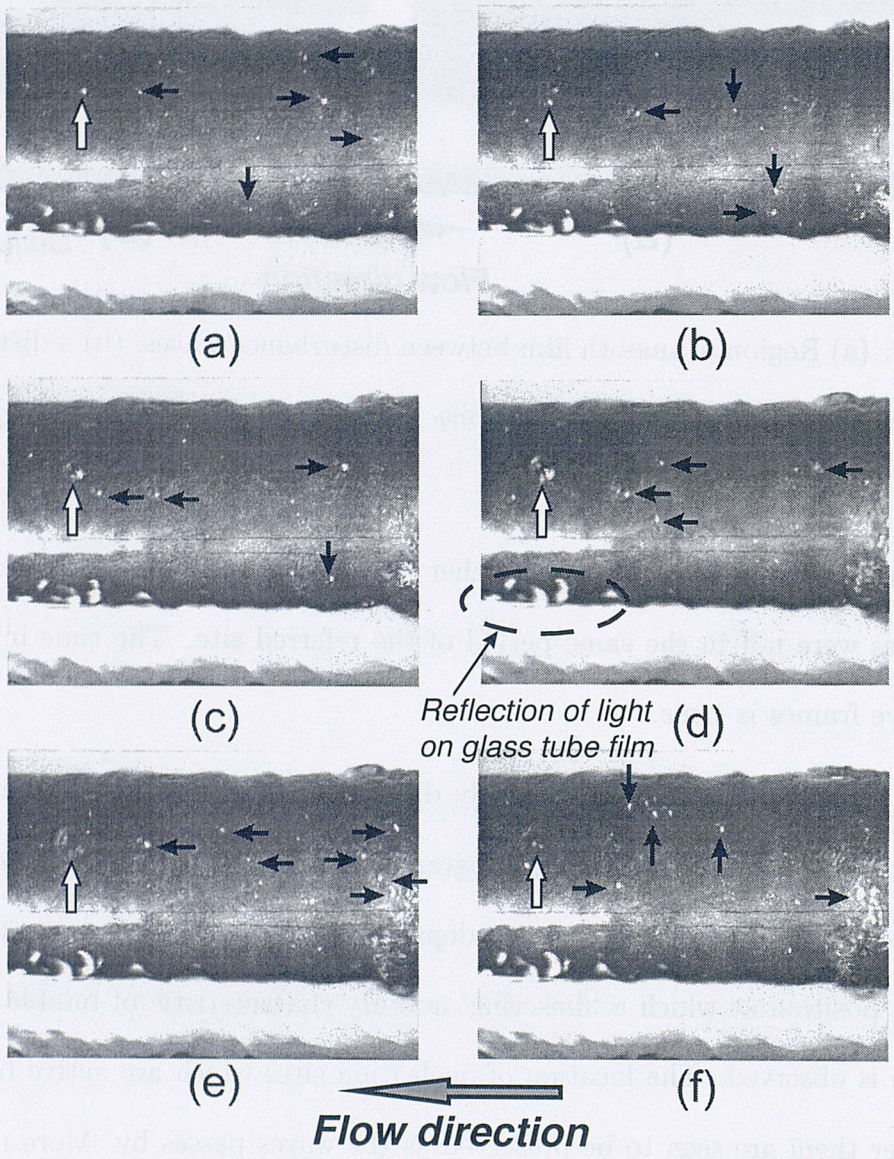


Figure 3.7: Illustration of nucleation in a smooth film between waves. Experimental conditions: $p_{in} = 1.9$ bar, $\dot{m}_T = 30.2$ kg m^{-2} s^{-1}, $X_{in} = 0.63$, $\dot{q}_w = 158.7$ kW m^{-2}, $\Delta T_{in} \approx 30$ K.

In annular flow, the droplet entrainment process is intimately related to the existence of

waves in the liquid film (Azzopardi and Whalley, 1980). Some of the available criteria for wave inception were summarised in Section 2.2.3.

Figure 3.8 presents a sequence in which liquid entrainment from the crest of a disturbance wave takes place ($Re_{LF} \approx 350$). In this sequence of frames, the entrainment process begins at frame 3.8.c and, in the subsequent frames, the droplets are all situated left of the wave in a faster-moving vapour flow. As will be seen from frame 3.8.e, the droplets appear as streaks being ejected from the wave. Nucleating bubbles are present in all frames (some were marked with black arrows in frames a, b and c). In frame 3.8.d, the visible active nucleation sites are marked by arrows. The greater number of arrows immediately upstream of the wave provide an indication of the increased bubble nucleation induced locally by the passage of the wave. This issue will be dealt with in detail later. In frame 3.8.f, some of the droplets entrained from the wave deposit on the glass tube. The time interval between consecutive frames is 1 ms.

Figure 3.9 illustrates a sequence of 12 frames in which $Re_{LF} = 166$. For the conditions of this case, approximate Re_{LFC} values given by the criteria presented in Section 2.2.3 are, Ishii and Grolmes (1975), 340; Asali *et al.* (1984), 610; Owen (1986), 710; Azzopardi (1997), 170. In this figure, the processes of wave break-up (formation of a filament which eventually breaks away from the body of the wave) and liquid entrainment are depicted. No disturbance waves were observed at Re_{LF} lower than that of the case illustrated in Fig. 3.9 ($Re_{LF} \approx 90$).

An increase in the wall heat flux leads to fully developed nucleate boiling in the liquid film. This is shown in Fig. 3.10. In this figure, one cannot identify the process of droplet entrainment from the disturbance wave. This is due to a thicker film of water on the glass tube. However, the presence of this film is, in itself, an indication of the enhancement of droplet entrainment at higher heat fluxes. There is also a significant increase in the number of active nucleation sites. From these frames, it is not possible to distinguish the

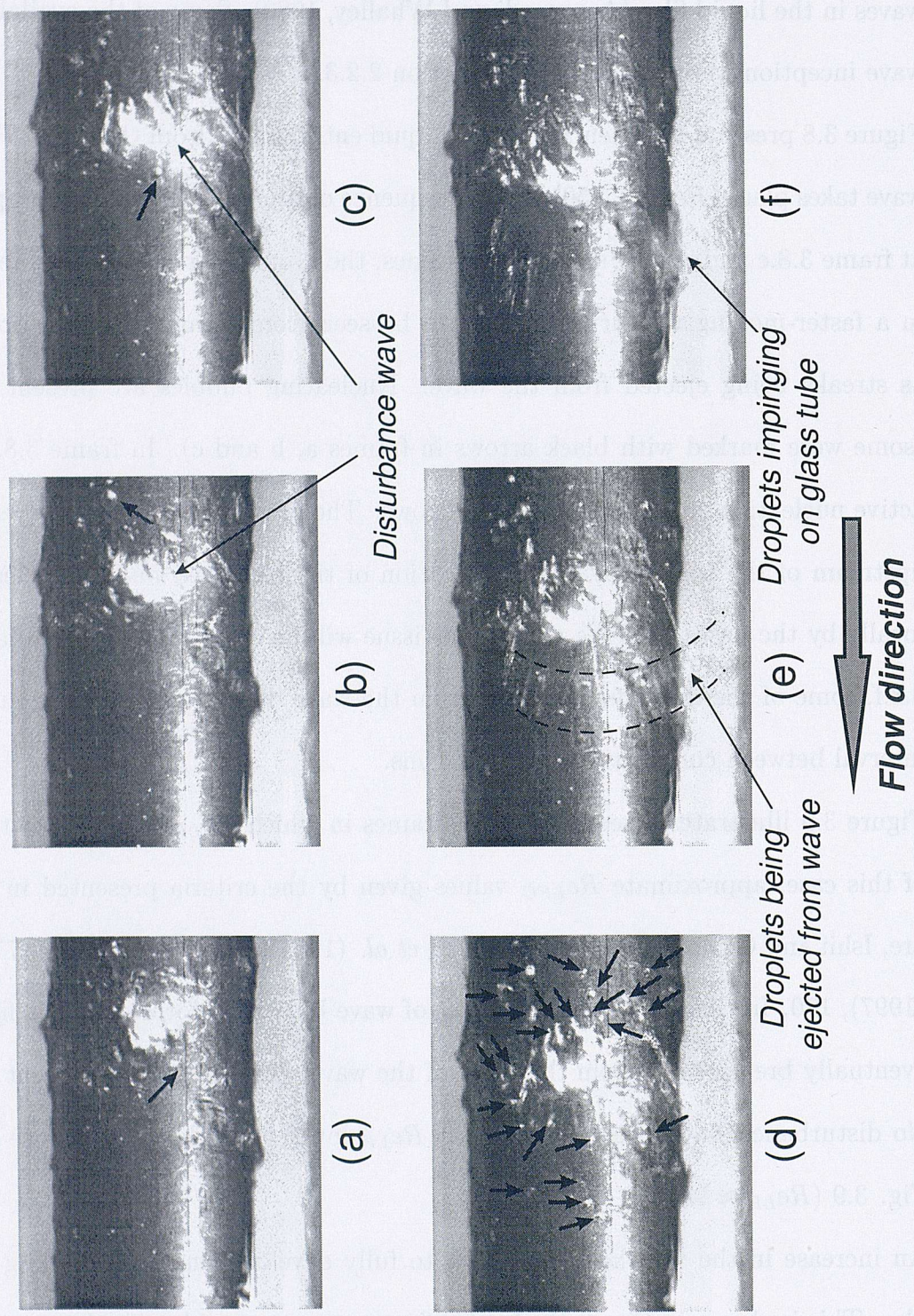


Figure 3.8: Droplet entrainment from the crest of a disturbance wave. Experimental conditions: $p_{in} = 2.0$ bar, $\dot{m}_T = 27.3$ kg m^{-2} s^{-1}, $X_{in} = 0.77$, $\dot{q}_w = 146.2$ kW m^{-2}, $\Delta T_{in} \approx 30$ K.

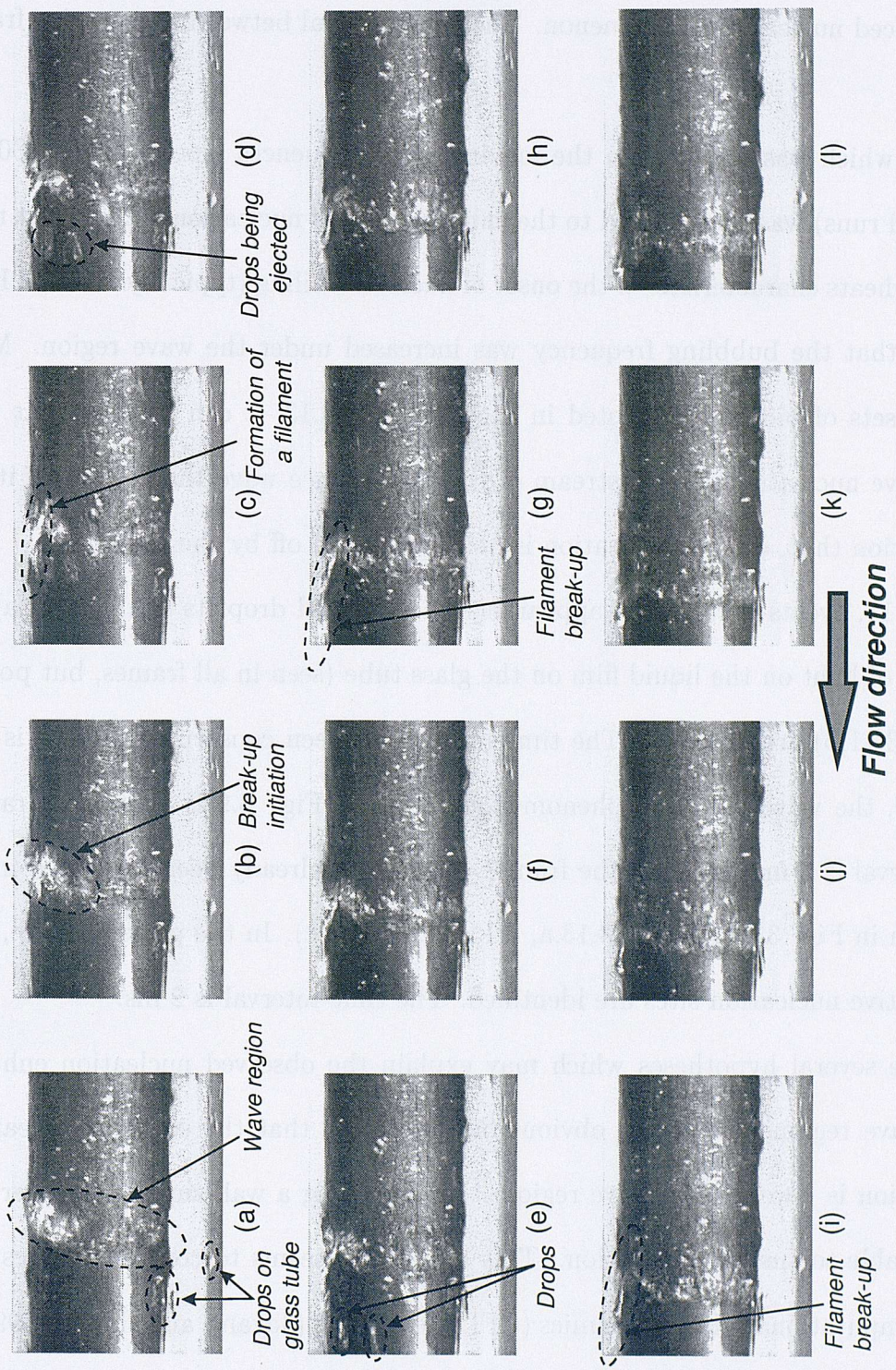


Figure 3.9: Nucleation and droplet entrainment at a low film flow rate. Experimental conditions: $p_{in} = 1.9$ bar, $\dot{m}_T = 24.0$ kg m^{-2} s^{-1}, $X_{in} = 0.87$, $\dot{q}_w = 195.8$ kW m^{-2}, $\Delta T_{in} \approx 30$ K.

wave-induced nucleation phenomenon. The time interval between consecutive frames is 3 ms.

An event which was observed in the moving video sequences (specially the 2000 frames per second runs) was that related to the enhancement of nucleation activity. At measured wall superheats characteristic of the onset of nucleate boiling (typically 10 to 12 K), it was observed that the bubbling frequency was increased under the wave region. Moreover, from the sets of pictures presented in Figs. 3.11 to 3.13, it can be seen that there are more active nucleation sites upstream of the disturbance wave than ahead of it. This is an indication that, *locally*, nucleation is being triggered off by the wave.

In Fig. 3.11, events such as the appearance of entrained droplets (frame 3.11.a) and the reflection of light on the liquid film on the glass tube (seen in all frames, but pointed out in frame 3.11.b) are depicted. The time interval between consecutive frames is 5 ms. In Fig. 3.12, the wave break-up phenomenon shown in Fig. 3.9 is again illustrated. The time interval is 3 ms. Some of the frames which have already been presented in Fig. 3.8 are shown in Fig. 3.13 (frames 3.13.a, 3.13.b and 3.13.c). In the present figure, however, all the active nucleation sites are identified. The time interval is 2 ms.

There are several hypotheses which may explain the observed nucleation enhancement in the wave region. The most obvious one would be that the convective heat transfer contribution is lower in the wave region; thus requiring a wall superheat lower than the one available to sustain nucleation. This hypothesis seems to contradict latest findings using Computational Fluid Dynamics (CFD) Modelling (Jayanti and Hewitt, 1997). From this CFD study, it was concluded that disturbance waves can be seen as 'packets' of turbulence travelling over a laminar film substrate. Figures 3.14 and 3.15 show the profiles of turbulent viscosity and the temperature contours in the wave region. In light of this analysis, it is difficult to explain the increased activity of the sites. Since the temperature gradient near the wall is presumably steeper in the highly turbulent wave region than

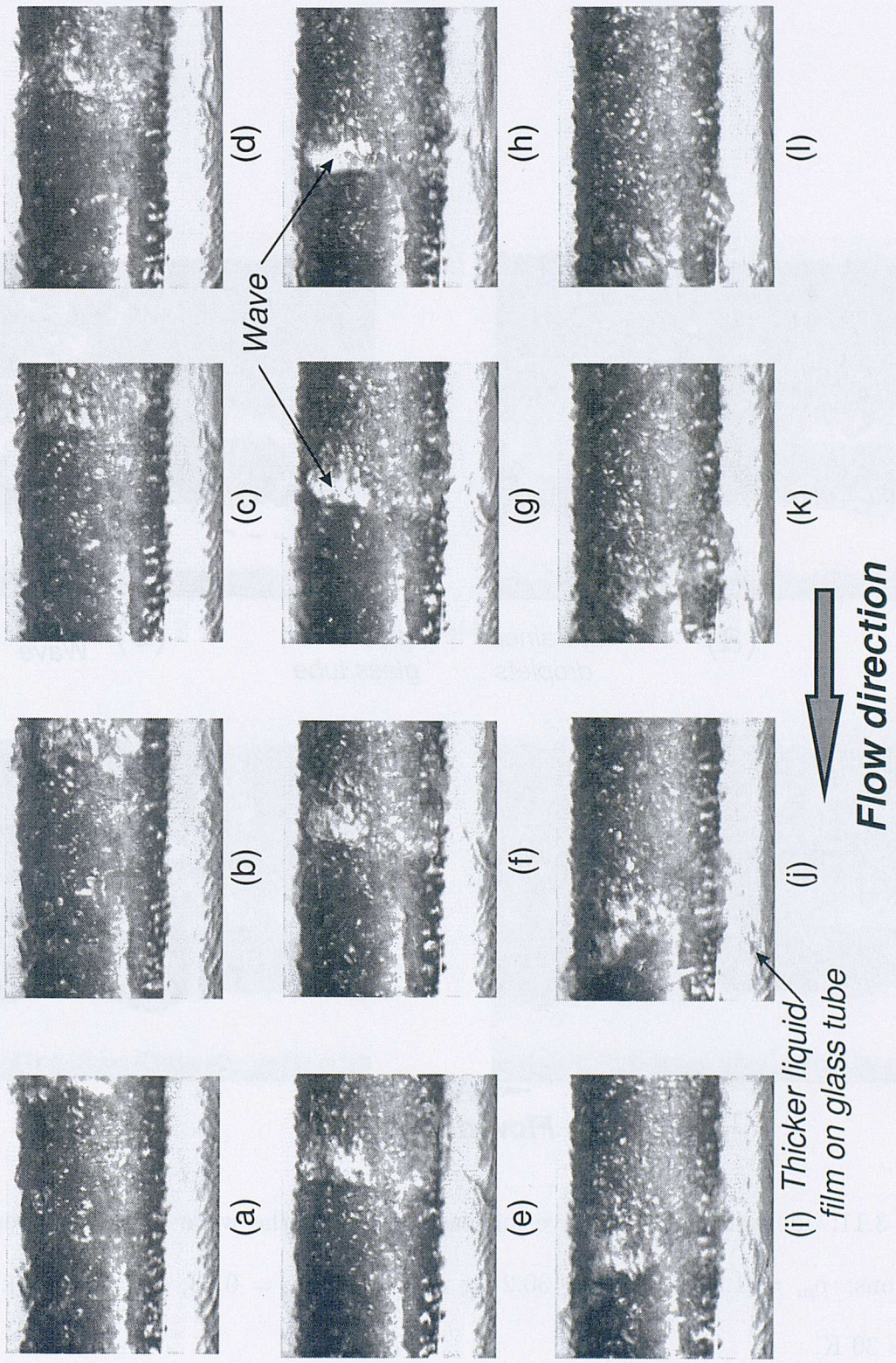


Figure 3.10: Fully developed nucleate boiling in the liquid film. Experimental conditions: $p_{in} = 2.0$ bar, $\dot{m}_T = 30.2$ kg m^{-2} s^{-1}, $X_{in} = 0.63$, $\dot{q}_w = 485.6$ kW m^{-2}, $\Delta T_{in} \approx 30$ K.

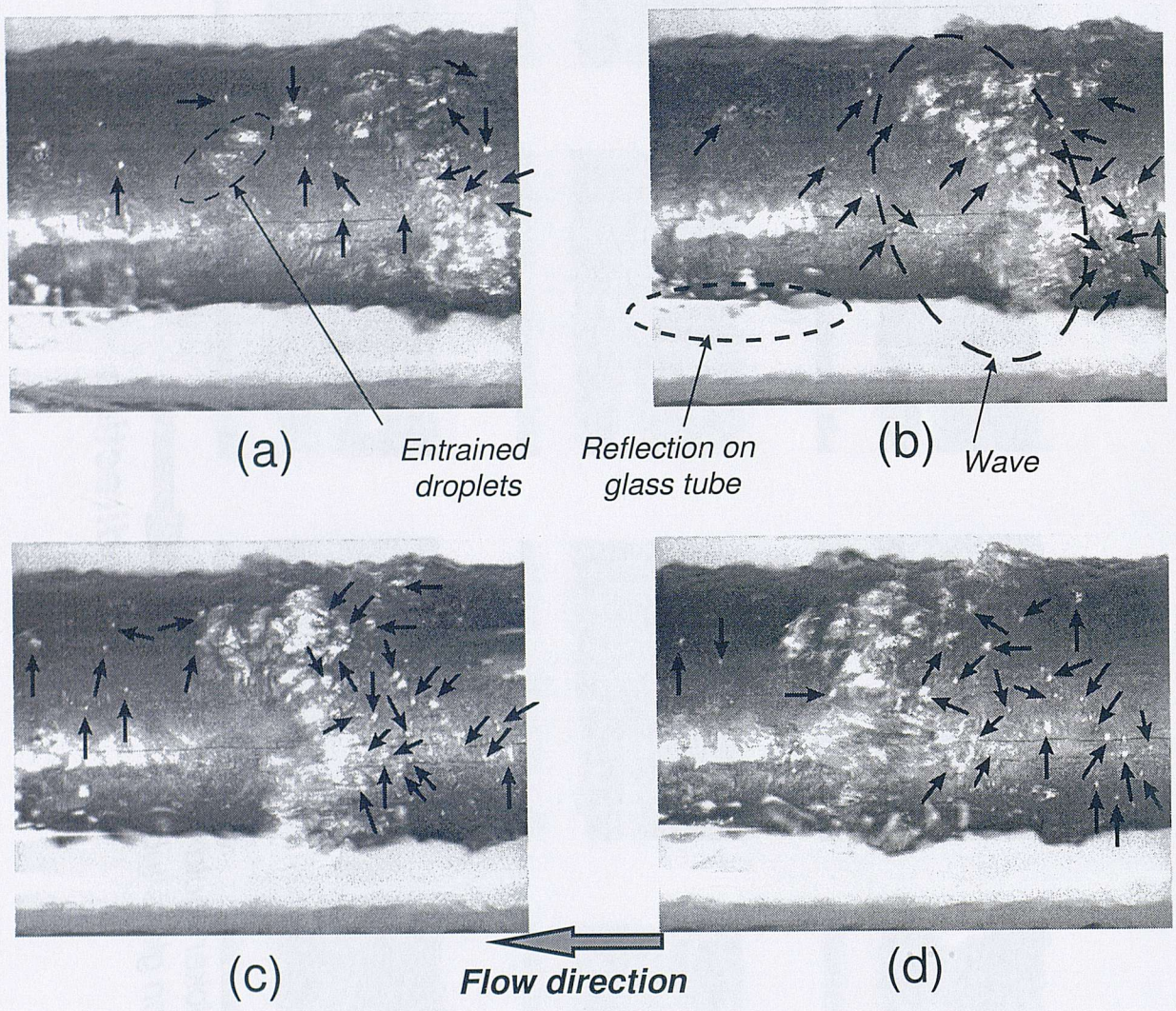


Figure 3.11: Identification of active nucleation sites in the wave region. Experimental conditions: $p_{in} = 1.9$ bar, $\dot{m}_T = 30.2$ kg m^{-2} s^{-1}, $X_{in} = 0.63$, $\dot{q}_w = 158.7$ kW m^{-2}, $\Delta T_{in} \approx 30$ K.

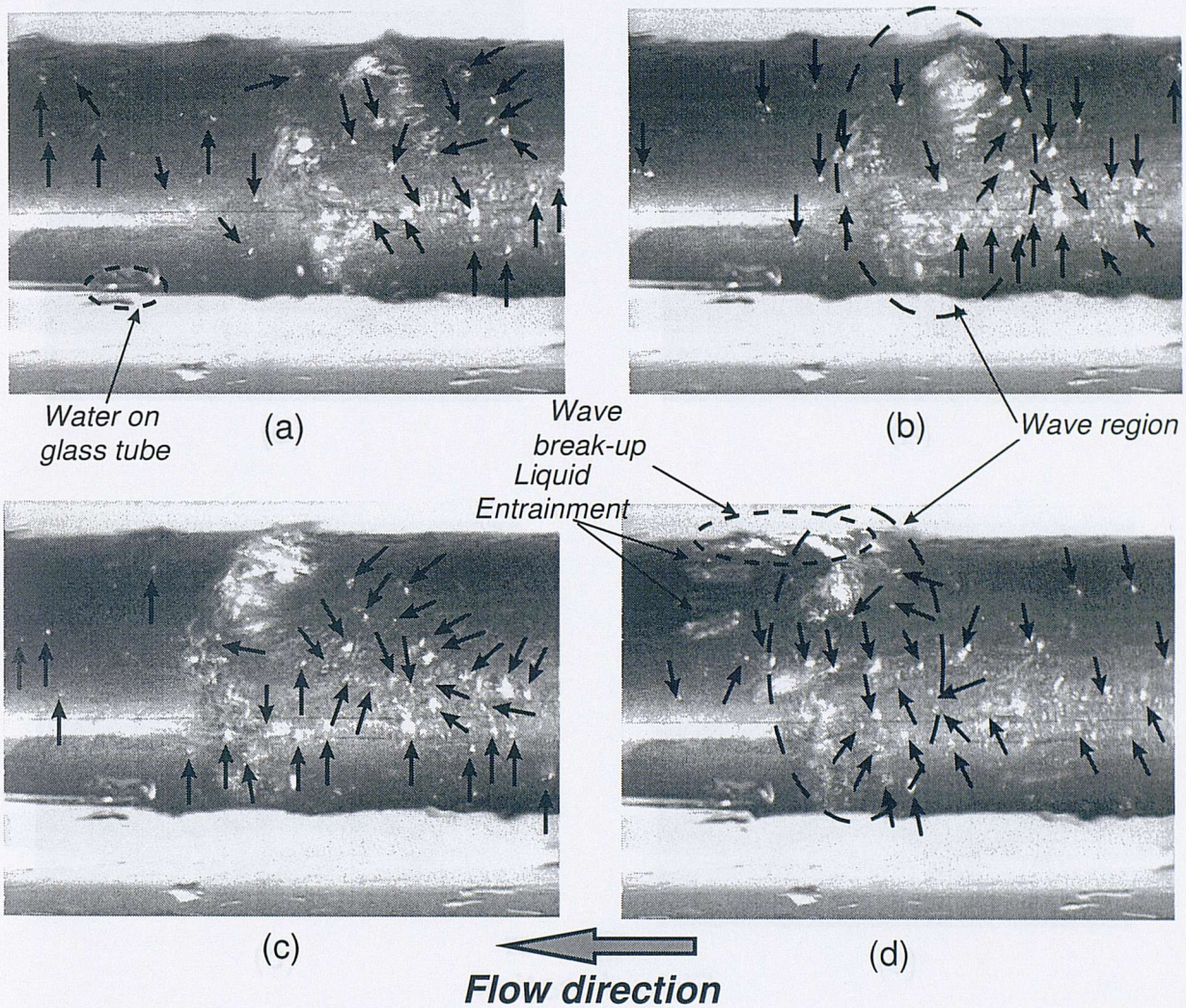


Figure 3.12: Identification of active nucleation sites in the wave region. Experimental conditions: $p_{in} = 1.9$ bar, $\dot{m}_T = 24.0$ kg m^{-2} s^{-1}, $X_{in} = 0.87$, $\dot{q}_w = 195.8$ kW m^{-2}, $\Delta T_{in} \approx 30$ K.

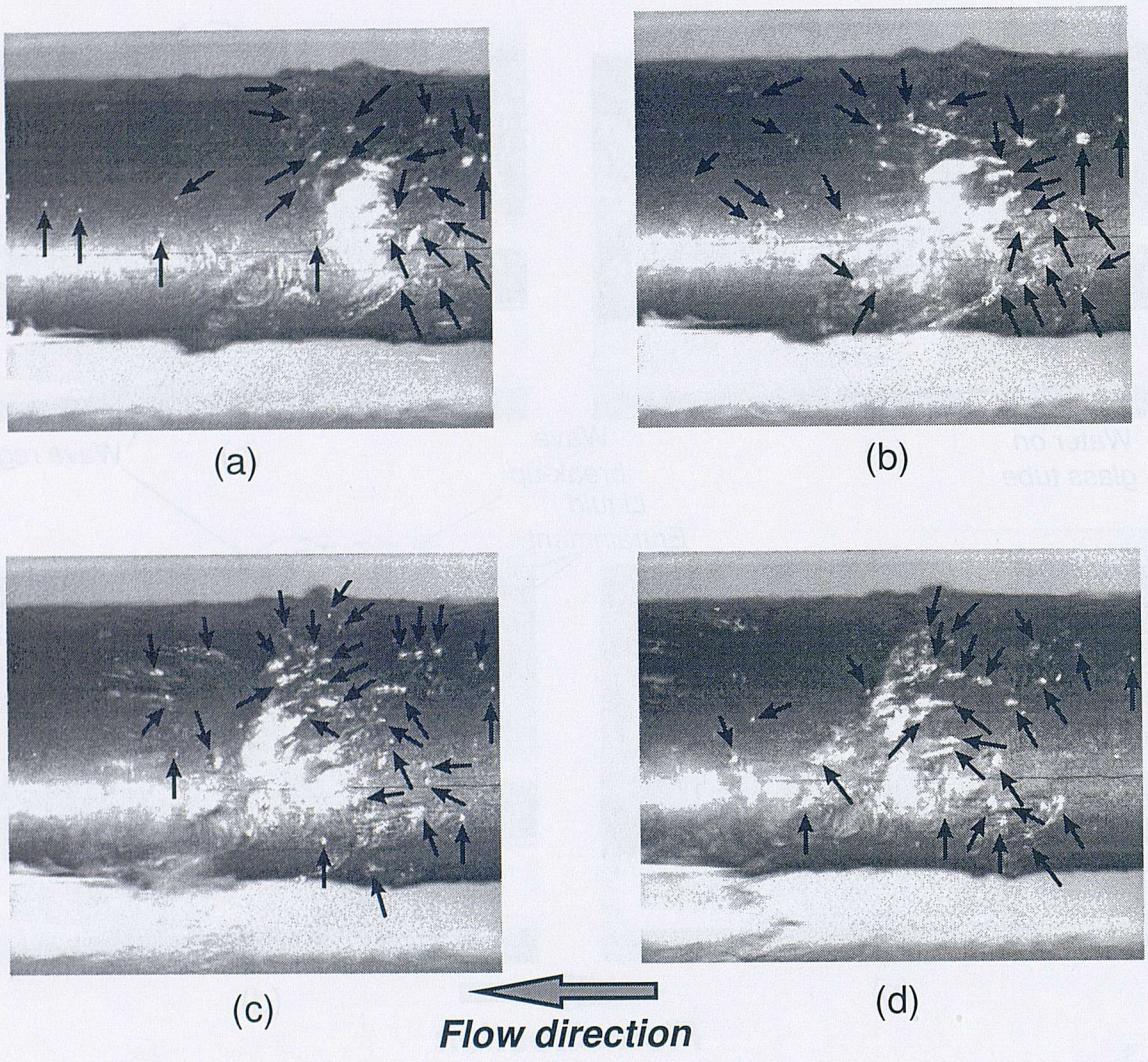


Figure 3.13: Identification of active nucleation sites in the wave region. Experimental conditions: $p_{in} = 2.0$ bar, $\dot{m}_T = 27.3$ kg m^{-2} s^{-1}, $X_{in} = 0.77$, $\dot{q}_w = 146.2$ kW m^{-2}, $\Delta T_{in} \approx 30$ K.

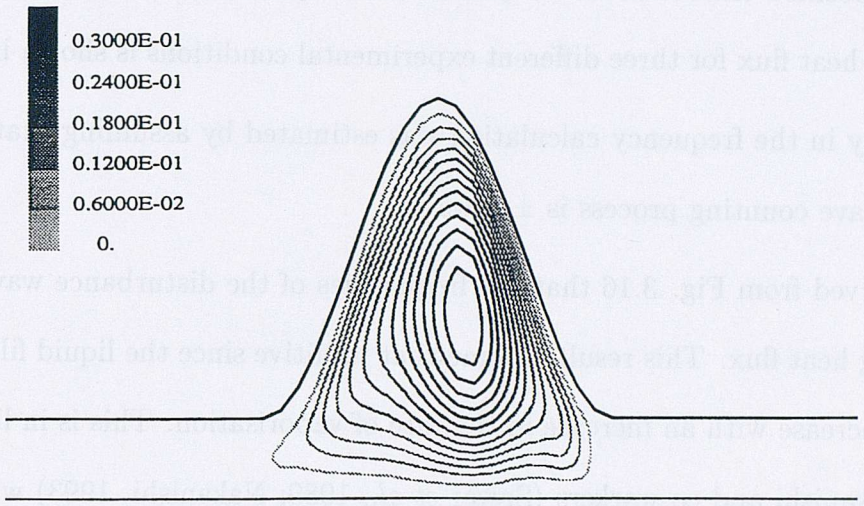


Figure 3.14: Turbulent viscosity distribution in the disturbance wave calculated using a low Reynolds number $\kappa - \varepsilon$ model (Jayanti and Hewitt, 1997).

in the film region, one should expect the associated lower wall superheat to suppress nucleation in the wave region.

The second postulation, as pointed out by Klausner (2000), is that, regardless of the flow regime in the wave region (laminar or turbulent), waves are also regions of reduced local pressure. Therefore, the decrease in the local saturation temperature due to the pressure reduction in the wave may be sufficient to counterbalance or even overcome the reduction of the wall superheat required to support nucleation under the more turbulent conditions in the wave region. This seems to be a likely explanation for the wave/nucleation sites interaction. However, it still requires experimental validation.

Wave frequencies and velocities

The frequency of disturbance waves could be obtained from the fixed axial position video sequences. This was achieved by counting the number of waves travelling along the view

frame over a specified time interval. A plot of the frequency of disturbance waves with increasing wall heat flux for three different experimental conditions is shown in Fig. 3.16. The uncertainty in the frequency calculation was estimated by assuming that the uncertainty of the wave counting process is $\pm$ 1 wave.

It can be observed from Fig. 3.16 that the frequencies of the disturbance waves decrease with increasing heat flux. This result is somewhat intuitive since the liquid film Reynolds number will decrease with an increase in the rate of vaporisation. This is in line with the findings of Nakanishi and co-workers (Sawai *et al.*, 1989; Nakanishi, 1993) who observed that the mean time separation (i.e., the time elapsed between the passing of two successive disturbance waves observed at a fixed time position) gradually increases as the the dryout region is approached.

From the difference in the frequencies of Runs 0824-1 and 0824-2 in Fig. 3.16, it can

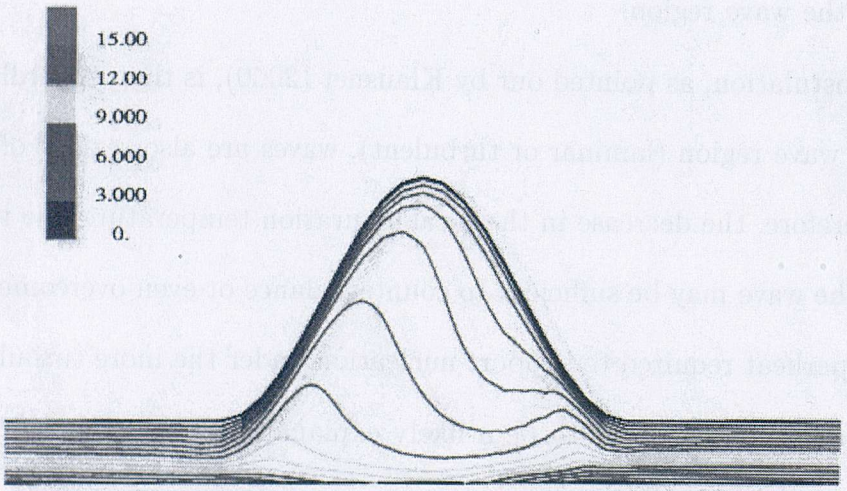


Figure 3.15: Temperature contours in the disturbance wave calculated using a low Reynolds number $\kappa - \varepsilon$ model. Interface at saturation (Jayanti and Hewitt, 1997).

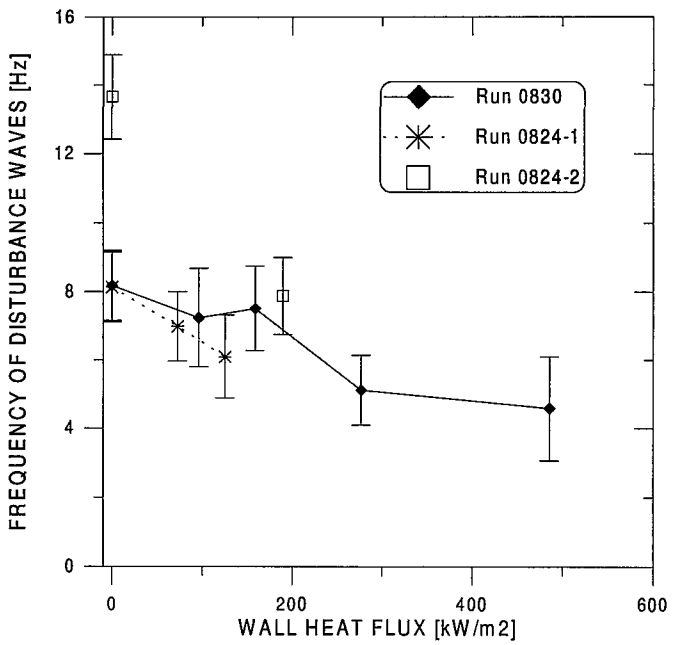


Figure 3.16: Variation of disturbance waves frequency with wall heat flux. Experimental conditions (Mass fluxes are initial values): Run 0824-1, $p_{in} = 1.6$ bar, $\dot{m}_G = 14.2$ kg m^{-2} s^{-1}, $\dot{m}_L = 8.0$ kg m^{-2} s^{-1}, $\Delta T_{in} \approx 10$ K, Run 0824-2, $p_{in} = 2.1$ bar, $\dot{m}_G = 22.0$ kg m^{-2} s^{-1}, $\dot{m}_L = 8.0$ kg m^{-2} s^{-1}, $\Delta T_{in} \approx 10$ K, Run 0830, $p_{in} = 2.0$ bar, $\dot{m}_G = 19.0$ kg m^{-2} s^{-1}, $\dot{m}_L = 11.2$ kg m^{-2} s^{-1}, $\Delta T_{in} \approx 10$ K.

be inferred that, as expected, the gas flow rate has also an effect on the frequency of disturbance waves. The wave frequency increases with an increase in the gas flow rate.

The approximate velocity of the disturbance waves could also be estimated from the analysis of the video recordings. This was calculated by counting the number of frames (and hence time) between the arrival of the wave front at two (previously measured) points.

The uncertainty in the velocity results was calculated by assuming that the uncertainty in the determination of the wave front arrival at the fixed points is $\pm$ 7 frames. The measured distance between the two points is assumed accurate.

Appendix A summarises the analysis of the video recordings by presenting a complete description of the frequency and velocity measurements in tabular form.

3.3.2 Wave axial development

In this section, experimental runs in which the camera was installed at various positions along the test section are reported. Video sequences were acquired at specific points of the visualisation section, such as the inlet porous sinter, the calming length and the bottom end of the heater) in order to obtain qualitative information on the formation and behaviour of the disturbance waves.

Figure 3.17 illustrates typical frames obtained at various points along the visualisation section. Regions of flow development, such as the inlet sinter and the calming section, are depicted together with frames acquired at a distance of approximately 0.25 m from the bottom of the heater (referred to as the *top of heater region*). Conditions in which a heat flux was applied to the inner rod are shown on the RHS of Fig. 3.17 (2 upper frames). The appearance of disturbance waves is quite different in situations where a heat flux is imposed (or not) to the heater.

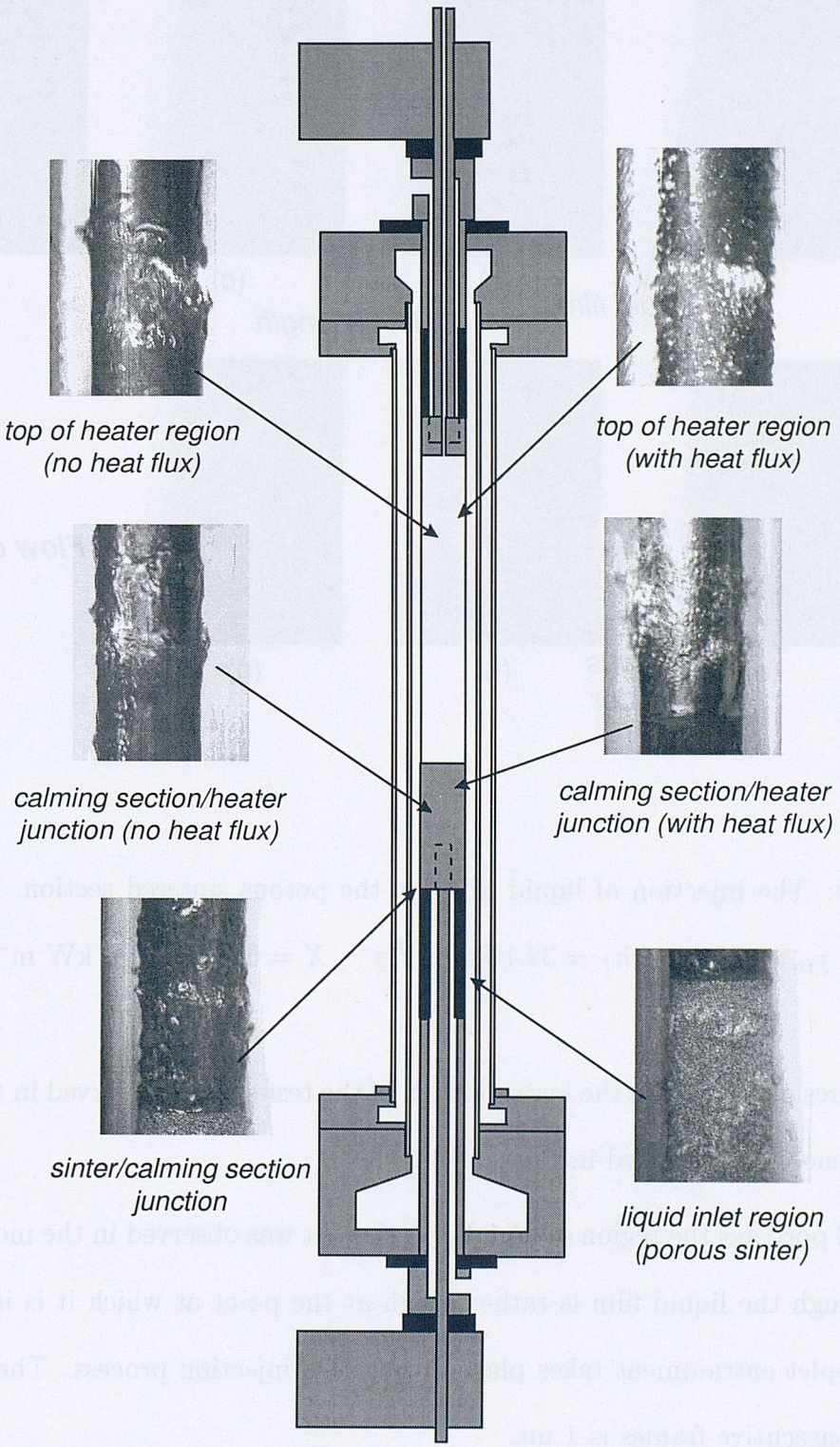


Figure 3.17: Illustration of axial development of the flow. Experimental conditions: $p_{in} = 1.9$ bar, $\dot{m}_T = 33$ kg m^{-2} s^{-1} (nominal), $X_{in} = 0.65$, $\dot{q}_w = 460$ kW m^{-2} (nominal: at frames indicating the presence of a heat flux. Others: $\dot{q}_w = 0$), $\Delta T_{in} \approx 30$ K (in *top of heater* frames. Approximately 10 K in others).

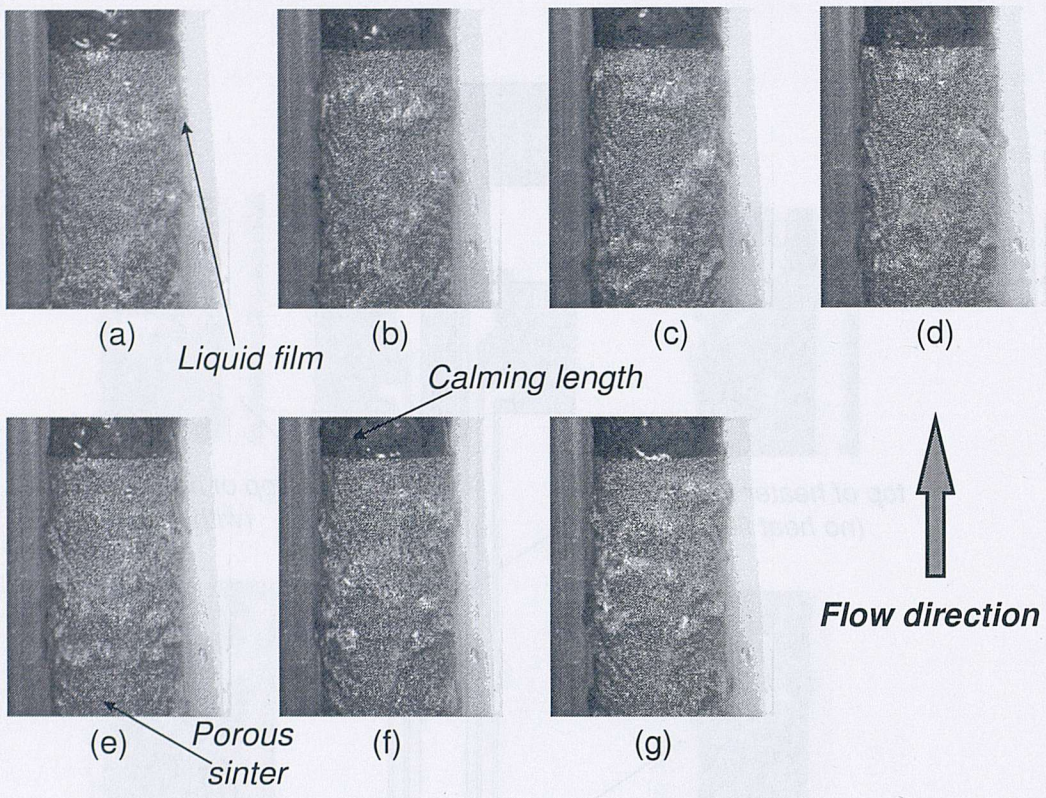


Figure 3.18: The injection of liquid through the porous sintered section. Experimental conditions: $p_{in} = 1.9$ bar, $\dot{m}_T = 32.1$ kg m^{-2} s^{-1}, $X = 0.66$, $\dot{q}_w = 0$ kW m^{-2}.

Some features of the flow in the lower portion of the test section observed in the high-speed video sequences are depicted in Figs. 3.18 to 3.22.

Figure 3.18 portrays the region of liquid injection. It was observed in the moving sequence that, although the liquid film is rather rough at the point at which it is injected, virtually no droplet entrainment takes place during this injection process. The time interval between consecutive frames is 1 ms.

Figure 3.19 depicts the liquid film at the junction between the porous sinter and the calming section. The underdeveloped nature of the flow in the liquid film is indicated by the multiple peak structure of the film interface. Some of these peaks are identified by

black arrows in some frames. The time interval between consecutive frames is 3 ms.

In Fig. 3.20, a sequence taken at the junction between the calming section and the heated section is shown. The ragged structure of the film as illustrated in Fig. 3.19 still prevails here, but some of the multiple peaks have died down. In this region, the circumferentially coherent waves observed further downstream start to develop. The time interval between consecutive frames is 1 ms.

Figures 3.21 and 3.22 also show sequences taken at the calming section/heater junction. In these figures, power was applied to the heater in order to observe the transition from a region in which no heat flux is present to one in which it is present and sufficiently high to give rise to bubble nucleation (some nucleation sites are marked with black arrows in some frames). Significant liquid entrainment was observed when the wave encounters the heated region. The time interval between consecutive frames in Figs. 3.21 and 3.22 is 2 ms.

Wave frequencies and velocities

The results of an assessment of the frequencies and velocities of the waves as a function of distance along the visualisation section is presented in this section.

Figure 3.23 shows the evolution of the frequency of disturbance waves with the distance along the heated section. There is a decay in the wave frequency, most probably as a result of wave merging and coalescence. In fact, these can be observed in some of the video sequences obtained at the junction between the calming section and the heater. This corresponds to $z = 0$ in Fig. 3.23.

In Fig. 3.23, the symbol $\diamond$ represents an attempt to measure the wave frequency at the calming section. However, large errors arose due to difficulty in the discrimination of the waves.

As far as the wave frequencies and velocities are concerned, conclusions similar to those

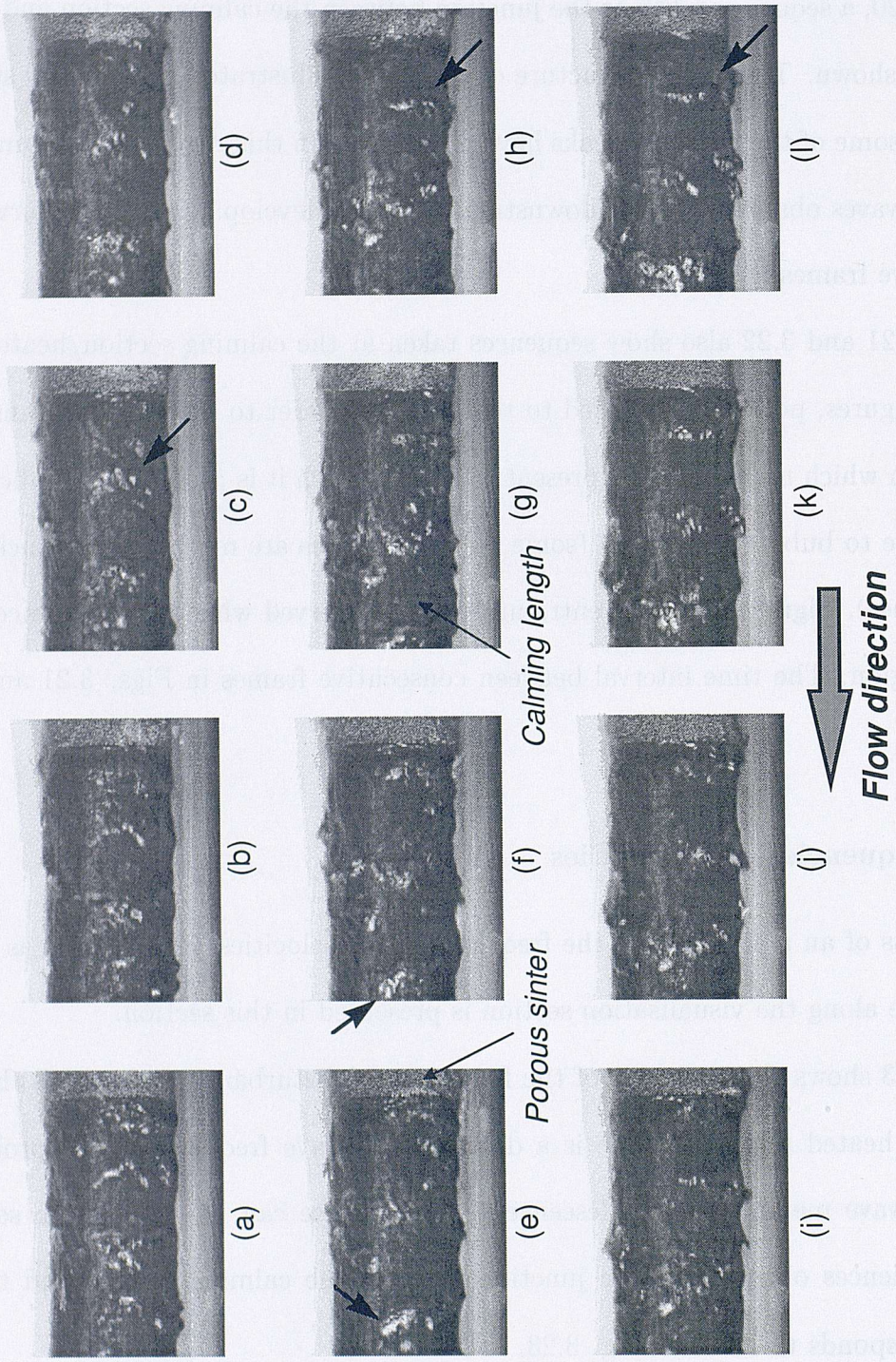


Figure 3.19: Illustration of the flow at the junction between the sinter and the calming section. Experimental conditions: $p_{in} = 1.9$ bar, $\dot{m}_T = 32.1$ kg m^{-2} s^{-1}, $X = 0.66$, $\dot{q}_w = 0$ kW m^{-2}.

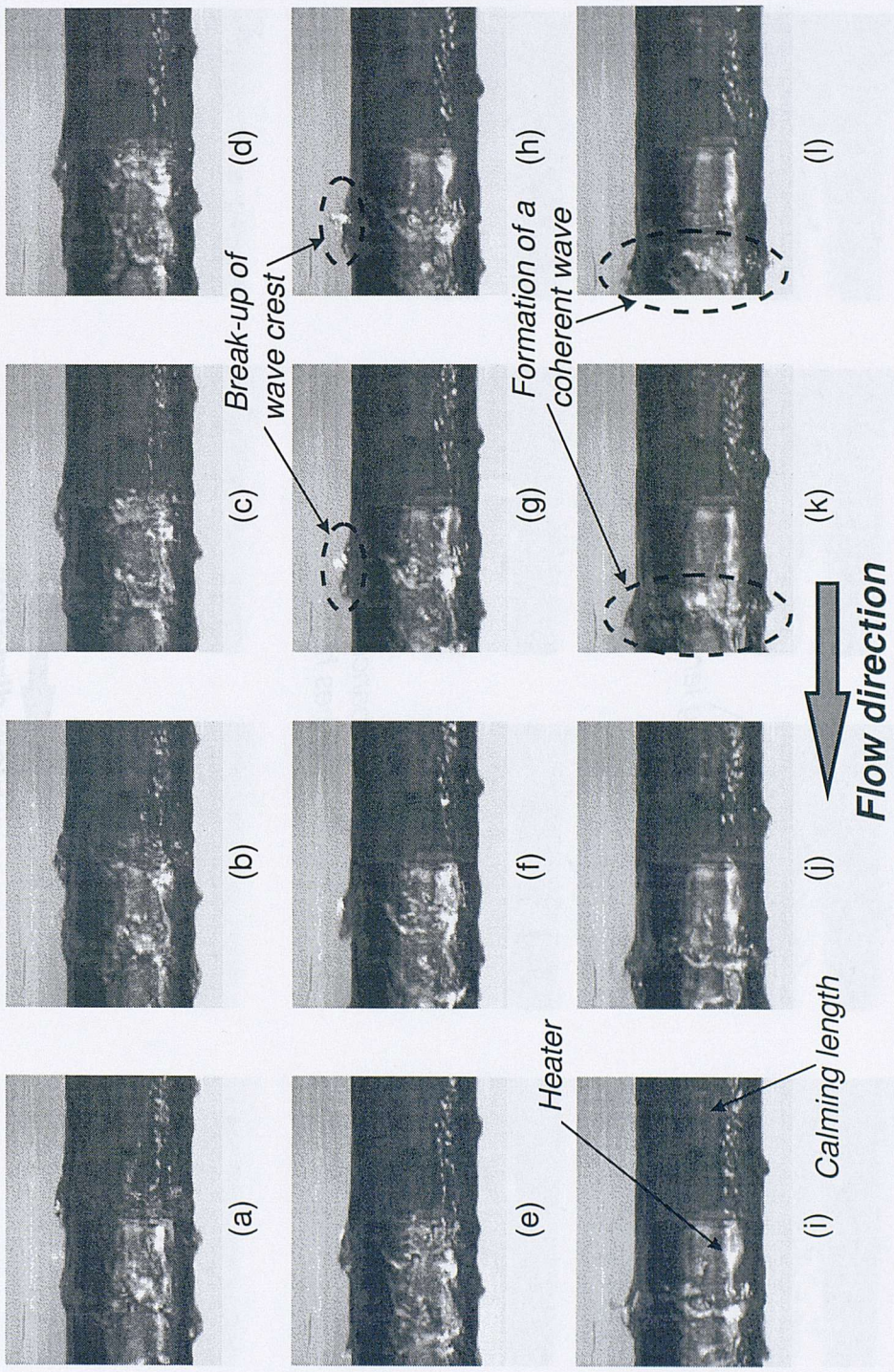


Figure 3.20: Illustration of the flow at the junction between the calming section and the heater. Experimental conditions: $p_{in} = 1.9$ bar, $\dot{m}_T = 32.1$ kg m^{-2} s^{-1}, $X = 0.66$, $\dot{q}_w = 0$ kW m^{-2}.

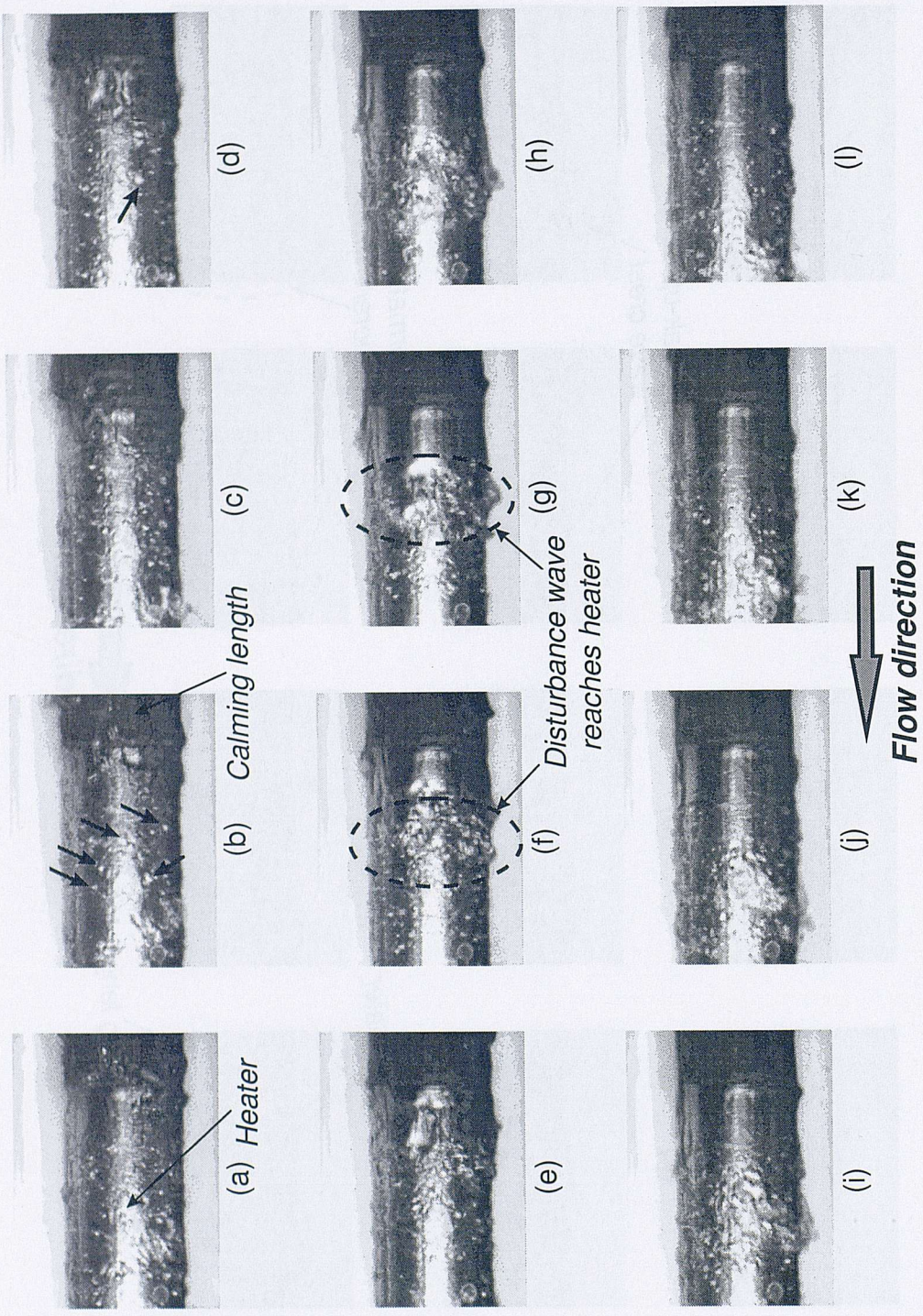


Figure 3.21: Illustration of the flow at the junction between the calming section and the heater. Experimental conditions: $p_{in} = 1.9$ bar, $\dot{m}_T = 32.1$ kg m^{-2} s^{-1}, $X_{in} = 0.66$, $\dot{q}_w = 309.6$ kW m^{-2}, $\Delta T_{in} \approx 10$ K.

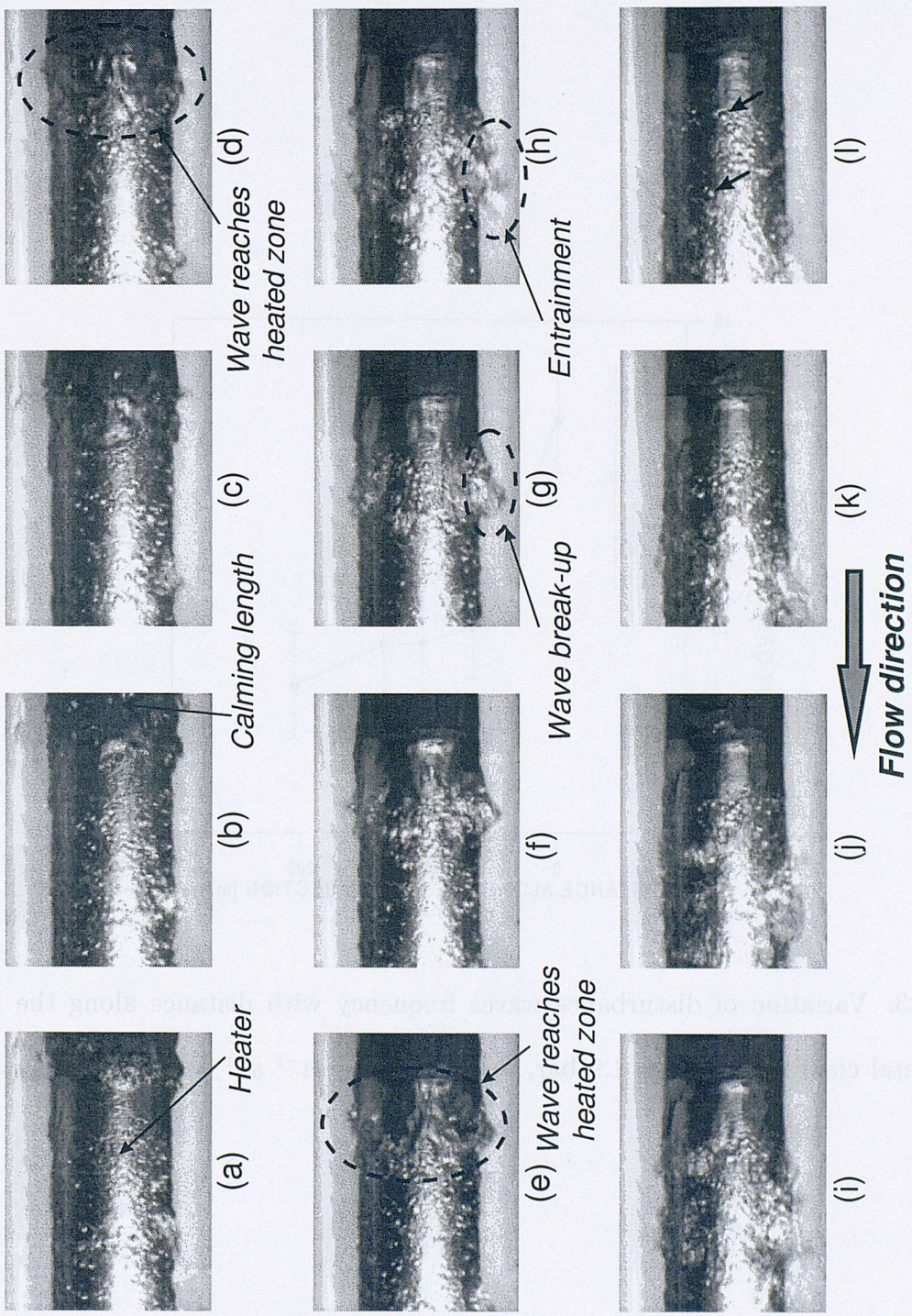


Figure 3.22: Illustration of the flow at the junction between the calming section and the heater. Experimental conditions: $p_{in} = 1.9$ bar, $\dot{m}_T = 32.1$ kg m^{-2} s^{-1}, $X_{in} = 0.66$, $\dot{q}_w = 437.2$ kW m^{-2}, $\Delta T_{in} \approx 10$ K.

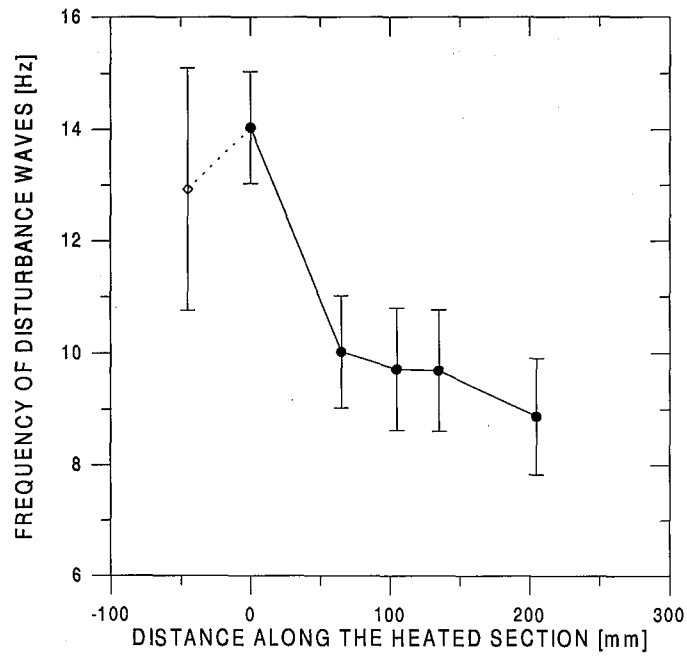


Figure 3.23: Variation of disturbance waves frequency with distance along the heater. Experimental conditions: $p_{in} = 1.9$ bar, $\dot{m}_T = 32.1$ kg m^{-2} s^{-1}, $X = 0.66$, $\dot{q}_w = 0$ kW m^{-2}.

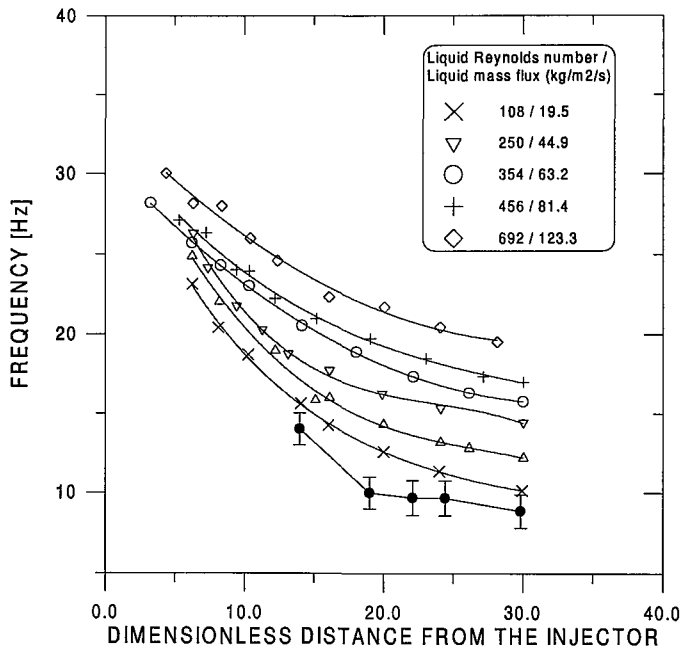


Figure 3.24: Wave frequency as a function of dimensionless distance (Hall-Taylor and Nedderman, 1968).

reported by Hall-Taylor and Nedderman (1968) can be made, even though the present database is very limited. It was found that the standard deviation of the wave velocities was around 0.12 m s^{-1} and roughly independent of the flow conditions.

The velocity of disturbance waves changed very slowly with position. However, as already seen, the wave frequency has a strong positional dependence. To illustrate this point, the data of Fig. 3.23 is plotted in Fig. 3.24 together with those of Hall-Taylor and Nedderman (1968).

As seen in Fig. 3.24, the experimental results are quite consistent and support the findings of Hall-Taylor and Nedderman.

Hall-Taylor and Nedderman (1968) also correlated graphically the velocities of disturbance waves in air-water and steam-water flows in pipes of about 25 mm internal diameter. This is shown in Fig. 3.25.

The data of the present work are better visualised at a close-up reproduction (Fig. 3.26).

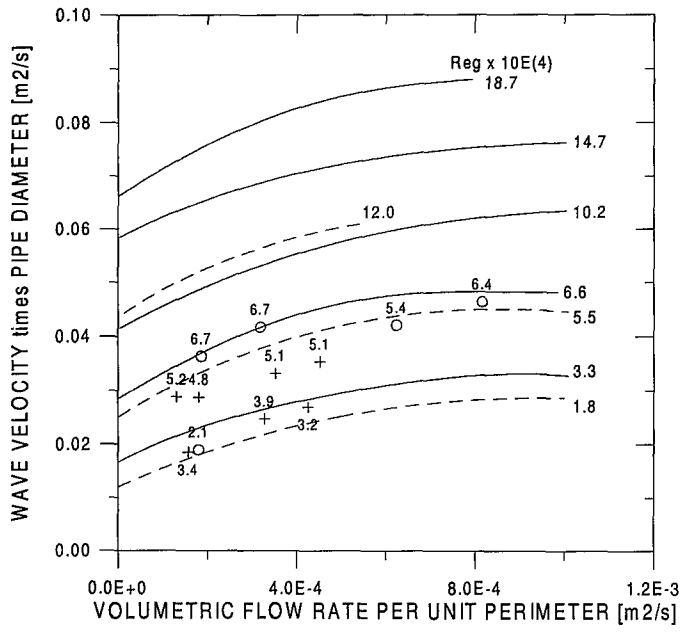


Figure 3.25: Wave velocity correlation (Hall-Taylor and Nedderman, 1968).

The data in Fig. 3.26 were obtained at a fixed position ($z_{HS} \approx 0.25$ m). The figures adjacent to the symbols in Figs. 3.25 and 3.26 correspond to the Reynolds number of the gas (Re_G). As will be seen, the agreement is quite good.

Figure 3.27 presents a comparison of the data obtained under no heat flux conditions and at a fixed position along the heater with those of Hall-Taylor and Nedderman (1968) for air-water and steam-water in a 25.4 mm internal diameter pipe for large distances from the injector. A curve through the experimental results by Shearer (1964) air-water data for 25.4 mm internal diameter and 15.9 mm internal diameter pipes is also shown.

The data are presented in terms of a Strouhal number based on the wave frequency and gas superficial velocity,

$$Sr = \frac{\mathrm{f} d_T}{U_{GS}}. \tag{3.4}$$

Similar conclusions to those of Hall-Taylor and Nedderman (1968) can be drawn concerning the correlation of frequency data, i.e., that it appears that Sr is strongly dependent

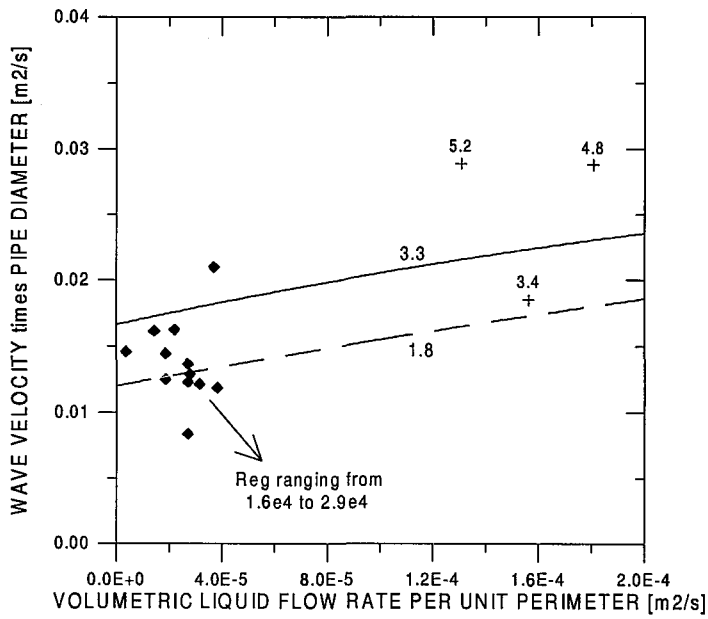


Figure 3.26: Comparison of the present data with the wave velocity correlation (Hall-Taylor and Nedderman, 1968).

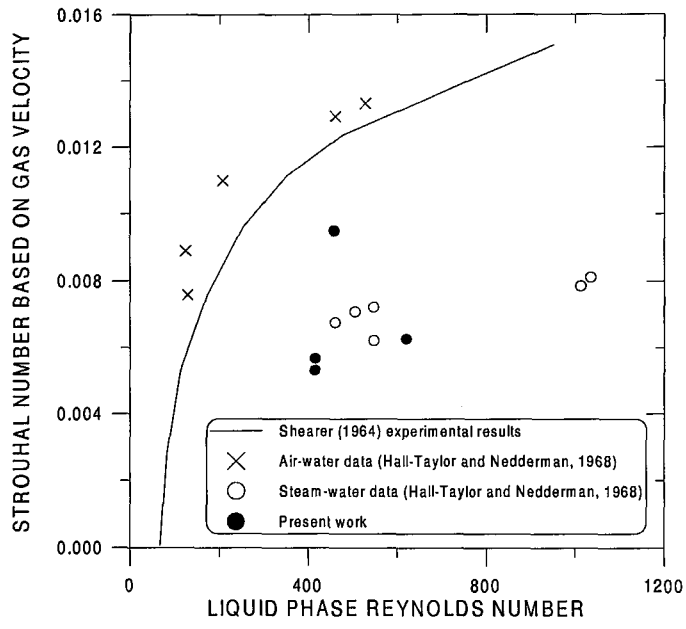


Figure 3.27: Comparison of wave frequency data with data of Shearer (1964) and Hall-Taylor and Nedderman (1968).

on the pair of fluids. Azzopardi (1997) attempted to modify the correlation by plotting the Strouhal number data as a function of an excess Reynolds number (based on the film flow rate over and above the critical film flow rate for wave inception). He correlated air-water data from various sources quite successfully, bringing together data whose frequencies would normally have covered two orders of magnitude. However, he suggested that before this approach is developed any further, more accurate prediction methods are required for the critical film flow rate. This is an important issue specially for systems other than air-water.

In the present work, the liquid film flow rates investigated are close to (above and below) the critical film flow rate for disturbance wave inception and onset of droplet entrainment according to several correlations. At the majority of this conditions (excluding the lowest of liquid flow rates), disturbance waves were observed. The values of Sr for the present

data are in good agreement with those in the modified correlation of Azzopardi (1997) for excess Reynolds numbers between 0.1 and 20.

Appendix A presents the values for Sr in tabular form. Also shown are the values of a Strouhal number based on the wave velocity,

$$Sr_W = \frac{\mathrm{f} d_T}{U_W}. \tag{3.5}$$

This is generally about one order of magnitude larger than Sr.

3.3.3 Heat transfer measurements

The range of experimental conditions over which the quantitative heat transfer (wall temperature measurement) experiments were carried out is shown in Table 3.2.

Table 3.2: Experimental conditions for the heat transfer tests.

Conditions	Unit	Range
Pressure (p)	bar	1.28 to 1.56
Total mass flux ($\dot{m}_T$)	kg m^{-2} s^{-1}	23.6 to 43.3
Heat flux ($\dot{q}_w$)	kW m^{-2}	9.3 to 326.9
Inlet subcooling (ΔT_{in})	K	around 10 (20 for $\dot{q}_w = 326.9$)
Inlet quality (X_{in})	-	0.48 to 0.79

Heat transfer coefficient and the effect of wall heat flux

The heat transfer coefficient is defined by the following relationship,

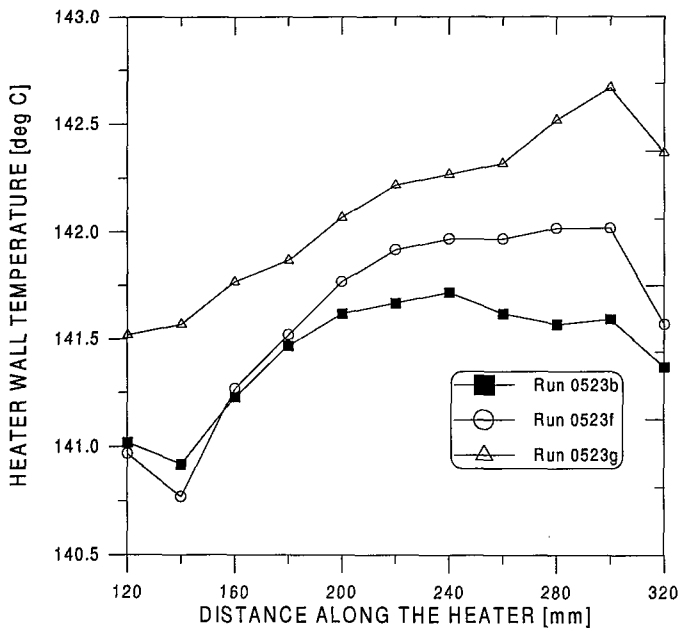


Figure 3.28: Profiles of measured wall temperature along the heated section. Experimental conditions: $\overline{p} = 1.6$ bar (nominal), $\dot{m}_{G,in} = 23$ kg m^{-2} s^{-1} (nominal), $\dot{q}_w = 326.9$ kW m^{-2}, $\Delta T_{in} \approx 10$ K, Run 0523b: $\dot{m}_{L,in} = 12.8$ kg m^{-2} s^{-1}, Run 0523f: $\dot{m}_{L,in} = 19.2$ kg m^{-2} s^{-1}, Run 0523g: $\dot{m}_{L,in} = 22.4$ kg m^{-2} s^{-1}.

$$\alpha = \frac{\dot{q}_w}{(T_{w_o} - T_{sat})}, \tag{3.6}$$

where T_{w_o} is the corrected outer wall temperature.

Figure 3.28 Illustrates typical distributions of T_{w_o} along the heated section.

A plot of $\overline{\alpha}$ against the wall heat flux, $\dot{q}_w$, is shown in Fig. 3.29. $\overline{\alpha}$ is the heat transfer coefficient averaged over the length of the heated section over which the wall temperature measurements were carried out, L^*_{HS}. This is defined as,

$$\overline{\alpha} = \frac{1}{L^*_{HS}} \int_0^{L^*_{HS}} \alpha dz. \tag{3.7}$$

Although the points in Fig. 3.29 is for a range of flow conditions, which might themselves

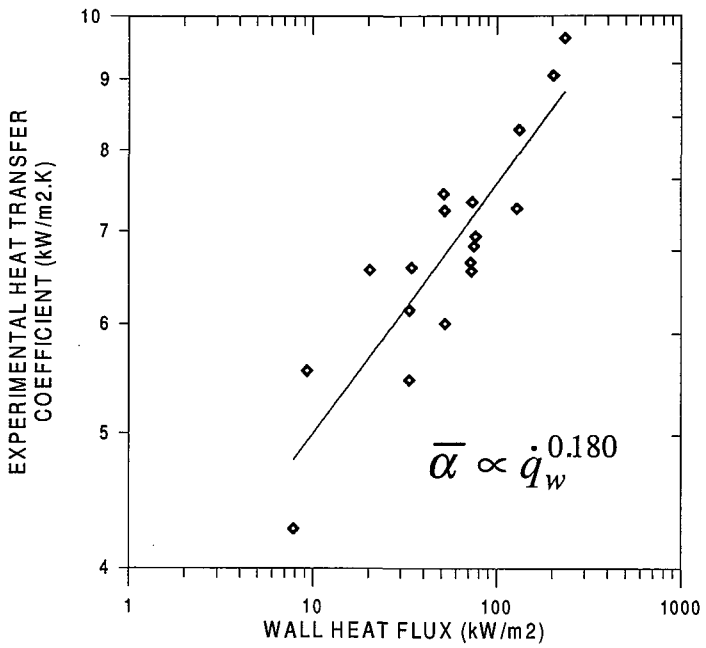


Figure 3.29: Variation of the experimental (average) heat transfer coefficient with wall heat flux.

depend on the heat flux (for example, changes in liquid film flow rate due to evaporation), this plot serves to indicate the dependence of the heat transfer coefficient on the heat flux. This dependence is given approximately by,

$$\overline{\alpha}_{exp} \propto \dot{q}_w^{0.180}. \tag{3.8}$$

Numerical integration of Eq. 3.7 was carried out using the trapezoidal rule.

A dependence of α on the heat flux of this sort was reported by Bennett *et al.* (1961) for very similar experiments (see Section 2.3.5).

Heat transfer coefficient predictions

This section shows predictions of α obtained from the application of some of the correlations presented in Section 2.3.5.

Figures 3.30 to 3.32 illustrate typical profiles of experimental and predicted local heat

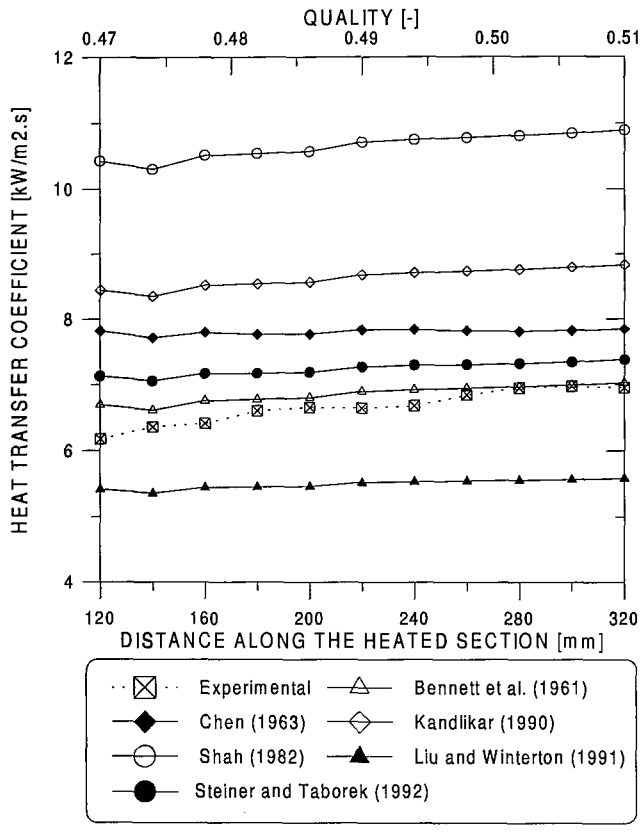


Figure 3.30: Predictions of the heat transfer coefficient by the various correlations. Experimental conditions: $\overline{p} = 1.42$ bar, $\dot{m}_T = 38.1$ kg m^{-2} s^{-1}, $\dot{q}_w = 33.4$ kW m^{-2}, $\overline{\Delta T}_w = 5.0$ K, $\Delta T_{in} \approx 10$ K.

transfer coefficient with distance and quality.

The correlation by Bennett *et al.* (1961) gives the best results over the entire range of flow conditions. This is not a surprising fact, since this correlation was devised based on experimental data obtained at very similar conditions (internally heated annulus). The second best performance is that of the Steiner and Taborek (1992) correlation, which slightly overpredicts the data at a low heat flux (Fig. 3.30) and has a rather steep slope with distance (quality) at higher heat fluxes. The Liu and Winterton (1991) correlation is the only method that always underpredicts the data. At a low heat flux, when nucleate boiling is suppressed, the Chen (1966) correlation performs better than the Shah (1982)

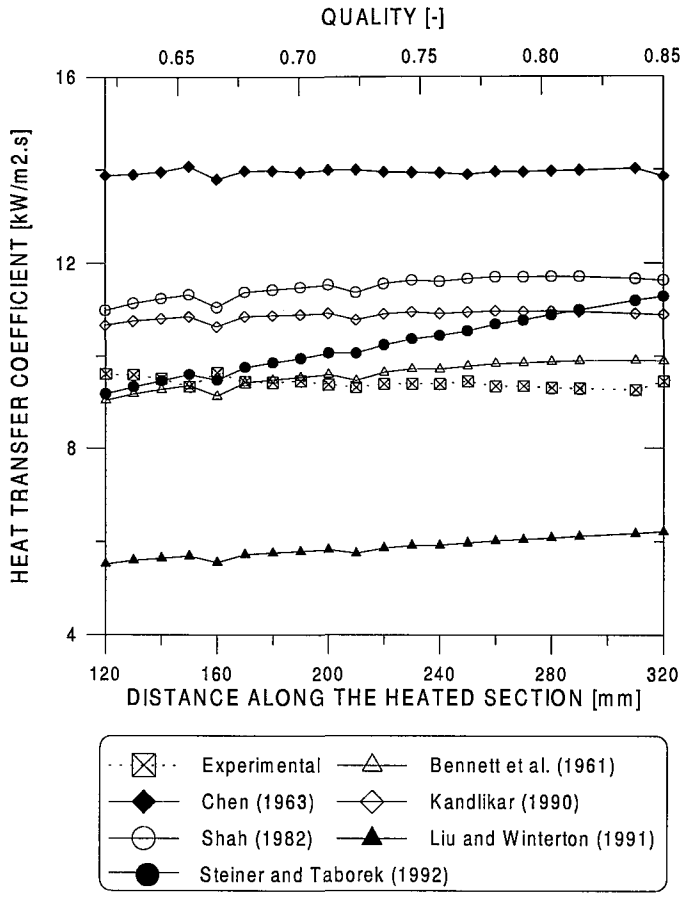


Figure 3.31: Predictions of the heat transfer coefficient by the various correlations. Experimental conditions: $\overline{p} = 1.52$ bar, $\dot{m}_T = 32.6$ kg m^{-2} s^{-1}, $\dot{q}_w = 202.3$ kW m^{-2}, $\overline{\Delta T}_w = 21.5$ K, $\Delta T_{in} \approx 10$ K.

and Kandlikar (1990) correlations. This role is inverted at high heat fluxes and it is possibly due to a severe overprediction of the nucleate boiling component of the Chen (1963) correlation.

It was observed that some of the correlations gave systematically better predictions when the definition of the equivalent diameter given by Eq. 2.147 was used. This was the case in the Chen (1966), Kandlikar (1990) and Steiner and Taborek (1992) correlations. Therefore, such a definition of the equivalent diameter was used for these methods. It was also used, as explicitly suggested by the authors, in the Liu and Winterton (1991)

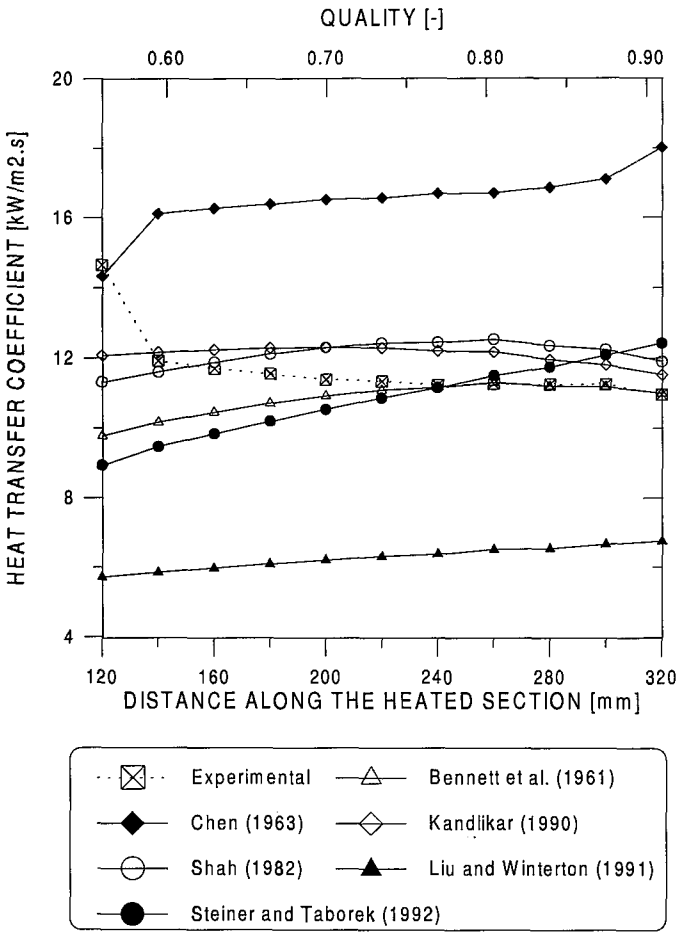


Figure 3.32: Predictions of the heat transfer coefficient by the various correlations. Experimental conditions: $\overline{p} = 1.55$ bar, $\dot{m}_T = 38.9$ kg m^{-2} s^{-1}, $\dot{q}_w = 326.9$ kW m^{-2}, $\overline{\Delta T}_w = 28.34$ K, $\Delta T_{in} \approx 30$ K.

correlation. On the other hand, Shah (1982) recommends that Eq. 2.147 should only be used if the *clearance* defined as,

$$\frac{d_a - d_o}{2}, \tag{3.9}$$

is less than 4 mm. In the present experiments, the clearance is equal to 6.45 mm. Therefore, the definition $d_e = d_a - d_o$ was employed in the Shah (1982) correlation.

The overall performance of the predictive methods is shown if Figs. 3.33 to 3.38.

The mean errors of the heat transfer coefficient prediction by each correlation is presented

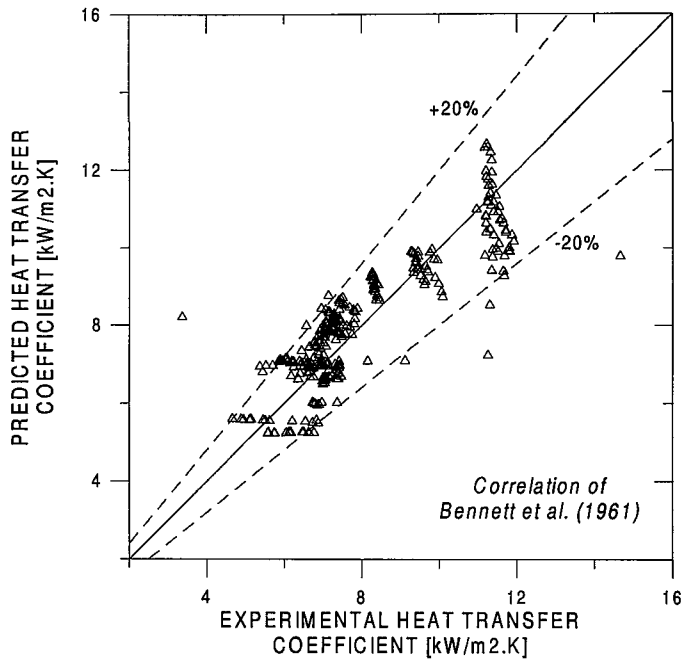


Figure 3.33: Predictions of the heat transfer coefficient using the Bennett *et al.* (1961) correlation.

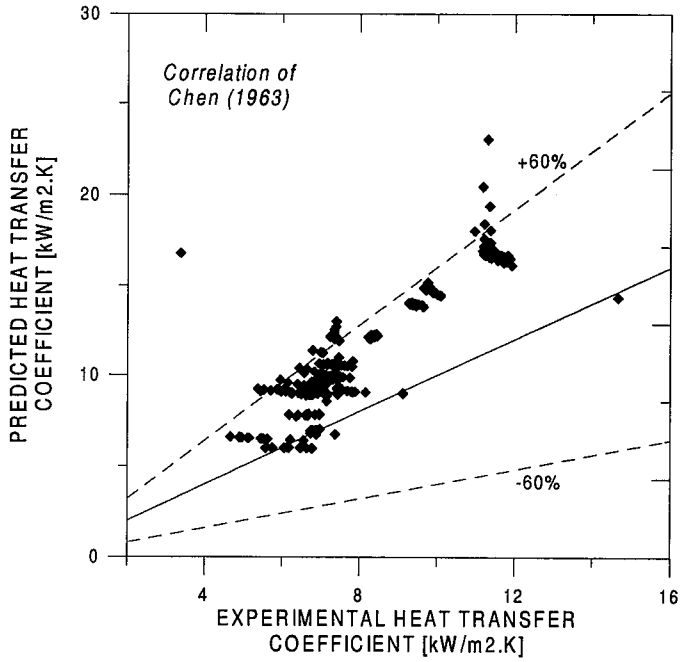


Figure 3.34: Predictions of the heat transfer coefficient using the Chen (1966) correlation.

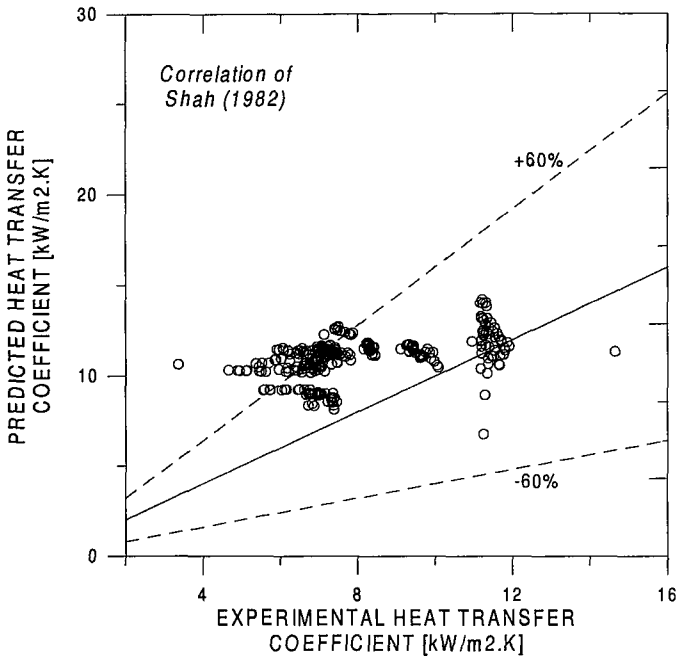


Figure 3.35: Predictions of the heat transfer coefficient using the Shah (1982) correlation.

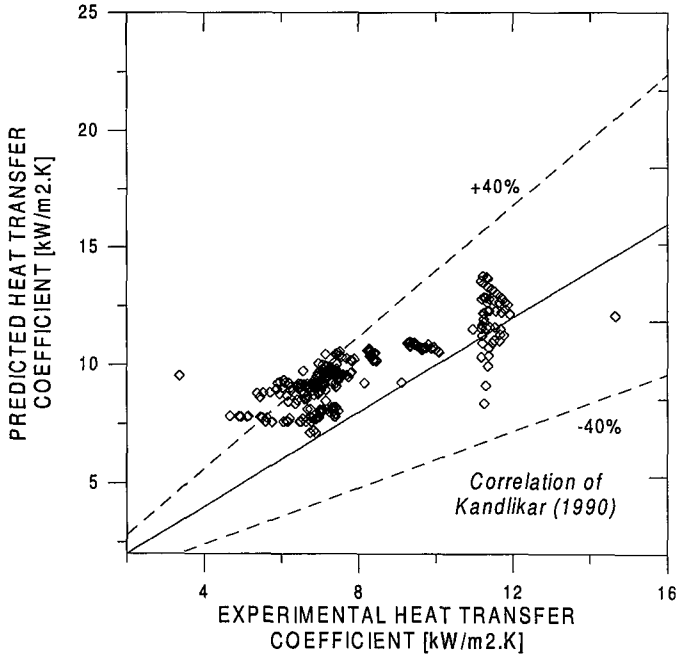


Figure 3.36: Predictions of the heat transfer coefficient using the Kandlikar (1990) correlation.

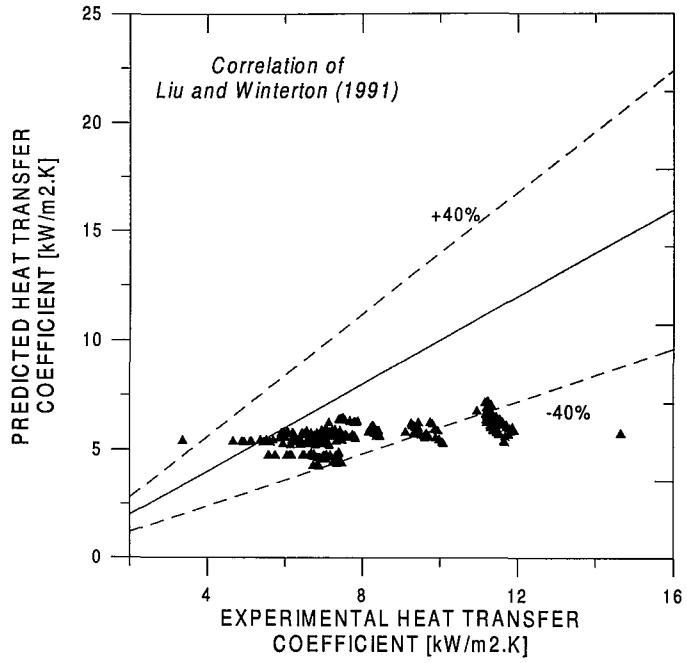


Figure 3.37: Predictions of the heat transfer coefficient using the Liu and Winterton (1991) correlation.

in Table 3.3. The mean error is defined as,

$$\text{error}_\alpha = \frac{1}{N_p} \sum_{j=1}^{N_p} \frac{|\alpha_{pred,j} - \alpha_{exp,j}|}{\alpha_{exp,j}}. \tag{3.10}$$

Discussion of the heat transfer results in light of the Classical Interpretation

A few comments regarding the experiments described in this chapter are needed to clarify some of the main findings. First of all, it should be emphasised that the primary goal of the boiling experiments in this thesis was the observation of the interaction between disturbance waves and nucleation sites.

With that in mind and based on previous experimental work of the same nature (Hewitt *et al.*, 1965), the present experiments were not designed to allow a wide range of total mass fluxes to be analysed. Therefore, it may be that this study does not provide a clear

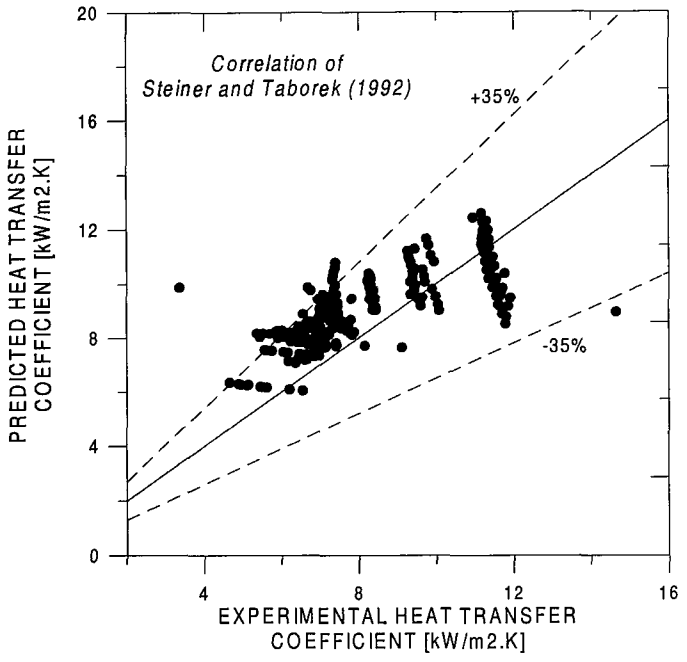


Figure 3.38: Predictions of the heat transfer coefficient using the Steiner and Taborek (1992) correlation.

Table 3.3: Errors of various correlations in predicting the heat transfer coefficient.

Correlation	error_α (%)
Bennett *et al.* (1961)	9.7
Chen (1966)	40.2
Shah (1982)	43.6
Kandlikar (1990)	25.8
Liu and Winterton (1991)	27.7
Steiner and Taborek (1992)	18.3

assessment of its effects on the heat transfer behaviour. On the other hand, a wide range of heat fluxes was tested and a fairly strong effect of this on the heat transfer coefficient

was observed (see Fig. 3.29). The question to be asked is to what extent does the inability of the apparatus to investigate the mass flux effect exaggerates the heat flux contribution. Without a confident answer to this question, no conclusion can be drawn as to which heat transfer mechanism is the dominant one. Nevertheless, this should not lead to the invalidation of the data. In defence of the genuineness of the results is the good agreement with the Bennett *et al.* (1961) correlation, which was devised based on a wide range of experimental data obtained using a very similar test section.

3.3.4 Error analysis

Table 3.4 presents the estimated uncertainties of the measured values used in the determination of the experimental heat transfer coefficient.

Table 3.4: Estimated uncertainty of measured parameters used in the determination of the experimental heat transfer coefficient.

Parameter	Uncertainty
Temperature (wall and saturation)	± 0.1 K
Pressure	0.1% full scale
Voltage across the heater (V)	± 0.5 V
Current across the heater (I)	± 5 to 10 A (assumed 7.5 A)
Heated length (L_{HS})	± 2 mm

The uncertainty in the heat transfer coefficient measurement is estimated as follows,

$$\delta\alpha^2 = \left(\frac{\partial\alpha}{\partial\dot{q}_w}\right)^2 \delta\dot{q}_w^2 + \left(\frac{\partial\alpha}{\partial\left(T_{w_o} - T_{sat}\right)}\right)^2 \delta\left(T_{w_o} - T_{sat}\right)^2, \tag{3.11}$$

where,

$$\delta \dot{q}_w^2 = \left(\frac{\partial \dot{q}_w}{\partial V}\right)^2 \delta V^2 + \left(\frac{\partial \dot{q}_w}{\partial I}\right)^2 \delta I^2 + \left(\frac{\partial \dot{q}_w}{\partial L_{HS}}\right)^2 \delta L_{HS}^2. \tag{3.12}$$

The partial derivatives of Eq. 3.6 and of,

$$\dot{q}_w = \frac{VI}{\pi d_o L_{HS}}, \tag{3.13}$$

are given by,

$$\frac{\partial \alpha}{\partial \dot{q}_w} = \frac{1}{(T_w - T_{sat})}, \tag{3.14}$$

$$\partial \left(T_{w_o} - T_{sat}\right) = -\frac{\dot{q}_w}{\left(T_w - T_{sat}\right)^2}, \tag{3.15}$$

$$\frac{\partial \dot{q}_w}{\partial V} = \frac{I}{\pi d_o L_{HS}}, \tag{3.16}$$

$$\frac{\partial \dot{q}_w}{\partial I} = \frac{V}{\pi d_o L_{HS}}, \tag{3.17}$$

$$\frac{\partial \dot{q}_w}{\partial L_{HS}} = -\frac{VI}{\pi d_o L_{HS}^2}. \tag{3.18}$$

An application of the above equations to the range of conditions investigated here gave errors around $\pm 12\%$ for the experimental heat transfer coefficient.

3.4 Prediction of ONB in climbing films

3.4.1 Onset and suppression of nucleation in forced convection

As mentioned in Section 2.3.2, it is the direction from which the critical temperature difference for nucleation is approached that dictates whether the phenomenon under in-

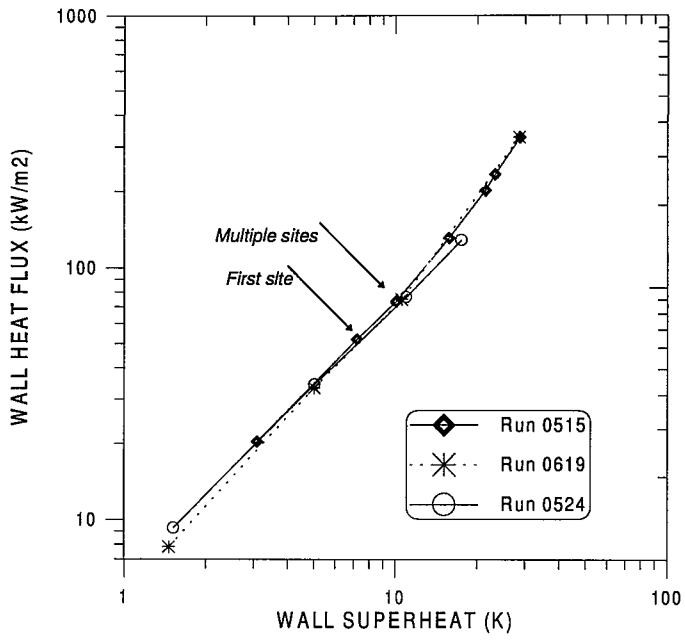


Figure 3.39: Typical boiling curves indicating the appearance of active nucleation sites. Experimental conditions: Run 0515. $\overline{p} = 1.5$ bar, $\dot{m}_T = 36.0$ kg m^{-2} s^{-1}, $\Delta T_{in} \approx 30$ K; Run 0524. $\overline{p} = 1.3$ bar, $\dot{m}_T = 38.1$ kg m^{-2} s^{-1}, $\Delta T_{in} \approx 10$ K; Run 0619. $\overline{p} = 1.5$ bar, $\dot{m}_T = 25$ kg m^{-2} s^{-1}, $\Delta T_{in} \approx 10$ K.

vestigation is one of onset or suppression of nucleate boiling.

In this section, a simple theory is applied in order to predict the Onset of Nucleate Boiling (ONB) in climbing films characteristic of those encountered in the heat transfer experiments.

Figure 3.39 presents typical boiling curves obtained in the series of heat transfer tests. The heat fluxes at which the very first nucleation site was spotted are indicated. So are those at which a number of other active sites were observed at various locations along the heater.

As seen in Section 2.3.2, there are several theories to predict the incipience of nucleation in forced convection. Amongst these, one can cite those of Davis and Anderson (1966),

$$(T_w - T_{sat})^2 = \frac{8C_1\sigma T_{sat}\dot{q}_w}{\lambda_L \Delta h_v}\left(\frac{1}{\rho_G} - \frac{1}{\rho_L}\right), \tag{3.19}$$

where $C_1 = 1$,

Frost and Dzakowic (1967),

$$(T_w - T_{sat})^2 = \frac{8\sigma T_{sat}\dot{q}_w}{\lambda_L \Delta h_v}\left(\frac{1}{\rho_G} - \frac{1}{\rho_L}\right) Pr_L^2, \tag{3.20}$$

and Marsh and Mudawar (1989),

$$T_w - T_{sat} = \left[\frac{8\sigma T_{sat}\left(\frac{1}{\rho_G} - \frac{1}{\rho_L}\right)\dot{q}_w}{\Delta h_v \lambda_L}\right]^{1/2} \Psi_m^{1/2}. \tag{3.21}$$

The Hsu (1962) relationship for the wall superheat above which nucleation occurs is given by,

$$\frac{\delta_{ts}\left(\theta_w - \theta_{sat}\right)^2}{\theta_w} = \frac{8\sigma T_{sat} C_3}{\rho_G \Delta h_v}, \tag{3.22}$$

where $C_3 = 1.6$ and δ_{ts} is the thermal boundary layer thickness. Equation 3.22 can only be applied if the thickness of the thermal sublayer is known. A classical value assigned to the thickness of the laminar sublayer is (Schlichting, 1987),

$$\mathrm{y}^+ = \frac{\rho \mathrm{y} u^*}{\eta} = 5, \tag{3.23}$$

where $u^* = \sqrt{\frac{\tau_w}{\rho}}$. Although the application of the Reynolds analogy in the laminar sublayer is debatable, it still may give reasonable results for liquid Prandtl numbers fairly close to unity. As an example of an analysis similar to that carried out here, Collier *et al.* (1964) applied Eq. 3.23 quite successfully to predict the changeover points from nucleate boiling to evaporation of water at about atmospheric pressure. Therefore, it is postulated that the dimensionless thermal sublayer thickness, δ_{ts}, can be calculated using Eq. 3.23. Substituting Eq. 3.23 in Eq. 3.22 gives,

$$T_w - T_{sat} = \frac{12.8\sigma T_{sat}\sqrt{\tau_w \rho_L}}{5\eta_L \rho_G \Delta h_v}, \tag{3.24}$$

with $T_\infty = T_{sat}$.

A procedure for calculating the shear stress, τ_w, in Eq. 3.24 for the case of annular flow in annuli is the subject of the next section.

3.4.2 Interpretation of the present data set

In order to compare the experimental data of Fig. 3.39 with the Hsu (1962) relationship (Eq. 3.24), it is necessary to know the shear stress distribution on the liquid film flowing on the inner rod. Hewitt (1964) proposed an approximate method to calculate the flow parameters in an annulus having one smooth surface and one rough surface. Since the velocity profile is not known and the shear stress on both surfaces are different due to the difference in roughness, an interpretation of experimental results (e.g., those involving the interfacial shear stress and liquid film thickness) is difficult.

Figure 3.40 presents the geometry of the channel. r_o and r_a are the inner and outer radii of the annular cavity, respectively. The channel is divided in two regions bounded by the surface of zero wall shear stress (and maximum velocity) r_m. Equations are derived for the Reynolds numbers, equivalent diameters (four times the flow area divided by the wetted perimeter) and friction factors of each region are given by,

$$d_{eo} = \frac{2\left(r_m^2 - r_o^2\right)}{r_o}, \tag{3.25}$$

$$d_{ea} = \frac{2\left(r_a^2 - r_m^2\right)}{r_a}, \tag{3.26}$$

$$Re_o = \frac{\rho U_o d_{eo}}{\eta}, \tag{3.27}$$

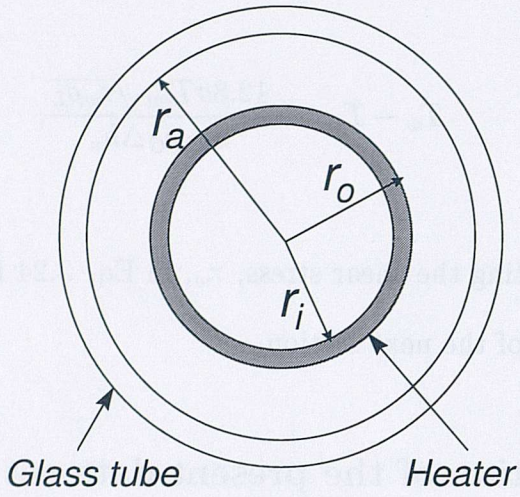


Figure 3.40: Geometry of the annular channel.

$$Re_a = \frac{\rho U_a d_{ea}}{\eta}, \tag{3.28}$$

$$f_o = \frac{\tau_{wo}}{\rho U_o^2}, \tag{3.29}$$

$$f_a = \frac{\tau_{wa}}{\rho U_a^2}. \tag{3.30}$$

In the above equations, U_o and U_a are the average velocities in the inner and outer regions, respectively. ρ and η are the density and viscosity of the flowing fluid and τ_{wo} and τ_{wa} are the shear stresses at the inner and outer walls. By applying a force balance and eliminating the shear stresses from Eqs. 3.29 and 3.30, it follows,

$$f_o = -\frac{dp}{dz}\frac{d_{eo}}{4}\frac{1}{\rho U_o^2}, \tag{3.31}$$

$$f_a = -\frac{dp}{dz}\frac{d_{ea}}{4}\frac{1}{\rho U_a^2}. \tag{3.32}$$

Additional relationships are (i) the overall mass balance,

$$U_o\left(r_m^2 - r_o^2\right) + U_a\left(r_a^2 - r_m^2\right) = \overline{U}\left(r_a^2 - r_o^2\right), \tag{3.33}$$

where $\overline{U}$ is the overall mean velocity; (ii) an empirical relationship for the friction factor for the smooth surface (Hewitt suggested the use of the Koo equation),

$$f_a = 0.00070 + 0.0625 Re_a^{-0.32}; \tag{3.34}$$

and (iii) a relationship between U_o and U_a,

$$\frac{U_o}{U_a} = \frac{\left[\frac{\sqrt{f_a}}{k}\left(\frac{r_m+3r_a}{2r_m+2r_a}\right)+1\right]}{\left[\frac{\sqrt{f_o}}{k}\left(\frac{r_m+3r_o}{2r_m+2r_o}\right)+1\right]}, \tag{3.35}$$

where $k = 0.368$. The equation above was derived based on an integration of the Universal Velocity Profile over both regions. Full details are given in Hewitt (1964).

The system of equations can be solved iteratively for the nine unknown parameters, viz., Re_o, Re_a, f_o, f_a, U_o, U_a, d_{eo}, d_{ea} and r_m. Once f_o and U_o are determined, the shear stress τ_{wo} is calculated using Eq. 3.29.

In the application of climbing film flow, the methodology serves to determine the interfacial shear stress on the film flowing over the inner rod. $\overline{U}$ is calculated using only the vapour flow rate. For the majority of experimental cases dealt with in the present work, the injected film flow rate was very close to that at which the onset of droplet entrainment takes place (see Sections 2.2.3 and 3.3.1). Therefore, entrained droplets are not likely to play a major part in the determination of the interfacial shear stress.

In upwards co-current annular flow, the film is very thin, generally turbulent for $Re_{LF} > 200$ (Collier and Thome, 1994) and the frictional pressure gradient is substantially higher than the gravitational component. Therefore, it can be assumed that the shear stress in the liquid film is approximately constant and equal to the interfacial shear. This would

result in the use of τ_{wo} in Eq. 3.24 to calculate the wall superheat for boiling incipience according to Hsu (1962).

3.4.3 Results

Figure 3.41 presents the experimental data for the ONB together with predictions from various methods. The correlations of Davis and Anderson (1966), Frost and Dzakowic (1967) and Marsh and Mudawar (1989) exhibit significant deviations from the experimental data. The curves in Fig 3.41 are for one specific experimental condition (Run 0619c), but can be seen as representative of the prediction of the correlations as no noteworthy differences arise between experimental conditions reported in Fig. 3.41.

The range of predicted wall superheat values given by the application of the Hsu (1962) methodology for annuli is depicted. In this case, the wall shear stress is calculated by applying the annulus transformation with the measured experimental pressure gradient and mass fluxes as input parameters.

The minimum and maximum wall superheats obtained from the Hsu (1962) analysis for the conditions presented in Fig. 3.41 are 10.4 and 11.8 K.

Also shown in Fig. 3.41 is the prediction obtained from the Marsh and Mudawar (1989) model using a modified multiplier, Ψ_m, which gives a better fit to the experimental data ($\Psi_m \approx 10$).

3.5 Summary

This chapter provided both qualitative and quantitative information on the heat transfer to a steam-water mixture flowing in an annulus test section heated internally.

Visualisation of the flow field was carried out using a high-speed video system, which enabled the observation of the interaction between disturbance waves and the activity of

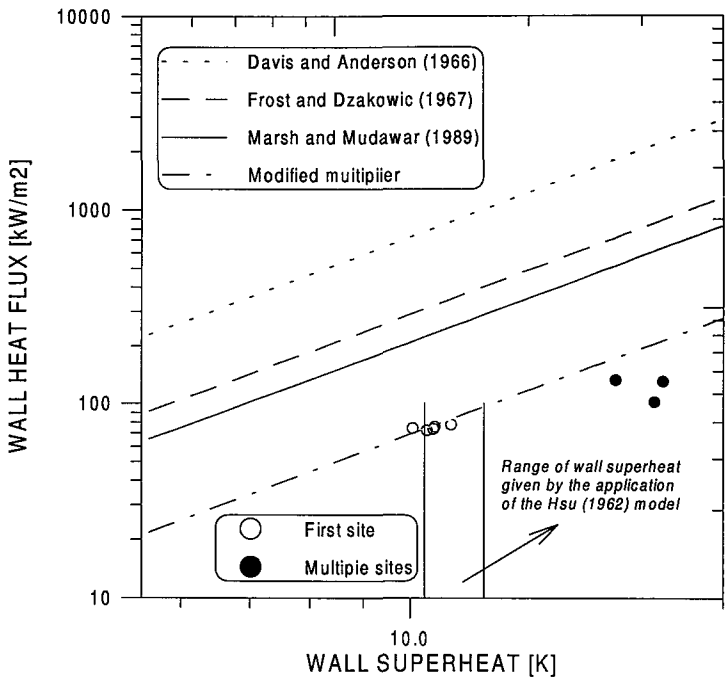
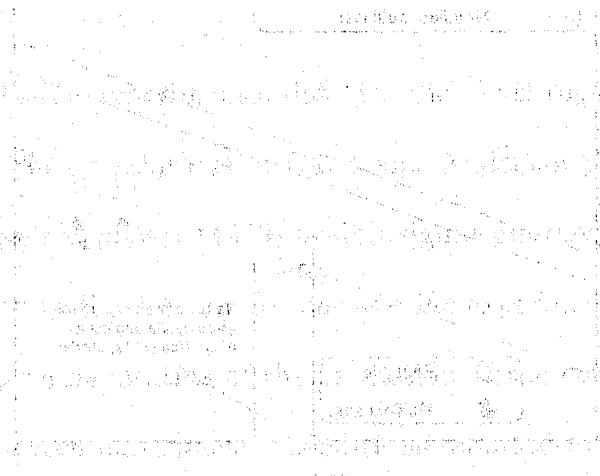


Figure 3.41: Predictions of the onset of nucleate boiling.

nucleation sites.

Estimates of the heat transfer coefficient were made possible through the use of a traversing radiation equilibrium thermocouple, which was used to measure the temperature of the heated section.

The main conclusions from this chapter are presented in Section 7.1.



Chapter 4

A Model for Flow Boiling of Multicomponent Mixtures

This chapter presents a model for forced convective boiling of multicomponent mixtures. In the first section, the motivation for the study is described and the problem is introduced. In Section 4.2, the hydrodynamics of multicomponent mixtures in annular flow is discussed and the mechanisms of droplet entrainment and deposition in such systems are described. Heat and mass transfer are dealt with in Section 4.3. For simplification, the binary systems case will be presented first and the description of the multicomponent case will be carried out as a natural extension of a scalar (binary case) to a vectorial analysis. Section 4.4 deals with the algorithm and numerical schemes associated with the solution of the system of governing equations derived in Sections 4.2 and 4.3. A brief theoretical appraisal of the problem of condensation of multicomponent mixtures is carried out in Section 4.5. Finally, results are presented in Section 4.6 and conclusions are drawn in Section 4.7.

4.1 Introduction

4.1.1 Motivation

Phase change heat transfer to mixtures is of indisputable technological relevance. Operations in which boiling of multicomponent organic mixtures take place are the rule rather than the exception in the process industry. For instance, by definition, feeds to distillation tower reboilers are mixtures of two or more substances. In some cases, as in a typical petroleum feed, up to 40 pure substances may form the mixture.

Despite the evident importance of the subject, there is a dearth of experimental data for hydrocarbon mixtures and of adequately detailed predictive models. Of the methods available in the open literature, the majority deal with the binary case. Moreover, of the number of studies devoted to the multicomponent case, most are related to condensation (Webb, 1982; Taylor and Krishna, 1993; Koyama and Lee, 1998). Experimental data obtained recently using a high pressure multicomponent boiling rig at the Harwell Laboratory of AEA Technology revealed many new features of forced convective multicomponent evaporation (Kandlbinder, 1997; Kandlbinder *et al.*, 1998). For instance, the increase in the heat transfer coefficient with quality characteristic of forced convective boiling often did not occur in these systems; indeed the coefficient sometimes actually decreases with increasing quality. These trends are not predicted either quantitatively or qualitatively by existing methods and it was this failure in prediction which led to the present study.

The heat transfer coefficient for mixture systems is defined by the following equation,

$$\alpha = \frac{\dot{q}_w}{T_w - T_E}, \tag{4.1}$$

where $\dot{q}_w$ is the heat flux applied to the channel wall, T_w is the temperature of the inner

wall and T_E is an equilibrium temperature calculated based on the system local pressure and enthalpy. For mixtures undergoing condensation T_E is the dew point temperature, whereas for boiling or evaporation T_E is the bubble point temperature.

A possible explanation for the decreasing heat transfer coefficient trends observed in forced convective boiling of mixtures may be due to the combined effect of droplet interchange and mass transfer resistance (mainly on the vapour side). This section introduces the physical arguments behind these hypotheses in a qualitative way. The hydrodynamic issues are dealt with firstly, then the mass transfer considerations are taken into account.

4.1.2 Hydrodynamic equilibrium considerations

As seen in Chapter 2, droplet entrainment and deposition are vigorous mass exchange phenomena which disrupt the hydrodynamic equilibrium of annular flow. Amongst many other effects, these phenomena are known to exert a large influence on important flow parameters like pressure drop. Nevertheless, the significance of droplet interchange on forced convective boiling of mixtures seems to have been overlooked in previous studies and the correct prediction of this mechanism may hold the key to understanding the deterioration associated with the heat transfer coefficient at high qualities.

Figure 4.1 depicts an interpretation of the physics of the problem. In design calculations, the two-phase flow pattern is usually ignored and it is implicitly assumed that the whole of the liquid flow is available for evaporation (Figure 4.1.b). Usually, a flash calculation is used to determine the amount of liquid which has evaporated for a given wall heat flux and the saturation (bubble point) temperature of the mixture. The preferential evaporation of the more volatile component gives rise to axial gradients of saturation temperature and of mean concentration in both phases.

If the system pressure is assumed to remain constant (i.e., pressure changes along the

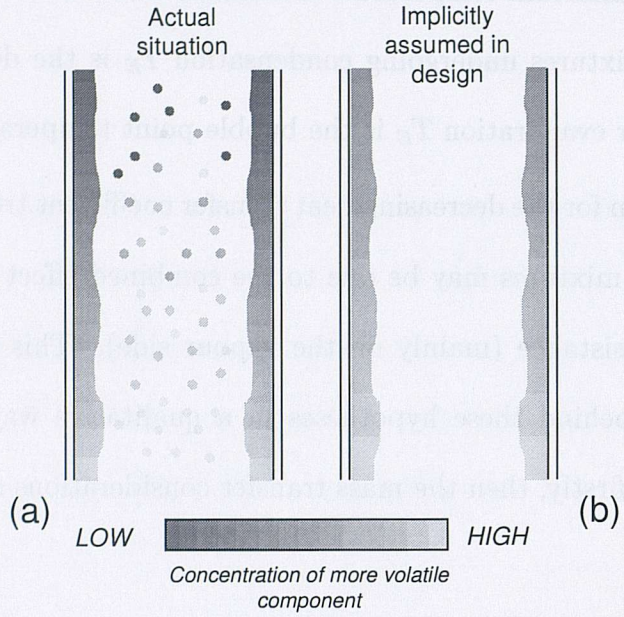


Figure 4.1: Evaporation of mixtures in annular flow. (a) Real situation, (b) Implicitly assumed in design (no droplets).

channel are small compared to the total pressure), a single vapour-liquid equilibrium diagram is then sufficient to express the temperature and concentration variations as a function of quality (the molar or mass fraction of the flow which is vapour). In the equilibrium diagram shown in Fig. 4.2, the mixture molar quality is given by the ratio between the lengths TU and TV,

$$\tilde{X} = \frac{\tilde{x}_{ov} - \tilde{x}}{\tilde{y} - \tilde{x}}. \tag{4.2}$$

where $\tilde{x}_{ov}$ is the overall mole fraction and $\tilde{x}$ and $\tilde{y}$ are the equilibrium liquid and vapour mole fraction at a given temperature. In terms of mass fractions, the mass quality can be expressed as,

$$X = \frac{x_{ov} - x}{y - x}. \tag{4.3}$$

From Fig. 4.2, one can also identify a relationship between quality and mixture saturation

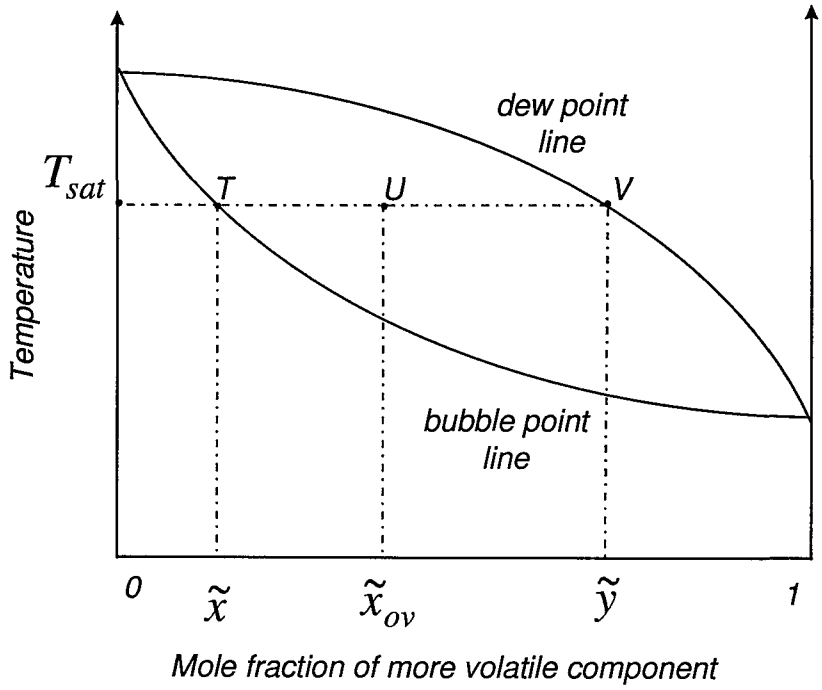


Figure 4.2: Phase diagram for a binary non-azeotropic mixture.

temperature which exists at this equilibrium situation. The bounds of such a relationship are as follows (the equations below are true for both molar and mass quantities),

$$T\left(X=0\right)=T_{bub}\left(x_{ov}\right), \tag{4.4}$$

$$T\left(X=1\right)=T_{dew}\left(x_{ov}\right). \tag{4.5}$$

The temperature may vary with enthalpy in a manner similar to that shown in Fig. 4.3. In a real situation, however, where the annular flow pattern is the dominant configuration, not all of the liquid is present as a film coating the inner wall of the pipe. Rather, droplets are generated from the crests of disturbance waves which travel along the liquid film and these droplets become entrained in the vapour core. The droplets travel at approximately the same velocity as the vapour. All along the channel, droplets are being exchanged

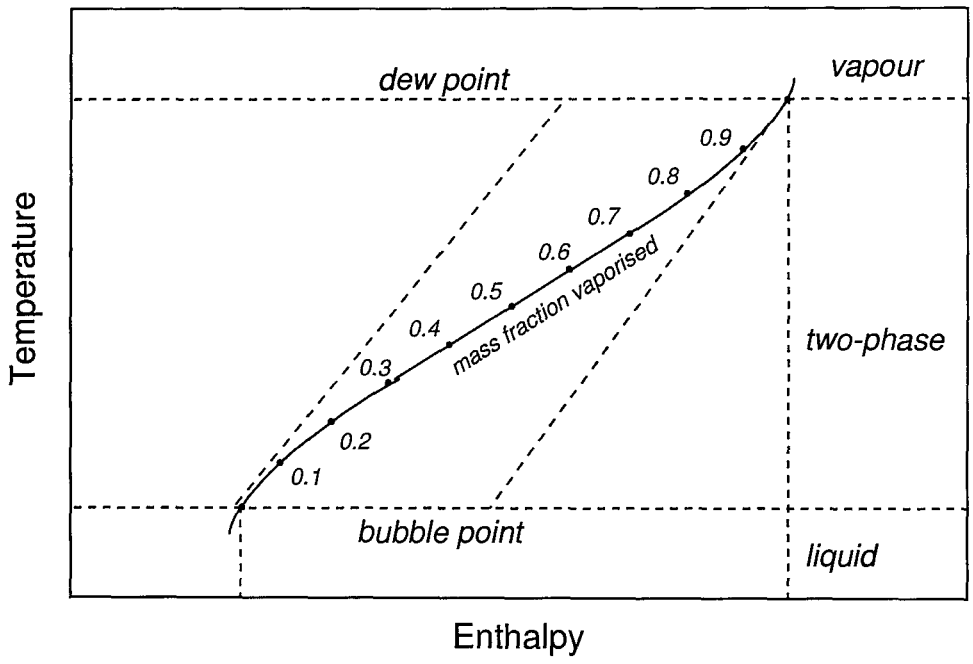


Figure 4.3: Saturation temperature against enthalpy for binary mixtures.

between the film and the core by entrainment and deposition. However, this exchange is not rapid enough (as we shall see) to maintain equality of composition between the droplets and the film. Bearing in mind that droplet evaporation may be negligible when compared to that of the liquid film (the temperature driving force in the liquid film is much higher), one can argue that in the actual situation not all of the liquid phase will be available for evaporation at a given distance along the pipe. This hydrodynamic effect breaks down the equilibrium relationship existing between quality and mixture saturation temperature (Eqs. 4.4 and 4.5) in the following manner.

For the sake of clarity, consider the simplified situation in which a certain amount of liquid is entrained as droplets at the onset of annular flow and in which no further entrainment or deposition occurs downstream of this point. Therefore, the initial film flow rate (amount of liquid initially available for evaporation) is equal to that where all the liquid in the film less the initial entrained droplet flow rate.

Even for this ideal situation where the entrained liquid flow is disregarded in the thermodynamic calculation, vapour-liquid equilibrium still demands that the same amount of liquid must be lost by evaporation for a given wall heat flux and, at the point of film depletion (dryout), the film (saturation) temperature must be equal to the dew point temperature at the overall composition. Since the film flow rate is less than the total liquid flow rate, then dryout will occur at a shorter distance along the channel than it would if all the liquid were in the film, and at a quality less than unity. The situation is analogous to carrying out the calculation using a pseudo-quality defined as the ratio between the vapour mass flux and the film mass flux plus the vapour mass flux ($X' = \frac{\dot{m}_{GC}}{\dot{m}_{GC}+\dot{m}_{LF}}$). Figure 4.4.a illustrates the film temperature profiles against quality which would be obtained for different initial liquid entrained fractions.

This simplified idea concerning the development of differences between drop and film concentration in mixture systems was first pursued by Kandlbinder *et al.* (1998) and plots of wall temperature and of heat transfer coefficient calculated using this approach are shown in Fig. 4.4.b. The higher wall temperatures obtained for the higher initial entrained fractions give rise to lower heat transfer coefficients (Eq. 4.1) in a trend similar to that observed in the experimental data. Though Kandlbinder *et al.*'s investigation gave qualitatively encouraging results, there remained the challenge of representing the processes quantitatively. One of the objectives of the present study is thus to put forward a quantitative model capable of representing correctly the droplet entrainment and deposition processes.

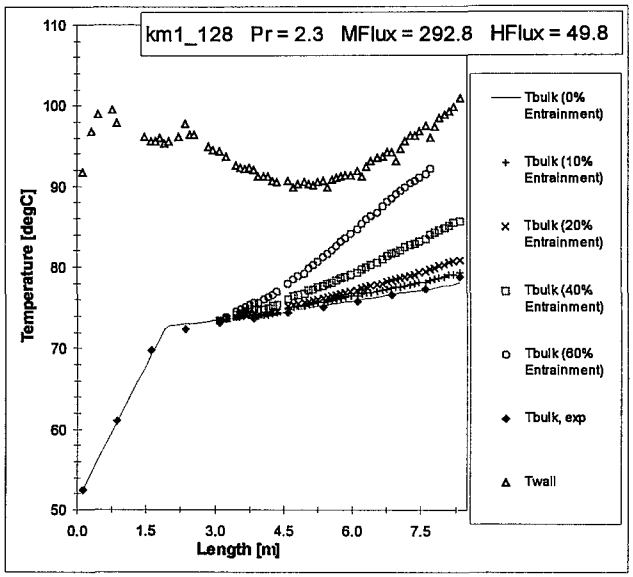
In the forced convective region (absence of nucleate boiling), the *liquid film* heat transfer coefficient is primarily a function of local turbulence and of physical properties. In general, however, the temperature change in the liquid film is dominated by that occurring in the region near the wall where the flow is laminar and turbulence is suppressed. Between this near-wall zone and the interface, the temperature changes little due to the mixing

caused by turbulence. This same mixing process in the film leads to a situation where the *component concentrations* in the liquid film are relatively constant and the interface concentration is close to the mean (fully mixed) concentration in the liquid film. This result was demonstrated quantitatively by Shock (1976), who showed that for any mixture, irrespective of the width of its boiling range, the effect of mass transfer in the *liquid film* is small enough to be ignored; that is, the interface concentration is close to that of the fully mixed film. Shock's calculations on the effect of mass transfer in the liquid film heat transfer are summarised in Appendix B.

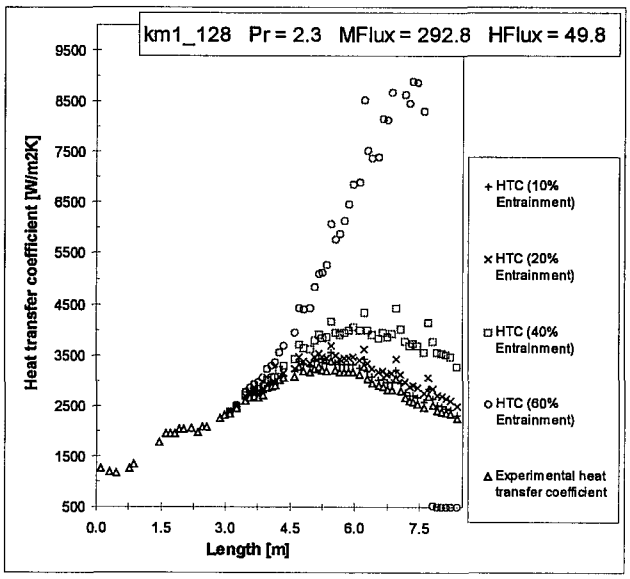
Shock (1976) also investigated the influence of mass transfer in the vapour core. He found that the effects were more significant than those for the liquid film (though still small). The vapour created by evaporation at the interface has to be transported through a laminar-like layer in the vapour adjacent to the interface. This transport process is achieved by a flow normal to the interface coupled with diffusive mass transfer, the latter depending on the concentration gradient of the components. In the present work, these mass transfer processes have been considered in detail. It transpires that their effect is small compared to the drop/film concentration difference effect mentioned above, though they could become significant in some circumstances.

4.1.3 The influence of droplet interchange

In Figure 4.1.a, a situation where droplet entrainment and deposition takes place was illustrated. The bottom end of the picture represents the onset of annular flow. If droplet evaporation is ignored, then it is not illogical to assume that the droplets will retain a concentration equal to that of the liquid film at the point at which they were created (entrained). As an axial gradient of concentration is established in the liquid film due to the preferential evaporation of the more volatile component(s), droplets generated at



(A)



(B)

Figure 4.4: Calculations of (a) wall temperature and (b) heat transfer coefficient using the simplified droplet interchange formulation (Kandlbinder *et al.*, 1998). Conditions of calculations: mixture n-pentane/iso-octane (0.7/0.3 mole fraction), $p = 3.2$ bar, $\dot{q}_w = 49.3$ kW m^{-2}, $\dot{m}_T = 305.0$ kg m^{-2} s^{-1}.

distinct (axial) positions will have distinct concentrations. Thus, at a particular position, a spectrum of concentration is found in the population of depositing droplets, these droplets having arisen from a variety of positions upstream. When calculating the rate of droplet deposition at a certain distance, one must take into account two important facts, (i) the difference in concentration between groups of droplets, and (ii) the liquid film at that distance is richer in the less volatile component than any depositing droplet. This would tend to smooth the difference between distributions of film concentration (and of liquid film temperature — see Fig. 4.4.a) obtained using the simplified approach for each initial entrained fraction. In fact, one can see the simplified approach carried out by Kandlbinder *et al.* as an extreme case, where no droplet deposition takes place, of the real situation where continuous entrainment and deposition takes place.

A detailed description of the model for hydrodynamics and droplet entrainment and deposition in annular flow of mixtures is carried out in Section 4.2.

4.1.4 Mass transfer considerations

Gradients of concentration building up adjacent to both sides of the interface would manifest a resistance to mass transfer and give consequential changes to the interface temperature and hence to the apparent heat transfer coefficient. As seen in Appendix B, the theoretical work by Shock (1976) revealed that these effects are negligible on the liquid film side. However, they may be of some significance in the vapour phase. Shock analysed the evaporation of a water-ethanol mixture, with a boiling range of the order of 20 K. He could not evaluate precisely the significance of mixture effects as the differences in wall temperature due to such effects may be small compared with the differences due to errors in his calculations of the temperature drop across the film. The systems studied here have boiling ranges at atmospheric pressure nearly 2.5 times greater than those analysed by

Shock and mass transfer effects are likely to be more significant.

One can learn about the problem of evaporation in annular flow by looking at its analogous counterpart, condensation. It is well known (Price and Bell, 1974) that heat transfer in condensation is significantly affected by the presence of inert gases and that the decrease in the heat transfer coefficient associated with mixture effects is well predicted by relatively simple (one-dimensional) methods for a variety of condenser geometries. In the so-called *film methods*, the degree of mixing in the liquid phase (condensate) is modelled in accordance with the geometry of the condenser. The level of mixing is an important factor in the calculation of the interfacial mass fluxes (condensation rates), which are based on vapour-liquid equilibrium calculations at the interface. For example, in the case of a horizontal shell-and-tube condenser where condensation takes place on the shell side, the condensate flows along the bottom of the shell and may not be intimately contacted with the vapour stream. Therefore, it can be hypothesised that as condensation occurs the condensate is added to the liquid stream without the stream reaching equilibrium with the vapour. On the other hand, one may envisage a situation where complete equilibrium is maintained between the condensate and vapour at all points along the condenser. This is equivalent to saying that the condensate is *fully-mixed* with respect to concentration and no concentration gradients take place in the direction transverse to the flow. A practical situation where this ideal concept is virtually fulfilled is that of condensation of multicomponent vapours in a vertical co-current tube-side condenser. Of course, the real situation concerning the nature of mass transfer on the liquid side lies somewhere between these two extremes. However, the adoption of a suitable hypotheses (total mixing or non-mixing) has proven to be very efficient in design calculations, especially when the calculation of liquid phase mass transfer coefficients is difficult or when adequate correlations are not available. The effects of droplet interchange on condensation will be discussed with more detail in Section 4.5.

In the present boiling/evaporation study, an approach similar to that for mass transfer in condensation is pursued. An assumption concerning the degree of mixing in the liquid film is made based on the distribution of the phases in the channel. It is believed that the liquid film is turbulent and thin enough so that radial gradients of concentration can be neglected and the liquid in the film can be regarded as *fully-mixed.* Moreover, even if one takes a more realistic view of the flow in the film (Jayanti and Hewitt, 1997), the one which depicts the film as packets of turbulence (disturbance waves) flowing over and separated by laminar substrates, the action of the disturbance waves would still be that of smoothing the gradients of concentration. The calculation methodology carried out here and presented in Section 4.3 is based on the widely applied method by Colburn and Drew (1937). More recent applications and extensions of the methodology were put forward by Price and Bell (1974) and by Webb (1982).

4.1.5 Nucleate boiling considerations

Section 2.4 dealt briefly with the occurrence and prediction of bubble nucleation in multicomponent systems and it was observed that there is no complete phenomenological model capable of fully explaining the hydrodynamic, heat transfer and coupled mass transfer phenomena associated with bubble generation at a solid wall under the influence of a velocity gradient. In order to determine the heat transfer coefficient in the liquid film, an empirical correction factor for mixture effects (Palen and Small, 1964) was applied to the nucleate boiling component of a superposition correlation devised for single component fluids (Chen, 1963). It is believed that such an approach would not lead to considerable errors since the nucleate boiling contribution is not likely to be large (less than 30%) as forced convection is largely dominant. Section 4.3.3 introduces the model for heat transfer in the liquid film.

4.2 Hydrodynamics

This section presents the model for hydrodynamics of annular flow of multicomponent mixtures. Firstly, the methodology used for computing the rates of droplet entrainment and deposition is shown. Subsequently, the mass and momentum conservation equations are derived and the model closure relationships are presented.

4.2.1 Droplet interchange

The physical model of the problem is schematically illustrated in Fig. 4.5. The portion of the vertical pipe (internal diameter d_T) over which annular flow occurs is divided into M sections, 0 being the section at which the onset of annular flow takes place. The mass flow rates per unit cross-sectional area, $\dot{m}$, of the three fields, viz., liquid film, LF, vapour core, GC, and entrained liquid, LE, are shown. The initial bulk concentrations (in terms of mass fractions) of the i^{th} component in the liquid film, entrained droplets and vapour core are $x^0_{LF,i}$, $x^0_{LE,i}$ and $y^0_{GC,i}$, respectively. An initial value is assumed for the fraction of liquid entrained as droplets at the point of initiation of the annular regime ($m = 0$) and the concentration of the respective components in this initially entrained liquid is assumed equal (at this point) to that of the liquid film — though differences develop later. The transition to annular flow is taken to be determined by the critical velocity criterion for flow reversal by Wallis (1969),

$$U^*_{GS} = 1.0, \tag{4.6}$$

where,

$$U^*_{GS} = U_{GS}\sqrt{\frac{\rho_G}{g d_T(\rho_L - \rho_G)}}. \tag{4.7}$$

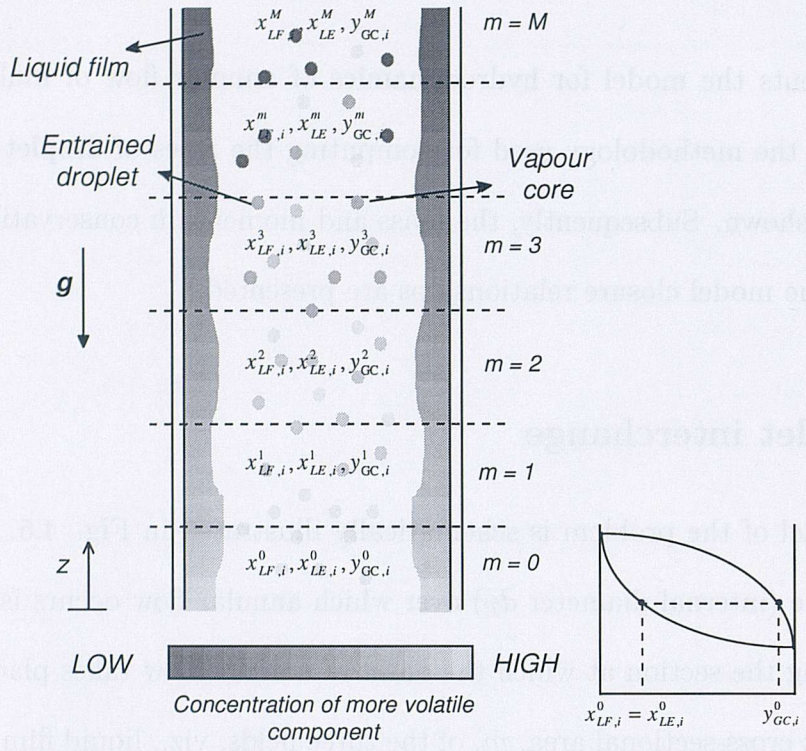


Figure 4.5: An illustration of the model.

The number of droplets depositing per unit time per unit area of tube wall at section m is defined as,

$$\langle n_D^m \rangle = \sum_{j=0}^{m} n_D^{j,m}, \tag{4.8}$$

where, $n_D^{j,m}$ is the number per unit time per unit area of tube wall of droplets entrained at section j (lower than m) that deposit at section m. Analogously, n_E^m is defined as the number per unit time per unit area of tube wall of droplets created (entrained) at section m. If the entrainment and deposition rates at any point in the channel are known, $n_D^{j,m}$ and n_E^m are given by Bennett *et al.* (1967a) ,

$$n_E^m = \frac{E^m}{M_{pc}^m}, \tag{4.9}$$

and

$$n_D^{j,m} = \frac{D^{j,m}}{M_p^{j,m}}, \tag{4.10}$$

where M_{pc}^m and $M_p^{j,m}$ are the mass of a droplet at creation at a section m and the mass, at section m, of a droplet generated at section j, respectively. If droplet evaporation and break-up/coalescence effects are not considered, then $M_p^{j,m} = M_{pc}^m$. Assuming that the droplets have a spherical shape, M_{pc}^m is given by,

$$M_{pc}^m = \frac{\pi \rho_{LF}^m (d_{pc}^m)^3}{6}, \tag{4.11}$$

where d_{pc}^m is the diameter of a droplet when created at section m. In the present study, d_{pc} is calculated through a correlation by Azzopardi *et al.* (1980) for the Sauter mean diameter of droplets in vertical annular flow. This is as follows,

$$\frac{d_{pc}}{d_T} = 1.91 \frac{Re_G^{0.1}}{We^{0.6}} + 0.4 \frac{\dot{m}_{LE}}{\rho_L U_{GS}}, \tag{4.12}$$

where the Weber number and the gas phase Reynolds numbers are given by,

$$We = \frac{\rho_G U_{GS}^2 d_T}{\sigma}, \tag{4.13}$$

and,

$$Re_G = \frac{\rho_G U_{GS} d_T}{\eta_G}. \tag{4.14}$$

The second term in the RHS of Eq. 4.12 accounts for coalescence and was not used in the present analysis since such coalescence is likely to be small. The entrainment and deposition rates, E^m and $D^{j,m}$, are a modification to the set of correlations developed by Govan *et al.* (1988). For the multicomponent case, the equations can be extended as follows,

$$E^m = \begin{cases} 0 & \text{if } \dot{m}^m_{LF} \leq \dot{m}^m_{LFC} \\ 5.75 \times 10^{-5} \dot{m}^m_{GC} \left[\frac{\rho^m_{LF} d_T}{\sigma^m_{LF} \rho^2_G} (\dot{m}^m_{LF} - \dot{m}^m_{LFC})^2 \right]^{0.316} & \text{if } \dot{m}^m_{LF} > \dot{m}^m_{LFC}, \end{cases} \tag{4.15}$$

where $\dot{m}^m_{LFC}$ is a critical liquid film mass flux given by,

$$\dot{m}^m_{LFC} = \frac{\eta^m_{LF}}{d_T} \exp \left[5.8504 + 0.4249 \left(\frac{\eta^m_G}{\eta^m_{LF}} \right) \left(\frac{\rho^m_{LF}}{\rho_G} \right)^{0.5} \right]. \tag{4.16}$$

The droplet deposition rate is expressed as,

$$D^{j,m} = k^{j,m}_D C^{j,m}, \tag{4.17}$$

where $C^{j,m}$ is the concentration, at section m, of droplets entrained at section j,

$$C^{j,m} = \frac{\dot{m}^{j,m}_{LE}}{\frac{\dot{m}^m_G}{\rho^m_G} + \langle \frac{\dot{m}^m_{LE}}{\rho^m_{LE}} \rangle}, \tag{4.18}$$

and the deposition transfer coefficient, $k^{j,m}_D$, is given by,

$$k^{j,m}_D = \begin{cases} 0.18 \left(\frac{\sigma^{j,m}_{LE}}{\rho^m_G d_T} \right)^{0.5} & \text{if } \frac{\langle C^m \rangle}{\rho^m_G} \leq 0.3 \\ 0.083 \left(\frac{\rho^m_G}{\langle C^m \rangle} \right)^{0.65} \left(\frac{\sigma^{j,m}_{LE}}{\rho^m_G d_T} \right)^{0.5} & \text{if } \frac{\langle C^m \rangle}{\rho^m_G} > 0.3. \end{cases} \tag{4.19}$$

$\langle C^m \rangle$ is the cumulative droplet concentration defined as,

$$\langle C^m \rangle = \frac{\langle \dot{m}^m_{LE} \rangle}{\frac{\dot{m}^m_G}{\rho^m_G} + \langle \frac{\dot{m}^m_{LE}}{\rho^m_{LE}} \rangle}, \tag{4.20}$$

with the cumulative operator $\langle \rangle$ defined in Eq. 4.8.

The number flowing per unit time per unit pipe cross-sectional area, at section m, of droplets generated at section j, $NOD^{j,m}$, can be calculated through a balance of the number of droplets in the vapour core over a length Δz. This gives,

$$\frac{\Delta NOD^{j,m}}{\Delta z} = \frac{4}{d_T} \left(n^j_E - \sum_{k=j}^{m} n^{j,m}_D \right). \tag{4.21}$$

Writing $NOD^{j,m}$ in terms of $\dot{m}_{LE}^{j,m}$,

$$NOD^{j,m} = \frac{\dot{m}_{LE}^{j,m}}{M_p^{j,m}}. \tag{4.22}$$

After some algebraic manipulation, a combination of Eqs. 4.8 to 4.21 leads to the following system of equations,

$$\mathsf{F}^{j,m} \equiv \Omega^{j,m}\left(n_E^j - \sum_{k=j}^{m} n_E^{j,k}\right) - n_D^{j,m}\left[\frac{\dot{m}_{GC}^m}{\rho_G^m} + \sum_{j=0}^{m}\Psi^{j,m}\left(n_E^j - \sum_{k=j}^{m} n_D^{j,k}\right)\right] = 0, \tag{4.23}$$

where,

$$\Omega^{j,m} = \frac{4\Delta z}{d_T} k_D^{j,m}, \tag{4.24}$$

and,

$$\Psi^{j,m} = \frac{4\Delta z}{d_T}\frac{M_p^{j,m}}{\rho_{LE}^{j,m}}. \tag{4.25}$$

The above $(m+1)\times(m+1)$ system of equations may be solved for $n_D^{j,m}$ via a multi-dimensional method, e.g., a multi-dimensional Newton-Raphson algorithm (Press *et al.*, 1992). The elements of the associated Jacobian matrix, $\frac{\partial \mathsf{F}^{j,m}}{\partial n_D^{j,m}}$ are given by,

$$\frac{\partial \mathsf{F}^{j,m}}{\partial n_D^{j,m}} = \begin{cases} -\Omega^{j,m} - \left[\frac{\dot{m}_{GC}^m}{\rho_G^m} + \sum_{j=0}^{m}\Psi^{j,m}\left(n_E^j - \sum_{k=j}^{m} n_D^{j,k}\right)\right] + \Psi^{j,m} n_D^{j,m} & \text{if } j = k \\ \Psi^{k,m} n_D^{j,m} & \text{if } j \neq k. \end{cases} \tag{4.26}$$

Due to the non-linearity involving $\langle C^m \rangle$ and $k_D^{j,m}$ in the second portion of Eq. 4.19, the Newton-Raphson algorithm was implemented as a part of an outer iterative scheme. The initial condition for $n_D^{j,m}$ was set equal to $0.001 n_E^j$.

The set of equations presented in this section enables one to determine the cumulative, $\langle D \rangle$, and individual, $D^{j,m}$, rates of droplet deposition in vertical annular flow of binary

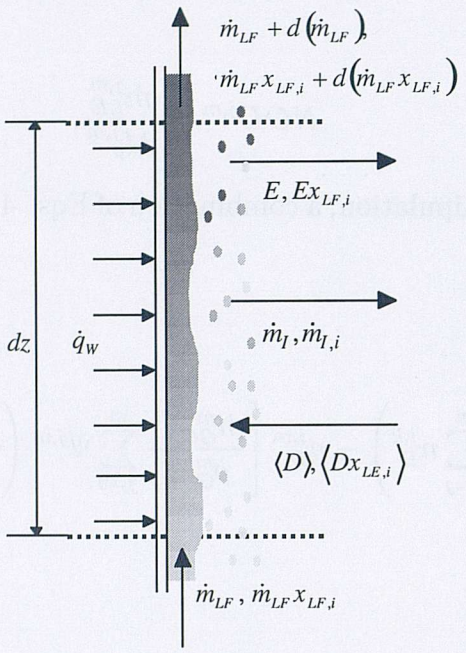


Figure 4.6: Mass conservation over an incremental pipe length.

and multicomponent mixtures. When these are coupled with mass and energy conservation equations, it is possible to calculate the distributions of mean concentration and temperature in the liquid film and in the droplet core.

4.2.2 Mass and momentum conservation

Once the method for calculating the individual and cumulative rates of droplet entrainment and deposition is established, it is possible to derive equations of conservation for the flow. A balance of mass and momentum over the incremental length of pipe shown in Fig. 4.6 is carried out below.

In an one-dimensional analysis, it is common to express momentum balances in terms of a sum of pressure gradient contributions (Collier and Thome, 1994). The total pressure gradient over an element dz is given by a contribution of frictional, f, accelerational, a, and gravitational, g, effects,

$$\frac{dp}{dz} = \frac{dp}{dz_a} + \frac{dp}{dz_f} + \frac{dp}{dz_g}. \tag{4.27}$$

In the gas core, a force balance over an element dz gives the following expressions for the components of the pressure gradient (Hawkes, 1996),

$$\frac{dp}{dz_a} = -\left(U_C - U_{LF}\right)\left[\frac{d\dot{m}_{GC}}{dz} + \frac{4}{d_T}\left(E + D\right)\right] - \frac{dU_C}{dz}\left[\dot{m}_{GC} + \dot{m}_{LE}\right], \tag{4.28}$$

$$\frac{dp}{dz_f} = -4\frac{\tau_I}{(d_T - 2\delta)}, \tag{4.29}$$

$$\frac{dp}{dz_g} = -\rho_C g, \tag{4.30}$$

where,

$$\frac{dU_C}{dz} = \frac{\frac{d\dot{m}_{LE}}{dz}\frac{1}{\rho_{LE}} + \frac{d\dot{m}_{GC}}{dz}\frac{1}{\rho_{GC}}}{\left(1 - \frac{2\delta}{d_T}\right)^2}. \tag{4.31}$$

The accelerational pressure drop is comprised by three terms, (i) the acceleration of droplets and vaporised gas from the liquid film velocity to the mean gas core velocity; (ii) the deceleration of droplets deposited on the annular film and (iii) the acceleration of mass in the gas core due to velocity changes.

The homogeneous core density and mean core velocity, ρ_C and U_C are given by,

$$\rho_C = \frac{\dot{m}_{LE} + \dot{m}_{GC}}{\frac{\dot{m}_{LE}}{\rho_{LE}} + \frac{\dot{m}_{GC}}{\rho_{GC}}}, \tag{4.32}$$

and,

$$U_C = \frac{\frac{\dot{m}_{LE}}{\rho_{LE}} + \frac{\dot{m}_{GC}}{\rho_{GC}}}{\left(1 - \frac{2\delta}{d_T}\right)^2}. \tag{4.33}$$

The following differential equations are obtained through mass balances over an element of tube of length dz (Fig. 4.6). Equations 4.34 to 4.36 represent overall mass conservation for the liquid film, vapour core and liquid entrained as droplets. Equation 4.37 is a component mass balance for the liquid film. The effect of deposition of droplets having different concentrations is characterised by the expression in parenthesis in the RHS of Eq. 4.37.

$$\frac{d}{dz}\dot{m}_{LF} = \frac{4}{d_T}\left(\langle D\rangle - E - \dot{m}_I\right), \tag{4.34}$$

$$\frac{d}{dz}\dot{m}_{GC} = \frac{4}{d_T}\dot{m}_I, \tag{4.35}$$

$$\frac{d}{dz}\dot{m}_{LE} = \frac{4}{d_T}\left(E - \langle D\rangle\right), \tag{4.36}$$

$$\frac{d}{dz}x_{LF,i} = \frac{4}{d_T\dot{m}_{LF}}\left[\left(\langle Dx_{LF,i}\rangle - \langle D\rangle x_{LF,i}\right) + \dot{m}_I x_{LF,i} - \dot{m}_{I,i}\right]. \tag{4.37}$$

$\dot{m}_{I,i}$ is the mass flux of component i in the evaporating stream. The calculation of $\dot{m}_{I,i}$ (and hence of $\dot{m}_I = \sum_{i=1}^{NOC}\dot{m}_{I,i}$) is carried out using a model for simultaneous heat and mass transfer, whose detailed description is within the scope of Section 4.3. The heat and mass transfer model is based on a film (or Colburn) method in which the effect of droplet interchange is taken into account in the interfacial heat balance.

The set of equations derived above enables one to calculate the mass fraction of droplets which, having been created at a section j, are still entrained in the core at a section m downstream,

$$e^{j,m} = \frac{\dot{m}_{LE}^{j,m}}{\langle\dot{m}_{LE}^{m}\rangle}, \tag{4.38}$$

and the mean concentration of the droplets in the core (at a given section or distance),

$$x_{LE,i} = \frac{\langle \dot{m}^m_{LE} x^m_{LE,i} \rangle}{\langle \dot{m}^m_{LE} \rangle}. \tag{4.39}$$

These quantities are of crucial importance to the analysis as they indicate the unbalance of concentration between the droplet core and the liquid film ($x_{LE,i}$) and between groups of droplets ($e^{j,m}$). Again, such imbalances develop due to the preferential evaporation of the more volatile component(s) from the liquid film interface.

4.2.3 Additional closure relationships for hydrodynamics

The calculation framework described in the above sections was embodied into an annular flow modelling programme — GRAMP code — (Hawkes, 1996) in which the triangular relationship between film thickness, film flow rate and interfacial shear stress is invoked together with the relationships for entrainment and deposition rates. In its simplest form, the triangular relationship can be expressed as,

$$\dot{m}_{LF} = \frac{4}{d_T} \delta \sqrt{\frac{2\tau_I \rho_{LF}}{f_{LF}}}, \tag{4.40}$$

where f_{LF} is the liquid film friction factor. f_{LF} is derived from results for the integration of the turbulent velocity profile in the liquid film (Hewitt, 1961) expressed in non-dimensional form as friction factor as a function of film Reynolds number (Hewitt and Hall-Taylor, 1970) , this function being fitted numerically. The interfacial shear stress is given by,

$$\tau_I = \frac{1}{2} \rho_C f_I (U_C - U_I)^2. \tag{4.41}$$

The interfacial friction factor, f_I is calculated through a correlation suggested by Hewitt and Whalley (1978) ,

$$f_I = f_{SC} \left[1 + 24 \left(\frac{\rho_{LF}}{\rho_G} \right)^{1/3} \frac{\delta}{d_T} \right], \tag{4.42}$$

where f_{SC} is the friction factor for a single phase vapour flow in a tube with the same diameter, the flow having a density ρ_C, velocity U_C and viscosity equal to that of the gas phase.

In an evaporating system in which single phase liquid is fed to the channel, annular flow will not occur until the vapour velocity is sufficient to satisfy Eq. 4.6. For sub-annular flow regimes occurring in the first part of the channel, the Friedel (1979) correlation is used to compute the wall shear stress. According to the Friedel correlation, the frictional pressure gradient for vertical upward flow is given by,

$$\frac{dp}{dz}_f = \phi_{LO}^2 \frac{2 f_{LO} \rho_L}{d_T} \left(\frac{\rho_L U_{LS} + \rho_G U_{GS}}{\rho_L} \right)^2, \tag{4.43}$$

where,

$$\phi_{LO}^2 = H_1 + \frac{3.24 H_2 H_3}{Fr^{0.045} We^{0.035}}, \tag{4.44}$$

$$H_1 = (1-X)^2 + X^2 \frac{\rho_L f_{GO}}{\rho_G f_{LO}}, \tag{4.45}$$

$$H_2 = X^{0.78} (1-X)^{0.24}, \tag{4.46}$$

$$H_3 = \left(\frac{\rho_L}{\rho_G} \right)^{0.91} \left(\frac{\eta_G}{\eta_L} \right)^{0.19} \left(1 - \frac{\eta_G}{\eta_L} \right)^{0.7}, \tag{4.47}$$

$$Fr = \frac{\dot{m}_T^2}{g d_T \rho_{tp}^2}, \tag{4.48}$$

$$We = \frac{\dot{m}_T^2 d_T}{\rho_{tp} \sigma}, \tag{4.49}$$

$$\rho_{tp} = \left(\frac{X}{\rho_G} + \frac{1-X}{\rho_L} \right)^{-1} . \tag{4.50}$$

f_{GO} and f_{LO} are the friction factor for the total mass flux flowing with gas and liquid properties, respectively.

4.3 Heat and mass transfer

4.3.1 Binary systems

As mentioned in Section 4.1, an interfacial heat and mass transfer methodology analogous to that for condensation problems is pursued here. A detailed description of the procedure applied to condensation is given by Webb and McNaught (1980), Taylor and Krishna (1993) and Webb (1995).

The model for interfacial heat and mass transfer is schematically illustrated in Fig. 4.7. It is postulated that the annular flow regime prevails and liquid is present in the core in the form of small entrained droplets. Droplet interchange between the core and the liquid film occurs as described in Section 4.2.1. The gas phase is a saturated or subcooled mixture which may contain non-condensing gases as well as vapours. All the resistances to heat and mass transfer in the gas side are assumed to lie in thin layers of thicknesses s_h and s_m adjacent to the interface. This approach is often referred to as the *equivalent laminar boundary layer* model (Hewitt *et al.*, 1994). The flow in such layers is assumed to be steady, laminar, and one-dimensional. In this theory, the velocity, temperature and concentration profiles are assumed to be linear across the layer. Transport properties are considered constant. Chemical reactions, viscous dissipation, and radiant-emission or absorption in the fluid are neglected.

Energy is transferred to the vapour flowing in the core in the form of latent and sensible

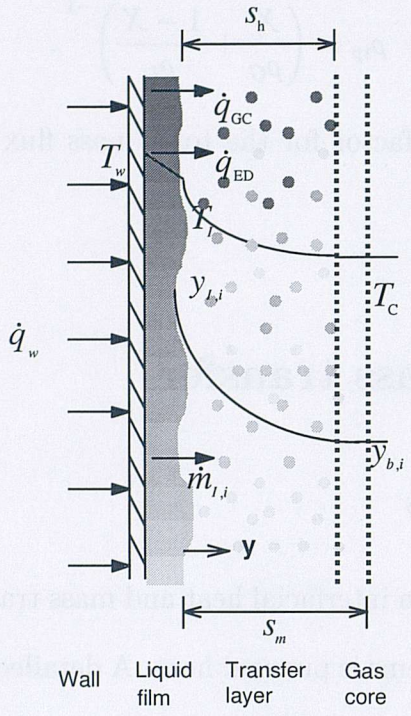


Figure 4.7: Schematic of the model for interphase transfer.

heat,

$$\dot{q}_{GC} = \dot{q}_{GC,L} + \dot{q}_{GC,S}. \tag{4.51}$$

Latent energy is released due to evaporation taking place at the interface. It is given by,

$$\dot{q}_{GC,L} = \sum_{i=1}^{2} \dot{m}_{I,i} \Delta h_{v,i}. \tag{4.52}$$

The release of sensible energy to the vapour is due to two distinct mechanisms, (i) convection of heat by the evaporating component as it travels from the interface to the bulk and, (ii) heating of the vapour in the core by conduction of heat through the laminar layer. At any given position within the laminar layer, these two processes are summed as follows,

$$\dot{q}_{GC,S} = \sum_{i=1}^{2} \dot{m}_{I,i} c_{pGC,i}(T - T_C) - \lambda \frac{dT}{dy}. \tag{4.53}$$

Integrating from y = 0 to y = s_h, with the boundary conditions shown in Fig. 4.7, gives,

$$\dot{q}_{GC,S} = \alpha^{\bullet}_{GC} e^{\phi_T}(T_I - T_C), \tag{4.54}$$

where,

$$\alpha^{\bullet}_{GC} = \frac{\alpha_{GC}\phi_T}{e^{\phi_T} - 1}, \tag{4.55}$$

$$\alpha_{GC} = \frac{\lambda_{GC}}{s_h}, \tag{4.56}$$

and,

$$\phi_T = \frac{1}{\alpha_{GC}} \sum_{i=1}^{2} \dot{m}_{I,i} c_{pGC,i}. \tag{4.57}$$

The total rate of energy released to the vapour in the core is thus,

$$\dot{q}_{GC} = \sum_{i=1}^{2} \dot{m}_{I,i} \Delta h_{v,i} + \alpha^{\bullet}_{GC} e^{\phi_T}(T_I - T_C). \tag{4.58}$$

With the above simplifying assumptions and using Fick's Law as the constitutive relationship for the diffusive mass fluxes, the equations of change for the vapour mass fluxes in the layer are (Bird *et al.*, 1960),

$$\frac{d}{dy}\left[y_i \sum_{i=1}^{2} \dot{m}_i - \rho_{GC} \Delta_{12} \frac{d}{dy} y_i \right] = 0. \tag{4.59}$$

Integration over the limits y = 0 and y = s_m with the appropriate boundary conditions gives,

$$\dot{m}_I = \rho_{GC}\beta^{\bullet}_{12}\left(\frac{y_{I1} - y_{b1}}{z - y_{I1}}\right), \tag{4.60}$$

where,

$$\dot{m}_I = \dot{m}_{I,1} + \dot{m}_{I,2}, \tag{4.61}$$

$$z = \frac{\dot{m}_{I,1}}{\dot{m}_I}, \tag{4.62}$$

$$\beta^{\bullet}_{12} = \beta_{12}\frac{\phi}{(e^{\phi} - 1)}, \tag{4.63}$$

and,

$$\phi = \frac{\dot{m}_I}{\rho_{GC}\beta_{12}}. \tag{4.64}$$

The zero-flux mass transfer coefficient, β_{12}, is given by a Dittus-Boelter type relationship,

$$\frac{\beta_{12}d_T}{\Delta_{12}} = 0.023Re^{0.8}_{GC}Sc^{0.4}_{GC}, \tag{4.65}$$

where,

$$Sc_{GC} = \frac{\rho_{GC}}{\eta_{GC}\Delta_{12}}. \tag{4.66}$$

Equation 4.60 is not a complete description of the evaporation process as only its diffusional part was specified. Another relationship is needed (determinacy condition) so that $\dot{m}_I$ is known. Two kinds of determinacy condition may be used; as in condensation, they are linked to degree of mixing in the liquid film (condensate). The first determinacy condition — *fully mixed liquid film* — is appropriate for vertical tubes where the liquid film flow is turbulent. It is assumed that no radial gradients of concentration exist in the

film. Thus, $x_{LF_{I,1}} = x_{LF_{b,1}} = \frac{\dot{m}_{I,1}}{\dot{m}_I}$. The second determinacy condition — *unmixed liquid film* — is typical of laminar liquid film flow in vertical tubes and of horizontal geometries. For this condition, $x_{LF_{I,1}} = \frac{\dot{m}_{I,1}}{\dot{m}_I}$. It is expected that real cases lie between these two extremes. For the present geometry and flow regime in the liquid film, the first determinacy condition — *fully mixed liquid* — seems more appropriate (the action of disturbance waves is towards a homogenisation of the concentration in the film). In this case, the interfacial liquid composition is known *a priori* (previous liquid film evaporation) and a bubble point calculation defines the interfacial state (vapour composition and interfacial temperature).

An energy balance over an element of the homogeneous core of length dz (see Fig. 4.6) gives,

$$\dot{m}_C c_{pC} \frac{d}{dz} T_C = \frac{4}{d_T} \left[\dot{\alpha}_{GC} \left(T_I - T_C \right) + \left(E - \langle D \rangle \right) c_{pLE} \left(T_I - T_C \right) \right], \tag{4.67}$$

where the first term in the RHS is the conductive contribution of the heat flux to the vapour phase. The second term in the RHS is the enthalpy released or absorbed by the core due to entrainment and deposition. $\dot{m}_C$, c_{pC} and T_C are the homogeneous core mass flux, specific heat capacity and temperature, respectively. These are given by,

$$\dot{m}_C = \dot{m}_{GC} + \langle \dot{m}_{LE} \rangle, \tag{4.68}$$

$$c_{pC} = \frac{\dot{m}_{GC} + \langle \dot{m}_{LE} \rangle}{\frac{\dot{m}_{GC}}{c_{pGC}} + \langle \frac{\dot{m}_{LE}}{c_{pLE}} \rangle}, \tag{4.69}$$

and,

$$T_C = \frac{\dot{m}_{GC} c_{pGC} + \langle \dot{m}_{LE} c_{pLE} \rangle}{\frac{\dot{m}_{GC} c_{pGC}}{T_{GC}} + \langle \frac{\dot{m}_{LE} c_{pLE}}{T_{LE}} \rangle}, \tag{4.70}$$

where the cumulative operator $\langle\rangle$ is defined by Eq. 4.8.

An additional closure hypothesis is as follows,

$$\dot{q}_{GC} = \dot{q}_w - \dot{q}_{ED}, \tag{4.71}$$

where,

$$\dot{q}_{ED} = (E - \langle D \rangle) c_{pLE} (T_I - T_C). \tag{4.72}$$

This assumption states that the wall heat flux is equal to the sum of the energy absorbed by the vapour and that absorbed by the entrained droplets due to entrainment and deposition.

Finally, a conservation equation for the bulk vapour concentration is as follows,

$$\frac{d}{dz} y_{b,i} = \frac{4}{d_T \dot{m}_{GC}} (\dot{m}_{I,i} - \dot{m}_I y_{b,i}). \tag{4.73}$$

4.3.2 Multicomponent systems

In multicomponent systems, the relationships for the interfacial mass fluxes, $\dot{m}_{I,i}$, can be written in the vectorial form. This is because the diffusion coefficient ceases to be a scalar and takes the form of a $(NOC-1)^{th}$ order tensor.

Fick's Law for the layer geometry (Fig. 4.7) is given by,

$$\dot{m}_{I,i} = y_{I,i} \sum_{j=1}^{NOC} \dot{m}_{I,j} - \rho_{GC} \sum_{k=1}^{NOC-1} \Delta_{i,k} \frac{dy_k}{dy}. \tag{4.74}$$

In terms of the elements of a finite-flux matrix of mass transfer coefficients, the evaporating mass flux vector is as follows (Taylor and Krishna, 1993),

$$\dot{m}_{I,i} = y_{I,i} \sum_{j=1}^{NOC} \dot{m}_{I,j} + \rho_{GC} \sum_{k=1}^{NOC-1} B^{\bullet}_{G_{i,k}} (y_{I,i} - y_{b,i}), \tag{4.75}$$

where,

$$[B_G^{\bullet}] = [B_G]\,[\Phi]\,\{\exp[\Phi] - [I]\}^{-1}, \tag{4.76}$$

and,

$$[\Phi] = \frac{1}{\rho_{GC}} \sum_{j=1}^{NOC} \dot{m}_{I,j} [B_G]^{-1}. \tag{4.77}$$

The zero-flux matrix of mass transfer coefficients is also given by a Dittus-Boelter type relationship. As suggested by Webb *et al.* (1993), no enhancement due to interfacial wave effects or entrainment was taken into account in such calculations.

$$[B_G]\, d_T [\Delta]^{-1} = 0.023 Re_{GC}^{0.8} [Sc_{GC}]^{0.4}, \tag{4.78}$$

where,

$$[Sc_{GC}] = \frac{\rho_{GC}}{\eta_{GC}} [\Delta]^{-1}, \tag{4.79}$$

and $[\Delta]$ is the matrix of Fickian diffusion coefficients.

The diffusive fluxes are given by the second term on the RHS of Eqs. 4.74 and 4.75. Unlike the binary case, for multicomponent systems the concentration gradients of each component may be different. If the elements off the main diagonal of $[\Delta]$ are not equal to zero, then interaction effects (Toor, 1957) are bound to occur.

Taylor and Krishna (1993) pointed out a criterion for quantifying diffusive interaction effects. This is as follows (in terms of a matrix of mass transfer coefficients),

$$Ip_i = \frac{|B_{G_{ij}}^{\bullet} (y_{I,j} - y_{b,j})|}{|B_{G_{ii}}^{\bullet} (y_{I,i} - y_{b,i})|} \sim O(1). \tag{4.80}$$

Thus, the higher Ip_i, the higher the significance of interaction effects, e.g., the tendency of species i to diffuse in a direction opposite to that indicated by its own gradient of concentration (*reverse diffusion*).

When calculating the diffusion coefficient tensor (and hence the mass transfer coefficient tensor, $B^{\bullet}_{G_{ik}}$), two basic approaches are used, (i) the Effective Diffusivity Method, where each constituent is assumed to transfer at a rate equal to that at which it would transfer if it alone were present in an arbitrarily chosen reference species at the same concentration, and (ii) the so-called Interactive Method, a more refined theory put forward by Toor (1964) and Stewart and Prober (1964), that assumes a linear dependence of the diffusive fluxes on *all* concentration driving forces. A description of calculation procedures for condenser design using both approaches is also presented by Webb (1982).

The two methods are summarised and illustrated below for the case of a ternary mixture. In both formulations, the the elements of $[\Delta]$ can be obtained assuming ideal gas behaviour in the vapour side. The Maxwell-Stefan diffusion coefficients, δ_{ij}, for the binary pairs can be calculated using a standard correlation, e.g., the one proposed by Fuller *et al.* (1964).

a. Interactive Method

In the interactive approach, the elements of $[\Delta]$ for a ternary system are given by (Taylor and Krishna, 1993),

$$\Delta_{11} = \delta_{13}\left[y_{b,1}\delta_{23} + (1 - y_{b,1})\,\delta_{12}\right]/S, \tag{4.81}$$

$$\Delta_{12} = y_{b,1}\delta_{23}\left(\delta_{13} - \delta_{12}\right)/S, \tag{4.82}$$

$$\Delta_{21} = y_{b,2}\delta_{13}\left(\delta_{23} - \delta_{12}\right)/S, \tag{4.83}$$

$$\Delta_{22} = \delta_{23}\left[y_{b,2}\delta_{13} + (1 - y_{b,2})\,\delta_{12}\right]/S, \tag{4.84}$$

where $S = y_{b,1}\delta_{23} + y_{b,2}\delta_{13} + y_{b,3}\delta_{12}$.

b. Effective Diffusivity Method

In this approach, only the main diagonal elements of the matrix of Fickian diffusion coefficients are different from zero. These are given by,

$$\Delta_{ii} = \delta_{i3}, \tag{4.85}$$

where $i = 1, 2$.

Therefore, interaction effects are not accounted for by the Effective Diffusivity Method.

4.3.3 Calculation of the wall temperature

As mentioned earlier, the heat transfer coefficient in the liquid film is obtained through the application of a simple correlation corrected for mixture effects. An employment of more refined methodologies, e.g., those based on an integration of the Universal Velocity Profile in the liquid film (Kosky and Staub, 1971) may not be worthwhile as they tend to overestimate the heat transfer coefficient for the case of evaporation. Other methods that were devised to cope with this overprediction by subdividing the liquid film into layers with different turbulence intensities (Moeck and Staichiewicz, 1972; Dobran, 1983), or by introducing damping functions to account for suppression of turbulence at the interface (Sun, 1996) are either too complicated or too restricted in terms of range of applicability. Here, the much tested correlation by Chen (1963) was chosen. The predictions of the Chen (1963) correlation are reasonably good at high qualities when nucleation is largely suppressed (Aounallah and Kenning, 1987), this seems to be the best alternative at the present stage. It must be said, however, that this is not the ideal solution and this is clearly an area for improvements in subsequent studies. For this calculation, properties of the liquid film (flow rate, Reynolds number etc.) are used. Moreover, a correction factor

proposed by Palen and Small (1964) is introduced so as to cope with the reduction of the already small nucleate boiling component due to mixture effects.

The liquid film heat transfer coefficient is given by,

$$\alpha_{LF} = \alpha_{LF_{FC}} F + k_{mix} \alpha_{LF_{NB}} S, \tag{4.86}$$

where,

$$\alpha_{LF_{FC}} = 0.023 \frac{\lambda_{LF}}{d_T} Re_{LF}^{0.8} Pr_{LF}^{0.4}, \tag{4.87}$$

$$Re_{LF} = \frac{\dot{m}_{LF} d_T}{\eta_{LF}}, \tag{4.88}$$

$$Pr_{LF} = \frac{\eta_{LF} c_{p_{LF}}}{\lambda_{LF}}, \tag{4.89}$$

$$F = \begin{cases} 1 & \text{if } \frac{1}{X_{tt_{LF}}} > 0.1 \\ 2.35\left[\frac{1}{X_{tt_{LF}}} + 0.213\right]^{0.736} & \text{if } \frac{1}{X_{tt_{LF}}} \leq 0.1, \end{cases} \tag{4.90}$$

$$\frac{1}{X_{tt_{LF}}} = \left(\frac{\rho_{LF}}{\rho_G}\right)^{0.5} \left(\frac{\eta_G}{\eta_{LF}}\right)^{0.1} \left(\frac{\dot{m}_G}{\dot{m}_{LF}}\right)^{0.9}, \tag{4.91}$$

$$\alpha_{LF_{NB}} = 0.00122 \frac{\lambda_{LF}^{0.79} c_{p_{LF}}^{0.45} \rho_{LF}^{0.49} \Delta T_{sat}^{0.24} \Delta p_{sat}^{0.75}}{\sigma_{LF}^{0.5} \eta_{LF}^{0.29} \rho_G^{0.24} \Delta h_V}, \tag{4.92}$$

$$S = \frac{1}{1 + 2.53 \times 10^{-6} Re_{tp_{LF}}^{1.17}}, \tag{4.93}$$

$$\Delta T_{sat} = T_w - T_{sat}, \tag{4.94}$$

$$\Delta p_{sat} = p_{sat}(T_w) - p_{sat}(T_{sat}), \tag{4.95}$$

and,

$$Re_{tp_{LF}} = Re_{LF}F^{1.25}. \tag{4.96}$$

The correction factor for mixture effects is given by,

$$k_{mix} = \exp(-0.027\Delta T_{bp}). \tag{4.97}$$

The wall temperature is finally calculated as follows,

$$T_w = \frac{\dot{q}_w}{\alpha_{LF}} + T_I. \tag{4.98}$$

4.4 Solution of the governing equations

4.4.1 Numerical schemes and algorithm

The task of solving the governing equations involves several stages of numerical computation. The objective of this section is to explain these stages and the methods used in each one of them as well as the solution procedure employed.

The total number (NEQ) of differential equations (for conservation of mass, momentum and energy) to be solved by the model grows with the number of components (NOC) according to the following relationship,

$$NEQ = 2NOC + 5. \tag{4.99}$$

In addition to the unknown variables present in the single component formulation, viz., $\dot{m}_{LF}$, $\dot{m}_{LE}$, $\dot{m}_{GC}$, $\frac{dp}{dz}_a$, $\frac{dp}{dz}_f$, $\frac{dp}{dz}_g$ and T_C, the mixture analysis requires individual component conservation equations; $x_{LF,1}$ and $y_{b,1}$ for the binary case and $x_{LF,1}$, $x_{LF,2}$, $y_{b,1}$ and $y_{b,2}$ for the ternary case.

As far as initial conditions at the onset of annular flow are concerned, a significant amount of liquid may be entrained as droplets in this region, perhaps as a result of high liquid entrainment associated with the large waves formed in churn flow (Hewitt and Hall-Taylor, 1970). The correlation developed in Chapter 5 is the only method available for calculating the entrained fraction at the onset of annular flow. However, this was obtained for air-water data and may not entirely hold for diabatic hydrocarbon data. A crude assumption is that rates of deposition and entrainment are at equilibrium (i.e., equal) at this point; for the present analysis, this would give entrained fractions in the range 5-10% at the onset of annular flow. However, this takes no account of the proximity to churn flow and the actual values are likely to be higher (as those obtained using the correlation). In the present work, the approach has been to assume a series of values covering the likely range (i.e., 0, 10, 20 and 40%) and to carry out calculations for each one of these values.

The variables known *a priori* are the total mass flux (subcooled liquid at the bottom of the pipe), the wall heat flux, the total pressure at the bottom of the pipe, the overall composition of the mixture and the length and diameter of the pipe.

In the annular flow region, the balance equations for mass (three fields plus liquid film and bulk vapour components), momentum (pressure drop) and energy (core temperature) are solved by a fifth order Runge-Kutta Method with an adaptative error control (Press *et al.*, 1992).

At each marching step m of length dz, the values of $n_D^{j,m}$ (and consequently of $D^{j,m}$, $\langle D^m \rangle$ and E^m) are calculated and used to compute the conservation equations. The variables associated with the interfacial heat and mass transfer analysis ($\dot{m}_{I,i}$, $y_{I,i}$ and T_I) are also computed at each marching step. The solution algorithm is comprised by the following steps (multicomponent case),

1. Known: $x_{LF_{I,i}} (= x_{LF_{b,i}}$, fully mixed film hypothesis), $y_{b,i}$, T_C;

2. Calculate: $y_{I,i}$, $T_I \rightarrow$ Bubble point temperature subroutine;

3. Guess: $\sum_{j=1}^{NOC} \dot{m}_{I,j}$;

4. Calculate: $\frac{\dot{m}_{I,j}}{\sum_{j=1}^{NOC} \dot{m}_{I,j}} \rightarrow$ Eq. 4.60 or Eq. 4.75;

5. Calculate: $\dot{q}_{GC} \rightarrow$ Eq. 4.58 (substitute 2 for NOC in the multicomponent case);

6. Compare: If $\dot{q}_{GC} \neq \dot{q}_w - \dot{q}_{ED}$, update $\sum_{j=1}^{NOC} \dot{m}_{I,j}$ and return to step 4.

Published routines for calculating physical and thermodynamic properties of mixtures (Assael *et al.*, 1996) were incorporated in the code. Densities and enthalpies were calculated using the Peng and Robinson (1976) equation of state. Specific heat capacities were calculated through the method of Lee and Kesler (1975), viscosities and thermal conductivities via the method by Ely and Hanley (1981,1983), surface tension using the method by Sprow and Prausnitz (1967) and the vapour side mass diffusivities via the correlation by Fuller *et al.* (1964).

4.5 Droplet interchange and condensation

It is intuitive to think that the effect of hydrodynamic non-equilibrium due to droplet interchange described in Section 4.1 will work in an opposite way for condensation, i.e., it will make the film become locally richer in the more volatile component than the droplets and than in the liquid film in a hypothetical situation where no droplet interchange takes place. The implications of this mechanism for condensation (see Fig. 4.8) will be that, at a certain distance along the pipe, the local saturation temperature at the film interface, T_I, lower than that expected (T_E) for equilibrium between a mixed liquid phase and the vapour. For a given heat flux and for a given temperature difference across the film, the wall temperature T_w will be *lower* than for the case where the liquid phase has a uniform

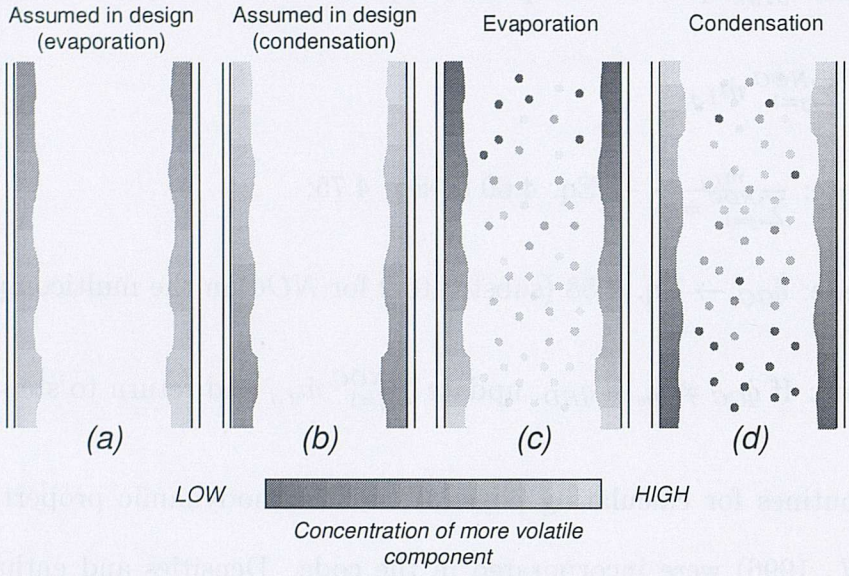


Figure 4.8: Droplet interchange and condensation of mixtures in annular flow.

concentration and thus $(T_w - T_E)$ will be lower. This will give an apparent *increase* in heat transfer coefficient, in contrast to the evaporation case where differences in drop and film concentration lead to an apparent *decrease* in heat transfer coefficient.

As mentioned before, there is some experimental evidence (Cavallini *et al.*, 1999; Cavallini *et al.*, 2000) of a slight increase in the heat transfer coefficient in condensation of R-407C and of a mixture R-125/R-236ea (0.46/0.54 mass fraction) at high qualities. A comparison between the data of Cavallini *et al.* and results obtained using an empirical correlation for condensation in annular flow (Tang, 1997) is presented in Fig. 4.9. As will be seen, the data for the mixture are higher than the correlation predicts whereas the single component data lie below the correlation.

The effect of droplet interchange on the condensation heat transfer may be more difficult to identify than in evaporation due to two reasons. Firstly, typical boiling ranges of mixtures used in condensing systems (and therefore experiments) are much lower than some observed in boiling experiments (R-407C at 1.5 MPa has a boiling range of the order

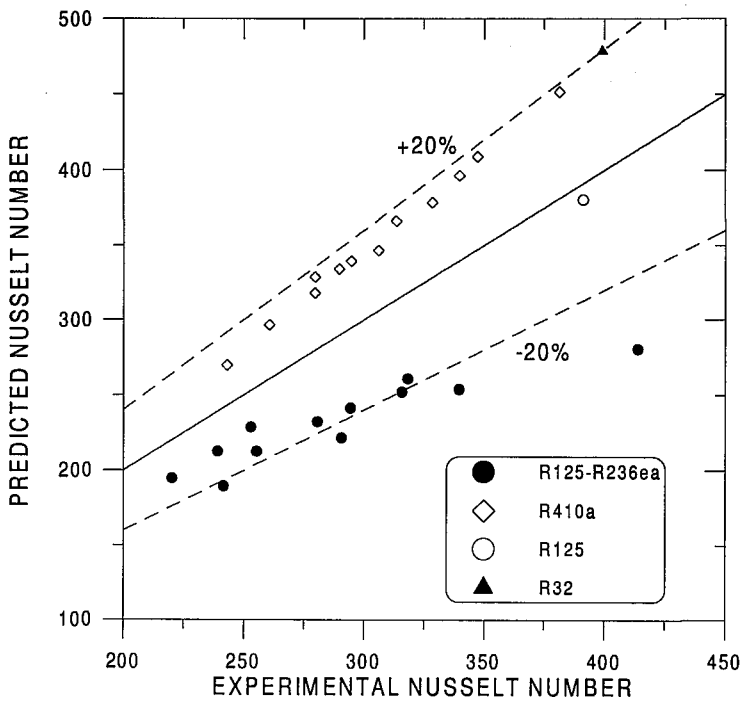


Figure 4.9: Comparison of predicted and experimental dimensionless heat transfer coefficients (Nusselt number) for condensation of refrigerants with the correlation of Tang (1997). Data of Cavallini *et al.* (2000).

of 5 K). This makes the saturation temperature imbalance between the liquid film and droplets much more subtle. Secondly, in evaporation, diffusive mass transfer resistance and droplet interchange work in the same way, i.e., towards a decrease in the heat transfer coefficient [1]. In condensation, however, the heat transfer coefficient deterioration due to mass transfer resistance may be sufficient to cancel out or overcome any increase associated with droplet interchange.

4.6 Results

4.6.1 Convective boiling of hydrocarbon mixtures

The main data set against which the present methodology is compared was collected at a high pressure multicomponent boiling facility situated at the AEA Technology plc site at Harwell, Oxfordshire, UK. The facility was operated under a collaborative experiment between Imperial College and the Heat Transfer and Fluid Flow Service (HTFS), the latter being part of AEA Technology. A detailed description of the apparatus is given in the PhD thesis of Kandlbinder (1997). Kandlbinder carried out an extensive experimental campaign using single component hydrocarbons (n-pentane and iso-octane), two sets of n-pentane/iso-octane binary mixtures (0.7/0.3 – mixture 1 and 0.37/0.63 – mixture 2, overall mole fraction) and one set of n-pentane/n-hexane/iso-octane ternary mixture (0.31/0.22/0.47 – mixture 3, overall mole fraction). The system pressure ranged from 2 to 11 bara, the total mass fluxes from 100 to 550 kg m^{-2} s^{-1} and the wall heat flux from 30 to 100 kW m^{-2}. The 8.68 m long vertical test section is made of 321 stainless steel. The inner and outer diameters are 25.4 and 38.0 mm, respectively. A schematic diagram of the experimental facility is shown in Fig. 4.10.

[1] The sole influence of droplet interchange effects on heat transfer was quantified in previous work (Barbosa and Hewitt, 1999) by assuming no mass transfer resistance in both phases (flash calculation).

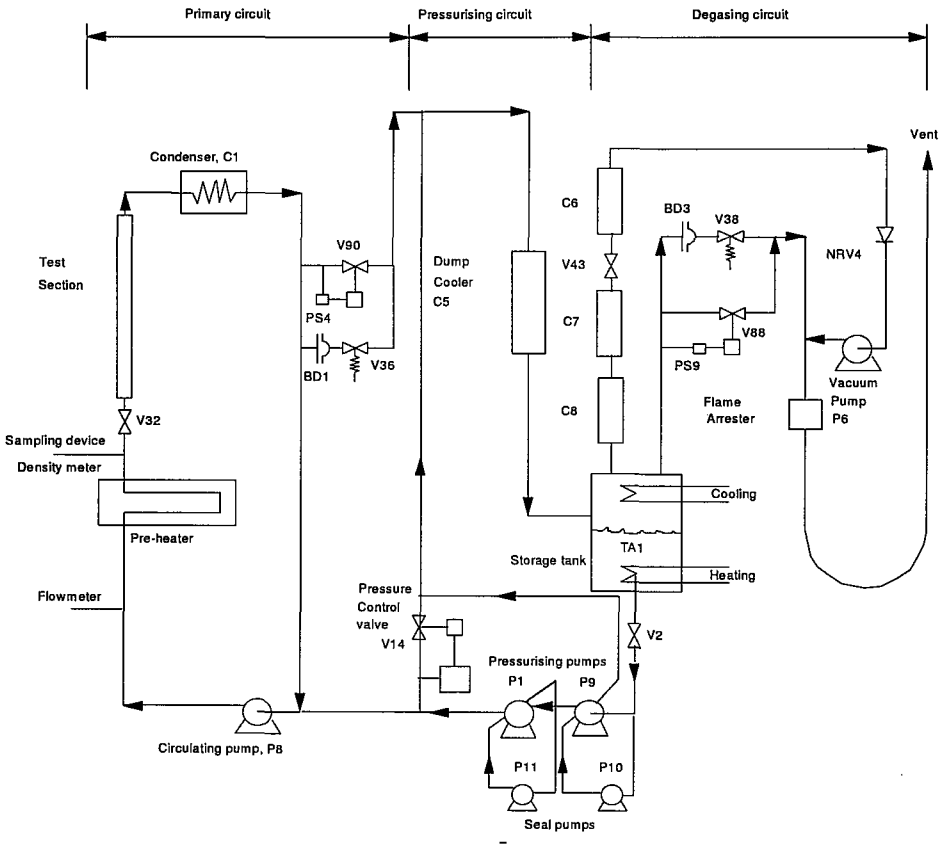


Figure 4.10: Schematic diagram of the High Pressure Boiling Facility.

Along the test section, bulk fluid and wall temperatures were measured. Bulk temperatures, the temperature of the fluid at the centre line of the tube, were measured at 12 equally spaced (750 mm) locations. Wall temperatures were measured at 74 points along the test section. Three absolute pressure transducers were located at the bottom, middle and top of the test section, with differential pressure cells located every 750 mm along the test section.

Estimated uncertainties of measured values by Kandlbinder (1997) are presented in Table 4.1. The experimental procedure by Kandlbinder was as follows. In the main series of

experiments, the heat flux was increased further in steps of 10 kW m^{-2}; to avoid dryout, the inlet temperature had often to be reduced with increasing heat flux. Another series of experiments were carried out where the heat flux, mass flux and pressure were kept constant and only the inlet temperature was increased up to a maximum value, typically 5 to 15°C below saturation. In addition, runs with reduction in the inlet temperature were performed to allow examination of hysteresis effects. In this context, experiments were also conducted by increasing and decreasing the heat flux. A test matrix for the experiments is shown in Table 4.2.

Table 4.1: Estimated uncertainty of measured values used in the determination of the experimental heat transfer coefficient.

Temperature (wall and bulk)	± 0.3 K
Pressure	0.1% full scale
Voltage across the test section	± 1.0%
Current across the test section	± 1.0%
Thermal conductivity of the test section	± 4.0%
Heat loss	± 20%
Heated length	± 10 mm
Inner diameter of test section	± 0.1 mm
Test section wall thickness	± 0.15 mm

According to Kandlbinder, the average error in the experimental heat transfer coefficient is ±10%.

Table 4.2: Test matrix for two-phase experiments (Kandlbinder, 1997).

Conditions	Unit	Range
Pressure	bar	2.3, 3.0, 6.0, 10.0
Mass flux	kg m^{-2} s^{-1}	100, 200, 300, 500
Heat flux	kW m^{-2}	10, 20, 30, 40, 50, 60, 70
Inlet subcooling	K	minimum of 5 to 15
Exit quality	-	≤ 0.8

Hydrodynamics results

In Eq. 4.38, $e^{j,m}$ was defined as the fraction of droplets created at section j which are still entrained at section m downstream. Of special interest is $e^{0,m}$ which represents the fraction of the droplets assumed to be present at the onset of annular flow which are still present at section m which is at a distance z_A from the point of onset of annular flow. Figures 4.11 and 4.12 show typical curves for the decay of $e^{0,m}$ against z_A, where $z_A = z - z_{OA}$, z_{OA} being the distance at which the onset of annular flow takes place. In each graph, the value of total initial entrained fraction, defined as the mass flux of entrained liquid divided by the total mass flux of liquid (in the film and in the droplets), is varied from 0% to 40%. It can be observed that the higher the initial entrained fraction, the lower the rate of decay of $e^{0,m}$, suggesting that the mean concentration of the entrained droplets is affected by the variation of initial entrained fraction.

Table 4.3 compares the values of $e^{0,m}$ for both mixtures under similar conditions using different initial entrained fractions. As the portion of the pipe over which annular flow occurs is different for each condition (basically due to distinct sub-cooling temperature differences at the pipe inlet), $e^{0,m}$ values are compared at a distance one metre downstream

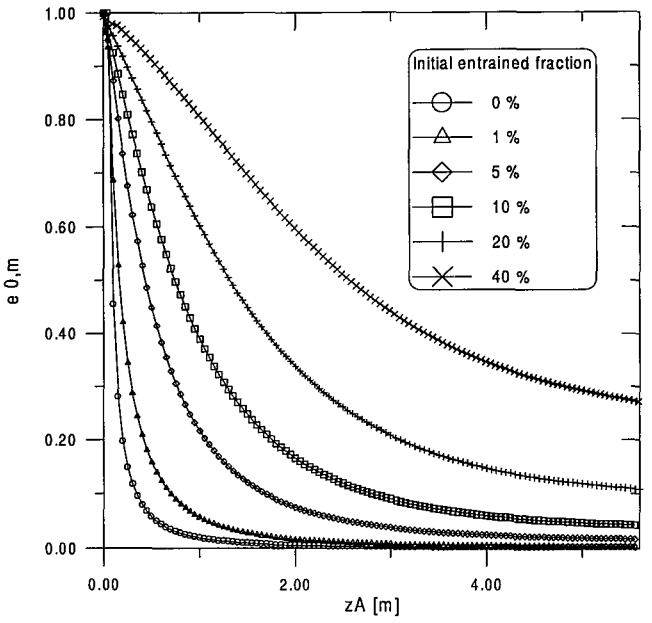


Figure 4.11: $e^{0,m}$ for different initial entrained fractions; mixture 1, $p = 2.3$ bar, $\dot{q}_w = 57.7$ kW m^{-2}, $\dot{m}_T = 286.6$ kg m^{-2} s^{-1}.

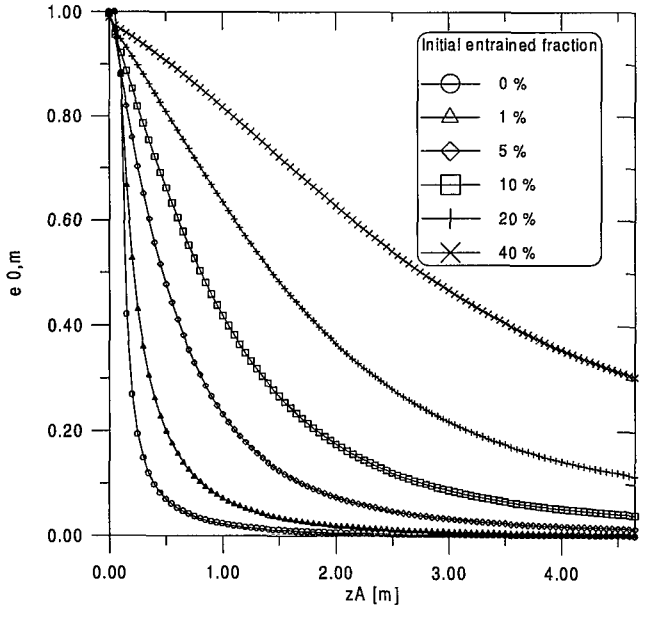


Figure 4.12: $e^{0,m}$ for different initial entrained fractions; mixture 1, $p = 6.0$ bar, $\dot{q}_w = 60.2$ kW m^{-2}, $\dot{m}_T = 295.0$ kg m^{-2} s^{-1}.

Table 4.3: Values of $e^{0,m}$, at $z_A = 1m$, for different values of initial entrained fraction.

Mixture 1					Mixture 2				
Run No	0%	10%	20%	40%	Run No	0%	10%	20%	40%
Run 1	0.019	0.389	0.602	0.797	Run 4	0.019	0.396	0.607	0.800
Run 2	0.019	0.398	0.611	0.804	Run 5	0.022	0.407	0.621	0.810
Run 3	0.022	0.418	0.634	0.818	Run 6	0.023	0.430	0.642	0.822

of the point of onset of annular flow, z_{OA}.

The data in Table 4.3 reveal that $e^{0,m}$ increases with pressure and is comparatively higher for mixture 2 (richer in the less volatile component). In addition, the rate of increase of $e^{0,m}$ with pressure is also higher for mixture 2. An explanation for these trends lies in the change in the physical properties of the mixture with both pressure and overall composition. This is, in turn, reflected in a variation of entrainment and deposition rates. The conditions of Runs 1 to 6 are given in Table 4.4.

The reason for having values of $e^{0,m}$ different than zero in the 0% initial entrained fraction columns is that, in the algorithm, section $m = 0$ is set as the first one after that in which U^*_{GS} exceeds 1 and the first drops are entrained.

Profiles of bulk concentration (mass fraction) of n-pentane for the film and for the droplets are shown in Figs. 4.13, 4.14 and 4.15 for various conditions. In each graph, the initial amount of liquid entrained as droplets is again varied from 0% to 40%. This alteration provokes an opposite effect in the behaviour of concentration in both streams; higher values of initial $\dot{m}_{LE}$ induce lower profiles of $x_{LF,1}$ and higher profiles of $x_{LE,1}$. In Fig. 4.15, the concentration of the liquid phase calculated assuming no droplet entrainment (all liquid in the film) and no mass transfer resistance (fiash calculation) is also shown.

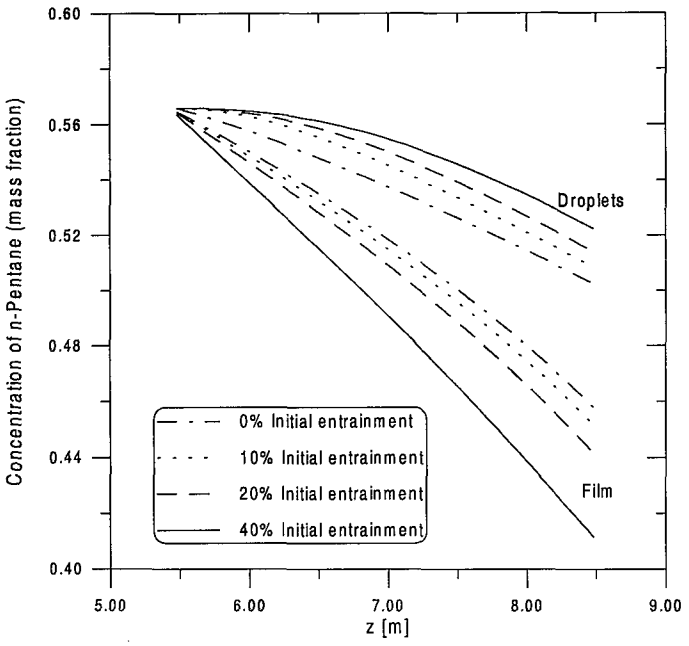


Figure 4.13: Mean concentration of n-pentane in the liquid film and in the droplets; mixture 1, $p = 6.1$ bar, $\dot{q}_w = 68.4$ kW m^{-2}, $\dot{m}_T = 503.8$ kg m^{-2} s^{-1}.

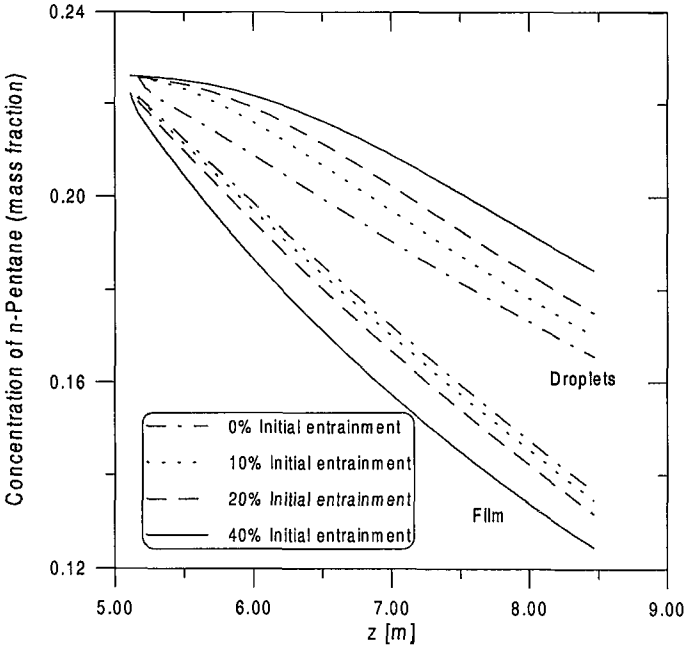


Figure 4.14: Mean concentration of n-pentane in the liquid film and in the droplets; mixture 2, $p = 2.2$ bar, $\dot{q}_w = 49.3$ kW m^{-2}, $\dot{m}_T = 297.1$ kg m^{-2} s^{-1}.

Table 4.4: Summary of conditions in calculations of $e^{0,m}$.

Run No	$\tilde{x}_{ov}$	$p[MPa]$	$\dot{q}_W[kWm^{-2}]$	$\dot{m}_T[kgm^{-2}s^{-1}]$
Run 1	0.7/0.3	0.23	57.7	286.6
Run 2	0.7/0.3	0.30	59.6	303.1
Run 3	0.7/0.3	0.60	60.2	295.0
Run 4	0.37/0.63	0.22	59.4	295.2
Run 5	0.37/0.63	0.29	58.9	302.2
Run 6	0.37/0.63	0.61	59.1	304.9

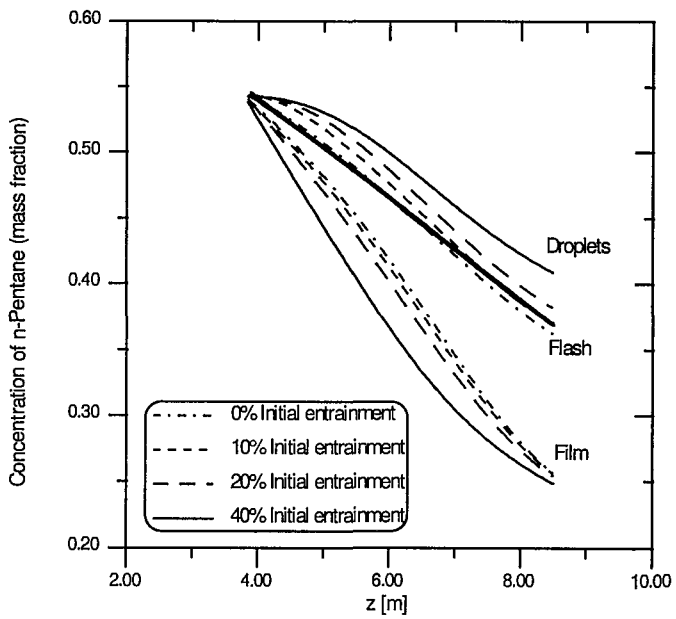


Figure 4.15: Mean concentration of n-pentane in the liquid film and in the droplets; mixture 1, $p = 6.0$ bar, $\dot{q}_w = 60.2$ kW m^{-2}, $\dot{m}_T = 295.0$ kg m^{-2} s^{-1}.

Figures 4.16 and 4.17 show comparisons between experimental data and predictions of absolute pressure distributions. As expected (Govan, 1990), the influence of the initial liquid entrained fraction on the pressure gradient is not as pronounced as on the profiles of liquid concentration. The average deviation in the absolute pressure predictions at high qualities lies within the 10%-15% range. However, it can be observed that the predicted gradients of pressure in the annular flow region are in very good agreement with those observed from the experimental data. This leads to the conclusion that the discrepancies in the absolute pressure values at high qualities are due to a poor prediction of pressure gradients at moderate qualities (mainly churn flow regime). A detailed understanding of the physics of such flows is not yet fully achieved and the need for more physically based models (especially for churn flow) is evident.

Heat transfer results for binary mixtures

In what follows, the heat transfer results are compared with the experimental data obtained by Kandlbinder (1997) for binary (n-pentane/iso-octane) mixtures. In Kandlbinder's experiments, thermocouples were located at the outer wall and at the centreline of the tube. In order to estimate the inner wall temperature (values with which the present predictions are compared), Kandlbinder solved the heat conduction equation with internal heat generation, having the outer wall temperatures as boundary conditions. As far as the bulk temperature measurements are concerned, it is expected that, due to the distribution of the phases in the annular flow pattern (the thickness of the liquid film is of the order of a fraction of millimetre), the temperature profiles recorded by the bulk (centreline) thermocouples are those corresponding to the homogeneous core. Thus, the predicted distributions of T_C are compared with the experimental data.

Figures 4.18 to 4.21 show the predictions of wall, interface and core temperatures for different initial entrained fractions at various conditions. As for the distributions of mean

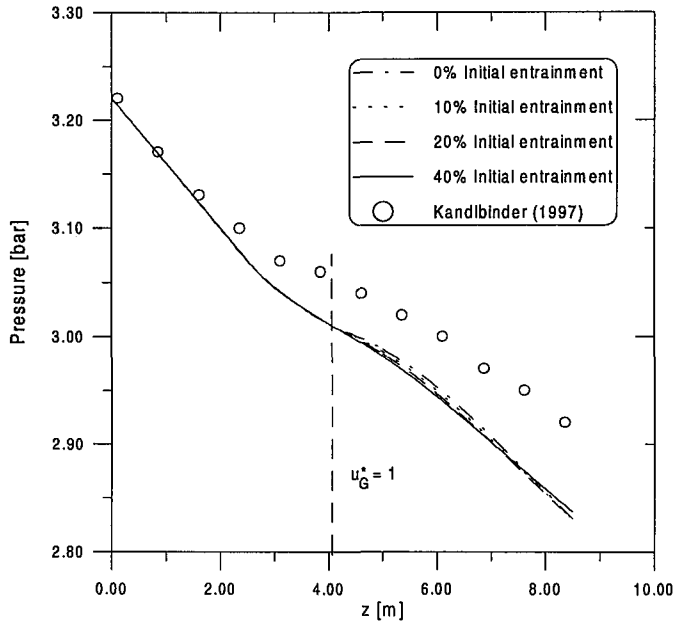


Figure 4.16: Profiles of absolute pressure; mixture 1, $p = 3.2$ bar, $\dot{q}_w = 49.3$ kW m^{-2}, $\dot{m}_T = 305.0$ kg m^{-2} s^{-1}.

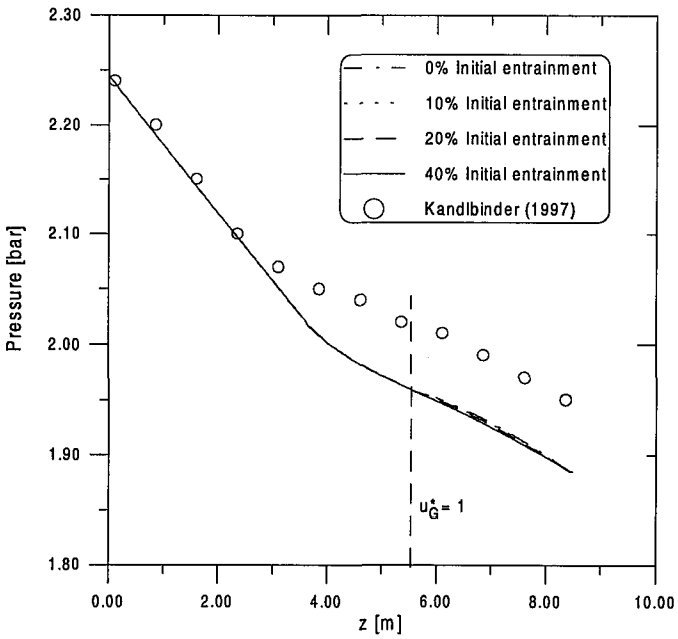


Figure 4.17: Profiles of absolute pressure; mixture 2, $p = 2.2$ bar, $\dot{q}_w = 40.7$ kW m^{-2}, $\dot{m}_T = 195.8$ kg m^{-2} s^{-1}.

concentration in the film and in the entrained droplets, a variation in the initial entrained fraction provokes an opposite effect in the behaviour of mean temperatures; higher values of initial $\dot{m}_{LE}$ induce lower profiles of T_C and higher profiles of T_I. It can be observed that the measured temperature trends are well picked up by the formulation, but the agreement decreases somewhat with increasing pressure. The probable reason for the discrepancy between the present model and the data at higher pressures is that the various correlations and methods embodied in the proposed formulation were originally obtained from low-pressure data.

The measured heat transfer coefficients (calculated by introducing the known wall heat flux, the measured wall temperature and the calculated value of T_E into Eq. 4.1 are compared with those calculated using the present methodology in Figs. 4.22 to 4.25 for the same conditions as in Figs. 4.18 to 4.21. Again, the capability of the formulation at predicting the decrease in the heat transfer coefficient with increasing quality is evident. Also shown in Figs. 4.22 to 4.25 are the predictions obtained from the Chen (1963) correlation taking account of mixture effects on the (small) nucleate boiling coefficient using the correlation of Palen and Small (1964). As will be seen, this modified version of the Chen correlation overpredicts the heat transfer coefficients. Since the Chen/Palen method was also used in the present methodology for calculating the film coefficient, the difference between the Chen/Palen predictions based on a conventional interpretation and those arising from the present model (combined effect of droplet interchange and mass transfer resistance) give a direct indication of the importance of these mechanisms. As observed, a very significant effect is predicted.

As mentioned before, there is at present no method for calculating the initial entrained fraction (though work towards this goal was carried out in the present project and is presented in Chapter 5) and it is expected that such a value is higher than that obtained by equating the entrainment and deposition rates (equilibrium value) at the point of onset

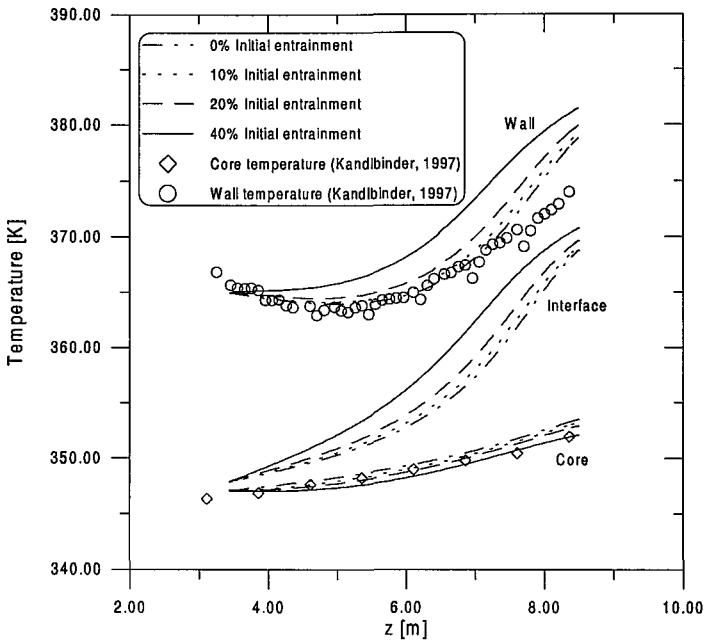


Figure 4.18: Predictions of wall, interface and core temperature; mixture 1, $p = 2.3$ bar, $\dot{q}_w = 49.8$ kW m^{-2}, $\dot{m}_T = 292.8$ kg m^{-2} s^{-1}.

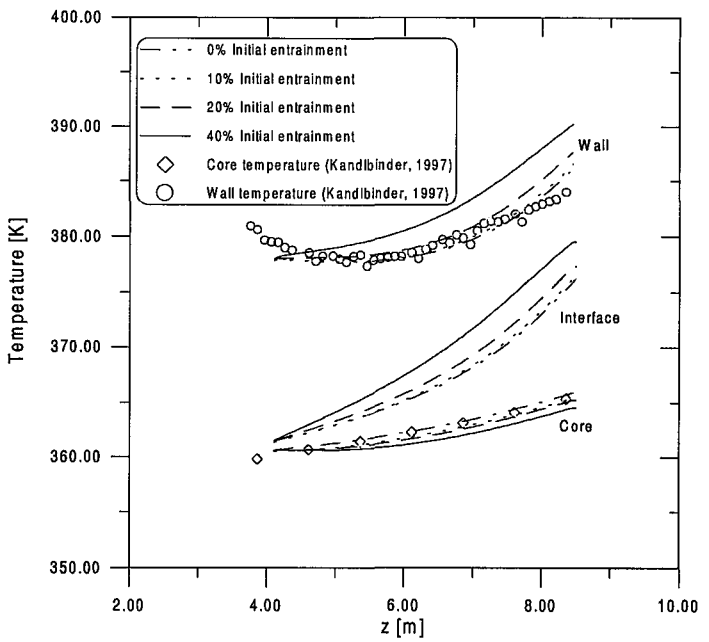


Figure 4.19: Predictions of wall, interface and core temperature; mixture 1, $p = 3.2$ bar, $\dot{q}_w = 49.3$ kW m^{-2}, $\dot{m}_T = 305.0$ kg m^{-2} s^{-1}.

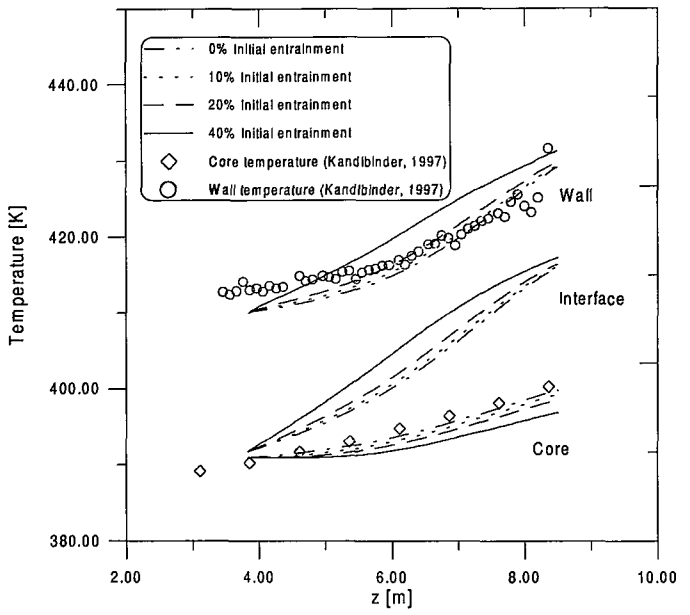


Figure 4.20: Predictions of wall, interface and core temperature; mixture 1, $p = 6.0$ bar, $\dot{q}_w = 60.2$ kW m^{-2}, $\dot{m}_T = 295.0$ kg m^{-2} s^{-1}.

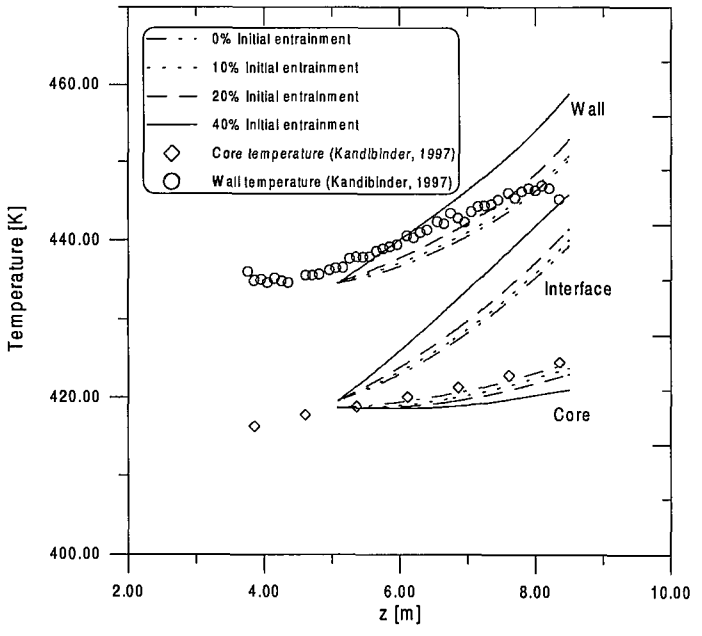


Figure 4.21: Predictions of wall, interface and core temperature; mixture 1, $p = 10.0$ bar, $\dot{q}_w = 49.8$ kW m^{-2}, $\dot{m}_T = 299.2$ kg m^{-2} s^{-1}.

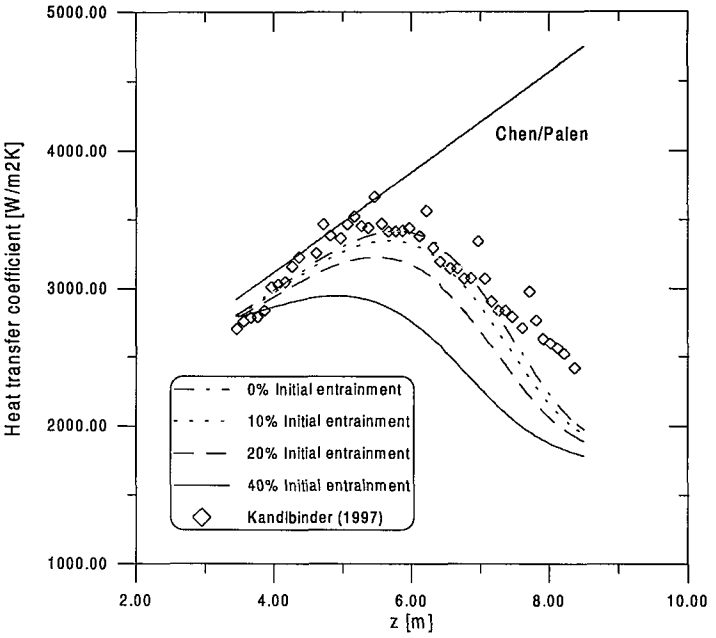


Figure 4.22: Predictions of heat transfer coefficient; mixture 1, $p = 2.3$ bar, $\dot{q}_w = 49.8$ kW m^{-2}, $\dot{m}_T = 292.8$ kg m^{-2} s^{-1}.

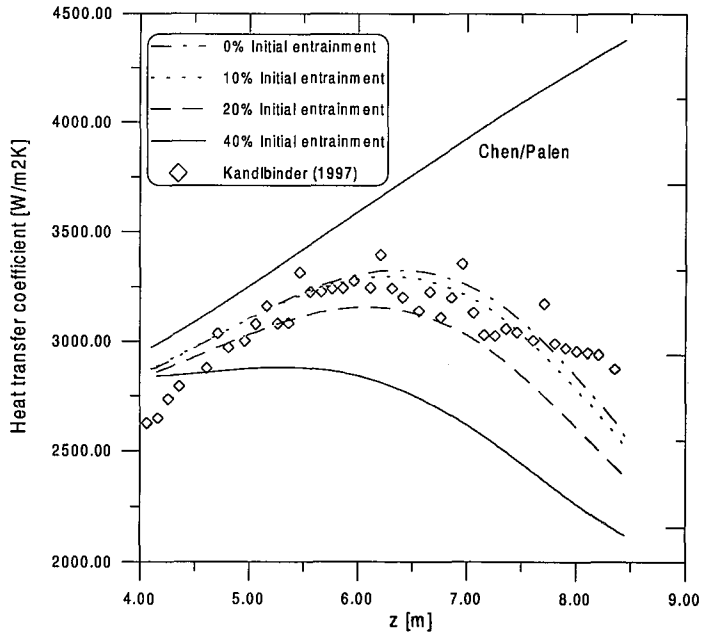


Figure 4.23: Predictions of heat transfer coefficient; mixture 1, $p = 3.2$ bar, $\dot{q}_w = 49.3$ kW m^{-2}, $\dot{m}_T = 305.0$ kg m^{-2} s^{-1}.

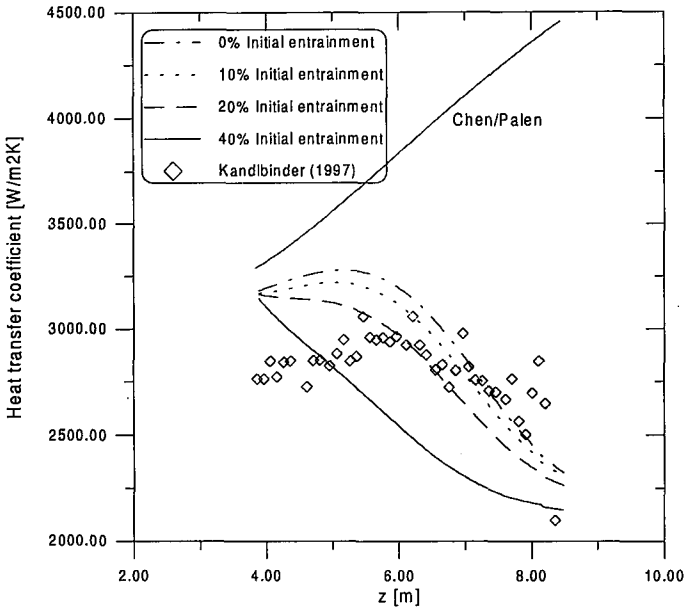


Figure 4.24: Predictions of heat transfer coefficient; mixture 1, $p = 6.0$ bar, $\dot{q}_w = 60.2$ kW m^{-2}, $\dot{m}_T = 295.0$ kg m^{-2} s^{-1}.

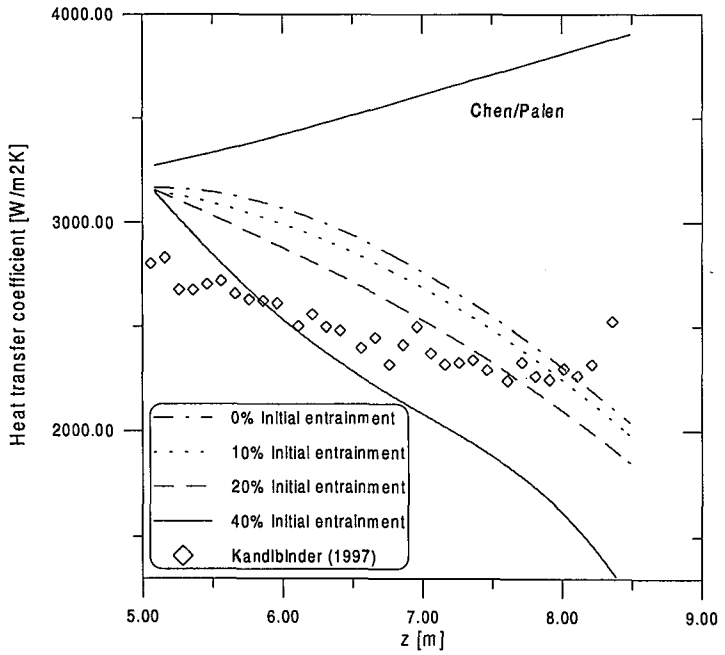


Figure 4.25: Predictions of heat transfer coefficient; mixture 1, $p = 10.0$ bar, $\dot{q}_w = 49.8$ kW m^{-2}, $\dot{m}_T = 299.2$ kg m^{-2} s^{-1}.

of annular flow. An analysis of Figs. 4.18 to 4.25 suggests that the likely value of the initial entrained fraction for the cases studied lies in the 10 to 20% range (higher than the 5 to 10% equilibrium value range).

In Figs. 4.26 and 4.27, typical profiles of bulk and interfacial vapour concentration are presented for various initial entrained fractions. As expected, an increase in the initial entrained fraction gives lower predictions of $y_{b,1}$ and $y_{I,1}$, as a lower amount of liquid is available in the film for evaporation. As will be seen, the bulk concentrations are higher than those at the interface. On the liquid side of the interface, the concentration of the more volatile component (n-pentane) are lower still (compare Figs. 4.13 and 4.26), the difference being consistent with vapour-liquid equilibrium at the interface position. The results shown in Figs. 4.26 and 4.27 are a manifestation of the balance between the two terms in brackets in Eq. 4.59. The first term represents convection away from the interface and the second term represents diffusion. For the cases shown in Figs. 4.26 and 4.27, there will be diffusion of the more volatile component (n-pentane) across the equivalent laminar layer *towards* the interface and diffusion of the less volatile component (iso-octane) *away* from the interface. However, the net transport of both components is away from the interface due to the infiuence of the first (convective) term in brackets in Eq. 4.59. Results similar to those shown in Figs. 4.26 and 4.27 were also obtained by Shock (1976).

Figures 4.28 and 4.29 show typical plots of the ratio $\frac{\dot{q}_{ED}}{\dot{q}_w}$ against the axial distance. It is observed that the enthalpy absorbed or released by the entrained droplets due to droplet interchange is lowcr than 10% of the wall heat flux. Moreover, as the liquid film gets thinner (due to entrainment and phase change), the entrainment rate decreases and the contribution due to droplet deposition in Eq. 4.71 becomes more significant. This leads to the maxima observed towards the end of the pipe in Figs. 4.26 and 4.27.

Figures 4.30 to 4.32 illustrate the performance of various methods in predicting the wall

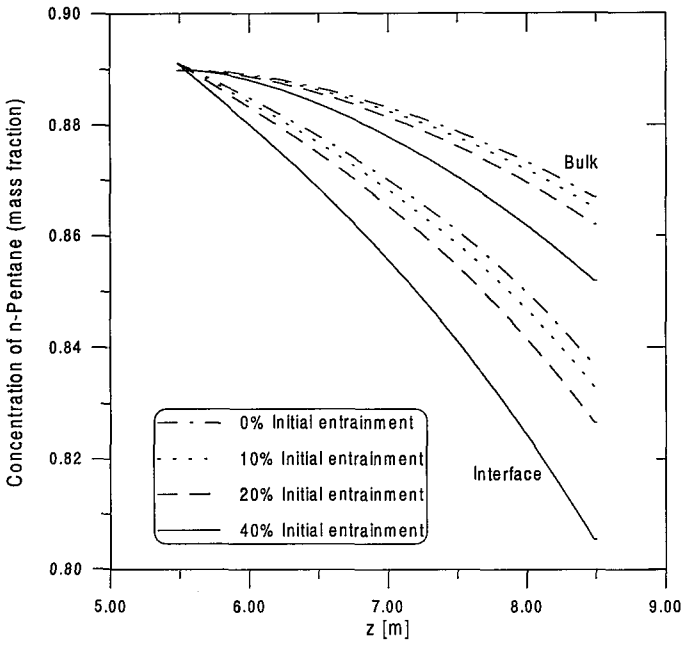


Figure 4.26: Profiles of bulk and interfacial concentration of n-pentane in the vapour core; mixture 1, $p = 6.1$ bar, $\dot{q}_w = 68.4$ kW m^{-2}, $\dot{m}_T = 503.8$ kg m^{-2} s^{-1}.

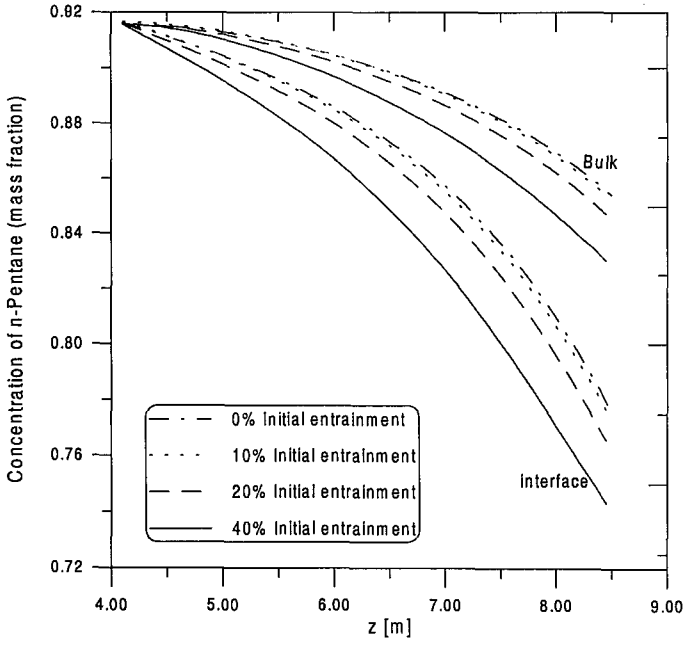


Figure 4.27: Profiles of bulk and interfacial concentration of n-pentane in the vapour core; mixture 1, $p = 3.2$ bar, $\dot{q}_w = 49.3$ kW m^{-2}, $\dot{m}_T = 305.0$ kg m^{-2} s^{-1}.

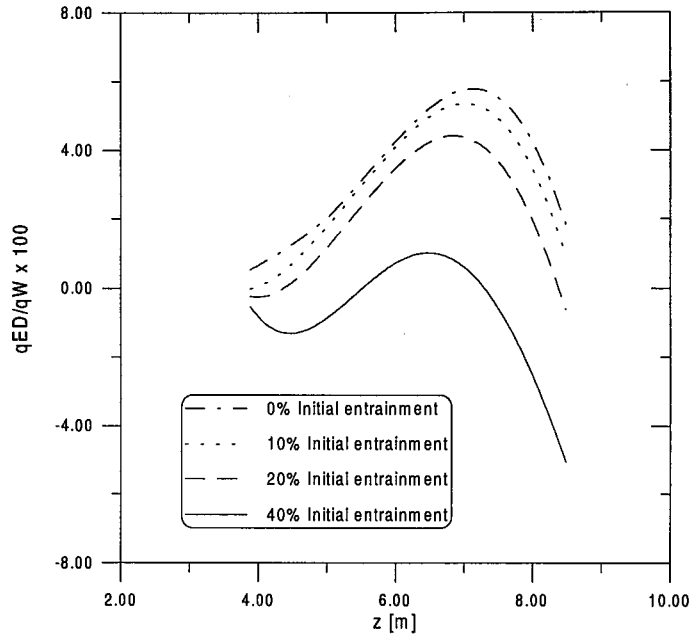


Figure 4.28: Profiles of enthalpy released or absorbed by the droplets normalised by the wall heat flux; mixture 1, $p = 6.0$ bar, $\dot{q}_w = 60.2$ kW m^{-2}, $\dot{m}_T = 295.0$ kg m^{-2} s^{-1}.

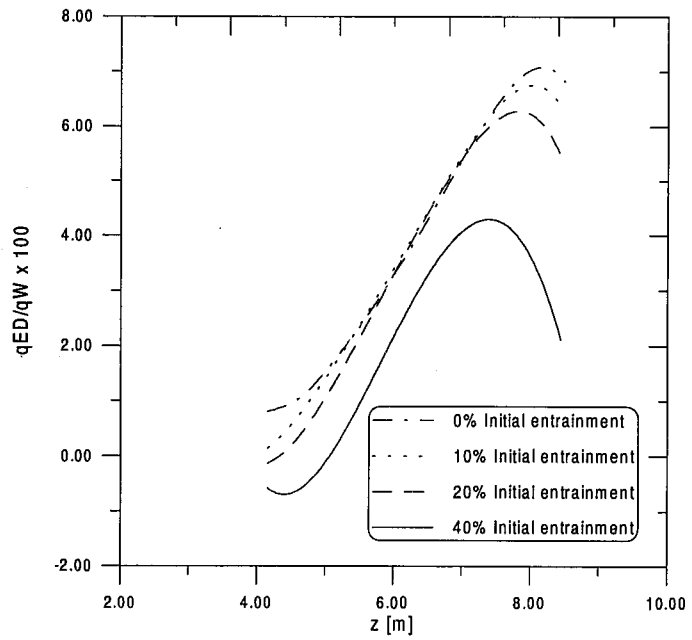


Figure 4.29: Profiles of enthalpy released or absorbed by the droplets normalised by the wall heat flux; mixture 1, $p = 3.2$ bar, $\dot{q}_w = 49.3$ kW m^{-2}, $\dot{m}_T = 305.0$ kg m^{-2} s^{-1}.

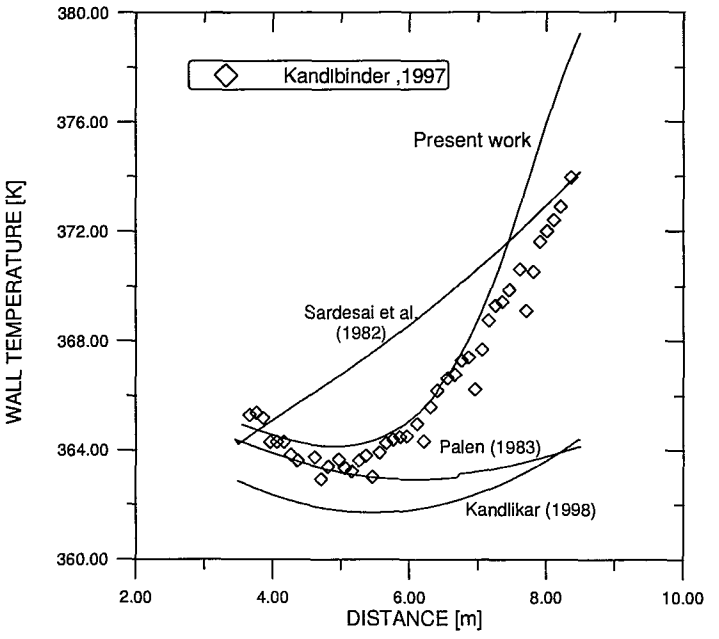


Figure 4.30: Predictions of local wall temperature by various methods; mixture 1, $p = 2.3$ bar, $\dot{q}_w = 49.8$ kW m^{-2}, $\dot{m}_T = 292.8$ kg m^{-2} s^{-1}.

temperature profile with distance. The best prediction is obtained with the present formulation (using a value of 10% for the initial entrained fraction). The experimental data are overpredicted in the intermediate range by the equilibrium method (Sardesai *et al.*, 1982) and underpredicted by the correlations of Kandlikar (1998) and Chen (1963) with the nucleate boiling term corrected according to Palen and Small (1964).

As observed in Figs. 4.33 to 4.35, and as expected from an analysis of Figs. 4.30 to 4.32, the correlation by Kandlikar (1998) and the equilibrium approach (Sardesai *et al.*, 1982) over and underpredict the experimental data, respectively. However, the performance of the equilibrium approach is significantly better.

Figure 4.36 shows a comparison between experimental and predicted heat transfer coefficients averaged over the length of pipe over which annular flow occurs. The average coefficient is defined as,

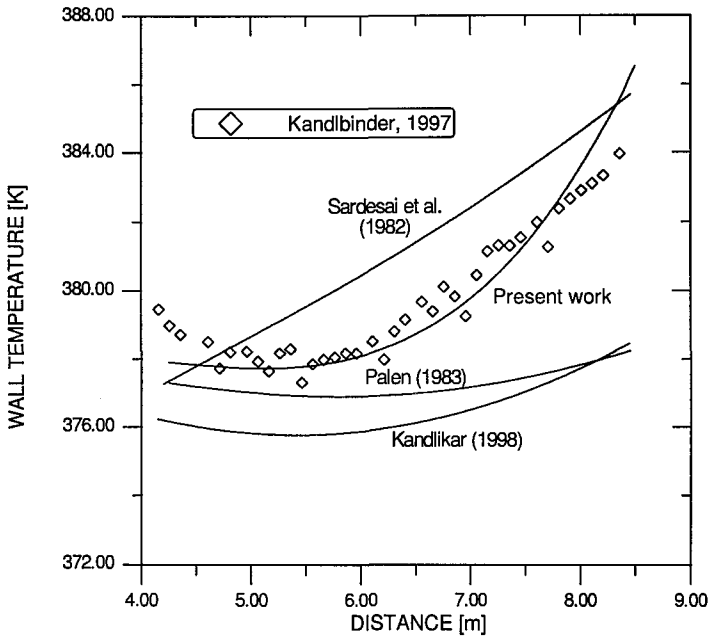


Figure 4.31: Predictions of local wall temperature by various methods; mixture 1, $p = 3.2$ bar, $\dot{q}_w = 49.3$ kW m^{-2}, $\dot{m}_T = 305.0$ kg m^{-2} s^{-1}.

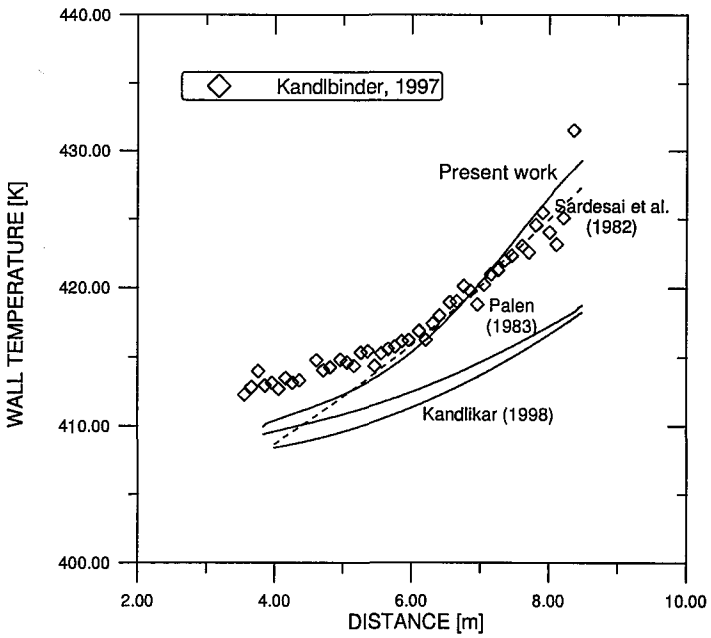


Figure 4.32: Predictions of local wall temperature by various methods; mixture 1, $p = 6.1$ bar, $\dot{q}_w = 60.2$ kW m^{-2}, $\dot{m}_T = 295.0$ kg m^{-2} s^{-1}.

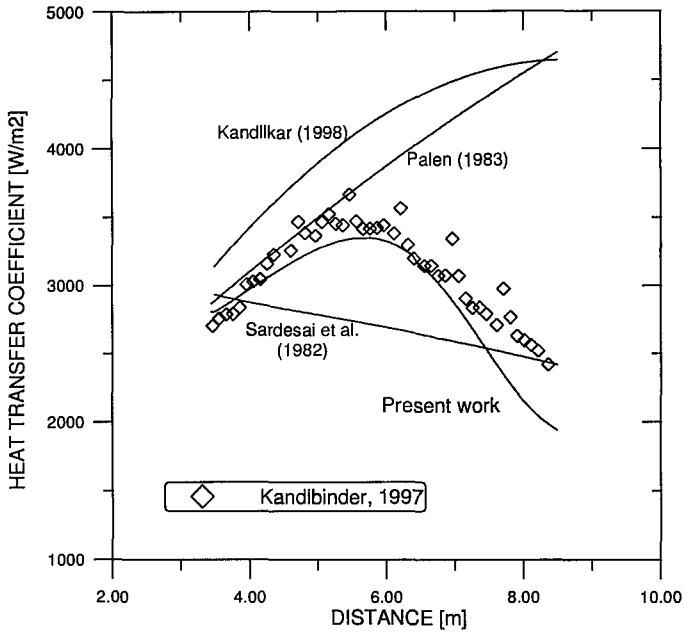


Figure 4.33: Predictions of local heat transfer coefficients by various methods; mixture 1, $p = 2.3$ bar, $\dot{q}_w = 49.8$ kW m^{-2}, $\dot{m}_T = 292.8$ kg m^{-2} s^{-1}.

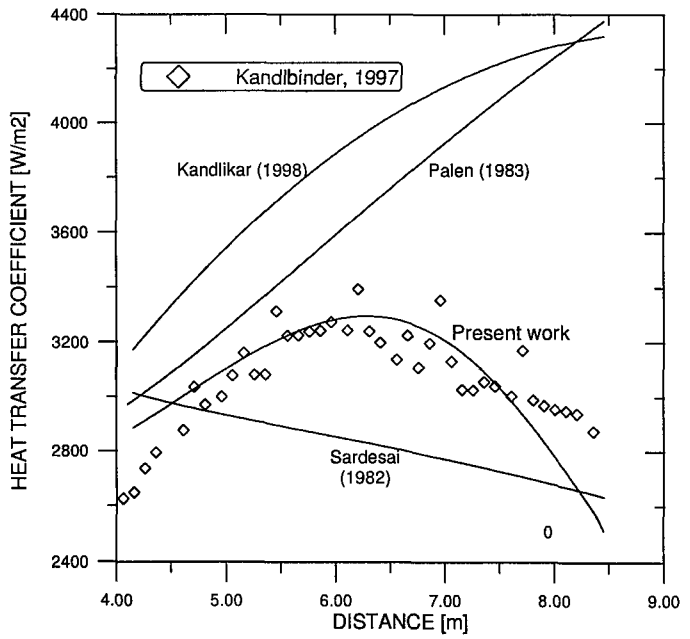


Figure 4.34: Predictions of local heat transfer coefficients by various methods; mixture 1, $p = 3.2$ bar, $\dot{q}_w = 49.3$ kW m^{-2}, $\dot{m}_T = 305.0$ kg m^{-2} s^{-1}.

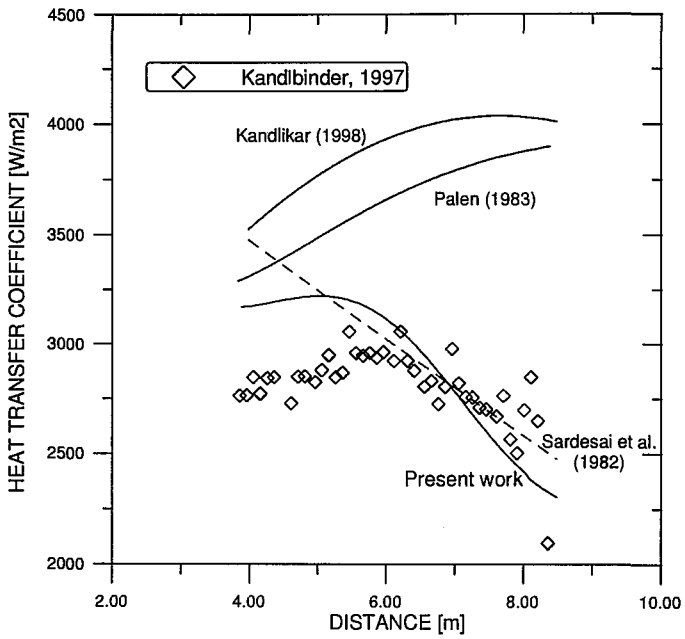


Figure 4.35: Predictions of local heat transfer coefficients by various methods; mixture 1, $p = 6.1$ bar, $\dot{q}_w = 60.2$ kW m^{-2}, $\dot{m}_T = 295.0$ kg m^{-2} s^{-1}.

$$\alpha_{av} = \frac{1}{L_A} \int_0^{L_A} \alpha dz. \tag{4.100}$$

The agreement of the proposed model is very good, with the majority of data being predicted within a ± 20% error band. The effects of system pressure, total mass flux and wall heat flux are presented in Figs. 4.37 to 4.39. The predicted heat transfer coefficients were obtained using an initial entrained fraction of 10%, this being a value close to that estimated for hydrodynamic equilibrium (equal entrainment and deposition rates).

The prediction of average heat transfer using other methods is also analysed in Fig. 4.36. The methods by Chen (1963) using the Palen and Small (1964) mixture correction factor (Chen/Palen), Murata and Hashizume (1993), and Kandlikar (1998) are compared with Kandlbinder's database. As will be seen, the performance of the present methodology is much better than that of the models above.

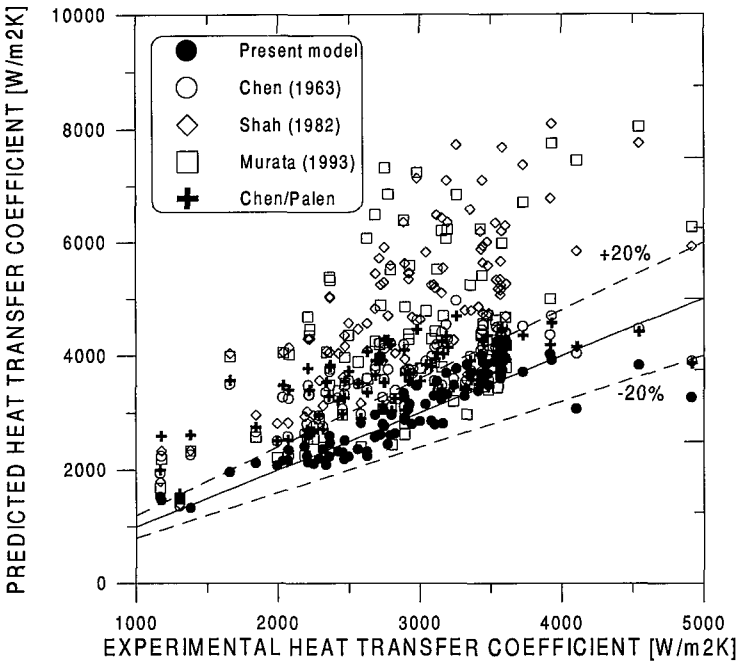


Figure 4.36: Predictions of average heat transfer coefficient.

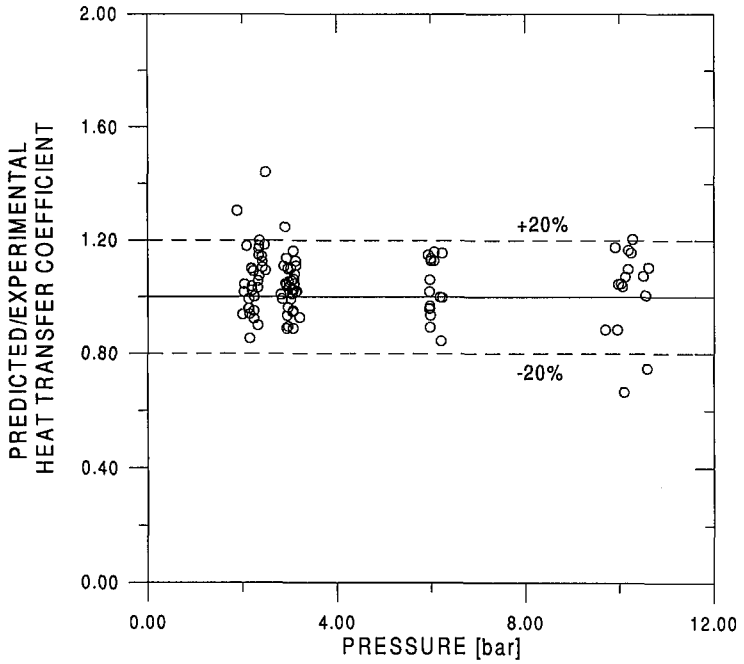


Figure 4.37: Behaviour of average heat transfer coefficient predictions with pressure.

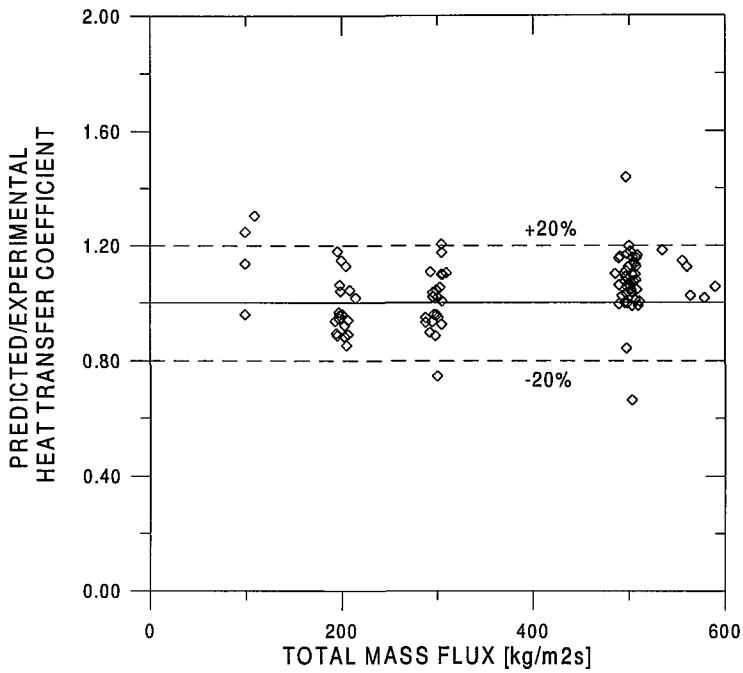


Figure 4.38: Behaviour of average heat transfer coefficient predictions with total mass flux.

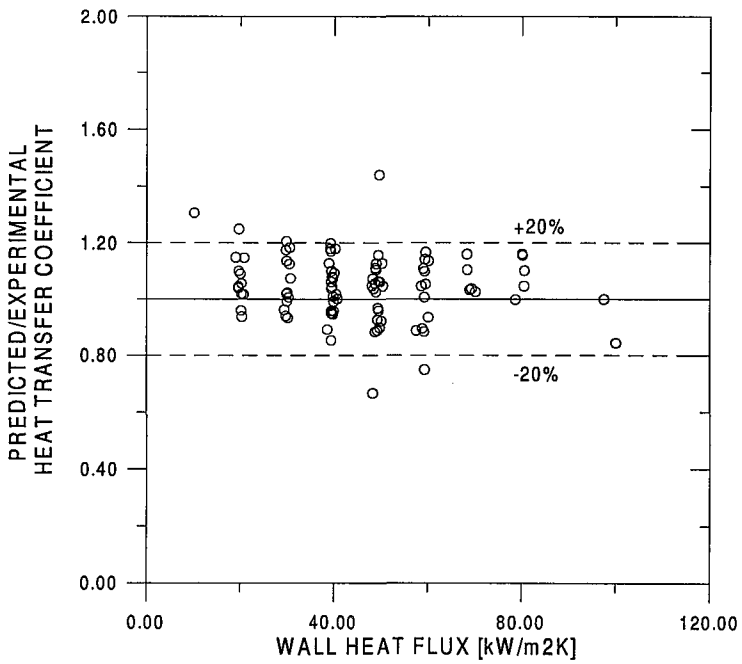


Figure 4.39: Behaviour of average heat transfer coefficient predictions with wall heat flux.

Heat transfer results for ternary mixtures

Figures 4.40 and 4.41 illustrate typical variations of liquid phase (film and droplets) mean concentration and of bulk and interfacial vapour concentration calculated using an interactive formulation. As will be seen in Figs. 4.42 and 4.43, which show typical plots of the interaction parameters Ip_1 and Ip_2, interaction effects are not important for the cases studied. For other runs, the values of Ip_i were never higher than 10^{-3}. Therefore, for the conditions evaluated, diffusive interaction effects are not relevant.

Figures 4.44 and 4.45 show the predictions of wall, interface and core temperatures for different initial entrained fractions at various conditions. A variation in the initial entrained fraction provokes an opposite effect in the behaviour of mean temperatures; higher values of initial $\dot{m}_{LE}$ induce lower profiles of T_C and higher profiles of T_I. As observed in the binary mixture temperature predictions, the measured temperature trends are well picked up by the formulation, but the agreement somewhat decreases with increasing pressure.

The measured heat transfer coefficients (calculated by introducing the known wall heat flux, the measured wall temperature and the calculated value of T_E into Eq. 4.1) are compared with those calculated using the present methodology in Figs. 4.46 and 4.47. Again, the capability of the formulation at predicting the decrease in the heat transfer coefficient with increasing quality is well observed.

The predictions in Figs. 4.44 to 4.47 were obtained applying the Effective Diffusivity Method. As seen before, the difference between the results given by this method and those given by the Interactive Method is negligible. The computing time, however, is as expected, shorter for the Effective Diffusivity Method.

As far as diffusion interaction effects are concerned, it can be seen that the effective diffusivity methodology can, at least for the hydrocarbon mixture analysed, be considered satisfactory. There is some evidence (Copati and Krishna, 2000) that this may not be the

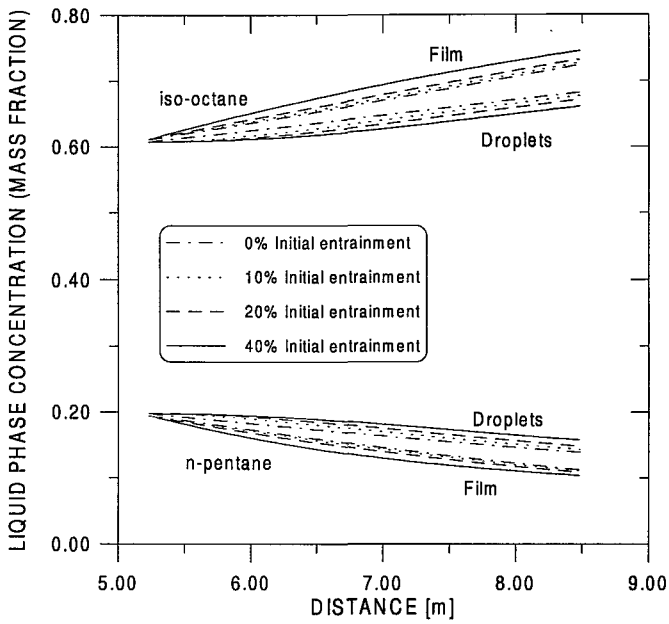


Figure 4.40: Profiles of liquid phase concentration; mixture 3, $p = 2.3$ bar, $\dot{q}_w = 40.5$ kW m^{-2}, $\dot{m}_T = 297.5$ kg m^{-2} s^{-1}.

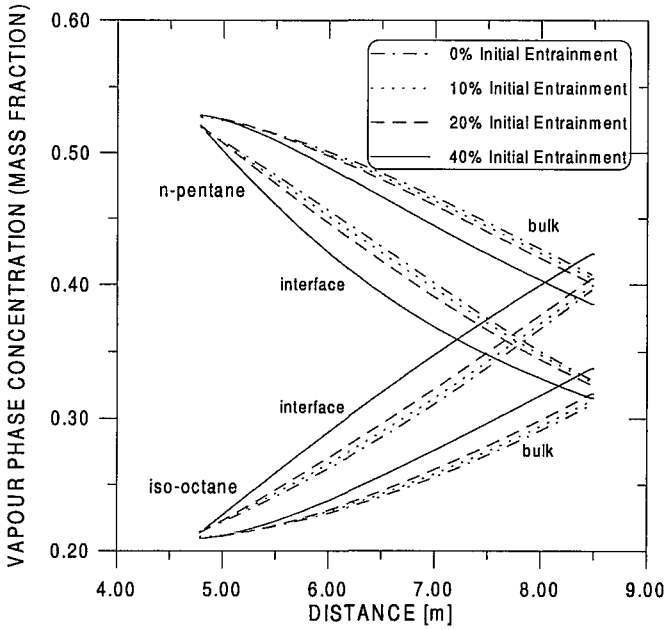


Figure 4.41: Profiles of vapour phase concentration; mixture 3, $p = 2.3$ bar, $\dot{q}_w = 40.5$ kW m^{-2}, $\dot{m}_T = 297.5$ kg m^{-2} s^{-1}.

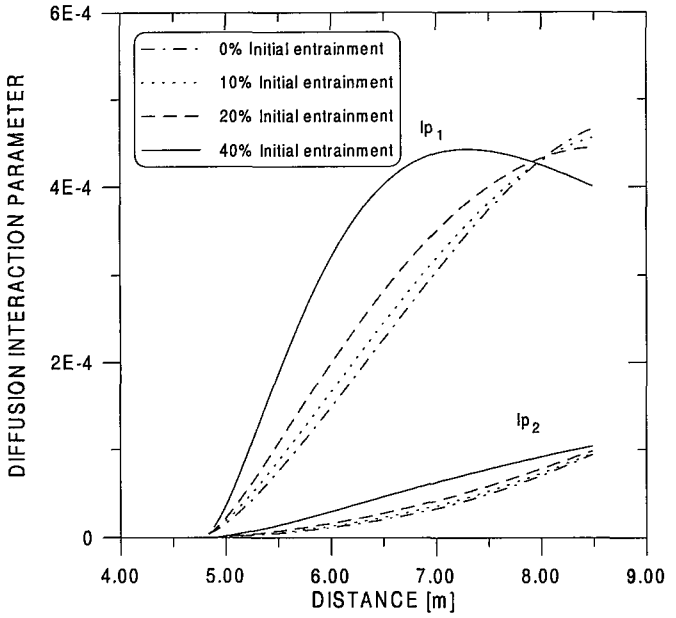


Figure 4.42: Distributions of Diffusion Interaction Parameters; mixture 3, $p = 3.1$ bar, $\dot{q}_w = 49.5$ kW m^{-2}, $\dot{m}_T = 296.0$ kg m^{-2} s^{-1}.

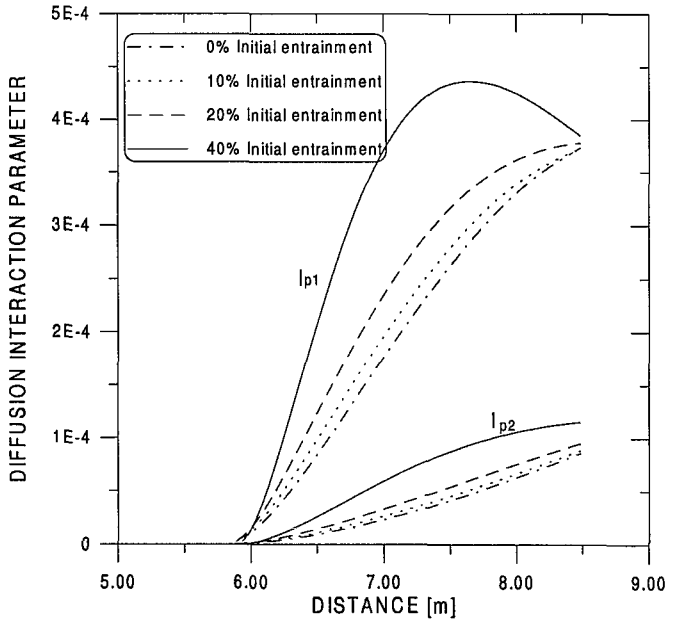


Figure 4.43: Distributions of Diffusion Interaction Parameters; mixture 3, $p = 6.0$ bar, $\dot{q}_w = 48.9$ kW m^{-2}, $\dot{m}_T = 300.5$ kg m^{-2} s^{-1}.

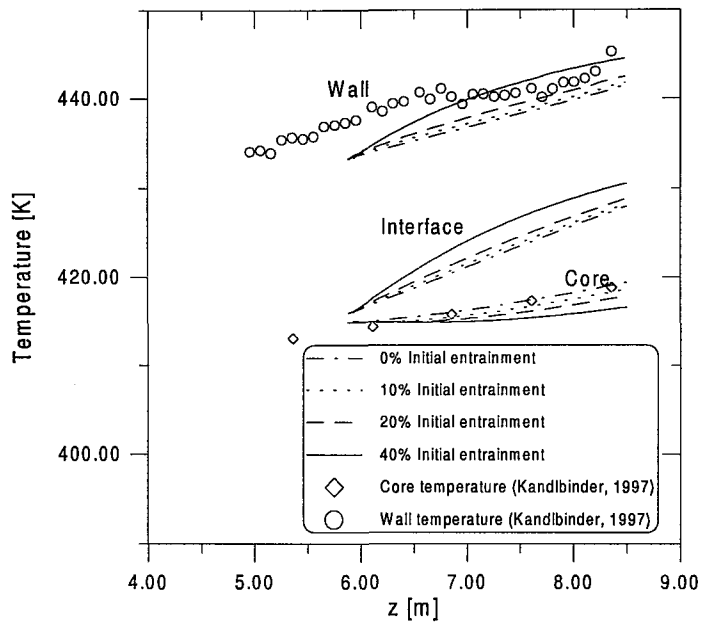


Figure 4.44: Distributions of wall, interface and core temperatures; mixture 3, $p = 6.0$ bar, $\dot{q}_w = 48.9$ kW m^{-2}, $\dot{m}_T = 300.5$ kg m^{-2} s^{-1}.

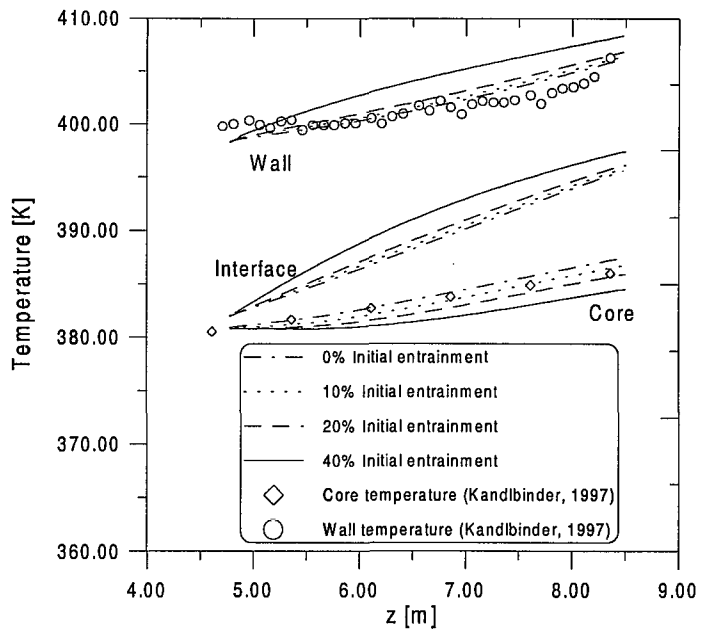


Figure 4.45: Distributions of wall, interface and core temperatures; mixture 3, $p = 3.1$ bar, $\dot{q}_w = 49.5$ kW m^{-2}, $\dot{m}_T = 296.0$ kg m^{-2} s^{-1}.

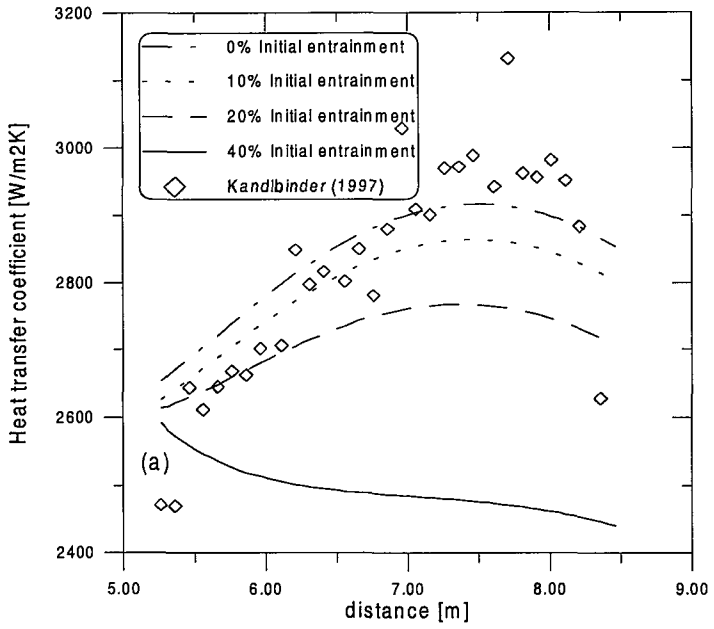


Figure 4.46: Heat transfer coefficient predictions; mixture 3, $p = 2.3$ bar, $\dot{q}_w = 40.5$ kW m^{-2}, $\dot{m}_T = 297.5$ kg m^{-2} s^{-1}.

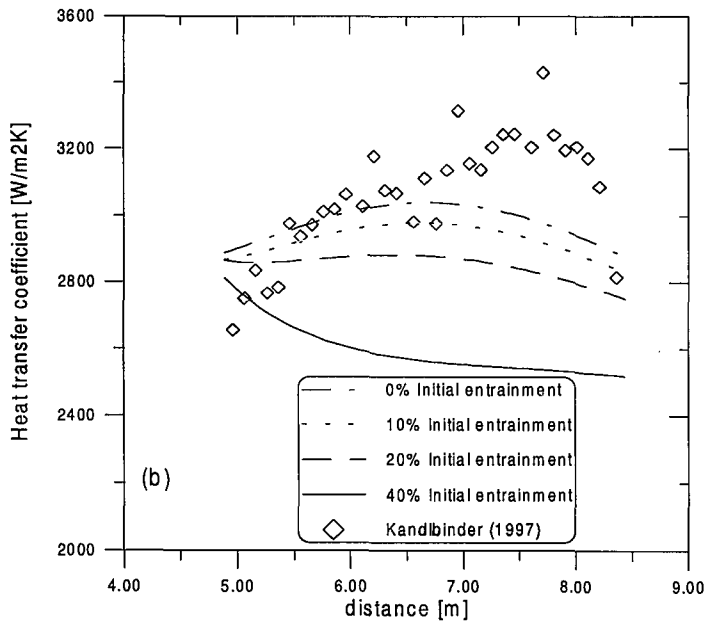


Figure 4.47: Heat transfer coefficient predictions; mixture 3, $p = 3.1$ bar, $\dot{q}_w = 49.5$ kW m^{-2}, $\dot{m}_T = 296.0$ kg m^{-2} s^{-1}.

case in condensation of mixed water and hydrocarbon vapours in the presence of an inert gas, where an effective diffusivity formulation gives an overprediction of the condenser area required for a specified condenser duty.

Figure 4.48 shows a comparison between experimental and predicted heat transfer coefficients averaged over the segment of pipe over which annular flow took place. The predictions obtained with the Chen (1963) correlation using the correction factor by Palen and Small (1964) for mixture effects are also shown for comparison purposes.

The agreement of the present methodology's results with the experimental data is also good for the ternary case, with the majority of data points lying within a ±20% error boundary. It was found that the data points from the proposed methodology that presented the largest deviation (outside that range) were those obtained at high pressure (10 bar), low total mass flow rate (100, 200 kg m^{-2} s^{-1}) and high wall heat flux (50, 60 kW m^{-2}). This may be due to presence of additional nucleate boiling or due to an unsuitability of some methods and correlations employed in the model to deal with higher pressures. Again, the predicted heat transfer coefficients were obtained using an initial entrained fraction of 10%.

The effects of system pressure, total mass flux and wall heat flux are investigated in Figs. 4.49 to 4.51. No particular trend is evident from any of these plots.

4.6.2 Dryout Prediction of Single Components and Mixtures

The occurrence of dryout is generally identified by an abrupt increase in wall temperature and this was captured by the wall thermocouples. In the simulation of the experiments by Kandlbinder (1997) the dryout position was given by the arithmetic mean between the position of the two thermocouples that recognised the temperature excursion. Figure 4.52 illustrates the wall and bulk temperature profiles of an experimental run in which

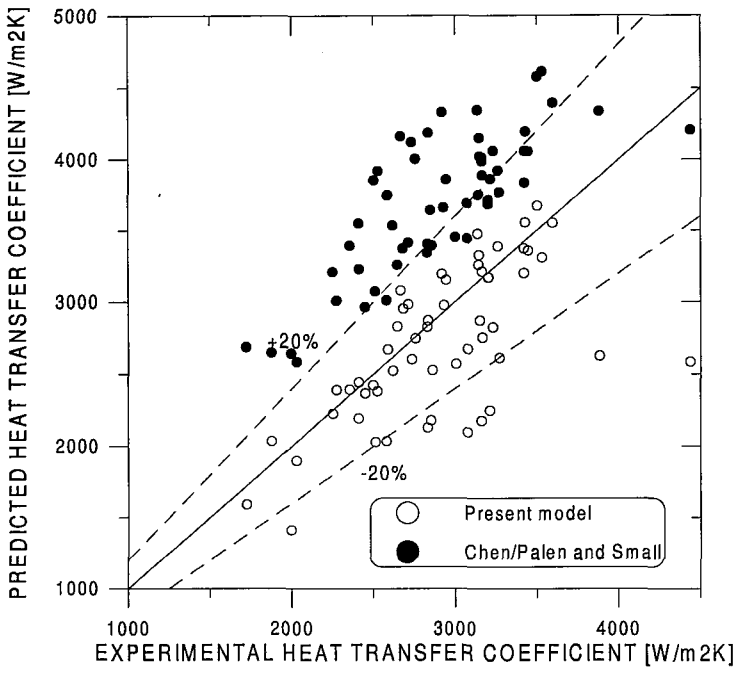


Figure 4.48: Predictions of average heat transfer coefficient in annular flow.

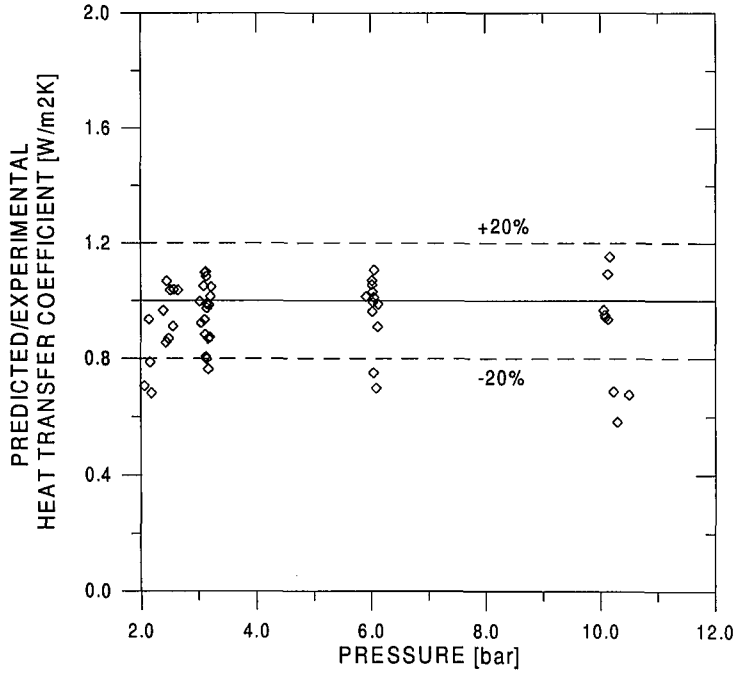


Figure 4.49: Behaviour of predicted average heat transfer coefficient with pressure.

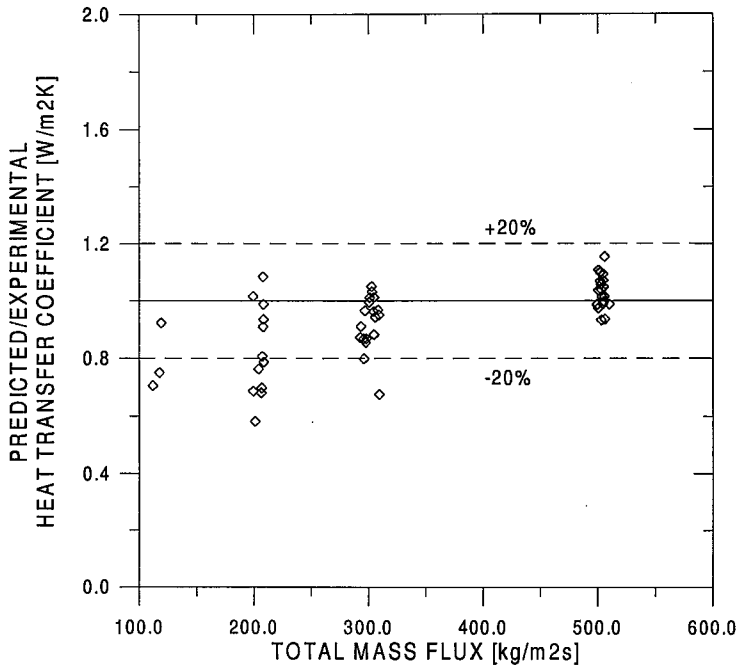


Figure 4.50: Behaviour of predicted average heat transfer coefficient with total mass flux.

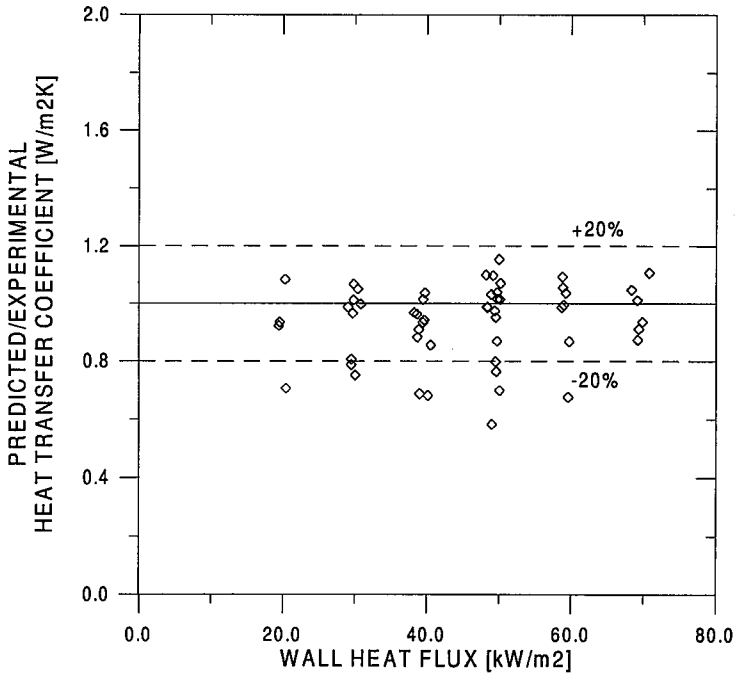


Figure 4.51: Behaviour of predicted average heat transfer coefficient with wall heat flux.

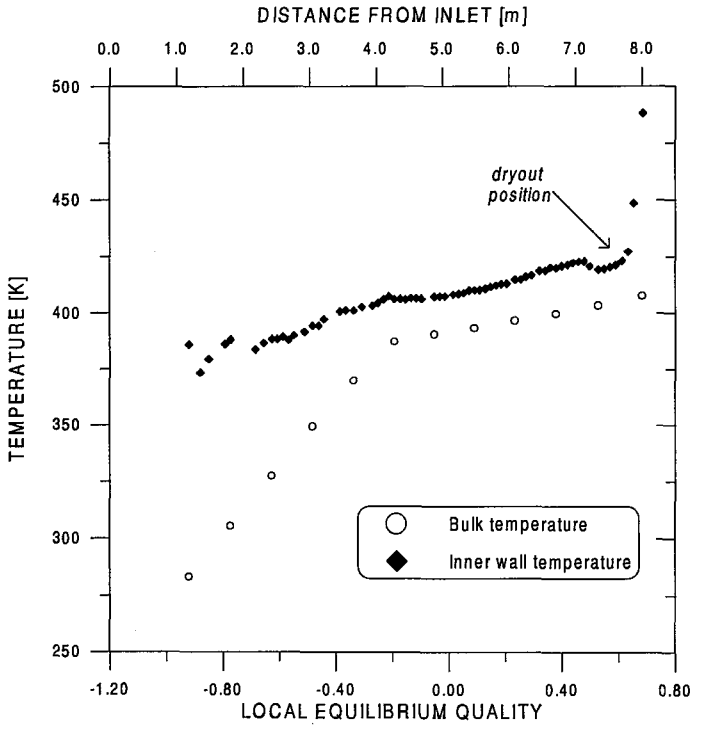


Figure 4.52: Temperature profiles in a run in which dryout occurred; mixture 1, $p = 6.1$ bar, $\dot{q}_w = 30.5$ kW m^{-2}, $\dot{m}_T = 92.3$ kg m^{-2} s^{-1}.

dryout took place. The experimental local quality (ratio between the vapour mass flow rate to the total flow rate) of the flow was calculated by means of a heat balance using the recorded values of absolute pressure to determine the latent heat of vaporisation of the flow. Critical quality is defined as the quality at which CHF (dryout) occurs.

For heated tubes, it has been demonstrated (Bennett *et al.*, 1967) that dryout takes place when the liquid film flow rate proceeds smoothly to zero, i.e., when the entrainment flow rate equals the total liquid flow rate. The predicted critical quality (in both single and multicomponent systems) is thus given by,

$$X_{cr} = \frac{\dot{m}_{GC}}{\dot{m}_{GC} + \dot{m}_{LE}}, \tag{4.101}$$

at the point where dryout takes place.

The critical heat flux is defined by,

$$CHF = \frac{\dot{m}_T d_T \Delta h_v}{4z} \left[X_{cr} + \frac{cp_L \left(\Delta T_{sub}\right)_{inlet}}{\Delta h_v} \right]. \tag{4.102}$$

Critical quality

A comparison between experimental and predicted critical qualities is shown in Figs. 4.53 and 4.54. The calculated values were obtained by applying the annular flow model with the Govan *et al.* (1988) entrainment and deposition correlations. A non-conservative over-prediction of the dryout quality can be observed for both single components (n-pentane and iso-octane) and for the binary and ternary mixtures. There are several possible reasons for such discrepancies, all of them in some way related to an inadequacy of the entrainment and deposition correlations for the hydrocarbon systems being studied here. Originally, the correlations were not developed for hydrocarbons. Most of the data used by Govan *et al.* (1988) (also Govan, 1990) to develop the entrainment and deposition correlations were obtained from aqueous, adiabatic systems. 98% of the deposition data were acquired using air-water flows. Therefore, it is expected that the method will not be so successful in predicting droplet interchange in fluids with so different physical properties. Particularly, as far as low surface tension fluids are concerned (the values of surface tension for hydrocarbons are approximately 5 to 10 times less than that of water), the prediction of entrainment and deposition rates and of entrained fraction (Willets *et al.*, 1986) is really very poor.

The presence of a heat flux may itself affect the droplet entrainment and deposition rates. Two specific mechanisms can be recognised, (i) the radial motion of steam due to vaporisation at the film interface, $\dot{m}_I$, may inhibit the deposition of droplets on the interface; (ii) if the heat flux is sufficient to cause generation of vapour bubbles at the

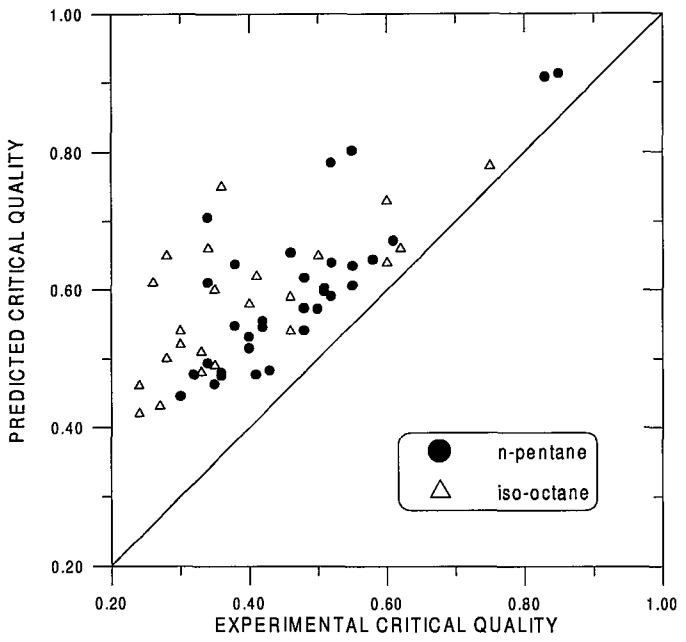


Figure 4.53: Predictions of critical quality for single components.

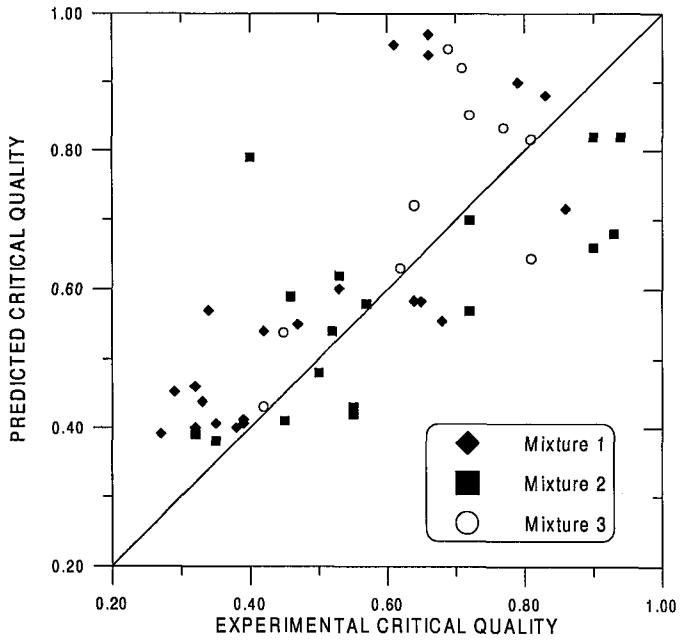


Figure 4.54: Predictions of critical quality for mixtures.

solid wall within the liquid film, then these bubbles can burst through the film giving rise to extra entrainment. These effects, often termed heat flux effects, were quantified by Milashenko *et al.* (1989), who observed an increase in the total entrainment rate with increasing wall heat flux in high pressure, high flow rate steam-water systems. Milashenko *et al.* produced a dimensional correlation for the change in net entrainment rate resulting from the heat flux in the form,

$$E_t = 1.75\frac{\dot{m}_{LF}}{4\pi}\left(\dot{q}_w \times 10^{-6}\frac{\rho_G}{\rho_L}\right)^{1.3}. \tag{4.103}$$

As most of Govan's entrainment data were obtained for adiabatic systems, the entrainment rate correlation given by Govan (1990) may characterise only the contribution of hydrodynamic effects (break-up of crests of disturbance waves due to vapour shear and shock entrainment due to droplet deposition) to the total entrainment rate. For diabatic steam-water systems, Govan (1990) used Eq. 4.103 in conjunction with Eqs. 2.35 and 2.37 and obtained good predictions of CHF.

An attempt to estimate the value of the entrainment rate due to heat flux effects for the conditions of the present study was carried out using Eq. 4.103. However, values of $\dot{q}_w$ employed in Kandlbinder (1997) experiments are much lower than those evaluated by Milashenko *et al.* (1989) and Govan (1990). This lead to the calculation of very low heat flux induced entrainment rates (several times less than the dynamically induced rate). This fact leaves an open question concerning the importance of heat flux induced entrainment in the hydrocarbon experiments. If heat flux effects are significant, then they are not well quantified by the empirical relationship of Milashenko *et al.* (1989). On the other hand, if the effects are not important, then the most likely reason for the over-prediction of the experimental data lies on the inadequacy of the entrainment and deposition correlations in dealing with non-aqueous systems. This question cannot be

totally answered in the light of the currently available experimental and modelling data.

A justification for neglecting the significance of heat flux induced entrainment (at least in the present work) is that bubble nucleation has already been assumed of secondary order in the heat and mass transfer calculations. The modelling results for wall and core temperatures and heat transfer coefficients were in good agreement with the experiments and it would be inconsistent to treat bubble nucleation as a governing phenomenon as far as droplet entrainment is concerned. Thus, one may suggest that the most likely reason for the critical quality over-prediction is the incapability of the entrainment and deposition correlations of dealing with hydrocarbons.

It can be seen from Fig. 2.6 that the air-fluoroheptane data ($\sigma = 0.012$ N m^{-1}) lie well below the best-fit line, suggesting that the deposition rate is lower in low surface tension systems. Furthermore, one can postulate based on the argument that droplet formation is facilitated in hydrocarbon systems (where the cohesion or surface tension forces are weaker), that higher entrainment rates are attained for the same value of gas superficial velocity.

Rates of entrainment and deposition are remarkably difficult to measure and, as there is considerable scatter in both correlations, the approach followed here was to add one standard deviation (+30%) to the entrainment and to subtract one standard deviation (−30%) from the deposition relationships. This would tend to give lower predicted critical qualities and therefore compensate the over-prediction of the CHF.

Figures 4.55 and 4.56 show the predicted versus experimental critical quality using the proposed correction for the entrainment and deposition correlations. Despite the scatter, it can be seen that the agreement has improved considerably. More detailed discussion of these results is presented in next two sections.

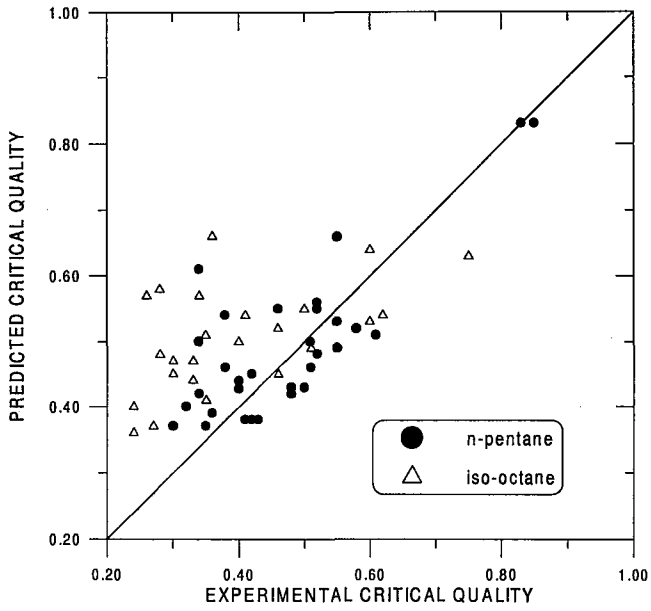


Figure 4.55: Predictions of dryout for single components using the modified entrainment and deposition correlations.

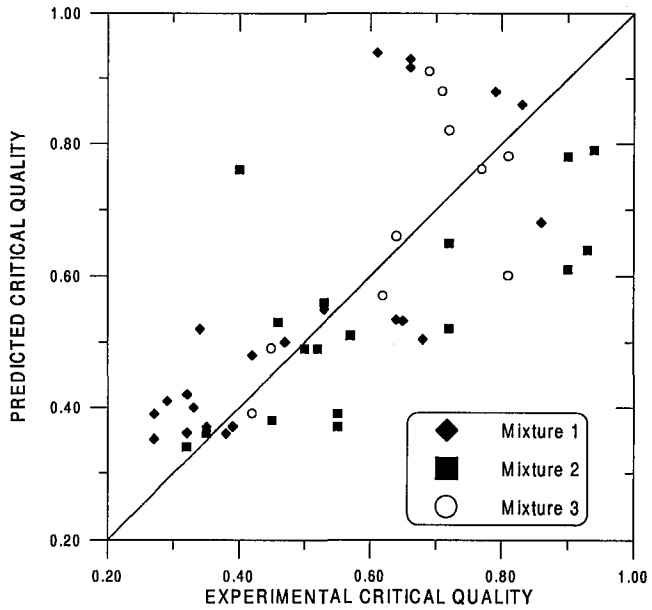


Figure 4.56: Predictions of dryout for mixtures using the modified entrainment and deposition correlations.

Single components

The ratio of experimental to predicted CHF is plotted as a function of pressure, inlet subcooling, total mass flux and wall heat flux in Figs. 4.57 to 4.59. The predicted values are those calculated using the droplet interchange correlations, enhancing the entrainment rate by 30% and decreasing the deposition rate by 30% as described above (the 30% value being chosen to represent the standard deviation). A non-conservative underprediction of the CHF is still observed for part of the data set. However, all the of the data is predicted by less than $\pm$ 25%.

Binary and Ternary Mixtures

As for the single component case, an underprediction of the CHF is observed in part of the binary and ternary mixtures data studied. Figures 4.60 to 4.62 show the ratio of experimental to predicted CHF as a function of pressure, inlet subcooling, total mass flux and wall heat flux. The scatter in the mixture predictions is higher than that for the single components and there appears to be a pattern in the variation of the experimental to predicted CHF ratio with inlet subcooling.

Figure 4.63 shows a typical variation of mixture surface tension calculated using the method by Sprow and Prausnitz (1967) with axial distance and with mean concentration of n-pentane (mass fraction) in the liquid film. Collier and Thome (1994) suggest that for positive binary mixtures, those in which the surface tension of the more volatile component is the lowest (van Stralen and Cole, 1979), breakdown of the liquid film into rivulets may occur somewhat earlier than for a pure liquid due to surface tension and temperature gradient effects (on the same grounds, breakdown may be delayed for negative mixtures). This fact may explain the additional underprediction of critical quality for some of the mixture data in Fig. 4.54. However, a more confident assertion cannot be made due to

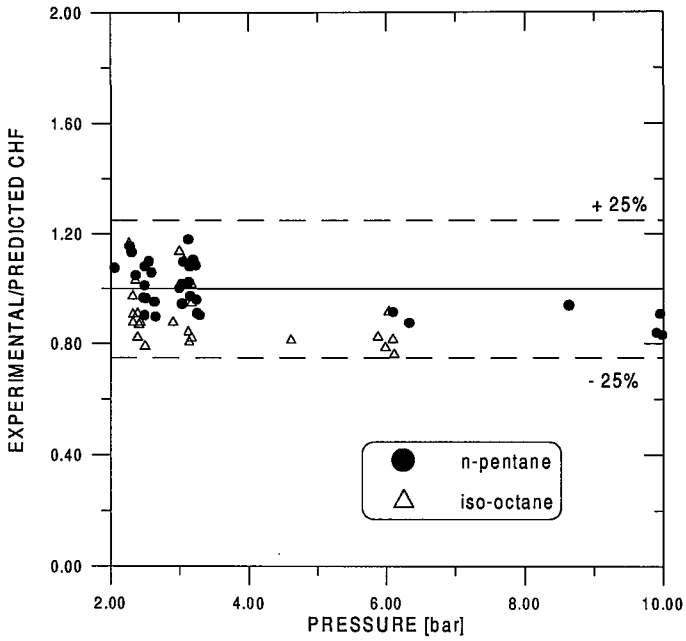


Figure 4.57: CHF versus pressure for single components.

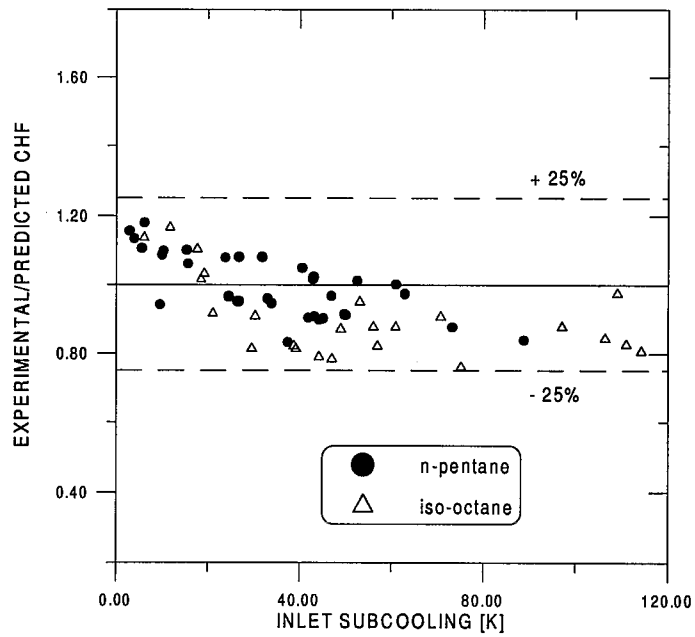


Figure 4.58: CHF versus inlet subcooling for single components.

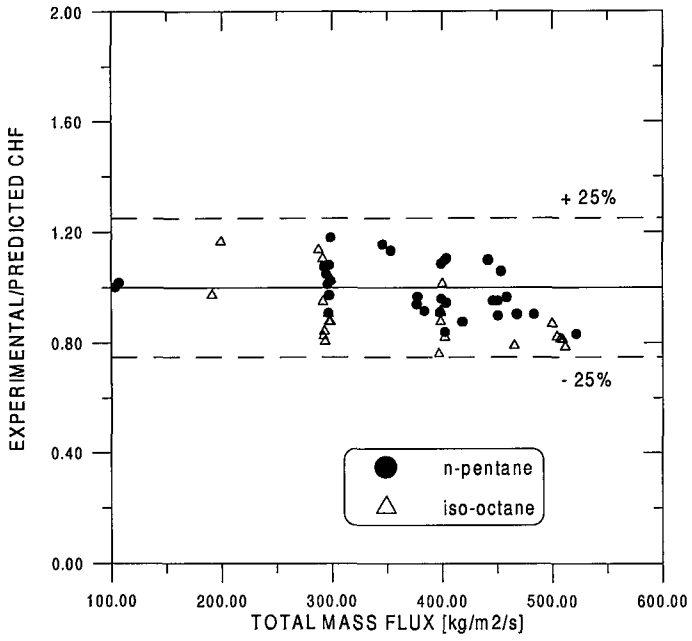


Figure 4.59: CHF versus total mass flux for single components.

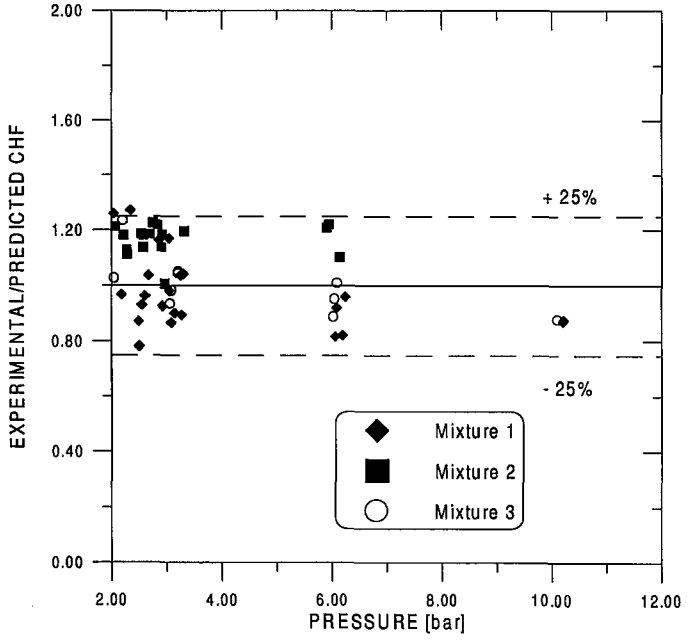


Figure 4.60: CHF versus pressure for mixtures.

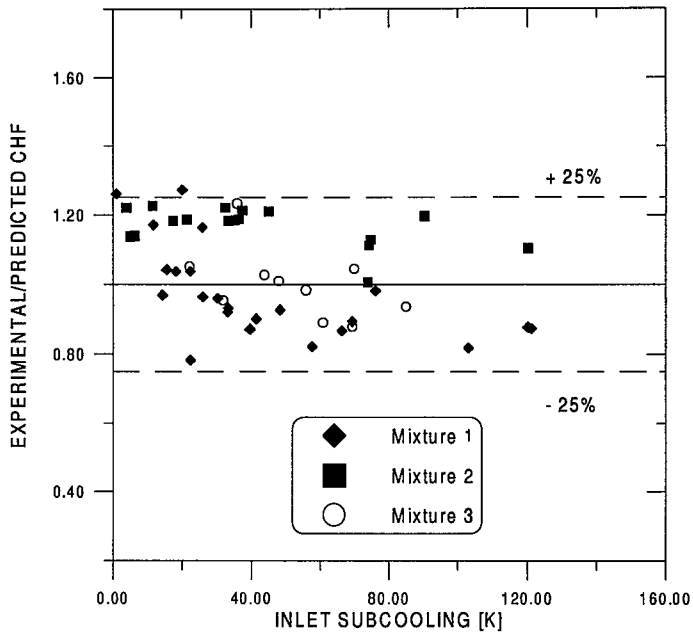


Figure 4.61: CHF versus inlet subcooling for mixtures.

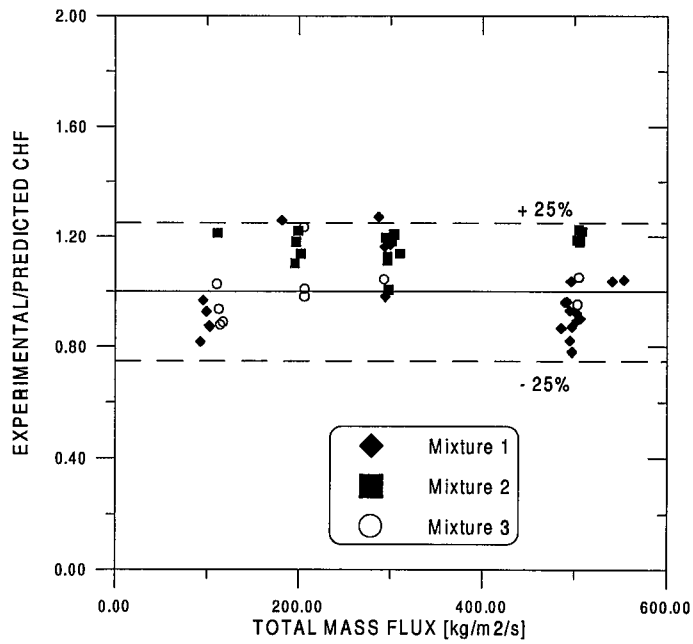


Figure 4.62: CHF versus total mass flux for mixtures.

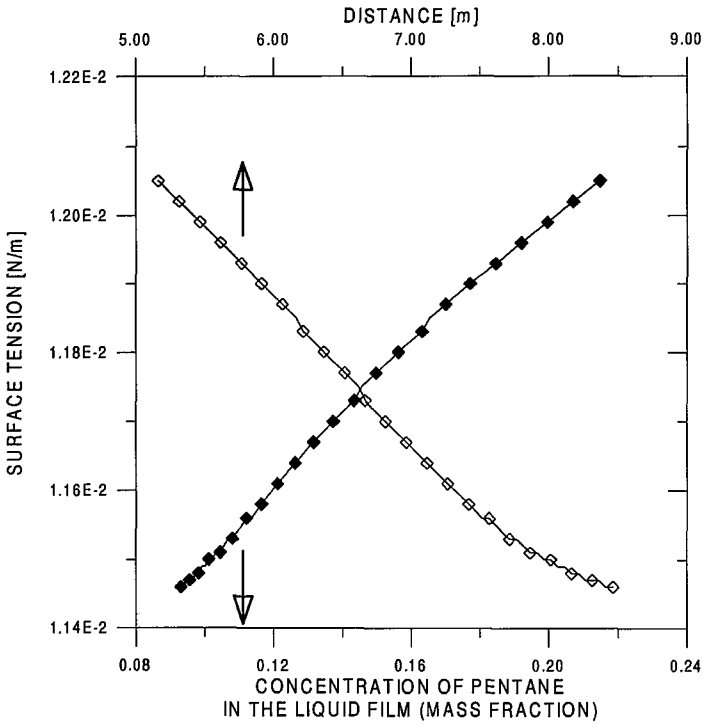


Figure 4.63: Variation of the surface tension of pentane/iso-octane mixture with axial distance and concentration; mixture 2, $p = 2.2$ bar, $\dot{q}_w = 49.3$ kW m^{-2}, $\dot{m}_T = 297.1$ kg m^{-2} s^{-1}.

the unsuitability of the entrainment and deposition correlations to hydrocarbon systems.

Influence of the modification to the interchange correlations on the heat transfer predictions

It will, of course, be true that the modification carried out in the droplet interchange equations (30% more entrainment, 30% less deposition) will also affect the heat transfer coefficient results. However, this effect is not as pronounced as that on the dryout prediction. An investigation of such effects has been performed and typical plots of local wall temperature and of local heat transfer coefficients predicted with and without the

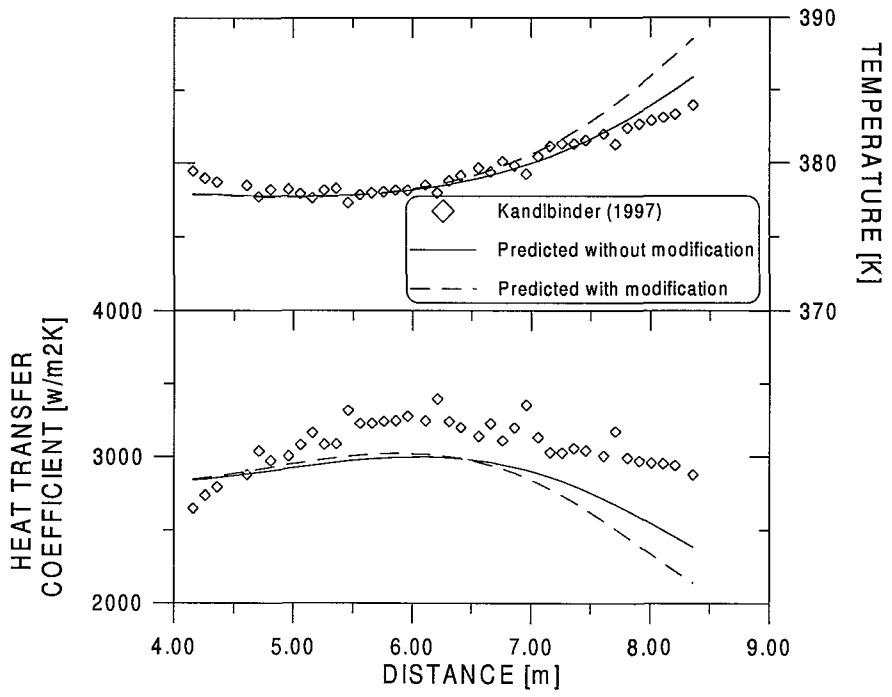


Figure 4.64: Illustration of the effects of the modification in the interchange correlations on the wall temperature and heat transfer coefficient predictions; mixture 1, $p = 3.2$ bar, $\dot{q}_w = 49.3$ kW m^{-2}, $\dot{m}_T = 305.0$ kg m^{-2} s^{-1}.

modification are shown in Fig. 4.64. Similar predictions were obtained for many other cases tested. For this particular run, the average experimental heat transfer coefficient is 3081 W m^{-2} K^{-1}, the average predicted heat transfer coefficient (10% initial entrainment) without modification is 2853 W m^{-2} K^{-1} and the average predicted heat transfer coefficient (10% initial entrainment) with modification is 2810 W m^{-2} K^{-1} (which corresponds to a difference of 1.5%).

CHF Predictions Using Other Methods

The Katto and Ohno (1984) CHF correlation was also implemented. This correlation has been tested for refrigerant (R12-R114) mixtures (Celata *et al.*, 1994) and gave a

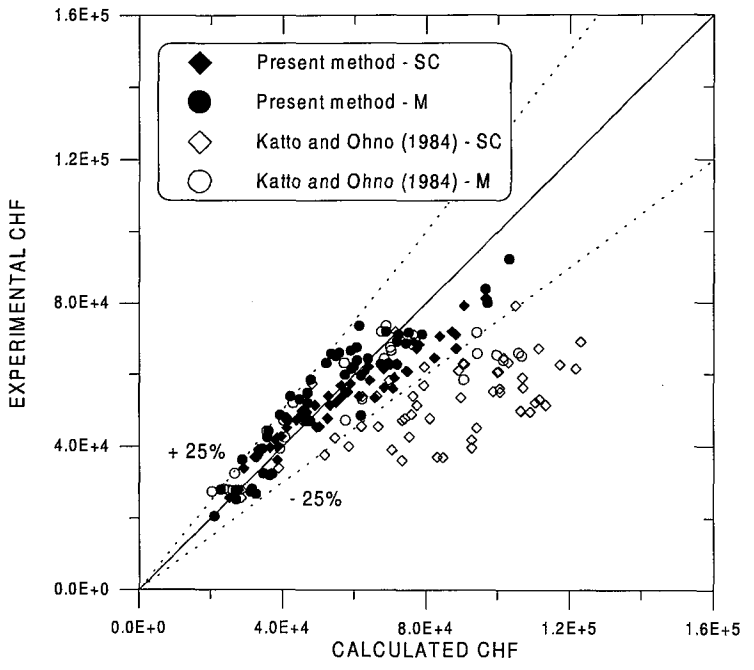


Figure 4.65: Comparison of calculated CHF using the present formulation and the correlation by Katto and Ohno (1984); SC, single component; M, mixture.

satisfactory performance (±15% with a systematic overprediction).

Figure 4.65 shows a comparison between the performance of the present methodology and that of Katto and Ohno's correlation. A much better agreement can be observed between the experimental data and the present analysis prediction. The Katto and Ohno correlation shows an over-prediction of the CHF for both single component and mixture data. The overall errors of the present method and of the Katto and Ohno's correlation is 11.4% and 48.4%, respectively.

4.6.3 Predictions of condensation data

As mentioned in an previous section, Cavallini *et al.* (2000) conducted condensation experiments using R-407C (a non-azeotropic ternary mixture of R-32, R-125 and R134a, the components having respectively, 23, 25 and 52 % by weight) at pressures of the order

of 17.0 bara in a 1 m long, horizontal stainless steel double pipe test section. The inner diameter of the inner pipe was 8.0 mm and condensation of the test fluid was achieved by passing cold water through the outer annular gap. In the present study, care was taken so that the conditions analysed fell on the annular/semi-annular flow regime in the flow pattern map presented by Cavallini *et al.* (2000). Refrigerant and wall temperatures at the inlet and outlet of the test section were measured using thermocouples inserted at both the centre line of the inner tube and at the tube wall. The average condensation heat transfer coefficient is given by the ratio between the wall heat flux (obtained from the axial temperature gradient on the coolant side) and the logarithmic mean temperature difference between the two-phase mixture (dew point temperature) and the pipe wall.

Figure 4.66 illustrate typical variations of mean concentration in the film and in the droplets for condensation of R-407C. The effect of hydrodynamic non-equilibrium can be observed in both cases. In the boiling cases, as the quality increases, the droplets become richer in the more volatile component than the liquid film. In condensation, the film gets richer in the more volatile component(s) as the quality increases.

As mentioned before, the relative changes in concentration for the R-407C case are not very large. However, in order to compare the results for condensation and evaporation, it is convenient to compare a case where the flow, pressure and composition are similar to one of the cases addressed for evaporation is Section 4.6.1. Here, we chose the case of mixture 1 with a pressure of 2.3 bar and a total mass flux of 292.8 kg m^{-2} s^{-1}; the results for temperature profiles in evaporation for this case are shown in Fig. 4.18. For the condensation case we assumed that saturated vapour enters the tube and is condensed. Here, annular flow exists immediately and the initial entrained fraction is zero. The results for film and drop concentrations for the condensation and evaporation cases are compared in Figs. 4.67 and 4.68. As will be seen, the expected reversal of the concentration differences in the drops and film is observed. In the case of condensation, the differences

as smaller but still significant. The smaller effect in condensation may be due to a joint effect of mass transfer resistance on the vapour side. Further analysis is required on this matter.

The analysis was used to predict the data of Cavallini *et al.* (1999) and comparisons of average experimental and measured values are shown in Fig. 4.69 for three different total mass fluxes, namely 200, 400 and 750 kg m^{-2} s^{-1}. The agreement between experimental and predicted data is satisfactory, with deviations always lower than $\pm$ 20%.

4.7 Summary

This chapter presented a model for forced convective boiling in annular flow of binary and multicomponent mixtures in vertical pipes. The deterioration in the local heat transfer coefficient observed by Kandlbinder (1997) were successfully predicted by the theory, which takes account of both concentration differences between drops and film and also mass transfer effects in the vapour core. The analysis was also applied in a preliminary way to the multicomponent case. Conclusions will be drawn in Section 7.2.

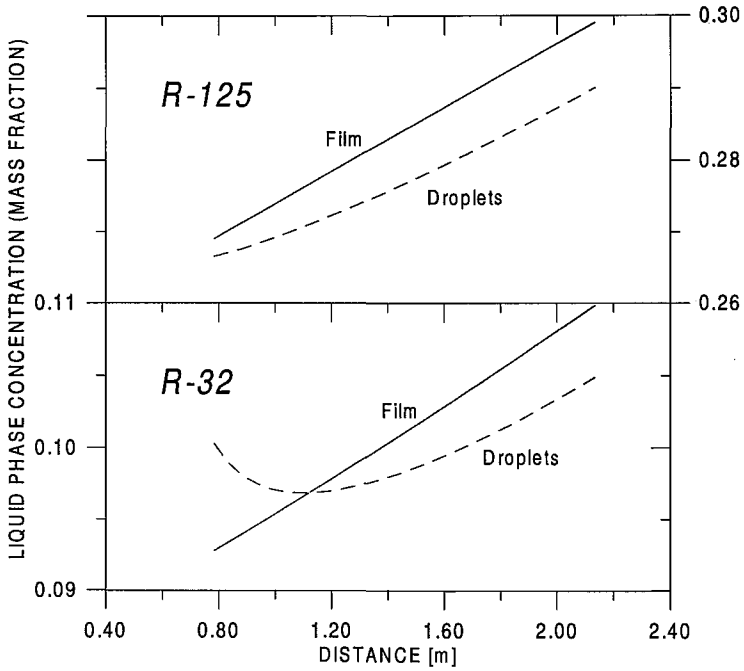


Figure 4.66: Liquid film concentration in condensation. R-407C, $p = 17$ bar, $\dot{q}_w = -33.7$ kW m^{-2}, $\dot{m}_L = 402$ kg m^{-2} s^{-1}.

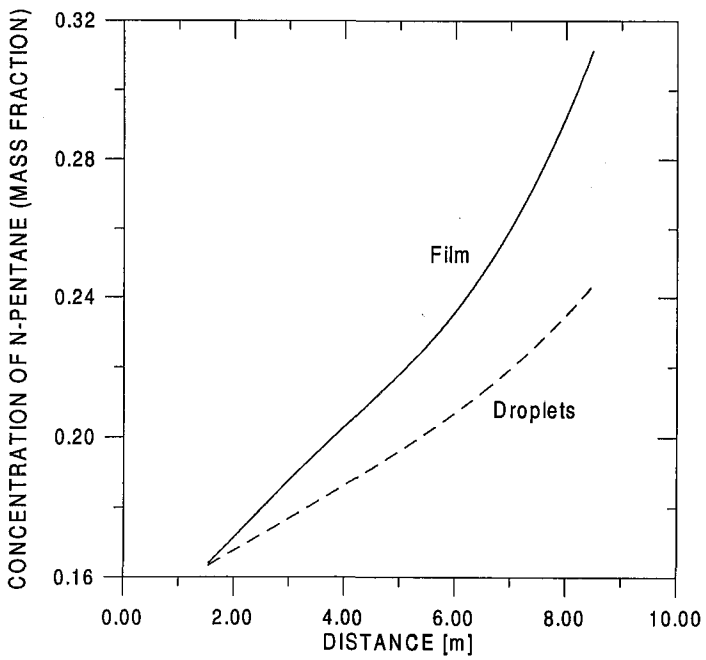


Figure 4.67: Liquid film and droplet concentration in condensation (hypothetical case); mixture 1, $p = 2.3$ bar, $\dot{q}_w = -49.8$ kW m^{-2}, $\dot{m}_L = 292.8$ kg m^{-2} s^{-1}.

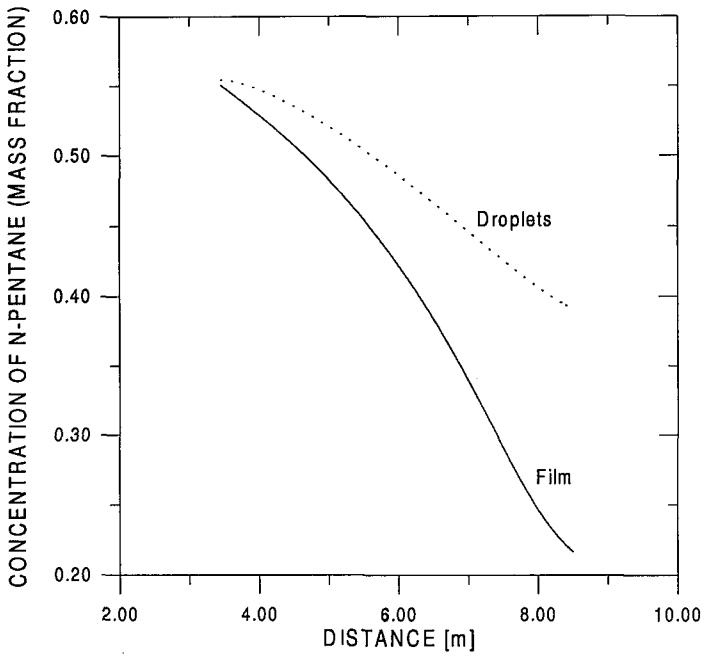


Figure 4.68: Liquid film and droplet concentration in evaporation (initial entrained fraction assumed equal to 10%); mixture 1, $p = 2.3$ bar, $\dot{q}_w = -49.8$ kW m^{-2}, $\dot{m}_L = 292.8$ kg m^{-2} s^{-1}.

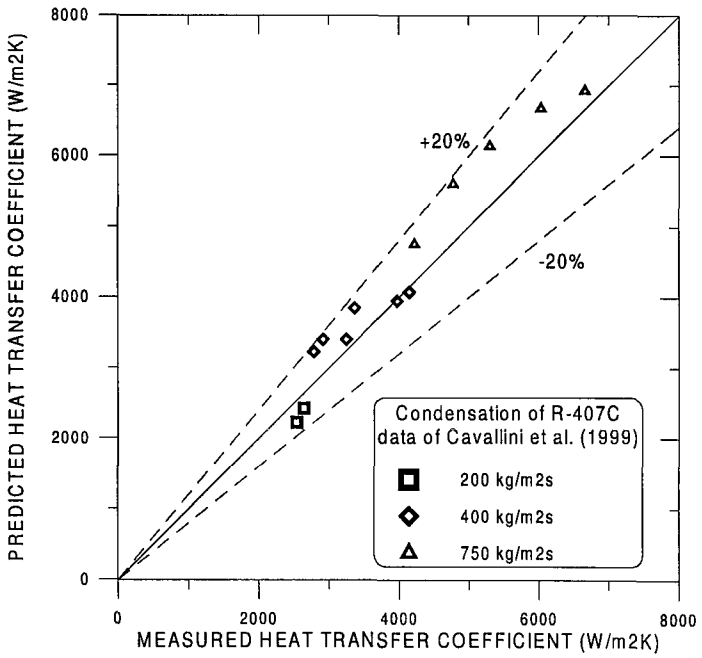


Figure 4.69: Prediction of condensation heat transfer coefficients for R-407C.

Chapter 5

Droplet Entrainment at the Onset of Annular Flow

This chapter presents an experimental study on droplet entrainment in churn flow with particular reference to establishing the entrainment at the transition from churn to annular flow in a vertical pipe. This value is needed for analyses of the type described in Chapter 4. In the first section of this chapter, some aspects of the churn-to-annular transition are addressed and the motivation for this study is presented. A brief review of earlier studies in which the objectives of the present work are brought into context is carried out in Section 5.2. Section 5.3 presents the experimental apparatus, the experimental technique and the experimental methodology. A specially constructed isokinetic probe system is used to measure the local radial mass fluxes of liquid and of gas. Results are presented in Section 5.4. An empirical correlation based on data obtained from this study and from the open literature is proposed so as to predict the fraction of liquid entrained as droplets at the onset of annular flow.

5.1 Introduction

In this chapter, as throughout this thesis, churn flow is defined as the regime occurring after the breakdown of slug flow. In the churn flow regime, there exists a thick, highly oscillatory liquid film which is swept by large flooding-type waves. Between the waves, the flow in the film reverses and there is a period of falling film flow until the next wave arrives. The gas core is continuous and there is a considerable amount of liquid entrained as droplets. As the gas flow rate increases, there is a cessation of downwards film flow giving rise to upwards, unidirectional annular flow.

As discussed in Section 2.2.2.c, a series of events which take place at the churn-annular boundary provide a number of possible criteria for correlating this flow pattern transition. Amongst these, the most common is the flow reversal point criterion. A simple expression to determine this is given by (Hewitt and Wallis, 1963; Wallis, 1969),

$$U_{GS}^{*} = U_{GS}\left[\frac{\rho_G}{g d_T\left(\rho_L - \rho_G\right)}\right]^{1/2} \approx 1. \tag{5.1}$$

Although parameters such as pressure gradient and wall shear stress are well characterised in the churn-annular region (Owen, 1986; Whalley and McQuillan, 1985; Govan, 1990), there is a dearth of experimental data on the mass fraction of the liquid flow initially entrained as droplets at the onset of annular flow. It is believed that this lack of experimental data may exist due to the following reasons,

1. the commonly acknowledged fact that the prediction of heat transfer coefficients and of critical heat flux (CHF) for annular flow of single component systems is only mildly affected by a variation of the initial entrained fraction. Such predictions are given by earlier (Whalley *et al.*, 1974) and more recent annular flow models (Govan, 1990);

2. the complex features of the liquid film in the churn-annular region make the application of experimental techniques that employ film removal devices (porous sinters, slits) very difficult. Hewitt (1978) described in detail the use of these techniques in cocurrent annular flow. More recently, Azzopardi and Zaidi (2000) pointed out the problems associated with the interpretation of entrainment measurements obtained using porous sinters under the flow conditions characteristic of churn flow.

Modelling results presented in Chapter 4 showed that, as opposed to single component systems, the role of the initial entrained fraction is a major one in determining the heat transfer coefficient and CHF in annular flow of mixtures. As seen before, the relationship existing between quality and saturation temperature at ideal hydrodynamic equilibrium conditions is broken down by liquid entrainment (see Figs. 4.3 and 4.4) and local differences in concentration between the liquid film and droplets develop significantly along the channel. This makes the knowledge of the initial conditions for mass conservation in annular flow very important to the correct description of the heat transfer behaviour of mixtures.

As discussed above, the use of techniques that do not rely on a direct measurement of the film flow rate to determine the initial entrained fraction may overcome the problem of measuring entrained flow in the churn-annular region. In this respect, techniques based on the collection of a sample of the droplet flow by means of a probe inserted in the gas core seem to be viable.

In a generic way, Azzopardi and Zaidi (2000) discussed the main disadvantages of the film suction and core sampling techniques. In the film suction technique, the entrained liquid flow rate is calculated by subtracting the film flow rate from the total liquid flow rate. In this method, problems are due to reproducibility of the results as well as to interpretation of the data (those of the fraction of liquid against fraction of gas taken

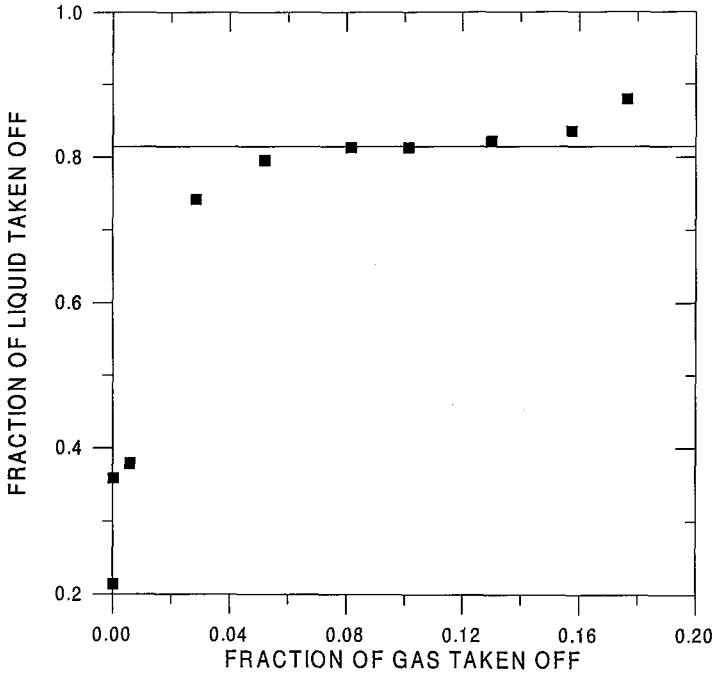


Figure 5.1: Results of take off through a porous wall section (air-water annular flow). $d_T = 0.032$ mm, $p = 1.5$ bara, $U_{LS} = 0.08$ m s^{-1}, $U_{GS} = 17.4$ m s^{-1} (Azzopardi and Zaidi, 2000).

off). As an illustration, Figs. 5.1 and 5.2 (Azzopardi and Zaidi, 2000) show plots of the rate of liquid extracted against the rate of extracted gas for flow conditions typical of the annular and churn flow region, respectively. In Fig. 5.1, there is a sharp rise in the fraction of liquid taken off and this is followed by an easily identifiable plateau (for values of the fraction of gas taken off from 0.05 to 0.13), where the fraction of liquid extracted is approximately independent of the fraction of gas extracted. In Fig. 5.2, the complication arises from the additional region of intermediate gradient. There are two interpretations for these data, (i) there is an apparent plateau that starts when approximately 20% of the gas has been extracted and gives an entrained fraction of 5%, and (ii) the film flow rate can be deduced from the intercept of the inclined line with the y axis. This gives an entrained fraction of 60%.

Difficulties with the core sampling techniques also exist and are mostly related to the

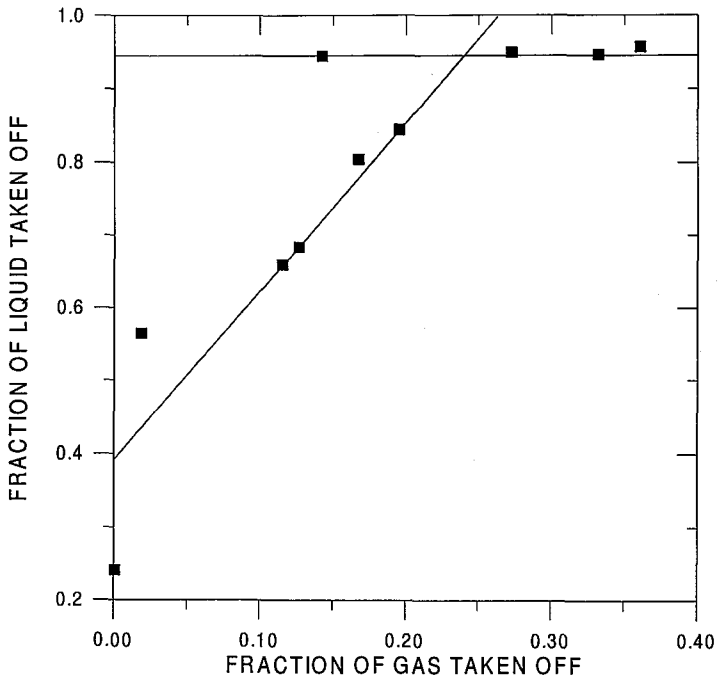


Figure 5.2: Results of take off through a porous wall section (air-water churn flow). $d_T = 0.032$ mm, $p = 1.5$ bara, $U_{LS} = 0.08$ m s^{-1}, $U_{GS} = 4.4$ m s^{-1} (Azzopardi and Zaidi, 2000).

setting of integration limits (when liquid can be erroneously withdrawn from the tip of the waves if the probe is placed too close to the fllm interface) and to droplet evaporation, which occurs when droplets pass to a lower pressure region outside the test section. The second problem is relevant to low liquid flow rates and Azzopardi and Whalley (1980) estimated the percentage of liquid evaporated during sampling by introducing a nonvolatile dye whose concentration is measured in both the collected liquid and the liquid in the test section.

In the present chapter, a core sampling technique that uses an *isokinetic probe* is employed so that simultaneous measurements of local entrained liquid and gas mass fluxes can be carried out. The experiments were performed in a vertical, adiabatic, air-water facility (LOTUS rig). The internal diameter of the test section is 31.8 mm and experimental conditions were such that considerable ranges of liquid mass fluxes and pressures were

covered. Typically, the superficial gas velocities were such that U_{GS}^{*} ranged from 0.5 to 1.7 (a value that is well into fully developed annular flow).

5.2 Background

Having explained the motivation for this study in Section 5.1, this section attempts to bring the practical objectives of the present experiments into the context of previous work in annular flow at low gas flow rates.

As seen in Chapter 2, Wallis (1962) provided the first information on the behaviour of the entrained fraction in the churn-annular flow region. He carried out experiments in a 12.7 mm internal diameter vertical pipe and his results are shown in Fig. 2.13 for both cocurrent upflow and downflow conditions.

Gill and co-workers (Gill *et al.*, 1963, 1964; Gill and Hewitt, 1966) presented a series of studies on the nature of the gas core in annular flow. They made use of a single sampling (Pitot-type) probe (1.57 mm internal diameter) which could be traversed both axially and radially in a 9 m long, 31.8 mm internal diameter vertical pipe. Air and water were used in the experiments. The flow rates ranged from 0.013 to 0.088 kg s^{-1} (16.3 to 110.8 kg m^{-2} s^{-1}) for air and 0.004 to 0.156 kg s^{-1} (5.0 to 196.4 kg m^{-2} s^{-1}) for water. Gill *et al.* measured the impact pressure, Δp_i, on the probe and, by assuming that the droplet-air mixture behaved homogeneously, they could use the well known Pitôt relationship given by,

$$\Delta p_i = \frac{1}{2}\rho_C U_M^2, \tag{5.2}$$

where,

$$U_M = \frac{\dot{m}_{LE} + \dot{m}_G}{\rho_C}, \tag{5.3}$$

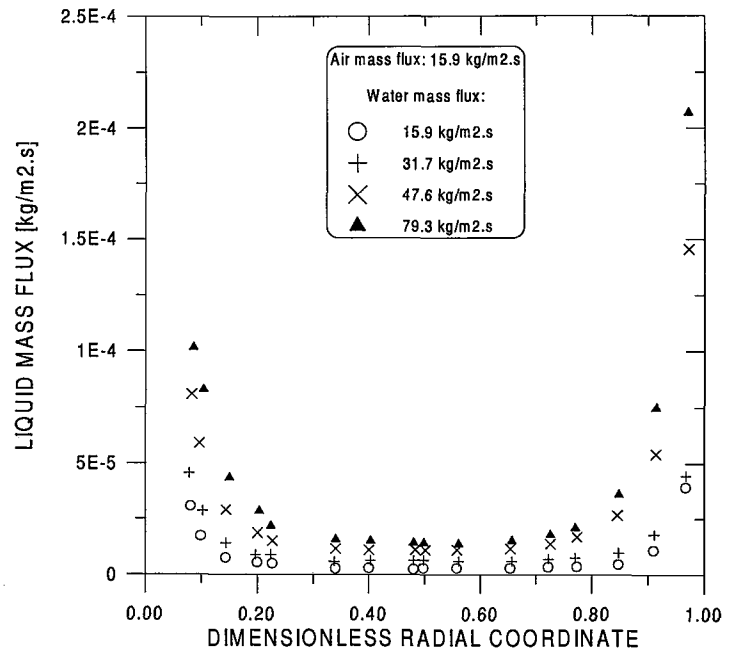


Figure 5.3: Local liquid mass flux profiles (Gill *et al.*, 1964).

and,

$$\rho_C = \frac{\rho_G \rho_L \left(\dot{m}_G + \dot{m}_{LE}\right)}{\left(\dot{m}_G \rho_L + \dot{m}_{LE} \rho_G\right)}. \tag{5.4}$$

Using the set of equations above, they could obtain the local gas mass flux, $\dot{m}_G$, from measurements of $\dot{m}_{LE}$ (the local droplet collection rate) and of Δp_i.

Gill *et al.* (1964) observed a different pattern of entrainment flow at low gas flow rates (0.013 kg s^{-1}). As it can be seen in Figs. 5.3 and 5.4, the low gas flow rate curve exhibit flat minima whereas that for high gas flow rate presents maxima at all water mass flow rates. Gill *et al.* found that this change in the nature of the curves is consistent with the approach to sub-annular regimes. They also observed a reversal in the effect of the air rate on entrainment; the data for 0.013 kg s^{-1} of air ($U^*_{GS} \approx 0.67$) showing consistently a higher entrainment than those for 0.026 kg s^{-1} ($U^*_{GS} \approx 1.34$). The entrained fraction would subsequently increase with increasing gas flow rate. Again, they attributed this behaviour to churn flow.

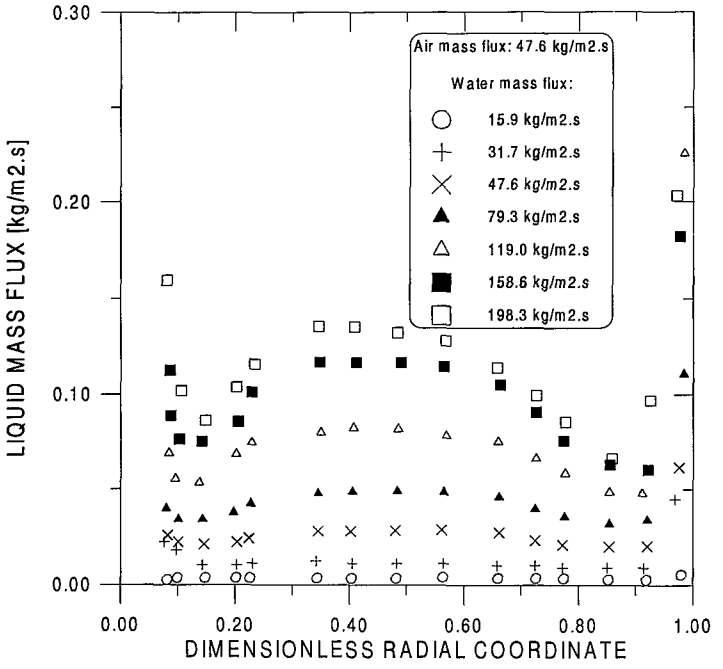


Figure 5.4: Local liquid mass flux profiles (Gill *et al.*, 1964).

As far as the measurements in the churn-annular region are concerned, Gill *et al.* (1964) reported that it was not possible to obtain reasonably satisfactory mass flux profiles because of the lack of precision in the readings of impact pressure. For $\dot{M}_G = 0.013$ kg s^{-1}, the impact pressure was, at the maximum, only 10 mm of water. They concluded that due to the high fluctuations imposed by the approach to churn flow it was not possible to measure the pressure differential accurately, even with a highly damped manometer. It is believed that the use of an isokinetic probe connected to an acquisition system in which electronic signal filtering and damping can be applied would allow more accurate measurements in this region. These issues are explored further below.

Perhaps the most significant contribution of Gill *et al.*'s work is concerned with the behaviour of the local droplet concentration, C. C is defined as the ratio of the local liquid mass flux to the local linear homogeneous core velocity,

$$\mathsf{C}(r) = \frac{\rho_G \dot{m}_{LE}(r)}{\rho_L \dot{m}_G(r) + \rho_G \dot{m}_{LE}(r)}, \tag{5.5}$$

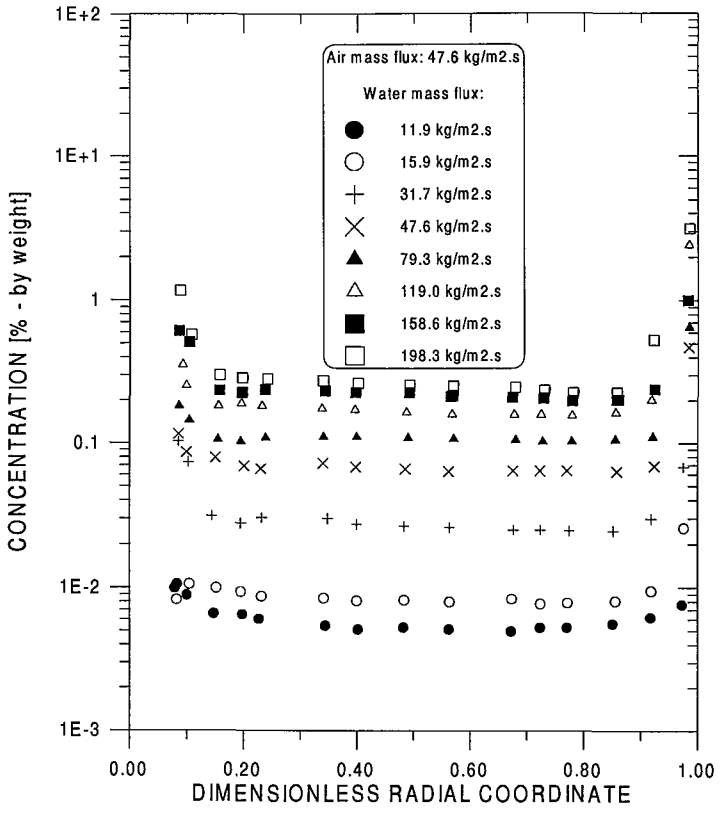


Figure 5.5: Local droplet concentration profiles (Gill *et al.*, 1964).

Gill *et al.* found that, apart from the regions very close to the wall, the concentration remains fairly constant across the tube at higher gas flow rates. This observation is consistent with the droplet diffusion equilibrium assumption often assigned to the behaviour of the droplet core. Furthermore, as it can be seen in Figs. 5.5 and 5.6, the concentration is virtually independent of the gas flow rate for fully cocurrent annular flow.

The question that remains partially unanswered since the work of Gill *et al.* (1964) is that concerning the behaviour of the local droplet concentration in the churn-annular region. Therefore, one of the goals of the present study is to investigate the behaviour of the droplet concentration at lower gas flow rates by making extensive measurements of localised mass fluxes of gas and liquid in the droplet core.

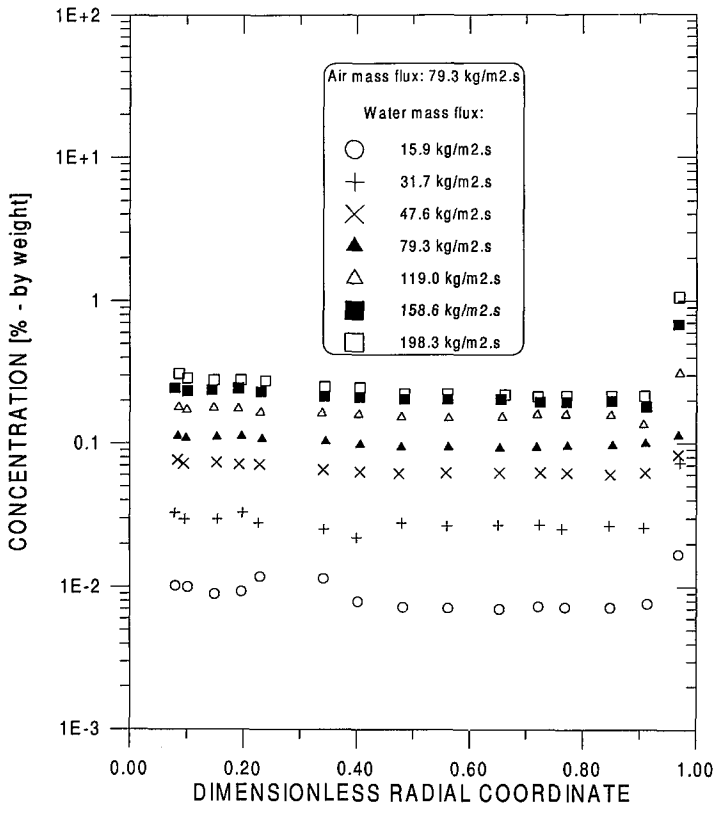


Figure 5.6: Local droplet concentration profiles (Gill *et al.*, 1964).

5.3 Experimental apparatus

5.3.1 The LOTUS Facility

A schematic diagram of the LOTUS (Long TUbe System) air-water facility is shown in Fig. 5.7. The facility consists of a 10.8 m long, 31.8 mm (1.25") internal diameter vertical copper tube. The tube is made up of sections of various lengths which were attached to an accurately aligned vertical fixed beam.

Air supplied from the site mains at approximately 7.5 bara is fed to the bottom of the tube via a large radius U-bend and and measured using a differential pressure transducer connected to either of two lines. One of 50.8 mm (2") internal diameter, the other of 76.2 mm (3") internal diameter. Both lines contained changeable orifice plates and calming lengths which conformed to BS1042. During the course of this investigation, the 50.8

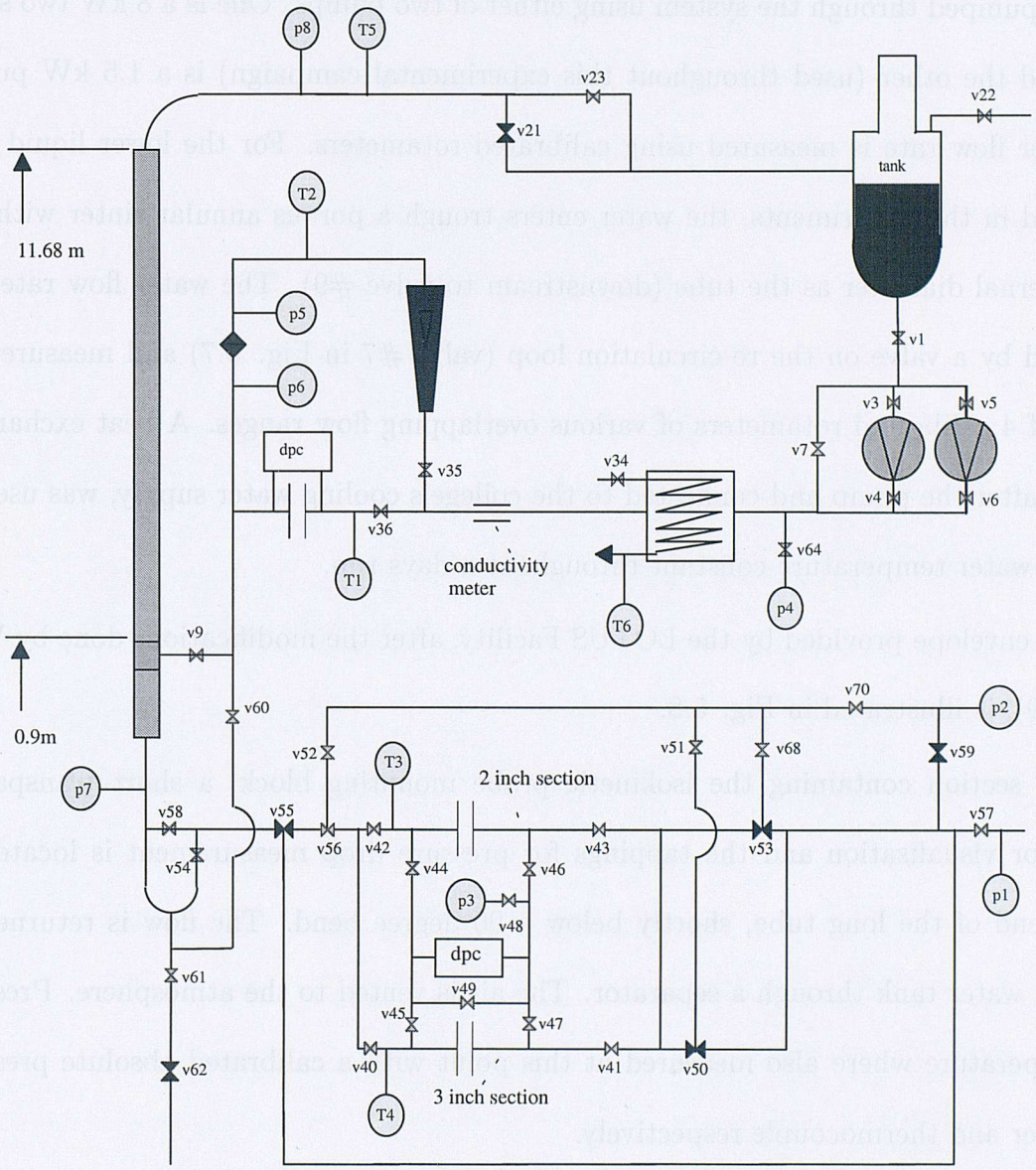


Figure 5.7: A diagram of the LOTUS air-water facility.

mm internal diameter line (in which a 25 mm diameter orifice plate was installed) was employed. The 76.2 mm internal diameter air line had a 31.8 mm diameter plate and was not used.

Water is pumped through the system using either of two pumps. One is a 8 kW two stage pump and the other (used throughout this experimental campaign) is a 1.5 kW pump. The water flow rate is measured using calibrated rotameters. For the lower liquid flow rates used in the experiments, the water enters trough a porous annular sinter with the same internal diameter as the tube (downstream to valve #9). The water flow rate was controlled by a valve on the re-circulation loop (valve #7 in Fig. 5.7) and measured by a bank of 4 calibrated rotameters of various overlapping flow ranges. A heat exchanger, situated after the pump and connected to the college's cooling water supply, was used to keep the water temperature constant throughout a days run.

The flow envelope provided by the LOTUS Facility, after the modifications done by Watson (1999), is illustrated in Fig. 5.8.

The test section containing the isokinetic probe mounting block, a short transparent section for visualisation and the tappings for pressure drop measurement is located at the top end of the long tube, shortly below a 90 degree bend. The flow is returned to the main water tank through a separator. The air is vented to the atmosphere. Pressure and temperature where also measured at this point with a calibrated absolute pressure transducer and thermocouple respectively.

Appendix C describes the operating instructions for the LOTUS Facility.

5.3.2 Pressure gradient measurement

The pressure gradient was evaluated using Eq. 5.6, where Δp is the pressure drop between two points distant Δz_{tap} along the test section. A differential pressure transducer (Druck

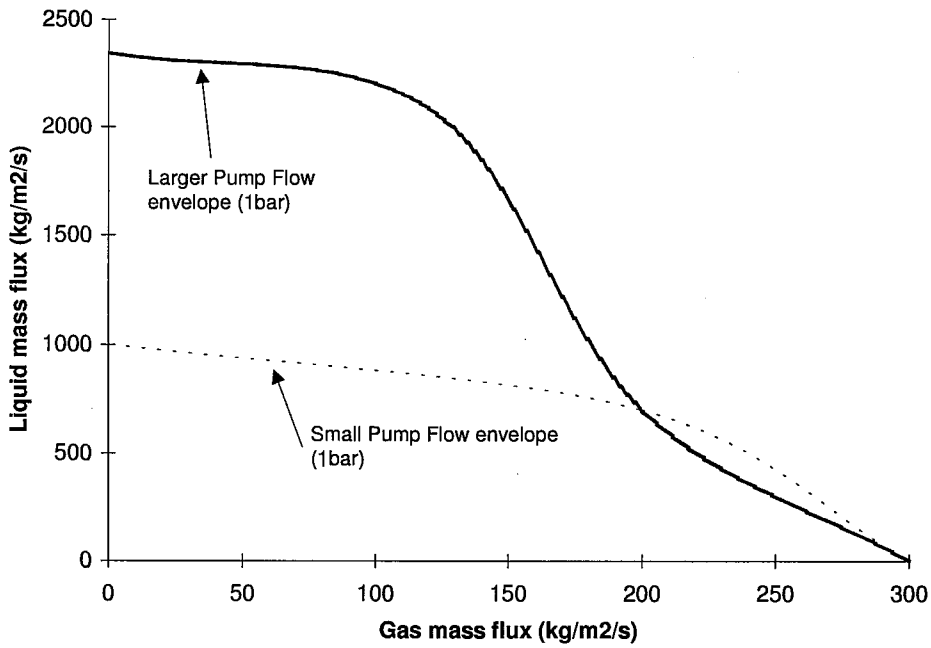


Figure 5.8: Operating range of the LOTUS Facility (Watson, 1999).

PMP4170) connected to two pressure tappings (3 mm internal diameter) was used for such a measurement. An absolute pressure transducer (Druck PMP4171) was also connected to one of the tappings. The distance between the tappings is 830 $\pm$ 1 mm.

$$\frac{dp}{dz} \approx \frac{\Delta p}{\Delta z_{tap}}. \tag{5.6}$$

A liquid purge system (Hewitt, 1978) was installed to avoid ambiguities in the pressure drop measurements associated with the presence of two phases in the tapping lines (see Fig. 5.9). The lines were kept free of gas bubbles by passing a very small liquid flow rate through them. The flow rates to each tapping were kept at a constant and identical value (via needle valves and calibrated rotameters) so as to avoid dynamic pressure differences due to the flow in the lines. The tapping flow rates are of the order of 0.1% to 1% of the liquid flow rate supplied to the test section and these are added to the supplied flow rate

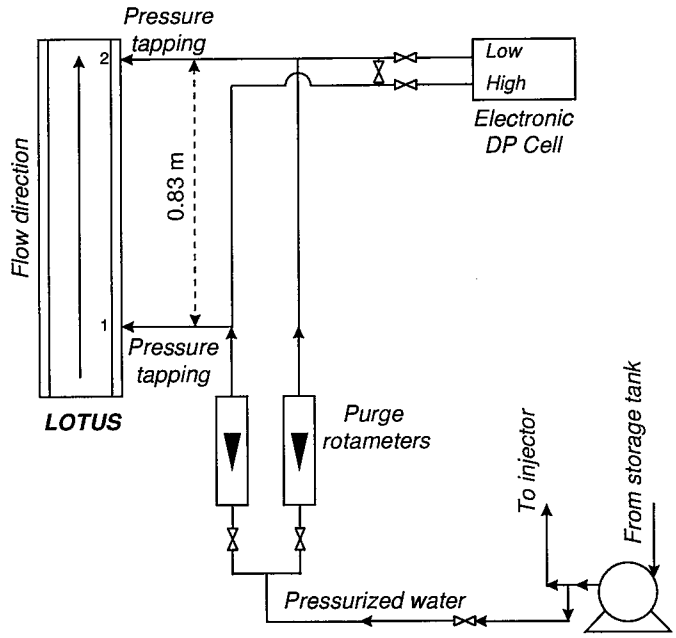


Figure 5.9: Schematic diagram of the liquid purge system.

to find the total liquid flow rate.

The signals from the absolute and differential pressure transducers were sent to a computer equipped with a data acquisition card. The sampling frequency was 1000 Hz and the data averaged over a period of approximately 10 s.

5.3.3 The Isokinetic Probe Technique

Working principle and applicability

The isokinetic sampling technique, shown in Fig. 5.10, is based on a single probe which is similar in structure to a Pitôt-static tube, but with a pressure tapping at the mouth, B, which measures the difference between the pressure in the mouth of the probe and the static pressure in the flow channel, S. The probe is mounted with its mouth facing the flow and the oncoming fluid is collected at a controlled rate. The rate of collection can be regulated so that the fluids enter the probe, A, in the same mixture proportions and

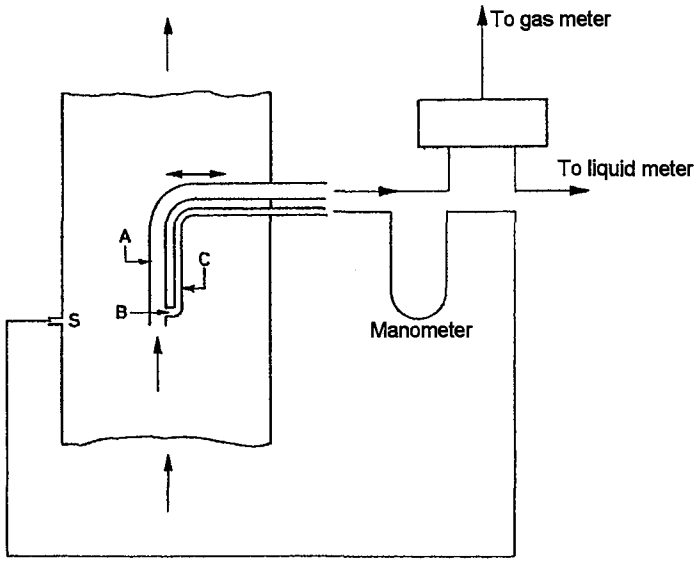


Figure 5.10: Isokinetic probe sampling principle.

at the same velocities as the flow would have in the absence of the probe. The *isokinetic* behaviour is achieved by establishing a collection rate which gives a null difference between the apparent dynamic pressure and the static pressure near the mouth of the probe, a condition indicating that (unless the velocity is *very* low — which is certainly not true for the present case) the velocity upstream and within the probe are identical.

The measured pressure difference when the collection rate is zero is the actual dynamic pressure of the fluid stream (as in a Pitôt-tube). There have been a number of models for interpretation of such pressures in two-phase flow (Schraub, 1969). However, in order to use this impact pressure measurement to obtain local information about the flow (e.g., slip), an independent assessment of the local void fraction, ε_G, is required. As no simultaneous measurements of ε_G were made in the present study, the probe was never operated under zero collection rate conditions.

Much of the earlier applications of isokinetic probes in two-phase flows was devoted to high quality gas-liquid systems (Gill *et al.*, 1963; Adorni *et al.*, 1963; Cousins and Hewitt, 1968).

For various geometries, these studies attempted to investigate the complex phenomena in the droplet laden gas core of annular flow.

Recently, Khor (1998) carried out a thorough review of the literature on the use of isokinetic probes. Khor covered in detail the usage of isokinetic sampling in many other applications, such as bubbly flows, aerosols and submerged jets.

The probe

The isokinetic probe used in the present work is identical to that designed and used by Khor (1998). A schematic of the probe and the mounting section is presented in Fig. 5.11.

The probe is made of stainless steel and its main dimensions are shown in Fig. 5.12 and in Table 5.1. The horizontal length of the probe is 180 mm and the vertical stem is 300 mm. The sampling probe could be traversed across the pipe cross section by means of a screw turning mechanism. A fine thread screw adjustment allowed the probe to be positioned with an accuracy of approximately $\pm$ 0.2 mm.

Table 5.1: Dimensions of the isokinetic sampling probe.

Tube	Outer Diameter (mm)	Inner Diameter (mm)	Wall Thickness (mm)
Sampling	6.35	5.842	0.254
Wall Static Pressure	1.588	1.181	0.201
Probe Static Pressure	1.588	1.181	0.201

In the probe design exercise, Khor (1998) concluded that the pressure difference between the throat and the inside (probe static) tapping position was negligible. The ratio between the probe outer diameter and the pipe diameter is 0.2 and it is therefore likely that the

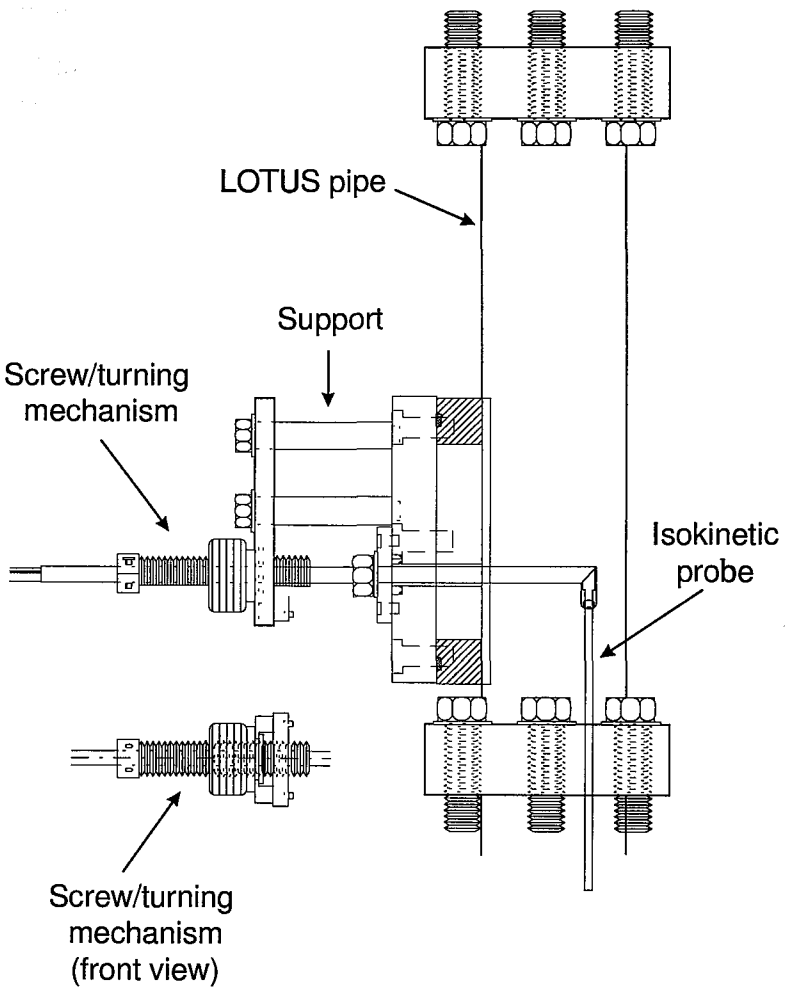


Figure 5.11: The isokinetic probe used in the present study and the mounting section. Not to scale (Khor, 1998).

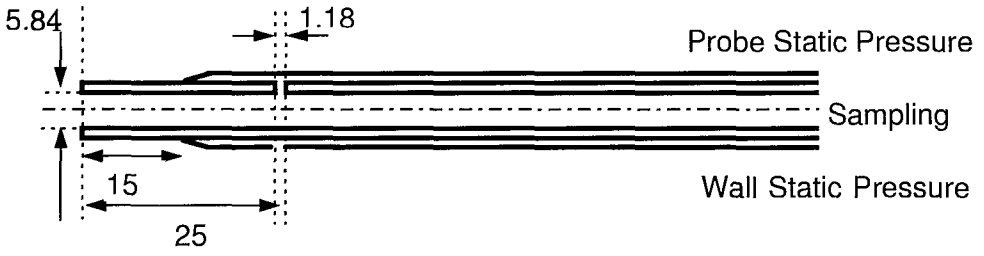


Figure 5.12: A detailed view of the tip of the isokinetic probe (Khor, 1998).

presence of the probe significantly affects the flow in the probe surroundings. Nevertheless, when the probe is operated at isokinetic conditions, the disturbances due to the probe are negligible and a measurement of the true flow conditions which would be present in the absence of the probe is achieved. This was described by Khor (1998) who carried out single phase air velocity measurements under zero collection rate and isokinetic conditions. Isokinetic single phase air tests were also performed by the present author in LOTUS. These are described in Section 5.4.5.

Measurement arrangement

The system for collection of entrained liquid and gas mass fluxes is schematically presented in Fig. 5.13. The two-phase sample collected by the probe is diverted via a 3-way valve into an acrylic resin gas-liquid separator. From the separator, the gas flowed to a calibrated rotameter. The liquid was accumulated in the separator for a given time interval (measured using a digital chronometer with an uncertainty of $\pm$ 0.05 s). After each measurement, the collected liquid was drained from the separator into a vessel whose weight was measured with an uncertainty of $\pm$ 0.005 kg before and after each collection. The collected liquid flow rate is given by the ratio between the weight of the collected

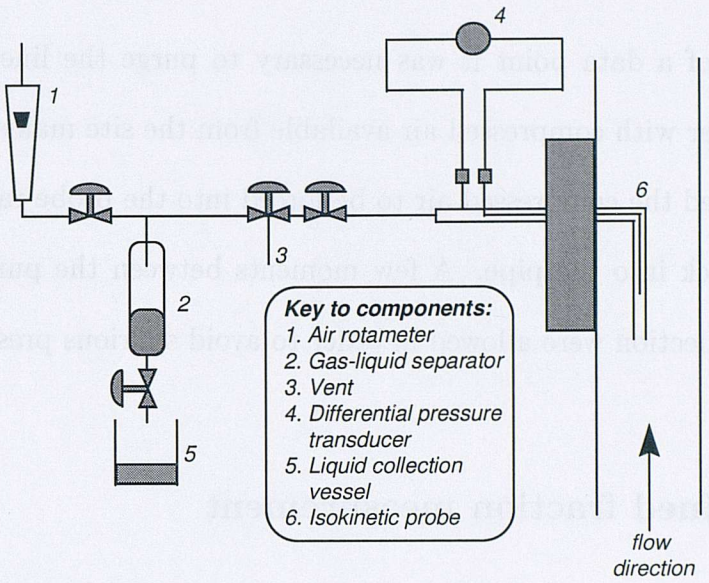


Figure 5.13: Experimental setup for gas and liquid collection using the isokinetic sampling probe.

liquid and the collection time interval.

The isokinetic operation condition was obtained by adjusting the manual needle valve until the difference between probe static pressure and the wall static pressure was zero. The probe tappings were connected to a pressure transducer (Rosemount 3051C) which was set to operate within the range −200 to 400 Pa. The electrical signal from the transducer was amplified (range 2 to 10 V) and then sent to a digital bench voltmeter (Keithley 195A). The voltmeter was equipped with filtering devices which were used to damp the severe signal fluctuations associated with churn flow. The uncertainty in the voltmeter reading was ± 0.01 V, which corresponded to ± 0.75 Pa.

As pointed out by Khor (1998), it is not sufficient only to have an accurate measurement of the differential pressure. Great care is also needed to ensure that the measurements are unambiguous; of crucial importance is that the lines connecting the differential pressure transducer to the pressure tappings on the probe are full of a known single phase. For the measurement of the pressure drop in the isokinetic probe, it was found that prior

to the collection of a data point it was necessary to purge the lines of the differential pressure transducer with compressed air available from the site mains. A system of valve connections allowed the compressed air to be forced into the probe tappings, purging the trapped liquid back into the pipe. A few moments between the purging operation and the data point collection were allowed in order to avoid spurious pressure fluctuations.

5.3.4 Entrained fraction measurement

The mass flow rate of liquid entrained as droplets, $\dot{M}_{LE}$, is calculated through an averaging of the local entrained liquid mass flux profile over the area of the gas core. Generally, the associated integration process has the difficulty that, as the probe approaches the liquid film it may intercept waves on the film which may be wrongly ascribed to entrainment. In the present study, the following procedure was carried out. Due to the relative size of the mouth of probe to the diameter of the tube, there were only five non-overlapping radial positions through which the probe could be traversed (see Fig. 5.14). Measurements were carried out at the three inner positions (shaded circles in Fig. 5.14) and the droplet fluxes in the outer positions (indicated by the dashed circle) were obtained via a linear extrapolation of the measured data points.

The integration of the local liquid mass flux profiles was carried out for the cases with and without extrapolation. It was found that approximately 11% was a representative value for the error associated with the integration of the extrapolated values. This is in accordance with the work of Asali *et al.* (1985), who also performed an extrapolation procedure and found that the maximum possible error (difference between the integrated extrapolated and not extrapolated profiles) was 18%.

Based on modelling predictions of the critical amplitude of interfacial waves characteristic of the churn-annular region (see Table 6.1), it is believed that the region covered by the

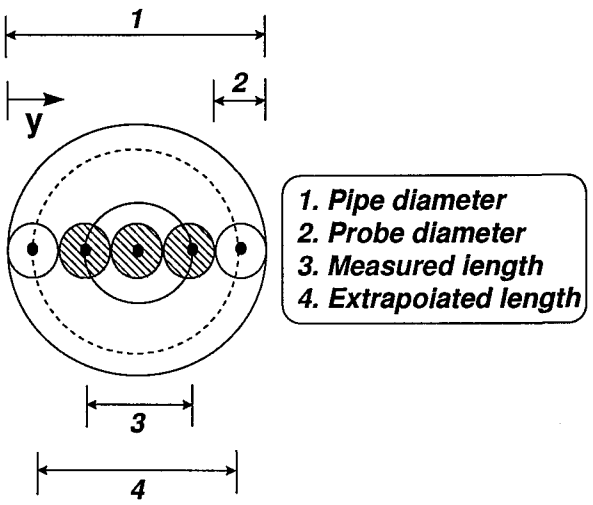


Figure 5.14: Traversing positions attained by the isokinetic probe and averaging dimensions.

three inner probe positions is free from the influence of waves.

The entrained liquid mass flux averaged over the pipe cross-sectional area and integrated using the extrapolated profile is given by,

$$\overline{\dot{m}_{LE}} = \frac{1}{d_T}\int_0^{d_T} \dot{m}_{LE}\,(\mathrm{y})\,d\mathrm{y}. \tag{5.7}$$

The integration of 5.7 is performed using the Simpson rule,

$$\overline{\dot{m}_{LE}} = \frac{1}{6}\left(\dot{m}_{LE_1} + 4\dot{m}_{LE_2} + \dot{m}_{LE_3}\right), \tag{5.8}$$

where $\dot{m}_{LE_1}$, $\dot{m}_{LE_2}$ and $\dot{m}_{LE_3}$ are the mass fluxes at the three sampling positions (from left to right). $\dot{m}_{LE_1}$ and $\dot{m}_{LE_3}$ are the extrapolated values.

The entrained fraction, $e\%$, given by,

$$e\% = 100\frac{\overline{\dot{m}_{LE}}A_{CS}}{\dot{M}_L}, \tag{5.9}$$

where A_{CS} is the cross-sectional area of the pipe.

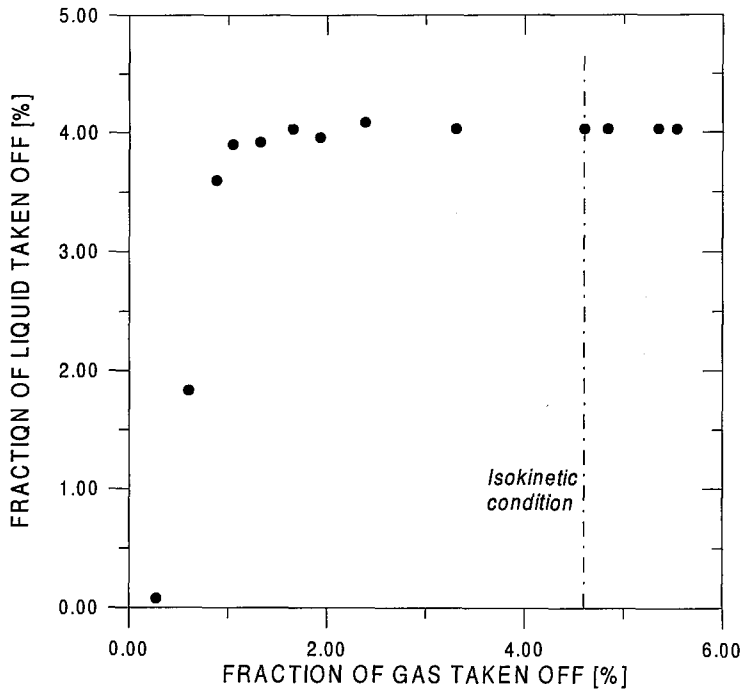


Figure 5.15: Liquid collection using the isokinetic probe. Experimental conditions: $p = 3$ bara, $\dot{m}_L = 45$ kg m^{-2} s^{-1}, $U^*_{GS} = 1.3$.

The insensitivity of the liquid collection rate to changes in air rate through the probe at one particular radial position is illustrated in Fig. 5.15. The probe's high droplet capture efficiency over a wide range of gas extraction rates can be observed. The isokinetic air rate is also shown.

The porous sinter technique

To serve as a mean of assessment of the isokinetic sampling measurements, a series of runs were carried out in which the liquid film flow rate (and indirectly the entrained fraction) was measured by extracting the film through a porous wall section (sinter). This consisted of a 0.1 m long, porous-wall tube mounted concentric to the test section. The measurement arrangement was similar to that shown in Fig. 5.13 for the isokinetic probe; the collected mixture was diverted to a gas-liquid separator and subsequently the

individual streams to a liquid collection vessel and to an air flow rotameter.

The entrained fraction measured using the sintered section is given by,

$$e\% = 100\frac{\dot{M}_L - \dot{M}_{LF}}{\dot{M}_L}. \tag{5.10}$$

Note that the comparative porous sinter measurements were undertaken at conditions in which the flow was unidirectional ($U^*_{GS} \approx 1.3$) and thus in the annular flow regime.

5.3.5 Experimental procedure

The procedure for the data acquisition was as follows. The test section pressure and the total liquid flow rate were set at the desired values. The flow pressure drop was measured and the pressure gradient calculated. The isokinetic probe was then traversed radially and samples were collected at three different radial positions. At each radial station, measurements of entrained liquid mass flux and of isokinetic gas flow rate were carried out. The collection time of entrained liquid at the separator was never less than 8 minutes for each position. After that, the air flow rate was set at another value and measurements were repeated after steady-state conditions had been reached. For a given set of flow conditions, tests were conducted in which the gas flow was *increased* to the required value and in which the gas flow was *reduced* from a higher value to the required value. No significant difference in the results for the two cases was observed.

5.4 Results

5.4.1 Local mass fluxes, velocities and droplet concentration

Typical radial profiles of entrained liquid mass flux (plotted against the dimensionless coordinate $\frac{y}{d_T}$), calculated by dividing the collected mass flow rate of water at each position

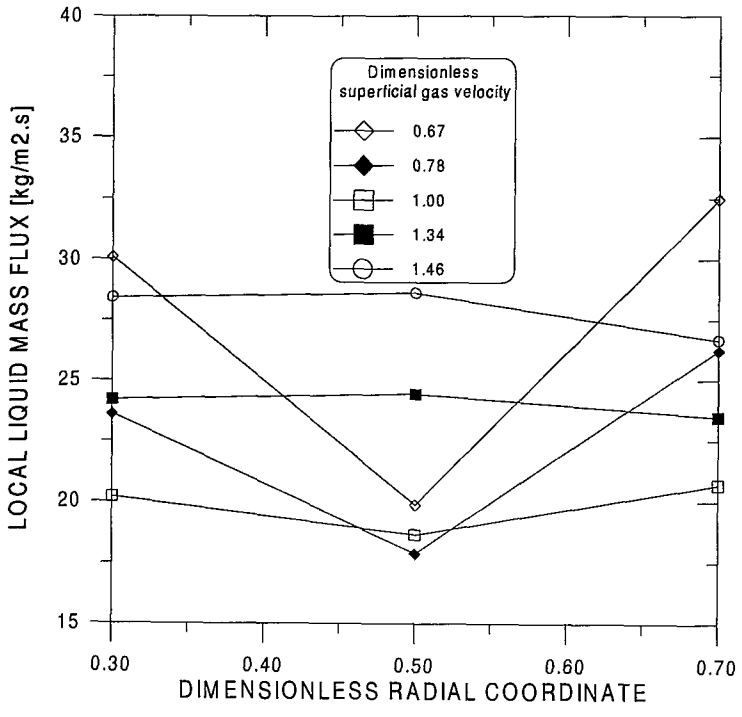


Figure 5.16: Local liquid mass flux profiles. $p = 2.1$ bara, $\dot{m}_L = 126.3$ kg m^{-2} s^{-1}.

by the cross-sectional area of the sampling probe, are shown in Figs. 5.16 and 5.17.

In these plots, U^*_{GS} is shown as a parameter. It can be observed that, at low U^*_{GS}, characteristic of the churn flow regime, the local entrained liquid mass flux goes through a minimum, which becomes less visible (and finally disappears) as U^*_{GS} increases. Also, as will be seen in the distributions of entrained fraction, there is a minimum average liquid mass flux at $U^*_{GS} \approx 1$.

Radial profiles of gas velocity are shown in Figs. 5.18 and 5.19 for the same conditions as in Figs. 5.16 and 5.17.

The point velocities are defined as the ratio of the measured air flow rate through the sampling probe (under isokinetic conditions) to the measured air density (calculated using the absolute pressure measurement in the test section). As expected, these velocity distributions exhibit maxima at the centre line of the pipe, despite the scatter at $\frac{y}{d_T} = 0.7$ at the higher superficial gas velocities in Fig. 5.19.

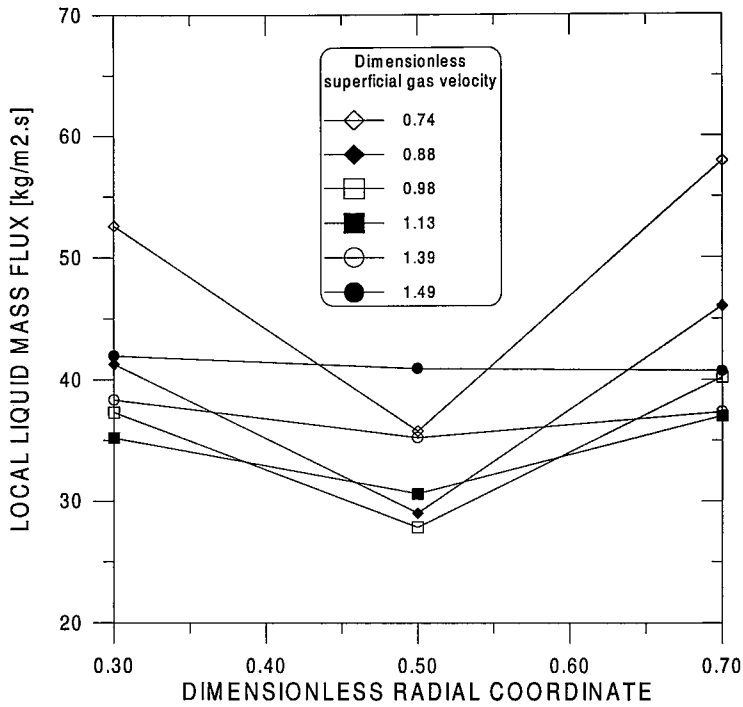


Figure 5.17: Local liquid mass flux profiles. $p = 3.7$ bara, $\dot{m}_L = 216.0$ kg m^{-2} s^{-1}.

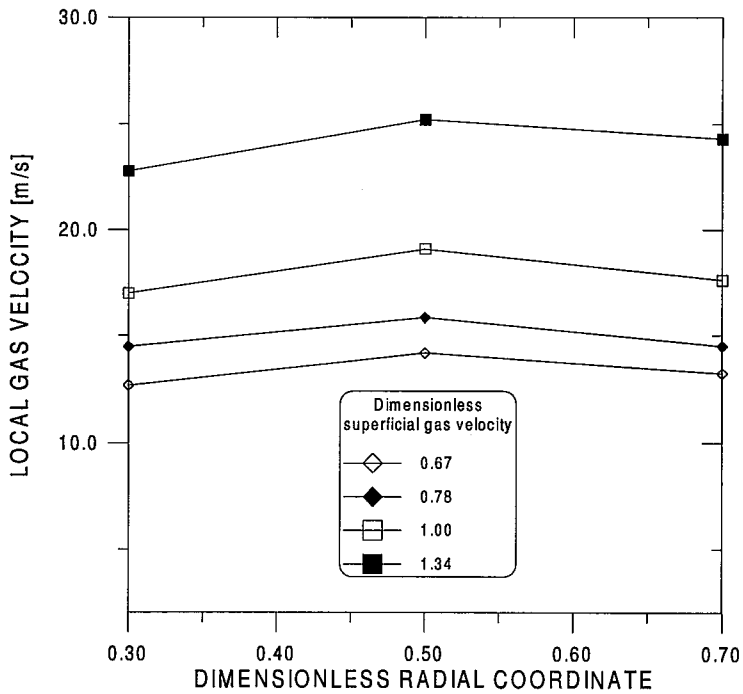


Figure 5.18: Local gas velocity profiles. $p = 2.1$ bara, $\dot{m}_L = 126.3$ kg m^{-2} s^{-1}.

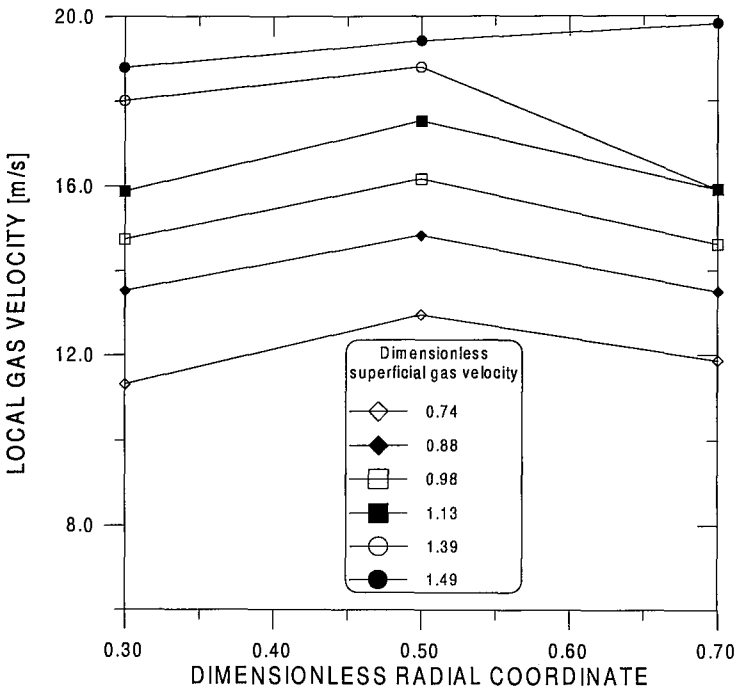


Figure 5.19: Local gas velocity profiles. $p = 3.7$ bara, $\dot{m}_L = 216.0$ kg m^{-2} s^{-1}.

Profiles of local concentration (Eq. 5.5) are shown in Figs. 5.20 and 5.21. As the superficial gas velocity increases and annular flow is approached (with U^*_{GS} tending to 1), the radial gradients are smoothed and the local concentration asymptotically approaches a constant value.

These results are in line with the measurements by Gill *et al.* (1964). However, in the present work, it was possible to obtain droplet concentration profiles at lower U^*_{GS} and thus to draw more thorough conclusions about the behaviour of entrained droplets in the churn flow regime.

Another view of the effect of gas flow rate on entrainment is provided by an analysis of the volumetric flow ratio in the gas core (or the apparent mean concentration), β. It is defined as (Gill *et al.*, 1964),

$$\beta = \frac{\dot{M}_{LE}\rho_G}{\dot{M}_G\rho_L}. \tag{5.11}$$

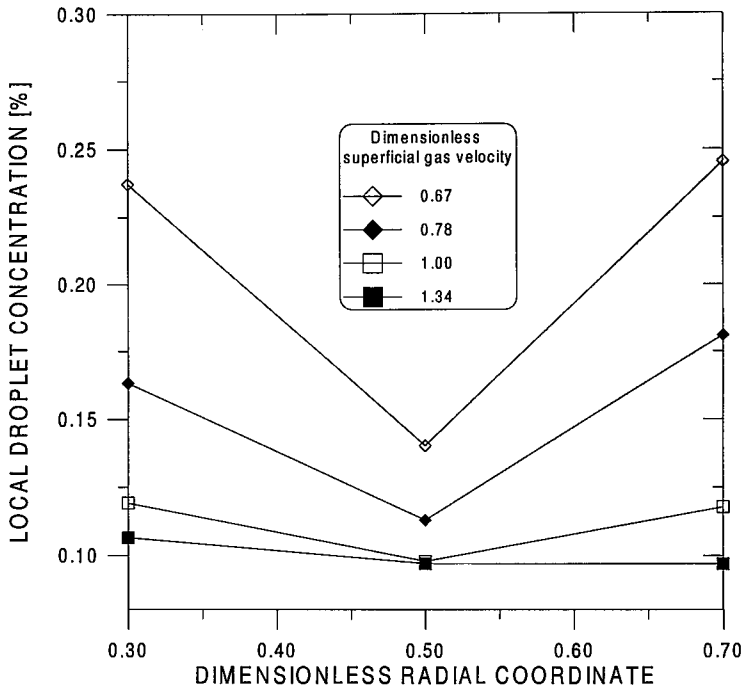


Figure 5.20: Profiles of local droplet concentration. $p = 2.1$ bara, $\dot{m}_L = 126.3$ kg m^{-2} s^{-1}.

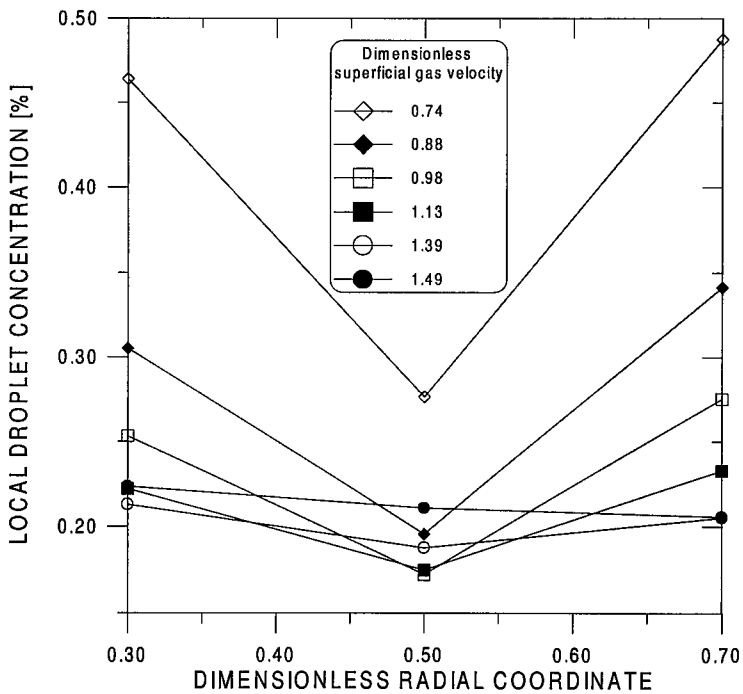


Figure 5.21: Profiles of local droplet concentration. $p = 3.7$ bara, $\dot{m}_L = 216.0$ kg m^{-2} s^{-1}.

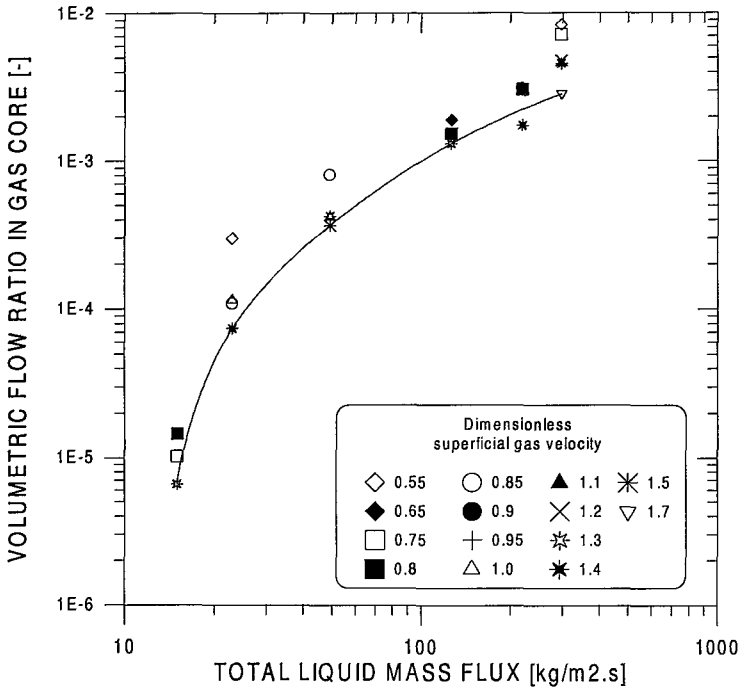


Figure 5.22: Volumetric flow ratio. $p = 2.0$ bara (nominal).

The variation of β with the liquid mass flux is illustrated in Figs. 5.22 to 5.24.

As previously observed by Gill *et al.* (1964), the data for U^*_{GS} greater than 1.0 fall approximately on a continuous curve with little deviation resulting in variations in air flow rate. The results for $U^*_{GS} < 1$ lie above the line; characterising the increase in entrainment associated with churn flow.

5.4.2 Liquid entrainment in the churn-annular region

The liquid entrained fraction calculated from Eq. 5.9 is plotted in Figs. 5.25 to 5.27 for different absolute pressures (2 to 5 bar).

In Figs. 5.25 to 5.27, the total liquid mass flux is varied from 11 to 330 kg m^{-2} s^{-1}. Error bars are shown. The issues concerned with uncertainty analysis are dealt with in a later section.

As observed in Figs. 5.25 to 5.27, the liquid entrained fraction decreases with increasing

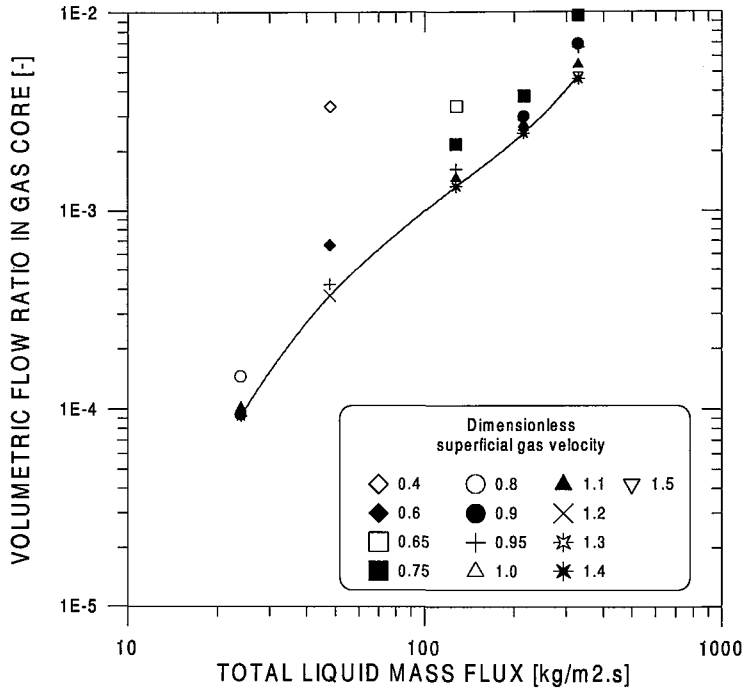


Figure 5.23: Volumetric flow ratio. $p = 3.6$ bara (nominal).

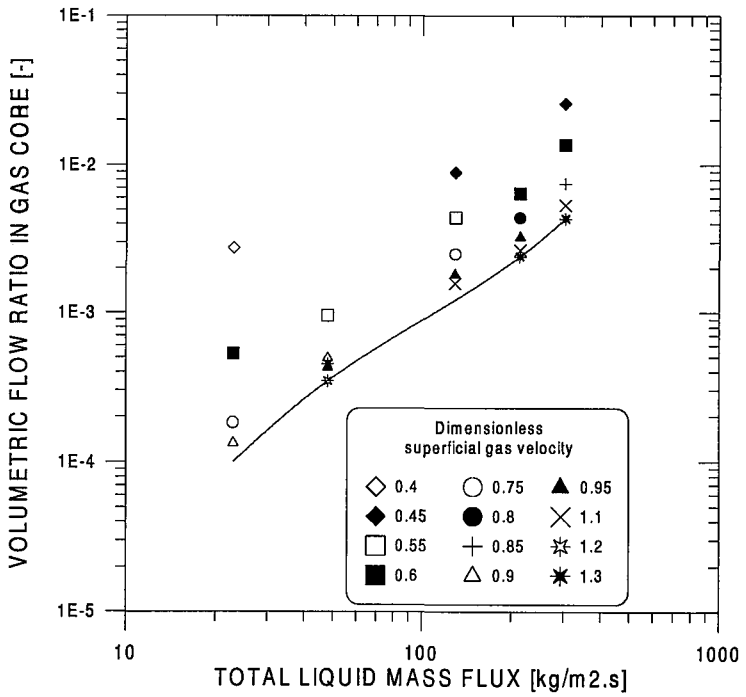


Figure 5.24: Volumetric flow ratio. $p = 5.2$ bara (nominal).

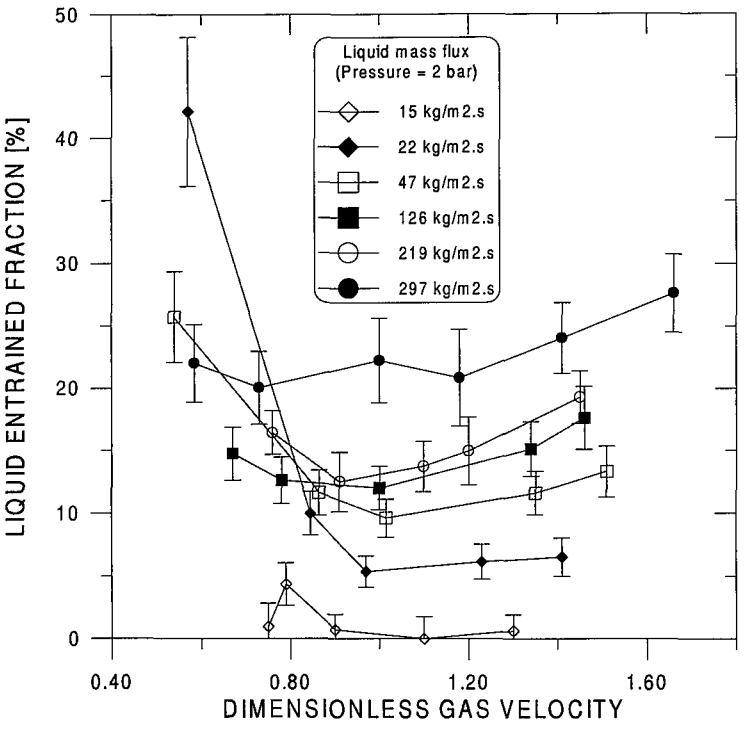


Figure 5.25: Liquid entrained fraction as a function of the total liquid mass flux. $p = 2.0$ bara (nominal).

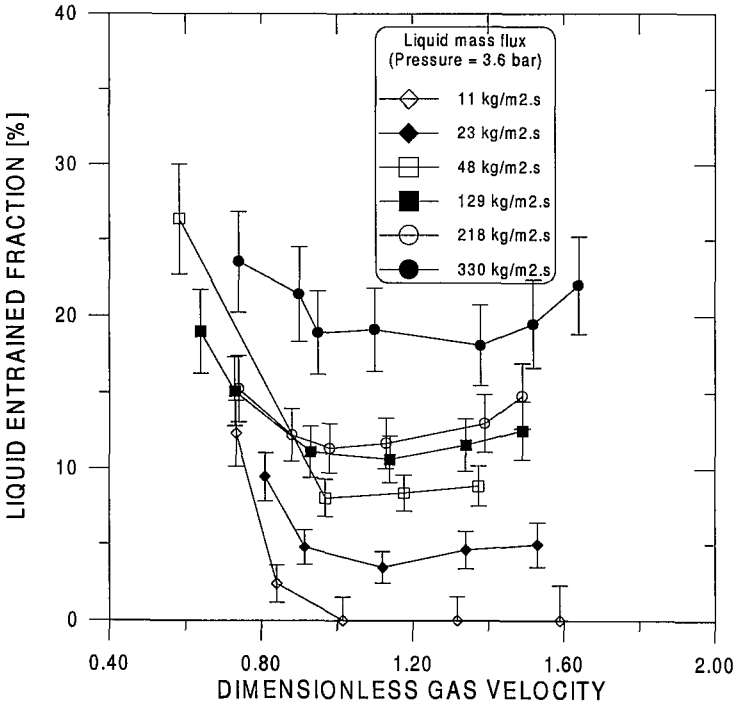


Figure 5.26: Liquid entrained fraction as a function of the total liquid mass flux. $p = 3.6$ bara (nominal).

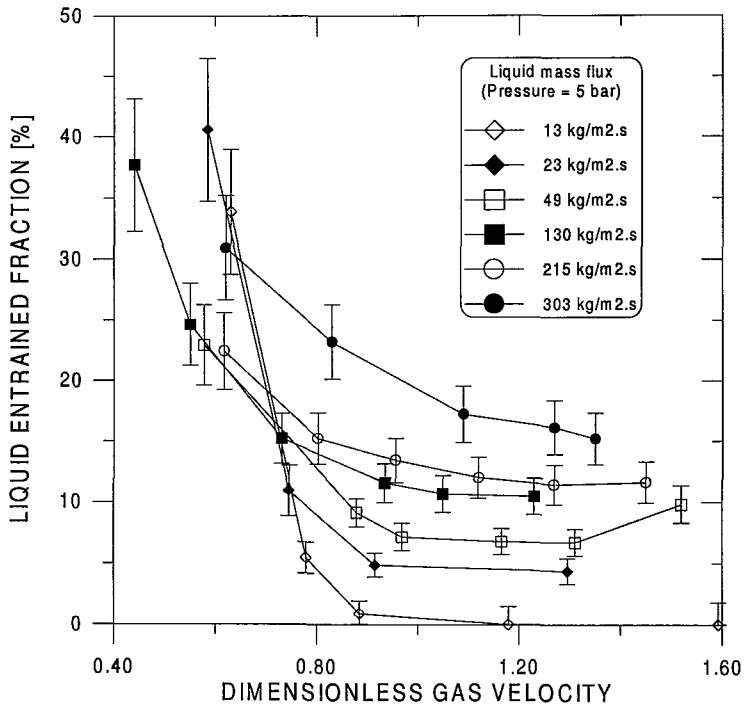


Figure 5.27: Liquid entrained fraction as a function of the total liquid mass flux. $p = 5.0$ bara (nominal).

U^*_{GS} in the churn flow region. It starts to increase again when the cocurrent annular region is entered. These observations are consistent with the data of Wallis (1962) (see Fig. 2.13). Also, the entrained fraction at the minimum region is always higher for the higher total liquid flow rates.

Although not very clear in the plots, it seems that the entrained fraction may go through an inversion region in churn flow ($0.6 < U^*_{GS} < 0.8$), with the higher entrained fractions being those of the lower liquid mass flux runs.

One can justify the behaviour of the entrained fraction in the churn-annular region based on the mechanisms by which droplets are generated from interfacial waves. As seen before, the nature of interfacial waves and the mechanisms by which they are formed are different in churn (flooding-type waves) and annular (disturbance waves) flow.

Azzopardi (1983) identified, from measurements of drop sizes and from flow visualisation

experiments, two mechanisms by which droplet entrainment takes place. An illustration of this processes is shown in Fig. 5.28. In the first mechanism, the gas apparently 'undercuts' a large wave forming and open-ended bubble with a thick filament rim. Gas pressure builds inside this bubble or bag and when this bag bursts, the pressure is released giving rise to a rapid transient acceleration of the gas phase which in turn accelerates the droplets. In the second mechanism, the crests of the waves are pulled forward in the form of ligaments, then these ligaments are broken into drops. This secondary break-up followed almost immediately after the initial ligament tear off. Azzopardi correlated the occurrence of each one of the mechanisms of droplet formation in annular flow to a critical Weber number. By assuming a wave height to mean film thickness ratio of approximately 3.5, good agreement with the transition boundary was found for,

$$We = \frac{\rho_G U_{GS}^2 \delta_w}{\sigma} = 25. \tag{5.12}$$

The results from Azzopardi's observations are shown in Fig. 5.29. Also, an important result obtained from experimental observations was that the sizes of droplets decrease with increasing gas flow rate. From such observations, it appears that the gas velocity is a key parameter in determining the dominant droplet formation mechanism. At low gas velocities, the bag (or filament) break-up mechanism is prevalent, whereas ligament break-up is dominant at high velocities.

James *et al.* (1980) carried out experimental and analytical studies on the motion of droplets in two-phase flow. As a result of their visualisation work (using a laser axial view technique), James *et al.* found that larger droplets ($> 200\mu$m), formed mainly from *bag break-up*, tend to travel in straight lines at velocities similar to those at the time of their formation. Moreover, because of their reduced size and therefore inertia, droplets formed by ligament break-up tend to stay in the core for much longer due to turbulent eddy

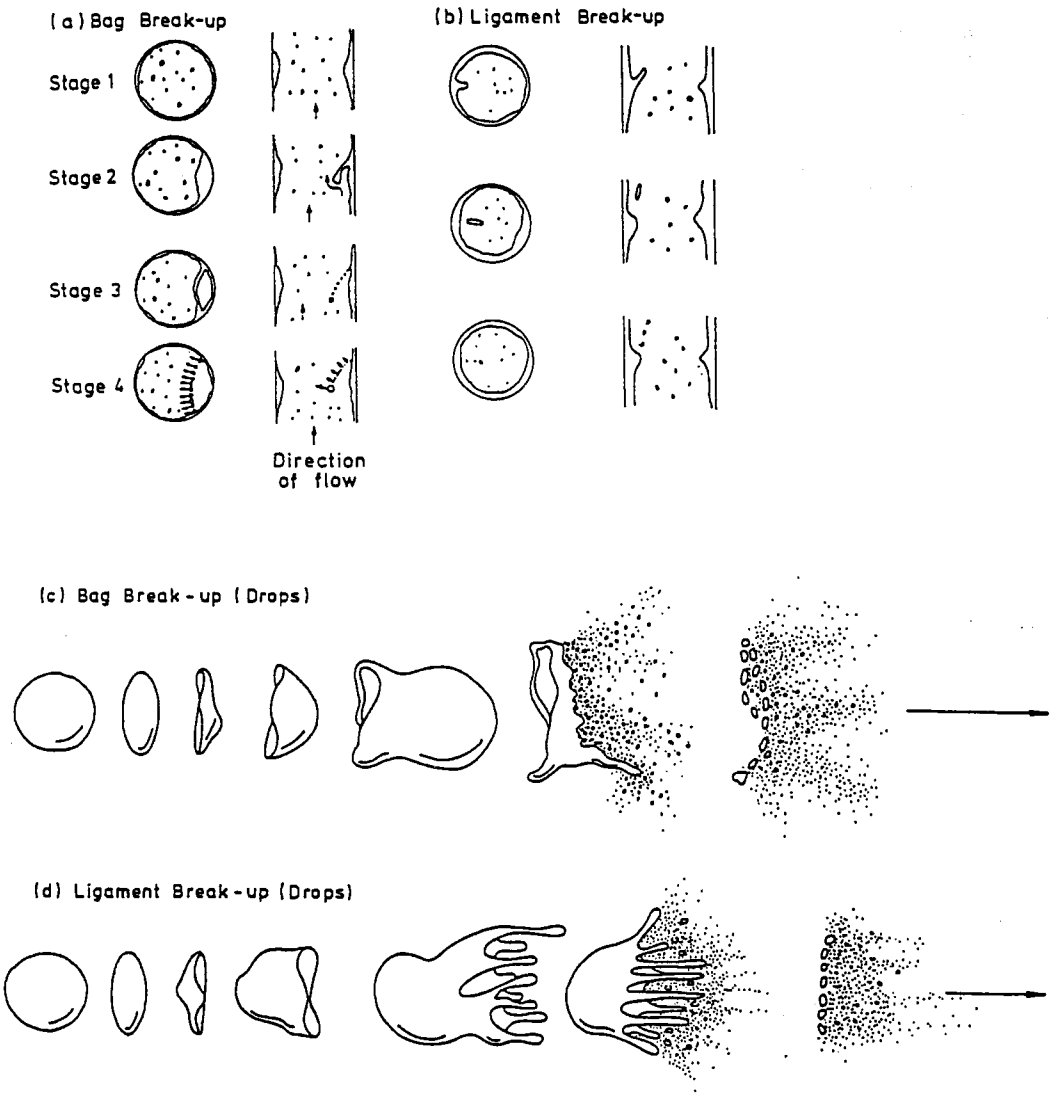


Figure 5.28: Mechanisms of entrainment and drop break-up (Azzopardi, 1983).

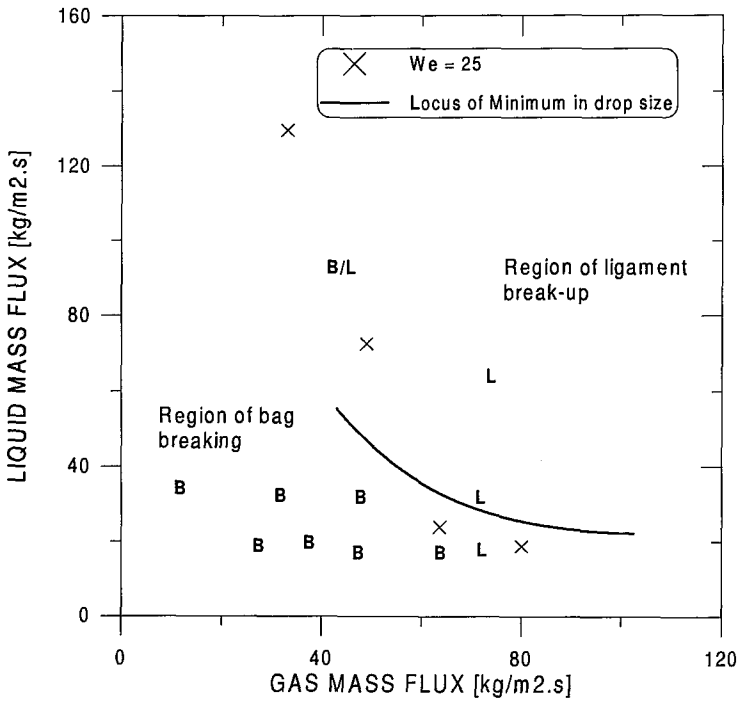


Figure 5.29: Map for droplet break-up mechanism (Azzopardi,1983).

interactions within the gas core. James *et al.*'s final conclusion was that both the direct impaction and the turbulent eddy interaction mechanisms are likely to be important at most practical situations, with the latter contributing to as much as 70% of the entrained fraction.

Based on the information above, one can retrace the entrainment curve on the light of the mechanisms of droplet formation. At low gas velocities the droplets are generated from the large flooding-type waves through the undercutting (bag break-up) mechanism. As the gas flow rate is increased and the occurrence of large flooding-type waves subsides, droplets cease to be generated by the (low gas velocity) undercutting mechanism, thus decreasing entrainment. With further and continuous increase of the gas flow rate, disturbance waves start to appear and both mechanisms may coexist, with the filament break-up mechanism gaining greater importance.

The effect of pressure on the liquid entrained fraction is investigated in Figs. 5.30 and 5.31.

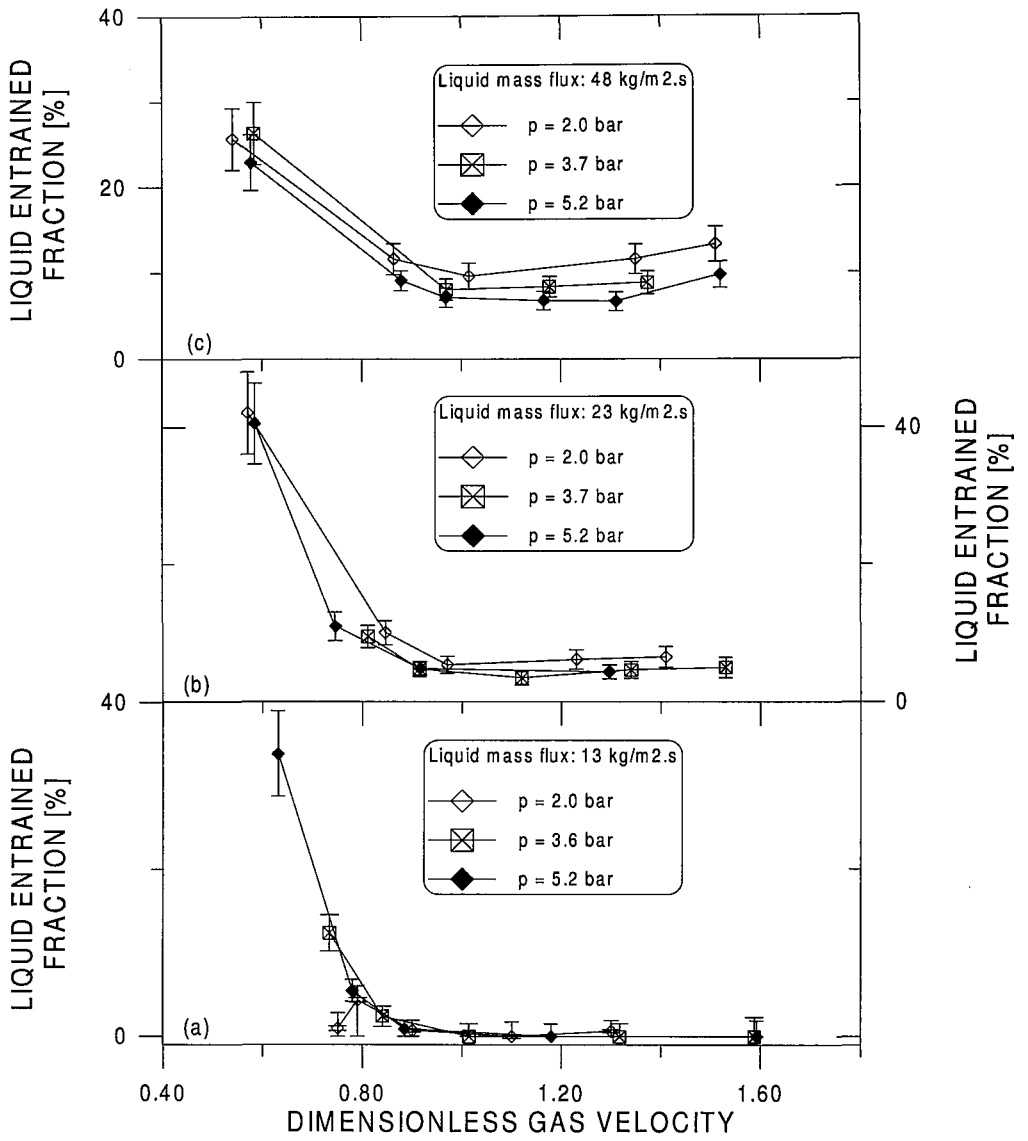


Figure 5.30: Liquid entrained fraction as a function of the absolute pressure. (a) $\dot{m}_L = 13$ kg m^{-2} s^{-1} (nominal), (b) $\dot{m}_L = 23$ kg m^{-2} s^{-1} (nominal), (c) $\dot{m}_L = 48$ kg m^{-2} s^{-1} (nominal).

The liquid entrained fraction is virtually constant in the churn region and the differences, though not very pronounced, develop in the annular region. A small suppression of entrainment is obtained with increasing pressure.

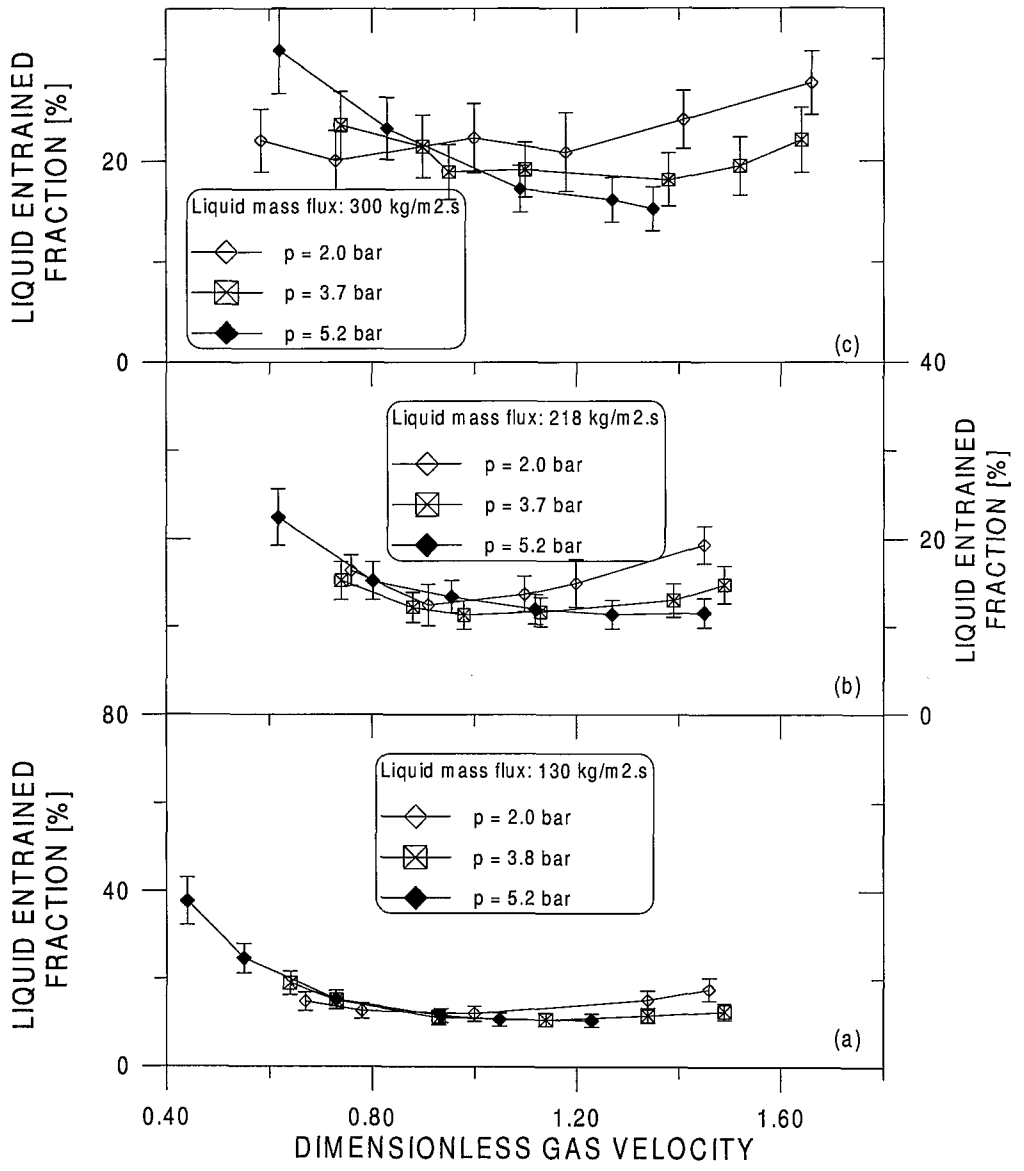


Figure 5.31: Liquid entrained fraction as a function of the absolute pressure. (a) $\dot{m}_L = 130$ kg m^{-2} s^{-1} (nominal), (b) $\dot{m}_L = 218$ kg m^{-2} s^{-1} (nominal), (c) $\dot{m}_L = 300$ kg m^{-2} s^{-1} (nominal).

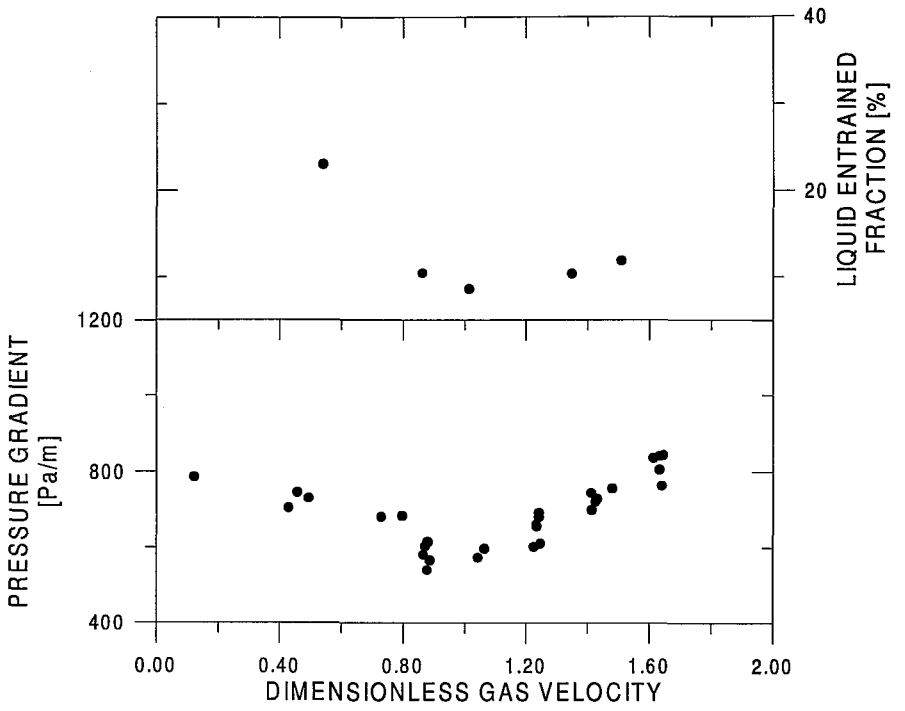


Figure 5.32: Entrainment and experimental pressure gradient in the churn-annular region. $p = 2.0$ bara, $\dot{m}_L = 47.0$ kg m^{-2} s^{-1} (nominal).

5.4.3 Entrained fraction and pressure gradient

Typical variations of pressure gradient and entrained liquid fraction with the dimensionless gas velocity, U^*_{GS}, are shown in Figs. 5.32 and 5.33.

The minima of each curve occur at $U^*_{GS} \approx 1$, which coincides with the criterion for flow reversal (Eq. 5.1). These trends were observed throughout the range of conditions investigated.

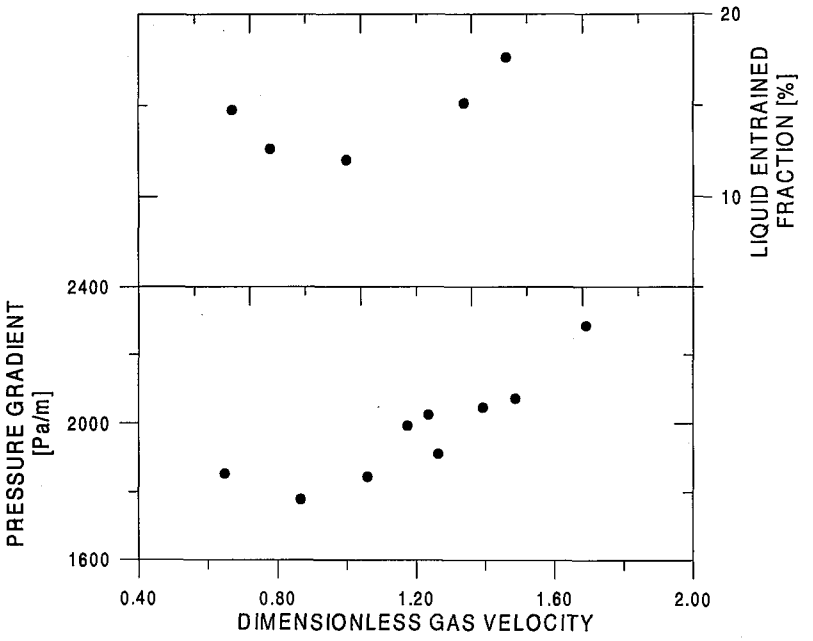


Figure 5.33: Entrainment and experimental pressure gradient in the churn-annular region. $p = 2.0$ bara, $\dot{m}_L = 138.0$ kg m^{-2} s^{-1} (nominal).

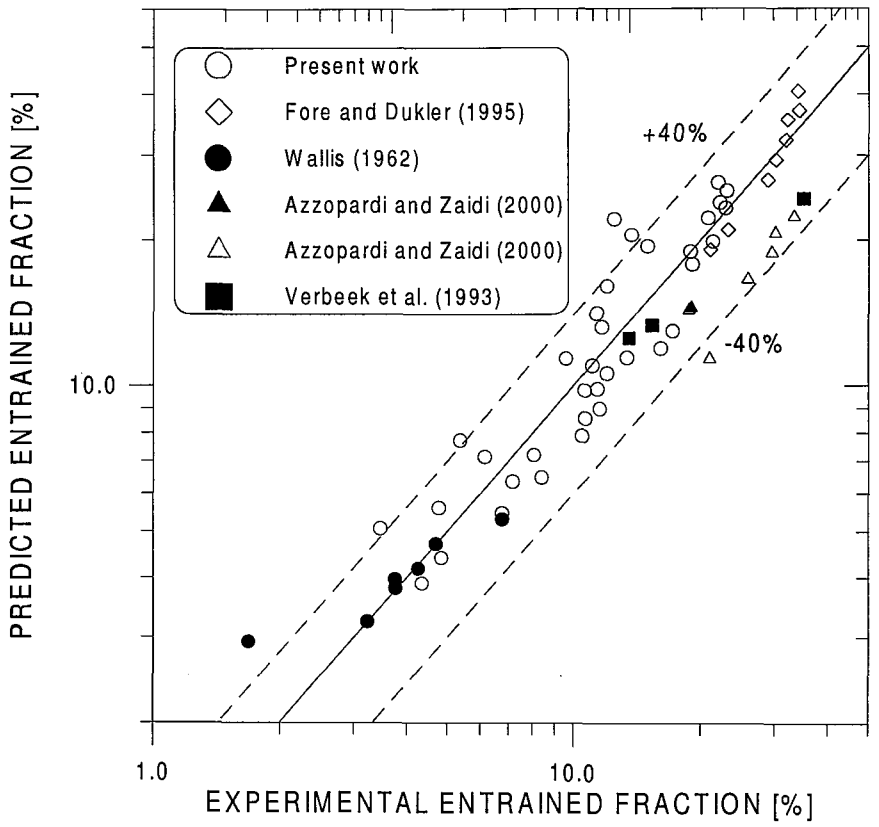


Figure 5.34: Prediction of entrained fraction using the proposed correlation.

5.4.4 A correlation for liquid entrained fraction at the onset of annular flow

An empirical correlation has been proposed for the prediction of the fraction of liquid entrained as droplets at the onset of annular flow, e_{OA}. This is as follows (parameters in SI Units),

$$e_{OA}\% = 0.95 + 342.55\sqrt{\frac{\rho_L \dot{m}_L}{\rho_G \dot{m}_G}} d_T^2. \tag{5.13}$$

Figure 5.34 illustrates the prediction of the experimental entrained fraction at the onset of annular flow. The data trend is reasonably well picked up by the correlation.

Equation 5.13 is valid for $0.9 \leq U_{GS}^* \leq 1.3$, $11 \leq \dot{m}_L \leq 334$ (in kg m^{-2} s^{-1}), $1.33 \leq p \leq 5.2$ (in bara) and $0.0127 \leq d_T \leq 0.0508$ (in m). The overall error is approximately equal to $\pm 18.9\%$.

As seen in Fig. 5.34, data from other sources are also well correlated. It is interesting to notice the effect of tube diameter on e_{OA}. The data of Fore and Dukler (1995) and Verbeek *et al.* (1993) (d_T =0.0508 m) exhibit the highest values of entrained fraction, whereas those of Wallis (1962) (d_T =0.0127 m) are amongst the lowest e_{OA}.

5.4.5 Measurement uncertainty

Single phase air runs were performed prior to the main series of experiments in order to evaluate the performance of the probe system. Under isokinetic conditions, average velocities were reproducible with an uncertainty of 5% for a wide range of air flow rates and pressures.

As pointed out in Section 5.3.4, in order to ensure the validity of the experimental technique, comparisons with experimental results obtained using a porous (sintered) section (100 mm long) mounted on the test section were carried out. The experiments were performed at sufficiently high gas superficial velocities, where the film flow is unidirectional and the film removal technique can be applied. The mass flux of entrained liquid was obtained by deduction of the measured film flow rate from the total liquid flow rate. The agreement between the techniques is shown in Table 5.2. This is of the same order of magnitude as the deviations reported by Azzopardi and Zaidi (2000) for comparisons of entrained liquid fraction in annular flow obtained using a porous sinter and a light scattering technique.

At low liquid flow rates, evaporation of the liquid phase (air humidification) may become significant as the amount of liquid evaporated is comparable to the amount of liquid entrained as droplets.

Owen (1986) carried out a theoretical analysis of the evaporation/mass transfer processes in a situation similar to that investigated here. He concluded that the air should be

Table 5.2: A comparison of entrained fraction obtained using a porous sinter and the isokinetic probe.

U^*_{GS} (-)	$\dot{m}_L$ (kg m^{-2} s^{-1})	$e\%_{sinter}$ (-)	$e\%_{probe}$ (-)
1.2	47	8.84	8.40
1.3	22	4.28	4.62
1.4	48	9.79	8.87
1.5	23	4.95	4.97

completely saturated with water vapour at the upper portion of the test section where the measurements are performed. The amount of film evaporated can be estimated by assuming that the air enters completely dry at the bottom of the test section.

The humidity of moist air in an air/water vapour mixture is defined as,

$$\mathsf{h} = \frac{M_W}{M_A}. \tag{5.14}$$

h is a function of both temperature and pressure of the system. For $T \approx 18$ °C, it can be interpolated by the following function (Owen, 1986),

$$\mathsf{h} = \frac{0.01293}{p^{0.9984}}, \tag{5.15}$$

for p in bara.

Therefore, for a given air flow rate, the amount of water 'entrained' due to evaporation can be easily calculated by applying the equations above. As an example, for a liquid flow rate of $\dot{m}_L \approx 12$ kg m^{-2} s^{-1} at $p = 2$ bar and $\dot{m}_G \approx 50$ kg m^{-2} s^{-1}, around 3% of $\dot{m}_L$, which is of the same order of magnitude of the measured entrained fraction under similar

conditions, is lost due to evaporation. In other words, it can be concluded that the effect of film evaporation is significant and together with the uncertainty in the film flow rate measurement as well as the uncertainty in the input liquid rate can account for all of the apparent entrainment at very low liquid flow rates.

Error propagation

It is postulated that the types of error occurring during the entrained fraction measurement are as follows,

1. sampling errors. These are the errors due to uncertainties in the collection measurement, time interval measurement and input liquid rate. A summary of these is given in Table 5.3;

Table 5.3: Uncertainties of measured parameters.

Parameter	Uncertainty
$\delta\Delta t_{coll,i}$	0.05 s
$\delta m_{coll,i}$	0.005 kg
$\delta\dot{M}_L$ (for 10, 20 and 50 kg m^{-2} s^{-1})	0.0002 kg s^{-1}
$\delta\dot{M}_L$ (for 100, 200 and 300 kg m^{-2} s^{-1})	0.0025 kg s^{-1}

2. error due to evaporation of the liquid (air humidification);

3. profile extrapolation and integration errors.

An error propagation analysis provides an estimate of the uncertainty associated with the measurement of $e\%$. Rewriting Eq. 5.9,

$$e = \frac{\overline{\dot{m}_{LE}} A_{CS}}{\dot{M}_L}. \tag{5.16}$$

The uncertainty in e is given by,

$$\delta e^2 = \left(\frac{\partial e}{\partial \overline{\dot{m}_{LE}}}\right)^2 \delta \overline{\dot{m}_{LE}}^2 + \left(\frac{\partial e}{\partial \dot{M}_L}\right)^2 \delta \dot{M}_L^2, \tag{5.17}$$

where,

$$\frac{\partial e}{\partial \overline{\dot{m}_{LE}}} = \frac{A_{CS}}{\dot{M}_L}, \tag{5.18}$$

and,

$$\frac{\partial e}{\partial \dot{M}_L} = -\frac{\overline{\dot{m}_{LE}} A_{CS}}{\dot{M}_L^2}. \tag{5.19}$$

The total error in the entrained liquid mass flux is made up of contributions due to the measurement uncertainty and extrapolation/integration,

$$\delta \overline{\dot{m}_{LE}} = \sqrt{\left(\delta \dot{m}_{LE_{meas}}\right)^2 + \left(\delta \dot{m}_{LE_{extrap}}\right)^2}, \tag{5.20}$$

where,

$$\delta \dot{m}_{LE_{meas}} = \sqrt{\left(\delta \dot{m}_{LE_{sampl}}\right)^2 + \left(\delta \dot{m}_{LE_{evap}}\right)^2}. \tag{5.21}$$

The error associated with the radial samples, $\dot{m}_{LE_i}$, is given by,

$$\delta \dot{m}_{LE_i}^2 = \left(\frac{\partial \dot{m}_{LE_i}}{\partial m_{coll,i}}\right)^2 \delta m_{coll,i}^2 + \left(\frac{\partial \dot{m}_{LE_i}}{\partial \Delta t_{coll,i}}\right)^2 \delta \Delta t_{coll,i}^2, \tag{5.22}$$

where,

$$\frac{\partial \dot{m}_{LE_i}}{\partial m_{coll,i}} = \frac{1}{\Delta t_{coll,i} A_{pr}}, \tag{5.23}$$

and,

$$\frac{\partial \dot{m}_{LE_i}}{\partial \Delta t_{coll,i}} = -\frac{m_{coll,i}}{\Delta t_{coll,i}^2 A_{pr}}. \tag{5.24}$$

The error in $\dot{m}_{LE_{meas}}$ is given by,

$$\delta \dot{m}_{LE_{meas}}^2 = \sum_{i=1}^{3} \left(\frac{\dot{m}_{LE_{meas}}}{\partial \dot{m}_{LE_i}} \right)^2 \delta \dot{m}_{LE_i}^2 + \left(\frac{0.01293}{p^{0.9984}} \dot{m}_G \right)^2, \tag{5.25}$$

where the second term on RHS of Eq. 5.25 is the definition of $\delta \dot{m}_{LE_{evap}}$ and it is found by combining Eqs. 5.14 and 5.15.

From Eq. 5.8 one has,

$$\frac{\partial \dot{m}_{LE_{meas}}}{\partial \dot{m}_{LE_1}} = \frac{1}{6}, \tag{5.26}$$

$$\frac{\partial \dot{m}_{LE_{meas}}}{\partial \dot{m}_{LE_2}} = \frac{2}{3}, \tag{5.27}$$

$$\frac{\partial \dot{m}_{LE_{meas}}}{\partial \dot{m}_{LE_3}} = \frac{1}{6}. \tag{5.28}$$

In the analysis described above, it was assumed that the system pressure, p, the cross-sectional area of the probe, A_{pr}, and the cross-sectional area of the pipe, A_{CS}, are accurately known.

Appendix D also provides the entrained fraction uncertainty data in tabular form.

5.4.6 Annular flow modelling and the onset of entrainment

As seen in Chapter 2, there are a number of correlations and methods that predict the processes of droplet entrainment and deposition in annular flow. In the present section, the performance of such models at the churn-annular boundary is investigated. In further detail, it may be interesting to assess their prediction of the equilibrium entrained fraction for cases identical to those of the present experiments and at $U_{GS}^* \approx 1$.

For the majority of the methods, (Govan, 1990; Schadel *et al.*, 1990) the equilibrium entrained fraction, e_{∞}, at a particular location can be calculated by equating the expressions for the entrainment and deposition rates, using local physical properties. This requires an iterative procedure to find e_{∞}. Some methods, provide an explicit relationship for calculating e_{∞}. This is the case of the Ishii and Mishima (1981) correlation, whose relationship for e_{∞} is also used in the latest correlation of Kataoka *et al.* (2000). According to them, the equilibrium entrained fraction is given by,

$$e_{\infty} = \tanh\left(7.25 \times 10^{-7} We^{1.25} Re_L^{0.25}\right), \tag{5.29}$$

where Re_L is the liquid phase Reynolds number and We is the Weber number for entrainment given by,

$$We = \frac{\rho_G U_{GS}^2 d_T}{\sigma} \left(\frac{\Delta\rho}{\rho_G}\right)^{1/3}. \tag{5.30}$$

Figures 5.35 to 5.37 present a comparison between the experimental data and the equilibrium entrained fraction calculated using the methods of Govan (1990), Schadel *et al.* (1990) and Ishii and Mishima (1981). In Fig. 5.35 the overall performance of the methods is also compared to that of the proposed correlation (Eq. 5.13).

As can be seen, the proposed correlation provides a much more accurate prediction of the data, whilst the other methods generally underpredict greatly the data.

Figure 5.37 shows that the effect of total liquid mass flux is a significant one as the discrepancies in the predictions of the equilibrium entrained fraction increases with increasing liquid mass flow rate. The effect of pressure (see Fig. 5.36) is less significant.

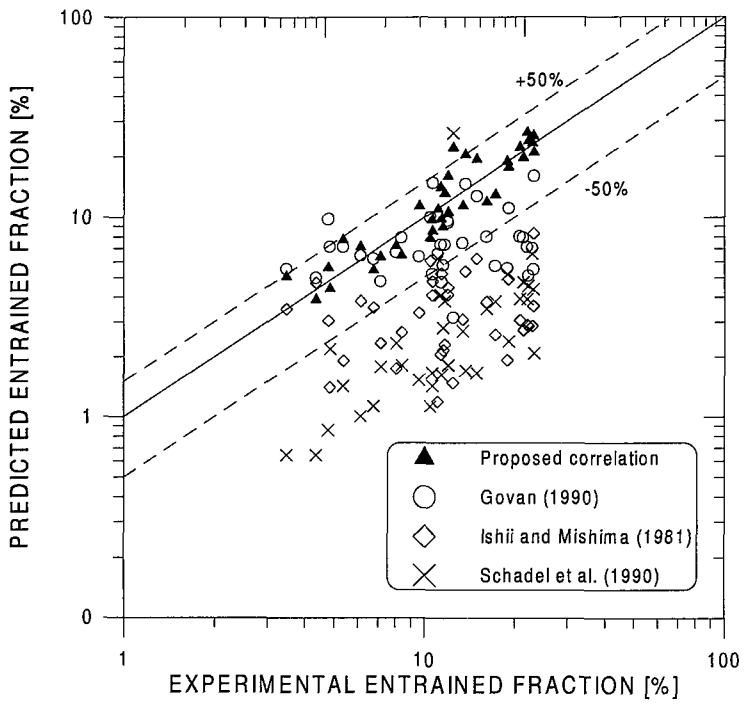


Figure 5.35: A comparison between experimental and predicted equilibrium entrained fraction according to various methods.

5.5 Summary

This chapter presented an experimental analysis of droplet entrainment at the region of transition between churn flow and annular flow in a vertical pipe. An isokinetic probe system was used to measure the local distributions of liquid and gas mass fluxes. The proposed empirical correlation for the entrained fraction at the onset of annular flow predicts data from the present work and from other sources with reasonable accuracy. A detailed description of the main conclusions arising from the studies presented in this chapter will be given in Section 7.3.

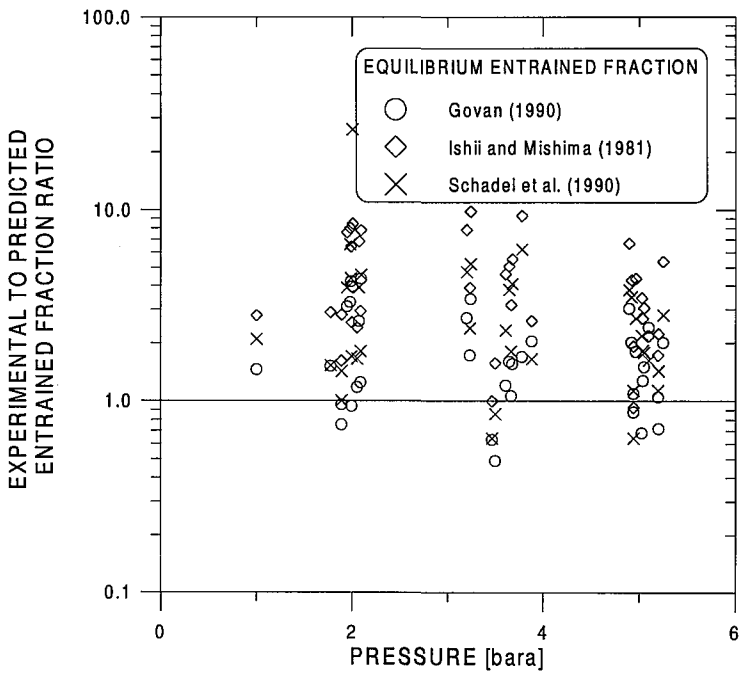


Figure 5.36: Effect of system pressure on the prediction of the equilibrium entrained fraction according to various methods.

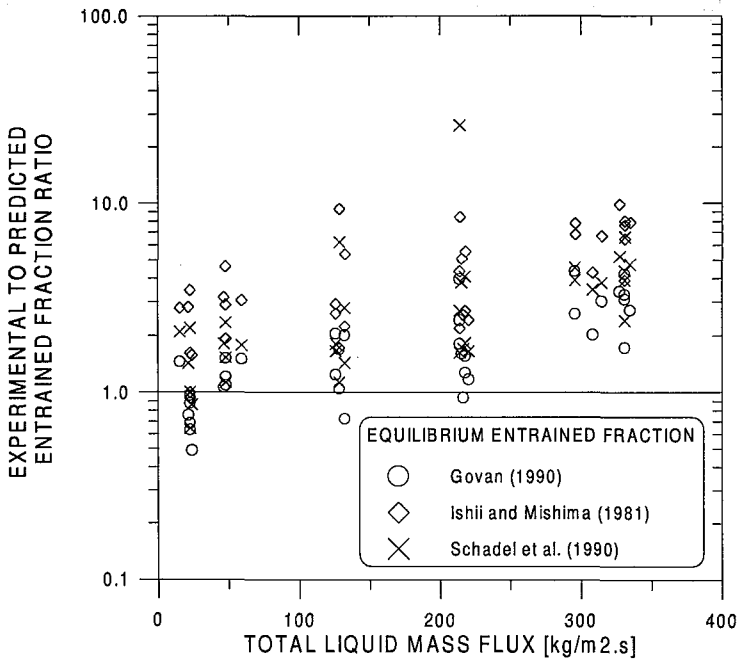


Figure 5.37: Effect of liquid mass flux on the prediction of the equilibrium entrained fraction according to various methods.

Chapter 6

A Theoretical Analysis of Interfacial Waves in Churn-Annular Flow

This chapter presents a simple model aimed at predicting some of the phenomena brought to attention by Govan (1990) during the churn flow visualisation experiments and in particular the levitation and motion of waves in the churn flow regime. The experimental findings of Hewitt *et al.* (1985), who also carried out visualisation experiments in churn flow, are also used as a basis for the assumptions made in the simplified model.

6.1 Conservation principles

The model for wave growth is based on macroscopic balances of mass and momentum over a control volume which encompasses the wave. The wave is assumed to be coherent around the periphery of the pipe.

Figure 6.1 illustrates the geometry of the problem. It has been experimentally observed that the waves generally grow at the bottom of the porous section before start moving upwards. There is a falling film downstream (above) the wave and liquid is shed by the

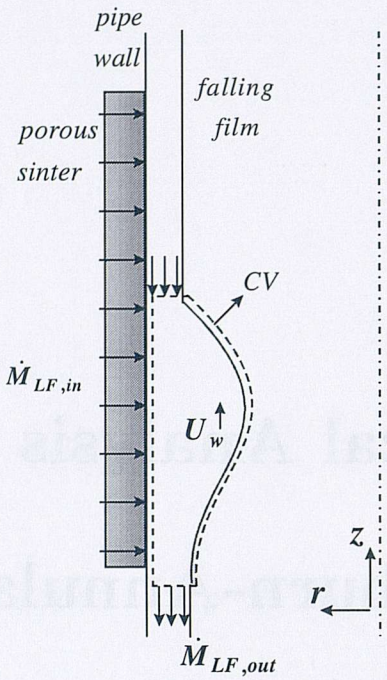


Figure 6.1: An illustration of the problem geometry.

wave as it grows. If the mass flowrates entering, $\dot{M}_{LF,in}$, and leaving, $\dot{M}_{LF,out}$, the wave are such that,

$$\dot{M}_{LF,out} < \dot{M}_{LF,in}, \tag{6.1}$$

then there will be mass storage in the control volume and the wave will grow. The wave will move upwards when it reaches a critical size and the net force acting on it is directed upwards.

A primary assumption of the macroscopic model is that the control volume encompassing the wave moves with velocity U_W relative to a fixed frame of reference. An application of the mass and momentum conservation principles is carried out as follows,

$$\rho_L \frac{d}{dt} \mathsf{V}_W = \dot{M}_{LF,in} - \dot{M}_{LF,out}, \tag{6.2}$$

and,

$$\sum \mathbf{F}_z = \rho_L \frac{d}{dt}(U_W \mathsf{V}_W) - U_{LF,in}\dot{M}_{LF,in} + U_{LF,out}\dot{M}_{LF,out}, \tag{6.3}$$

where V_W is the wave volume and $U_{LF,in}$ and $U_{LF,out}$ are the mean liquid film velocities in and out of the control volume. $\sum \mathbf{F}_z$ is the resultant force acting on the wave in the axial direction, z.

Equations 6.2 and 6.3 can be solved provided that V_W and $\sum \mathbf{F}_z$ are known. The wave volume is calculated by assuming that the shape of the wave is known and the resultant force is estimated through a force balance. These calculations are described in the following sections.

6.2 Wave shape and volumetric relationships

Direct calculation of the detailed shape of the large waves in churn flow may not be currently feasible. Thus, in any analysis, it is necessary to assume a shape. As was mentioned above, the waves are related to those formed in flooding; viable analyses of flooding have been performed by McQuillan *et al.* (1985) and by Costigan (1997) based on the assumption that the waves are hemispherical in form. However, it is unlikely that the waves would be of hemispherical shape; in an analysis of wave growth associated with flooding, Shearer and Davidson (1965) calculated a shape based on a force balance. The wave was somewhat asymmetric in form but it is not known whether waves in the developed churn flow region would have the same form (the Shearer and Davidson analysis was based on a stationary wave). In fact, Hewitt *et al.* (1985) measured wave shapes based on the visualisation experiments and compared them with the shape calculated by Shearer and Davidson. The results are shown in Fig. 6.2. Though there is considerable variation between the wave shapes, they clearly do not conform either to the shape predicted for the stationary wave by Shearer and Davidson or to the hemispherical shape assumed by

McQuillan *et al.* and Costigan. In the present analysis, therefore, it has been assumed that the wave is *sinusoidal* in shape. This is reasonably consistent with the results shown in Fig. 6.2 and is considered to be a better approximation than assuming a hemispherical shape. However, since the assumption of a hemispherical shape gives reasonable answers for flooding, it is not considered that the exact shape is significant in governing the qualitative results from the analysis. It is assumed that the shape of the wave is known and that this shape is retained as the wave grows. The thickness of the liquid film in wave region, δ_W, is given by (see Fig. 6.3),

$$\delta_W(z) = \begin{cases} \delta_{W1}; & 0 \le z \le L_W/2 \\ \delta_{W2}; & L_W/2 \le z \le L_W, \end{cases} \tag{6.4}$$

where,

$$\delta_{W1} = \frac{1}{2}\left[(\mathsf{A}_W + \delta_{s,out}) + (\mathsf{A}_W - \delta_{s,out})\cos\frac{2\pi\,(L_W/2 - z)}{L_W}\right], \tag{6.5}$$

and,

$$\delta_{W2} = \frac{1}{2}\left[(\mathsf{A}_W + \delta_{s,in}) - (\mathsf{A}_W - \delta_{s,in})\cos\frac{2\pi\,(L_W - z)}{L_W}\right]. \tag{6.6}$$

In Eqs. 6.4 to 6.6, L_W is the length of the wave, A_W is the wave amplitude and $\delta_{s,in}$ and $\delta_{s,out}$ are thickness of the liquid film at the top ($z = L_W$) and bottom ($z = 0$) of the wave, respectively. The wave volume is given by,

$$\mathsf{V}_W = \pi d_T\left[\int_0^{L_W/2}\delta_{W1}(z)\,dz + \int_{L_W/2}^{L_W}\delta_{W2}(z)\,dz\right]. \tag{6.7}$$

Integration of Eq. 6.7 gives,

$$\mathsf{V}_W = \frac{1}{4}\pi d_T L_W\,(2\mathsf{A}_W + \delta_{s,in} + \delta_{s,out}). \tag{6.8}$$

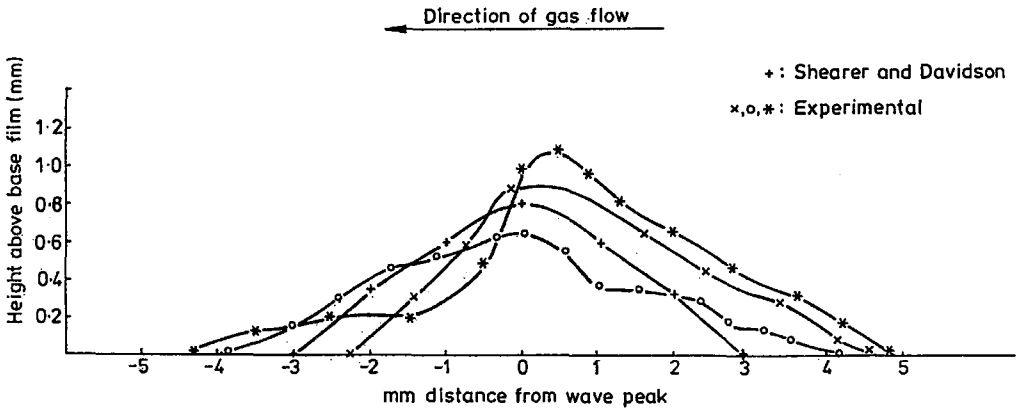


Figure 6.2: Measured churn flow wave shapes based on the visualisation experiments of Hewitt *et al.* (1985).

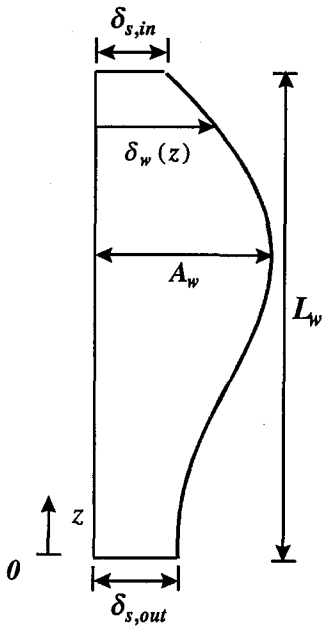


Figure 6.3: The assumed geometry of the wave.

The time derivative of the wave volume is calculated assuming that L_W is approximately constant. Thus,

$$\frac{d}{dt}\mathsf{V}_W = \frac{1}{4}\pi d_T L_W \left(2\frac{d}{dt}\mathsf{A}_W + \frac{d}{dt}\delta_{s,in} + \frac{d}{dt}\delta_{s,out}\right). \tag{6.9}$$

As the wave moves upwards along the sintered section (i.e., the porous wall section over which the liquid is introduced), the values of $\dot{M}_{LF,in}$ and $\dot{M}_{LF,out}$ are likely to vary with distance. At one extreme *all* of the liquid flowing into the injection region will enter the wave which is initially stationary at the bottom of the injector region; some of this liquid flows out from the bottom of the wave to form the downward falling film, but this is accounted for in the model. When the wave is transported to a position just above the top of the injector region, then *none* of the liquid entering the injector passes into the wave. An exact prediction of the amount of liquid entering the wave in between these two extreme conditions is difficult and a simple assumption is made that the amount of the liquid entering the injector which goes into a wave will depend linearly on the position of the wave in the injector region. It is not believed that this assumption affects the analysis materially. Figure 6.4 illustrates the variation of $\dot{M}_{LF,in}$ and $\dot{M}_{LF,out}$ with distance as the wave travels upwards along the sintered section. The idealised curves are as follows,

$$\dot{M}_{LF,in}(z) = \left(\dot{M}_L - \dot{M}_{LE}\right) - \frac{\left[\left(\dot{M}_L - \dot{M}_{LE}\right) - \dot{M}_{LF,ss}\right] z}{L_{sint}}, \tag{6.10}$$

and,

$$\dot{M}_{LF,out}(z) = \dot{M}_{LF,out}(0) - \frac{\left[\dot{M}_{LF,out}(0) - \dot{M}_{LF,ss}\right] z}{L_{sint}}, \tag{6.11}$$

where $\dot{M}_L$ is the total liquid flowrate, L_{sint} is the length of the sintered section, $\dot{M}_{LE}$ is the mass flowrate of entrained liquid and $\dot{M}_{LF,ss}$ is the flowrate in the falling film region between waves attained towards the end of the sintered section, where some sort

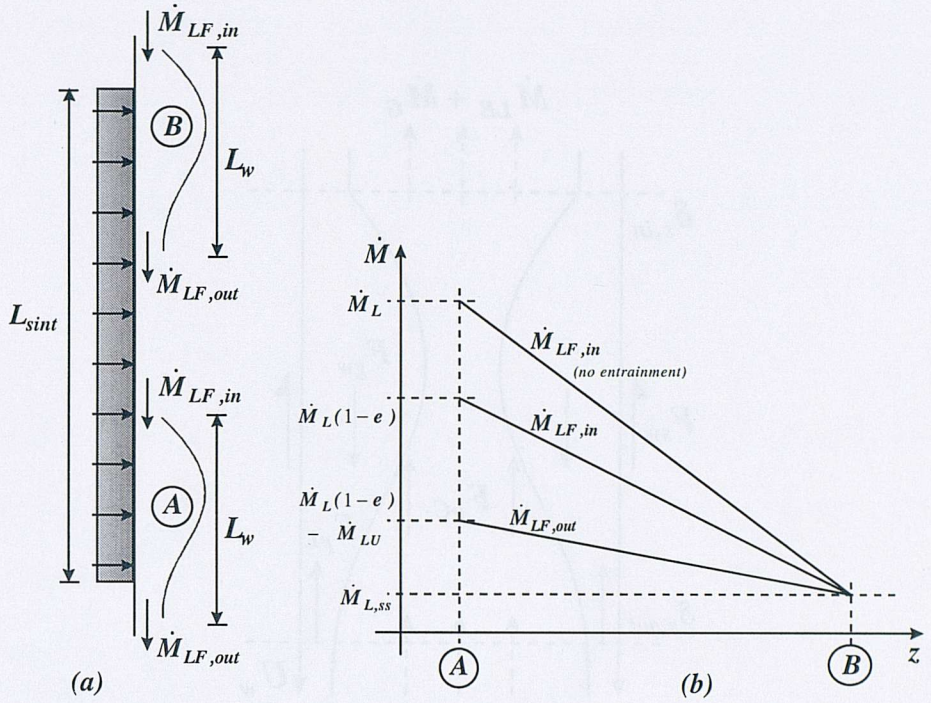


Figure 6.4: Illustration and model of flowrates in and out of the wave.

of steady-state is reached. The true value of $\dot{M}_{LF,ss}$ is not known, however calculations with values of $\dot{M}_{LF,ss}$ ranging from 5 to 15 per cent of $\dot{M}_L$ were carried out without causing any significant changes to the final results (basically, the values of the calculated wave parameters tended to remain approximately unchanged for values of $\dot{M}_{LF,ss}$ between $0.075\dot{M}_L$ and $0.15\dot{M}_L$).

$\delta_{s,in}$ and $\delta_{s,out}$, are calculated via the Nusselt film theory,

$$\delta_s = \left[\frac{3\eta_L \dot{M}_{LF}}{\pi d_T \rho_L g\,(\rho_L - \rho_C)}\right]^{1/3}, \tag{6.12}$$

where $\dot{M}_{LF}$ is the film flowrate in or out of the wave in a fixed frame of reference. η_L is the liquid kinematic viscosity and ρ_C is the core density, defined in Section 5.2.

In the experiments of Hewitt and Wallis (1963) film thickness measurements in counter-current flow showed that the mean film thickness agreed closely with the Nusselt equation.

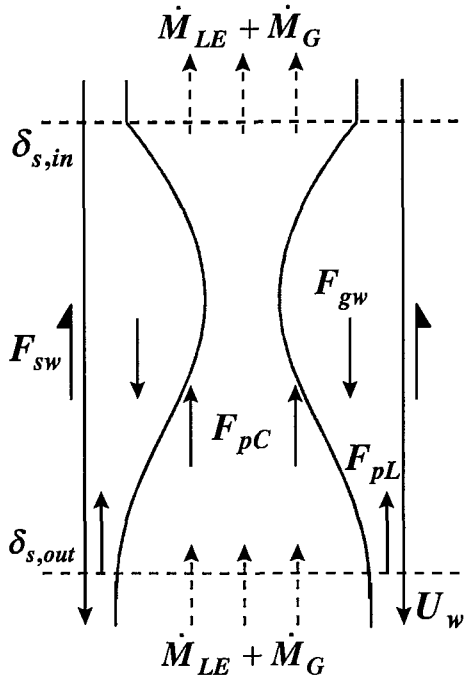


Figure 6.5: Force balance over a coherent wave.

6.3 Force balance over the coherent wave

The balance of forces on the wave is schematically shown in Fig. 6.5.

The analysis is based on that of Shearer and Davidson (1965), the main difference being that the shape of the wave is known *a priori* in the present simulation and is not the dependent variable as in Shearer and Davidson's calculation. A similar approach was also adopted by Hewitt *et al.* (1985) and McQuillan *et al.* (1985). The forces are as follows,

1. Gravitational force. $\mathbf{F}_{gw}$ is due to the action of the gravitational field on the mass of liquid that forms the wave.

$$\mathbf{F}_{gw} = \frac{1}{4}\pi\rho_L g d_T L_W \left(2\mathsf{A}_W + \delta_{s,in} + \delta_{s,out}\right). \tag{6.13}$$

2. Pressure force on the core. $\mathbf{F}_{pC}$ is due to the pressure unbalance over the wave in the core side (separation at the leeward side of the wave).

$$\mathbf{F}_{pC} = \frac{2\pi\rho_C}{(d_T - 2\mathrm{A}_W)^4}\left(U_C - U_W\right)^2\left(d_T - 2\delta_{s,out}\right)^2\left(\mathrm{A}_W - \delta_{s,out}\right)^2\left(\mathrm{A}_W + \delta_{s,out} - d_T\right)^2. \tag{6.14}$$

The above equation was derived by applying the Bernoulli equation to the flow in the core region, where it is assumed (Shearer and Davidson, 1965) that the pressure at the leeward side of the wave remains equal to its value at the wave crest. $\mathbf{F}_{pC}$ also accounts for the (opposite) force caused by the change in core velocity over the control volume as one assumes that the streamlines remain parallel downstream to the crest plane. ρ_C and U_C are the homogeneous core density and velocity, respectively. They are calculated assuming a homogeneous flow of gas and entrained droplets (if any) in the core. These are given by,

$$\rho_C = \frac{\dot{m}_{LE} + \dot{m}_G}{\frac{\dot{m}_{LE}}{\rho_L} + \frac{\dot{m}_G}{\rho_G}}, \tag{6.15}$$

and,

$$U_C = \frac{\frac{\dot{m}_{LE}}{\rho_L} + \frac{\dot{m}_G}{\rho_G}}{\left(1 - \frac{2\delta_s}{d_T}\right)^2}. \tag{6.16}$$

In Eqs. 6.15 and 6.16, $\dot{m}_{LE}$ and $\dot{m}_G$ are the entrained liquid and gas mass velocities. For consistency in the pressure calculations, U_C is always evaluated using $\delta_s = \delta_{s,out}$.

3. Pressure force on the liquid. $\mathbf{F}_{pL}$ is due to a pressure imbalance at the top and at the bottom of the wave on the liquid film. The magnitude of $\mathbf{F}_{pL}$ is given by,

$$|\mathbf{F}_{pL}| = |p_{L,in}A_{LF,in} - p_{L,out}A_{LF,out}|\,, \tag{6.17}$$

where $A_{LF,in}$ and $A_{LF,out}$ are the cross sectional area of the liquid film at the planes $z = L_W$ and $z = 0$, respectively. $p_{L,in}$ and $p_{L,out}$ are the pressures acting normal to these planes in the liquid film.

A simplification to Eq. 6.17 is carried out as follows,

$$p_{L,in}A_{LF,in} - p_{L,out}A_{LF,out} \cong (p_{L,in} - p_{L,out})\,\overline{A}_{LF}, \tag{6.18}$$

where $\overline{A}_{LF}$ is an average falling film area given by,

$$\overline{A}_{LF} = \frac{\pi}{2} d_T\,(\delta_{s,in} + \delta_{s,out})\,. \tag{6.19}$$

The pressure difference between the top and bottom of the wave on the liquid side is given by,

$$p_{L,in} - p_{L,out} = p_{C,in} - p_{C,out} + \sigma\left(\left.\frac{d^2\delta_s}{dz^2}\right|_{z=0} - \left.\frac{d^2\delta_s}{dz^2}\right|_{z=L_W}\right), \tag{6.20}$$

where σ is the surface tension. The pressure drop in the core side, $p_{C,in} - p_{C,out}$, is given by the same analysis which led to the calculation of $\mathbf{F}_{pC}$,

$$p_{C,in} - p_{C,out} = \frac{8\rho_C}{(d_T - 2\mathrm{A}_W)^4}\,(\mathrm{A}_W - \delta_{s,out})^2\,(U_C - U_W)^2\,(\mathrm{A}_W + \delta_{s,out} - d_T)^2\,, \tag{6.21}$$

and,

$$\left(\left.\frac{d^2\delta_s}{dz^2}\right|_{z=0} - \left.\frac{d^2\delta_s}{dz^2}\right|_{z=L_W}\right) = \frac{2\pi^2}{L_W^2}\,(\delta_{s,out} - \delta_{s,in})\,. \tag{6.22}$$

$\mathbf{F}_{pL}$ is finally given by,

$$\mathbf{F}_{pL} = (p_{L,out} - p_{L,in})\,\overline{A}_{LF}. \tag{6.23}$$

4. Wall shear force. To calculate the force due to shear stress at the wall in the wave region, the approach taken by Hewitt *et al.* (1985) based on studies on slug flows (Moalem Maron and Brauner, 1982) and on inclined wavy falling film flows (Brauner *et al.*, 1985) was adopted and it is illustrated in Fig. 6.6. The incoming fluid is brought to rest (with respect to the wave) in a mixing zone after which a new boundary layer is formed on the (moving) wall as illustrated. Assuming that the mixing zone is short, the boundary layer length may be taken as approximately equal to the wave region length. Thus, assuming the boundary layer to be laminar, the frictional force (in this case *downwards* with respect to the wave) can be calculated from the standard boundary layer expression,

$$\mathbf{F}_{sw} = \left(\frac{8\rho_L L_W U_W \eta_L}{15}\right)^{1/2}. \tag{6.24}$$

Visual observation of the velocity profile in the wave region by Hewitt *et al.* (1985) showed that the actual movement of the liquid in this region does not conform to this pattern. In fact, there is a strong liquid circulation which gives rise to a peak in the velocity profile. However, at the level of sophistication of the present methodology, where numerous simplifying assumptions were made, it is believed that a more realistic, and therefore more complicated, representation of the liquid velocity distribution in the wave region will not lead to a significant improvement of the results.

5. Interfacial shear force. The shear force exerted on the liquid surface by the gas

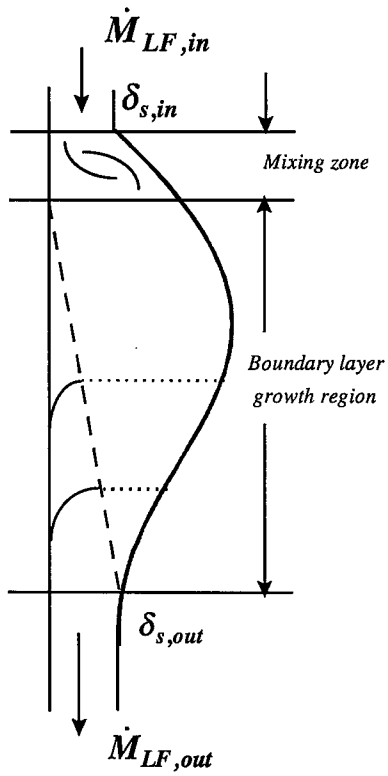


Figure 6.6: The boundary layer hypothesis for wall shear stress.

flow is neglected. Shearer and Davidson (1965) performed an order-of-magnitude calculation that showed a much greater influence of normal pressure forces. There is evidence that suggests that the interfacial shear stress is small compared with the gravitational force up to the point where flooding waves are generated; thus, in the experiments of Hewitt and Wallis (1963) there was little or no effect on mean film thickness as the gas velocity was increased from zero up to just before that required for flooding. However, the importance of shear stress once the wave is formed and is being transported cannot easily be deduced either from the Shearer and Davidson (1965) order-of-magnitude calculation or from the observations of Hewitt and Wallis (1963). In order to calculate the shear force, it is necessary to have recourse to Computational Fluid Dynamics (CFD) calculations and such calculations on flooding-type waves are reported by Jayanti *et al.* (1996). Their calculations show that the shear force on the wave is of the order of 20% of the pressure force. Since it is difficult to estimate the shear force without recourse to CFD, and since it is a relatively small proportion of the total force, it has been neglected in the current analysis. Note that the nature of flooding waves is different from that of disturbance waves characteristic of co-current annular flows. In the latter, interfacial shear plays a dominant role whereas pressure forces may by neglected.

The net force acting on the wave is thus,

$$\sum \mathbf{F}_z = \mathbf{F}_{pC} + \mathbf{F}_{pL} - \mathbf{F}_{sw} - \mathbf{F}_{gw}. \tag{6.25}$$

6.4 Solution of conservation equations

After combination of wave volumetric relationships, Eqs. 6.8 and 6.9, with Eqs. 6.2 and 6.3, the conservation principles can be written as,

$$\frac{d}{dt}\mathsf{A}_W = 2\frac{\dot{M}_{LF,in} - \dot{M}_{LF,out}}{\pi\rho_L d_T L_W} - \frac{U_W}{6L_{sint}}\left[\frac{\delta_{s,in}\left(\dot{M}_{LF,ss} + \dot{M}_{LE} - \dot{M}_L\right)}{\dot{M}_{LF,in}} + \frac{\delta_{s,out}\left(\dot{M}_{LF,ss} - \dot{M}_{LF,out}(0)\right)}{\dot{M}_{LF,out}}\right], \tag{6.26}$$

and,

$$\frac{d}{dt}U_W = 4\frac{\sum \mathbf{F}_z + \frac{\dot{M}^2_{LF,out}}{\pi d_T \rho_L \delta_{s,out}} - \frac{\dot{M}^2_{LF,in}}{\pi d_T \rho_L \delta_{s,in}}}{\pi\rho_L d_T L_W \left(2\mathsf{A}_W + \delta_{s,in} + \delta_{s,out}\right)}. \tag{6.27}$$

The distance travelled by the wave is given by,

$$\frac{d}{dt}z = U_W. \tag{6.28}$$

Equations 6.27 to 6.28 are solved using a fourth-order Runge-Kutta Method (Press *et al.*, 1992) with the following initial conditions,

$$\mathsf{A}_W(0) = \mathsf{A}_{W,crit}, \tag{6.29}$$

$$U_W(0) = 0, \tag{6.30}$$

$$z(0) = 0, \tag{6.31}$$

where $\mathsf{A}_{W,crit}$ is the critical wave amplitude, i.e., the amplitude at which the wave starts moving upwards. At this critical condition, the sum of forces acting on the wave is equal to zero. The resultant force is calculated applying an analysis similar to that by Costigan (1997).

The solution procedure of the mathematical model is as follows. $\dot{M}_{LF,in}$ is set equal to $\dot{M}_L\,(1-e)$, where e is the fraction of liquid entrained as droplets. e is not known *a*

priori and it is assumed constant. L_W and $\dot{M}_{LF,out}(0)$ are also not previously known. Therefore, L_W, $\dot{M}_{LF,out}(0)$ and e are set to vary over a wide range of values and at each iteration the system of Eqs. 6.27 to 6.28 is solved giving distributions of wave amplitude, velocity and distance travelled as a function of time. The set of parameters corresponding to the chosen solution is the one whose distribution gives the smallest deviation to the experimental data on the distance travelled by the wave.

For all conditions observed, the ranges of values assessed are as follows, L_W, $d_T/6$ to d_T; $\dot{M}_{LF,out}(0)$, 0 to $\left(\dot{M}_L - \dot{M}_{LU}\right)(1-e)$; and e, 0 to 0.25. $\dot{M}_{LU}$ is the flowrate of liquid carried upwards.

6.5 Analytical results

The values of critical wave amplitude, liquid entrained fraction and wave parameters that give the best fit to the experimental data for each sequence are summarised in Table 6.1. Also shown is the mean error associated with the prediction for each sequence defined as,

$$error = \frac{1}{N_p}\sum_{i=1}^{N_p}\frac{|z_{pred,i} - z_{exp,i}|}{z_{exp,i}}, \tag{6.32}$$

where N_p is the number of experimental points available for each sequence. z_{pred} and z_{exp} are the predicted and experimental axial distances travelled by the wave.

It can be seen from Table 6.1 that both the length of the wave, L_W, and the critical amplitude, $A_{W,crit}$, increase with decreasing gas flowrate at constant liquid flowrate (Sequences 3, 4 and 5) and with increasing liquid flowrate at constant gas flowrate (Sequences 1 and 2). This is consistent with what has been observed experimentally. By comparing the values of liquid flowrate out of the wave, $\dot{M}_{LF,out}(0)$, for Sequences 3 to 5, it can be observed that the mass storage in the control volume is higher for the higher gas flowrates. Therefore, the rate of growth is higher for such cases and the wave critical amplitude is

Table 6.1: Results obtained using the mathematical model.

Sequence No	$A_{W,crit}$ [mm]	e [-]	$\dot{M}_{LF,out}$ $\times 10^{-3}$ [kg/s]	L_W [mm]	Wave velocity [m/s]	E [%]
1	4.08	0.06	14.4	9.8	1.06	12.7
2	4.09	0.07	24.4	10.8	1.44	34.4
3	3.89	0.10	44.9	10.5	1.69	23.8
4	4.76	0.10	62.4	13.5	1.20	19.7
5	5.30	0.08	70.4	14.3	0.81	25.3

attained more rapidly. Also shown in Table 6.1 are the values of wave velocity at the end of the sinter ($z = 25$ mm) for each experimental sequence. With exception of Sequences 2, the agreement between these values and the mean velocities obtained experimentally is not so good. However, the range of predicted velocities is not inconsistent when compared to that obtained by Hewitt *et al.* (1985) for both air-water and air-trichlorethylene flows. The predicted entrained fraction remains approximately constant throughout the assessed range of parameters; though a small gas flowrate effect is picked up in Sequences 3, 4 and 5.

The solid lines in Fig. 6.7 correspond to the predictions of distance travelled by the waves for each one of the sequences (S1 to S5). The general trend of the experimental data is generally well picked-up by the methodology (with exception of Sequence 2). Figure 6.8 shows the calculated wave velocity distributions for each sequence. It can be observed that the wave of Sequence 5 has a slight negative velocity before starting to move upwards.

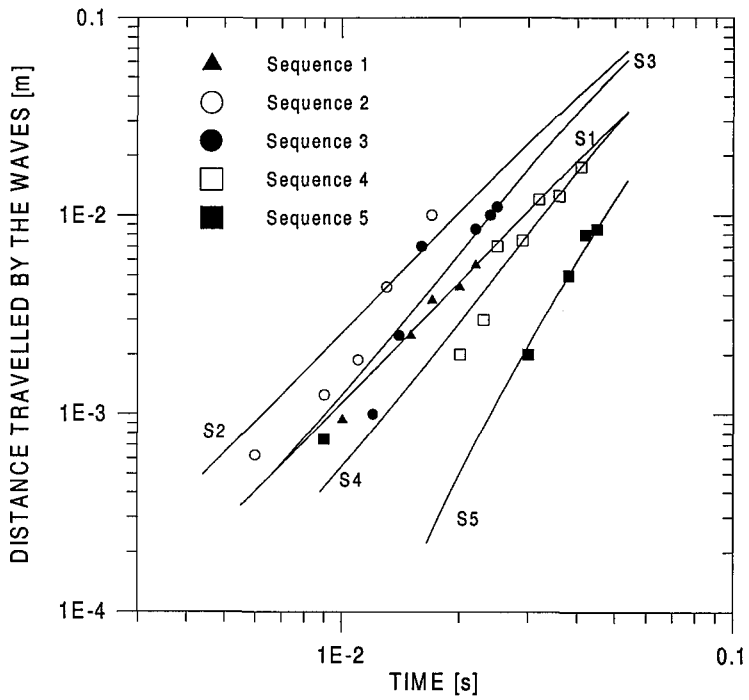


Figure 6.7: Wave position versus time. Symbols refer to Sequences in Govan (1990) experiments.

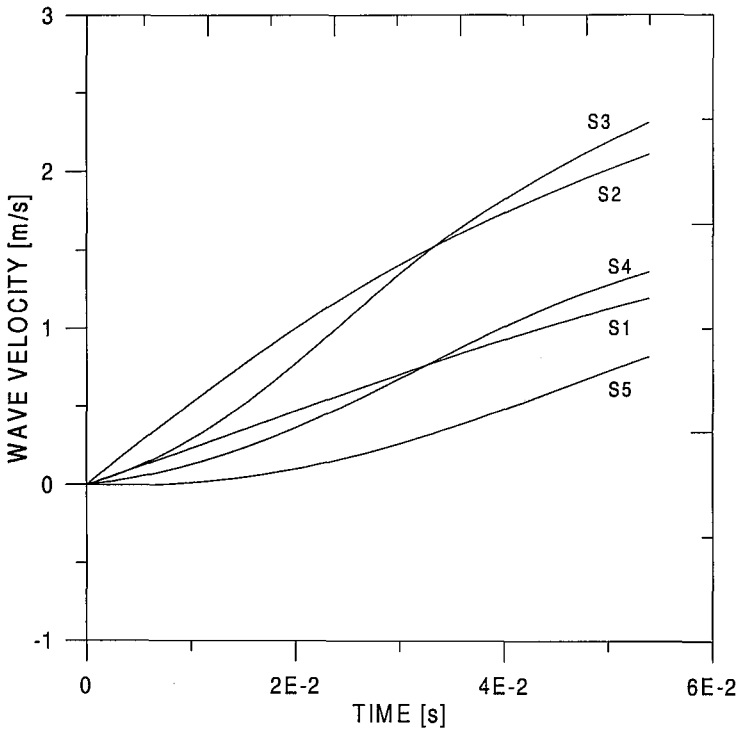


Figure 6.8: Calculated wave velocity distributions.

6.6 Summary

The present work has dealt with analysis of video sequences of churn flow of an air-water mixture in a vertical pipe and the development of a model for the flow. The video sequences analysed were those by Govan (1990) in studying the behaviour of the flow close to the liquid inlet in a specially constructed transparent porous-wall test section. The main conclusions arising from this study are presented in Section 7.4.

Chapter 7

Conclusions and Future Work

This Chapter presents the main conclusions arising from the studies carried out in this thesis. Sections 7.1 to 7.4 summarise the conclusions of Chapters 3 to 6. Recommendations for future work are also presented in each section.

7.1 Visualisation of nucleate boiling in annular flow

7.1.1 Conclusions

Chapter 3 presented an experimental investigation of nucleate boiling in a climbing film characteristic of annular flow. This was performed using a specially constructed, internally heated, annulus test section through which a direct observation of the flow could be carried out. Measurements of the heater wall temperature enabled the calculation of the local heat transfer coefficient. The main conclusions arising from this study are as follows,

1. From an analysis of high-speed video recordings (and of corresponding still frames), several qualitative features of the hydrodynamics and heat transfer in annular flow could be observed (e.g., wave break-up, droplet entrainment, bubble nucleation). From an analysis of such observations, it seems possible that bubble nucleation

is *locally* triggered off by disturbance waves travelling upwards on the liquid film. Although the series of experiments described in Chapter 3 did not allow a disclosure of the mechanism behind the observed phenomenon, an explanation for this local enhancement may be sought in the decrease of the local pressure associated with the passage of the wave. This is a point which requires further investigation;

2. Disturbance waves were present in all but the lowest of film flow rates investigated ($Re_{LF} \approx 90$). Droplet entrainment from the disturbance waves was observed. The value of the critical liquid Reynolds number for droplet entrainment inception was reasonably well predicted by the graphical correlation available in Azzopardi (1997);

3. Through an analysis of the video sequences, the frequency and velocity of the waves were determined. These were made at several locations along the test section. Although the database generated was very limited, general conclusions could be drawn which are in accordance with previous work (Shearer, 1964; Hall-Taylor and Nedderman, 1968). The main conclusions are, (i) the velocity of disturbance waves changed very slowly with position, (ii) the wave frequency, in contrast, had a stronger positional dependence and (iii) the Strouhal number (dimensionless frequency), Sr, did not agree with the correlation of Shearer (1964), based on his air and water data. Like Hall-Taylor and Nedderman (1968), one may conclude that Sr is dependent on the pair of fluids;

4. A simple analysis of the Onset of Nucleate Boiling (ONB) in a climbing film was presented. Some of the available correlations and methods for predicting the wall superheat at the ONB in convective systems (Davis and Anderson, 1966; Frost and Dzakovic, 1967) and falling films (Marsh and Mudawar, 1989) tended to underestimate the wall superheat as a function of the wall heat flux at the ONB and other system parameters. On the other hand, when use was made of a methodology which

combined the theory of Hsu (1962) for ONB and a procedure to estimate the wall shear stress from measurements of pressure gradient and phase mass fluxes in an annulus (Hewitt, 1964), a better prediction of the wall superheat at the ONB was achieved;

5. A weak (but noticeable) dependence of the heat transfer coefficient on the wall heat flux was observed. This was illustrated by a power-law fit to the average heat transfer coefficient. Six correlations were tested and the best agreement with the experimental data was given by the correlation of Bennett *et al.* (1961) for boiling in annuli;

6. For some of the boiling heat transfer correlations (Chen, 1966; Kandlikar, 1990; Steiner and Taborek, 1992), better results for annuli were obtained using the equivalent diameter defined as four times the ratio of the flow area to the *heated* perimeter.

7.1.2 Future Work

Recommendations for future investigations in pursuance of the work described in Chapter 3 are as follows,

1. To devise and perform an experimental campaign in which the pressure fluctuations associated with the passage of the wave are evaluated. This investigation could combine simultaneously the pressure measurement with a high-speed observation of the flow field;

2. To extend the database for wave frequency and velocities as a function of distance along the test section.

7.2 Modelling of forced convective multicomponent boiling

7.2.1 Conclusions

In Chapter 4, a comprehensive modelling framework for prediction of annular flow of binary and multicomponent mixtures undergoing phase change was presented. The methodology was tested using data from Kandlbinder (1997) for boiling of binary and ternary hydrocarbon mixtures in a vertical tube.

A droplet interchange model was proposed and embedded into the annular flow calculation methodology. The set of correlations of droplet entrainment and deposition by Govan *et al.* (1988) (see also Govan, 1990) for pure fluids was applied in this model. This was coupled with a model for interphase heat and mass transfer based on a Colburn-Drew type formulation. The application of this calculation methodology enabled the assessment of the behaviour of several flow parameters such as the mass fluxes and bulk concentrations of the liquid film, entrained droplets and vapour core, the interface temperature, the interface liquid and vapour concentrations, the wall temperature and the heat transfer coefficient.

The main conclusions arising from the study described in Chapter 4 are as follows,

1. In the annular flow regime, the processes of droplet entrainment and deposition coupled with the preferential evaporation of the more volatile component from the liquid film generates, at a given distance along the channel, a difference in the mean concentrations of the liquid film and entrained droplets. As a result, different axial gradients of mean concentration occur in the respective liquid streams;

2. The analysis of the parameter $e^{0,m}$, defined as the mass fraction of droplets which, having been created at the point of onset of annular flow, are still entrained in

the core at a section m downstream, permits an assessment of the influence of the amount of liquid initially entrained as droplets on the liquid concentration profiles;

3. In the model, an increase in the fraction of liquid entrained as droplets at the onset of annular flow gives rise to profiles of mean droplet concentration which are richer in the more volatile component. In contrast, the liquid film mean concentration distributions are richer in the less volatile component as less liquid was available in the film for evaporation;

4. The combined effect of mass transfer resistance (due to gradients of concentration building up adjacent to the interface) and of droplet interchange gives rise to interfacial temperatures higher than the equilibrium (T_{bub}) temperature (assuming no droplet entrainment and no mass transfer resistance). This leads to wall temperatures (calculated by the model) which are higher than those calculated assuming equilibrium. As the heat transfer coefficient, α, is defined as the ratio of the wall heat fiux, $\dot{q}_w$ to the wall superheat, $(T_w - T_{bub})$, the proposed methodology gives heat transfer coefficients lower than those predicted using the equilibrium assumption;

5. Predictions of heat transfer coefficient are compared with the experimental data of Kandlbinder (1997) for boiling of binary (n-pentane/iso-octane) and ternary (n-pentane/n-hexane/iso-octane) hydrocarbon mixtures under various conditions. The deterioration observed in the experimental heat transfer coefficient for mixtures at high qualities is well predicted by the methodology. The accuracy of the predictions reduces somewhat with increasing system pressure;

6. Other methods and correlations for predicting the heat transfer coefficient in mixture systems were implemented (Sardesai *et al.*, 1982; Palen, 1983; Kandlikar, 1998). It

was shown that the predictions of the present methodology are significantly better than those given by the methods for a wide range of conditions;

7. In modelling the interface mass and heat transfer for ternary mixtures, the diffusive fluxes present in the Colburn-Drew methodology were modelled via a linearly generalised Fick's Law (Toor, 1964; Stewart and Prober, 1964) or via an Effective Diffusivity (Taylor and Krishna, 1993) formulation. Diffusive interaction effects were found to be small for the set of conditions assessed and the results were very similar for both formulations;

8. The modified annular flow model was also employed to predict the data of Kandlbinder (1997) on dryout of single component hydrocarbons and hydrocarbon mixtures. When the model was applied using the original set of correlations for entrainment and deposition by Govan (1990), an overestimation of the dryout quality was observed. It is likely that this non-conservative over-prediction is due to an inability of the correlations to deal adequately with the low surface tension fluids like the hydrocarbon systems studied here. Based on a measure of the statistical variance of the data used in the correlation, a correction was proposed for the droplet interchange rates correlations. The correction improved the prediction of the data. The dryout predictions are significantly better than that given by a widely used empirical correlation (Katto and Ohno, 1984). It was also demonstrated that the proposed correction of the entrainment and deposition correlations to better predict dryout of hydrocarbons did not affected the heat transfer coefficient predictions significantly;

9. An analysis of the droplet interchange/mass transfer effects on condensation heat transfer of mixtures was carried out and preliminary results showed that the heat transfer coefficient may actually increase with increasing quality for condensation. The modelling results agreed well with experimental data of Cavallini *et al.* (1999)

for condensation of mixed refrigerants.

7.2.2 Future Work

Recommendations for future investigations on the work presented in Chapter 4 are as follows,

1. More experimental work is needed on entrainment and deposition in hydrocarbons and other non-aqueous systems so that better droplet interchange correlations can be developed for such systems. Also, a more thorough investigation of the role of heat flux induced entrainment in both aqueous and non-aqueous systems is needed;

2. The present methodology should be applied to systems other than organic mixtures (i.e., aqueous mixtures). The water/methanol data of Shatto (1998) could be used for comparison;

3. a more detailed set of experiments, aimed at investigating the influence of droplet interchange on condensation heat transfer of multicomponent mixtures, is required in order to consolidate the condensation analysis.

7.3 Entrainment at the onset of annular flow

7.3.1 Conclusions

Chapter 5 presented an experimental analysis of droplet entrainment in churn flow, with particular emphasis on determining the entrained droplet fraction in the region of transition between churn flow and annular flow in a vertical pipe. An isokinetic probe system was used to measure the local distributions of liquid and gas mass fluxes. The main conclusions arising from this study are as follows,

1. In the fully cocurrent annular region ($U^*_{GS} > 1$), the local droplet concentration is virtually constant within the gas core. In contrast, the churn flow regime exhibits sharp radial gradients of concentration which gradually disappear with increase in gas velocity;

2. Both pressure gradient behaviour and entrained fraction exhibit a minimum at $U^*_{GS} \approx 1$, before increasing again in the annular regime. An explanation for such a behaviour may by sought based on the mechanisms by which droplets are created from interfacial waves present on a liquid film (Azzopardi, 1983). Other features of the behaviour of the entrained fraction could be observed, namely (i) the entrained liquid flowrate (and the entrained fraction) increases with the total liquid flowrate; (ii) the effect of pressure on the entrained fraction is not as pronounced as that of the liquid flowrate, however the pressure seems to affect more the results in the annular flow region (for higher pressures, the entrained fraction increases less after the minimum is reached); (iii) for low water flowrates ($\dot{m}_L \approx 10$ kg m^{-2} s-1 and $\dot{m}_L \approx 20$ kg m^{-2} s-1) the higher uncertainty in the experimental data is attributed to evaporation of the liquid film (air humidification);

3. An empirical correlation was devised to predict the entrained fraction at the onset of annular flow ($0.9 < U^*_G < 1.3$). The correlation predicts data from the present study and from other sources with reasonable accuracy;

4. Predictions using an annular flow model indicated that, at the onset of annular flow and under equilibrium conditions identical to those of the experiments, the entrained fraction was severely underpredicted for $\dot{m}_L > 100$ kg m^{-2} s^{-1}.

7.3.2 Future Work

Recommendations for future work on the study presented in Chapter 5 are as follows,

1. Further experiments are needed to investigate in more detail the effect of physical properties on entrainment in churn flow and in the transition region between churn and annular flow;

2. Visualisation and other studies are required to clarify the mechanisms of entrainment in churn flow and in the churn/annular transition.

7.4 Modelling of churn flow waves

7.4.1 Conclusions

Chapter 6 presented a simple model describing the processes of wave formation and development in churn flow. The model was largely based on visual observations of the flow by means of high-speed video recording (Govan, 1990). These were also in general agreement with the mechanisms of wave formation postulated by Hewitt *et al.* (1985) and illustrated in Fig. 2.9. The main conclusions on this study are as follows,

1. The model was calibrated using the data obtained by Govan (1990) for the distance travelled by the waves. The results are in good agreement with these data;

2. Predicted wave parameters, such as critical amplitude, length, velocity and flowrates are also consistent with the experimental observations.

The model in its present form is far from being a predictive tool for a complex phenomenon such as churn flow. Rather, its mission is to give an insight on the mechanisms involved and to serve as a basis to more refined phenomenological methodologies capable also of predicting relevant engineering parameters such as pressure drop.

7.4.2 Future Work

Recommendations for additional work related to the work presented in Chapter 6 are as follows,

1. To generate more data on the wave formation and development in churn flow. The effect of physical properties such as surface tension and viscosity should be determined. The visualisation technique of Govan (1990) could be used for these studies, perhaps being coupled with axial view photography and photo-chromic dye tracing;

2. To develop more detailed models for formation and transport of waves in churn flow. Perhaps the CFD approach used by Jayanti and Hewitt (1997) and Watson (1999) could be used in this context.

Appendix A

Visualisation Data of Nucleate Boiling in Annular Flow

The purpose of this appendix is to present detailed data obtained from the analysis of the video sequences of boiling in annular flow in a vertical annulus section described in Chapter 3. Tables A.1 to A.12 present the visualisation data obtained at a single axial position (approximately 0.25 m from the bottom of heater). Tables A.13 to A.22 present the visualisation data obtained at different distances along the heater.

Table A.1: Wave velocity and frequency data. Experimental conditions: Run 0824a, $p_{in} = 1.6$ bar, $\dot{m}_T = 24.9$ kg m^{-2} s^{-1}, $X_{in} = 0.68$, $\dot{q}_w = 0$ kW m^{-2}, $\Delta T_{in} \approx 30$ K.

Wave No	Nucleate Boiling	Velocity (m s^{-1})	Frequency (Hz)	Wave Strouhal number	Strouhal number
1		0.56 ± 0.07		0.187	
2	no	0.74 ± 0.13	8.13 ± 0.97	0.142	0.0056

Table A.2: Wave velocity and frequency data. Experimental conditions: Run 0824c, $p_{in} = 1.6$ bar, $\dot{m}_T = 24.9$ kg m^{-2} s^{-1}, $X_{in} = 0.68$, $\dot{q}_w = 0$ kW m^{-2}, $\Delta T_{in} \approx 30$ K.

Wave No	Nucleate Boiling	Velocity (m s^{-1})	Frequency (Hz)	Wave Strouhal number	Strouhal number
1		0.85 ± 0.13		0.116	
2	no	1.06 ± 0.19	7.63 ± 0.95	0.093	0.0053

Table A.3: Wave velocity and frequency data. Experimental conditions: Run 0824e, $p_{in} = 1.6$ bar, $\dot{m}_T = 22.2$ kg m^{-2} s^{-1}, $X_{in} = 0.64$, $\dot{q}_w = 73.1$ kW m^{-2}, $\Delta T_{in} \approx 30$ K.

Wave No	Nucleate Boiling	Velocity (m s^{-1})	Frequency (Hz)	Wave Strouhal number	Strouhal number
1		1.29 ± 0.21		0.070	
2	1 site	1.23 ± 0.20	6.98 ± 0.94	0.073	0.0058

Table A.4: Wave velocity and frequency data. Experimental conditions: Run 0824f, $p_{in} = 1.6$ bar, $\dot{m}_T = 22.2$ kg m^{-2} s^{-1}, $X_{in} = 0.64$, $\dot{q}_w = 125.3$ kW m^{-2}, $\Delta T_{in} \approx 30$ K.

Wave No	Nucleate Boiling	Velocity (m s^{-1})	Frequency (Hz)	Wave Strouhal number	Strouhal number
1		1.06 ± 0.19		0.074	
2	ONB	1.00 ± 0.17	6.09 ± 0.91	0.079	0.051
3		0.85 ± 0.12		0.092	

Table A.5: Wave velocity and frequency data. Experimental conditions: Run 0824h, $p_{in} = 2.1$ bar, $\dot{m}_T = 30.1$ kg m^{-2} s^{-1}, $X_{in} = 0.73$, $\dot{q}_w = 0$ kW m^{-2}, $\Delta T_{in} \approx 30$ K.

Wave No	Nucleate Boiling	Velocity (m s^{-1})	Frequency (Hz)	Wave Strouhal number	Strouhal number
1		1.03 ± 0.18		0.172	
2	no	0.97 ± 0.16	13.7 ± 1.2	0.182	0.0095

Table A.6: Wave velocity and frequency data. Experimental conditions: Run 0824k, $p_{in} = 2.1$ bar, $\dot{m}_T = 30.1$ kg m^{-2} s^{-1}, $X_{in} = 0.73$, $\dot{q}_w = 189.5$ kW m^{-2}, $\Delta T_{in} \approx 30$ K.

Wave No	Nucleate Boiling	Velocity (m s^{-1})	Frequency (Hz)	Wave Strouhal number	Strouhal number
1		1.26 ± 0.26		0.081	
2	yes	1.31 ± 0.28	7.88 ± 0.96	0.076	0.0055
3		1.22 ± 0.24		0.083	
4		1.22 ± 0.24		0.083	

Table A.7: Wave velocity and frequency data. Experimental conditions: Run 0829b, $p_{in} = 2.0$ bar, $\dot{m}_T = 33.7$ kg m^{-2} s^{-1}, $X_{in} = 0.62$, $\dot{q}_w = 96.6$ kW m^{-2}, $\Delta T_{in} \approx 30$ K.

Wave No	Nucleate Boiling	Velocity (m s^{-1})	Frequency (Hz)	Wave Strouhal number	Strouhal number
1		1.36 ± 0.30		—	
2	no	1.89 ± 0.53	inconclusive	—	—

Table A.8: Wave velocity and frequency data. Experimental conditions: Run 0830a, $p_{in} = 2.0$ bar, $\dot{m}_T = 30.2$ kg m^{-2} s^{-1}, $X_{in} = 0.63$, $\dot{q}_w = 0$ kW m^{-2}, $\Delta T_{in} \approx 30$ K.

Wave No	Nucleate Boiling	Velocity (m s^{-1})	Frequency (Hz)	Wave Strouhal number	Strouhal number
1		0.97 ± 0.14		0.109	
2		1.14 ± 0.19		0.093	
3		0.83 ± 0.11		0.127	
4		0.77 ± 0.09		0.137	
5	no	1.14 ± 0.19	8.18 ± 0.97	0.093	0.0063
6		0.68 ± 0.07		0.155	
7		0.87 ± 0.12		0.121	
8		0.76 ± 0.09		0.139	
9		1.06 ± 0.17		0.099	
10		0.97 ± 0.14		0.109	

Table A.9: Wave velocity and frequency data. Experimental conditions: Run 0830b, $p_{in} = 2.0$ bar, $\dot{m}_T = 30.2$ kg m^{-2} s^{-1}, $X_{in} = 0.63$, $\dot{q}_w = 96.1$ kW m^{-2}, $\Delta T_{in} \approx 30$ K.

Wave No	Nucleate Boiling	Velocity (m s^{-1})	Frequency (Hz)	Wave Strouhal number	Strouhal number
1		1.22 ± 0.24		0.077	
2		1.06 ± 0.17		0.088	
3	3 sites	1.03 ± 0.16	7.24 ± 0.94	0.091	0.0055
4		0.59 ± 0.07		0.158	
5		1.06 ± 0.17		0.088	
6		0.77 ± 0.09		0.121	
7		0.87 ± 0.16		0.107	

Table A.10: Wave velocity and frequency data. Experimental conditions: Run 0830c, $p_{in} = 2.0$ bar, $\dot{m}_T = 30.2$ kg m^{-2} s^{-1}, $X_{in} = 0.63$, $\dot{q}_w = 158.7$ kW m^{-2}, $\Delta T_{in} \approx 30$ K.

Wave No	Nucleate Boiling	Velocity (m s^{-1})	Frequency (Hz)	Wave Strouhal number	Strouhal number
1	yes	0.92 ± 0.18	7.51 ± 0.94	0.105	0.0057
2		0.60 ± 0.08		0.161	
3		1.17 ± 0.20		0.083	
4		1.03 ± 0.16		0.094	
5		0.85 ± 0.11		0.114	
6		1.03 ± 0.16		0.094	
7		1.17 ± 0.20		0.083	
8		1.70 ± 0.44		0.057	

Table A.11: Wave velocity and frequency data. Experimental conditions: Run 0830d, $p_{in} = 2.0$ bar, $\dot{m}_T = 30.2$ kg m^{-2} s^{-1}, $X_{in} = 0.63$, $\dot{q}_w = 276.7$ kW m^{-2}, $\Delta T_{in} \approx 30$ K.

Wave No	Nucleate Boiling	Velocity (m s^{-1})	Frequency (Hz)	Wave Strouhal number	Strouhal number
1	yes	0.79 ± 0.11	5.01 ± 0.89	0.082	0.0038
2		1.21 ± 0.24		0.053	
3		1.36 ± 0.30		0.048	

Table A.12: Wave velocity and frequency data. Experimental conditions: Run 0830e, $p_{in} = 2.0$ bar, $\dot{m}_T = 30.2$ kg m^{-2} s^{-1}, $X_{in} = 0.63$, $\dot{q}_w = 485.6$ kW m^{-2}, $\Delta T_{in} \approx 30$ K.

Wave No	Nucleate Boiling	Velocity (m s^{-1})	Frequency (Hz)	Wave Strouhal number	Strouhal number
1		1.26 ± 0.23		0.046	
2	yes	1.00 ± 0.15	4.51 ± 0.88	0.058	0.0034

Table A.13: Wave velocity and frequency data. Experimental conditions: Run 1027a, Position from the bottom of heater = 0 m, $p_{in} = 1.9$ bar, $\dot{m}_T = 32.1$ kg m^{-2} s^{-1}, $X_{in} = 0.60$, $\dot{q}_w = 0$ kW m^{-2}, $\Delta T_{in} \approx 10$ K.

Wave No	Nucleate Boiling	Velocity (m s^{-1})	Frequency (Hz)	Wave Strouhal number	Strouhal number
1		0.96 ± 0.08		0.188	
2		0.98 ± 0.13		0.184	
3		1.08 ± 0.19		0.167	
4		1.00 ± 0.15		0.181	
5	no	1.00 ± 0.15	14.0 ± 1.0	0.181	0.010
6		0.89 ± 0.12		0.203	
7		0.77 ± 0.10		0.234	
8		0.79 ± 0.11		0.229	
9		1.08 ± 0.17		0.167	

Table A.14: Wave velocity and frequency data. Experimental conditions: Run 1027b, Position from the bottom of heater = 0 m, p_{in} = 1.9 bar, $\dot{m}_T$ = 32.1 kg m^{-2} s^{-1}, $X_{in} = 0.60$, $\dot{q}_w = 0$ kW m^{-2}, $\Delta T_{in} \approx 10$ K.

Wave No	Nucleate Boiling	Velocity (m s^{-1})	Frequency (Hz)	Wave Strouhal number	Strouhal number
1		0.87 ± 0.12		0.208	
2		1.18 ± 0.20		0.153	
3	no	1.34 ± 0.25	14.0 ± 1.0	0.135	0.010
4		0.89 ± 0.12		0.203	
5		0.85 ± 0.11		0.212	
6		0.98 ± 0.14		0.184	

Table A.15: Wave velocity and frequency data. Experimental conditions: Run 1027c, Position from the bottom of heater = 0.065 m, p_{in} = 1.9 bar, $\dot{m}_T$ = 32.1 kg m^{-2} s^{-1}, $X_{in} = 0.60$, $\dot{q}_w = 0$ kW m^{-2}, $\Delta T_{in} \approx 10$ K.

Wave No	Nucleate Boiling	Velocity (m s^{-1})	Frequency (Hz)	Wave Strouhal number	Strouhal number
1		0.87 ± 0.12		0.148	
2	no	1.08 ± 0.17	10.0 ± 1.0	0.119	0.0072
3		1.10 ± 0.20		0.117	

Table A.16: Wave velocity and frequency data. Experimental conditions: Run 1027d, Position from the bottom of heater = 0.065 m, p_{in} = 1.9 bar, $\dot{m}_T$ = 32.1 kg m^{-2} s^{-1}, $X_{in} = 0.60$, $\dot{q}_w = 0$ kW m^{-2}, $\Delta T_{in} \approx 10$ K.

Wave No	Nucleate Boiling	Velocity (m s^{-1})	Frequency (Hz)	Wave Strouhal number	Strouhal number
1	no	1.00 ± 0.15	10.0 ± 1.0	0.129	0.0072
2		0.98 ± 0.13		0.132	
3		0.96 ± 0.14		0.134	
4		0.82 ± 0.10		0.157	

Table A.17: Wave velocity and frequency data. Experimental conditions: Run 1027e, Position from the bottom of heater = 0.105 m, p_{in} = 1.9 bar, $\dot{m}_T$ = 32.1 kg m^{-2} s^{-1}, $X_{in} = 0.60$, $\dot{q}_w = 0$ kW m^{-2}, $\Delta T_{in} \approx 10$ K.

Wave No	Nucleate Boiling	Velocity (m s^{-1})	Frequency (Hz)	Wave Strouhal number	Strouhal number
1		1.08 ± 0.17		0.119	
2		0.89 ± 0.12		0.145	
3		0.93 ± 0.13		0.139	
4	no	1.08 ± 0.17	10.0 ± 1.0	0.119	0.0072
5		0.84 ± 0.11		0.154	
6		0.98 ± 0.14		0.132	
7		1.00 ± 0.15		0.129	

Table A.18: Wave velocity and frequency data. Experimental conditions: Run 1027f, Position from the bottom of heater = 0.105 m, p_{in} = 1.9 bar, $\dot{m}_T$ = 32.1 kg m^{-2} s^{-1}, $X_{in} = 0.60$, $\dot{q}_w = 0$ kW m^{-2}, $\Delta T_{in} \approx 10$ K.

Wave No	Nucleate Boiling	Velocity (m s^{-1})	Frequency (Hz)	Wave Strouhal number	Strouhal number
1		0.96 ± 0.14		0.126	
2	no	0.82 ± 0.10	9.4 ± 1.2	0.148	0.0068

Table A.19: Wave velocity and frequency data. Experimental conditions: Run 1027g, Position from the bottom of heater = 0.135 m, p_{in} = 1.9 bar, $\dot{m}_T$ = 32.1 kg m^{-2} s^{-1}, $X_{in} = 0.60$, $\dot{q}_w = 0$ kW m^{-2}, $\Delta T_{in} \approx 10$ K.

Wave No	Nucleate Boiling	Velocity (m s^{-1})	Frequency (Hz)	Wave Strouhal number	Strouhal number
1		1.00 ± 0.15		0.121	
2		1.06 ± 0.16		0.114	
3	no	0.85 ± 0.11	9.4 ± 1.0	0.143	0.0068
4		1.22 ± 0.21		0.099	
5		1.06 ± 0.16		0.114	

Table A.20: Wave velocity and frequency data. Experimental conditions: Run 1027h, Position from the bottom of heater = 0.135 m, p_{in} = 1.9 bar, $\dot{m}_T$ = 32.1 kg m^{-2} s^{-1}, $X_{in} = 0.60$, $\dot{q}_w = 0$ kW m^{-2}, $\Delta T_{in} \approx 10$ K.

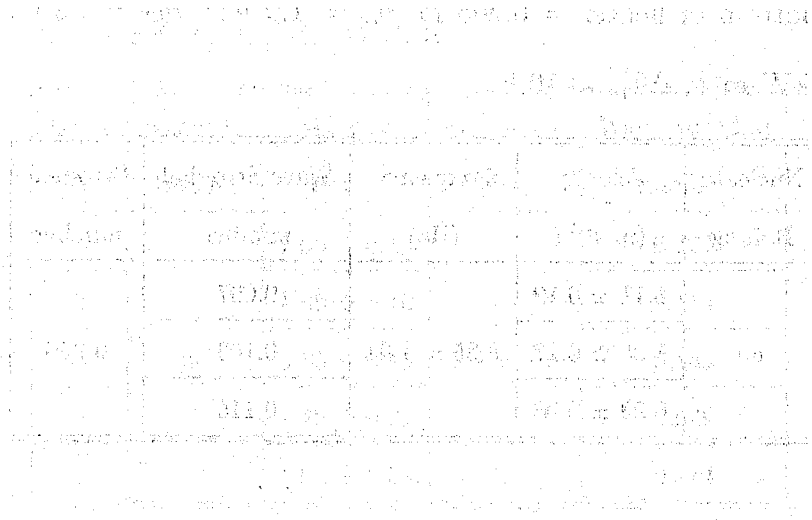
Wave No	Nucleate Boiling	Velocity (m s^{-1})	Frequency (Hz)	Wave Strouhal number	Strouhal number
1		1.08 ± 0.17		0.119	
2		1.29 ± 0.24		0.100	
3	no	0.96 ± 0.14	10.0 ± 1.1	0.134	0.0072
4		1.08 ± 0.17		0.119	
5		1.29 ± 0.24		0.100	

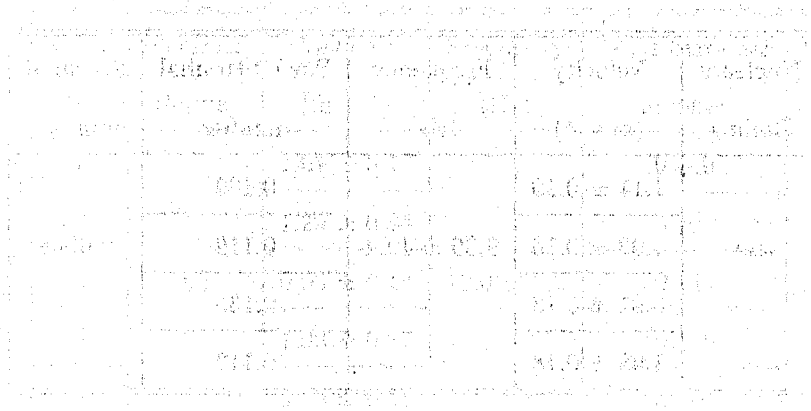
Table A.21: Wave velocity and frequency data. Experimental conditions: Run 1027i, Position from the bottom of heater = 0.205 m, p_{in} = 1.9 bar, $\dot{m}_T$ = 32.1 kg m^{-2} s^{-1}, $X_{in} = 0.60$, $\dot{q}_w = 0$ kW m^{-2}, $\Delta T_{in} \approx 10$ K.

Wave No	Nucleate Boiling	Velocity (m s^{-1})	Frequency (Hz)	Wave Strouhal number	Strouhal number
1		1.11 ± 0.19		0.097	
2	no	1.05 ± 0.17	8.35 ± 1.04	0.103	0.006
3		0.93 ± 0.08		0.116	

Table A.22: Wave velocity and frequency data. Experimental conditions: Run 1027j, Position from the bottom of heater = 0.205 m, p_{in} = 1.9 bar, $\dot{m}_T$ = 32.1 kg m^{-2} s^{-1}, $X_{in} = 0.60$, $\dot{q}_w = 0$ kW m^{-2}, $\Delta T_{in} \approx 10$ K.

Wave No	Nucleate Boiling	Velocity (m s^{-1})	Frequency (Hz)	Wave Strouhal number	Strouhal number
1		1.11 ± 0.19		0.109	
2	no	1.02 ± 0.16	9.39 ± 1.04	0.119	0.0068
3		0.91 ± 0.13		0.133	
4		1.08 ± 0.18		0.112	





Appendix B

Heat and mass transfer in the liquid film (Shock, 1976)

As mentioned in Chapter 2, Shock (1976) described a theory for simultaneous heat and mass transfer in annular flow of binary mixtures. The theory was based on the earlier theory by Hewitt (1961) for heat transfer in single component annular flow. According to Shock (1976), an energy balance for a turbulent film on a surface where curvature effects are negligible, where the rates of axial diffusion and conduction are also negligible and where the sensible heat contribution to the liquid film is small compared to the latent heat contribution,

$$\left|\dot{m}_{LF} c_{pLF} \frac{d\overline{T}_{LF}}{dz}\right| \ll \left|\frac{4}{d_T}\dot{m}_I \Delta h_v\right|, \tag{B.1}$$

gives,

$$\dot{q}_w = \left(\lambda_{LF} + \lambda_{LF}^{(t)}\right)\frac{dT_{LF}}{dy} + \sum_{i=1}^{NOC} h_i \sum_{k=1}^{NOC-1} \rho_{LF}\left(\Delta_{i,k} + \Delta_{i,k}^{(t)}\right)\frac{dx_{LF,k}}{dy}, \tag{B.2}$$

where the superscript (t) indicates a (mass and energy) transport enhancement due to turbulent fluctuations (Boussinesq assumption). Shock (1976) derived the equation above

for the binary mixture case ($NOC = 2$) using a Prandtl mixing length-type expression due to Deissler (1955) and to von Kármán (1930) (see Schlichting, 1987 and Kays and Crawford, 1993) to model the turbulence in the concentration, thermal and flow fields.

In dimensionless form, Eq. B.2 can be rewritten as (binary case),

$$\left(\frac{1}{Pr_{LF}} + \frac{1}{Pr_{LF}^{(t)}}\right)\frac{dT^+}{dy^+} + QT^+\int_0^{y^+} u^+ dy^+ = 1; \tag{B.3}$$

where the specific enthalpies, h_i, in Eq. B.2 were approximated by $c_{pLF,i}\,(T - T_{ref})$, with the wall temperature taken as a reference and the diffusive mass fluxes taken as,

$$\rho_{LF}\left(\Delta_{1,2} + \Delta_{1,2}^{(t)}\right)\frac{dx_{LF,1}}{dy} = -\rho_{LF}\frac{\partial x_{LF,1}}{\partial z}\int_0^{y} u dy, \tag{B.4}$$

The dimensionless parameters in Eq. B.3 are as follows,

$$T_{LF}^+ = \frac{c_{pLF,w}\rho_{LF,w}}{\dot{q}_w}u^*\left(T_{LF,w} - T_{LF}\right), \tag{B.5}$$

is the dimensionless liquid film temperature profile. u^* is the friction velocity given by $\sqrt{\frac{\tau_w}{\rho_{LF,w}}}$ and the subscript w stands for the value at the wall.

Q is a dimensionless group which characterises the effects of interdiffusion of the components on heat transfer; it can be positive or negative,

$$Q = \frac{c_{pLF,1} - c_{pLF,2}}{c_{pLF,m}}\frac{\eta_{LF}}{\rho_{LF}u^*}\frac{\partial x_{LF}}{\partial z}, \tag{B.6}$$

where $c_{pLF,m}$ is the mixture specific heat capacity. An improvement in heat transfer will occur with positive Q. Shock (1976) pointed out that it is unlikely that in practice Q would be greater than 10^{-6}. He solved Eq. B.3 numerically to obtain,

$$Nu_{LF} = \frac{\delta^+ Pr_{LF}}{T_I^+}, \tag{B.7}$$

for various values of Re_{LF}, Pr_{LF} and Q and found that the practical values of Q are small enough not to influence the temperature drop across the film. This fact decouples heat from mass transfer in the liquid film and the wall temperature can be calculated by applying a model for the heat transfer coefficient across the film to the interfacial temperature.

Appendix C

Operating Instructions for the LOTUS Facility

These are instructions for operation of the air-water facility (LOTUS rig). They were reviewed and agreed by the Departamental Safety Officer.

The rig should never be left unattended in an operating state, although all of the components of the pressurised loop are capable of withstanding the full mains pressure. Several points should be checked before start-up. These are as follows,

1. The main water tank should be sufficiently filled. This can be checked via a level meter on its side or, alternatively, filled until the level alarm sounds. If high liquid and gas mass fluxes are going to be used ($\dot{m}_G > 140$ kg m^{-2} s^{-1}, $\dot{m}_L > 400$ kg m^{-2} s^{-1}) then the water tank should be left approximately two-thirds full to avoid level oscillations which permanently trigger the alarm;

2. The valves of the pump to be used are open and the unused pump isolated from the power supply using the breaker switches located on the wall of the second floor. Watson (1999) recommended that the smaller pump should be used despite its lower

power consumption as it appears to be a much more efficient design, and it provides the same flow rates as the larger pump without the noise or vibration;

3. Switch on the control panel and switch bank on the third floor. The water alarm will test itself, therefore press buttons to confirm alarm and then reset it;

4. The following valves (see Table C.1) should be closed: 3, 4, 21, 22, 33, 34, 36, 42, 43, 46, 49, 55, 57, 58 60, 61. *All* other valves should be fully open with the exception of #59 which should be set to provide an outlet pressure of 25 psig as recorded by the pressure gauge (calibrate in psig). The pump bypass valve #7 along with the inlet and outlet valves to the flow meters can be used to control the water flow rate.

Regular start-up

To establish the air flow:

- open main air supply valve #57;
- open valve #52 fully and wait around 40 seconds;
- confirm that outlet of valve #59 is 25 psig (approximately);
- open valve #55 (switch on control panel);
- close valve #52 which gradually opens valve #56;
- to avoid shocks to the system, use valve #51 or the handle to valve #41 to control the air flow rate. The air flow is *very sensitive.*

To establish the water flow:

- confirm that air flow is sufficient (around 10 in of water on orifice);

- confirm that valve #1 (exit to water tank) is open;
- open the cooling water supply (especially for small water flow rates) using valve #34 on the second floor;
- open inlet to required flow meter;
- open pump bypass using handle on 3rd floor;
- slightly open flow meter outlet valve;
- turn on pump (switch on control panel);
- use the pump bypass valve #7 to increase the water flow rate along with the flow meter outlet valve;
- the pump outlet pressure should be between 20 and 55 psig;
- the gas and liquid flow rates can then be adjusted using the control valves #51, #41, #7, the outlet flow meter valve, or the test section exit throttling valve #23.

Regular shut-down

The water pump should be turned off first via the switch on the control panel and then the inlet and outlet valves to the flow meter used closed (ensuring that the increase in gas flow rate that will occur does not raise the exit pressure too high, to avoid damage to the pressure gauge at the test section exit). The air flow rate should then be throttled to around 10 to 15 in of water in order to purge the test section of water. This takes about 3 minutes. Valve #23 should be opened slowly. Valve #51 should be opened fully and valve #55 closed via the control panel to cut off the air supply. Close valves #57 and #1. Turn off the plug bank and control panel.

Emergency shut-down

1. switch off the water pump at the control panel;

2. close valve #55 by switch;

3. switch off the control panel and plug bank.

This will immediately cut off the air and water supplies. Valves #1 and #57 can then closed.

Table C.1 list the valves in the LOTUS rig.

Valve	Floor	Description	Type
1	2	closes tank at its bottom	ball
3	2	large pump inlet	ball
4	2	large pump outlet	ball
5	2	small pump inlet	ball
6	2	small pump outlet	ball
7	2	pre-cooler pump bypass	ball
9	1	water sinter inlet	ball
21	3	bypasses valves #20 and #23	safety
Continued on next page			

Table C.1 – continued from previous page

Valve	Floor	Description	Type
22	3	main water supply for tank	ball
23	3	test section outlet valve	ball
34	2	cooling water inlet	ball
35	3	flow meter bank inlet	ball
36	3	water orifice pipe inlet	ball
37	3	post-cooler pump bypass	ball
40	2	3" air orifice pipe outlet	ball
41	2	3" air orifice pipe inlet	ball
42	2	2" air orifice pipe outlet	ball
43	2	2" air orifice pipe inlet	ball
44	2	2" air pressure after orifice to dp cell	needle
45	2	3" air pressure after orifice to dp cell	needle
46	2	2" air pressure before orifice to dp cell	needle
47	2	3" air pressure before orifice to dp cell	needle
48	2	air pressure before orifice to gauge on 3rd floor	needle
49	2	pressure equaliser at air dp cell	needle
50	2	large air flow control valve, operated by valve #51, fails open	pneumatic
51	3	closes large air flow valve #50	ball
52	3	closes air flow on/off valve #56	ball

Continued on next page

Table C.1 – concluded from previous page

Valve	Floor	Description	Type
53	2	small air flow control valve, operated by valve #68, fails open	pneumatic
54	1	for 'elbow' air inlet	ball
55	2	air flow on/off valve, switch at 3rd floor, fails close	solenoid
56	2	air flow on/off valve, operated by valve #52, fails open	pneumatic
57	2	main air supply	ball
58	1	for 'T' air inlet	ball
59	2	pressure reducing valve, supplies air flow control loop pressure	reducing
60	1	water circuit drain valve	ball
61	1	drain pipe control, before valve #62	ball
62	1	drain pipe control, switch on 3rd floor, fails open	solenoid
64	2	at pump's high pressure side before gauge on 3rd floor	ball
68	3	closes small air flow control valve #53	ball
70	3	shuts off air flow control loop after valve #59	ball

Table C.1: List of valves in the LOTUS rig.

Appendix D

Data for the Entrained Fraction near the Onset of Annular Flow

The purpose of this Appendix is to archive the data obtained for entrained fraction in the region near (i.e., above and below) the onset of annular flow. Details of the experiments and discussion of the results are given in Chapter 5.

Table D.1: Entrained fraction data. Experimental conditions: $p = 2.1$ bara (nominal), $\dot{m}_L = 15$ kg m^{-2} s^{-1} (nominal).

p (bara)	ρ_G (kg m^{-3})	$\dot{m}_L$ (kg m^{-2} s^{-1})	$\dot{m}_G$ (kg m^{-2} s^{-1})	$U^{\star}_{GS}$ (-)	$\dot{m}_{LE}$ (kg m^{-2} s^{-1})	e (%)	$\delta\dot{m}_{LE}$ (kg m^{-2} s^{-1})	δe (%)
2.11	2.46	15.11	30.39	1.10	0	0	0.28	1.86
1.99	2.33	15.11	21.22	0.79	0.66	4.35	0.25	1.69
2.11	2.45	15.11	20.68	0.75	0.15	0.97	0.19	1.24
2.10	2.44	13.85	35.77	1.30	0.09	0.64	0.24	1.76
2.04	2.38	15.11	24.45	0.90	0.11	0.71	0.19	1.29

Table D.2: Entrained fraction data. Experimental conditions: $p = 3.6$ bara (nominal), $\dot{m}_L = 12$ kg m^{-2} s^{-1} (nominal).

p (bara)	ρ_G (kg m^{-3})	$\dot{m}_L$ (kg m^{-2} s^{-1})	$\dot{m}_G$ (kg m^{-2} s^{-1})	U^*_{GS} (-)	$\dot{m}_{LE}$ (kg m^{-2} s^{-1})	e (%)	$\delta\dot{m}_{LE}$ (kg m^{-2} s^{-1})	δe (%)
3.64	4.28	11.33	26.68	0.73	1.40	12.32	0.24	2.16
3.52	4.12	12.59	30.00	0.84	0.30	2.38	0.15	1.21
3.62	4.24	12.59	36.72	1.01	0	0	0.19	1.52
3.64	4.25	12.59	47.77	1.31	0	0	0.19	1.54
3.58	4.18	11.33	57.15	1.59	0	0	0.26	2.29

Table D.3: Entrained fraction data. Experimental conditions: $p = 5.0$ bara (nominal), $\dot{m}_L = 12$ kg m^{-2} s^{-1} (nominal).

p (bara)	ρ_G (kg m^{-3})	$\dot{m}_L$ (kg m^{-2} s^{-1})	$\dot{m}_G$ (kg m^{-2} s^{-1})	U^*_{GS} (-)	$\dot{m}_{LE}$ (kg m^{-2} s^{-1})	e (%)	$\delta\dot{m}_{LE}$ (kg m^{-2} s^{-1})	δe (%)
5.05	5.92	12.59	26.96	0.63	4.26	33.86	0.63	5.11
5.09	5.95	12.59	33.41	0.78	0.68	5.45	0.16	1.30
5.02	5.85	12.59	37.60	0.88	0.11	0.88	0.13	1.04
4.97	5.79	12.59	49.90	1.18	0	0	0.19	1.48
5.15	5.99	11.33	68.53	1.59	0	0	0.21	1.84

Table D.4: Entrained fraction data. Experimental conditions: $p = 1.9$ bara (nominal), $\dot{m}_L = 22$ kg m^{-2} s^{-1} (nominal).

p (bara)	ρ_G (kg m^{-3})	$\dot{m}_L$ (kg m^{-2} s^{-1})	$\dot{m}_G$ (kg m^{-2} s^{-1})	U^*_{GS} (-)	$\dot{m}_{LE}$ (kg m^{-2} s^{-1})	e (%)	$\delta\dot{m}_{LE}$ (kg m^{-2} s^{-1})	δe (%)
1.86	2.18	22.66	14.82	0.57	9.55	42.16	1.36	6.01
1.88	2.19	21.40	22.04	0.85	2.14	10.00	0.37	1.74
1.89	2.20	21.40	25.36	0.97	1.15	5.37	0.26	1.22
1.89	2.21	22.66	32.18	1.23	1.39	6.14	0.31	1.39
1.85	2.17	22.66	36.56	1.41	1.47	6.50	0.35	1.53

Table D.5: Entrained fraction data. Experimental conditions: $p = 3.5$ bara (nominal), $\dot{m}_L = 23$ kg m^{-2} s^{-1} (nominal).

p (bara)	ρ_G (kg m^{-3})	$\dot{m}_L$ (kg m^{-2} s^{-1})	$\dot{m}_G$ (kg m^{-2} s^{-1})	U^*_{GS} (-)	$\dot{m}_{LE}$ (kg m^{-2} s^{-1})	e (%)	$\delta\dot{m}_{LE}$ (kg m^{-2} s^{-1})	δe (%)
3.48	4.06	23.92	28.74	0.81	2.26	9.46	0.38	1.60
3.50	4.08	22.66	32.50	0.91	1.08	4.79	0.26	1.14
3.46	4.05	22.66	39.65	1.12	0.79	3.47	0.23	1.04
3.53	4.12	22.66	47.87	1.34	1.05	4.62	0.28	1.22
3.45	4.02	21.40	54.01	1.53	1.06	4.97	0.32	1.49

Table D.6: Entrained fraction data. Experimental conditions: $p = 5.0$ bara (nominal), $\dot{m}_L = 23$ kg m^{-2} s^{-1} (nominal).

p (bara)	ρ_G (kg m^{-3})	$\dot{m}_L$ (kg m^{-2} s^{-1})	$\dot{m}_G$ (kg m^{-2} s^{-1})	U^*_{GS} (-)	$\dot{m}_{LE}$ (kg m^{-2} s^{-1})	e (%)	$\delta\dot{m}_{LE}$ (kg m^{-2} s^{-1})	δe (%)
5.00	5.87	22.66	17.64	0.41	22.54	99.44	3.57	15.85
5.04	5.91	22.66	24.95	0.58	9.20	40.60	1.33	5.89
5.00	5.84	22.66	31.65	0.75	2.48	10.95	0.47	2.07
5.03	5.87	22.66	38.97	0.92	1.10	4.85	0.22	0.97
4.94	5.76	22.66	54.70	1.30	0.99	4.36	0.23	1.03

Table D.7: Entrained fraction data. Experimental conditions: $p = 1.8$ bara (nominal), $\dot{m}_L = 48$ kg m^{-2} s^{-1} (nominal).

p (bara)	ρ_G (kg m^{-3})	$\dot{m}_L$ (kg m^{-2} s^{-1})	$\dot{m}_G$ (kg m^{-2} s^{-1})	U^*_{GS} (-)	$\dot{m}_{LE}$ (kg m^{-2} s^{-1})	e (%)	$\delta\dot{m}_{LE}$ (kg m^{-2} s^{-1})	δe (%)
1.82	2.11	50.36	13.83	0.54	12.96	25.73	1.83	3.64
1.83	2.14	47.85	22.25	0.86	5.57	11.64	0.86	1.80
1.77	2.06	47.85	25.69	1.02	4.60	9.62	0.72	1.50
1.79	2.08	50.36	34.30	1.35	5.84	11.60	0.87	1.73
1.81	2.11	49.10	38.61	1.51	6.54	13.32	1.00	2.04

Table D.8: Entrained fraction data. Experimental conditions: $p = 3.6$ bara (nominal), $\dot{m}_L = 48$ kg m^{-2} s^{-1} (nominal).

p (bara)	ρ_G (kg m^{-3})	$\dot{m}_L$ (kg m^{-2} s^{-1})	$\dot{m}_G$ (kg m^{-2} s^{-1})	U^*_{GS} (-)	$\dot{m}_{LE}$ (kg m^{-2} s^{-1})	e (%)	$\delta\dot{m}_{LE}$ (kg m^{-2} s^{-1})	δe (%)
3.66	4.28	47.59	14.10	0.39	36.54	78.43	5.14	11.04
3.53	4.12	47.85	20.82	0.58	12.61	26.36	1.75	3.66
3.61	4.20	46.59	34.96	0.97	3.75	8.06	0.58	1.25
3.66	4.27	50.36	42.80	1.18	4.23	8.40	0.60	1.19
3.67	4.28	47.85	50.01	1.37	4.24	8.87	0.64	1.33

Table D.9: Entrained fraction data. Experimental conditions: $p = 5.0$ bara (nominal), $\dot{m}_L = 48$ kg m^{-2} s^{-1} (nominal).

p (bara)	ρ_G (kg m^{-3})	$\dot{m}_L$ (kg m^{-2} s^{-1})	$\dot{m}_G$ (kg m^{-2} s^{-1})	U^*_{GS} (-)	$\dot{m}_{LE}$ (kg m^{-2} s^{-1})	e (%)	$\delta\dot{m}_{LE}$ (kg m^{-2} s^{-1})	δe (%)
5.00	5.81	49.10	24.46	0.58	11.25	22.93	1.62	3.31
5.00	5.81	59.18	37.27	0.88	5.40	9.13	0.67	1.13
5.05	5.87	47.85	41.30	0.97	3.42	7.15	0.54	1.13
4.94	5.75	47.85	49.15	1.17	3.24	6.78	0.52	1.08
4.93	5.75	47.85	55.29	1.31	3.21	6.70	0.52	1.10
5.00	5.82	47.85	64.47	1.52	4.70	9.82	0.73	1.53

Table D.10: Entrained fraction data. Experimental conditions: $p = 2.1$ bara (nominal), $\dot{m}_L = 126$ kg m^{-2} s^{-1} (nominal).

p (bara)	ρ_G (kg m^{-3})	$\dot{m}_L$ (kg m^{-2} s^{-1})	$\dot{m}_G$ (kg m^{-2} s^{-1})	U^*_{GS} (-)	$\dot{m}_{LE}$ (kg m^{-2} s^{-1})	e (%)	$\delta\dot{m}_{LE}$ (kg m^{-2} s^{-1})	δe (%)
2.13	2.48	125.91	18.58	0.67	18.58	14.76	2.62	2.13
2.09	2.43	125.91	21.40	0.78	15.87	12.61	2.24	1.83
2.09	2.42	125.91	27.38	1.00	15.11	12.00	2.14	1.74
2.07	2.40	125.91	36.53	1.34	19.02	15.11	2.69	2.19
2.18	2.52	125.91	40.85	1.46	22.18	17.62	3.13	2.55

Table D.11: Entrained fraction data. Experimental conditions: $p = 3.8$ bara (nominal), $\dot{m}_L = 128$ kg m^{-2} s^{-1} (nominal).

p (bara)	ρ_G (kg m^{-3})	$\dot{m}_L$ (kg m^{-2} s^{-1})	$\dot{m}_G$ (kg m^{-2} s^{-1})	U^*_{GS} (-)	$\dot{m}_{LE}$ (kg m^{-2} s^{-1})	e (%)	$\delta\dot{m}_{LE}$ (kg m^{-2} s^{-1})	δe (%)
3.80	4.48	132.20	23.84	0.64	25.10	18.99	3.53	2.73
3.81	4.48	128.43	27.18	0.73	19.37	15.08	2.84	2.26
3.78	4.43	125.91	34.43	0.93	13.99	11.11	2.07	1.69
3.88	4.54	132.20	42.73	1.14	14.06	10.63	1.99	1.54
3.78	4.42	128.43	49.57	1.34	14.86	11.57	2.16	1.72
3.77	4.41	125.91	55.08	1.49	15.78	12.53	2.34	1.91

Table D.12: Entrained fraction data. Experimental conditions: $p = 5.2$ bara (nominal), $\dot{m}_L = 105$ kg m^{-2} s^{-1} (nominal).

p (bara)	ρ_G (kg m^{-3})	$\dot{m}_L$ (kg m^{-2} s^{-1})	$\dot{m}_G$ (kg m^{-2} s^{-1})	U^*_{GS} (-)	$\dot{m}_{LE}$ (kg m^{-2} s^{-1})	e (%)	$\delta\dot{m}_{LE}$ (kg m^{-2} s^{-1})	δe (%)
5.27	6.13	125.91	19.15	0.44	47.48	37.71	6.66	5.42
5.27	6.13	132.20	23.93	0.55	32.55	24.62	4.37	3.38
5.15	5.98	132.20	31.39	0.73	20.13	15.23	2.71	2.10
5.25	6.09	132.20	40.55	0.94	15.28	11.56	2.06	1.59
5.20	6.03	128.43	45.32	1.05	13.70	10.67	1.90	1.51
5.20	6.02	128.43	53.04	1.23	13.46	10.48	1.87	1.49

Table D.13: Entrained fraction data. Experimental conditions: $p = 2.0$ bara (nominal), $\dot{m}_L = 218$ kg m^{-2} s^{-1} (nominal).

p (bara)	ρ_G (kg m^{-3})	$\dot{m}_L$ (kg m^{-2} s^{-1})	$\dot{m}_G$ (kg m^{-2} s^{-1})	U^*_{GS} (-)	$\dot{m}_{LE}$ (kg m^{-2} s^{-1})	e (%)	$\delta\dot{m}_{LE}$ (kg m^{-2} s^{-1})	δe (%)
2.00	2.34	220.34	24.50	0.91	27.51	12.49	3.85	3.86
1.98	2.30	216.56	20.28	0.76	35.56	16.42	5.07	5.08
2.00	2.31	214.04	29.44	1.10	29.37	13.72	4.23	4.25
1.96	2.28	220.34	38.55	1.45	42.50	19.29	5.95	5.97
2.05	2.38	220.34	32.58	1.20	32.97	14.96	4.62	4.63

Table D.14: Entrained fraction data. Experimental conditions: $p = 3.7$ bara (nominal), $\dot{m}_L = 215$ kg m^{-2} s^{-1} (nominal).

p (bara)	ρ_G (kg m^{-3})	$\dot{m}_L$ (kg m^{-2} s^{-1})	$\dot{m}_G$ (kg m^{-2} s^{-1})	U^*_{GS} (-)	$\dot{m}_{LE}$ (kg m^{-2} s^{-1})	e (%)	$\delta\dot{m}_{LE}$ (kg m^{-2} s^{-1})	δe (%)
3.69	4.27	217.82	26.91	0.74	33.19	15.24	4.66	2.16
3.75	4.33	217.82	32.24	0.88	26.61	12.22	3.74	1.73
3.68	4.26	215.30	35.57	0.98	24.43	11.35	3.48	1.63
3.64	4.22	216.56	40.83	1.13	25.33	11.69	3.59	1.67
3.75	4.32	210.27	50.85	1.39	27.36	13.01	3.99	1.91
3.67	4.25	214.04	54.07	1.49	31.69	14.81	4.54	2.14

Table D.15: Entrained fraction data. Experimental conditions: $p = 5.1$ bara (nominal), $\dot{m}_L = 214$ kg m^{-2} s^{-1} (nominal).

p (bara)	ρ_G (kg m^{-3})	$\dot{m}_L$ (kg m^{-2} s^{-1})	$\dot{m}_G$ (kg m^{-2} s^{-1})	U^*_{GS} (-)	$\dot{m}_{LE}$ (kg m^{-2} s^{-1})	e (%)	$\delta\dot{m}_{LE}$ (kg m^{-2} s^{-1})	δe (%)
5.06	5.91	210.27	26.36	0.62	47.15	22.43	6.63	3.18
5.09	5.94	214.04	34.36	0.80	32.61	15.24	4.52	2.13
4.97	5.80	217.82	40.48	0.96	29.25	13.43	3.98	1.84
5.04	5.88	214.04	47.75	1.12	25.70	12.01	3.58	1.68
5.10	5.95	211.53	54.47	1.27	24.14	11.41	3.39	1.61
5.11	5.96	207.75	62.24	1.45	24.12	11.61	3.47	1.70

Table D.16: Entrained fraction data. Experimental conditions: $p = 2.0$ bara (nominal), $\dot{m}_L = 331$ kg m^{-2} s^{-1} (nominal).

p (bara)	ρ_G (kg m^{-3})	$\dot{m}_L$ (kg m^{-2} s^{-1})	$\dot{m}_G$ (kg m^{-2} s^{-1})	U^*_{GS} (-)	$\dot{m}_{LE}$ (kg m^{-2} s^{-1})	e (%)	$\delta\dot{m}_{LE}$ (kg m^{-2} s^{-1})	δe (%)
1.97	2.28	331.14	22.36	0.84	86.55	26.14	13.55	4.11
1.94	2.25	331.14	27.43	1.04	65.33	19.73	10.25	3.10
1.99	2.30	331.14	29.12	1.09	68.51	20.69	10.74	3.25
1.98	2.29	331.14	34.65	1.30	68.03	20.54	10.67	3.23
1.98	2.29	328.62	37.57	1.41	71.38	21.72	11.27	3.44
1.92	2.23	331.14	43.64	1.66	90.25	27.25	14.14	4.28

Table D.17: Entrained fraction data. Experimental conditions: $p = 3.2$ bara (nominal), $\dot{m}_L = 330$ kg m^{-2} s^{-1} (nominal).

p (bara)	ρ_G (kg m^{-3})	$\dot{m}_L$ (kg m^{-2} s^{-1})	$\dot{m}_G$ (kg m^{-2} s^{-1})	U^*_{GS} (-)	$\dot{m}_{LE}$ (kg m^{-2} s^{-1})	e (%)	$\delta\dot{m}_{LE}$ (kg m^{-2} s^{-1})	δe (%)
3.28	3.80	334.91	25.39	0.74	78.80	23.53	11.06	3.31
3.20	3.70	327.36	30.47	0.90	70.11	21.42	10.07	3.09
3.24	3.75	331.14	32.38	0.95	62.60	18.91	8.90	2.70
3.23	3.74	333.66	37.45	1.10	63.80	19.12	9.00	2.71
3.18	3.68	324.84	46.60	1.38	58.85	18.12	8.53	2.64
3.26	3.77	321.07	51.95	1.52	62.60	19.50	9.18	2.87
3.07	3.55	327.36	54.40	1.64	72.11	22.03	10.36	3.18

Table D.18: Entrained fraction data. Experimental conditions: $p = 5.0$ bara (nominal), $\dot{m}_L = 302$ kg m^{-2} s^{-1} (nominal).

p (bara)	ρ_G (kg m^{-3})	$\dot{m}_L$ (kg m^{-2} s^{-1})	$\dot{m}_G$ (kg m^{-2} s^{-1})	U^*_{GS} (-)	$\dot{m}_{LE}$ (kg m^{-2} s^{-1})	e (%)	$\delta\dot{m}_{LE}$ (kg m^{-2} s^{-1})	δe (%)
4.98	5.83	302.18	26.31	0.62	93.42	30.91	12.84	4.27
4.86	5.69	314.77	34.80	0.83	73.01	23.20	9.63	3.07
4.90	5.72	308.48	45.85	1.09	53.18	17.24	7.18	2.34
4.92	5.75	302.18	53.53	1.27	48.75	16.13	6.72	2.23
4.95	5.78	295.89	57.08	1.35	45.05	15.23	6.33	2.15

Appendix E

Papers covering the work described in this thesis

1. Barbosa, Jr., J.R., Kandlbinder, T. and Hewitt, G.F., 2001, 'Forced convective boiling of ternary mixtures at high qualities'. Submitted to *International Journal of Heat and Mass Transfer.*

2. Barbosa, Jr., J.R., Hewitt, G.F. and Richardson, S.M., 2001, 'A note on the influence of droplet interchange on evaporation and condensation of multicomponent mixtures in annular flow'. Submitted to *International Journal of Heat and Mass Transfer.*

3. Barbosa, Jr., J.R., Hewitt, G.F., König, G. and Richardson, S.M., 2001, 'Liquid entrainment, droplet concentration and pressure gradient at the onset of annular flow in a vertical pipe'. Submitted to *International Journal of Multiphase Flow.*

4. Barbosa, Jr., J.R., Govan, A.H. and Hewitt, G.F., 2001, 'Visualisation and modelling studies of churn flow in a vertical pipe'. Submitted to *International Journal of Multiphase Flow.*

5. Barbosa, Jr., J.R., Hewitt, G.F. and Richardson, S.M., 2001, 'Nucleate boiling

in climbing films: a flow visualisation study'. To be presented at the 5th World Conference on Experimental Heat Transfer, Fluid Mechanics and Thermodynamics, September 24 – 28, Thessaloniki, Greece.

6. Barbosa, Jr., J.R., Hewitt, G.F. and Richardson, S.M., 2001, 'Phase change of multicomponent mixtures in annular flow'. To be presented at the 4th International Conference on Multiphase Flow, May 27 – June 1, New Orleans, Lousiana, USA.

7. Barbosa, Jr., J.R. and Hewitt, G.F., 2001, 'Forced convective boiling of binary mixtures in annular Flow. Part I: Liquid phase mass transport'. *International Journal of Heat and Mass Transfer*, Vol. 44, pp. 1465–1474.

8. Barbosa, Jr., J.R. and Hewitt, G.F., 2001, 'Forced convective boiling of binary mixtures in annular Flow. Part H: Heat and mass transfer'. *International Journal of Heat and Mass Transfer*, Vol. 44, pp. 1475–1484.

9. Barbosa, Jr., J.R. and Hewitt, G.F., 2000, 'A note on diffusion interaction effects in convective boiling of ternary mixtures'. Proc. HTFS Annual Meeting, November, Amsterdam, The Netherlands, HTFS Report RS1089.

10. Barbosa, Jr., J.R., Kandlbinder, T. and Hewitt, G.F., 2000, 'A study of dryout in annular flow of single component hydrocarbons and their mixtures'. Proceedings of the Boiling 2000: Phenomena and Emerging Applications Conference, United Engineering Foundation, April 30 – May 5, Anchorage, Alaska, USA, pp. 585–606 (To be published in *Multiphase Science and Technology*).

11. Barbosa, Jr., J.R., Wadekar, V.V. and Hewitt, G.F., 2000, 'A review of heat and mass transfer in flow boiling of binary mixtures'. Proceedings of the Boiling 2000: Phenomena and Emerging Applications Conference, United Engineering Founda-

tion, April 30 – May 5, Anchorage, Alaska, USA, pp. 754–751 (Also: Proc. HTFS Annual Meeting, October, Dublin, Ireland, RS1065, pp. 265–279).

12. Barbosa, Jr., J.R. and Hewitt, G.F., 1999, 'Forced convective boiling of hydrocarbon mixtures', *International Journal of Heat and Technology — Calore e Tecnologia*, Vol.17, No.2, pp.37–48.

13. Barbosa, Jr., J.R. and Hewitt, G.F., 1999, 'The influence of droplet interchange on forced convective boiling of binary mixtures in annular flow'. Proc. HTFS Annual Meeting, October, Dublin, Ireland, RS1064, pp. 251–264.

14. Barbosa, Jr., J.R. and Hewitt, G.F., 1999, 'A model for forced convective boiling of ternary mixtures', Proceedings of the 6^{th} UK National Heat Transfer Conference, 15–16 September, Heriot-Watt University, Edinburgh, IMechE, pp. 169–174. **This paper was awarded the HTFS Prize for the best paper presented at the Conference.**

Bibliography

[1] Y. Abe, H. Akimoto, and Y. Murao. Estimation of shear stress in countercurrent anular flow. *Journal of Nuclear Science and Technology*, 28(3):208–217, 1991.

[2] N Adorni, P. Alia, L. Cravarolo, A. Hassan, and E. Pedrocchi. An isokinetic sampling probe flow phase and velocity distribution measurements in two-phase flow near the wall of the conduit. Technical report, CISE Milan, Report No R-89, 1963.

[3] G.H. Anderson and G.B. Mantzouranis. Two-phase (gas-liquid) flow phenomena. 1: Pressure drop and hold-up for two-phase flow in vertical tubes. *Chemical Engineering Science*, 12:109–126, 1960.

[4] Y. Aounallah and D.B.R. Kenning. Nucleate boiling and the chen correlation for flow boiling heat transfer. *Experimental Heat Transfer*, 1:87–92, 1987.

[5] Y. Aounallah, D.B.R. Kenning, P.B. Whalley, and G.F. Hewitt. Boiling heat transfer in annular flow. In U. Grigull, editor, *Proceedings of the Seventh International Heat Transfer Conference*, volume 5, pages 452–457, Munich, West Germany, September 1982. Hemisphere Publishing Co., New York, NY.

[6] J.C. Asali, W. Leman, and T.J. Hanratty. Entrainment measurements and their use in design equations. *PhysicoChemical Hydrodynamics*, 6(1/2):207–221, 1985.

[7] M.J. Assael, J.P.M. Trusler, and T.F. Tsolakis. *Thermophysical Properties of Fluids.* Imperial College Press, London, 1996.

[8] B.J. Azzopardi. Mechanisms of entrainment in annular two-phase flow. Technical report, UKAEA Report AERE R-11068, 1983.

[9] B.J. Azzopardi. Drops in annular two-phase flow. *International Journal of Multiphase Flow*, 23, Suppl.:1–53, 1997.

[10] B.J. Azzopardi. Links across flow patterns in gas/liquid flow in vertical pipes. In *European-Japan Two-Phase Flow Meeting*, Tsukuba, Japan, 2000.

[11] B.J. Azzopardi, G. Freeman, and D.J. King. Drop sizes and deposition in annular two-phase flow. Technical report, UKAEA Report AERE R-9634, 1980.

[12] B.J. Azzopardi, S. Taylor, and D.B. Gibbons. Annular two-phase flow in large diameter pipes. In *Proceedings of the International Conference on Physical Modelling of Multiphase Flow*, pages 267–282, Coventry, UK, 1983.

[13] B.J. Azzopardi and P.B. Whalley. Artificial waves in annular two-phase flow. In *Basic Mechanisms in Two-Phase Flow and Heat Transfer*, pages 1–8. ASME, 1980.

[14] B.J. Azzopardi and S.H. Zaidi. Determination of entrained fraction in vertical annular gas-liquid flow. *Journal of Fluids Engineering, Transactions of the ASME*, 122:146–150, 2000.

[15] J.R. Barbosa, Jr. and G.F. Hewitt. Forced convective boiling of hydrocarbon mixtures. *International Journal of Heat and Technology — Calore e Tecnologia*, 17(2):37–48, 1999.

[16] H.S. Bean. *Fluid Meters: Their Theory and Application.* ASME, New York, sixth edition, 1971.

[17] D.R.H. Beattie and W.J. Green. The existence of nucleate boiling in diabatic two-phase annular flow. *International Journal of Heat Mass Transfer*, 27(2):315–317, 1984.

[18] D.R.H. Beattie and K.R. Lawther. Letter to the editor. *AIChE Journal*, 25(2):384, 1979.

[19] K.J. Bell and M.A. Ghaly. An approximate generalized design for multicomponent partial condensers. *AIChE Symposium Series*, 69(131):72–79, 1973.

[20] A.W. Bennett, G.F. Hewitt, H.A. Kearsey, and R.K.F. Keeys. Heat transfer to steam-water mixtures flowing in uniformly heated tubes in which the critical heat flux has been exceeded. In *Thermodynamics and Fluid Mechanics Convention*, Bristol, UK, 1967a. Institution of Mechanical Engineers. Paper 27.

[21] A.W. Bennett, G.F. Hewitt, H.A. Kearsey, R.K.F. Keeys, and D.J. Pulling. Studies of burnout in boiling heat transfer. *Transactions of the Institution of Chemical Engineers*, 45:319–333, 1967b.

[22] D.L. Bennett, M.W. Davis, and B.L. Hertzler. The suppression of saturated nucleate boiling by forced convective flow. *AIChE Symposium Series*, 76(199):91–103, 1980.

[23] A.E. Bergles and W.M. Rohsenow. The determination of forced convection surface-boiling heat transfer. *Journal of Heat Transfer, Transactions of the ASME*, 86:365–372, 1964.

[24] K.E. Bett, J.S. Rowlinson, and G. Saville. *Thermodynamics for Chemical Engineers.* The Athlone Press, London, 1975.

[25] D. Bharathan and G.B. Wallis. Air-water countercurrent annular flow. *International Journal of Multiphase Flow*, 9(4):349–366, 1983.

[26] A. Biesheuvel and W.M.C. Gorissen. Void fraction disturbances in a uniform bubbly fluids. *International Journal of Multiphase Flow*, 16(2):211–231, 1990.

[27] R.B. Bird, W.E. Stewart, and E.N. Lightfoot. *Transport Phenomena.* John Wiley & Sons, New York, 1960.

[28] R.W. Bjorge, G.R. Hall, and W.M. Rohsenow. Correlation of forced convection boiling heat transfer data. *International Journal of Heat Mass Transfer*, 25(6):753–757, 1982.

[29] J.A. Boure. Wave phenomena and one-dimensional two-phase flow models. In G.F. Hewitt and J.M. Delhaye, editors, *Multiphase Science and Technology*, volume 9. Hemisphere Publishing Co., New York, 1997.

[30] N. Brauner and D. Barnea. Slug/churn transition in upward gas liquid flow. *Chemical Engineering Science*, 41(1):159–163, 1986.

[31] N. Brauner, D.M. Moalem Maron, and A.E. Dukler. Modelling of wavy flow in inclined thin films in the presence of interfacial shear. *Chemical Engineering Science*, 40:923–937, 1985.

[32] W. Brotz. Uber die vorausberechnung der absorptiongeschwindigkeit von gasen in stromenden flussigkeitsschichten. *Chemie Ingeniur Technik*, 26:470, 1954.

[33] L.K. Brumfleld and T.G. Theofanous. On the prediction of heat transfer across turbulent liquid films. *Journal of Heat Transfer, Transactions of the ASME*, August:496–502, 1976.

[34] D. Butterworth and R.A.W. Shock. Flow boiling. In U. Grigull, editor, *Proceedings of the Seventh International Heat Transfer Conference*, volume 1, pages 11–30,

Munich, West Germany, September 1982. Hemisphere Publishing Co., New York, NY.

[35] S. Calvert and B. Williams. Upwards co-current annular flow of air and water in short tubes. *AIChE Journal*, 1:78–86, 1955.

[36] A. Cavallini, G. Censi, D. Del Col, L. Doretti, G.A. Longo, and L. Rossetto. Condensation of pure and blended hfc refrigerants. In *38th European Two-Phase Flow Group Meeting*, Karlsruhe, Germany, 2000.

[37] A. Cavallini, D. del Col, L. Doretti, G.A. Longo, and L. Rossetto. Condensation of r-22 and r-407c inside a horizontal tube. In *20th International Congress of Refrigeration, IIR/IIF*, Sydney, Australia, 1999.

[38] G.P. Celata, M. Cumo, and T. Setaro. Forced convective boiling in binary mixtures. *International Journal of Heat Mass Transfer*, 36(13):3299–3309, 1993.

[39] G.P. Celata, M. Cumo, and T. Setaro. Critical heat flux in upflow convective boiling of refrigerant binary mixtures. *International Journal of Heat Mass Transfer*, 37(7):1143–1153, 1994.

[40] W.H.G.T. Chan. *Evaporation and condensation in annular vertical upward flow of water-steam.* PhD thesis, University of London, Imperial College, 1990.

[41] J.C. Chen. A correlation for boiling heat transfer to saturated fluids in convective flow. *Industrial and Engineering Chemistry*, 5:322–329, 1966.

[42] X.T. Chen and J.P. Brill. Slug to churn transition in upward vertical two-phase flow. *Chemical Engineering Science*, 52(23):4269–4272, 1997.

[43] A.P. Colburn and D.A. Drew. The condensation of mixed vapours. *Transactions of the AIChE*, 33:197–212, 1937.

[44] J.G. Collier, P.M.C. Lacey, and D.J. Pulling. Heat transfer to two-phase gas-liquid systems. 2: Further data on steam-water mixtures in the liquid-dispersed region in an annulus. *Transactions of the Institution of Chemical Engineers*, 42:127–139, 1964.

[45] J.G. Collier and J.R. Thome. *Convective Boiling and Condensation.* Oxford University Press, Oxford, UK, third edition, 1994.

[46] M.G. Cooper. Heat flow rates in saturated nucleate pool boiling — a wide ranging examination using reduced properties. *Advances in Heat Transfer*, 16:155–239, 1984.

[47] J.A. Copati and R. Krishna. Influence of non-condensables on the condensation of vapour mixtures forming immiscible liquids. *International Communications in Heat Mass Transfer*, 27(3):425–434, 2000.

[48] G. Costigan. *Flow pattern transitions in vertical gas-liquid flows*, 1997. D.Phil. Thesis, Oxford University.

[49] L.B. Cousins, W.H. Denton, and G.F. Hewitt. Liquid phase mass transfer in annular two-phase flow. Technical report, UKAEA Report AERE-R 4926, 1965.

[50] L.B. Cousins and G.F. Hewitt. Liquid phase mass transfer in annular two-phase flow: radial liquid mixing. Technical report, UKAEA Report AERE-R 5657, 1968.

[51] G. Das, P.K. Das, N.K. Purohit, and A.K. Mitra. Flow pattern transition during gas liquid upflow through vertical concentric annuli. 1: Experimental investigations. *Journal of Fluids Engineering, Transactions of the ASME*, 121:895–901, 1999a.

[52] G. Das, P.K. Das, N.K. Purohit, and A.K. Mitra. Flow pattern transition during gas liquid upflow through vertical concentric annuli. 2: Mechanistic models. *Journal of Fluids Engineering, Transactions of the ASME*, 121:902–907, 1999b.

[53] E.J. Davis and G.H. Anderson. The incipience of nucleate boiling in forced convection flow. *AIChE Journal*, 12:774–780, 1966.

[54] C.E. Dengler and J.N. Addoms. Heat transfer mechanism for vaporisation of water in a vertical tube. *Chemical Engineering Progress Symposium Series*, 52(18):85–103, 1956.

[55] V.K. Dhir. Boiling heat transfer. *Annual Review of Fluid Mechanics*, 30:365–401, 1998.

[56] F. Dobran. Hydrodynamic and heat transfer analysis of two-phase annular flow with a new liquid film model of turbulence. *International Journal of Heat Mass Transfer*, 26(8):1159–1171, 1983.

[57] A.E. Dukler. Fluid mechanics and heat transfer in falling film systems. *Chemical Engineering Progress Symposium Series*, 56(30):1–10, 1960.

[58] A.E. Dukler and Y. Taitel. Flow pattern transition in gas-liquid systems: measurement and modelling. In G.F. Hewitt, J.M. Delhaye, and N. Zuber, editors, *Multiphase Science and Technology*, volume 2, pages 1–94. Hemisphere Publishing Co., New York, 1986.

[59] J.F. Ely and H.J.M. Hanley. Prediction of transport properties. 1. viscosities of fluids and mixtures. *Industrial and Engineering Chemistry Fundamentals*, 20:323–332, 1981.

[60] J.F. Ely and H.J.M. Hanley. Prediction of transport properties. 2. thermal conductivity of pure fluids and mixtures. *Industrial and Engineering Chemistry Fundamentals*, 22:90–97, 1983.

[61] L.B. Fore and A.E. Dukler. Droplet deposition and momentum transfer in annular flow. *AIChE Journal*, 41(9):2040–2046, 1995.

[62] H.K. Forster and N. Zuber. Dynamics of vapor bubbles and boiling heat transfer. *AIChE Journal*, 1:531–535, 1955.

[63] L. Friedel. Improved friction pressure drop correlations for horizontal and vertical two-phase pipe flow. In *European Two-Phase Flow Group Meeting*, Ispra, Italy, 1979. Paper E2.

[64] W. Frost and G.S. Dzakowic. An extension of the method of predicting incipient boiling on commercially finished surfaces. In *ASME Paper No. 67-HT-61*, 1967.

[65] F. Fu and J.F. Klausner. A separated flow model for predicting two-phase pressure drop and evaporative heat transfer for vertical annular flow. *International Journal of Heat and Fluid Flow*, 18(6):541–549, 1997.

[66] Y. Fujita and M. Tsutsui. Flow boiling heat transfer of binary mixtures in a uniformly heated vertical tube. In J.S. Lee, editor, *Proceedings of the Eleventh International Heat Transfer Conference*, volume 2, pages 243–248, Kyongju, Korea, August 1998. Taylor and Francis, Philadelphia, PA.

[67] E. Fuller, P.D. Schettler, and J.C. Giddings. A new method for prediction of binary gas phase diffusion coefficients. *Industrial and Engineering Chemistry*, 58(5):19–23, 1966.

[68] L.E. Gill and G.F. Hewitt. Sampling probe studies of the gas core in two-phase flow: Iii, distribution of velocity and droplet flowrate after injection through an axial jet. Technical report, UKAEA Report AERE-M 1202, 1966.

[69] L.E. Gill, G.F. Hewitt, J.W. Hitchon, and P.M.C. Lacey. Sampling probe studies of the gas core in two-phase flow: I, the effect of length on phase velocity distribution. Technical report, UKAEA Report AERE-R 3954, 1963. (also: *Chemical Engineering Science*, 18, pp. 525–535).

[70] L.E. Gill, G.F. Hewitt, and P.M.C. Lacey. Sampling probe studies of the gas core in two-phase flow: Ii, studies of the effect of phase flowrates on phase velocity distribution. Technical report, UKAEA Report AERE-R 3955, 1964. (also: *Chemical Engineering Science*, 19, pp. 665–682).

[71] V. Gnielinski. New equations for heat and mass transfer in turbulent pipe and channel flow. *International Chemical Engineering*, 16(2):359–368, 1976. (Also in: G.F. Hewitt (Ed.), *Handbook of Heat Exchanger Design (HEDH)*, Begell House, Inc., New York, 1992).

[72] A.H. Govan. *Modelling of vertical annular and dispersed two-phase flows.* PhD thesis, University of London, Imperial College, 1990.

[73] A.H. Govan, G.F. Hewitt, D.G. Owen, and T.R. Bott. An improved chf modelling code. In *Proceedings of the Second UK National Heat Transfer Conference*, Glasgow, UK, 1988. Institution of Mechanical Engineers. Paper No. C175.

[74] A.H. Govan, G.F. Hewitt, H.J. Richter, and A. Scott. Flooding and churn flow in vertical pipes. *International Journal of Multiphase Flow*, 17:27–44, 1991.

[75] S.A. Guerrieri and R.D. Talty. A study of heat transfer to organic liquids in single tube, natural circulation, vertical tube boilers. *Chemical Engineering Progress Symposium Series*, 52(18):69–77, 1956.

[76] N.S. Hall-Taylor and R.M. Nedderman. The coalescence of disturbance waves in annular two-phase flow. *Chemical Engineering Science*, 23:551–564, 1968.

[77] N.J. Hawkes. *Wispy-annular flow.* PhD thesis, University of London, Imperial College, 1996.

[78] G.F. Hewitt. Analysis of annular two-phase flow; application of the dukler analysis to vertical upward flow in a tube. Technical report, UKAEA Report AERE-3680, 1961.

[79] G.F. Hewitt. Interpretation of pressure drop data from an annular channel. Technical report, UKAEA Report AERE-R 4340, 1964.

[80] G.F. Hewitt. *Measurement of two-phase flow parameters.* Academic Press, London, UK, 1978.

[81] G.F. Hewitt. Phenomenological issues in forced convective boiling. In J.C. Chen, editor, *Convective Boiling.* Taylor and Francis, Philadelphia, PA, 1996. Keynote Lecture 2.

[82] G.F. Hewitt and N.S. Hall-Taylor. *Annular two-phase flow.* Pergamon Press, Oxford, UK, 1970.

[83] G.F. Hewitt and S. Jayanti. To churn or not to churn. *International Journal of Multiphase Flow*, 19:527–529, 1993.

[84] G.F. Hewitt, H.A. Kersey, P.M.C. Lacey, and D.J. Pulling. Burnout and nucleation in climbing film flow. *International Journal of Heat Mass Transfer*, 8:793–814, 1965.

[85] G.F. Hewitt, C.J. Martin, and N.S. Wilkes. Experimental and modelling studies of annular flow in the region between flow reversal and the pressure drop minimum. *PhysicoChemical Hydrodynamics*, 6(1/2):69–86, 1985.

[86] G.F. Hewitt and D.N. Roberts. Studies of in two-phase flow patterns by simultaneous x-ray and flash photography. Technical report, UKAEA Report AERE-M 2159, 1969.

[87] G.F. Hewitt, G.L. Shires, and T.R. Bott. *Process Heat Transfer.* CRC Press Inc., Boca Raton, Florida, 1994.

[88] G.F. Hewitt and G.B. Wallis. Flooding and associated phenomena in falling film in a vertical tube. In *Proceedings of Multi-Phase Flow Symposium*, pages 62–74, Philadelphia, PA, 1963.

[89] G.F. Hewitt and P.B. Whalley. The correlation of liquid entrained fraction and entrainment rate in annular two-phase flow. Technical report, UKAEA Report AERE-9187, 1978.

[90] Y.Y. Hsu. On the size range of active nucleation cavities on a heating surface. *Journal of Heat Transfer, Transactions of the ASME*, 84:207–216, 1962.

[91] P. Hutchinson and P.B. Whalley. A possible characterisation of entrainment in annular flow. *Chemical Engineering Science*, 28:974–975, 1973.

[92] M. Ishii and K. Mishima. Correlation for liquid entrainment in annular two-phase flow of low viscous fluid. Technical report, ANL Report ANL/RAS/LWR 81-2, 1981.

[93] P.W. James, G.F. Hewitt, and P.B. Whalley. Droplet motion in two-phase flow. Technical report, UKAEA Report AERE-R 9711, 1980.

[94] S. Jayanti and G.F. Hewitt. Prediction of the slug to churn flow transition in vertical two-phase flow. *International Journal of Multiphase Flow*, 18:847–860, 1992.

[95] S. Jayanti and G.F. Hewitt. Hydrodynamics and heat transfer in wavy annular gas-liquid flow: a computational fluid dynamics study. *International Journal of Heat Mass Transfer*, 40:2445–2460, 1997.

[96] S. Jayanti, G.F. Hewitt, D.E.F. Low, and E. Hervieu. Observation of flooding in the taylor bubble of co-current upwards slug flow. *International Journal of Multiphase Flow*, 19:531–534, 1993.

[97] S. Jayanti, A. Tokarz, and G.F. Hewitt. Theoretical investigation of the diameter effect on flooding in countercurrent flow. *International Journal of Multiphase Flow*, 22:307–324, 1996.

[98] T. Kandlbinder. *Experimental investigation of forced convective boiling of hydrocarbons and hydrocarbon mixtures.* PhD thesis, University of London, Imperial College, 1997.

[99] T. Kandlbinder, V.V. Wadekar, and G.F. Hewitt. Mixture effects for flow boiling of a binary hydrocarbon mixture. In J.S. Lee, editor, *Proceedings of the Eleventh International Heat Transfer Conference*, volume 2, pages 303–305, Kyongju, Korea, August 1998. Taylor and Francis, Philadelphia, PA.

[100] S.G. Kandlikar. A general correlation for saturated two-phase flow boiling heat transfer inside horizontal and vertical tubes. *Journal of Heat Transfer, Transactions of the ASME*, 112:219–228, 1990.

[101] S.G. Kandlikar. Boiling heat transfer with binary mixtures. 2: Flow boiling in plain tubes. *Journal of Heat Transfer, Transactions of the ASME*, 120:388–394, 1998.

[102] S.G. Kandlikar, M.D. Cartwright, and V.R. Mizo. A photographic study of nucleation characteristics of cavities in flow boiling. In *Proceedings of the International*

Conference on Convective Flow Boiling, Banff, Canada, April-May 1995. United Engineering Foundation, New York, NY. paper II-1.

[103] I. Kataoka, M. Ishii, and A. Nakayama. Entrainment and deposition of droplets in annular two-phase flow. *International Journal of Heat Mass Transfer*, 43:1573–1589, 2000.

[104] Y. Katto and H. Ohno. An improved version of the generalised correlation of critical heat flux for forced convective boiling in uniformly heated vertical tubes. *International Journal of Heat Mass Transfer*, 27:1641–1648, 1984.

[105] W.M. Kays and M.E. Crawford. *Convective Heat and Mass Transfer*. McGraw-Hill, New York, third edition, 1993.

[106] J.M. Kelly and R.L. Freitas. Interfacial friction in low flowrate vertical annular flow. In *Proceedings of the Sixth International Meeting on Nuclear Reactor Thermal Hydraulics*, volume 1, pages 154–160, 1993.

[107] D.B.R. Kenning and M.G. Cooper. Flow patterns near nuclei and the initiation of boiling during forced convection heat transfer. In *Symposium on Boiling Heat Transfer in Steam Generating Units and Heat Exchangers*, Manchester, UK, September 1965. Institution of Mechanical Engineers.

[108] S.H. Khor. *Three-phase liquid-liquid-gas stratified flow in pipelines*. PhD thesis, University of London, Imperial College, 1998.

[109] J.F. Klausner. Private communication, 2000.

[110] P.G. Kosky and F.W. Staub. Local condensing heat transfer coefficients in annular flow regimes. *AIChE Journal*, 17:1037–1043, 1971.

[111] S. Koyama and S.M. Lee. A prediction model for condensation of ternary refrigerant mixtures inside a horizontal smooth tube. In J.S. Lee, editor, *Proceedings of the Eleventh International Heat Transfer Conference*, volume 2, pages 427–432, Kyongju, Korea, August 1998. Taylor and Francis, Philadelphia, PA.

[112] B.I. Lee and M.G. Kesler. A generalized thermodynamic correlation based on three-parameter corresponding states. *AIChE Journal*, 21:510–527, 1975.

[113] S. Levy. Theory of pressure drop and heat transfer for annular steady-state two-phase two-component flow in pipes. In *Proceedings of the Second Midwestern Conference on Fluid Mechanics*, page 337, 1952. (Also in: S. Levy, *Two-Phase Flow in Complex Systems*, Wiley, New York, 1999).

[114] S. Levy. *Two-Phase Flow in Complex Systems.* John Wiley & Sons, New York, 1999.

[115] Z. Liu and R.H.S. Winterton. A general correlation for saturated and subcooled flow boiling in tubes and annuli, based on a nucleate pool boiling equation. *International Journal of Heat Mass Transfer*, 34(11):2759–2766, 1991.

[116] R.W. Lockhart and R.C. Martinelli. Proposed correlation of data for isothermal two-phase two-component flow in pipes. *Chemical Engineering Progress*, 45:39, 1949.

[117] Z. Lu and X. Zhang. Identification of flow patterns of two-phase flow by mathematical modelling. *Nuclear Engineering and Design*, 149:111–116, 1994.

[118] Z.S. Mao and A.E. Dukler. The myth of churn flow? *International Journal of Multiphase Flow*, 19:377–383, 1993.

[119] W.J. Marsh and I. Mudawar. Predicting the onset of nucleate boiling in wavy free-falling turbulent liquid films. *International Journal of Heat Mass Transfer*, 32(2):361–378, 1989.

[120] C.J. Martin and B.J. Azzopardi. Waves in vertical annular flow. *PhysicoChemical Hydrodynamics*, 6(1/2):257–265, 1985.

[121] R.C. Martinelli and D.B. Nelson. Prediction of pressure drop during forced circulation boiling of water. *Transactions of the ASME*, 70:695, 1948.

[122] J. McNaught. Mass transfer correction terms in design methods for multicomponent-partial condensers. In *18th National Heat Transfer Conference*, San Diego, 1979. ASME-AIChE.

[123] K.W. McQuillan and P.B. Whalley. Flow patterns in vertical two-phase flow. *International Journal of Multiphase Flow*, 11:161–175, 1985.

[124] K.W. McQuillan, P.B. Whalley, and G.F. Hewitt. Flooding in vertical two-phase flow. *International Journal of Multiphase Flow*, 11:741–760, 1985.

[125] R.B. Mesler. An alternate to the dengler and addoms convection concept of forced convection boiling heat transfer. *AIChE Journal*, 23(4):448–453, 1977.

[126] V.I. Milashenko, B.I. Nigmatulin, V.V. Pethukov, and N.I. Trubkin. Burnout and distribution of liquid in evaporative channels of various lengths. *International Journal of Multiphase Flow*, 15:393–401, 1989.

[127] K. Mishima and M. Ishii. Flow regime transition criteria for two-phase flow in vertical tubes. *International Journal of Heat Mass Transfer*, 27:723–734, 1984.

[128] M.P. Mishra, H.K. Varma, and C.P. Sharma. Heat transfer coefficients in forced convective evaporation of refrigerant mixtures. *Letters in Heat and Mass Transfer*, 8(2):127–136, 1981.

[129] D.M. Moalem Maron and N. Brauner. New thoughts on the mechanism of gas-liquid slug flow. *Letters in Heat and Mass Transfer*, 9:333–342, 1982.

[130] E.O. Moeck and J.W. Stachiewicz. A droplet interchange model for annular-dipersed, two-phase flow. *International Journal of Heat Mass Transfer*, 15:637–653, 1972.

[131] I.A. Mudawwar and M.A. El-Masri. Momentum and heat transfer across freely-falling turbulent liquid films. *International Journal of Multiphase Flow*, 12(5):771–790, 1986.

[132] K. Murata and K. Hashizume. Forced convective boiling of nonazeotropic refrigerant mixtures inside tubes. *Journal of Heat Transfer, Transactions of the ASME*, 115:680–689, 1993.

[133] S. Nakanishi. Disturbance wave in boiling flow. In O.C. Jones, Jr. and I. Michiyoshi, editors, *Dynamics of Two-Phase Flows*, pages 185–211. CRC Press, 1993.

[134] D.J. Nicklin and J.F. Davidson. The onset of instability in two-phase slug flow. In *Proceedings of the Symposium on Two-Phase Flow*, UK, 1962. Institution of Mechanical Engineers. 7 February, Paper No. 4.

[135] R.I. Nigmatulin, B.I. Nigmatulin, Y.A. Khodzaev, and V.E. Kroshilin. Entrainment and deposition rates in a dispersed-film flow. *International Journal of Multiphase Flow*, 22:19–30, 1996.

[136] K. Nishikawa, Y. Fujita, H. Ohta, and S. Hidaja. Effect of the surface roughness on the nucleate boiling heat transfer over the wide range of pressure. In U. Grigull, editor, *Proceedings of the Seventh International Heat Transfer Conference*, volume 4, pages 61–66, Munich, West Germany, September 1982. Hemisphere Publishing Co., New York, NY.

[137] D.G. Owen. *An experimental and theoretical analysis of equilibrium annular flow.* PhD thesis, University of Birmingham, UK, 1986.

[138] J.W. Palen. Shell-and-tube reboilers: Thermal design. In G.F. Hewitt, editor, *Handbook of Heat Exchanger Design (HEDH)*, pages 3.6.2–1–3.6.2–12. Begell House, Inc., New York, 1992.

[139] J.W. Palen and W.M. Small. A new way to design kettle and internal reboilers. *Hydrocarbon Processing*, 43(11):199–208, 1964.

[140] J.W. Palen, C.C. Yang, and J. Taborek. Application of the resistance proration method to boiling in tubes in the presence of inert gas. *AIChE Symposium Series*, 76(199):282–288, 1980.

[141] C. Pauchon and S. Banerjee. Interphase momentum effects in the averaged multifield model. 1: Void propagation in bubble flows. *International Journal of Multiphase Flow*, 12:559–573, 1986.

[142] B.S. Pethukov and V.N. Popov. Theoretical calculation of heat exchange and frictional resistance in turbulent flow in tubes of an incompressible fluid with variable physical properties. *High Temperature (USSR)*, 1(1):69–83, 1963. (Also in: G.F. Hewitt (Ed.), *Handbook of Heat Exchanger Design (HEDH)*, Begell House, Inc., New York, 1992).

[143] W.H. Press, S.A. Teukolsky, W.T. Vetterling, and B.P. Flannery. *Numerical Recipes in FORTRAN - The Art of Scientific Computing.* Cambridge University Press, New York, second edition, 1992.

[144] B.C. Price and K.J. Bell. Design of binary vapor condensers using the colburn-drew equations. *AIChE Symposium Series*, 70(138):163–171, 1974.

[145] O.L. Pushkina and Y.L. Sorokin. Breakdown of liquid film motion in vertical tubes. *Heat Transfer — Soviet Research*, 1(5):56–64, 1969.

[146] E.R. Quandt. Measurement of some basic parameters in two-phase annular flow. *AIChE Journal*, 11:311–318, 1965.

[147] R.G. Sardesai, R.A.W. Shock, and D. Butterworth. Heat and mass transfer in multicomponent condensation and boiling. *Heat Transfer Engineering*, 3(3–4):104–104, 1982.

[148] T. Sawai, S. Yamauchi, and S. Nakanishi. Behavior of disturbance waves under non-equilibrium conditions. *International Journal of Multiphase Flow*, 15(3):341–356, 1989.

[149] S.A. Schadel, G.W. Leman, J.L. Binder, and T.J. Hanratty. Rates of atomisation and deposition in vertical annular flow. *International Journal of Multiphase Flow*, 16:363–374, 1990.

[150] H. Schlichting. *Boundary Layer Theory.* McGraw-Hill, New York, seventh edition, 1987.

[151] F.A. Schraub. Isokinetic probes and other sampling devices: a survey. In *11th National ASME/AIChE Heat Transfer Conference*, Minneapolis, MN, 1969.

[152] L.E. Scriven. On the dynamics of phase growth. *Chemical Engineering Science*, 27:1687–1697, 1959.

[153] M.M. Shah. Chart correlation for saturated boiling heat transfer: equations and further study. *ASHRAE Transactions*, 88:185–196, 1982.

[154] D.P. Shatto. *Vertical in-tube flow boiling of mixtures.* PhD thesis, Texas A&M University, 1998.

[155] C.J. Shearer. *Interfacial wave phenomena in two-phase flow.* PhD thesis, Cambridge University, 1964.

[156] Y. Shibata, H. Tezuka, Y. Hagiwara, and K. Suzuki. A numerical study of evaporative heat transfer of nonazeotropic binary mixtures in a vertical tube (the effect of nonideality of mixtures). In G.F. Hewitt, editor, *Proceedings of the Tenth International Heat Transfer Conference*, volume 7, pages 533–538, Brighton, UK, August 1994. Taylor and Francis, Philadelphia, PA.

[157] R.A.W. Shock. Evaporation of binary mixtures in upward annular flow. *International Journal of Multiphase Flow*, 2:411–433, 1976.

[158] R.A.W. Shock. Boiling in multicomponent fluids. In G.F. Hewitt, J.M. Delhaye, and N. Zuber, editors, *Multiphase Science and Technology*, volume 1, pages 281–383. Hemisphere Publishing Corp., New York, 1982.

[159] L. Silver. Gas cooling with aqueous condensation. *Transactions of the Institution of Chemical Engineers*, 25:30–42, 1947.

[160] F.B. Sprow and J.M. Prausnitz. Surface thermodynamics of liquid mixtures. *Canadian Journal of Chemical Engineering*, 45:25–28, 1967.

[161] F.C. Standiford. Letter to the editor. *AIChE Journal*, 24(4):750–751, 1978.

[162] D. Steiner and J. Taborek. Flow boiling heat transfer in vertical tubes correlated by an asymptotic model. *Heat Transfer Engineering*, 13(2):43–69, 1992.

[163] K. Stephan and M. Abdelsalam. Heat transfer correlations for natural convection boiling. *International Journal of Heat Mass Transfer*, 23:73–87, 1980.

[164] K. Stephan and M. Korner. Calculation of heat transfer in evaporating binary liquid mixtures. *Chemie Ingeniur Technik*, 41(7):409–417, 1969.

[165] W.E. Stewart and R. Prober. Matrix calculation of multicomponent mass transfer in isothermal systems. *Industrial and Engineering Chemistry Fundamentals*, 3(3):224–235, 1964.

[166] G. Sun. *Heat transfer in forced convective flow boiling.* PhD thesis, University of London, Imperial College, 1996.

[167] Y. Taitel, D. Barnea, and A.E. Dukler. Modelling of flow pattern transitions for steady upward gas-liquid flow in vertical tubes. *AIChE Journal*, 26:345–354, 1980.

[168] L. Tang. *Empirical study of new refrigerant flow condensation inside horizontal tubes.* PhD thesis, University of Maryland, 1997.

[169] R. Taylor and R. Krishna. *Multicomponent Mass Transfer.* John Wiley & Sons, New York, 1993.

[170] J.R. Thome and R.A.W. Shock. Boiling of multicomponent liquid mixtures. *Advances in Heat Transfer*, 16:59–156, 1984.

[171] H.L. Toor. Diffusion in three component gas mixtures. *AIChE Journal*, 3:198–207, 1957.

[172] H.L. Toor. Solution of the linearized equations of multicomponent mass transfer. 2: Matrix methods. *AIChE Journal*, 10(4):460–465, 1964.

[173] T. Ueda. Entrainment rate and size of entrained droplets in annular two-phase flow. *Bulletin of the JSME*, 22:1258–1265, 1979.

[174] S. van Stralen and R. Cole. *Boiling Phenomena - Physicochemical and Engineering Fundamental Applications, Volume 1.* McGraw-Hill, New York, 1979.

[175] P. Vassallo. Near wall structure in vertical air-water annular flows. *International Journal of Multiphase Flow*, 25:459–476, 1999.

[176] P.H.J. Verbeek, R. Miesen, and C.J. Schellenkens. Liquid entrainment in annular dispersed upflow. In *European Two-Phase Flow Group Meeting*, Hannover, Germany, 1993.

[177] V.V. Wadekar. Convective heat transfer to binary mixtures in annular two-phase flow. Technical report, UKAEA Report AERE-R 13815, 1990.

[178] V.V. Wadekar. Convective heat transfer to binary mixtures in annular two-phase flow. In G.F. Hewitt, editor, *Proceedings of the Tenth International Heat Transfer Conference*, volume 7, pages 557–562, Brighton, UK, August 1994. Taylor and Francis, Philadelphia, PA.

[179] G.B. Wallis. Flooding velocities for air and water in vertical tubes. Technical report, UKAEA Report AEEW R-1234, 1961.

[180] G.B. Wallis. The onset of droplet entrainment in annular gas-liquid flow. Technical report, General Electric No. 62 GL127, 1962.

[181] G.B. Wallis. *One Dimensional Two-Phase Flow.* McGraw-Hill, New York, 1969.

[182] M.J. Watson. *Flow pattern transitions and associated phenomena.* PhD thesis, University of London, Imperial College, 1999.

[183] M.J. Watson and G.F. Hewitt. Pressure effects on the slug to churn transition. *International Journal of Multiphase Flow*, 25:1225–1241, 1999.

[184] D.R. Webb. Heat and mass transfer in condensation of multicomponent vapours. In U. Grigull, editor, *Proceedings of the Seventh International Heat Transfer Conference*, volume 1, pages 167–174, Munich, West Germany, September 1982. Hemisphere Publishing Co., New York, NY.

[185] D.R. Webb. Condensation of vapour mixtures. In G.F. Hewitt, editor, *Handbook of Heat Exchanger Design (HEDH)*, pages 2.6.3–1–2.6.3–25. Begell House, Inc., New York, 1995. Second Edition.

[186] D.R. Webb, M. Fahrner, and R. Schwaab. The relationship between the colburn and silver methods for condenser design. *International Journal of Heat Mass Transfer*, 39(15):3147–3156, 1993.

[187] D.R. Webb and J.M. McNaught. Condensers. In *Developments in Heat Exchanger Technology*, Barking, UK, 1980. Applied Science.

[188] M. Wettermann and D. Steiner. Flow boiling heat transfer characteristics of wide-boiling mixtures. *International Journal of Thermal Sciences — Revue Generale de Thermique*, 39:225–235, 2000.

[189] P.B. Whalley. *Two-Phase Flow and Heat Transfer.* Oxford University Press, Oxford, 1996.

[190] I.P. Willets, B.J. Azzopardi, and P.B. Whalley. A study of the effect of gas and liquid properties on annular two-phase flow. Technical report, UKAEA Report AERE-R 11976, 1986.

[191] D.D. Williams and R.B. Mesler. The effect of surface orientation on delay time of bubbles from artificial sites during nucleate boiling. *AIChE Journal*, 13(5):1020–1024, 1967.

[192] A. Wolf. *Liquid film structure in annular two-phase flow.* PhD thesis, University of London, Imperial College, 1995.

[193] L. Zhang, E. Hihara, T. Saito, and J.T. Oh. Boiling heat transfer of a ternary refrigerant mixture inside a horizontal smooth tube. *International Journal of Heat Mass Transfer*, 40(9):2009–2017, 1997.

[194] N. Zuber and J.A. Findlay. Average volumetric concentration in two-phase flow systems. *Journal of Heat Transfer, Transactions of the ASME*, 87:453–468, 1965.

Reference Addendum

1. S. Jayanti and N. Brauner, Churn flow. In: Multiphase Science and Technology, Volume 8 - Two-Phase Flow Fundamentals. G.F. Hewitt, J.M. Delhaye, N. Zuber, J.H. Kim and R.T. Lahey, Jr. (Eds.), Begell House, Inc., New York, Chapter 8, pp. 471–521, 1994.

2. J.A.R. Bennett, J.G. Collier, H.R.C. Pratt and D. Thornton, Heat transfer to two-phase gas-liquid systems. Steam-water mixtures in the liquid-dispersed region in an annulus. *Transactions of the Institution of Chemical Engineers*, vol. 39, pp. 113–26, 1961.